Detonation diffraction in mixtures with various degrees of instability

Thesis by

Florian Pintgen

In Partial Fulfillment of the Requirements

for the Degree of

Doctor of Philosophy

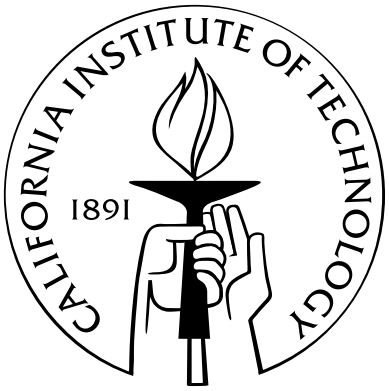

California Institute of Technology

Pasadena, California

2004

(Submitted December, 2004)

Abstract

Planar laser induced fluorescence (PLIF) is widely used in combustion diagnostics but has only recently been successfully applied to detonation. The strong spatial variations in temperature, pressure, and background composition under these conditions influence the quantitative link between OH-number density and fluorescence intensity seen on images. Up to now, this has lead to uncertainties in interpreting the features seen on PLIF images obtained in detonations. A one-dimensional fluorescence model has been developed, which takes into account light sheet attenuation by absorption, collisional quenching, and changing absorption line shape. The model predicts the fluorescence profile based on a one-dimensional distribution in pressure, temperature, and mixture composition. The fluorescence profiles based on a calculated ZND detonation profile were found to be in good agreement with experiments.

The PLIF technique is used to study the diffraction process of a self-sustained detonation wave into an unconfined space through an abrupt area change. Simultaneous schlieren images enable direct comparison of shock and reaction fronts. Two mixture types of different effective activation energy θ are studied in detail, these represent extreme cases in the classification of detonation front instability and cellular regularity. Striking differences are seen in the failure mechanisms for the very regular H_2-O_2-Ar mixture ($\theta \sim 4.5$) and the highly irregular H_2-N_2O mixture ($\theta \sim 9.4$). Detailed image analysis quantifies the observed differences. Stereoscopic imaging reveals the complex three-dimensional structure of the transverse detonation and its location with respect to the shock front. The study is concluded by using the experimentally-obtained shock and reaction front profiles in a simplified model to examine the decoupling of the shock from the chemical reaction. The rapid increase in activation energy for the

H_2-O_2-Ar mixtures with decreasing shock velocity is proposed as an important new element in the analysis of diffraction for these mixture.

Contents

List of Figures

List of Tables

Nomenclature

Roman characters, lower case

a	Voigt a-parameter	
c	speed of light	m/s
	concentration of absorbing species	$1/cm^3$
c_2	second radiative constant	cm· K
d_c	critical tube diameter	m
f_B	Boltzmann fraction	
h	Planck's constant	J·s
	light sheet height	m
k	Boltzmann's constant	J/K
	absorption coefficient	1/cm
m_A	mass of absorbing molecule	u
n	number density	$molecules/cm^3$
s	Shock decay rate	m/s^2
t_c	time after which corner disturbance signals collide	m
t_d	shock decay time	s
t_{TEP}	time after the detonation has reached the tube exit plane	s
u	post-shock velocity in lab fixed frame	
v	vibrational level	
w	fluid velocity in shock fixed coordinates	m/s
x_c	distance after which corner disturbance signals collide	m
t_{TEP}	distance from tube exit plane	mm

Roman characters, upper case

A_{12}	Einstein coefficient for spontaneous emission	1/s
B_{12}	Einstein coefficient for absorption	$cm^2/J{\cdot}s$
B_{21}	Einstein coefficient for stimulated emission	$cm^2/J{\cdot}s$
D	detonation tube diameter	m

	effective dimension	
E_a	activation energy	J/mol
F	fluorescence signal power	
F_{pred}	predicted fluorescence power	
I_ν	spectral irradiance	$W/m^2 \cdot cm^{-1}$
I^ν_{sat}	saturation spectral irradiance	$W/m^2 \cdot cm^{-1}$
L	coverage length	m
$L_L(\nu)$	spectral distribution function of the laser	
N	number density	mol/m^3
	rotational level	
M	Mach number	
P	pressure	Pa
P_O	initial mixture pressure	Pa
Q_{21}	quenching rate	1/s
$Q(T)$	partition function	
R	universal gas constant	J/ mol ·K
S	spectral line intensity	cm/molecule
	cell size (only Chapter 4)	m
S_L	laminar burning velocity	m/s
S_T	turbulent burning velocity	m/s
T	temperature	K
T_O	initial mixture temperature	K
U	detonation velocity	m/s
$V(a,x)$	Voigt-profile	
$Y_A(\nu)$	spectral line-shape function	$1/cm^{-1}$

Greek characters, lower case

α	track angle measured on soot foils	$^\circ$
	corner disturbance propagation half angle	$^\circ$
β	line shift parameter	

γ	ratio of specific heats	
γ_i	collisional broadening coefficient of species i	
ε_i	inner cut-off scale	m
ε_o	outer cut-off scale	m
θ	effective activation energy	
λ	wave length	m
	cell size	m
ν	frequency	1/cm
ν_{0A}	center line frequency of absorbing transition line	1/cm
σ	absorption cross section	cm^2/molecule
τ	average time between collisions of molecules	s
τ_i	induction time	s

Greek characters, upper case

Δ	induction zone length	m
$\Delta\nu_D$	Doppler width	1/cm
$\Delta\nu_c$	collision width	1/cm
Γ	spectral overlap fraction/ integral	

Sub-scripts

O	initial mixture conditions
CJ	Chapman-Jouguet conditions
L	laser
ps	vonNeumann (post-shock) conditions
P	fluid particle
TEP	measured from tube exit plane
vN	vonNeumann (post-shock) conditions

Super-scripts

$''$	lower (ground) level
$'$	upper (excited) level

Chapter 1

Fundamentals of Detonations

A detonation is a supersonic combustion wave characterized by an exothermic chemical reaction which takes place behind a strong leading shock front. Due to the increased pressure and temperature behind the shock wave, the reactive material ignites after a short period of time, the induction time τ_i. The volume expansion caused by the large increase in temperature during the exothermic reaction drives the shock. This leads to a coupling between the shock and reaction fronts. The chemical reaction is shock-induced as opposed to being controlled by heat conduction or diffusion as observed in ordinary flames. Two simplified one-dimensional detonation models, the Chapman Jouguet (CJ) and the ZND model, are described in Section 1.1. Detonation wave cellular structure is discussed in Section 1.2 and 1.3. An introduction to the diffraction of detonations is given in Sections 1.4.

1.1 Simple Models

The hydrodynamic model of a detonation assumes a steady wave within which reactants are instantaneously converted from reactants to products. The products are in chemical equilibrium and constrained by the conservation of mass, momentum and energy to take a specific set of values. The locus of states defined by the conservation laws form a curve known as the detonation adiabat or Hugoniot. The CJ solution (Chapman, 1899, Jouguet, 1905) is a particular state, the CJ-point, which is the unique solution observed in the laboratory. The CJ point corresponds to the

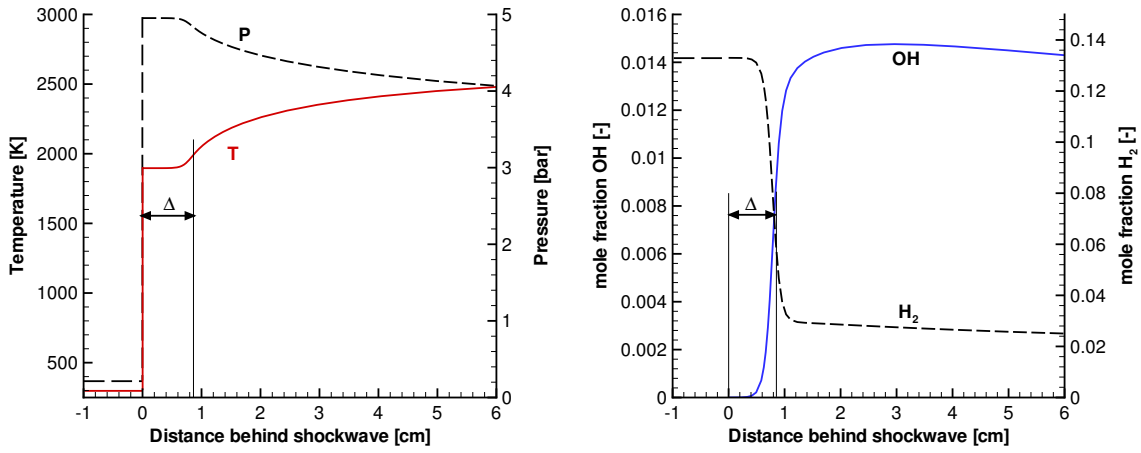

a) b)

Figure 1.1: ZND-calculated profiles of thermodynamics conditions (a) and species mole fraction (b) for a detonation wave calculated with the ZND model using the code of Shepherd (1986). $0.14H_2+0.07O_2+0.8Ar$ mixture, T_0=300 K, P_0=20 kPa.

minimum wave speed and the sonic outflow of the products from the wave. Using the CJ solution to the hydrodynamic model, the wave speed and the properties of the products can be uniquely determined. The specific heat capacities of real gases are temperature-dependent and the exact product composition, also due to dissociation, is unknown. This makes an iterative calculation of the CJ point necessary. An overview of iteration methods is given in Kuo (1986). In the present study, the chemical equilibrium code STANJAN, Reynolds (1986), is used, which is based on the method of element potentials. Given the mixture composition and initial conditions, the code enables the determination of the CJ detonation velocity. Despite the simplicity of this model, the CJ detonation velocity agrees to within 2% of the experimentally measured velocities of fully-developed detonations.

The ZND model (Zel'dovich, 1950, von Neumann, 1942, Döring, 1943) assumes that the wave travels at the CJ velocity but includes finite reaction rates and therefore a finite induction time. In a time τ_i, a fluid particle is convected a distance, the induction zone length Δ, from the lead shock position. The induction zone behind the leading shock is usually thermally neutral or slightly endothermic as the fuel is consumed and the concentration of radicals (e.g., OH) increases (Fig. 1.1). The conditions at the beginning of the induction zone are the post-shock or von Neumann

thermodynamic state. At the end of the induction zone, the temperature increases due to the strongly exothermic recombination reaction of intermediate species and radicals as they form the primary products. The reaction takes place via many individual elementary reactions, which can be modeled by a detailed reaction mechanism. When chemical equilibrium is reached, the reactions terminate, the CJ point is reached, and the fluid velocity is sonic with respect to the shock wave. There are several ways of defining the induction zone length. In this study, the distance Δ is defined from the lead shock to the point of maximum increase in temperature. Other definitions use the location of the maximum in thermicity, which usually falls close to the point used here.

The induction time of a mixture is highly temperature-dependent. Lower temperatures lead to longer induction times. The induction time calculation using detailed chemistry can be simplified when modeling τ_i by an Arrhenius-type dependence on the temperature,

$$\tau_i = A_i \exp \theta = A_i \exp \left(\frac{E_a}{R T_{vN}} \right), \tag{1.1}$$

where A_i is a parameter depending on the mixture composition, θ is the effective or non-dimensional activation energy, E_a is the activation energy, R is the universal gas constant, and T_{vN} is the temperature at von Neumann conditions. The activation energy E_a is a measure of how sensitive the induction time is to perturbations in temperature, or in the case of the post-shock conditions, to perturbations in the leading shock speed.

1.2 Cellular structure

Detonation waves observed in experiments are intrinsically unstable, as discovered from optical visualizations by White (1961). Instabilities lead to the development of a multi-front detonation, which involves a complex three-dimensional shock structure known as cellular structure of the detonation front. The structure includes a

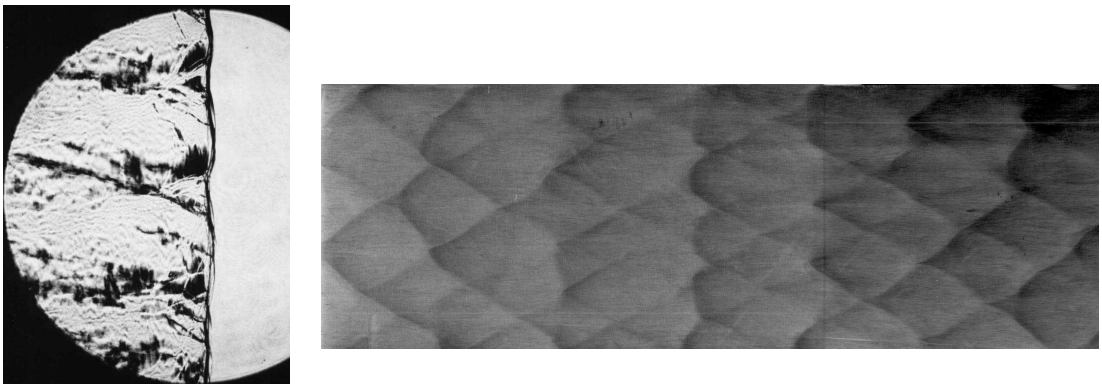

a) b)

Figure 1.2: a) Schlieren image of fully-developed detonation in 150 mm square cross section tube showing transverse waves and segmented lead shock front. b) Soot-foil showing cellular pattern of detonation. (a) and (b): Image height 150 mm. Mixture: $2H_2+O_2+17Ar$, P_0=20 kPa, T_0=300 K. Flow direction left to right.

segmented leading shock with transverse waves extending into the reacting gas as observed on schlieren images (Fig. 1.2a). When sooted foils are placed on the side wall of the tube or channel, the cellular pattern is evident after the detonation wave has passed over (Fig. 1.2b). This technique was first applied to detonations by Denisov and Troshin (1959) and Shchelkin and Troshin (1965).

The detonation multi-front wave involves a periodically varying leading shock velocity (Voitsekhovskii et al., 1966). The leading shock is divided into segments of incident shock and Mach stem, following the nomenclature of a non-reactive three shock configuration (Fig. 1.3a). Incident shock, Mach stem, and transverse wave meet at the triple-point. The tracks that are seen on soot-foils describe a diamond-shape or cellular pattern and seem to closely follow the path of the triple-point, discussed further below. After the collision of the triple-points, the Mach stem is over-driven, i.e., travels with a velocity higher than the CJ velocity. The shock velocity decays further downstream in the cell, and the Mach stem, which has become an incident wave, travels slower than the CJ velocity. Due to the strong temperature-dependence of the induction zone length (Fig. 1.3b and c), a keystone shaped region of lower chemical reaction rate is created behind the incident shock. This can be observed on planar laser induced fluorescence (PLIF) images, which enable the visualization

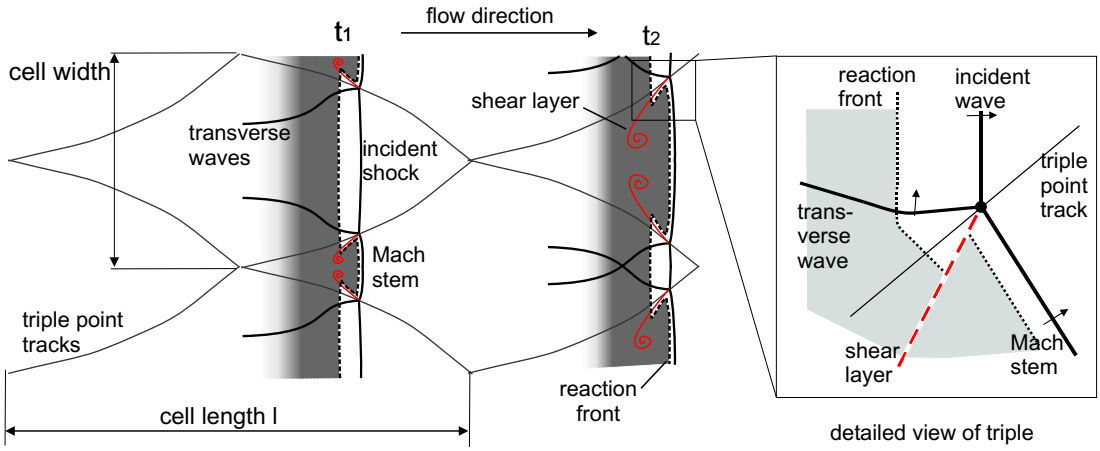

a)

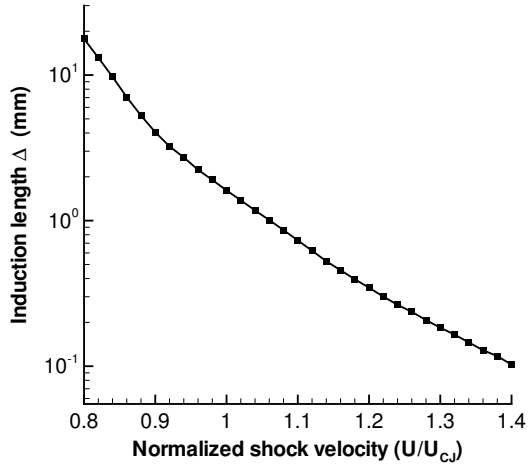

b)

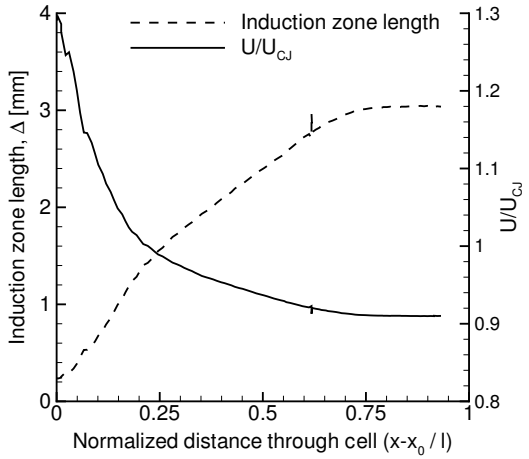

c)

Figure 1.3: a) Schematic of cellular structure of detonation front. b) Induction zone length calculated with detailed chemical reaction mechanism of Warnatz. $2H_2+O_2+17Ar$, P_0=20 kPa, T_0=300 K. c) Shock velocity on centerline through one cellular cycle from two-dimensional numerical simulation, $2H_2+O_2+7Ar$, 6.7 kPa, Eckett (2000).

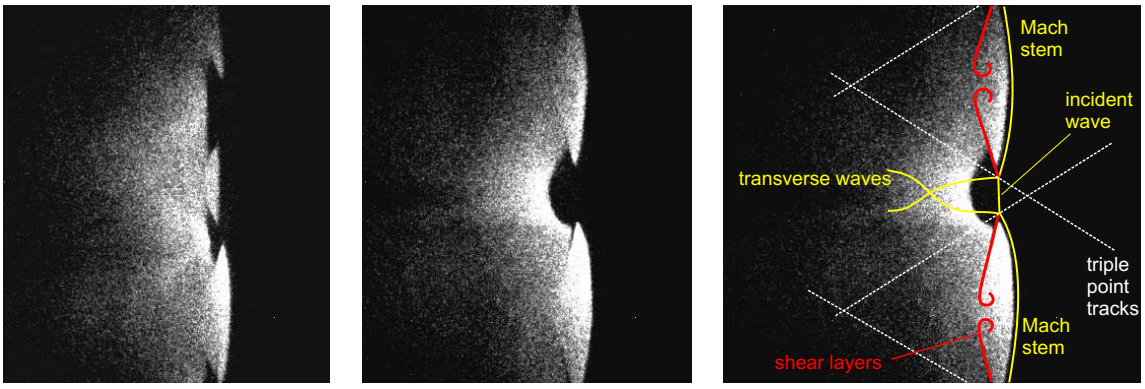

a) b) c)

Figure 1.4: PLIF image of detonation (Pintgen et al., 2003b). Flow direction is left to right. Image height 75 mm. Mixture: $2H_2+O_2+17Ar$, P_0=20 kPa, T_0=300 K. (a) and (b) are separate experiments. c) Explanation of features seen in (b).

of the OH radical, an intermediate species in the combustion process (Fig. 1.4). In detonations, the OH radical functions as a natural marker for chemical reactions taking place. Higher fluorescence intensity on the PLIF images corresponds to higher OH concentration. The PLIF technique allows the selective visualization of certain species concentrations in a thin layer (corresponding to the light sheet plane) within the flow field and is discussed in more detail in Chapter 3. Behind the Mach stem, a keystone of higher fluorescence is observed. The keystones sometimes appear to be bounded on the sides by the shear layer. The shear layer is the dividing line between particles which have passed through the incident shock and transverse wave, and the particles which have passed through the Mach stem (Fig. 1.3a). The details in the corner of the keystone were observed to depend on the mixture type (Pintgen et al., 2003a).

Note that the cellular structure is three-dimensional and the triple-points shown in the two-dimensional view shown in Fig. 1.3a are actually triple lines which extend into the paper plane. Furthermore, a second set of transverse waves traveling in the direction perpendicular to the paper plane exists. The triple lines do not necessarily form an orthogonal grid but may have a random phase and orientation. For detonations with a regular cellular structure propagating in a rectangular cross section channel, the transverse waves are more likely to be aligned parallel to the channel

walls. This can be observed on soot-foils which are placed on the channel end-plate.

The cell width λ (Fig. 1.3a) is, despite its large uncertainty, the most commonly used characteristic length scale and is one of the most widely used parameters (Lee, 1984). The cell width can be empirically correlated to the induction zone length as $\lambda = C\Delta$, whereas the value for the proportionality factor C varies between approximately 10 and 100. The proportionality is valid only for modest variations in mixture composition, but nonetheless enables a rough estimate of the cell size λ from Δ. The induction zone length Δ can be calculated fairly quickly using the ZND model whereas a direct reliable cell size calculation is not possible at this point.

The soot-foil technique is the standard experimental technique for determining the cell size and shock wave configuration of multi-front detonations. While it is clear that soot gets redistributed or removed by the passing detonation, the physical principle behind the soot-foil technique is not yet completely understood. It is commonly supposed that the soot-tracks coincide with the triple point path of the detonation. As long as the triple line is perpendicular to the wall, the tracks on the soot-foils allow for an estimation of the transverse wave strength from the track-angle α via a shock polar analysis. The track-angle is defined as the angle between the main flow propagation direction and the tracks seen on soot-foils and varies during a cellular cycle as the triple point configuration changes. The transverse wave Mach number is (depending on the mixture) on the order of $M \sim 1.3$, relatively weak compared to the Mach number of the incident wave and Mach stem of $M \sim 5$. Note that the apparent track-angle on the soot-foil increases if the triple line is inclined to the wall. This is because the contact point of the triple line at the wall has an additional velocity component along the triple line. This effect has to be considered when interpreting the soot-tracks, especially for geometries like tubes of circular cross section in which the transverse waves do not have a preferred propagation direction.

In order to illustrate the cellular detonation structure, some results of a study (Pintgen and Shepherd, 2003) conducted to investigate the correlation between triple-point location and soot-tracks are shown in this paragraph. The PLIF technique employing the OH radical was used for an independent visualization of the cellular

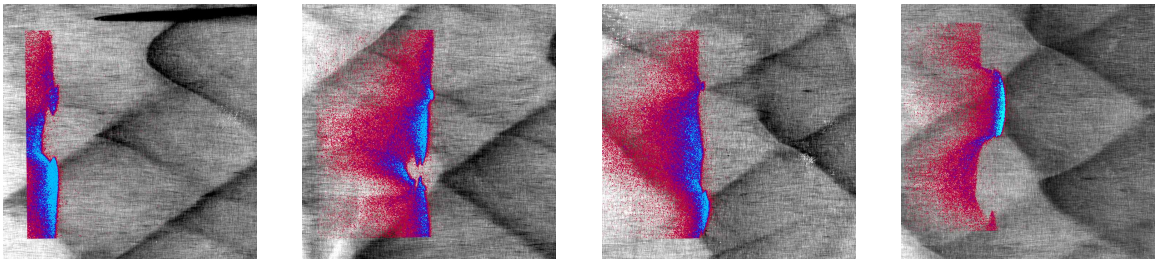

(a) Shot 1651 (b) Shot 1652 (c) Shot 1653 (d) Shot 1654

Figure 1.5: Overlay of soot-foils and PLIF-images, flow direction left to right. The region of higher fluorescence of the PLIF image is shown in false color. Image height: 85 mm, $2H_2+O_2+17Ar$, P_0=20 kPa, T_0=294 K.

structure simultaneous to the soot-foil technique. The light sheet for the PLIF visualization was oriented parallel to the soot-foil, at a distance of approximately 1 mm, which allows for an overlay of the PLIF and soot-foil images (Fig. 1.5). The soot-tracks for the highly argon-diluted H_2-O_2-mixture appear as a dividing line between brighter and darker regions on the soot-foil. The keystones of lower fluorescence correlate well with the "closing" portion of cell patterns, which correspond to the second half in the cellular cycle, where the bounding soot tracks converge. Keystones of a higher fluorescence correlate with the "opening" portions of the cell patterns, in the first half of the cellular cycle. This is a consequence of the higher lead shock velocity at the beginning of the cell compared to the end of the cell. The triple-point location derived from the PLIF images by an idealized triple-point analysis was shifted approximately 3 mm from the soot track, consistently toward the side of the incident wave. The influence of viscous effects of the fluid on the detonation and visualization technique is investigated by considering the boundary layer. A non-reacting similarity solution behind the shock wave traveling with CJ velocity (1415 m/s) was obtained by numerically solving the equations of motion. The post-shock velocity of the free stream is 1087 m/s. The velocity component, which is wall parallel in the lab fixed coordinate system, is plotted in Fig. 1.6 against the distance to the shock front. Also shown is the location of the light sheet and the induction zone length for CJ velocity, U_{CJ}, and 0.9 U_{CJ}. This calculation assumes laminar flow. At $Re \approx 3.5\ 10^5$ to 10^6,

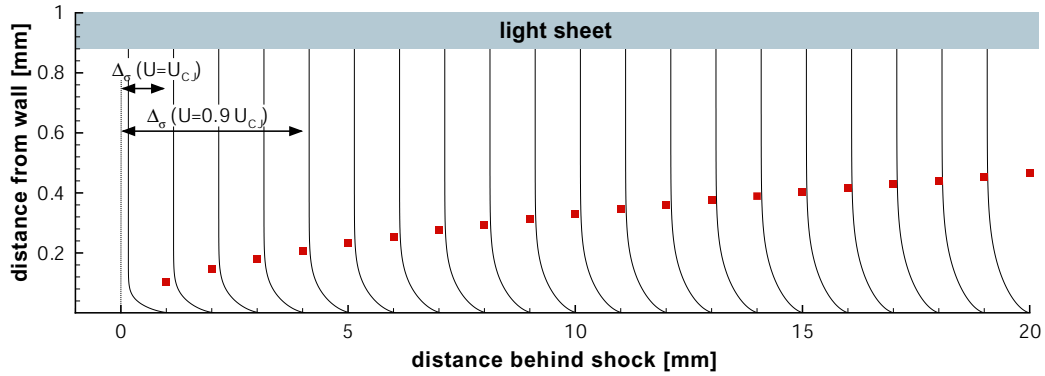

Figure 1.6: Calculated wall parallel velocity profiles behind a shock wave traveling with CJ velocity; Filled squares mark the location of U=0.99 U_{ps}.

the boundary layer transitions to turbulence; this corresponds to a distance of 10 to 28 mm behind the shock front. Neglecting the influence of transverse waves, the boundary layer is laminar in the induction zone and does not reach the light sheet. The location of the distinct OH front seen on the PLIF images is, therefore, not influenced by the boundary layer. This supports the notion that the triple-point location does not exactly coincide with the soot-foil tracks for this mixture.

For an idealized two-dimensional detonation (Fig. 1.3a), the cell size is equal to the transverse wave spacing, which is the distance between two transverse waves traveling in the same direction. The transverse wave spacing, obtained from PLIF images by measuring the distance between two keystone tips pointing in the same direction (e.g., Fig. 1.4a), is usually smaller than the cell size obtained from soot-foils (Pintgen, 2000). This is attributed to three-dimensional effects caused by the orientation of the cellular structure relative to the light sheet plane of the PLIF system. Only if triple lines are oriented perpendicular to the light sheet plane does the result seen on the PLIF images correspond to the two-dimensional view shown in Fig. 1.3. Note that soot-foils are, in a sense, also a two-dimensional cut through the three-dimensional shock structure, similar to the light sheet. Nevertheless, it seems that the imprints on the soot-tracks are more pronounced for the triple lines that are almost perpendicular to the soot-foil. The less distinct triple lines which are approximately parallel to the soot-foil result in vertical line structures perpendicular to the main flow direction on the soot-foils. Furthermore, a continuous spectrum of track-angles was not observed

on soot-foils, even in tubes. This could also be caused by wave interactions at the boundary. Soot-foils are, in contrast to PLIF, a highly intrusive diagnostic. These effects could contribute to the range of cell sizes measured from a single soot-foil, even for regular mixtures. The soot-foil interpretation and definition of a "cell" is quite subjective, especially for more irregular mixtures, which are discussed in the next section.

1.3 Regularity of detonations

For highly argon-diluted stoichiometric H_2-O_2-mixtures, the cellular pattern observed on the soot-foil is regular, only one dominant length scale is observed, and the variations in track-angle are small. On the PLIF images, the smooth reaction front is punctuated with distinct keystones. The degree of regularity depends on the mixture composition and was classified by Strehlow (1968) into various qualitative categories (excellent, good, irregular, and poor). For undiluted H_2-N_2O-mixtures, an example of highly irregular mixture, sub-structure on a smaller length scale is observed on soot-foils (Fig. 1.7a). On PLIF images, the keystone-shaped features are not as distinct and the reaction front appears more subdivided and rough (Fig. 1.7b). Since all detonations are, to a certain degree, unstable, the more regular mixtures are also termed "weakly unstable", whereas the highly irregular mixtures are also termed "highly unstable".

Linking system properties to the observed instability has received considerable attention in theoretical, numerical, and experimental studies (Lee and Stewart, 1990, Short and Quirk, 1997, Austin, 2003). The normalized heat release, the effective activation energy, and the lead shock velocity influence the stability. Furthermore, the thermicity pulse length, a measure of how rapidly the chemical energy is released, play a role. A figure of merit quantifying the degree of irregularity is the effective activation energy θ. It can be calculated from the mixture composition and initial conditions. A method of quantifying the degree of regularity from experimentally obtained PLIF images is given in Chapter 4. The activation energy θ is calculated

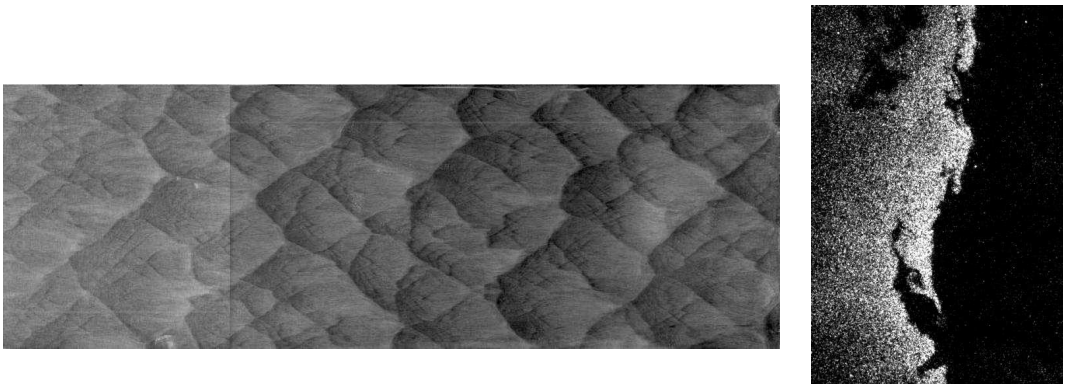

a) Shot 1643 b) Shot 1607

Figure 1.7: Example of observation in mixtures with irregular structure. Flow direction left to right. a) Sootfoil, image height: 150 mm, H_2-N_2O-$3N_2$, P_0=20 kPa. b) PLIF image, image height: 45 mm, H_2-N_2O-$3N_2$, P_0=20 kPa.

by evaluating numerically the induction time τ_i for a perturbation in T_{vN} assuming the Arrhenius-type dependence (Eq. 1.1),

$$\theta = \frac{1}{T_{vN}} \frac{\ln \tau_{ia} - \ln \tau_{ib}}{1/T_a - 1/T_b}, \tag{1.2}$$

where τ_{ia} and τ_{ib} are induction times corresponding to the perturbed temperatures T_a and T_b, so that $T_{a/b} = T_{vN} \pm 0.01 T_{vN}$. This leads to slightly more accurate determination of the activation energy than the method of perturbing the shock Mach number, since the post-shock density is not constant with varying shock velocity. The choice of the detailed chemical mechanism used for the calculation of the induction times has the biggest influence on the results. The induction times are calculated with the zero-dimensional code CV (Shepherd, 1986) that models a constant volume adiabatic explosion. The perturbation magnitude has to be large enough to avoid the influence of numerical errors and small enough to reflect a good approximation at the given thermodynamic condition. Perturbations of smaller than 0.1% and larger than 10% on T_{vN} were found to give erratic results (Pintgen and Shepherd, 2004).

Larger effective activation energies seem to correspond with a higher degree of irregularity, as confirmed by experimental observations (Pintgen et al., 2003a). This is motivated by the appearance of the neutral stability boundary in θ versus Mach

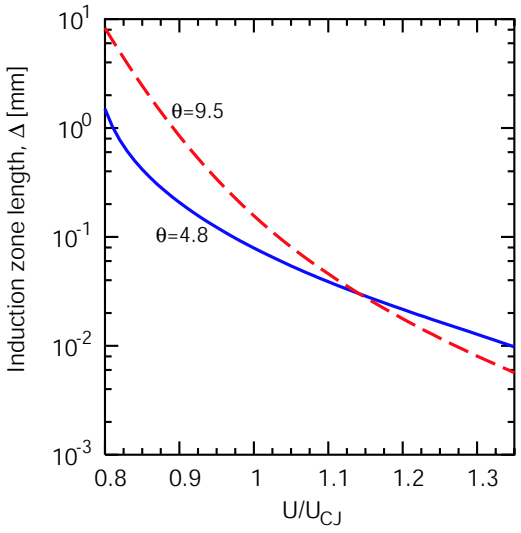

Figure 1.8: Change in induction zone length as a function of normalized lead shock velocity for two mixtures with different effective activation energy: θ=4.8, $2H_2+O_2+7Ar$, P_0=100 kPa, T_0=300 K. θ=9.5, H_2+N_2O, P_0=45 kPa, T_0=300 K.

number coordinates (Lee and Stewart, 1990, Austin et al., 2004). Furthermore, the effective activation energy was found to be the determining parameter in amplification of small disturbances (Lee and Stewart, 1990, Short and Quirk, 1997). For the highly argon-diluted mixture shown in Fig. 1.2, θ is calculated to be 5.4 whereas it is 12.4 for the H_2-N_2O-N_2-mixtures shown in Fig. 1.7. The different values of θ are also evident in the induction zone length Δ versus shock velocity computations (Fig. 1.8).

1.4 Detonation diffraction

If a detonation wave, propagating in a rigid tube or channel, suddenly emerges into an unconfined volume, the planar wave will diffract and transform into an approximately spherical wave (Fig 1.9a). Detonation transition from planar to spherical geometry may result in detonation failure or initiation, and involves mechanisms of both unsteadiness and wave curvature (Eckett, 2000, Arienti, 2002). An understanding of this process is of fundamental importance for the combustion community since it gives insight into the relative role of these mechanisms, which occur simultaneously during the diffraction process. Depending on the mixture parameters and geometry,

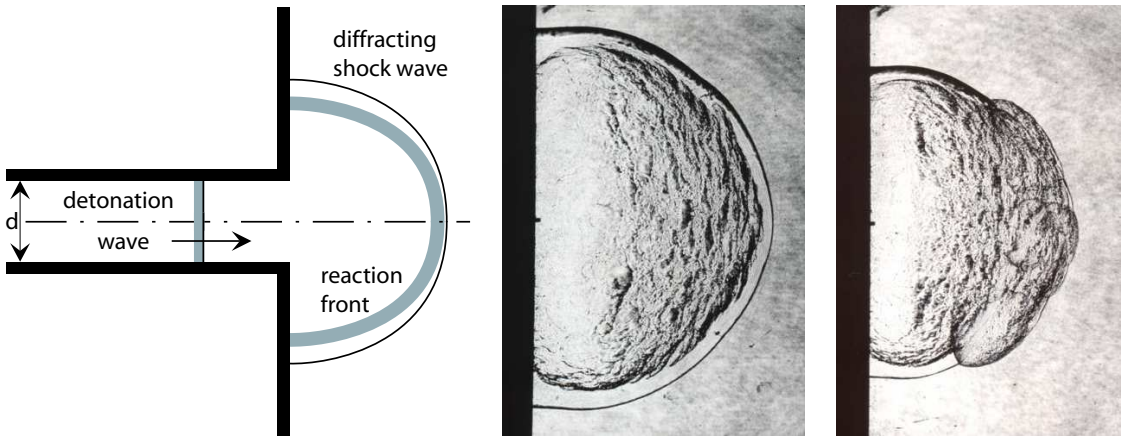

Figure 1.9: a) Sketch of diffracting detonation wave out of circular tube. b) Sub-critical outcome, H_2+N_2O, P_0=42.5 kPa. c) Super-critical outcome, H_2+N_2O, P_0=45 kPa. (b) and (c) Schlieren images, image heights: 125 mm, tube diameter: 38 mm, flow from left to right.

decoupling and re-initiation phenomena occur. The coupling of shock and reaction fronts is fundamentally different during one cellular cycle for mixtures with different degrees of regularity. This is observed in fully-developed detonations traveling near the CJ velocity (Strehlow, 1968). However, the effects of the degree of regularity on the detonation diffraction process have not been characterized and quantified rigorously at this point. The goal of the present experimental investigation of the detonation diffraction process, is to characterize and quantify the differences observed for mixtures with a varying degree of regularity.

If the detonation transitions successfully, the shock and reaction zone remain coupled; this is the super-critical case. If the detonation wave fails, the shock and reaction zone decouple; this is the sub-critical case. The outcome is determined by the following parameters: mixture composition and thermodynamic conditions, the detonation velocity as the detonation exits the tube, and the geometry of the area expansion and tube cross section. The transition point from the sub- to super-critical experimental outcome is known as the critical condition. In the literature, these conditions are quantified as the "critical tube diameter" d_c for a given mixture. A super-critical outcome of the experiment is observed if the tube diameter d, from

which the detonation wave emerges, is larger than the critical diameter; a sub-critical outcome is observed if $d < d_c$. From the experimental data collected by previous researchers, empirical correlations between the cell size λ and d_c were derived. The critical tube diameter d_c is 10 to 30 times larger than λ, depending on the mixture composition (Mitrofanov and Soloukhin, 1965, Knystautas et al., 1982, Shepherd et al., 1986). An extensive literature review on the critical tube diameter including modeling can be found in Schultz (2000).

1.5 Goals of this study

The goal of the detonation diffraction experiments conducted for the present study is to compare and identify the different patterns and mechanisms observed for decoupling and recoupling of shock and reaction fronts in mixtures with a varying degree of regularity. The focus is on the failure and re-ignition phenomena occurring in the critical regime. In the critical regime, super- and sub-critical experimental outcomes are possible for nominally identical initial conditions. In this intermediate regime, the re-ignition and failure processes are very sensitive to small perturbations in initial conditions, which are beyond experimental control. In the super-critical regime the experimental outcome is always a successful detonation transition, whereas in the sub-critical regime, the detonation always fails. Note that there are three regimes documented, but only two possible experimental outcomes.

Previous work on visualization of the diffraction process was often conducted in a rectangular high aspect ratio channels, e.g., Edwards et al. (1979), Vasil'ev (1999) and Pantow et al. (1996), resulting in a cylindrical diffraction process. Soot-foils and schlieren and open shutter chemiluminescence imaging was used. While this enables a better interpretation of the images, the detonation structure is still three-dimensional and the transverse waves reflecting off the side walls could influence the diffraction process especially in the critical regime. Narrow channel experiments for fully-developed detonations with a cell size smaller than the channel width have shown the presence of a small amplitude instability which remains in the narrow

dimension (Austin, 2003, p. 71). A strictly two-dimensional detonation is apparently very difficult to achieve experimentally. The present study of detonation diffraction is carried out in a rotationally symmetric geometry for the area change and no preferred orientation of the transverse wave structure is given ab initio by the geometry. The effects of shock reflections off the side walls, which are downstream from the sudden expansion, are beyond the scope of the present work. The understanding of the exact mechanisms by which detonations transition or fail through an area expansion is from the practical point of view, of particular interest to the field of propulsion and safety analysis.

1.6 Thesis outline

An introduction about the detonation cellular structure and detonation regularity is given in Chapter 1. Furthermore, the goals of this work are described.

The experimental setup and optical diagnostic techniques used for the experimental work are explained in Chapter 2. The facilities used for the detonation diffraction experiments and study of fully-developed detonations are discussed.

In Chapter 3, a detailed description of the PLIF technique is presented together with a fluorescence model. The model-predicted fluorescence is compared to experimentally obtained fluorescence profiles in fully-developed detonations.

A method for quantifying the degree of regularity of a mixture based on PLIF images is contained in Chapter 4. Techniques used in fractal analysis are applied to the edge-detected OH-front, visible on PLIF images.

The results of the detonation diffraction experiments are presented and discussed in Chapter 5. The focus is on comparing two mixture types, one of them with a highly regular structure; the other one with a highly irregular structure. The differences observed on schlieren, PLIF and chemiluminescence images, and pressure traces are shown. Also the stereoscopic imaging technique and results are described in Chapter 5.

The results are further analyzed on the basis of a model in Chapter 6. The

conclusion and future work are given in Chapter 7.

Chapter 2

Experimental Setup

In this study, two experimental facilities were used: The gaseous detonation tube (GDT) was used for the investigation of fully developed Chapman Jouguet detonations and the detonation diffraction facility for the study of self-sustaining detonation waves diffracting from confinement into an unconfined space through an abrupt area change. The same setup of optical diagnostic techniques including schlieren, planar laser induced fluorescence (PLIF), and multiple exposure and open shutter chemiluminescence imaging was used with both facilities. Pressure history data from transducers mounted in the tube and test section side walls were recorded in both cases with a 14 bit digital data acquisition system and a sampling rate of 1 MHz.

2.1 Facilities

The GDT is a 7.6 m long tube with an inner diameter of 280 mm attached with a "cookie-cutter" to a test section (Fig. 2.1, 2.2) described in more detail in Akbar (1997). The facility is evacuated prior to each experiment to a pressure level below 4 Pa. The filling procedure is based on the partial pressure method with a filling gauge accuracy of ± 7 Pa. In order to ensure a homogeneous mixture, the entire tube volume was circulated for five minutes with a bellows pump through a circulation line, not shown in Fig. 2.1. The detonation is initiated with an exploding wire and a short section of acetylene-oxygen mixture injected immediately before the wire explosion, which results in a highly repeatable operation of the initiation phase. The propagating

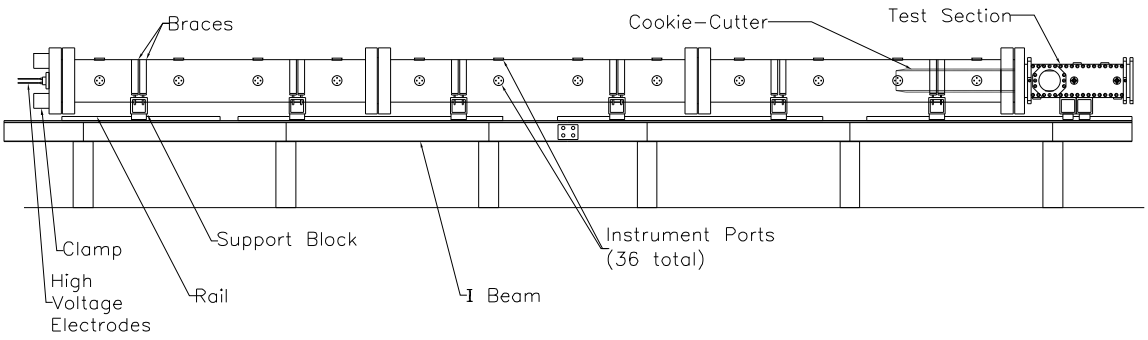

Figure 2.1: Schematic of gaseous detonation tube. Courtesy of Tong Wa Chao

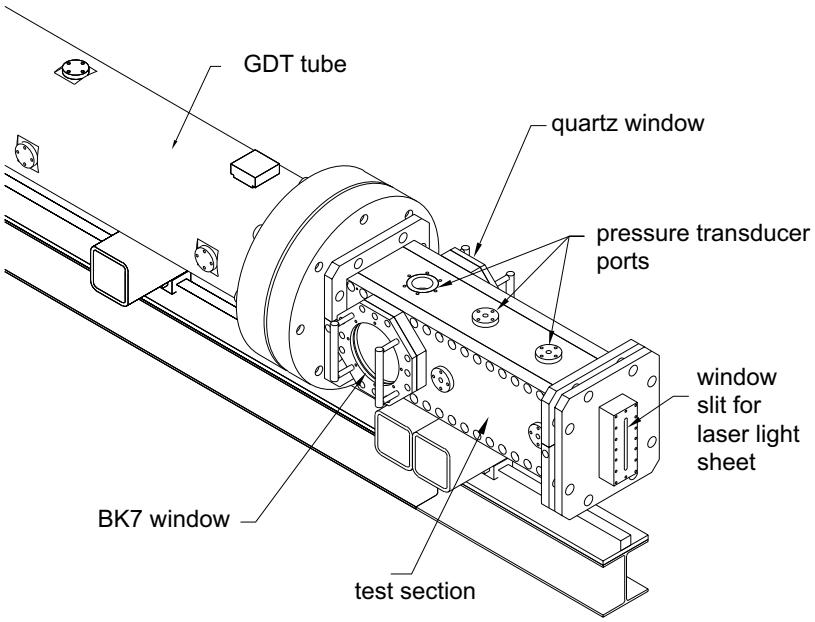

Figure 2.2: Schematic of test section attached to GDT tube. Courtesy of Tong Wa Chao

detonation is cut at the end of the tube by four plates with sharp edges, the 1 m long "cookie-cutter", which form a 150 mm square cross-section channel and transitions into the 1.8 m long, 150 mm square section of the facility. Experiments conducted in this facility are discussed in Chapters 3 and 4. Six pressure transducers, three of them in the test section, were used to obtain the pressure histories and detonation velocity from time of arrival data of the detonation wave.

The detonation diffraction facility consists of a 1.5 m long tube with an inner diameter of 38 mm, described in detail in Schultz (2000). The tube is attached to the 0.8 m long aforementioned test section as shown in Fig. 2.3. The GDT and

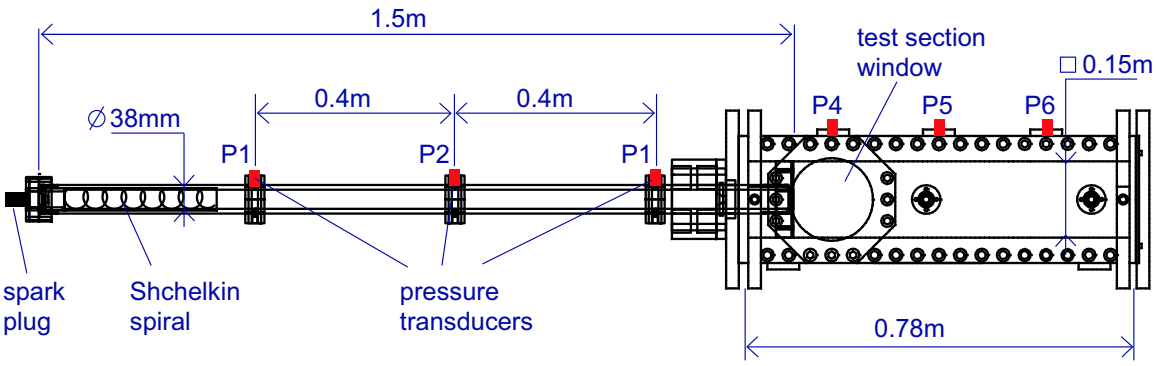

Figure 2.3: Schematic of detonation diffraction tube. Courtesy of Eric Schultz

the detonation diffraction facility use the same test section, Kaneshige (1999), which could be attached to either facility. The O-ring sealed clamp connection between the tube and the test section allows for variable positioning of the tube end face with respect to the window center. For most of the shots, the tube end face was located 50 mm upstream of the window center. The tube end face plate attached to the diffraction tube inside the test section creates a rotationally symmetric sharp concave corner of 90 °. The corner radius was measured to be less than 0.3 mm. The facility was evacuated to a pressure of 6 Pa or less, filled with the mixture components by the method of partial pressures, and, finally, circulated for eight minutes with a bellows pump to ensure a uniform mixture. The circulation line includes a segment connected to the small volume behind the tube end face plate. Furthermore, the filling lines leading to the facility are included in the circulation loop minimizing the filling error possibly created by unmixed gas volumes. The volume of the filling line not circulated was 4 cm^3 compared to 0.2 m^3 of total facility volume. The gauge accuracy used for the gas filling was ± 7 Pa. The detonation is initiated by an electrical spark (total stored energy of 225 mJ) and a Shchelkin spiral for enhancing the deflagration to detonation transition. The Shchelkin spiral covers a tube length of 305 mm, has a wire diameter of 4 mm and a pitch of 12 mm. Pressure histories were recorded by a total of six pressure transducers equally spaced in the tube and test section.

2.2 Diagnostics

The test section used for both facilities has three points of optical accesses, two windows, each 64 mm thick and 150 mm in diameter. These are located opposite each other, 0.5 m from the end plate. This allows the parallel schlieren light beam to enter and exit the test section (Fig. 2.2, 2.5). The third window is a UV-transmitting quartz window in the end plate, which permits the laser light sheet for the PLIF diagnostics to enter the test section.

2.2.1 Schlieren setup

The schlieren setup is a classical Z-setup with two parabolic mirrors of focal length 1000 mm. The light source is a ruby laser with a pulse length of approximately 50 ns (Akbar, 1997). The test section volume is imaged onto a 83 × 105 mm black and white Polaroid 667 (3000 ISO), Fig. 2.4a. An electro-mechanical electronic capping shutter (3 s open time) and a laser line filter avoid fogging of the film by light in the room prior to the experiment or by light emission from the reacting flow. The schlieren system and triggering scheme are shown in Fig.2.7 and described below and, in more detail, in Pintgen (2000).

2.2.2 Chemiluminescence

For some detonation diffraction experiments, a second camera was used to obtain chemiluminescence images. A 105 mm f/2.8 Micro Nikkor lens (Nikkon) was used to acquire an image by the ICCD assembly (Princeton Instruments PI Max) with a resolution of 512×512 pixel, a 16 bit dynamic range, and a built-in high voltage pulser. The f-number was increased for experiments with strong chemiluminescence intensity like mixtures including hydrocarbons. Additionally, depending on the experiment, the gate width was varied between 50 and 300 ns to employ the full dynamic range of the ICCD system. The camera position was tilted 8° with respect to the horizontal to avoid interference with the optical path of the schlieren system (Fig. 2.5). The line of

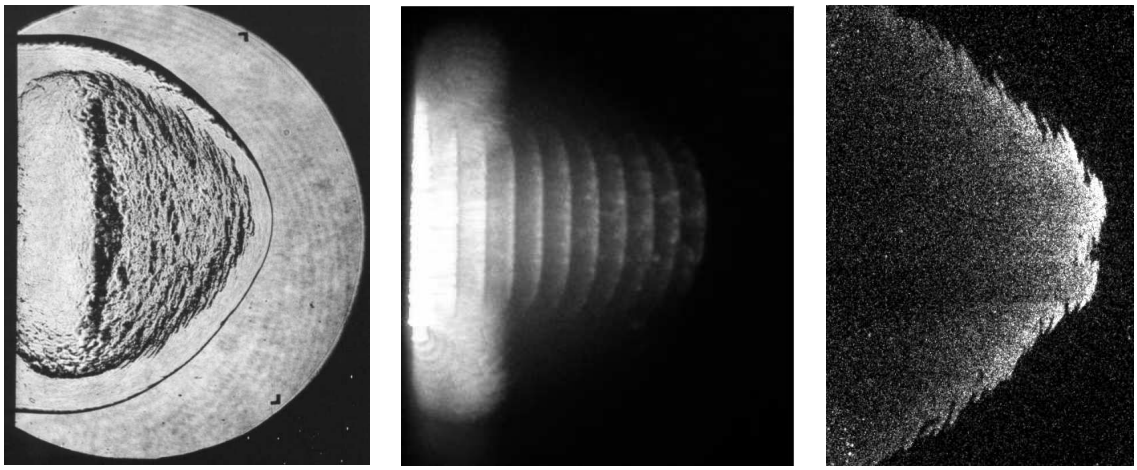

a) b) c)

Figure 2.4: Examples of images obtained with the optical diagnostics in the diffraction experiment. The detonation is traveling from left to right and the tube exit plane is located on the left side on all images. a) Schlieren image, H_2+2O_2+7Ar, P_0=1 bar, image height 150 mm, shot 71. b) Multiple burst image obtained from a detonation diffraction experiment. The timing between the 10 burst was set to 3 μs, gate width 300 ns, H_2+2O_2+6Ar, P_0=1 bar, image height 77 mm, shot 148. c) PLIF image, H_2+2O_2+7Ar, P_0=1 bar, image height 70 mm.

sight of the camera thereby remained perpendicular to the direction of the main flow. The camera can be operated in multiple gate mode enabling several intensifier gating pulses before the CCD read-out occurs. The camera system controller unit includes a pulse timing generator so each trigger in this mode initiates a burst of intensifier gate pulses. The temporal sequence of events appears overlaid on the image. The leading reaction front for every gate pulse can be clearly located, as long as they are spaced sufficiently far apart, Fig. 2.4b. There is a trade-off between the total number of bursts and their spacing, far apart and how distinct each front is. For the image height of 109 mm and the mixtures investigated, a temporal spacing between each pulse of 3 to 6 μs and a total number of up to 15 pulses have been found to produce good results. From the multiple-pulse images, the average velocity of the leading luminescence front between gate pulses could be determined.

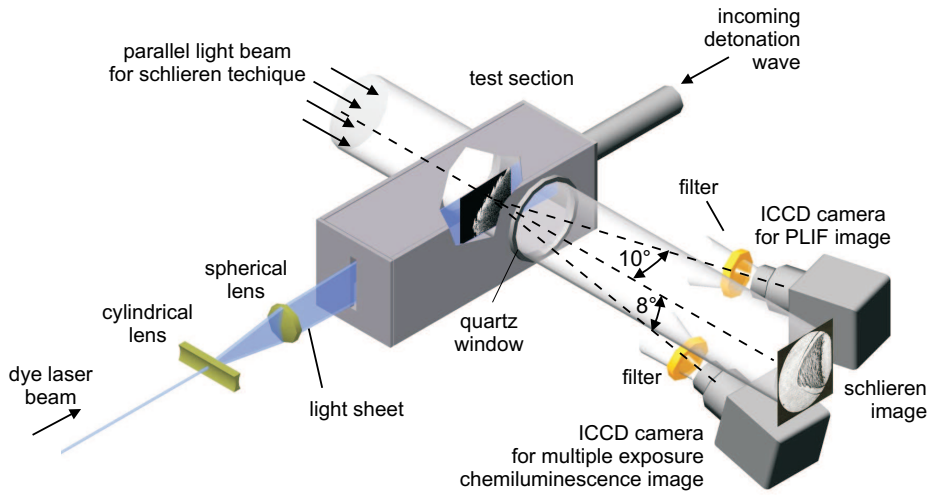

Figure 2.5: Schematic of experimental setup used for detonation diffraction experiment including the camera used to obtain multiple exposure chemiluminescence images.

2.2.3 Planar laser induced fluorescence

As part of the PLIF system, an excimer pumped tunable dye laser (Scanmate2E, Lambda Physik) with a frequency doubling unit delivers a pulse of narrow bandwidth UV-light with a pulse length of approximately 20ns and pulse energy of about 6.5 mJ. The frequency was tuned to the immediate vicinity of two OH-transition lines close to 284 nm: $A^2\Sigma^+ \leftarrow X^2\Pi_i(1,0)$ $Q_2(8)$ at 284.009 nm and $A^2\Sigma^+ \leftarrow X^2\Pi_i(1,0)$ $Q_1(9)$ at 284.007 nm. A light sheet was formed by the combination of a cylindrical lens (focal length -25 mm) and a spherical lens (focal length 1000 mm). The light sheet enters the test section through the quartz window and slit at the end plate of the test section. The induced fluorescence passes through the UV-transmitting quartz window and is filtered by a bandpass filter with a centerline of 313 nm and FWHM 10 nm.

The peak fractional transition for the interference transmission bandpass filter (Andover Cooperation, No. 313FS1-50) is about 0.16. For the pumped transition line the non-resonant fluorescence, mainly from the (1,1) and (0,0) transition band, occurs in the wavelength region between 306 nm and approximately 320 nm. Therefore, the fluorescence range overlaps well with the bandpass filter transition range, blocking

out all possible sources of noise like elastic scattering and chemiluminescence arising from the hot reacting flow. For experiments in the detonation diffraction facility, the fluorescence yield is significantly lower, which is explained by the higher pressure and correspondingly higher quenching rate (see Chapter 3). Despite the fast optics used, the fluorescence intensity was at the limit of being detectable over a reasonable dynamic range (> 4 bits) by the camera. For some of these cases, a UG11 black glass filter was used instead of the interference filter. The peak fractional transmission is given as 0.84 at 315 nm. The wavelength transition range reaches from 260 to 380 nm and therefore includes the fluorescence arising from the resonant (1,0) band. Furthermore, it contains contributions from Raman and Rayleigh scattering. By tuning the laser 0.02 nm off the pumping transition line, the scattering effects were isolated and minor compared with the fluorescence signal obtained. This can be explained by the thin spectral width of the pumping line of the laser, which facilitates effective pumping while keeping the scattering contributions far below the fluorescence intensities. In the future, for low fluorescence yield situations, the use of reflection filter sets should be considered since they provide a higher peak reflectance than the peak transmission of interference filters.

The fluorescence signal is collected perpendicularly to the light sheet by a 576×384 pixel 12-bit intensified CCD-Camera (Princeton Instruments ITE/ICCD-576, 22×22 μm pixel size). The camera was gated by a 30 ns pulse of 1000 V, which allows for a minimization of chemiluminescence as a source of noise. Since the characteristic quenching time is far smaller than the fluorescence life time, the fluorescence signal does temporally coincide (discussed in detail in Chapter 3) with the dye laser pulse of approximately 20 ns length. The image is formed by a 105 mm f/4.5 UV-transmitting lens (Nikkon UV-Nikkor). The height of the imaged region was between 30 and 80 mm depending on the particular experiment (Fig. 2.4c). For the simultaneous use of the PLIF and schlieren system, the camera had to be moved out of the optical path of the schlieren system. The resulting distortion of the image was corrected by means of post-processing the PLIF image. The PLIF and schlieren images were obtained within 80 ns which allows for an overlay of both images with a minimal displace-

ment (less than 0.48 μm, including the uncertainties in the overlay process) of spatial features. To ensure alignment of the superimposed images, a set of target images was used. After the alignment of the optical systems and prior to the experiment, a transparent target was placed in the plane of the light sheet. An image of the same target was taken with both the schlieren and PLIF systems. To obtain sufficient signal strength on the target image of the room light with the PLIF camera, the filter was removed, the light sheet was blocked, and the exposure time increased. For the overlay of images obtained in an experiment, identical transformations of target and experimentally obtained images were performed while matching the targets on the PLIF and schlieren images. One PLIF image, one schlieren image, and one multiple exposure chemiluminescence image could be acquired simultaneously per experiment.

The development of the PLIF system is discussed in detail in Pintgen (2000) and quantitative aspects of the PLIF technique are described on a theoretical basis in Chapter 3. Here, the triggering of the simultaneous PLIF and schlieren systems is addressed in detail, since it was modified from the system described in the references given above and allows for an optimized camera gate width on the order of the dye laser pulse length.

2.2.4 Triggering of the imaging system

A timing diagram and wiring schematic of the experimental setup is shown in Figs. 2.7 and 2.6. The firing sequence is initiated by the manual triggering of delay generator A, which immediately sets off the charging sequence of the ruby laser flash lamp capacitor. The charging of the flash lamp capacitor takes, depending on the voltage setting, approximately 5 s, and the flash lamp has to be fired within 10 s after the charging is completed before it discharges automatically. After the flash lamp capacitor is fully charged up, delay generator A triggers the spark plug circuit. Following the deflagration to detonation transition process, the detonation wave reaches, after a certain period of time, the field of view for the optical system. This period of time, between the spark firing and the point in time the detonation wave reaches the field

of view, depends on mixture sensitivity as well as CJ velocity of the specific mixture. Roughly 1 ms before the detonation wave reaches the field of view, the ruby laser flash lamp has to be fired. The delay between the spark plug firing and the detonation wave reaching the field of view is very repeatable and can be estimated for the first shot with a specific mixture composition from the calculated CJ velocity. Note that for fast propagating detonations in sensitive mixtures, the delay between ignition and the point in time when the detonation front reaches the window can be less than 1 ms. In this case, the flash lamp is actually fired before the spark ignition. To ensure precise timing for the detonation diffraction experiment, the closest pressure transducer, 298 mm upstream to the tube exit plane, is used for triggering the optical systems. The pressure transducer signal is "teed" from the data acquisition system and processed by a latching edge detection trigger circuit. This circuit consists of a Schmitt-trigger and an AND-gate. The purpose is to inhibit any trigger output for 0.5 ms after the firing signal. This avoids false triggering by noise on the pressure transducer signal induced by the HV spark plug or exploding wire circuit. The TTL level output of this circuit is used as input for delay generator B.

A trigger signal is sent from delay generator B to the excimer laser accounting for the time the detonation front needs to travel from the pressure transducer to the desired location in the field of view of the schlieren and PLIF system. The light output of the excimer pumped dye laser occurs approximately 1.2 μs after the trigger input signal and is afflicted with a jitter of approximately 200 ns. The laser monitor output signal also shows a shot-to-shot variation of 150 ns between trigger output and light output as measured by a photo-diode. As a result, triggering of the camera gate precisely coinciding with the laser light output is not possible in a repeatable fashion as long as the camera system is triggered based on the laser input trigger or laser monitor output. To overcome this difficulty, an induction coil was placed inside the excimer casing to obtain the high frequency noise signal arising from the discharge of the capacitors of the excimer laser 85 ns prior to the light output. The high frequency noise was processed with a high speed comparator circuit to obtain a TTL-level signal 70 ns before the light output. The circuit consists of a rectifier, an RC-low-pass filter,

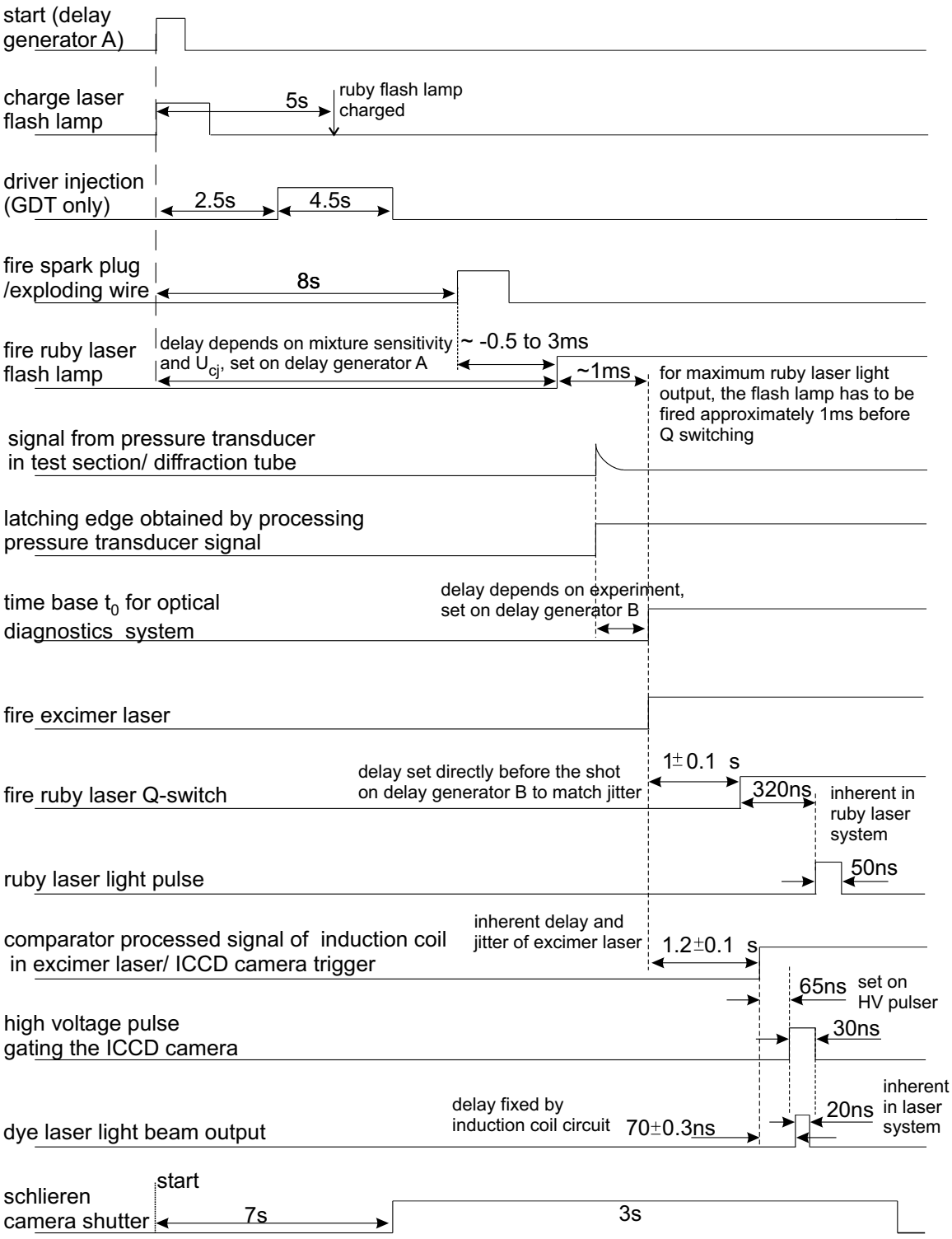

Figure 2.6: Timing diagram of triggering sequence for simultaneous schlieren and PLIF setup.

and an integrated comparator circuit (LM362, National Semiconductor). Tests with a photo-diode showed that the jitter of the delay between the TTL output signal of the high speed comparator circuit and the actual light output is 0.3 ns, allowing a highly repeatable gating of the camera with respect to the laser light pulse. The delays for the camera gate pulse timing are set on the HV gate generator to coincide with the light output. The entire PLIF system is, therefore, solely triggered by the input signal to the excimer laser. The ruby laser system has an inherent delay of approximately 320 ns from the trigger input signal to the Q-switch to the beginning of the light pulse of 50 ns length. If the Q-switch were triggered by the inductor coil signal, the schlieren picture would be consistently taken 250 ns after the PLIF image. This corresponds to a spatial displacement of 0.5 mm for a detonation traveling at 2000 m/s. In order to decrease the delay between obtaining the PLIF and schlieren images, the Q-switch is triggered prior to the inductor coil signal by delay generator B. The disadvantage is that the point in time of the PLIF image being taken is afflicted with a jitter of 200 ns with respect to the time base on the delay generator. This required the Q-switch timing to be tested and adjusted prior to each experiment to compensate for the varying delay between the delay generator B time base and the PLIF image being taken. This is only possible because the jitter of the excimer laser drifts only 50 ns over about one minute while, over several minutes, the drift can be up to 200 ns (Pintgen, 2000). This technique allows for a delay of 20 to 70 ns at the maximum between acquiring the PLIF and schlieren images, corresponding to a spatial displacement of 0.14 mm for a front velocity of 2000 m/s, which is on the order of one pixel resolution in the CCD camera. Since the UG11 filter used for some experiments in the PLIF system has a second transition band close to the ruby laser wave length of 694 nm, overlap between the PLIF camera gate and the ruby laser pulse was avoided. The camera shutter on the Polaroid film for the schlieren image was actuated by delay generator A prior to the spark ignition and closed after the ruby laser fired.

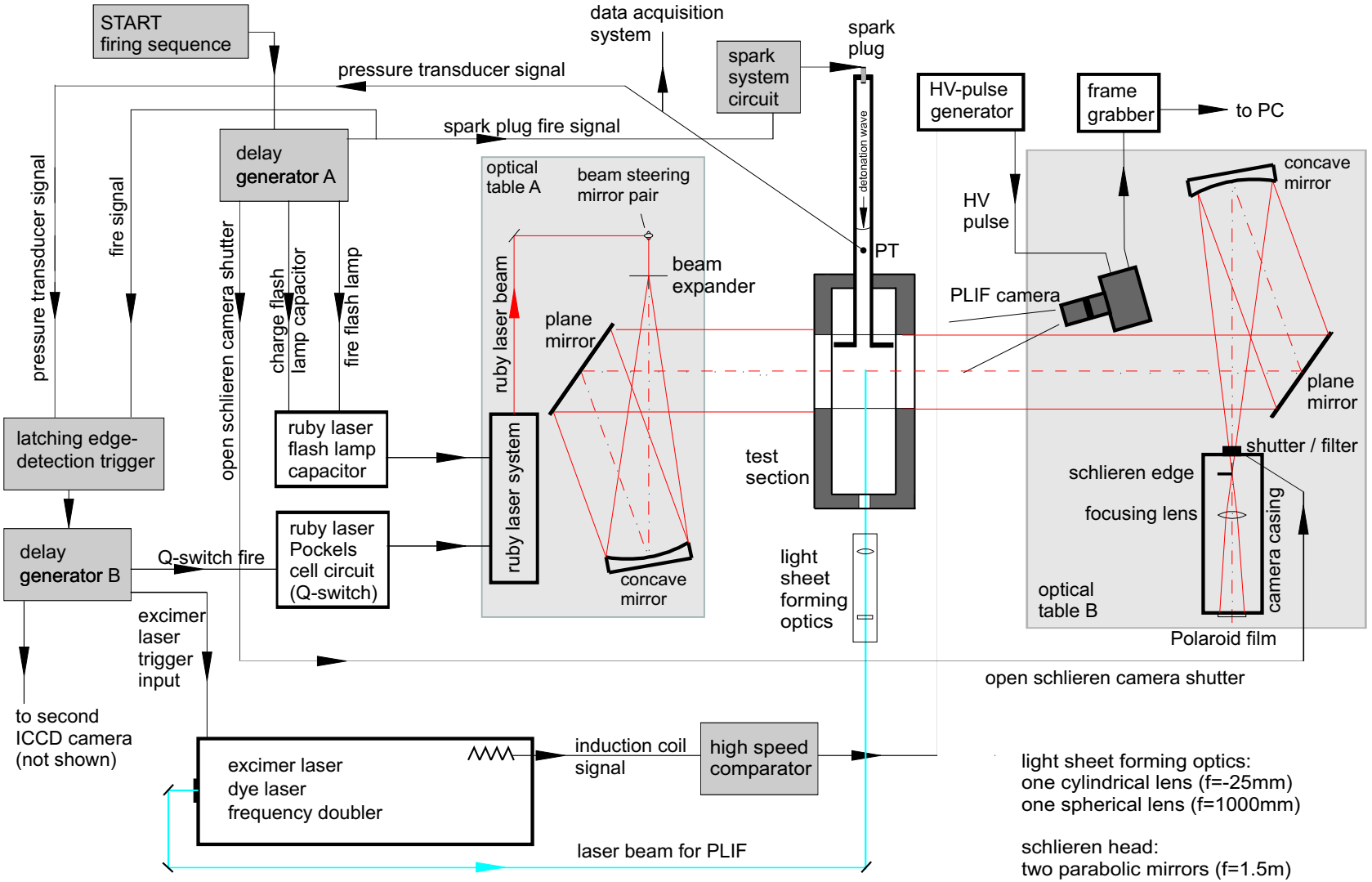

Figure 2.7: Schematic of experimental setup and triggering layout of simultaneous schlieren and PLIF setup for the detonation diffraction experiment.

Chapter 3

Quantitative Considerations for PLIF Signals

Planar laser induced fluorescence (PLIF) of the OH radical has been used to visualize the distribution of OH concentration in a flow field with locally strongly varying background composition and thermodynamical conditions in the detonation front. The quantitative relationship between the PLIF signal intensity and number density of OH molecules is discussed in this chapter, including the effects of shape and strength of the absorption line, quenching, and light sheet energy attenuation by absorption.

In the first Section, the general principle of laser induced fluorescence is discussed. The purpose of the subsequent three Sections in this chapter is to provide a theoretical spectroscopic background for the PLIF model discussed in Section 3.5. In Section 3.7, experimentally obtained fluorescence intensities from fully developed detonations are compared to the model predictions.

3.1 Laser induced fluorescence

Laser induced fluorescence (LIF) techniques are one of the most widely used non-intrusive techniques for the probing of gases, and it facilitates selective species concentration measurements. The high signal strength often makes it preferable to Rayleigh and Raman scattering. With PLIF, one can obtain two-dimensional species concentration distributions and slices of the probed volume, which enables the study of three-dimensional phenomena.

All LIF techniques rely on properties of the natural fluorescence of the probed atom or molecule. Since the natural fluorescence occurs from, in general, weakly populated higher energy levels, natural fluorescence signals are small. The incoming laser light temporarily populates the higher levels by exciting molecules in the lower and more densely populated levels. This leads to a much higher signal strength from the subsequent downward transition. LIF is therefore a two-step process involving excitation and fluorescence.

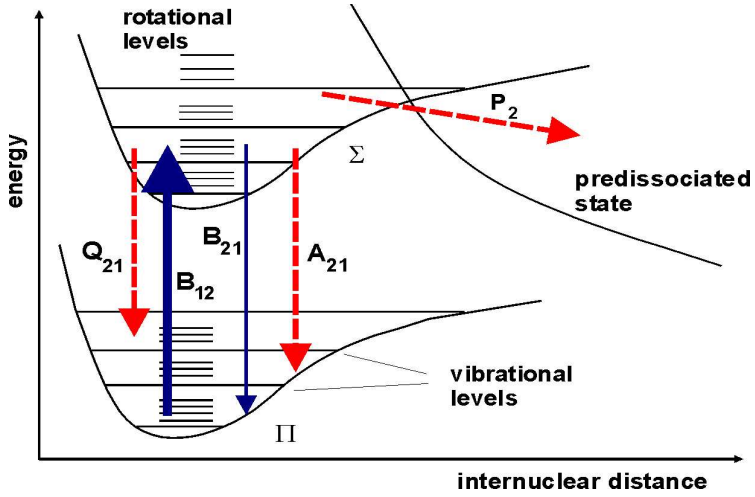

Figure 3.1: Energy level scheme of the OH radical.

In Fig. 3.1, the various transition mechanisms that play a role in the LIF technique are illustrated, each specified by the corresponding rate coefficient. The lower, $X^2\Pi$, and upper, $A^2\Sigma^+$, electronic levels of the OH radical are subdivided into vibrational levels denoted by arabic numbers for v'' and v', respectively. Each vibrational level is further subdivided into rotational levels, denoted by N'' and N', respectively. The Einstein B coefficient for absorption B_{12} [$\mathrm{cm}^2/(\mathrm{Js})$] represents the absorption of photons. The emission of a photon can be caused by two processes. In stimulated emission, the excited molecule transitions, under the influence of the incoming laser light, to the lower state, represented by the Einstein coefficient for stimulated emission B_{21}. The emitted photon carries an energy, $E_{phot} = h\nu_{laser}$, equivalent to that of the laser radiation, where ν_{laser} is the frequency of the laser. For spontaneous emission, expressed by the Einstein coefficient for spontaneous emission, A_{21} [1/s], the

transition occurs to a lower level, which, in general, is not the initial level. Furthermore, the molecule in the upper state can get de-excited by intermolecular collisional quenching involving either two electronic states with a quenching rate Q_{21} [1/s] or only one electronic state with a quenching rate $Q_{rot,vib}$ [1/s]. Effects of predissociation denoted by P_2 are neglected here since they are negligible for the transition line pumped in the experiment. The Einstein B absorption coefficients are related to the corresponding rate constants b in units of 1/s by

$$b = \frac{BI_\nu}{c}, \tag{3.1}$$

where c is the speed of light and I_ν [W/(cm^2 cm^{-1})] is the spectral laser irradiance. The units of I_ν show that the physical quantity represented is an energy amount [J] per unit time [s] per unit area [cm^2] per unit wavenumber [cm^{-1}]. Note that the units for wavenumber are denoted throughout this chapter as cm^{-1} as compared to 1/cm. The units are not simplified to allow for a faster physical interpretation of the physical quantity. For now, I_ν is assumed as a simplification to be constant over the absorption line-shape. In contrast to Q, which is dependent on temperature, pressure, and background composition, the rate constants for emission and absorption are fixed quantities for each transition line. Assuming a simple two-level model (Eckbreth, 1996), the rate equations are given as

$$\begin{aligned} \frac{dN_1}{dt} &= -N_1 B_{12} + N_2(b_{21} + A_{21} + Q_{21}), \\ \frac{dN_2}{dt} &= N_1 B_{12} - N_2(b_{21} + A_{21} + Q_{21}) \end{aligned} \tag{3.2}$$

and lower and upper state population densities N_1 and N_2 can be written as a function of time during the laser pulse as

$$N_2(t) = \frac{b_{12} N_1^0}{r}(1 - \exp(-rt)), \tag{3.3}$$

$$r = b_{12} + b_{21} + A_{21} + Q_{21}, \tag{3.4}$$

where

$$N_1(t) + N_2(t) = N_1^0, \quad N_2(t=0) = 0. \tag{3.5}$$

For $t \gg 1/r$, the system reaches a steady state and the upper state population is

$$N_2 = \frac{b_{12} N_1^0}{r}. \tag{3.6}$$

The steady-state number density of molecules in the upper state can also be written as

$$N_2 = N_1^0 \frac{B_{12}}{B_{12} + B_{21}} \frac{1}{1 + \frac{I_\nu^{sat}}{I_\nu}}, \tag{3.7}$$

$$\tag{3.8}$$

where

$$I_\nu^{sat} = c \frac{A_{21} + Q_{21}}{B_{12} + B_{21}} \tag{3.9}$$

is the saturation spectral irradiance. The detected fluorescence signal power, F, is proportional to the product of the the absolute number of molecules in the upper state, $N_2 V$, and the downward transition rate constant, $A_{21} N_2$, and can be written as

$$\begin{aligned} F &= C A_{21} \delta V N_2 \\ &= C A_{21} \delta V N_1^0 \frac{B_{12}}{B_{12} + B_{21}} \frac{1}{1 + \frac{I_\nu^{sat}}{I_\nu}}, \end{aligned} \tag{3.10}$$

where C is a lumped constant containing the collection solid angle, and δV is the laser irradiated volume from which fluorescence is detected. The volume δV can be pictured as the intersection of the total light sheet irradiated volume and the conical region imaged onto the detector, e.g. one pixel of the camera. Light sheet attenuation effects

are discussed in Section 3.3 but neglected in this Section. Depending on the magnitude of I_ν^{sat} and I_ν, two operational regimes for a PLIF system can be distinguished. For $I_\nu \ll I_\nu^{sat}$, the last term in Eq. 3.10 can be approximated by I_ν. The fluorescence signal power is then proportional to the laser irradiance, and the system is operating in the linear regime. Note that in this case, F is proportional to $I_\nu \delta V$ and therefore independent of the light sheet thickness t. The irradiated volume δV is proportional to t since $\delta V = At$, where A is the projected area of δV. I_ν is proportional to $1/t$ as for a fixed light sheet height h and fixed laser power. The cross section area of the light sheet decreases linearly with t. The product $I_\nu \delta V$ is therefore independent of the thickness t. Since the detected fluorescence signal gets integrated over the thickness t, the spatial resolution of the PLIF system is limited by the light sheet thickness.

When reducing the light sheet height h, the volume δV from which fluorescence emerges is constant while I_ν increases proportional to $1/h$ for a constant magnification of the imaging system. This leads to a higher fluorescence signal detected and an increased signal-to-noise ratio as long as the noise is not proportional to I_ν. In the case where the noise arises mainly from elastic scattering processes, no improved signal-to-noise ratio can be expected, whereas the signal-to-noise ratio will improve in the case where the noise arises mainly from chemiluminescence, which is obviously independent of the laser irradiance. Nevertheless, there are limits in decreasing the light sheet height. If the light sheet height, is smaller than the field of view height the detected fluorescence power F does not increase for all pixels on the detector, since the so-called "wings" of the light sheet profile have a lower intensity.

In the case of $I_\nu \gg I_\nu^{sat}$, F becomes independent of I_ν and I_ν^{sat} and therefore independent of Q. This LIF technique is known as laser induced saturation fluorescence (LISF). The energy transfer into and out of the directly pumped levels is then controlled by the rates of laser absorption and stimulated emission. The saturation approach leads to a maximum fluorescence yield and, therefore, maximum species detectivity. However, it is often due to the magnitude of I_ν^{sat} challenging to achieve complete saturation over the entire light sheet plane. This is due to the spatial wings of the laser beam which result in lower intensities in the regions in the outer edges of

the light sheet. Furthermore, the condition $I_\nu \gg I_\nu^{sat}$ might not hold over the entire laser pulse duration. For the present study, saturation effects are not considered since $I_\nu \sim I_\nu^{sat}$ as discussed in Section 3.9. A more detailed discussion about LISF is found in Eckbreth (1996). The spectral distribution of the laser and absorption line are not included in this highly simplified fluorescence signal strength description, Eq. 3.10, and are discussed in the next Section.

3.2 Line shapes

Spectral line-shapes of the laser and the absorption lines have to be considered in order to determine how much of the laser energy actually goes into exciting the desired transition line. This is measured by the spectral overlap fraction Γ of the excited molecular transition line and the laser line. The spectral overlap fraction is also referred to as the spectral overlap integral or overlap term and describes the spectrally distributed interaction between the molecular transitions and laser radiation, as there exists a frequency spread of the absorption by the transition line and of the emission by the laser line. In the literature concerning this topic (Palma et al., 1998), this quantity is defined in several ways, sometimes termed g with dimensions of $1/cm^{-1}$. Here, the definition of Partridge and Laurendeau (1995) is followed and the overlap integral Γ is defined as a dimensionless quantity

$$\Gamma = \int_{-\infty}^{+\infty} Y_A(\nu) L_L(\nu)\, d\nu \tag{3.11}$$

where $Y_A(\nu)$ $[1/cm^{-1}]$ is the spectral line-shape function of the absorption line, which is normalized to unity, and $L_L(\nu)$ is the dimensionless spectral distribution function of the laser, normalized to the spectral full width half maximum (FWHM) $\Delta\nu_L$ of the laser:

$$\int_{-\infty}^{+\infty} Y_A(\nu) d\nu = 1, \tag{3.12}$$

$$\int_{-\infty}^{+\infty} L_L(\nu) d\nu = \Delta\nu_L. \tag{3.13}$$

The spectral line-shape function describes the absorption and emission strength as a function of wavelength since there exists a spread in frequency and the energy levels in atoms and molecules are not infinitely sharp. The overlap integral represents the fraction in energy of the laser line, which actually gets absorbed by a specific transition line.

3.2.1 Line shape of absorption line

This discussion is limited to the quantitative calculation of the absorption line-shape and the influence of two effects, temperature and pressure broadening. Effects such as natural line broadening are neglected as these effects are, in the present application, small compared to the ones considered.

3.2.1.1 Temperature broadening

The temperature broadening is caused by the thermal motion of the absorbing species in the gas and the resulting Doppler effect. The Doppler line-shape function is mathematically described as a Gaussian function and can be written (Eckbreth, 1996) in its normalized form as

$$Y_D(\nu) = \frac{c}{\nu_0}\sqrt{\frac{m_A}{2\pi kT}}\ \exp\left(-4\ln 2\frac{(\nu-\nu_0)^2}{\Delta\nu_D^2}\right), \tag{3.14}$$

where k is the Boltzmann constant, c the speed of light, m_A the molecular mass of the absorbing molecule, ν_{0A} the centerline transition frequency, and $\Delta\nu_D$ the transition width. The transition width (FWHM) is given by Fowles (1968) as

$$\Delta\nu_D = \frac{2\nu_0}{c}\sqrt{\frac{2\ln 2kT}{m_A}}. \tag{3.15}$$

3.2.1.2 Pressure broadening

Pressure broadening occurs when the absorption process of the molecule is interrupted by collisions with other molecules or atoms. These collisions can occur with different species than the absorbing molecule or the same species, a process called

self-broadening. The spread in the power spectrum or spread in frequency $\Delta\nu_C$ of the finite wave train absorbed by the molecule is inversely proportional to the average time τ between collisions of molecules, $\Delta\nu_C = (\pi\tau)^{-1}$. The collision-broadened line-shape is given by a Lorentzian, Kessler et al. (1993), as

$$Y_C(\nu) = \frac{\Delta\nu_C}{2\pi} \frac{1}{(\nu - \nu_0)^2 + (\Delta\nu_C/2)^2}, \tag{3.16}$$

where $\Delta\nu_C$ is the collision width. The collision width is temperature and pressure dependent and, furthermore, specific to each collisional partner. The collisional line width is calculated by considering the sum of the contributions of all species present in the background gas and self-broadening. The contribution of each species can be modeled to be proportional to the product of the partial pressure P_i and the collisional broadening coefficient, γ_i, of each species i, (Rea et al., 1987). The total collisional line width can be expressed as

$$\Delta\nu_C \; = \sum_i 2\,\gamma_i P_i \; . \tag{3.17}$$

The collisional broadening coefficient of intermediate combustion species like OH has been measured for a variety of broadening species from absorption data obtained in shock tubes by Rea et al. (1989), water vapor discharge cells by Shirinzadeh et al. (1985), or from flat-flame burners. The temperature dependence of the collisional broadening coefficient can be described (Rea et al., 1987) by

$$2\,\gamma \; = \; 2\,\gamma_0 \left(\frac{T}{T_{ref}}\right)^n , \tag{3.18}$$

where γ_0 is the value of the collisional broadening coefficient measured at the reference temperature T_{ref}. The exponent n is determined from experimental fits for each species and varies between 0.1 and -1.0. Besides the vibrational band dependence, γ_0 can be a function of the rotational level of the ground state. For example, the collisional broadening coefficient of the OH radical in the (0,0) band at 2000 K varies for N_2 as a colliding species from 0.051 $cm^{-1}atm^{-1}$ for a rotational quantum number

J of 0.5 to 0.038 $cm^{-1}atm^{-1}$ for J = 9.5 (Rea et al., 1987). However, γ seems to be fairly independent ($2\gamma \approx 0.034$ $cm^{-1}atm^{-1}$) of the quantum number for Ar. Besides the collision-induced broadening, a collision-induced shift ν_s of the absorption line can be observed. This shift can be expressed as a fraction of the collisional width ν_C:

$$\nu_s = \beta \nu_C, \tag{3.19}$$

where β is determined experimentally and varies between 0.1 and 0.3 (Shirinzadeh et al., 1985). The shift of the centerline frequency can be either negative or positive depending on the colliding species. Data for the major collision species in combustion research are available for the (0,0) and (1,0) band of the OH radical in Rea et al. (1987), Rea et al. (1989), and Kessler et al. (1993).

3.2.1.3 The Voigt profile

If temperature and pressure broadening are both significant, a line-shape combination of Gaussian and Lorentzian is used, the so-called Voigt profile $V(a,x)$. The absorption line-shape function $\gamma(\nu)$ is given by

$$\gamma(\nu) = 2\sqrt{\frac{\ln 2}{\pi}}\,\frac{V(a,x)}{\Delta\nu_D} \tag{3.20}$$

and the Voigt profile $V(a,x)$ is

$$V(a,x) \equiv \frac{a}{\pi}\int_{-\infty}^{\infty}\frac{\exp(-y^2)}{a^2+(x-y)^2}\,dy\,, \tag{3.21}$$

where the parameter, x and a are given by

$$x \equiv 2\sqrt{\ln 2}\,\frac{\nu-\nu_0}{\Delta\nu_D}\,, \tag{3.22}$$

$$a \equiv \sqrt{\ln 2}\,\frac{\Delta\nu_C}{\Delta\nu_D}\,. \tag{3.23}$$

The parameter a is a measurement of the contribution by the two broadening processes and can be evaluated with Eq. 3.15 and 3.17.

3.2.2 Determination of the spectral line-shape of the laser

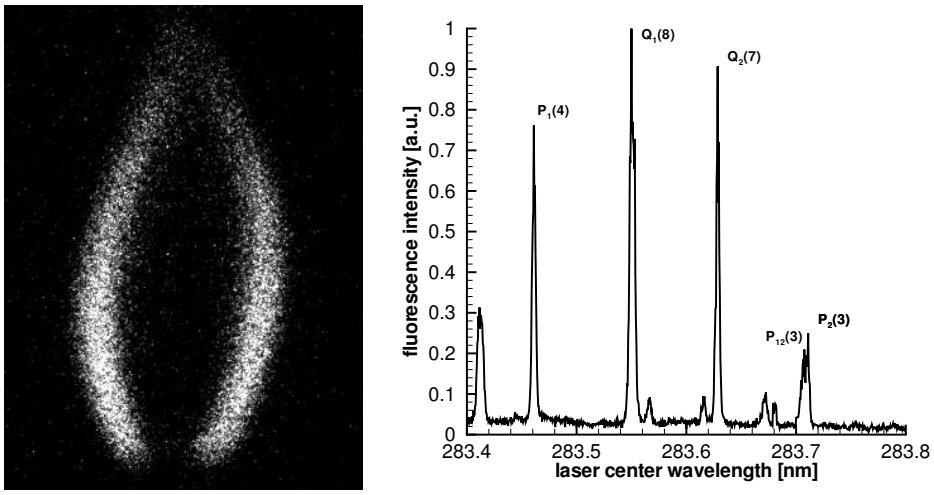

a) b)

Figure 3.2: a) PLIF image of test-flame. Image height: 75 mm. b) Fluorescence intensity as a function of the center excitation wavelength of the dye laser. The fluorescence is averaged over the entire field of view.

The spectral laser line-shape can be determined from the excitation spectrum, which is the fluorescence intensity occurring as a function of the center excitation wavelength ν_{0L} of the laser. The fluorescence intensity is thereby integrated over a wide range of wavelengths, as a bandpass filter of 10 nm FWHM is placed in front of the detector, which is the ICCD camera in this setup. Note that the excitation spectrum is fundamentally different from the fluorescence spectrum, which describes the fluorescence intensity as a function of wavelength for a fixed excitation frequency. For the determination of the fluorescence spectrum, a spectrometer is necessary. An experimentally obtained excitation spectrum over a spectral range including several transition lines is shown in Fig. 3.2. The dye laser is scanned in frequency over an absorption line and the total fluorescence from a test-flame is detected. A highly resolved excitation spectrum of an isolated transition line is ideal for gaining quantitative information about the laser line-shape if the line-shape of the excited transition

line is known beforehand. An experimentally obtained excitation spectrum of the $P_1(4)$ absorption line of the (1,0) band of the OH radical in the vicinity of 283.4 nm is shown in Fig. 3.3. In this measurement the wavelength increment of the dye laser is set to its minimum value of $5{\cdot}10^{-4}$nm ($\approx$ 1.86 GHz). The fluorescence was detected by the ICCD camera broad-band through a bandpass filter with a centerline of 313 nm and 10 nm FWHM. A source of error is the lack of complete stability of the flame geometry. Due to small movements of the flame, the cross sectional area of the reaction zone with the light sheet changes and thus introduces noise to the excitation spectrum measurement. In order to minimize this and improve the signal-to-noise ratio, the excitation spectrum of the $P_1(4)$ transition line is averaged over 10 shots for each wavelength. The obtained excitation spectrum $I(\nu_{0L})$ is proportional to the convolution of the absorption line and the laser line,

$$I(\nu_{0L}) = C L_L(\nu_{0L}, \nu) * Y_A = C \int_{-\infty}^{\infty} L_L(\nu_{0L}, \nu) Y_A(\nu) d\nu \,, \tag{3.24}$$

where C is necessary overall scaling constant, since the detected fluorescence signal is not measured in absolute units so that the convolution integral is in arbitrary units.

There are two ways to determine the spectral line-shape of the laser from the excitation spectrum. Assuming a priori an analytical expression for the spectral laser line-shape, only the parameters in this analytical expression need to be determined. For the Gaussian line-shape assumed here, the Gaussian width $\Delta\nu_L$ is the only parameter to be evaluated. The laser spectral profile can, following Eq. 3.14, be written as

$$L_L(\nu) = \sqrt{\frac{4\ln 2}{\pi}} \exp\left(-4\,\ln(2)\left(\frac{\nu - \nu_{0L}}{\Delta\nu_L}\right)^2\right), \tag{3.25}$$

where ν_{0L} is the centerline frequency of the spectral laser profile. The laser line-shape is normalized as defined in Eq. 3.13. The line-shape of the $P_1(4)$ absorption line $g_{abs}(\nu)$ is approximated as a Voigt profile as discussed in Section 3.2.1.3 with estimated values for the temperature and collisional broadening coefficients based on the major species present in the test-flame. The absorption line-shape parameters for

H_2-air flames at atmospheric conditions can also be taken from the literature (Kessler et al., 1993). Once the absorption line-shape in known, Eq. 3.24 can be evaluated and $\Delta\nu_L$ determined by a least-squares fit to the experimentally obtained data points.

A different approach to determining the laser line-shape is to assume a priori no analytical expression for the spectral laser profile, but fit a Voigt profile $\mathrm{V}_{exp}(\nu_{0L})$ to the experimentally obtained excitation spectrum $I(\nu_{0L})$. From this, one can obtain an expression for $\mathrm{L}_L(\nu)$ by Fourier transforming Eq. 3.24:

$$\begin{aligned}
&\int_{-\infty}^{\infty} \exp(-ik\nu_{0L}) I(\nu_{0L})\, d\nu_{0L} \qquad (3.26)\\
&= \int_{-\infty}^{\infty}\int_{-\infty}^{\infty} \exp(-ik\nu_{0L}) L_L(\nu_{0L}-\nu)\, Y_A(\nu)\, d\nu\, d\nu_{0L}\\
&= \int_{-\infty}^{\infty}\int_{-\infty}^{\infty} \exp(-ik(\nu+x)) L_L(x)\, Y_A(\nu)\, d\nu\, dx\\
&= \int_{-\infty}^{\infty} \exp(-ik\nu)\, L_L(x)\, d\nu \int_{-\infty}^{\infty} \exp(-ik\nu)\, Y_A(\nu)\, dx.
\end{aligned}$$

Equation. 3.26 can be solved numerically for L_L by an inverse Fourier transformation. In the present study, the first approach is followed.

In order to determine the line-shape parameters at the test-flame conditions, the temperature and background composition have to be specified. The adiabatic flame temperature for a stoichiometric H_2-air flame is calculated to be 2340K. Since it is a non-premixed diffusion flame, there are regions in the flame with temperatures much lower than the adiabatic flame temperature. The temperature in the regions where the OH radical occurs in detectable amounts is assumed to be fairly close to the adiabatic flame temperature. This is seen in an experimental and computational investigation of the OH radical field in a two-dimensional, axisymmetric, laminar, methane-air diffusion flame by Smooke et al. (1992). The adiabatic flame temperature is calculated to be 2220 K. In the region in which the OH radical was found in amounts larger than 50% of the peak mole fraction, the temperature was calculated to be between

Species	partial pressure (kPa)
N_2	66.0
H_2O	31.4
H_2	1.3
OH	0.6
O_2	0.4
NO	0.2

Table 3.1: Partial pressure of major species from equilibrium calculation for stoichiometric H_2-air flame at 100kPa total pressure.

approximately 1900 and 2050 K, which is 170 to 320 K below the adiabatic flame temperature. Non-intrusive flame temperature measurements 10 mm above a 25-mm diameter burner surface in a premixed stoichiometric H_2-air flame (Kessler et al., 1993) give results in the order of 2050 K. This temperature is about 300 K below the adiabatic flame temperature. This difference can be explained by the heat transfer to the large burner surface in that case. In the present study, a H_2-air diffusion flame is used for the calibration. The average flame temperature in the region where OH radicals are detected is assumed to be 2100 K, which is 240 K below the adiabatic flame temperature. This simplification does not take into account that there is OH fluorescence, even though in small amounts, arising from a region colder than this temperature. In this region the Doppler line width $\Delta\nu_D$ is correspondingly smaller. Note that $\Delta\nu_D$ is proportional to the square root of the temperature and the error introduced by the small uncertainty in the temperature insignificant.

The Doppler line width $\Delta\nu_D$ of the absorption line was calculated from the temperature (T = 2100 K) and the molecular weight of the OH radical (m_{OH} = 17.007 amu), Eq. 3.15, to be 0.28 cm^{-1}. The partial pressures of the major species present in the diffusion flame are calculated (Reynolds, 1986) by assuming chemical equilibrium and are given in Table 3.1.

The collision width can be evaluated based on the values given in Table 3.1 and Eq. 3.17. Only the major species H_2O and N_2 are considered as colliding species. Broadening coefficients are available for only a limited number of species in the literature (Bessler et al., 2003). The vibrational band dependence in the OH system

Species	2γ ($cm^{-1}atm^{-1}$)	n
N2	$0.043\ _{T=2000K}$	0.83
H2O	$0.13\ _{T=2370K}$	0.66
CO2	$0.035\ _{T=2290K}$	1.2
Ar	$0.031_{T=2000K}$	0.80

Table 3.2: Values for collisional broadening coefficient for several species of interest. The values for 2γ and the temperature exponent n are taken from Shirinzadeh et al. (1985) and Rea et al. (1987) for a rotational level J = 5.5 for the (0,0) band.

	$2\gamma(N_2)$	$2\gamma(H_2O)$	$\Delta(\nu_C)$ $[1/cm]$
$P_1(4)$	0.042	0.124	0.065

Table 3.3: Calculated values for 2γ [cm^{-1} atm $^{-1}$] for $P_1(4)$ transition line and total collision width [GHz] for atmospheric H_2-air flame.

for the species H_2O and N_2 is rather weak (Kessler et al., 1993) so the values for the (0,0) band can be used as a good approximation for the (1,0) band, the case studied here. The results for calculated collisional width are given in Table 3.3. The transition lines considered in the test-flame are mainly affected by temperature broadening. The Voigt a-parameter is evaluated to be

$$\begin{aligned} \frac{\Delta\nu_C}{\Delta\nu_D} &= 0.234, \\ a(P_1(4)) &= 0.195. \end{aligned} \tag{3.27}$$

The calculated values are in good agreement with a best fit Voigt profile to the directly measured (Kessler et al., 1993) absorption profile of the $P_1(7)$ transition in the (1,0) band near 283 nm, with a reported a-parameter value of a = 0.19.

The experimental data were fitted by the least-squares method to the calculated excitation spectrum, Eq. 3.24, by optimizing three parameters: The Gaussian width of the laser line $\Delta\nu_L$, an overall scaling factor C, in order to match the arbitrary units of the experimental data to the arbitrary units of I_ν, Eq. 3.24, and a wavelength shift parameter $\Delta\nu_{fit}$. Since the dye laser is not calibrated to absolute wavelength, the calculated absorption line and, therefore, the excitation spectrum, will be shifted relative to the nominal wavelength given by the dye laser readout. The wavelength shift parameter $\Delta\nu_{fit}$ takes this into account. The analytical expression for the laser

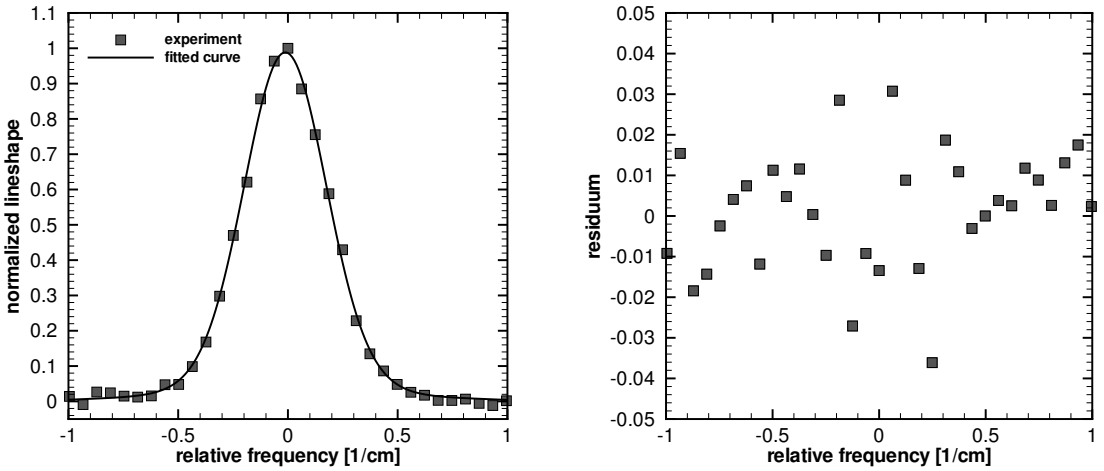

a) b)

Figure 3.3: a) Experimentally obtained excitation spectrum of the $P_1(4)$ (1,0) line of the OH radical near 284 nm from atmospheric H_2-air test-flame. Each data point is obtained by integrating the total intensity and averaging over ten individual images obtained for fixed excitation wavelength. The fitted curve shows the predicted excitation profile based on the laser line parameters determined. Arbitrary units on ordinate, normalized and centered to maximum experimental fluorescence intensity. b) Residuum of fitted curve.

line spectral profile is

$$L_L(\nu - \nu_{0L}, \Delta\nu_L, C, \Delta\nu_{fit}) = C\sqrt{\frac{4\ln 2}{\pi}}\ \exp\left(4\ \ln(2)\left(\frac{\nu - \nu_{0L} - \Delta\nu_{fit}}{\Delta\nu_L}\right)^2\right). \tag{3.28}$$

For the absorption line profile the expression for $\gamma(\nu)$ from Eq. 3.21 was used with the parameters shown in Eq. 3.27. The objective function E to be minimized in the least-squares fit can thus be written as

$$\begin{aligned} & E(\Delta\nu_L, C, \Delta\nu_{fit}) \\ & = \sum_{p=1}^{n}\left(\int_{-\infty}^{\infty} L_L(\nu - \nu_p, \Delta\nu_L, C, \Delta\nu_f it)\cdot\gamma_{abs}(\nu)\,d\nu\ -\ M(\nu_p)\right)^2 \end{aligned} \tag{3.29}$$

$M(\nu_p)$ is the measured fluorescence for the data point p, which corresponds to a wavelength of ν_p as taken from the dye laser display. The experimentally obtained

profile was normalized and and shifted to the maximum, see Fig. 3.3a squares. The best fit was found for $\Delta\nu_L$=0.305 cm^{-1}, $\Delta\nu_{fit}$ =-0.012 cm^{-1}, and C =0.985 and is shown in Fig. 3.3a as a solid line. The corresponding residuum, which describes the normalized difference in the line-shape between the fitted values and experimentally obtained values, was at the maximum 4% and is shown in Fig. 3.3b. The laser line width is for flame conditions close to the line width of the absorption line of 0.32 cm^{-1}, Fig. 3.4. For the test-flame conditions, the overlap integral, Eq. 3.11, was determined to be Γ=0.60. The assumption of a constant spectral irradiance over the absorption line used sometimes in quantitative PLIF analysis does not hold true in this case. In the proceeding analysis, the spectrally resolved interaction between the absorption and laser line has to be accounted for. The excitation spectrum is also used to calibrate the laser wavelength, which is based on the known centerline frequency of a specific absorption line. The excitation spectrum can be obtained with the simulation tool for spectral analysis, LIFBASE (Luque and Crosley, 1999). The simulated excitation spectrum was then compared with the experimental one to evaluate the effective wavelength output corresponding to a specific grating position of the tunable dye laser. The grating position is the quantity set on the laser control unit, which determines the output wavelength. The calibration process is described in detail Pintgen (2000). The calibration process is not affected by the spectral interaction since the maximum in the convolution integral occurs when the absorption line center coincides with the centerline of the laser line, regardless of the line width of both lines. The absorption line-shapes at conditions occurring behind detonation fronts and their implications for the overlap integral and PLIF signal are discussed in Section 3.6.

3.3 Absorption

The effect of light sheet energy attenuation by absorption can be divided into absorption by the distinct transition lines and broadband absorption arising from species with very dense and overlapping transition lines. The absorption by distinct transition

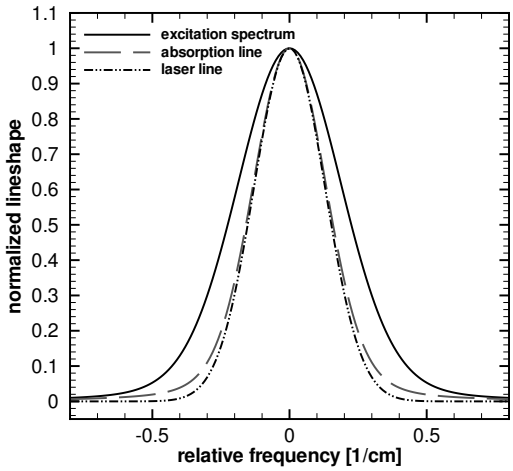

Figure 3.4: Comparison of the fitted excitation spectrum (convolution), the absorption line-shape and the laser line-shape, all normalized to their maximum, for the conditions in the atmospheric H_2-air-flame.

lines of the OH radical and broadband absorption by H_2O and CO_2 are considered. The Beer-Lambert law relates the absorption of radiation to the properties of the material the light is traveling through.

3.3.1 Beer-Lambert law

When monochromatic radiation of frequency ν and incident intensity I_0 passes through an absorbing gas of path length L, the transmitted intensity I_t can, according to the Beer-Lambert law, be written as

$$I_t = I_0 \exp\left(-\alpha(\nu)\right), \tag{3.30}$$

where α is the absorbance, defined as the integral over the path length L of the product of spectral line intensity S [cm/molecule] (Section 3.3.2), number density n of the absorbing species [molecules/cm^3], and spectral line function $Y_A(\nu)$ [cm], Eq. 3.13:

$$\alpha(\nu) = \int_0^L S\, n\, Y_A(\nu)\; d\nu. \tag{3.31}$$

In general, S, n, and $Y_A(\nu)$ depend on the thermodynamical properties and gas composition. If the medium is assumed uniform, Eq. 3.31 simplifies to

$$\alpha(\nu) = S\, n\, Y_A(\nu) L = k(\nu) L, \tag{3.32}$$

where k with units of inverse length is often referred to as the absorption coefficient. Yet another commonly used quantity is the spectral absorption cross section $\sigma(\nu)$ [cm^2/molecule], which describes, from the view point of geometrical optics the area being blocked by each absorbing molecule. The cross section is related to the absorption coefficient through the concentration of the absorbing species n by

$$k(\nu) = \sigma(\nu) n. \tag{3.33}$$

3.3.2 Spectral line intensity

The spectral line intensity for two states of a vibrational-rotational system is defined (Penner, 1959) as

$$S \;=\; \frac{n''}{n} \left\{ 1 - \frac{n' g''}{g' n''} \right\} B_{12} \frac{h\nu_0}{c}, \tag{3.34}$$

and for local thermodynamic equilibrium as

$$S(T) \;=\; f_B(T) \left\{ 1 - \exp\left(-c_2 \frac{\nu_0}{T} \right) \right\} B_{12} \frac{h\nu_0}{c}, \tag{3.35}$$

where f_B is the Boltzmann fraction, c_2 [cm K] is the second radiative constant defined as $c_2 = hc/k$, h is the Planck constant, B_{12} is the Einstein coefficient for induced absorption and ν_0 [1/cm] is the transition frequency between the two states. The populations of the lower and upper states, n'' and n', respectively, follow at a temperature T for local thermodynamic equilibrium Boltzmann statistics. The statistical weights of the states are denoted by g. Boltzmann's formula relates the ratio of the numbers n_1 and n_2 of molecules occupying the two energy states E_1 and E_2 [1/cm] in

thermodynamic equilibrium at a temperature T by

$$\frac{n_1}{n_2} = \frac{g_1}{g_2} \exp\left(-c_2 \frac{(E_1 - E_2)}{T}\right) . \tag{3.36}$$

Therefore, the Boltzmann fraction of the lower level, describing the fraction of molecules occupying that level, can be written as

$$f_B = \frac{g'' \exp\left(-c_2 \frac{E''}{T}\right)}{\sum_{i=0}^{\infty} g_i \exp\left(-c_2 \frac{E_i}{T}\right)} = \frac{g'' \exp\left(-c_2 \frac{E''}{T}\right)}{Q(T)}, \tag{3.37}$$

where the sum is taken over all possible states, $Q(T)$ is referred to as the partition function or state sum, and E'' is the lower state energy of the transition. For the numerical evaluation of Eq. 3.37, $Q(T)$ is taken from the spectroscopic database *HITRAN* (Rothman et al., 2003), which lists $Q(T)$ for the OH radical up to 3000 K in 1 K increments in T. An example evaluation for f_B for the $Q_2(8)$ transition line (E''=1368.7216 cm^{-1}) of the OH radical is shown in Fig. 3.5. The temperature dependence of f_B for this transition line between 1000 and 2800 K is rather weak as it changes by only 16%. The second term in Eq. 3.35 describes the effects of stimulated

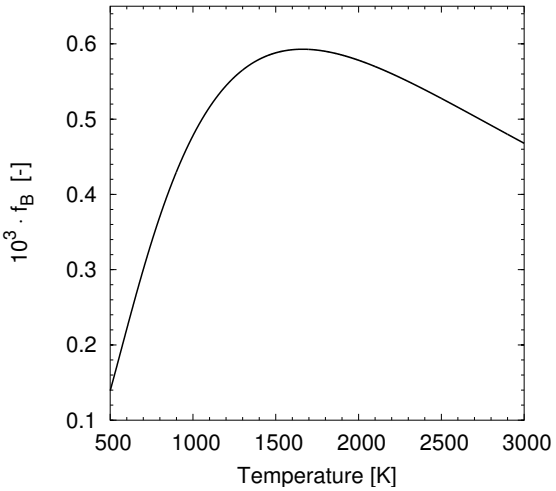

Figure 3.5: Boltzmann fraction f_B for $Q_2(8)$ transition line of OH radical.

emission, which are minor for the regime of the PLIF system in the experiment

considered here. The temperature dependence of the line strength arises in this case mainly from the temperature dependent Boltzmann fraction, since the Einstein B_{12} coefficient is independent of temperature. The line intensity can be written in other commonly used units S' [cm^{-2}/atm] by using the ideal gas law, $p = nkT$,

$$S'(T) = n_L \frac{T_0}{T} S(T), \tag{3.38}$$

where n_L [molecules/cm] is the Loschmidt constant and $T_0 = 273.15$ K. Using Eq. 3.35, the knowledge of the line strength S for a reference temperature T_{ref} enables the calculation of S at any temperature T via

$$S(T) = S(T_{ref}) \frac{Q(T_{ref})}{Q(T)} \frac{\exp\left(-c_2 \dfrac{E''}{T}\right)}{\exp\left(-c_2 \dfrac{E''}{T_{ref}}\right)} \frac{1 - \exp\left(-c_2 \dfrac{\nu_0}{T}\right)}{1 - \exp\left(-c_2 \dfrac{\nu_0}{T_{ref}}\right)}. \tag{3.39}$$

The line strength for the transition lines of the OH radical is tabulated for a reference temperature of $T_{ref} = 293$ K in the spectroscopic database *HITRAN* (Rothman et al., 2003) which, together with $Q(T)$ and Eq. 3.39, enables the numerical evaluation of $S(T)$. The self-absorption of the light sheet intensity by the OH transition lines is calculated in this fashion together with Eq. 3.30 and 3.31.

In the LIF model subsequently discussed, broadband absorption by H_2O and CO_2 is considered. Limited data for broadband absorption of UV light by H_2O and CO_2 at elevated temperatures was available. The ultraviolet absorption spectrum of CO_2 shifts significantly to longer wavelengths with increasing temperature (Jensen et al., 1997). Hildenbrandt and Schulz (2001) and Schulz et al. (2002b) report spectrally resolved UV absorption cross-sections between 190 and 320 nm in shock-heated CO_2 and H_2O between 880 and 3050 K. Schulz et al. (2002a) report a fit to the temperature-dependent absorption spectra measured in the form of an analytical expression and enabling the estimation of the absorption cross section. A more detailed description of the model is found in Appendix A. The light sheet attenuation is evaluated by the analytical expression given in Schulz et al. (2002a) σ and using Eq. 3.32 and 3.33.

3.4 Quenching

To be able to quantitatively link the fluorescence signal strength and the probed molecule concentration through Eq. 3.10, the effects of collisional quenching and vibrational energy transfer have to be considered. There are LIF techniques which avoid the effects of quenching on the fluorescence signal strength like LISF or laser induced predissociation fluorescence (LIPF). However, the PLIF system used in the present experiment is operating in the linear regime and one has to account for quenching effects. The quenching rate constant Q for an excited molecule is a function of temperature and pressure and is furthermore dependent on the background composition. Since these parameters are sometimes difficult to determine and strongly vary within the probed measurement volume, the determination of Q and correction for quenching effects is often difficult when operating in the linear LIF regime.

The quenching rate also depends on the rotational and vibrational level of the excited molecule. Rotational-level-dependent quenching rate data for the OH radical are available only for a limited number of colliders and rotational states (Jeffries et al., 1988, Köllner et al., 1990, Beaud et al., 1998, Stepowski and Cottereau, 1981). Rotational energy transfer (RET), a process faster than vibrational energy transfer (VET) for the upper state of the OH radical, redistributes the rotational state population within the vibronic state. Eventually, the population within the vibronic state would equilibrate and the rotational population distribution would reflect the ambient temperature. Therefore, this process is also termed thermalization and the equilibrium state is termed the thermal distribution. Due to the population of the one specific rotational level excited during the laser pulse and the constant VET and quenching, the actual rotational distribution within the vibronic state might be different from the thermal distribution (Crosley, 1989).

This possibility depends on the timescales the depletion process of the vibronic state and the redistribution within the vibronic state acts on. The depletion can take place by quenching of the vibronic state and by vibrational energy transfer, as transitions to other vibrational level, within the same electronic level take place.

rotational level	rate constants [10^8 1/s]		
	Q_1	v_{10}	k_L
$N' = 4$	8.9	5.0	57
$N' = 12$	6.0	1.9	30

Table 3.4: Quenching (Q_1), VET (v_{10}) and total RET (k_L) rate constants for the OH radical in an atmospheric pressure CH_4-air flame measured directly after a 1 ps excitation pulse of the ($v' = 1$, $N' = 4, 12$) level, maximum error 8%, Beaud et al. (1998).

The corresponding timescales are the quenching rate coefficient Q and the VET-rate coefficient v. Re-distribution within the rotational level is characterized by the RET rate coefficient k. If the redistribution process is taking place much faster than the depletion process, a thermally equilibrated state can be assumed.

No data on the rate coefficient were available for the thermodynamic conditions which are present behind the detonation fronts studied. The data available (Beaud et al., 1998) are for atmospheric pressure environments, whereas spectrally and pico-second time resolved measurements of the fluorescence decay are necessary to determine the rate coefficients. The pressure behind the investigated detonation fronts is on the order of 4 bar and are therefore four times higher than the pressure for the data obtained by Beaud et al. (1998), who investigated a CH_4-air flame. The background composition is apart from the CO_2 and CO present in the case of the CH_4-air flame similar to the one behind the detonation front. The rotational-level-dependent numbers given here are nevertheless only an estimate for the ratio of the rate constants occurring for the conditions behind the detonation front (Table 3.4). The RET is found approximately one order of magnitude faster than the VET and quenching. Note that the numbers given in Table 3.4 are measured directly after the laser excitation pulse and are not the equilibrium rate constants, which were found to be in between the values given for $N' = 4$ and $N' = 12$. The exact value of the overall quenching rate Q occurring in the experiment depends on the interaction between the quenching rate for each rotational level and RET and the VET rate constants, which are not available for the majority of states and colliding species. This would require a dynamic model describing the energy transfer at experimental conditions, as

done for flames (Monkhouse and Selle, 1998). Spontaneous emission can be neglected as a depletion process in this context as it takes place on a much slower timescale ($A_{21} \sim 2 \cdot 10^5$ 1/s). The rate constant b (corresponding to Einstein B absorption coefficient) for population of the specific rotational level during the laser pulse was estimated to be $b \sim 2 \cdot 10^7$ 1/s. Therefore a light sheet height of 50 mm, a light sheet thickness of 0.3 mm, a laser pulse length of 20 ns, and a laser pulse energy of 5 mJ was assumed. The population of the vibronic state is therefore approximately two orders of magnitude slower than the redistribution within the vibronic state.

From the considerations and estimation above, it seems a reasonable simplification to assume thermalization in the vibronic state for the evaluation of Q in the following. Based on the Boltzmann distribution within a vibronic state, the thermally averaged quenching rate for the OH radical can be written as (Paul, 1994)

$$Q = \frac{P}{k_b T} \langle u_{OH} \rangle \sum_p \chi_p (1 + m_{OH}/m_p)^{1/2} \langle\langle \sigma_p(T) \rangle\rangle \,, \tag{3.40}$$

where the summation is taken over all perturbing species p, χ_p is the mole fraction of the perturber p, $\langle u_{OH} \rangle$ is the average velocity of the OH radical given as

$$\langle u_{OH} \rangle = \left(\frac{8 k_B T}{\pi m_{OH}} \right)^{1/2} \tag{3.41}$$

m_{OH} and m_p are the mass of the OH molecule and the perturber, respectively, and $\langle\langle \sigma_p(T) \rangle\rangle$ is the thermally averaged quenching cross section given as

$$\langle\langle \sigma_p(T) \rangle\rangle = \int_0^\infty f_B(T, N) \langle\langle \sigma_{pN}(T) \rangle\rangle dN \,, \tag{3.42}$$

where N is the rotational quantum number and $\langle\langle \sigma_{pN}(T) \rangle\rangle$ is the cross section for the perturber p and a rotational quantum number of N. Two models from the literature, Paul (1994) and Tamura et al. (1998), are used to evaluate the quenching cross sections $\langle\langle \sigma_p(T) \rangle\rangle$ (Appendix B). The models together cover at least 99% of the perturber species present in the background. Composition and conditions behind the

investigated detonation waves were calculated from a one-dimensional ZND model. Experimentally measured quenching cross sections show reasonable agreement with both models as explained in detail in Appendix B.

3.5 PLIF Model

We use a simple non-transient three-level LIF model to describe in quantitative terms the fluorescence signal observed. It is based on the model by Bessler et al. (2003) used for nitric oxide LIF spectra. Models including more levels, e.g. Allen et al. (1995), often require detailed knowledge regarding rate processes, which are at this point in time, not available for the regime the PLIF system operates in the experiment.

3.5.1 Three-level model

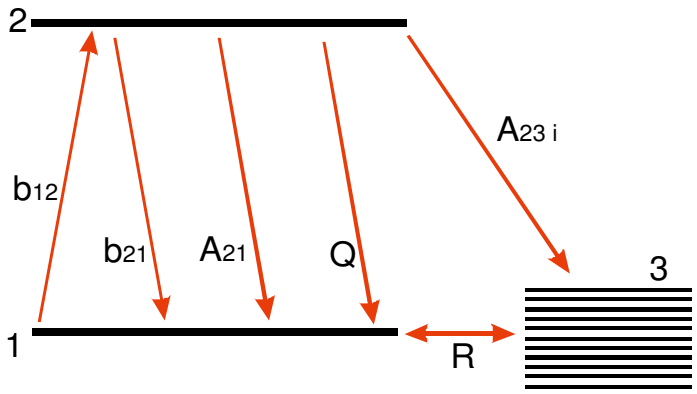

Figure 3.6: Three-level diagram showing the energy levels and rate coefficients considered in the fluorescence model.

The three-level model, Fig. 3.6, assumes equilibrium population of the laser coupled ground state 1. The ground state RET rate constant R between level 1 and all other levels in the electronic ground states, level 3, is supposed to be fast. The fluorescence emission occurs from a single laser coupled upper state, level 2, to all possible rotational and vibrational levels in the electronic ground state, and is expressed by the Einstein coefficient for spontaneous emission A_{23i}. Levels 1 and 2 are coupled in the upward direction via the rate constant for absorption, b_{12}, and in the

downward direction via the rate constant for stimulated and spontaneous emission, b_{21} and A_{21}, respectively, and the quenching rate constant Q. Predissociation processes occur significantly for the OH radical in the v'=3 level (Andresen et al., 1988), but are neglected for the v'=1 level employed here. Since photo-dissociation processes are also neglected, quenching is the only non-radiative transition from the excited upper state. Solving the steady-state rate equations system (Eq. 3.2) in the linear regime for the system considered (Eckbreth, 1996), the fluorescence intensity detected from one single pumped transition can be written as

$$F \sim f_B \; \Gamma \; I_\nu^0 \; I_b \; N_{OH} \; B \; \frac{1}{Q} \; \sum_i \; A_i. \tag{3.43}$$

Therefore, f_B is the Boltzmann fraction of OH molecules in the ground state (Section 3.3.2), Γ is the dimensionless overlap integral (Section 3.2), I_ν^0 [W/(cm^{2}cm^{-1})] is the normalized spectral laser irradiance (Section 3.1), I_b is a dimensionless factor accounting for the light sheet energy broad-band absorption along the direction the light sheet is traveling in, N_{OH} [1/cm^3] is the number density of OH radicals, B [m^3/Js^2] and A_i [1/s] the Einstein coefficients (Section 3.1) and Q [1/s] the quenching rate (Section 3.4). The total fluorescence is calculated by looping over all transitions with transition energies in the vicinity of the excitation wave number, calculating F via Eq. 3.43, and adding up the individual contributions. Some factors in Eq. 3.43 depend on the background composition and thermodynamic conditions. The Boltzmann factor is purely dependent on the temperature T. Γ is due to the considered temperature and pressure broadening a function of T, pressure p, the background composition and the spectral distribution function of the laser. The quenching rate Q as modeled here is determined by the temperature, pressure, and background composition. In order to take into account light sheet energy absorption, the thermodynamic conditions and background composition have to be known as a function of distance along the light sheet. Given these quantities, the model predicts the one-dimensional fluorescence intensity distribution that would be observed. Note that it is not possible to calculate the OH number density distribution from the experimentally measured in-

tensity distribution without making the assumptions. To do this, a code based on a one-dimensional ZND model (Shepherd, 1986) is used to calculate the species mole fractions, temperature, and pressure as a function of distance behind the shock front (Section 1.1). The input parameters to the steady-state ZND code are the leading shock velocity and the mixture composition together with the initial conditions for temperature and pressure.

3.5.2 Implementation

The CJ detonation velocity was calculated using the `STANJAN` thermodynamic equilibrium code, and the results of the ZND code containing temperature, pressure, and species mole fractions were stored in a text file. The results are given as data points in approximately 0.02 mm increments behind the leading shock wave. The variables for the quenching rate model and line broadening parameters from the literature were stored in ASCII files, as well as the spectroscopic data provided by the HITRAN database (Rothman et al., 2003). This simplifies changing or adding of model parameters and species. Computationally intensive calculations like the numerical evaluation of integrals occurring (e.g., for the evaluation of the Voigt profile) were performed in `OCTAVE` (Eaton, 1998), a high-level language compatible with `MATLAB`. The main program, written in `PERL`, reads in data from the ZND results file, and the spectroscopic database files, and the parameter files derived from the literature. Based on this, a command sequence is created for each step and passed on to `OCTAVE`, which evaluates the predicted fluorescence intensity. The spectral distribution of the laser intensity was discretized and represented by 200 points equally spaced over 1 cm^{-1}. The product of Γ, I_ν^0, and I_B was evaluated and numerically evaluated stepwise. The spectral profile of the laser, modified to account for absorption, is returned by `OCTAVE` after each step and used as an input for the next step. The absorption by all discrete OH absorption lines in the vicinity of the laser line is considered, which can lead to an asymmetric spectral profile of the laser.

The implementation is far from being optimized, but the run time is fast enough

for the cases evaluated. A calculation of a fluorescence signal distribution based on 1000 spatial points takes approximately 30 minutes on a 1.5 GHz Pentium CPU.

3.6 Application of model to detonations

The one-dimensional fluorescence intensity distribution was calculated for detonations in stoichiometric H_2-O_2, H_2-N_2O, and hydrocarbon-oxygen mixtures diluted with Ar or N_2. The initial temperature and pressure for all mixtures considered was 300 K and 20 kPa, respectively. The case considered in most detail is a detonation in a $2H_2$-O_2-$5.5N_2$ mixture at the CJ velocity of 1799 m/s using the detailed chemistry mechanism by Konnov (2000) for the ZND calculation (Fig 3.7a). The model predicts the fluorescence intensity in arbitrary units and in order to compare the expected PLIF intensity with the OH number density, the fluorescence intensity is normalized to the peak OH number density (Fig. 3.7b). The predicted fluorescence intensity F_{pred} shows, as does the OH number density $N(\mathrm{OH})$, a sharp rise at the end of the induction zone, i.e., the region of radical chain reaction. The maximum of F_{pred} and $N(OH)$ are located very close together (Fig 3.8). After reaching a maximum, the predicted fluorescence intensity falls very rapidly while the OH number density remains for up to 3 cm behind the leading shock at a level of approximately one-half of the maximum. The strong decay in fluorescence intensity can be mainly contributed to the absorption of the incoming light sheet energy by the OH molecules themselves. Note that the laser beam is assumed to propagate in the opposite direction from the detonation and corresponds to a light sheet coming in from the left in Fig. 3.7.

The effects on the predicted fluorescence intensity can be divided into three groups: OH absorption line-shape and the resulting effects in Γ, collisional quenching, and light sheet energy absorption. Due to the increasing temperature behind the shock front the Doppler width $\Delta\nu_D$ of the pumped absorption line, $Q_1(9)$ (1,0), increases from 0.62 cm^{-1} at post shock conditions to approximately 0.7 cm^{-1} far behind the leading shock wave (Fig 3.9a). Despite the decreasing pressure with increasing distance behind the leading shock at the end of the induction zone, the collisional width

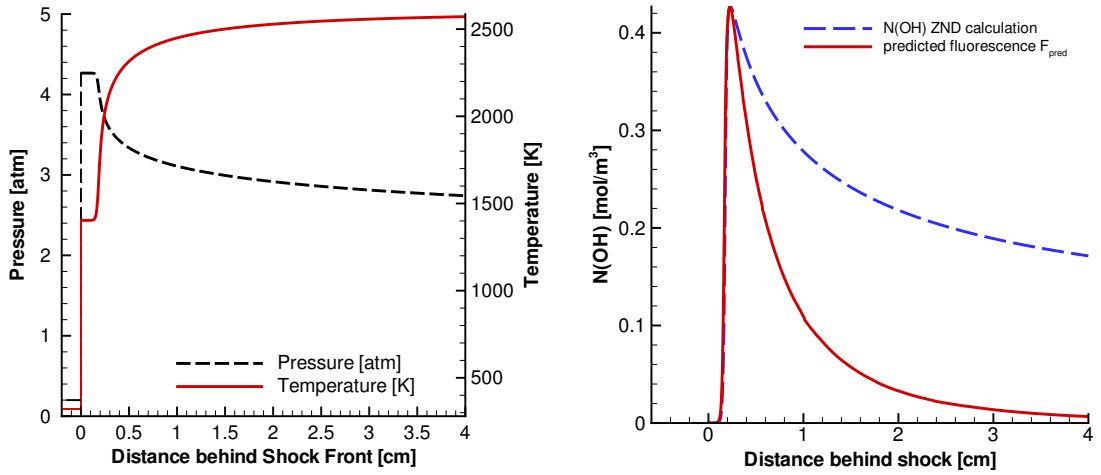

a) b)

Figure 3.7: a) ZND profiles of pressure and temperature for a CJ detonation in $2H_2$-O_2-$5.5N_2$, T_0=300 K, p_0=20 kPa. b) ZND profile of OH number density and predicted fluorescence profile based on model. The abscissa orientation corresponds in all ZND profile plots in this Section to the detonation traveling from right to left.

$\Delta\nu_C$ sharply increases by about 10% (Fig 3.9a). This can be explained by the growing mole fraction of H_2O at the beginning of the energy release zone and the large broadening coefficient of H_2O, which over-compensates for the decrease in pressure. Once the water mole fraction is equilibrated, $\Delta\nu_C$ decreases slightly with pressure. The Voigt a-parameter throughout the profile is approximately 0.7, which indicates that neither pressure nor temperature broadening is dominant. To illustrate the effect of the changing absorption line-shape effect on the fluorescence signal, the overlap integral Γ was calculated through the ZND profile neglecting the light sheet absorption effect (Fig. 3.9a). The abrupt broadening of the absorption line at the end of the induction zone leads to a decrease of Γ from 0.52 at post shock conditions to a fairly constant value of 0.44 far behind the front. The predicted fluorescence within the induction zone is small due to the OH number density being close to zero. The changing absorption line-shape therefore affects the fluorescence front since the increases in N(OH), $\Delta\nu_D$ and $\Delta\nu_C$ all approximately coincide. The decrease in Γ leads to a smaller increase in fluorescence intensity compared to the increase in OH number density.

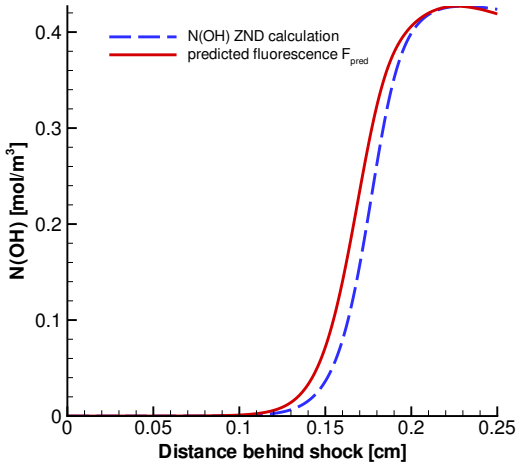

Figure 3.8: Detailed view of sharp OH number density rise and predicted fluorescence signal.

A higher characteristic quenching rate Q leads to a lower fluorescence signal (Eq. 3.43). The characteristic quenching time $1/Q$ is in units of ns in Fig. 3.10a. The characteristic quenching time shows a sharp dip by a factor of approximately two at the end of the induction zone. This is seemingly contrary to the linear dependence of Q on p (Eq.3.40) and the pressure decreasing with increasing distance in the reaction zone. The sharp dip can be attributed to the large quenching cross section and increasing mole fraction of H_2O at this point in the profile. The total quenching rate can be broken down into the contributions of specific species by examining the magnitude of each summand in Eq. 3.40. The H_2O molecule is clearly the dominant quenching species behind the induction zone (Fig. 3.10b).

The rapid reduction in characteristic quenching time and overlap integral at the end of the induction zone results in the constant of proportionality between the fluorescence intensity and the OH number density. The decrease in $1/Q$ and Γ with increasing distance from the shock leads to a gradually reducing proportionality factor between F_{pred} and N(OH) as shown in Fig. 3.8; F_{pred} is normalized to the maximum of N(OH). At the maximum in the predicted profile, the fluorescence efficiency is low. The predicted fluorescence front, defined as the point of 50% rise to maximum and the point of steepest increase, is therefore shifted towards the shock front by about 0.08 mm and 0.12 mm compared to the N(OH) front, but still occurs as a distinct

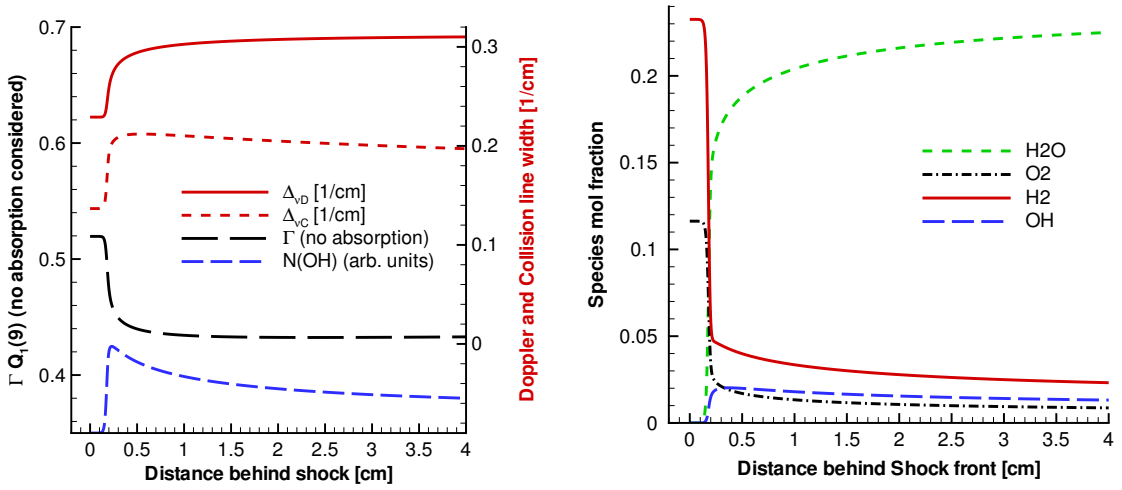

a) b)

Figure 3.9: a) Absorption line parameters for $Q_1 9$ (1,0) transition in a CJ detonation in $2H_2$-O_2-$5.5N_2$, T_0=300K, p_0=20kPa, based on ZND model and corresponding overlap integral Γ neglecting absorption effects. b) Mole fraction of major species except N2.

front.

Since the characteristic quenching time is below 1 ns throughout the profile, which is far below the radiative lifetime of approximately 750 ns of the excited state, the LIF system is operating in the quenching dominated regime. The effective lifetime can therefore be assumed to be close to the characteristic quenching time. Since the laser pulse width of 20 ns is significantly longer than the effective lifetime of the upper state, the time window in which fluorescence can be observed is comparable to the laser pulse duration. Neglecting the details of the temporal distribution function of the laser, the optimum signal-to-noise ratio for the experiment can be expected for a camera gate width equal to the laser pulse width. The main source of noise on the PLIF images is chemiluminescence from the hot products which decreases the signal-to-noise ratio if accumulated on the detector before or after the fluorescence signal occurs.

In order to analyze the absorption of incoming light sheet intensity, the parameter $I_\nu^0 I_b$ is considered (Fig. 3.11a). $I_\nu^0 I_b$ shows a rapid decrease to 30% of its post shock value after only 1 cm behind the leading shock front. The light sheet absorption is

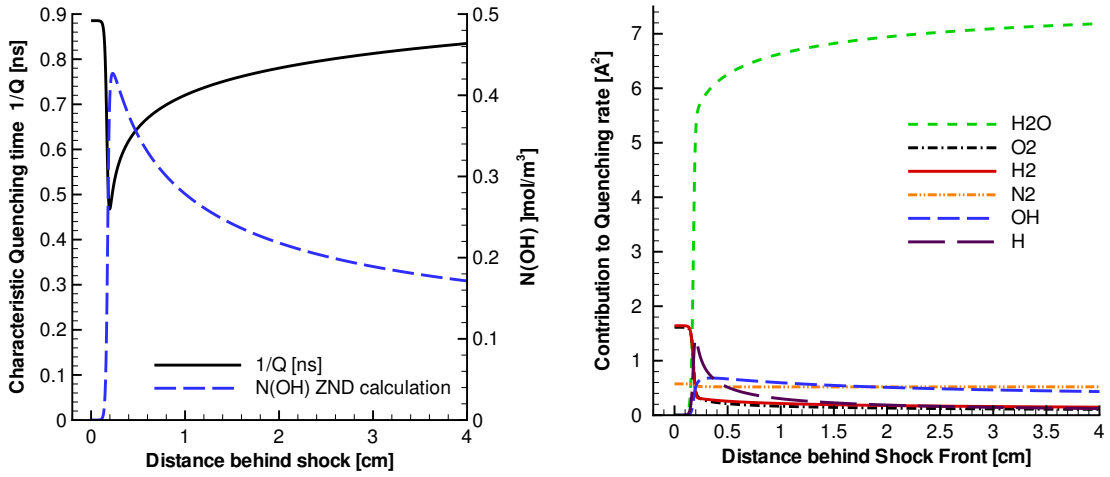

a) b)

Figure 3.10: a) Characteristic quenching time and OH number density in a CJ detonation in $2H_2$-O_2-$5.5N_2$, T_0=300K, p_0=20kPa, based on ZND model. b) Contribution of selected species to total quenching cross section. Plotted are the summands for each species in Eq. 3.40 which includes the mole fraction as a function of distance behind the shock front.

caused mainly by the OH molecules. The broad-band absorption by H_2O was found to be negligible. Two OH absorption lines in the vicinity of the laser center frequency contribute to the absorption process, which leads to an asymmetric spectral laser intensity distribution (Fig. 3.11b). The absorption of incoming light sheet energy by OH molecules is predominantly responsible for the stronger decay of the predicted fluorescence signal in the recombination zone compared to the modest decrease in OH number density. The absorption process does not influence the sharp rise of the fluorescence signals at the end of the induction zone since $I_\nu I_b$ changes insignificantly in this region of the profile. The Boltzmann factor is found to be temperature independent for both transition lines in the vicinity of the pumping wavelength and has a negligible effect on the PLIF signal (Fig 3.11a).

3.7 Comparison of model with experiment

In order to compare the model predicted fluorescence with the experimentally obtained fluorescence, a one-dimensional profile of the fluorescence intensity was ex-

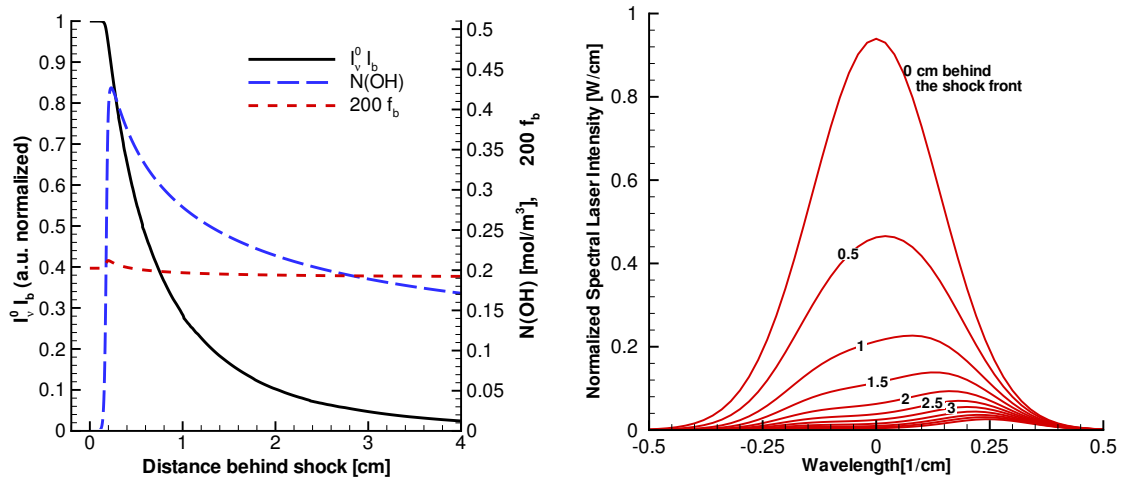

a) b)

Figure 3.11: a) Lumped parameter $I_\nu^0 I_b$, illustrating the effects of incoming light sheet intensity absorption, OH number density N(OH) and Boltzmann factor f_B for the $Q_1(9)$ transition in a CJ detonation in $2H_2$-O_2-$5.5N_2$, T_0 = 300 K, p_0 = 20kPa, based on the ZND model. b) Spectral distribution of laser intensity as a function of distance behind the shock front. Two absorption lines are considered.

tracted from a PLIF image. Due to the limitations discussed below, the comparison is qualitative rather than quantitative. The experimental fluorescence intensity was averaged transversely to the flow direction over a 1 cm wide stripe oriented in the flow direction (Fig. 3.12a). A segment of the incident shock, which does not appear to be influenced by any three-dimensional effects, was chosen and the leading shock velocity can be assumed approximately constant over the stripe width at the instant in time the image is taken (Fig. 3.12a). The shock velocity is oscillating in time due to the cellular nature of the detonation, which is a key limitation in the comparison of the steady-state ZND model with experimental data. Steel and Oppenheim (1966) measured for a marginal detonation in a $2H_2$-O_2-$7.1N_2$ mixture at 13.3 kPa, a lead shock velocity decay from the CJ value U_{CJ} at the cell center to 0.8 U_{CJ} at the end of the cell. The portion of the leading shock front in the latter part of the cell is also denoted as an incident wave in contrast to the Mach-stem in the earlier part of the cellular cycle (Chapter 1). The leading shock front is divided up into segments corresponding to either Mach stem or incident wave. For the incident wave the decay rate appears to be smaller and the lead shock velocity closer to U_{CJ} as compared to

the Mach stem, which makes incident wave segments of the front more preferable to compare with the model evaluated at CJ conditions. The experimental fluorescence profiles obtained from several experiments with the same mixtures were normalized, aligned using the maximum value, and averaged. Since the exact location of the shock front can not be derived from the PLIF image, the experimentally obtained fluorescence profile is normalized and shifted so that the maxima of experimental and predicted fluorescence profiles coincide (Fig. 3.12b). The case considered shows good agreement between the rapid fall off in the measured and predicted fluorescence intensity. The uncertainties and limitations associated with this comparison prevent a quantitative interpretation of the fluorescence front. From inspections of individual experiment images, the distance from 10% to 90% of the maximum fluorescence appears to be on the order of 0.5 mm, which corresponds well with the predictions.

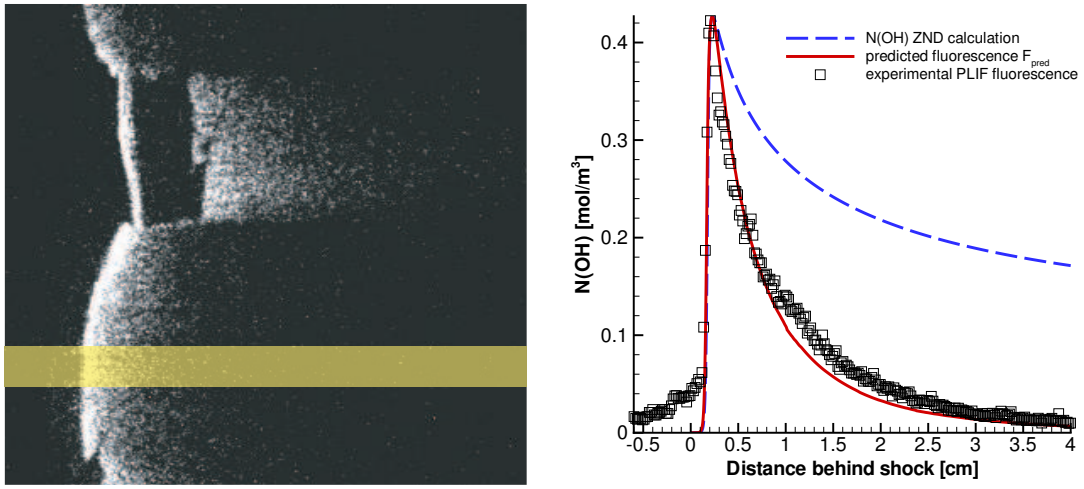

a) b)

Figure 3.12: a) Example of horizontal stripe placement on a PLIF image to obtain a fluorescence profile in a CJ detonation in $2H_2$-O_2-$5.5N_2$, T_0=300K, p_0=20kPa. b) Comparison of experimental and predicted fluorescence profile.

3.8 Lead shock strength unsteadiness

The ZND model with a fixed lead shock velocity does not take the oscillations in the lead shock velocity into account. The induction zone length is significantly shorter

at the beginning than at the end of the cellular cycle as seen in the overlay of the schlieren and PLIF images in Pintgen (2000) and Austin et al. (2004). Neglecting the effects of unsteadiness, the results are confirmed by the computed dependency of adiabatic explosion time on shock strength (Fig. 3.13a). The effect of unsteadiness on the reaction can be evaluated by defining a characteristic shock decay time

$$t_d = \frac{U}{\partial U/\partial t}, \tag{3.44}$$

where U is the lead shock velocity (Fig. 3.14). The influence of the unsteadiness depends strongly on the portion of the cellular cycle under consideration. At the beginning of the cellular cycle with high lead shock velocity the shock decay rates large and the induction zone length short. At the end of the cell shock the decay rates are smaller, but the induction zone length is larger. The effect of unsteadiness is based on the relative change of the induction zone length within the induction period. The less the induction zone length changes within an induction period, the closer conditions are to the steady-state model.

The absolute change in induction zone length Δ within the induction time can be written as

$$\frac{\partial \Delta}{\partial t}\tau = \frac{\partial \Delta}{\partial U}\frac{\partial U}{\partial t}\tau, \tag{3.45}$$

where the induction time τ is given by

$$\tau = \frac{\Delta}{w}, \tag{3.46}$$

and w is the post shock velocity in the shock fixed frame. The change in induction zone length within the induction time can be rewritten using Eq. 3.44 as

$$\frac{\partial \Delta}{\partial t}\tau = \frac{\partial \Delta}{\partial U}\frac{\Delta}{w}\frac{U}{t_d}. \tag{3.47}$$

The relative change in Δ within the induction time can be written as

$$\begin{aligned} \frac{\partial \Delta}{\partial t}\frac{\tau}{\Delta} &= \frac{\partial \Delta}{\partial U}\frac{\partial U}{\partial t}\frac{1}{w} \\ &= \frac{\partial \Delta}{\partial U}\frac{U}{w}\frac{1}{t_d}. \\ &= \frac{\mathcal{T}}{t_d}, \end{aligned} \tag{3.48}$$

where $\mathcal{T}$ is defined as

$$\mathcal{T} = \left[\frac{U}{\Delta}\frac{\partial \Delta}{\partial U}\right]\tau = \frac{\partial \Delta}{\partial U}\frac{U}{w}. \tag{3.49}$$

Here, the expression $\mathcal{T}/t_d$ is taken as a measure of the influence of the unsteadiness on the reaction. For large values of $\mathcal{T}/t_d$, the induction zone length changes significantly within the induction time, leading to a strong deviation from the steady-state approximation. For significantly small values of $\mathcal{T}/t_d$, the approximation of a steady-state solution is reasonable.

In order to numerically evaluate the expressions given above, a series of calculations with the steady-state ZND code (Shepherd, 1986) for a range of lead shock velocities U/U_{CJ} from 0.78 to 1.5 in steps of 0.02 were performed. The derivatives were approximated using finite difference quotients. Three mixtures were investigated: $2H_2$+O_2+17Ar, $2H_2$+O_2+5.5N_2, and H_2+N_2O all at initial conditions of 20 kPa and 300 K. A summary of relevant quantities for these mixtures is shown in Appendix D.

The lead shock velocity through the cell and corresponding shock decay times t_d were taken from a two-dimensional numerical simulation by Eckett (2000), who studied a mixture of $2H_2$+O_2+7Ar at 6.7 kPa (Fig. 3.14). For this estimate, the normalized lead shock velocity variation in a cell was assumed to be similar to the $2H_2$+O_2+17Ar case discussed here. The shock decay times were scaled according to the induction zone length of 1.3 mm for the numerical case and 1.4 mm for the experimental case. According to the results of the numerical simulation, the normalized shock velocity U/U_{CJ} varies from 1.3 at the beginning of the cell to 0.9 at the end of the cell and the shock decay times vary correspondingly from approximately 10^{-5} s

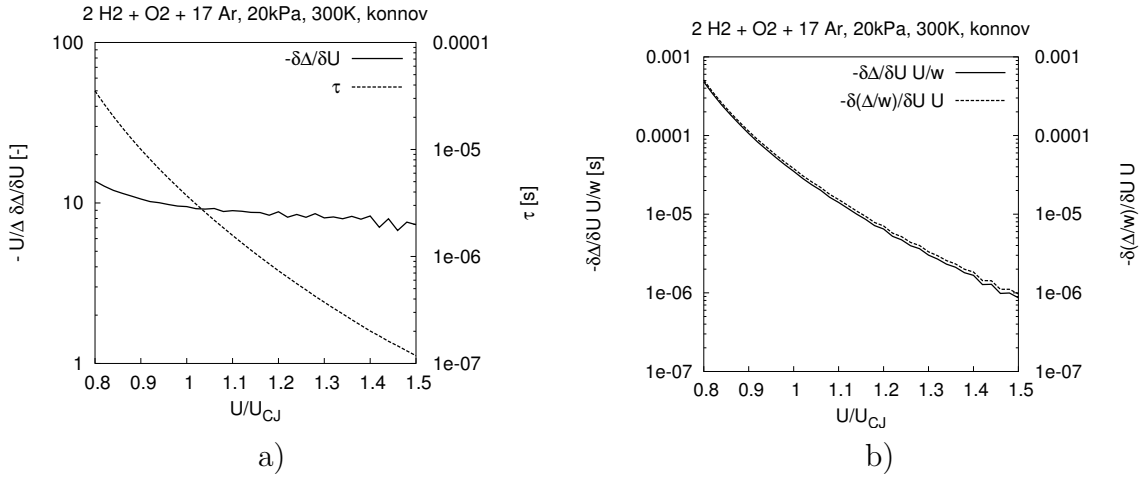

Figure 3.13: a) Change of induction zone length with normalized lead shock velocity (primary ordinate) and induction time τ (secondary ordinate). b) Absolute change in induction time with relative change in U, $\mathcal{T}$ (primary ordinate).

to 10^{-3} s (Fig. 3.14). The results of the evaluation are summarized for U/U_{CJ} of 1.3 and 0.9 in Table 3.8.

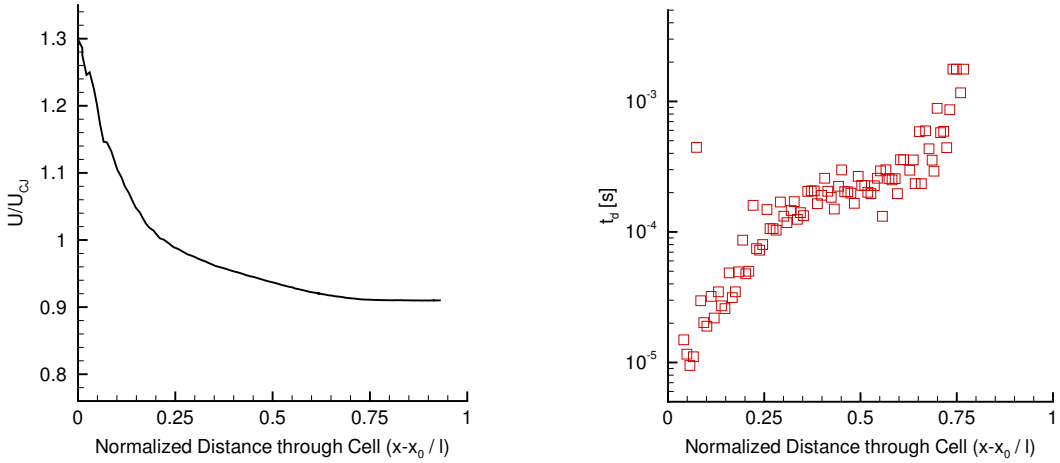

Figure 3.14: a) Normalized lead shock velocity through one cellular cycle, Eckett (2000), $2H_2$+O_2+7Ar at 6.7 kPa. b) Corresponding leading shock decay rate t_d.

The induction time is about 30 times longer at the end of the cell than at the beginning, whereas the dimensionless change in induction zone length with lead shock velocity stays approximately constant. This leads to values of $\mathcal{T}$ which are approximately 30 times larger at the end of the cell than at the beginning. The values for

U/U_{CJ}	$-\partial\Delta/\partial U\ U/\Delta$	τ [s]	$\mathcal{T}$ [s]	t_d [s]	$\partial\Delta/\partial t\,\tau/\Delta$
1.3	8	$3.7\ 10^{-7}$	$3\ 10^{-6}$	10^{-5}	0.3
0.9	10	$1\ 10^{-5}$	10^{-4}	10^{-3}	0.1

Table 3.5: Summary of calculated quantities at beginning and end of cellular cycle, $2H_2$+O_2+17Ar, 20 kPa, 300 K, Konnov mechanism.

$\partial\Delta/\partial t\,\tau/\Delta$ are obtained to be 0.3 and 0.1 at the beginning and end of the cell cycle, respectively. This suggests that the steady-state induction zone length increases by only 10% within the induction time at the end of the cell cycle. At the beginning of the cell cycle, the induction zone length increases by 30% within the induction time, which is due to the faster decay rate of the lead shock wave. Based on this criterion, the details of the induction zone are better approximated by the steady-state ZND model at the end of the cellular cycle. Eckett (2000) developed a critical decay rate model, which provides the shock velocity decay rate at which decoupling of the reaction front from the shock front occurs. As the present model assumes a coupled reaction front, the shock decay rate has to be below the critical decay rate. Furthermore, the induction time has to be significantly shorter than the cellular cycle time, as the shock velocity increases at the beginning of the next cell after the transverse wave collision. Both criteria are met for the example considered. For other mixtures, like H_2-N_2O mixtures, as shown in Appendix D, this is due to the large induction time for lower lead shock velocities. Shock decay time data for mixtures different than the case considered are needed to estimate the influence of the decaying shock wave for these mixtures.

3.9 Limitations of the model

The limitations of this model and the comparison of predicted and measured fluorescence can be divided into three groups: uncertainties within the model in predicting the fluorescence intensity based on the ZND calculation, errors arising from applying the predicted fluorescence to the three-dimensional cellular detonation, and experimental uncertainties.

PLIF model limitations:

- The steady-state model assumes that the laser excitation rate is less than the total de-excitation rate. Estimates of the spectral irradiance based on a light sheet thickness of 0.25 mm and a light sheet height of 80 mm show that the system is operating close to, but below, the saturation regime. The assumption is valid.

- Thermally averaged quenching rates were used for the model evaluation. The RET-rates in the A-state were measured to be slightly faster than the quenching rate (Beaud et al., 1998) which limits the error introduced by this assumption, especially since the total fluorescence is detected. The lack of inclusion of RET seems to be less important for determining the total PLIF signal intensity, since the dominating (0,0) and (1,1) transitions are both included in the broadband imaging. The RET rates in the v"=0 and both v'=0 and v'=1 levels were found to be comparable (Zizak et al., 1991, Kliner and Farrow, 1999), but not large enough such that hole burning could be ruled out. The assumed Boltzmann distribution in the ground state could introduce a significant error.

Restrictions in applying the ZND model:

- The decaying leading shock velocity through a cellular cycle is not taken into account in the steady-state ZND model, which assumes a constant CJ detonation velocity. To overcome this drawback, two- or three-dimensional, unsteady numerical simulations are needed. Estimates shown in the previous Section for the H_2-O_2-Ar system indicate that the details of the induction zone are for that particular case reasonably approximated by the steady-state ZND model at the end of the cellular cycle. For other mixture types, this might change. It is clear that the error arising from applying the steady-state model is increasing with distance behind the leading shock front, especially behind the induction zone. The good agreement with the experimental profile can be explained by the rapid decay in fluorescence intensity which is fairly insensitive to the details in the recombination zone.

- The ZND model is purely one-dimensional and the effects of transverse waves, which can have velocity components orthogonal to the light sheet plane, are not considered. These effects are clearly observed on the experimentally obtained fluorescence profile.

Experimental uncertainties:

- The fluorescence signal emitted from the light sheet plane will be absorbed on its way out of the test section. Since absorption is expected to occur mainly by OH molecules, which are non-uniformly distributed behind the detonation front, the magnitude of absorption will fluctuate. This could cause some error in the fluorescence profile obtained experimentally. For a methanol-air flame investigated by Deasgroux et al. (1995) the trapping was found negligible for the same excitation scheme which was used in the present study.

- The overlap integral and absorption depends on shifts in laser centerline frequency relative to the OH absorption line, which can arise from uncertainties when setting the dye-laser frequency. To investigate that effect, a laser centerline shift by 0.06 cm^{-1}, the step width of the dye laser grating, was assumed. The predicted fluorescence profile does not alter significantly (Fig. 3.15).

- Uncertainties in determining the spectral width of the laser were neglected.

3.10 Conclusions on model and comparison

Given the approximations in applying the steady ZND model to the detonations and the lack of absolute calibration in terms of OH number density, the comparison of experiments and model is limited to a qualitative interpretation of the features observed in both profiles. Two important conclusions can be drawn:

- The distinct fluorescence front seen on PLIF images correlates well with the sharp rise in OH number density. Due to the rapid change in the quenching

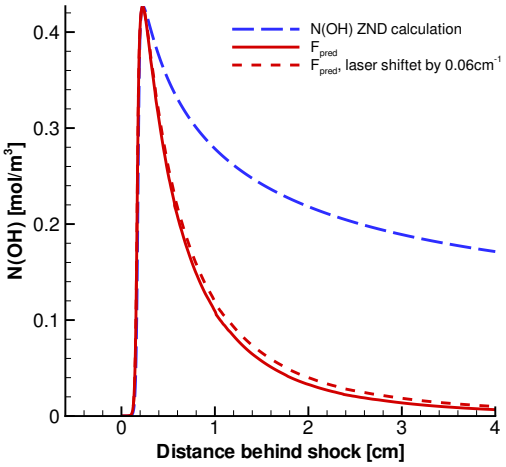

a)

Figure 3.15: a) The effect of shifting the laser centerline frequency by 0.06cm $^{-1}$ on predicted fluorescence profile is found to be minor. Mixture is $2H_2$-O_2-$5.5N_2$, T_0=300 K, p_0=20 kPa.

rate, an apparent shift of the fluorescence front up to 0.1 mm was found for the mixtures considered (see Appendix C). The direction and magnitude of the shift depends on the details of the species mole fraction at the end of the induction zone and which, in turn, were found to depend on the mixture composition.

- The experimentally observed rapid fluorescence decay seems predominantly due to absorption of incoming light sheet energy by OH molecules.

These conclusions are important for the interpretation of the PLIF images obtained and hold true for a variety of mixtures investigated including H_2-O_2-Ar, H_2-N_2O-N_2 and nitrogen-diluted hydrocarbon-oxygen mixtures. Evaluations of CJ detonations for these mixtures used are shown in Appendix C. To obtain a detailed qualitative comparison of the experimental and predicted fluorescence intensity, a fluorescence intensity model would have to be applied to a detonation profile from a multi-dimensional detonation simulation. Furthermore, an experimentally obtained, spectrally resolved, one-dimensional profile of the detonation could be useful in obtaining information on the thermodynamic conditions. To minimize the influence of the out-of-plane transverse waves, this should be done in a high-aspect-ratio facility.

Chapter 4

Quantifying the Degree of Regularity

In the last chapter, it was shown that the OH-front coincides with the fluorescence front seen on PLIF images despite the large local variations in thermodynamic conditions and background composition. In this chapter, a quantitative analysis of the PLIF images is given, taking into consideration the performance of the imaging system. The aim of the analysis is to quantify the degree of regularity of a mixture by analyzing the reaction front geometry.

In Section 4.1, the motivation for this analysis is given. In Section 4.2, the mixtures investigated are characterized. In Section 4.3, a detailed analysis of the imaging system is presented. In Sections 4.4 and 4.5, the results of the analysis are discussed. The experimental results analyzed in this chapter are from experiments in the GDT facility described in Chapter 2.

4.1 Motivation

Detonation structure exhibits a varying degree of regularity in different mixtures. The classification of mixtures can be made through experimental observations and mixture property calculations. A large number of experimental, and more recently numerical, studies were performed to characterize detonation front structure and the nature of the combustion process within the reaction zone. In experimental studies, the soot-foil technique is used extensively in order to classify the regularity as

excellent, good, poor, or irregular (Strehlow, 1968). Here, a method for quantifying the regularity based on the OH-front geometry as obtained from PLIF images is presented. The geometric complexity of the reaction front is characterized both in terms of the effective reaction front length and an effective dimensionality. In order to demonstrate the concept, a total of 68 detonation experiments with varying regularity was processed and the results correlated with a numerically calculated mixture property, the reduced activation energy θ, as computed from detailed chemical reaction mechanisms. The mixtures studied vary in the degree of cellular regularity from "regular" to "highly irregular", corresponding to effective reduced activation energies θ between 5.2 and 12.4.

Previous observations (Pintgen et al., 2003b, Pintgen, 2000) of the detonation reaction zone structure show that mixtures with very regular cellular patterns have smooth reaction fronts as visualized by PLIF images of the OH radical. Mixtures with more irregular cellular structure exhibit (Pintgen et al., 2003a, Austin, 2003) shear flow instabilities and fine scale wrinkling of the reaction front. The reaction front geometries visualized in Ar- and N_2-diluted mixtures of H_2-O_2 and H_2-N_2O show a broad spectrum of geometric complexity (Fig. 4.1). The extent of geometric complexity is an important issue (Singh et al., 2003) in determining the relative role of chemical reaction due to shock compression as compared to diffusive transport from the hotter into the cooler regions. At the present stage of development, only preliminary conclusions can be drawn from the image processing. A systematic parametric study is necessary to allow for more general statements about the role of diffusive transport for detonation propagation.

4.2 Characterization of mixtures

Stoichiometric H_2-O_2 and H_2-N_2O mixtures diluted with Ar or N_2 at initial conditions of 20 kPa and 20°C were investigated. One PLIF image is obtained from each experiment. The distinct fluorescence front seen in all PLIF images indicates the location of the sharp rise in the OH concentration at the end of the induction zone

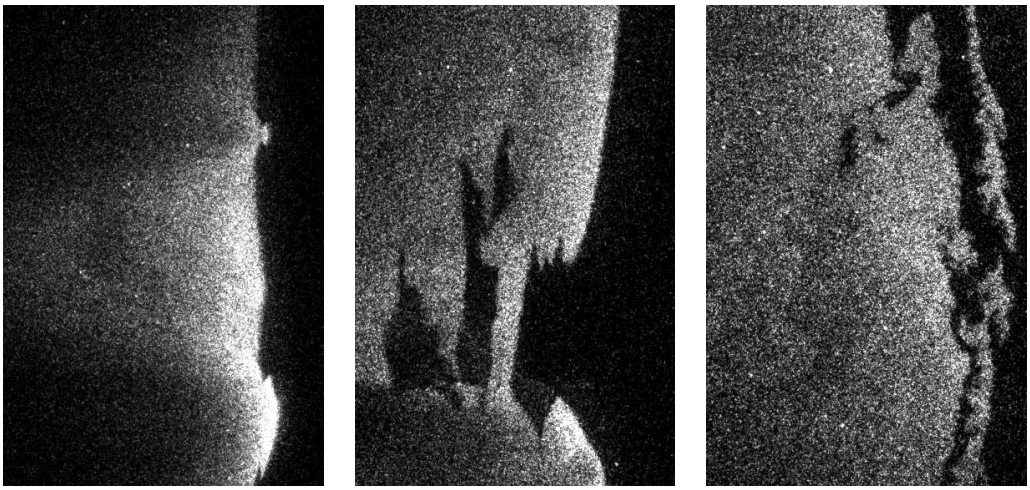

Figure 4.1: Three examples of PLIF images. a) Shot 1653, $2H_2$+O_2+17Ar, image height: 40 mm, cell size: 47 mm, $\theta = 5.6$; b) Shot 1619, $2H_2$+O_2+$6N_2$, image height: 30 mm, largest cell size observed on soot-foil 80 mm, $\theta = 7.8$; c) Shot 1591, H_2+N_2O+$3N_2$, image height 30 mm, largest cell size observed on soot-foil: 120 mm, $\theta = 12.4$.

(see Chapter 3). The exponential rise in OH concentration coincides approximately with the most rapid temperature increase (Fig. 4.2). In the present study, we will refer to the leading edge of the OH fluorescence front simply as the "reaction front".

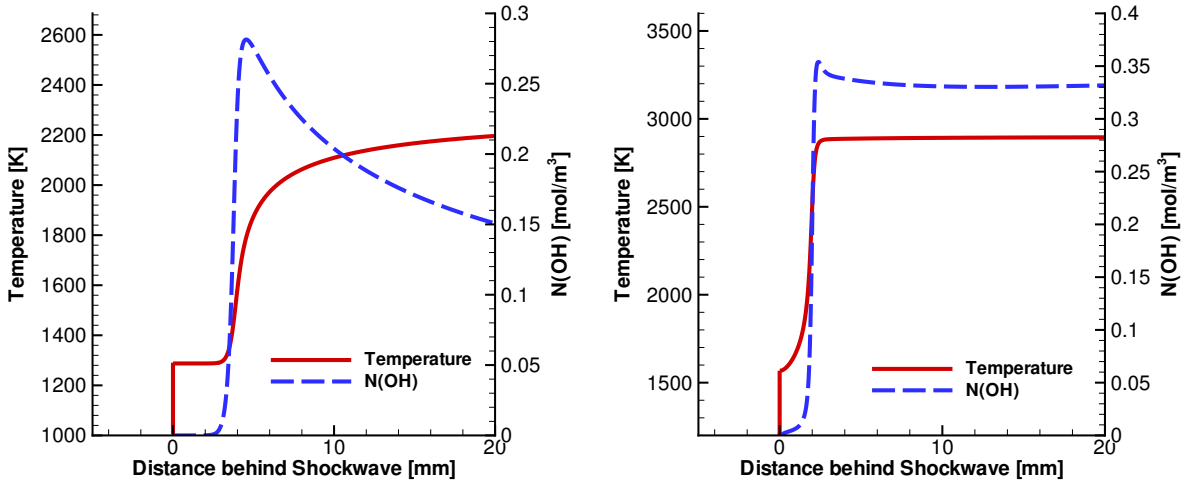

Figure 4.2: ZND profiles of temperature and OH number density for CJ detonation. a) $18H_2$+$9O_2$+$73N_2$, $P_0 = 320$kPa, $\theta = 7.9$, b) $25H_2$+$25N_2O$+$50N_2$, $P_0 = 30$ kPa, $\theta = 11.5$.

The induction zone length was calculated with the one-dimensional ZND model (Shepherd, 1986) together with the validated detailed chemical kinetics mechanism of Mueller et al. (2000) and the gas phase chemistry library of Kee et al. (1989). The location of the sharpest increase in OH concentration behind the leading shock wave is found to be within 3% of the location of the steepest temperature increase. The reaction zone length at CJ conditions varies from 0.8 to 7.5 mm (Table 4.1). The cell sizes ranged from 22 to 110 mm as measured with soot-foils placed on the side wall of the test section. It was difficult to assign a cell size S for the marginal mixtures, $S \geq 80$ mm, since a whole range of cell sizes was present. For these cases, the largest cell size observed on the soot-foils is given.

Mixture	θ	$(dT/dx)_{max}$ [mm]	$(dn(\mathrm{OH})/dx)_{max}$ [mm]	S [mm]
$13.3H_2+6.6O_2+80Ar$	5.2	0.7	0.68	22
$10H_2+5O_2+85Ar$	5.6	1.4	1.3	46
$22H_2+11_2+67N_2$	6.8	2.2	2.1	73
$18H_2+9O_2+73N_2$	7.9	3.9	3.8	104
$16.6H_2+8.3O_2+75N_2$	8.8	6.2	6	not measured
$25H_2+25N_2O+50N_2$	11.5	2.9	2.9	54
$20H_2+20N_2O+60N_2$	12.4	7.4	7.6	110

Table 4.1: Reduced activation energy θ, reaction zone length based on the maximum temperature gradient and OH number density gradient, and cell size.

The reduced activation energy θ was calculated by numerically evaluating the derivative of the induction time t_i with respect to the post shock temperature at the von Neumann state (subscript vN)

$$\theta == \left(\frac{T}{t_i}\frac{\partial t_i}{\partial T}\right)_{vN}, \tag{4.1}$$

as described in Section 1.3. Considering the reaction process as being modeled by a one-step reaction with an activation energy E_a, we can show that $\theta = E_a/RT_{vN}$, which is one of the key parameters controlling the instability of detonations to perturbations and by extension, the nonlinear evolution of highly unstable propagating waves. For the $2H_2$-O_2-βAr mixtures, θ varies from 5.2 to 5.6 ($\beta = 12$ to 17), and for the most

irregular mixtures of H_2-N_2O-βN_2, θ reaches values up to 12.4 for $\beta = 3$. Intermediate values of θ were found for the N_2-diluted mixtures of H_2-N_2O and H_2-O_2.

The usual subjective interpretation of the degree of regularity observed on soot-foils, classified as "regular", "irregular" and "highly irregular", correlates well (Pintgen et al., 2003a) with the magnitude of θ. Mixtures with higher values of θ exhibit a more irregular cellular pattern on soot-foils. The H_2-O_2-Ar mixture represents a mixture with a very regular cellular structure. The N_2-diluted H_2-O_2 mixture is an example of a more irregular mixture, whereas the H_2-N_2O mixture diluted with N_2 is highly irregular. Cellular substructure has been observed previously (Libouton et al., 1981) in the H_2-N_2O system . The irregularity and substructure seems to be a general feature of mixtures with high activation energy and has been shown (Austin, 2003) to also apply to hydrocarbon fuels.

4.3 Analysis of the imaging system

It is obvious from visual examination of the PLIF images (Fig. 4.1) that the reaction fronts of mixtures classified as "irregular" have a much greater geometric complexity than those of the "regular" mixtures. However, to go beyond this simple observation and make a quantitative analysis of the reaction front geometry requires an evaluation of the imaging system. The key issues of motion blur, modulation transfer function, light sheet thickness, and image processing are discussed in this Section.

The motion blur induced by the time span for which fluorescence is emitted was estimated to be, at the most, 33 μm at CJ conditions, which corresponds to 0.5 pixel for an image height of 45 mm. Here, a fluorescence time in the order of the laser pulse duration of 20 ns was assumed since the PLIF system is operating in the quenching dominated regime.

For an ideal imaging system, the image height of 30 to 75 mm corresponds to a nominal resolution of 50 to 130 μm/pixel. Due to aberrations occurring for the low f-number optics and the non-ideal modulation transfer function (MTF) of the ICCD-assembly, the point spread function (PSF) is known (Clemens, 2002) to have a

broader profile than the diffraction limited blur spot diameter. In the present study the f-number was 4.5 for all images. The diffraction limited blur spot diameter was calculated to be 7 μm for an image height of 45 mm.

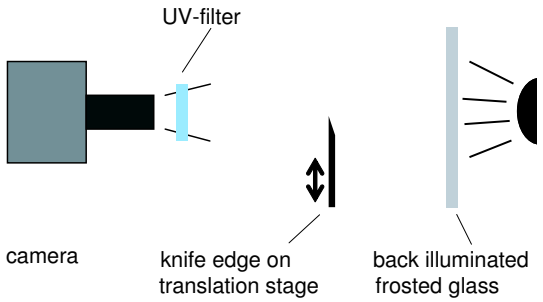

Figure 4.3: Experimental setup used for determining the line spread function.

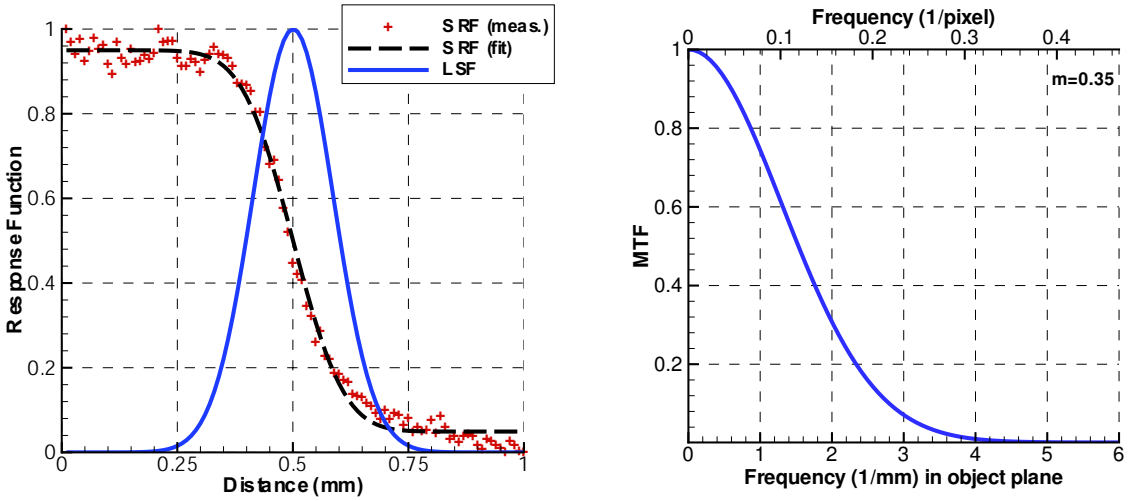

a) b)

Figure 4.4: a) Measured SRF and LSF derived from the error function curve fit for the camera system used; object height: 45 mm. b) Modulation transfer function inferred from the LSF.

The line spread function (LSF), the one-dimensional analog to the PSF, was determined by imaging a knife edge moving across the object plane in steps of 10 μm in front of back-illuminated frosted glass (Fig. 4.3). The camera is thereby focused on the knife edge. Note that the LSF data points are obtained by considering the signal on a particular pixel, as a function of the knife edge position as obtained from several

images, and not the intensity distribution transverse to the knife edge as obtained from several pixels. This procedure allows for determination of the PSF with a sub-pixel resolution, limited only by the precision of the micrometer on the translational stage. In the present case, this allowed for a 7-times sub-pixel resolution. The image height was set to 45 mm, which corresponds to a magnification m of 0.28. Since the MTF depends on m, we used the same setup as in the experiments except for the gate width, which had to be set to 3 ms in order to use the full dynamic range of the camera just as in the experiment. The 10 nm spectral line filter was placed in front of the lens in order to ensure the same amount of chromatic aberration as in the experiment.

The step response function (SRF), where LSF(x)=dSRF(x)/dx, was averaged over ten images and is shown in Fig. 4.4. In order to reduce the noise and enable the differentiation of the SRF, an error function was fitted least-squares to the SRF. The LSF has a $1/e^2$ full width of 350 μm, which corresponds to 5 pixel at this magnification. The MTF is the Fourier transform of the LSF and measures the contrast transfer as a function of the spatial frequency intensity modulation. For the MTF (Fig.4.4b), sine wave structures with a wavelength of 0.5 mm in the object plane will be imaged with only 30% of their original contrast. For the signal-to-noise ratio observed in the majority of the images, the cut-off frequency for a minimum visibility corresponding to a contrast ratio of 10% was estimated to be approximately 4.5 pixel. The knowledge of the MTF enables simulating the imaging characteristics of the camera system. An example of applying this to a model fractal, the Koch curve, is shown in Fig. 4.5a and b.

In order to obtain curves from the fluorescence images, the following procedure was used. The images were low-pass filtered before being down-sampled to half the resolution with bi-cubic interpolation. The images were then edge detected with a second-order edge detector (Laplacian of Gaussian, σ=2, filter size: 13×13 pixel) and the threshold for the Laplacian was set manually for each image. Due to fluorescence intensity fluctuations caused by the non-uniform light sheet intensity over the image height, each image had to be processed individually. The smallest feature size resolved

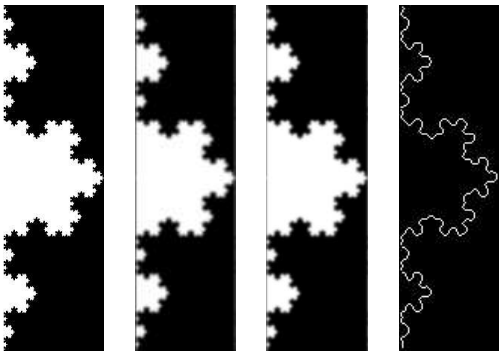

Figure 4.5: a) Filled segment of Koch curve b) Measured modulation transfer function of imaging system applied on Koch curve. c) Filtered and down-sampled image d) edge detected image.

with this technique was 6-7 pixel as determined by processing test images like the Koch curve. The test images were degraded with the MTF and processed in the same fashion as the actual images (Fig. 4.5). For an image height of 45 mm (m=0.28), the determined effective resolution corresponds to 410 μm in the object plane.

The light sheet thickness at the focal point was estimated to be 140 μm FWHM by measuring the expanded spatial profile of the laser output beam and assuming ideal focusing optics. For a Gaussian profile of the beam, 75% of the energy is within that thickness. Measurements of test burns on thermal paper indicate a larger thickness of 300μm; this might be caused by the high sensitivity of the thermal paper, which does not resolve the full range of the irradiance intensities. For $m = 0.28$, the light sheet thickness corresponds to 2 or 4.5 pixels depending on the thickness derived from the expanded beam profile or test burns. The distance over which the beam diameter does not exceed 1.4 times the value at the beam waist was estimated to be 15 cm. Therefore, the change in light sheet thickness in the region of interest is considered to be minimal.

After considering the effects of MTF, light sheet thickness, and motion blur, one can conclude that the resolution is not limited by the digital nature of the ICCD but rather by the illumination technique and the degradation of the image due to the contrast reduction resulting from the lens, the intensifier, and other optical components.

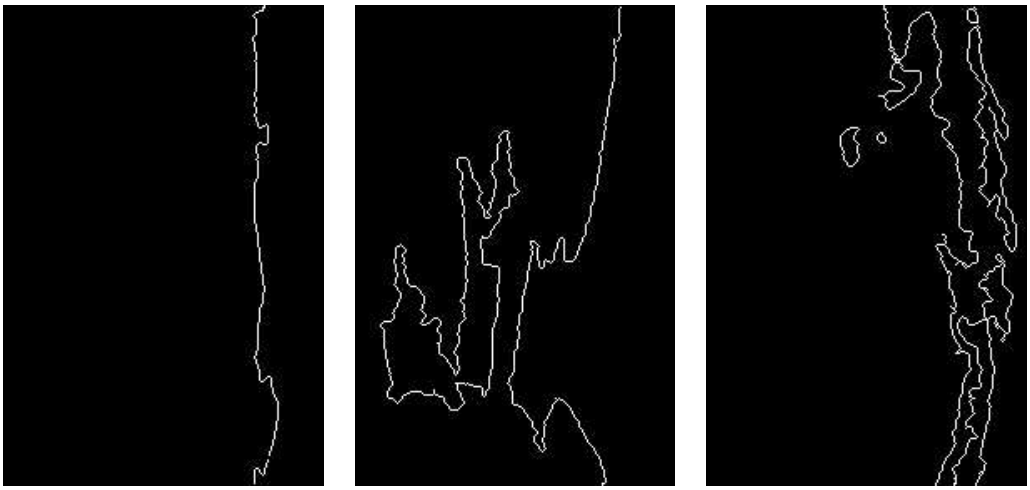

a) $\theta = 5.6$ b) $\theta = 7.8$ c) $\theta = 12.4$

Figure 4.6: Three examples of original PLIF and edge detected images. a) Shot 1653, $2H_2+O_2+17Ar$, image height: 40 mm, cell size: 47 mm; b) Shot 1619, $2H_2+O_2+6N_2$, image height: 30 mm, largest cell size observed on soot-foil 80 mm; c) Shot 1591, $H_2+N_2O+3N_2$, image height 30 mm, largest cell size observed on soot-foil: 120 mm

A further reduction in the smallest feature detectable arises from the image processing technique. The smallest resolvable scale depends on the image height (Table 4.2) and ranges for images between 30 to 70 mm high from 0.5 to 1.0 mm. This estimate is based on summing up the separate influences of the MTF, light sheet thickness, and motion blur. The MTF was measured only for $m = 0.28$ and approximated as constant for the range of magnifications used. The quoted resolution is in terms of actual physical dimensions of the object. Comparing the values in Tables 4.1 and 4.2, we see that we can resolve features that are, in the best cases, one order of magnitude smaller than the ZND-CJ reaction zone length and two orders of magnitude than the cell size. In the worst cases, the resolution is comparable with the ZND-CJ reaction zone length. Fortuitously, due to the larger cell size, the resolution is best for the irregular cases where it is most interesting to resolve the largest range of scales possible.

4.4 Normalized reaction front length

Three examples of edge detected images for $\theta = 5.3$, 7.8, and 12.4 are shown in Fig. 4.6. One measure describing the front geometry is the total edge length normalized by the image height. The minimum normalized edge length l is by construction one. Note that isolated regions of reacting and unreacting fluid increase the total edge length. The edge is, in some cases, not a continuous line, but made up of several segments (Fig. 4.6b and c), which are either closed (islands or lakes) or begin and end at the image edge. The total edge length is calculated by piecewise-linear approximations, counting all 4-connected pixel pairs of the edge as length 1 pixel and diagonally connected pixel pairs as length $\sqrt{2}$ pixel.

4.4.1 Results

The normalized edge lengths measured for the "regular" mixtures (Ar-diluted H_2-O_2) range from a minimum of 1 up to 1.8. This is small when compared with the other mixtures studied (Fig. 4.7). For higher reduced activation energies θ, the maximum normalized edge length and observed range of values increases. Mixtures with $\theta \approx 8$ reach values of normalized edge length up to 4.2. The minimum normalized edge length appears independent of θ and close to 1. For the "highly irregular" mixtures with $\theta = 12.4$, values of normalized edge length up to 7.5 are measured. The current analysis does not allow for a comprehensive statistical characterization, but the results clearly quantitatively show the increasing complexity of the reaction front for mixtures with increasing θ.

image height (mm)	30	45	70
magnification m	0.42	0.28	0.18
MTF and edge detection (mm)	0.36	0.54	0.85
light sheet and motion blur (mm)	0.14	0.14	0.14
smallest scale total resolvable (mm)	0.50	0.68	0.99

Table 4.2: Overview of smallest resolvable scale for various image heights considering the effects of the MTF and the edge detection process, motion blur, and light sheet thickness. The MTF itself was assumed to be constant for all magnifications.

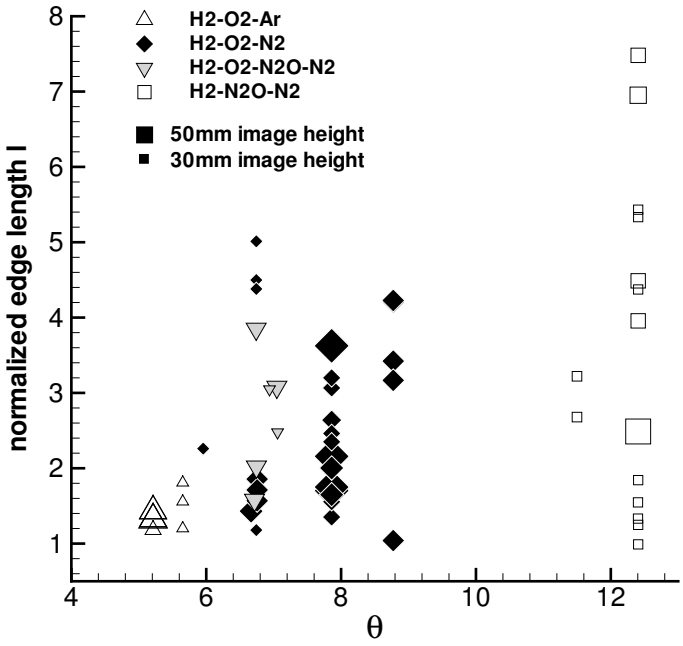

Figure 4.7: Total edge length as a function of the reduced activation energy θ. Symbol size scales with height of field of view.

4.4.2 Discussion

The key limitation of this and all other techniques based on light sheet illumination is the lack of out-of-plane information. Due to the high-speed nature of the flow and the apparatus we are using, we are also unable to obtain more than one realization per experiment. Based on our experience (Pintgen et al., 2003b) with more regular mixtures, we can identify several effects that these limitations can mask, which can lead to misconceptions when interpreting these images.

One of the most significant issues is that three-dimensional effects caused by the orientation of the cellular structure to the light sheet could not be resolved. This can lead to separated islands of higher and lower fluorescence regions, which significantly contribute to a larger normalized edge length. The orientation of the transverse wave system with respect to the light sheet is a stochastic process which contributes to the large range of normalized edge length measured. For irregular mixtures with sub-structure, this effect is more pronounced, since it is more likely that the light sheet

intersects a reaction front structure arising from transverse wave-like disturbances traveling perpendicular to the imaging plane. This partially accounts for the large range of normalized edge lengths measured for the N_2-H_2-O_2 mixtures. The image height and cell size are variables in this analysis which influence the probability of capturing images influenced by three-dimensional effects. The number of shots analyzed for one specific mixture, corresponding to one cell size, is too small to make a statement about the correlation between normalized edge length and image height or resolution. For the mixture $2H_2+O_2+8.1N_2$, $\theta = 7.8$, 14 shots have been analyzed with image heights of 40, 50 and 57 mm, and no trend of edge length dependence on image height can be seen (Fig 4.7).

Another effect is more noticeable if the image height is smaller than the cell size: due to the seemingly random variations in the phasing of the transverse waves, the field of view can correspond to different arrangements of the transverse waves and phases of the cellular cycle. The phase close to the end of a cellular cycle is known to exhibit, for more regular mixtures, a large-scale keystone-shaped region of lower fluorescence, which leads to a much larger edge length. In contrast, if the region in the middle of the cell cycle is captured, the reaction front is known to be smooth for Ar-diluted H_2-O_2 mixtures and the normalized edge length is close to its minimum value of one. These effects also contribute to the large range of observed edge lengths.

4.5 Box counting analysis on the reaction front

In a second approach to quantitatively describing the geometry of the reaction front, analysis commonly used for fractal-like objects (Catrakis and Dimotakis, 1996) was conducted on the edge detected images. The edge detected reaction front describes a convoluted curve with a scale-dependent length. Note that we do not claim that the edge detected OH-PLIF images are fractals, but simply are applying techniques used in fractal analysis to quantitatively describe the geometric complexity. The edge detected PLIF images describe curves whose topological dimension is one and embedding dimension is two. A variety of methods, all based on multiple resolution

analysis, are used to determine the dimension D of empirical curves. The key idea is to use the functional dependence of the curve length L on the scale λ to define D. The most common approaches are the yard stick and the box-coverage method, which will be applied here. The coverage length L is defined in terms of the box-coverage count $N(\lambda)$, the number of non overlapping boxes needed to cover the curve, and the box-size λ, here defined as the square-root of the box area.

$$L(\lambda) = \lambda N(\lambda) \tag{4.2}$$

$$D(\lambda) = -\frac{\mathrm{d}\log N(\lambda)}{\mathrm{d}\log \lambda} \tag{4.3}$$

By plotting $\log N(\lambda)$ versus $\log \lambda$, the dimension D can be visualized as the negative slope of this graph. If the slope is not constant the curve may be referred to as a scale-dependent fractal for which the dimension depends on the scale λ. The minimum dimension of a curve like object is the topological dimension 1, which corresponds to a straight line. For empirical fractals, a power law dependence typically occurs only over a range of scales $\varepsilon_i \leq \lambda \leq \varepsilon_o$, where ε_i and ε_o are the inner and outer cut-off, respectively. In the case of PLIF images, the fractal analysis could be applied only over a limited range of scales, bounded on the upper side by the field of view, and on the lower side by the resolution of the optical system.

Two sets of box or tile sizes were used. One set was chosen such that the image could be covered for every tile size in an integer number of tiles, which resulted in tiles of size 2×2, 4×4, 8×8, 16×16, 32×32, 96×96, and 288×192 pixel. The other set was chosen with dimensions $2^n \times 2^n$ with n = 0.8, which describes even horizontal and vertical subdivision of each tile in successive steps. When using the latter set of tile sizes, in some cases only fractions of tiles covered the image. This leads to coverage lengths $L(\lambda)$ which over-predict the true length since some tiles extend outside the image. This could be corrected by averaging the coverage counts for a specific tile size over several starting positions for the first tile. This approach led to very similar results. Here, only data from the tile set mentioned first were used.

Another effect, illustrated easiest by means of an example, arises from dividing

the tile size by two in the horizontal and three in the vertical direction when changing the tile size from 288×192 to 96×96; assume a straight vertical line in the right half of the image. For the tile size 288×192 $N = 1$ and $\lambda = L = 235$ and for the tile size 96×96 $N = 3$, $\lambda = 96$ and $L = 288$, which shows the unwanted effect of increasing coverage length for a one-dimensional object. To avoid this effect, the largest tile size was set to 288×288 and all tiles were square.

4.5.1 Results

Coverage counts N for six representative PLIF images, including the ones from Fig. 4.6, are shown in Fig. 4.8a as a function of the normalized tile size λ/λ_0, where λ_0 is the largest tile size used. The coverage count is a monotonically increasing function with decreasing tile size and the slope decreases slightly with decreasing λ. The H_2-O_2-Ar mixtures have the lowest slope, close to one, which indicates the least complexity in reaction front geometry. The trends for the coverage length, Fig. 4.8b, are consistent with the intuitive evaluation of the images and the range of total edge lengths shown in Fig. 4.7.

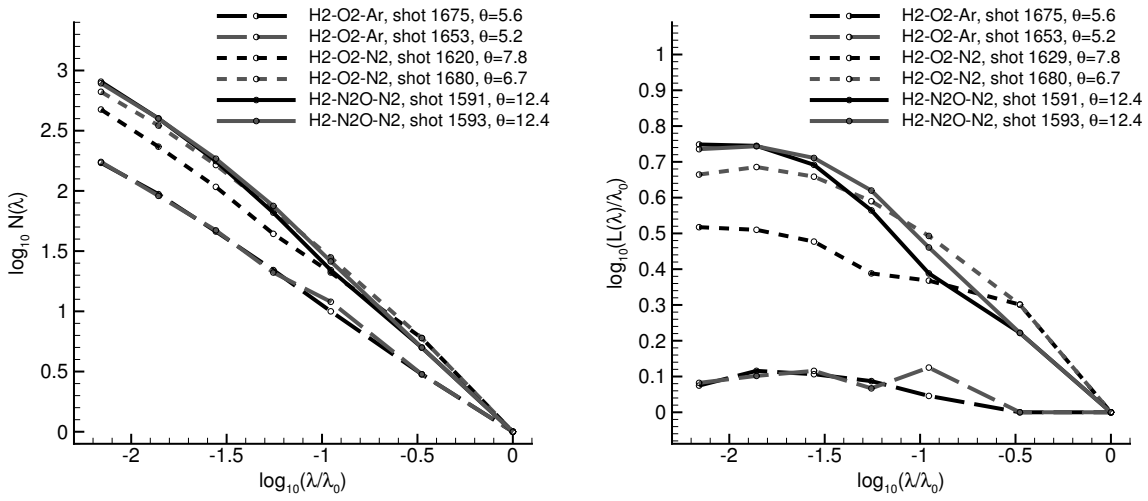

Figure 4.8: (a) Box-coverage count $N(\lambda)$ as a function of normalized scale for six representative images. (b) Normalized box coverage length L as a function of normalized scale.

The coverage length is almost independent of the tile size for the two lower activation energy mixtures and $L_{max}/\lambda_0 < 1.25$, indicating that these fronts are very smooth and made up of only a few line segments. For the higher activation energy cases, the normalized coverage length L/λ_0 increases rapidly with decreasing λ/λ_0. The coverage length appears to reach a limiting value at the smallest values of λ/λ_0 corresponding to tiles smaller than 8×8 pixel, which corresponds to object height of 1.25 mm for an image height of 45 mm. The limiting value of L/λ_0 is an increasing function of the reduced activation energy. For $\theta = 12.4$, the limiting value of $L/\lambda_0 = 5.6$, which is consistent with the maximum value of 7.5 from Fig. 4.7. The phenomena of a limiting value for L/λ_0 is, in part, caused by the continuously decreasing contrast ratio for higher spatial frequencies as described by the MTF, discussed further below.

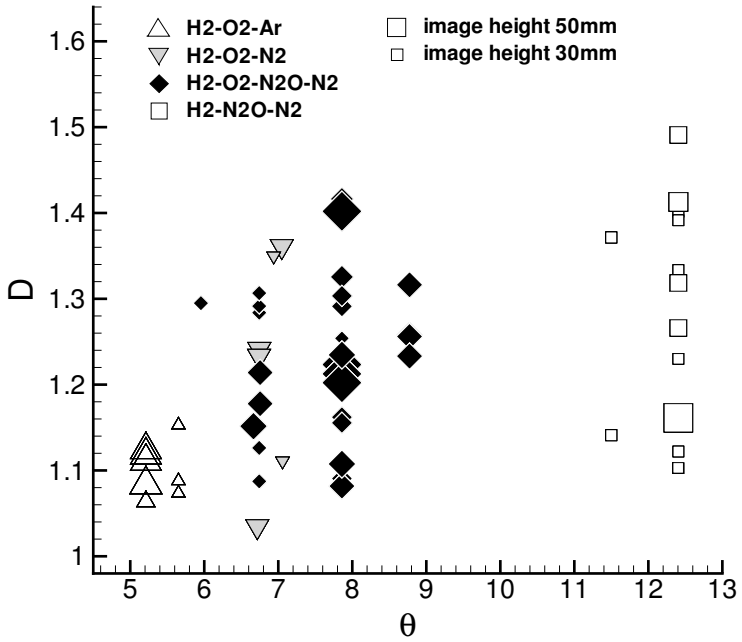

Figure 4.9: Dimension obtained from least-square linear fit as a function of the reduced activation energy θ. Symbol size scales with height of field of view.

The dimension (Fig. 4.9) was found for each image using a linear least-squares fit

to determine D in the relationship

$$\log(N/\lambda_0) = -D\log(\lambda/\lambda_0) + constant \tag{4.4}$$

for the range -2.1 $\leq \log(\lambda/\lambda_0) \leq$ -0.5, corresponding to tile sizes from 4×4 to 96×96. The choice of the inner cut-off for this fit is motivated by the previous considerations involving the MTF of the imaging system resolution. The inner cut-off scale corresponds to the smallest feature size that can be visualized according to our analysis of the imaging system. The upper bound was taken one size smaller than the 288×288 tile, which is larger than the image. The cut-off scales are somewhat arbitrary but similar results for the dimension were obtained by changing the cut-off scales by one tile size up or down.

As for the normalized edge length, a range of dimensions is obtained for each θ. For $\theta \leq 6$, the spread is small and the dimensions range from 1.05 up to 1.15. For intermediate values of θ, the dimensions range between 1.05 and 1.4 and for the highest value of $\theta = 12.4$, the maximum dimension of 1.5 is obtained. The larger maximum values of the dimensions obtained for higher values of θ are quantitative evidence for the increasing degree of corrugation of the reaction front for higher values of θ.

4.5.2 Discussion

The large range of dimensions obtained for $\theta > 6$ can be ascribed in part to the same effects that were discussed earlier in connection with the spread in values measured for the lengths shown in Fig. 4.7.

Additionally, the pixelation of the image and the edge representation affects the box counting method. The box count will vary depending on the edge orientation with respect to the pixel grid. For example, a straight line is represented as a straight line on all scales only if it is horizontal, vertical, or inclined to the pixel grid at 45°. When the box size approaches the pixel size, the inferred dimension will decrease towards one, which is to be expected, since the effective dimension at the pixel scale

must always be one. Analysis of synthetic images of the Koch curve show a decrease in $\mathrm{dlog}\, L(\lambda)/\mathrm{dlog}\, \lambda$ with decreasing λ, for $\lambda \leq 4$ pixel. With the box counting technique, $d \log L(\lambda)/d \log \lambda$ does not approach zero in a smooth fashion, a consequence of the pixel representation itself. A bounding box partition method (Catrakis and Dimotakis, 1996) based on the idea of representing the boundary outline as B-splines and subsequently subdividing the bounding box in both dimensions in each step, is shown to remove several difficulties based on pixel-based schemes. However, this technique is limited in its application with regard to the images processed here, since the bounding box has a high aspect ratio. This leads to a sub-pixel resolution in the horizontal direction after a few subdividing steps.

Another reason for the continuous decrease in the slope of $\mathrm{d}\, \log N(\lambda)/\mathrm{d}\, \log \lambda$ with decreasing λ is the steep fall-off in the MTF for low frequencies. The increasing blur for smaller features results in a smoother edge detected front at smaller scales, and, consequently, a decrease in $\mathrm{d}\, \log N(\lambda)/\mathrm{d}\, \log \lambda$ and $\mathrm{d}\, \log L(\lambda)/\mathrm{d}\, \log \lambda$. In addition, one has to consider the light sheet thickness, which further reduces the resolvable scale but at smaller scales. We can conclude that the decrease in dimension observed for some images of N_2-diluted H_2-O_2 and H_2-N_2O mixtures for scale sizes on the order of 1 mm is not likely to have been caused by the absence of smaller scale features in the flow, but rather from an effect arising from the box-counting technique applied here and the imaging system and technique.

4.5.3 Implications for possible diffusive transport phenomena

For the assumed cut-off scales and fractal dimensions fractal geometry concepts have been shown to provide estimates of the turbulent flame velocity in combustion research (Gouldin, 1987). The ratio of turbulent burning velocity S_T to laminar burning velocity S_L was first suggested by Damköhler (1940) to be proportional to the ratio of wrinkled flame surface area A_w to the flow cross section area A_0. Here, this concept is applied to investigate the possible contribution of a diffusion-controlled combustion

mode to detonation propagation, which, in the classical models, is considered to be due only to shock-induced reaction with no diffusive transport.

The surface area of the reaction front is estimated from the fractal dimension. From the PLIF images, we obtain only a two-dimensional cross section of the three dimensionally corrugated reaction front surface. Assuming fractal isotropy the fractal dimension D_3 of an object in three dimensions is, due to self-similarity, one greater than the fractal dimension D_2 of a two dimensional cross section of the same object (Smallwood et al., 1995). The fractal dimensions D_2 obtained from the PLIF images were at maximum 1.5, so, for the cases considered, D_3 is, at most, approximately 2.5. In order to compute the three-dimensional surface area from the fractal dimension, the following relationship used in low-speed turbulent combustion research (Gouldin, 1987) has been applied:

$$\frac{A_w}{A_0} = A \left(\frac{\varepsilon_o}{\varepsilon_i} \right)^{D_3 - 2}, \tag{4.5}$$

where A is a model constant on the order of one. For a model constant A=1, this leads to a value for A_w/A_0 of 4.8, using for the inner and outer cut-off 4 and 96, respectively. Based on mass conservation considerations, the ratio A_w/A_0 has to be on the order of w/S_L for a diffusion-dominated adiabatic flame to contribute to the combustion. w is the post shock velocity in the shock fixed frame, and S_L is the adiabatic flame speed for post shock conditions. The computation of the adiabatic burning velocity S_L at post shock conditions was performed with a numerical solution of the one-dimensional steady reactive Navier-Stokes equation with the detailed chemical reaction mechanism as described in Singh et al. (2003). The post shock conditions were evaluated for a detonation traveling with $U/U_{CJ} = 0.95$ in a mixture of $2H_2+O_2+8.1N_2$ ($P_0 = 20$ kPa, $T_0 = 300$ K) to be $P_{ps} = 0.39$ MPa and $T_{ps} = 1195$ K. The corresponding adiabatic burning velocity was calculated to be 30.4 m/s. The post shock velocity is 320 m/s at these conditions, which leads to criterion of $A_w/A_0 \approx 10.5$ for an adiabatic burning process contributing significantly to the combustion mode. This is a factor of two smaller than the surface area increase predicted from the fractal geometry approach. A better resolution of the PLIF images could allow for a smaller inner cut-off ε_i and

larger values for A_w/A_0, possibly larger than the criterion mentioned above. In the current analysis, the range of scales necessary to meet this criterion could not be resolved.

Chapter 5

Results of Detonation Diffraction Experiments

The results of the diffraction experiments are presented in this chapter together with a simplified model for the diffraction process. A characterization of the mixtures studied is given in Section 5.1. The data obtained from the pressure transducer traces are shown in Section 5.2. The diffraction process is described in Section 5.3 together with Skews' model for a diffracting wave. Even though this section is more an analysis than a result, it leads to a better understanding of the features seen on images presented in the following sections. The critical, sub-, and super-critical diffraction regime is documented in Section 5.4 on the basis of representative examples of the experimentally obtained PLIF, schlieren, and chemiluminescence images. To gain further insight into the complex three-dimensional combustion process, a stereoscopic image of a critical diffraction experiment was constructed, which is described in Section 5.5. In Sections 5.6 and 5.7, quantitative measurements of the distance from the shock to the reaction front and the axial velocity profile of both are presented. The data were derived from edge detected images, which are described in Section 5.8. Furthermore, the evolution of the shape of the diffracting wave and the velocity profile are discussed for sub-critical cases.

5.1 Mixture characterization

All mixtures investigated were at stoichiometric composition and the initial temperature was between 294 and 301 K. Within a series of experiments, the facility temperature increased with time due to the energy release by the combustion taking place, leading to a slightly higher temperature than the room temperature of 294 K. The experiments can be divided up with respect to their composition and initial pressure into six series, which are given in Table 5.1.

	mixture composition	P_0 [kPa]	diluent mole fraction of total mixture	nomenclature	number of shots
1	2 H_2 + O_2 + β Ar	100	50–72%	Ar dilution series	77
2	2 H_2 + O_2 + 3 Ar	45–100	-	Ar pressure series	19
3	2 H_2 + O_2 + β N_2	100	19–25%	N_2 series	14
4	H_2 + N_2O	40–80	-	N_2O series	71
5	CH_4 + 2 O_2	50–125	-	CH_4 series	19
6	C_2H_6 + 3.5 O_2	30–45	-	C_2H_6 series	35

Table 5.1: Summary of series of experiments conducted with the detonation diffraction experiment with respect to mixture composition and initial pressure.

A more detailed presentation of mixture parameters for all experiments is given in Appendix F. The amount of diluent was varied only for series 1–3, i.e., the Ar- and N_2-diluted H_2-O_2 mixtures. The mixture composition was fixed for all other series and the initial pressure was changed. Each experimental series ranges from the sub- to the super-critical detonation diffraction regime. Most of the 229 total experiments are conducted for the argon pressure and dilution series and the N_2O series. The focus in the following analysis is on three experimental series, two Ar-diluted. The argon diluted H_2-O_2 mixtures (series 1 and 2) served as an example of mixtures with regular cellular structure while the H_2-N_2O mixtures (series 3) represented those exhibiting irregular cell structure. Experiments indicate that mixtures with higher values of θ exhibit a more unstable and more irregular structure. Within one series of experiments, θ was changed little in comparison to Δ, the induction zone length. This allows the study of a mixture with a fixed degree of regularity in the sub- and super-

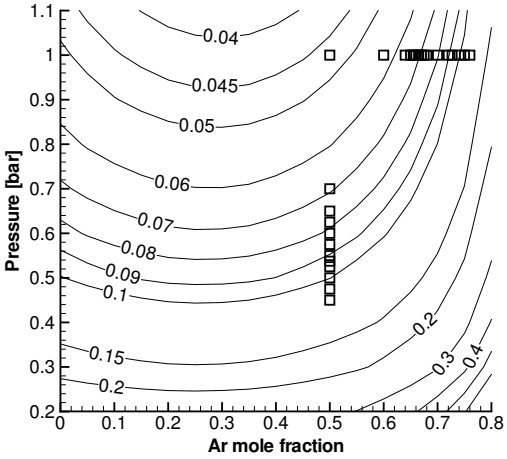

a) Δ [mm], $2H_2+O_2+\beta AR$ Warnatz mechanism.

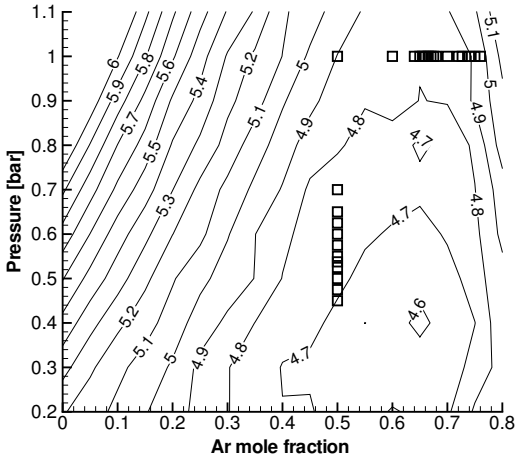

b) θ [-], $2H_2+O_2+\beta AR$ Warnatz mechanism.

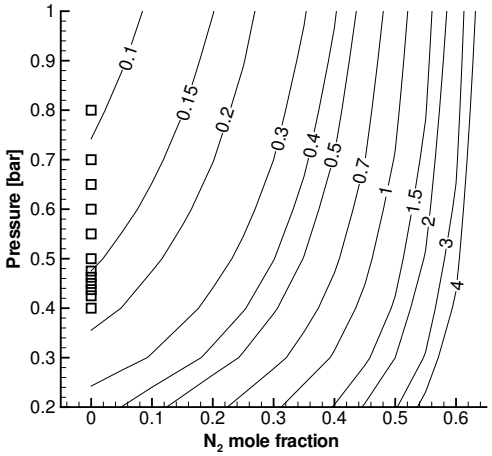

a) Δ [mm], $H_2+N_2O+\beta N_2$, Mueller mechanism.

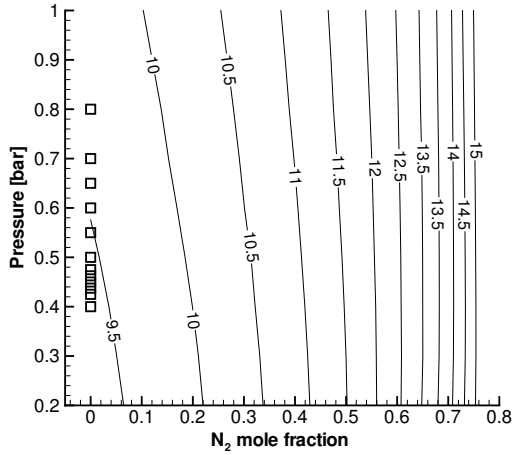

b) θ [-], $H_2+N_2O+\beta N_2$, Mueller mechanism.

Figure 5.1: Contour plots of induction zone length, Δ, and reduced activation energy, θ, as function of initial pressure and dilution amount for the Ar and N_2O series. Open square symbols represent the conditions of experiments. Multiple experiments are conducted for identical conditions, so the number of squares does not reflect the number of experiments.

critical diffraction regime. The induction zone length of a fuel-oxidizer-diluent system can be changed by various means, including stoichiometry, diluent mole fraction, and initial temperature and pressure. For the mixtures studied, the diluent amount and initial pressure were found to be parameters that could be changed easily in the experiment while keeping θ constant within one experimental series (Fig. 5.1). Contour plots of Δ and θ for all mixtures experimentally investigated are shown in Appendix H. For the argon pressure and dilution series, θ ranged from 4.5 to 4.9 while Δ varied from 0.05 to 0.12 mm. For the N_2O series, θ varied from 9.4 to 9.5 compared to Δ varying from 0.1 to 0.18 mm.

5.2 Pressure traces

Determination of whether an experiment was super-critical or sub-critical was made based on the pressure histories acquired. The three pressure transducers (P_1, P_2, and P_3) mounted in the detonation tube section (Fig. 2.5) were used to monitor the velocity of the incoming detonation wave by analyzing time of arrival data. An example of a set of pressure traces obtained from experiments of the Ar pressure series is shown in Fig. 5.2. The pressure histories of all experiments are shown in Appendix K. The time of arrival was defined as the time of the first data point for which the pressure is larger than one-half the peak pressure. The normalized velocity U/U_{CJ} was between 0.97 and 1.03 and the detonation wave was traveling close to CJ conditions before reaching the area change (Fig. 5.3).

The CJ velocity U_{CJ} was calculated with the thermodynamic equilibrium code STANJAN (Reynolds, 1986). In general, there is a slight decrease in detonation velocity while the detonation is traveling down the tube. The velocity U_{12}, measured between transducer P_1 (0.4 m from ignition point) and P_2 (0.8 m), is, for most experiments, larger than U_{23}, corresponding to the velocity derived from the pressure histories of transducers P_2 and P_3 (1.2m). This could be caused by P_1 being located directly after the Shchelkin spiral section. The deflagration to detonation transition (DDT) is enhanced by the section including the Shchelkin spiral and is presumably

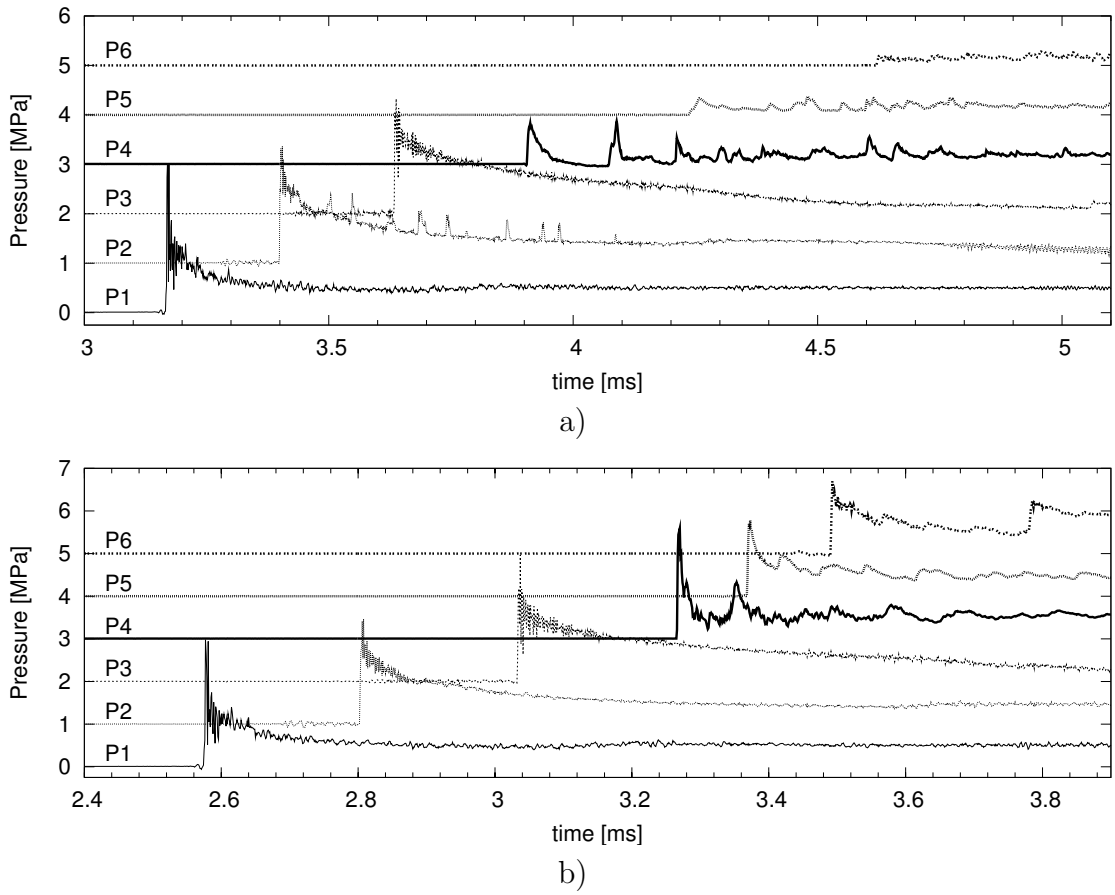

Figure 5.2: Pressure traces. a) Sub-critical experimental outcome. Shot 32, 0.213 H_2 + 0.107 O_2 + 0.68 Ar, P_0=100 kPa, T_0=296 K. b) Super-critical experimental outcome. Shot 44, 0.233 H_2 + 0.117 O_2 + 0.65 Ar, P_0=100 kPa, T_0=296 K.

taking place within that section of the tube. The DDT event itself is known to involve a "localized explosion" event and a detonation wave velocity above CJ condition directly after the event. The uncertainty in detonation velocity, obtained experimentally from pressure histories, was found to be ±3%. This includes the effect of finite sampling rate of the data acquisition system, the averaging effects arising from the 4 mm in diameter large active surface of the pressure transducer, and uncertainties in the spacing of the pressure transducers.

The discrete spacing in values obtained for U/U_{CJ} (Fig. 5.3) arises from the finite sampling rate of the data acquisition system. As U_{CJ} varies as a function of Ar-dilution and initial pressure, the data points obtained from individual experiments line up as curves.

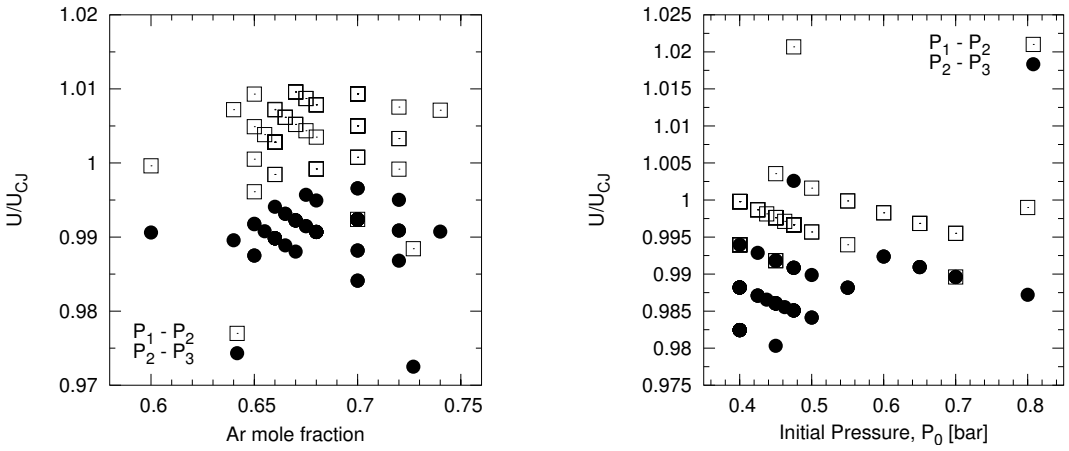

a) $2H_2+O_2+\beta$AR, P_0 1bar, dilution series. b) H_2+N_2O, pressure series.

Figure 5.3: Normalized velocity U/U_{CJ} as a function of (a) argon diluent amount for the Ar dilution series and (b) of initial pressure for the N_2O series. U is derived from pressure histories and corresponding detonation wave time of arrival data.

The normalized CJ velocity was found to be independent of the initial pressure or diluent amount in all of the experimental series. This indicates that for all mixture compositions investigated, the detonation tube was operated in normal propagation regimes and a self-sustained stable detonation wave traveling close to CJ conditions was present at the tube exit plane.

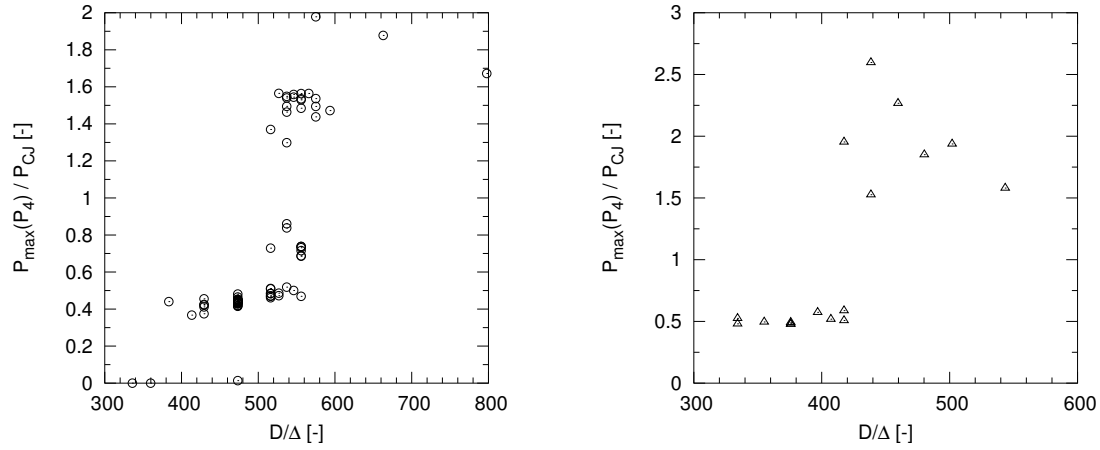

a) $2H_2+O_2+\beta$AR, P_0=1bar, dilution series. b) $2H_2+O_2+3$Ar, pressure series.

Figure 5.4: Maximum pressure measured within 100 μs at pressure transducer P_4 normalized by the pressure corresponding to the calculated CJ velocity versus D/Δ. D is the tube diameter (18 mm) and Δ the calculated induction zone length.

The pressure histories obtained from transducers (P_4, P_5, and P_6) mounted in the

	mixture composition	critical conditions		
		P_0 [kPa]	diluent mole fraction of total mixture	D/Δ
1	2 H_2 + O_2 + β Ar	100	67%	537
2	2 H_2 + O_2 + 3 Ar	55	-	417
3	2 H_2 + O_2 + β N_2	100	24%	494
4	H_2 + N_2O	43.75	-	232
5	CH_4 + 2 O_2	120	-	235
6	C_2H_6 + 3.5 O_2	37.25	-	353

Table 5.2: Summary of critical conditions for all series of experiments conducted. For the CH_4-O_2 mixtures, the critical conditions were determined upon inspection of the schlieren and multiple gates chemiluminescence images and for all other mixtures upon the maximum pressure measured at transducer P_4 as described in the text.

test section were used to determine whether the detonation successfully transitioned into the test section or detonation failure occurred. Two sets of pressure traces representative of the sub-critical and super-critical regime are shown in Fig. 5.2. In the sub-critical case, the pressure transducer in the test section registered a much lower pressure rise than the peak pressure in the detonation tube, which was found to be close to the calculated CJ pressure. The weaker shock wave can reflect off the side and end walls of the test section and can re-initiate a detonation wave (Murray and Lee, 1983, Thomas et al., 1986). In the present study, confinement influence is not investigated. The pressure signals from experiments in the super-critical regime show, for the pressure transducers in the test section, a peak pressure close to the one measured in the tube section (Fig. 5.2b). This indicates successful detonation transmission into the test section. The determination of the regime was based on the pressure trace of transducer P_4, the first pressure transducer in the test section. The maximum pressure within 100 μs after the first pressure rise was determined for each experiment and is denoted in the following as maximum pressure P_{max}. Note that P_{max} is not the overall maximum pressure from a pressure trace. The value for P_{max}, obtained from each experiment, was then normalized by the calculated CJ pressure, P_{CJ}, for the specific mixture and experimental conditions (Fig. 5.4).

For pressure transducers P_5 and P_6, which are located further downstream, normalized peak pressures larger than unity were detected for experiments with a smaller

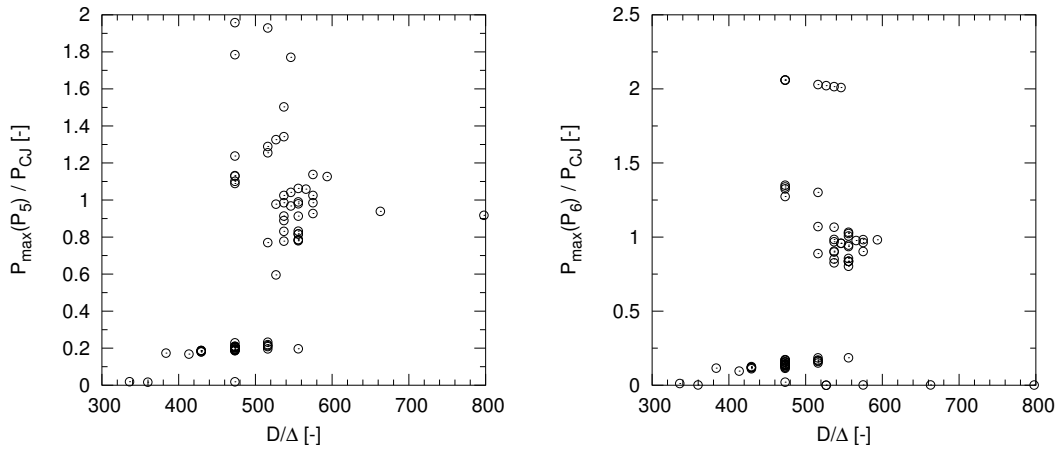

Figure 5.5: Maximum pressure measured within 100 μs at pressure transducer P_5 (a) and P_6 (b) normalized by the calculated CJ velocity versus D/Δ.

value for D/Δ than was detected at P_4 (Fig. 5.5). For the most insensitive mixture, $P_{max}(P_4)/P_{CJ}$ was measured to be larger than unity when D/Δ >520 compared to a D/Δ >475 for $P_{max}(P_6)/P_{CJ}$. This indicates that diffracting detonation waves in mixtures close to the critical regime do, in fact, re-ignite further downstream. The shift towards smaller values of D/Δ for re-initiation was observed for most experimental series as shown in the complete set of plots shown in Appendix I. The highest values for P_{max}/P_{CJ} were measured for pressure transducers P_4. This could arise from phenomena like oblique reflections and Mach stems, less likely to occur further downstream, since the detonation or shock wave has traveled a substantial distance in the test section.

If $P_{max}(P_4)/P_{CJ}$ was found to be smaller than unity, the experiment was considered sub-critical, otherwise it was considered super-critical. For some pressure traces, a high overall maximum pressure was observed at P_4. This could arise from a reflected shock wave of the test section side or end wall, which triggered a re-initiation event. This overall maximum pressure was often observed long after the first pressure rise was detected on P_4. Possible misinterpretation of these cases was avoided by taking the maximum pressure within 100 μs after the initial pressure rise. The magnitude of the pressure signal measured at P_4 can also be influenced by the fact that the

diffracting detonation wave is not traveling perpendicular to the top wall of the test section. Regardless of whether a re-initiation event is taking place, the leading shock wave will be reflected obliquely by the wall. The detected pressure will be different than for a wave perpendicular to the surface.

Schlieren and sequences of chemiluminescence images were taken along with the pressure traces to aid the interpretation of pressure histories. The determination of the critical conditions is not significantly influenced by reflection phenomena as they occur only for a narrow range of mixtures. Critical conditions given in Table 5.2 are defined as the average of the values bounding the critical regime. For experiments conducted in the critical regime, both sub-critical and super-critical outcomes were observed for a given mixture. The re-initiation process is a stochastic process in the critical diffraction regime and is apparently very sensitive to small, uncontrollable variations in initial conditions. These include the random variations in the phasing of the transverse waves within the cellular structure of the detonation front.

5.3 Disturbance propagation

In the following section, the diffraction process is discussed in a simplified manner using a model originally developed for unreactive shock waves. The detonation is assumed to travel at CJ conditions in the tube of diameter D towards the unconfined space. The tube and unconfined space are both occupied by the same mixture. The area change is described by the angle of divergence δ between the initial detonation propagation direction and the wall of the unconfined half space, an angle $\delta = 90°$ is shown on Fig. 5.6. In the case of the present experiments, δ was always 90 deg.

When the detonation wave reaches the corner, a disturbance created by the flow around the corner propagates with a finite transverse velocity component into the undisturbed part of the detonation front. For a constant transverse velocity, the point of interaction between the main wave and the disturbance defines a cone at angle α to the tube wall. The tip of the cone is located on the tube axis at a distance x_c from the tube end plate. The tip is the point at which the corner signals sent

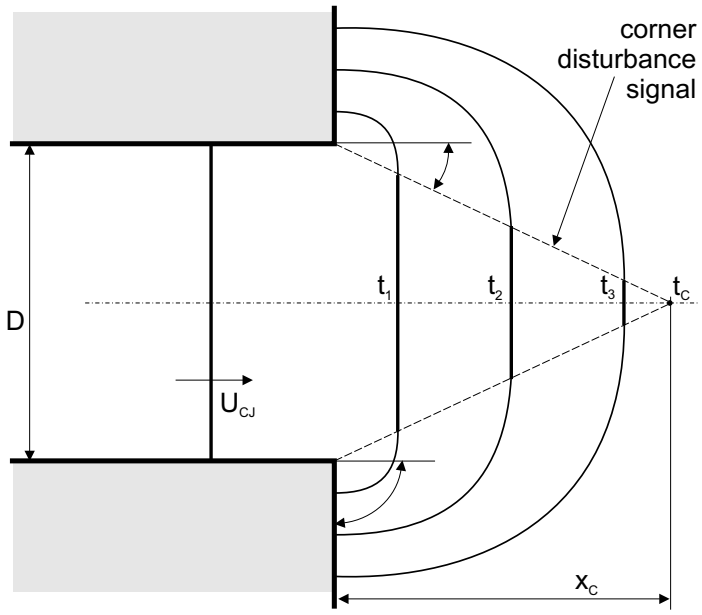

Figure 5.6: Sketch of diffracting detonation wave showing the cone of the corner disturbance signal.

out from points along the rotationally symmetric corner collide. The distance x_c and the time of collision t_c depend on the transverse disturbance propagation speed, the CJ velocity, and the tube diameter. Until that point in time, the detonation is undisturbed inside the cone described by the corner signal (Fig, 5.7).

The thermodynamic conditions normal to the detonation vary strongly, temporally as well as spatially. Furthermore, variations along the front arise from the cellular structure of the detonation. This makes it difficult to determine the effective transverse velocity component v with which the corner signal propagates into the undisturbed front. For a non-reacting shock wave with an uniform flow behind, the problem is much simpler and the transverse velocity is well defined. Using the geometric construction of Skews (1967) for non-reacting diffracting shocks v depends on the post-shock sound speed c and post-shock velocity in the lab frame u (Fig. 5.7).

The corner disturbance signal is traveling radially into the shocked material at the local sound speed c while being convected downstream with the velocity u, the post-shock velocity in the lab frame. The angle α is found by a Huygens' construction

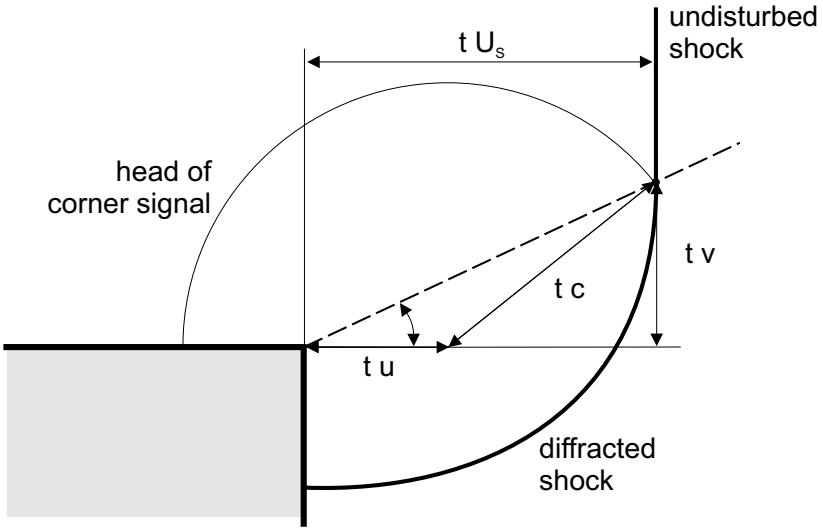

Figure 5.7: Skews' construction of disturbance propagation angle.

and, from the geometry shown, is

$$\tan\alpha = \frac{v}{U_S} = \frac{\sqrt{c^2-(U_S-u)^2}}{U_S} = \frac{\sqrt{c^2-w^2}}{U_S}\,, \tag{5.1}$$

where w is the fluid velocity behind the shock in the shock fixed frame. The distance x_c and time t_c at which the disturbance signal reaches the tube axis can be written as

$$x_c = \frac{D}{2\alpha}, \tag{5.2}$$

$$t_c = \frac{D}{2\alpha U_S}. \tag{5.3}$$

Skews' model can be adapted to the case of a diffracting detonation traveling at CJ conditions by assuming an incoming shock velocity equal to the CJ velocity and an appropriate choice for c and u. Previous researchers used the post-shock conditions at CJ conditions (Schultz, 2000), neglecting the details of the reaction zone and the oscillating strength of the lead shock wave, both discussed here. In order to calculate c and u, the details of the reaction front are simplified to an one-dimensional steady profile described by the ZND model. The sound speed and post-shock velocity are then a function of the distance to the lead shock only (Fig. 5.8). The sound speed

c is fairly constant within the induction zone and its rise at the beginning of the recombination zone is mainly due to the temperature increase. The reacting gas begins to expand at this point in the detonation profile, leading to a lower fluid density and a higher relative velocity w. After recombination is complete, a plateau in all properties is observed. The length of the reaction zone, which can vary from mixture to mixture, determines when the plateau in both properties is reached.

Transverse acoustic channels of different sound speeds c exist in the undisturbed part of the detonation. These depend, in the one-dimensional ZND model, on the distance to the lead shock front only. The post-shock velocity is also changing as a function of distance behind the shock. The disturbance propagation angle α has to be calculated with corresponding c and w as a function of distance behind the shock in order to determine the maximum in α (Fig. 5.8). The maximum in α gives a lower bound for t_c and x_t, the time and distance at which the acoustic disturbance signal reaches the tube axis. The quantity $(c^2 - w^2)^{1/2}$ is proportional to $\tan\alpha$ (Eq. 5.1) and is also shown in Fig. 5.8. The details of the rise in c and w determine the existence and location of a local maximum in α. For the H_2-O_2-Ar mixtures, the maximum in α is very broad and the post-shock values of properties are a good approximation to the maximum values. For the H_2-N_2O mixtures, c increases slightly earlier than w, leading to a more pronounced maximum in α. Using post-shock conditions to calculate α can introduce significant error in this case. The maximum in α was identified for all mixtures to occur within 1 mm behind the lead shock front. Note that the choice of detailed chemical reaction mechanism can influence the profiles of c and w and therefore influence the maximum value of α.

The angle α was calculated for post-shock conditions for all mixtures experimentally investigated. A complete set of results for all mixtures is plotted in Appendix J. The maximum in α for the ZND profile, corresponding to the minimum in x_c, was determined (Fig. 5.9). The distances are plotted versus the D/Δ parameter. Larger values of D/Δ correspond to mixtures with smaller induction zone length Δ, which in the present study, means higher initial pressure. For the dilution series, the more diluted mixtures correspond to smaller values of D/Δ. The distance x_c is fairly in-

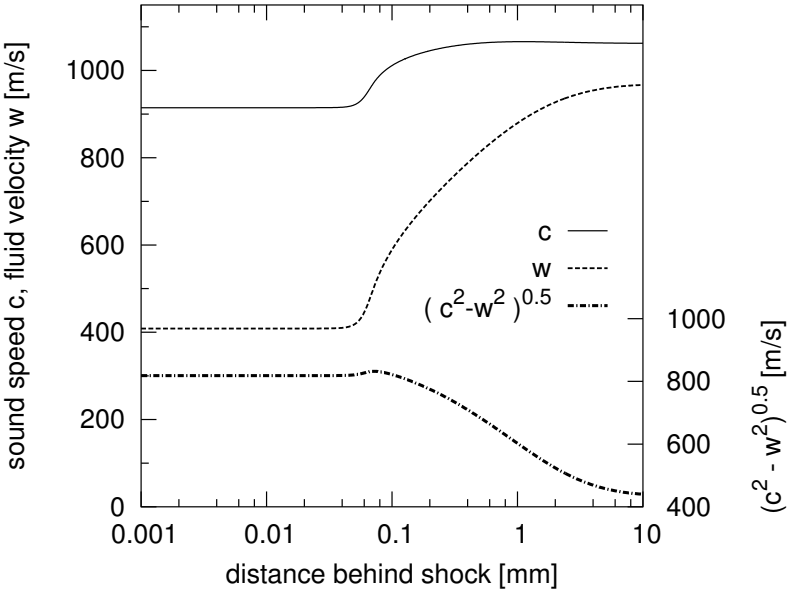

a) $0.233H_2$+$0.177O_2$+0.65Ar, 100 kPa, 300K, D/Δ = 575, Warnatz mechanism.

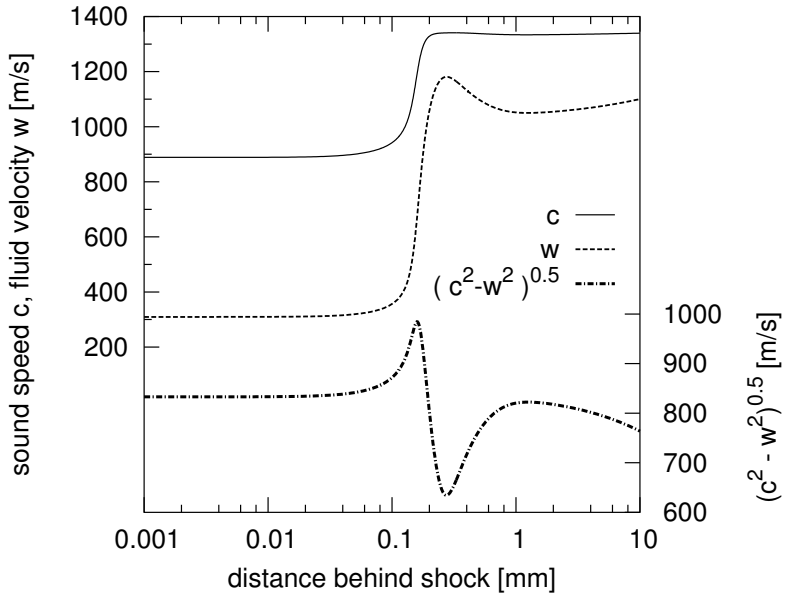

b) $0.5H_2$+$0.5N_2O$, 45 kPa, 300K, D/Δ = 237, Mueller mechanism.

Figure 5.8: Local sound speed and fluid velocity as a function of distance behind the lead shock wave. Calculations with the ZND model and reaction mechanisms of Warnatz and Mueller. The quantity $(c^2 - w^2)^{1/2}$ is proportional to $\tan\alpha$, the local disturbance propagation angle.

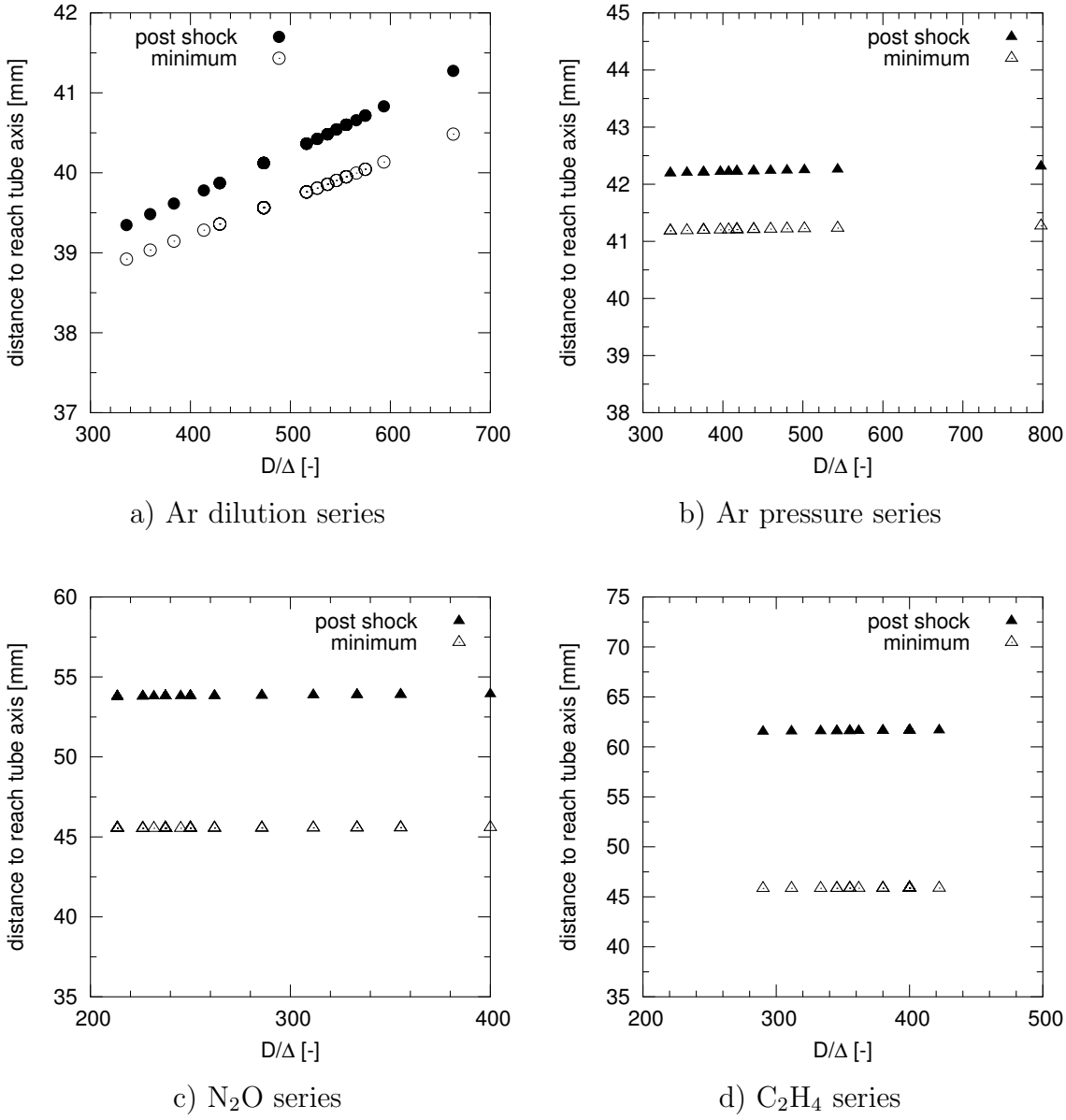

a) Ar dilution series

b) Ar pressure series

c) N_2O series

d) C_2H_4 series

Figure 5.9: Distance x_c at which corner disturbance signal reaches the tube center axis as a function of normalized induction zone length. x_c is calculated from the post-shock conditions, labeled "post shock", and from the maximum angle α found within the ZND calculated detonation profile. This angle corresponds to the minimum in x_c, labeled "minimum". a) H_2-O_2-Ar mixtures, dilution series, Warnatz mechanism. b) H_2-O_2-Ar mixtures, pressure series, Warnatz mechanism. c) H_2-N_2O mixtures, Mueller mechanism. d) C_2H_6-O_2 mixtures, GRI mechanism.

dependent of the initial pressure for a fixed mixture composition. This observation is valid for all mixtures investigated in this study. The smallest x_c was found to be 40 mm for the Ar-diluted H_2-O_2 mixtures. For all other mixtures investigated, the minimum x_c was found near 45 mm. For the dilution series, 50–72% Ar-diluted H_2-O_2 mixtures, the distance x_c for the smallest dilution is 5% higher than for the highest dilution. Neither the initial pressure nor the amount of diluent significantly influence the distance x_c for the Ar-diluted mixtures.

The model of a steady state ZND profile with a lead shock traveling at CJ conditions for the detonation front is highly simplified. The lead shock velocity is known to oscillate during a cellular cycle between 0.9 and up to 1.5 times the CJ velocity, depending on the mixture. In order to address this issue, ZND profiles were calculated for steady lead shock velocities in the range of $U_S/U_{CJ} = 0.9$ to 1.5. For each value of U_S/U_{CJ}, the maximum in α was found and compared to the value at CJ conditions. Even though this method does not include the unsteadiness of the front directly, it gives a good estimate of how much the transverse propagation speed of the corner signal at CJ conditions is influenced by a higher or lower lead shock velocity. Two mixtures are discussed here in detail: $0.223H_2$+$0.117O_2$+0.65Ar at $P_0 = 100$ kPa and $0.5H_2$+$0.5N_2O$ at $P_0 = 45$ kPa, both at $T_0 = 300$ K.

Larger values for U_S/U_{CJ} result in a higher post-shock temperature and post-shock sound speed (Fig. 5.10a and b). The absolute temperature rise in the reaction zone is smaller, since dissociation of the products is more significant at larger U_S/U_{CJ}. The absolute increase in sound speed c is also smaller for larger U_S/U_{CJ}. The fluid velocity demonstrates a similar trend for larger values of U_S/U_{CJ} (Fig. 5.10c and d). Despite the significantly higher sound speed for higher U_S/U_{CJ}, the angle α at post-shock conditions and the maximum in α varies insignificantly (Fig. 5.11).

This can be explained by the fact that the higher transverse propagation speed of the corner signal is associated with a higher leading shock velocity U_S. The larger value of U_S compensates for the increasing c (Eq. 5.1), changing α only by a small amount. For the Ar-diluted H_2-O_2 mixture, the minimum distance x_c increases from 40 mm for $U_S/U_{CJ} = 1$ monotonically up to 41.5 mm for $U_S/U_{CJ} = 1.4$ (Fig. 5.12a).

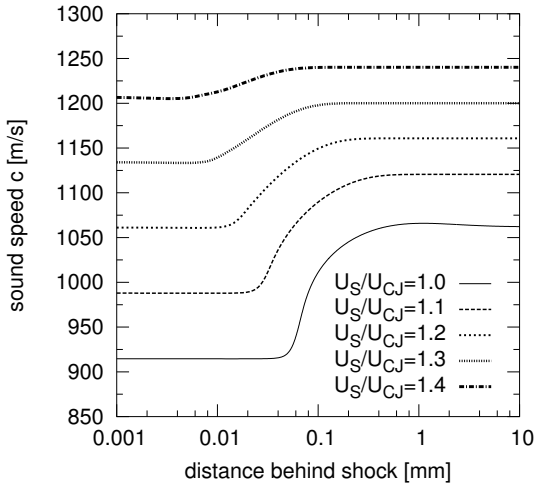

a) $0.223H_2+0.117O_2+0.65Ar$, P_0 100 kPa.

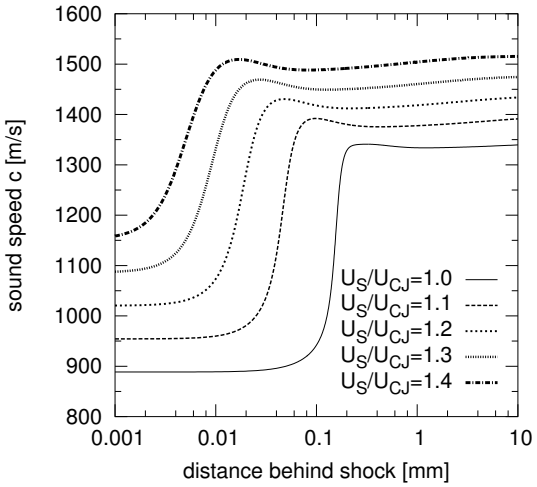

b) $0.5H_2+0.5N_2O$, P_0 45 kPa.

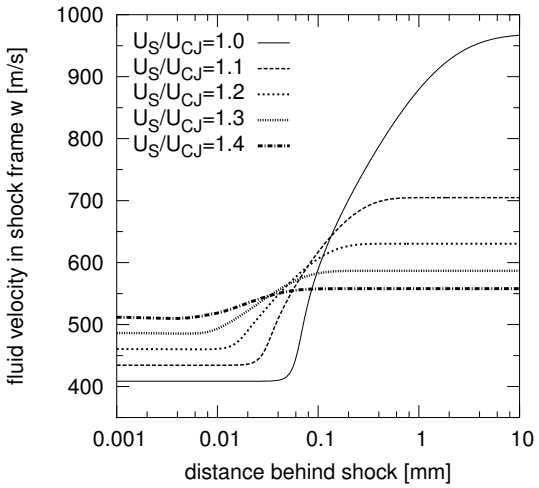

c) $0.223H_2+0.117O_2+0.65Ar$, P_0 100 kPa.

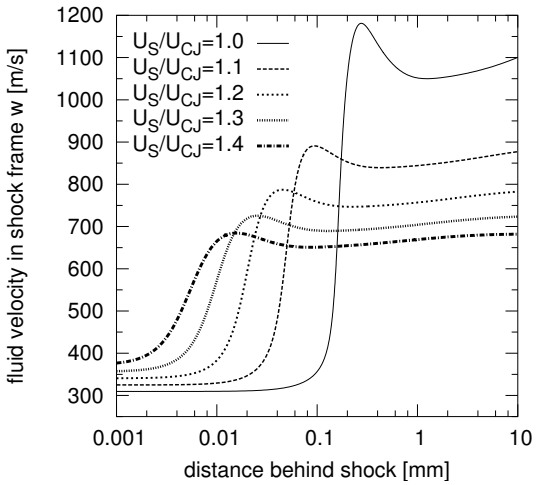

d) $0.5H_2+0.5N_2O$, P_0 45 kPa.

Figure 5.10: Profiles of sound speed, c, and fluid velocity in shock frame, w, calculated with the ZND code for several lead shock velocities.

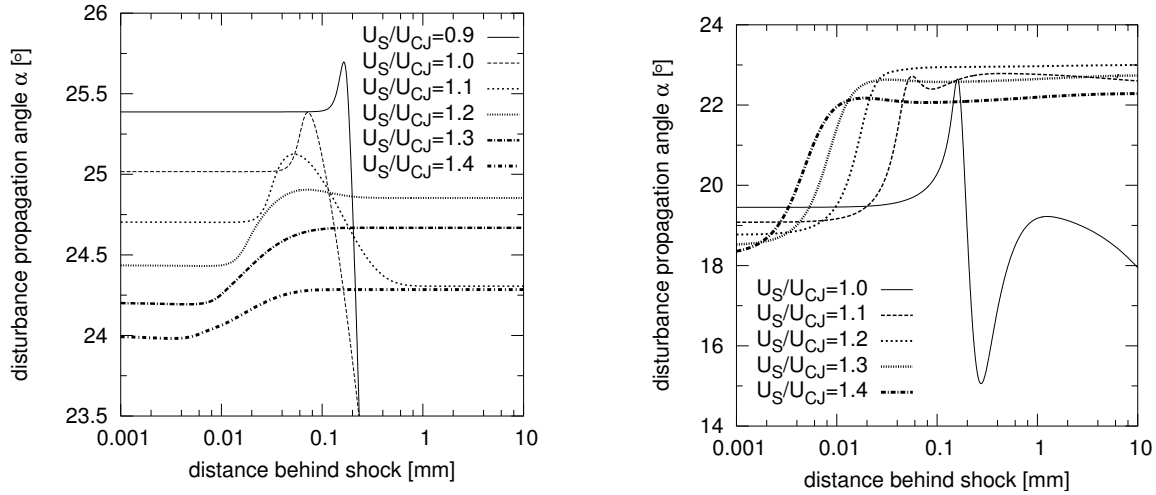

a) $0.223H_2$+$0.117O_2$+0.65Ar, P_0 = 100 kPa. b) $0.5H_2$+$0.5N_2O$, P_0 = 45 kPa.

Figure 5.11: Disturbance propagation angle α calculated with flow properties from ZND code for several lead shock velocities.

In contrast, the time t_c decreases for the same range of U_S/U_{CJ} from 23 μs to 17 μs. This decrease in t_c is due to the simultaneous increase in the transverse and horizontal velocity component of the interaction point of the corner disturbance signal with the undisturbed detonation front. The range of variation in x_c for 0.9$\leq U_S/U_{CJ} \leq$1.4 is 3 mm (Fig. 5.12b). The change in slope of x_c and t_c as a function of U_S/U_{CJ} observed for U_S/U_{CJ} = 1.095 can be explained by examining α for two cases of U_S/U_{CJ}, the abrupt change in slope. The profile of α as a function of distance behind the shock wave is shown for U_S/U_{CJ} = 1.09 and 1.1 in Fig. 5.13. For each profile, two local maxima in α exist. For the case of U_S/U_{CJ} = 1.09, the absolute maximum corresponds to the local maximum closest to the lead shock front. For U_S/U_{CJ} >1.1, the absolute maximum is found at the local maximum furthest behind the front. Since the overall maximum in α is used for the calculation of the minimum in x_c, x_c as a function of U_S/U_{CJ} appears continuous but not smooth.

5.4 Qualitative observations

In this section, the characteristic features observed on the schlieren, PLIF, and chemiluminescence images are described. Note that the features seen on the PLIF images

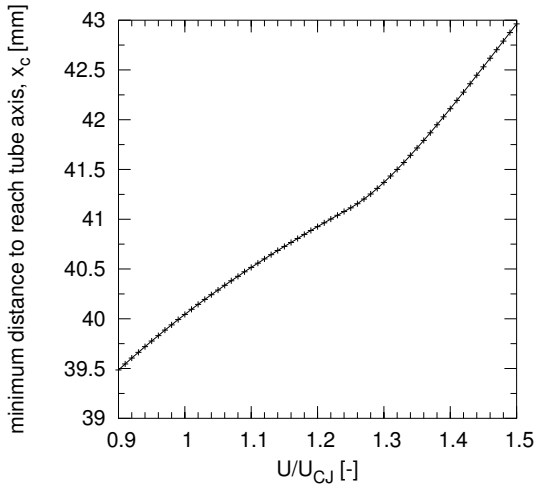

a) $0.223H_2$+$0.117O_2$+0.65Ar, $P_0 = 100$ kPa.

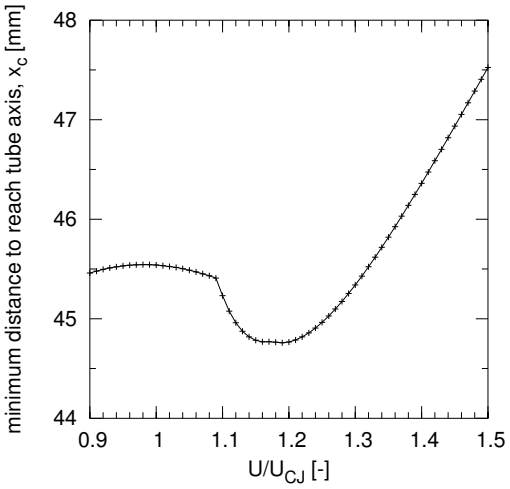

b) $0.5H_2$+$0.5N_2O$, $P_0 = 45$ kPa.

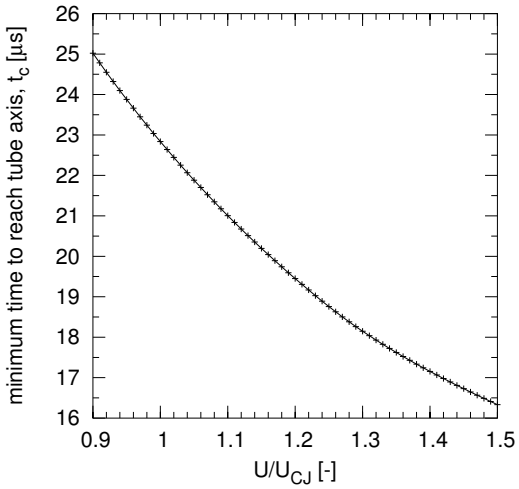

c) $0.223H_2$+$0.117O_2$+0.65Ar, $P_0 = 100$ kPa.

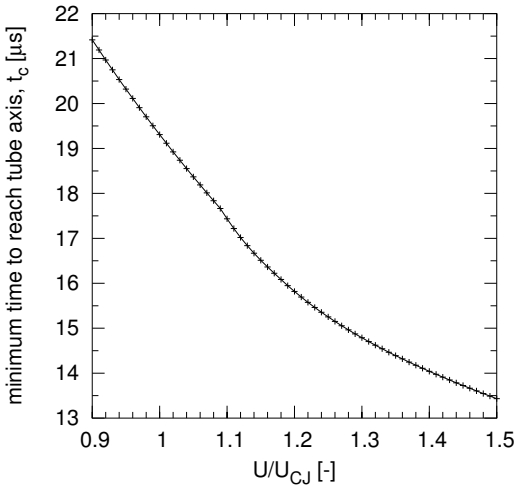

c) $0.5H_2$+$0.5N_2O$, $P_0 = 45$ kPa.

Figure 5.12: Minimum distance x_c and corresponding time t_c for corner disturbance signal to reach the tube axis as a function of lead shock velocity.

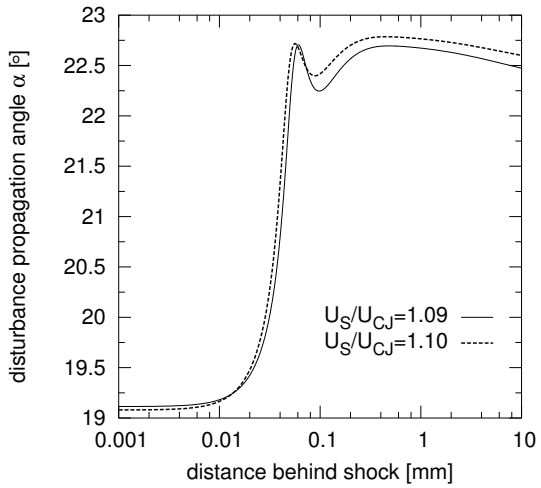

Figure 5.13: Disturbance propagation angle α calculated with flow properties from ZND code for two lead shock velocities.

correspond to a vertical cut through the flow field whereas the schlieren and chemiluminescence techniques integrate over the flow field in the direction of the optical axis of the system. Effects to be considered for the interpretation of multiple gates chemiluminescence images are discussed in Section 5.7. This section is divided up into experiments with H_2-O_2-Ar mixtures and experiments with H_2-N_2O mixtures. In each section, the observations for the sub-critical experiments are discussed first, followed by the observations for the super-critical experiments.

5.4.1 H_2-O_2-Ar mixtures

Note that a critical experiment per se does not exist. An experiment is classified as either sub- or super-critical. Nevertheless, the range of mixture parameters for which sub-critical and super-critical experimental outcomes are both possible is denoted as the critical diffraction regime. Most of the experiments in this study are conducted within the critical diffraction regime.

5.4.1.1 Sub-critical regime

In the sub-critical regime, schlieren images for the H_2-O_2-Ar mixtures show a planar detonation front directly after the detonation exits the tube. The diameter of the

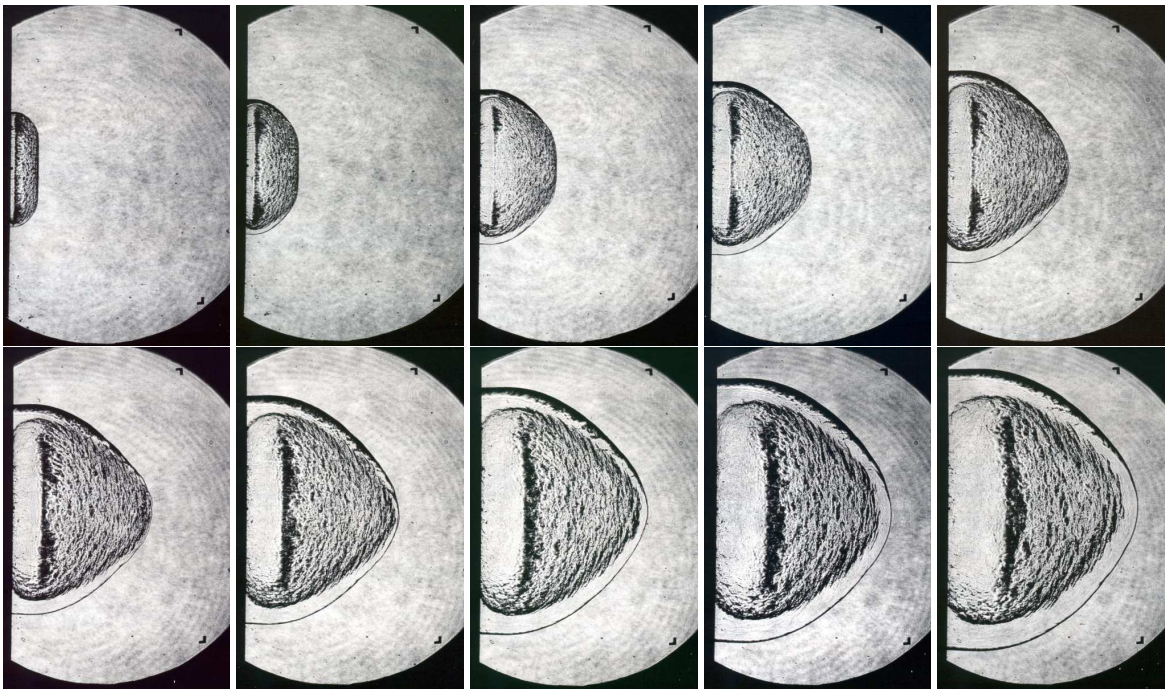

Figure 5.14: Schlieren images obtained from 10 separate experiments using the same $0.2H_2$+$0.1O_2$+0.7Ar mixture and initial conditions of P_0 = 100 kPa. The time increment between the point in time at which the schlieren image was taken is 6 μs. The shot numbers in the order shown are: 74, 73, 64, 65, 66, 67, 68, 69, 70, 71.

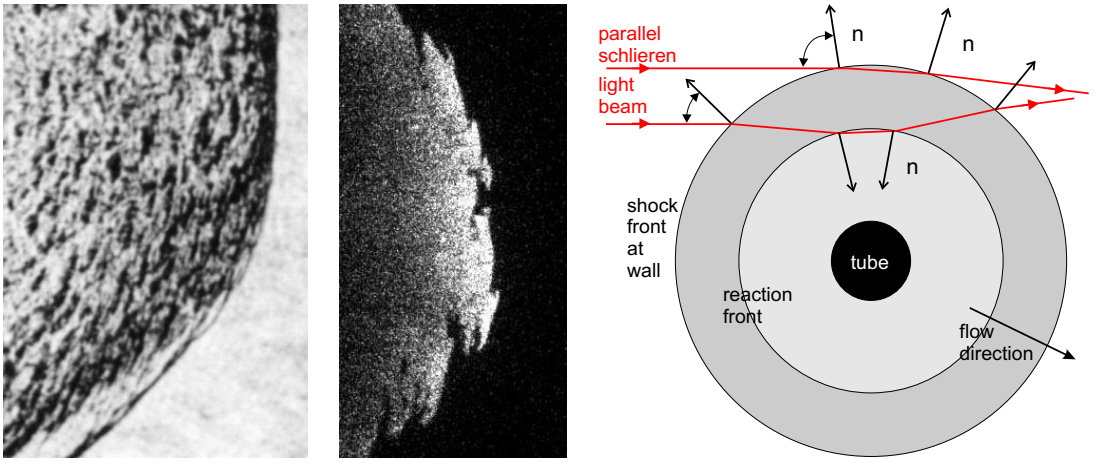

a) b) c)

Figure 5.15: a) Schlieren image of lead shock front, image height 30 mm, $0.2H_2$+$0.1O_2$+0.7Ar, P_0 = 100 kPa, shot 64. b) Keystone features on PLIF image observed close to tube axis, image height 50 mm, $0.33H_2$+$0.17O_2$+0.5Ar, P_0 = 50 kPa, shot 156. c) Sketch of schlieren system light beam deflections at shock and reaction front close to the wall, view along tube axis.

planar part of the shock front centered on the tube axis decreases with increasing time (Fig. 5.14). On a scale of about 1 mm, the planar part of the lead detonation front appears slightly corrugated and is not absolutely flat (Fig. 5.15a). Since the cell size at CJ conditions is approximately on that length scale, this corrugation might arise from the cellular structure of the detonation, as the kinks in lead shock occur where Mach stem and incident shock join. After the lead shock has reached a distance of approximately 70 mm, the lead shock is very smooth and without any kinks. The curvature along the front appears to be continuous and changing slowly. A clear separation between the leading shock and the following reaction front located behind the shock has taken place over the entire shock. The separation takes place gradually as the reaction front close to the wall decouples first and the region close to the axis decouples last. The wall shock appears at all times smooth on all scales resolved by the schlieren image. For times at which both coupled parts on the tube axis and decoupled parts at the wall exist, the lead shock in the intermediate region shows kinks along the outline at length approximately 5–10 times larger than the cell size at CJ conditions (Fig. 5.15a). Despite the integrating character of the schlieren images, this indicates a three-shock configuration and the existence of transverse waves and shear layers, which can be identified on some images. Weak transverse wave structures are also seen in schlieren images after the shock has clearly decoupled from the reaction front (Fig. 5.16a and b). They appear as darker lines or regions, branching off of the main shock into the shocked gas. Since the transverse waves are traveling away from the tube axis, the density gradient is oriented towards the tube axis and they are better visualized on the top half of the diffracting shock for reasons discussed in the next paragraph.

The wall shock on the top appears thicker and with more contrast than on the bottom. This is due to the horizontal schlieren knife edge placed on the bottom. Light deflections towards the bottom are therefore detected with more contrast. The parallel light beam passing the top wall shock is deflected downwards, since the wall shock creates a cylindrical region of higher optical density close to the wall. The bottom shock is also detected since the light ray deflection is so strong that lens

holders and the finite mirror extension block the deflected part of the light beam. Note that the opposite effect is observed for the reaction front close to the wall. The reaction front on the bottom appears with more contrast than the one on the top, which indicates that the optical density in the shocked but unburned gas is larger than in the hot gas. For gases of fixed composition, the optical refraction index n is a linearly increasing function of density. The density for the burned gas is significantly lower than the unburned gas at the same pressure. The light beam crossing the edge of the reaction front is less influenced by the density gradient of the shock since the angle α between the density gradient and the incoming light beam is not as close to 90° as for the visible portion of the leading shock (Fig. 5.15c). Since the radius R of light beam curvature is given $1/R = (\sin\alpha\nabla n)/n$ (Schardin, 1934) the amount of light beam deflection is larger the closer the angle α is to 90°. Furthermore, the total deflection increases with the distance the light beam is traveling through the region with a refraction index gradient.

In contrast to the very distinct smooth front of the lead shock seen on the schlieren images, the reaction front appears fuzzy. The simultaneous PLIF image and the overlay with the schlieren image reveals the exact location and detailed structure of the reaction front (Fig. 5.16). The signal-to-noise ratio on the OH fluorescence images with lower pressure, Fig. 5.16c, is better due to the lower quenching coefficient. Close to the tube axis, the reaction front appears to be fairly flat. In some experiments, keystone-shaped features are observed, similar to those in fully developed detonations traveling at CJ velocity. The keystones of higher fluorescence are pointing in both directions with respect to the tube axis. Further away from the tube axis, the reaction front more closely resembles a saw tooth geometry, where the teeth of higher fluorescence are, in general, pointing away from the tube axis and are slightly inclined towards the wall direction (Fig. 5.17). The length scale of the largest features is about 10 mm, which corresponds to approximately 5–10 times the cell size at CJ conditions. The large scale features appear with a smooth front in some cases and corrugated in others. The orientation of saw tooth-like features away from the tube axis is also observed on the schlieren images. The PLIF reaction front location corresponds well

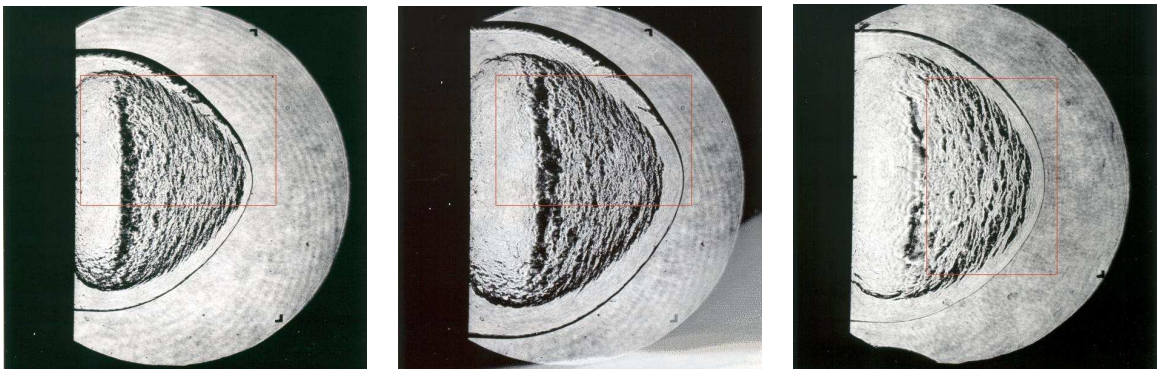

schlieren images, full field of view, red rectangle indicates region used for overlay.

schlieren images, cropped region used for overlay.

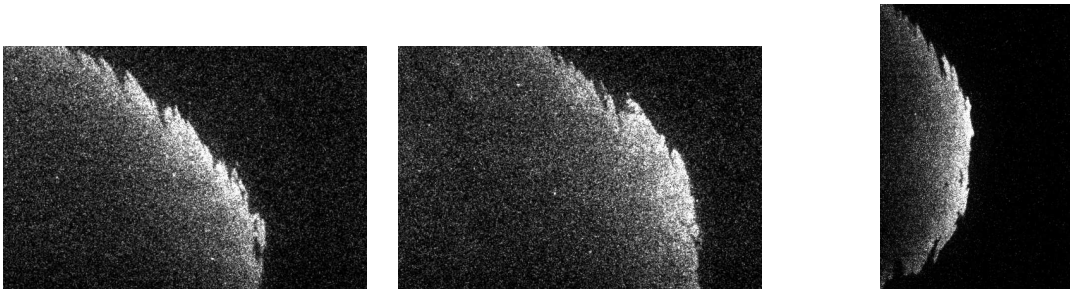

PLIF images.

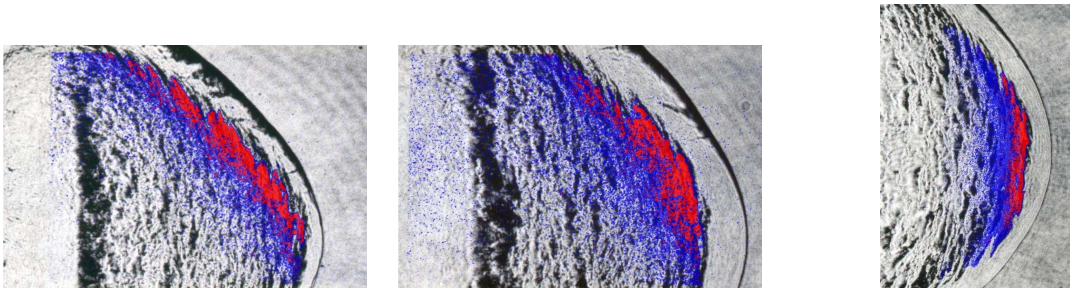

overlay of PLIF and schlieren images, PLIF layer in false color.

a) $0.2H_2+0.1O_2+0.7Ar$, $P_0 = 100$ kPa, shot 69.

b) $0.2H_2+0.1O_2+0.7Ar$, $P_0 = 100$ kPa, shot 72.

c) $0.333H_2+0.167O_2+0.5Ar$ $P_0 = 47.5$ kPa, shot 157.

Figure 5.16: Observations in the sub-critical regime for Ar-diluted mixture.

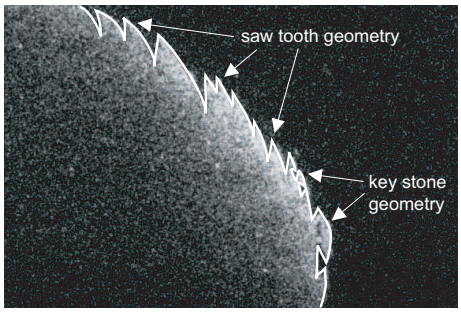

Figure 5.17: Illustration of saw tooth geometry observed for off-axis OH front. PLIF image in background is from shot 69, see Fig. 5.16a.

with the fuzzy front seen on the schlieren images. As long as the flow field is axially symmetric, the leading reaction front seen on schlieren images must be close to that seen in the light sheet plane. The geometry of the reaction front in the schlieren images can be clearly matched with the PLIF image for regions in which the integrating effect of the schlieren system is minor. For some experiments, the assumed reaction front seen on schlieren images appears ahead of the reaction front obtained from the PLIF images. This could be attributed to non-axially symmetric flow and parts of the reaction front outside the light sheet plane. The transverse waves seen on some schlieren images were, in most cases, located close to a tip of the reaction front geometry (Fig. 5.16).

On multiple exposure chemiluminescence images for sub-critical conditions, the leading front appears comparatively bright and flat immediately after the detonation exits the tube (Fig. 5.18). All chemiluminescence images are shown, as well as the PLIF images, normalized but not intensity clipped. By doing so, the full range of intensities is preserved and the lowest intensity corresponds to complete black and the highest to complete white. The grey scale is a linear representation of the counts registered by the camera for each pixel. The luminescence intensity of the front decays rapidly as the detonation travels further from the tube axis. At distances of approximately 50 mm from the tube exit plane, the front is hardly detectable by the camera system. The gain and exposure time settings on the 16 bit camera system were configured to utilize the full dynamic range of the camera. Since it was not possible to predict the brightness accurately prior to the experiment, some

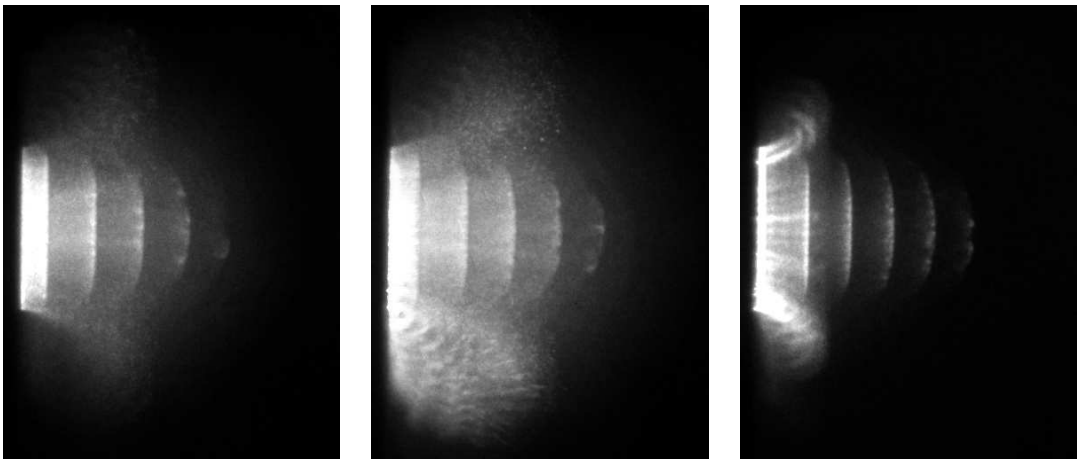

a) b) c)

Figure 5.18: Multiple exposure chemiluminescence images. Image height 109 mm. a) Shot 156, 0.333 H_2 + 0.167 O_2 + 0.5 Ar, P_0=45 kPa, T_0=296 K. Multiple exposure timing: $9\times6\mu s$. b) Shot 157, 0.333 H_2 + 0.167 O_2 + 0.5 Ar, P_0=47.5 kPa, T_0=296 K. Multiple exposure timing: $11\times6\mu s$. c) Shot 128, 0.2 H_2 + 0.1 O_2 + 0.7 Ar, P_0=100 kPa, T_0=295 K. Multiple exposure timing: $6\times6\mu s$.

images are overexposed in areas close to the tube exit plane. The intensities of a non-detectable front are approximately three orders of magnitude smaller than the maximum intensity observed. The intensity of the image is both highest and most persistent close to the tube axis. The region of higher luminescence can be bounded by a conical region in some cases, in others more by a frustum-like geometry. In general, a decrease in both brightness and extent of the leading front is observed as the wave propagates away from the tube. Due to the integrating nature of the chemiluminescence images one can not conclude a lower temperature or local energy release rate from a lower luminescence intensity. As long as the front is comparatively flat and parallel to the optical axis, the intensity is integrated over the depth as the plane is projected on a line. Assuming axial symmetry of the reaction front, luminous fronts with a larger vertical extent are brighter than those with a smaller extent. The diffuse edges of the conical region could be attributed in part to this effect.

The intensity distribution along the reaction front during a 6 μs exposure gate was obtained by averaging horizontally over a 15-pixel wide vertical stripe (Fig. 5.19a). Also shown is the intensity distribution from a disk of uniform local luminosity pro-

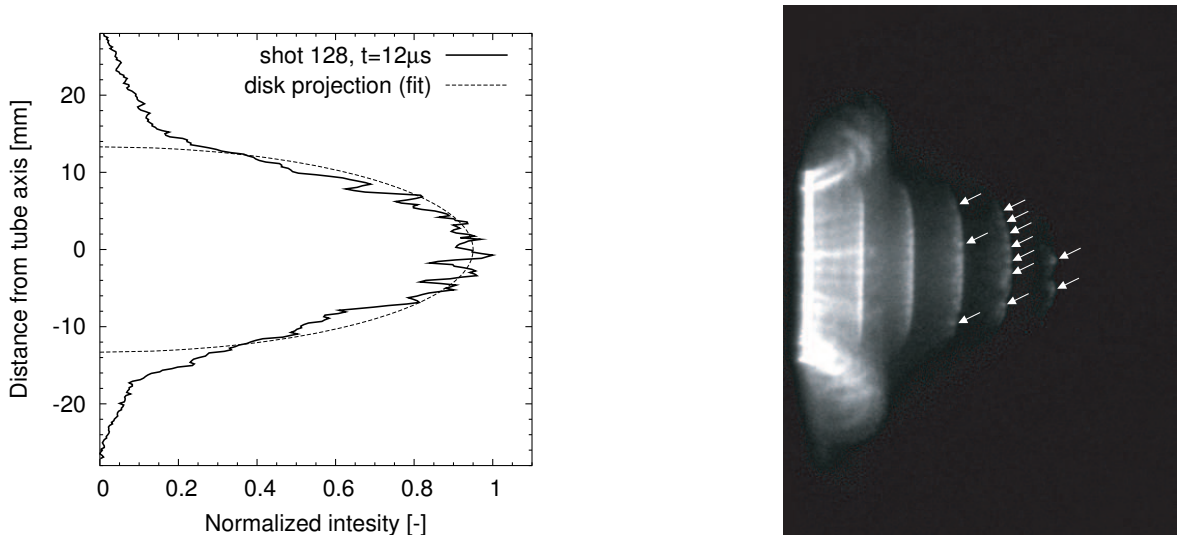

a) b)

Figure 5.19: a) Solid line: Experimentally obtained vertical intensity distribution along the chemiluminescence front for the third exposure gate (t = 6 μs), shot 128 (see Fig. 5.18c); 23 mm from tube exit plane. Averaged horizontally over 15 pixel. Dashed line: Ideal intensity distribution arising from a disk with an uniform intensity distribution, projected onto a line. b) Bright spots indicated by white arrows causing spatial modulation in reaction front intensity, Shot 128, 0.2 H_2 + 0.1 O_2 + 0.7 Ar, P_0=100 kPa, T_0=295 K. Multiple exposure timing: 6×6μs.

jected onto a line to the experimental profile. The profile shows two symmetric "wings" of higher intensity at distances beyond 17 mm from the tube axis. Otherwise, the idealized and experimental intensity profiles are in reasonable agreement.

The chemiluminescence front, especially for later times in the diffraction process, appears folded. Furthermore bright spots appear along the reaction front, causing the modulation in intensity as seen in Fig. 5.19. For later times in the diffraction process the number of bright spots close to the tube axis is decreasing (Fig. 5.19b).

In some images, bright streaks close to the tube exit were observed. Possible explanations include hot particles, e.g. from previous soot foil experiments, which follow the flow behind the detonation wave and exit the tube close to the tube wall.

5.4.1.2 Critical regime

In the critical regime the amount of argon dilution is decreased or the initial pressure increased compared to the mixtures in the sub-critical regime. In this section,

experiments without a re-initiation event are described.

For experiments in the critical regime with a sub-critical outcome, the shock and reaction front appear coupled close to the tube axis for much larger distances than in the sub-critical regime. The coupling is evident on the schlieren images by the corrugated lead shock front and on the simultaneous PLIF images by the close relation between OH front and shock (Fig. 5.23). On some images, the reaction front appears to be coupled up to 86 mm from the tube exit plane (Fig. 5.21). The wall shock is clearly decoupled, and the distance between the shock and reaction front appears to gradually decrease as one approaches the tube axis. Weak transverse wave structures and, more pronounced, the corresponding shear-layers are present on schlieren images in the decoupled regions in the sub-critical regime (Fig. 5.20a). The shear-layers join the lead shock in a weak triple point, which is indicative to the three shock structure. In some cases the optical density gradient across the transverse wave is too weak to be visualized by the schlieren system. The shear-layer structure bounds the saw tooth geometry of the OH-front. This indicates that the saw tooth geometry have the same origin as the keystone-shaped geometry observed for fully developed detonations (Fig. 1.4c). In case of the diffracting wave the transverse waves are in the decoupled region observed to travel only towards the wall as no new transverse waves are regenerated in this region. This results in saw tooth geometries pointing in the off-axis direction.

The geometry of the lead shock outline is altered compared to the sub-critical regime only in the region close to the tube axis. It appears further ahead, indicative of a larger propagation velocity of the coupled region close to the tube axis. The strict axial symmetry observed in the sub-critical regime is not seen in the critical regime. For later times in the diffraction process, the leading shock is sometimes asymmetric close to the tube axis. The asymmetry can also be observed on the chemiluminescence images (Fig. 5.22).

On the PLIF images, the saw tooth-like geometries appear as in the sub-critical regime in the off axis regions. The reaction front in the coupled region exhibits keystone-shaped elements, which appear more frequent and distinct than in the sub-

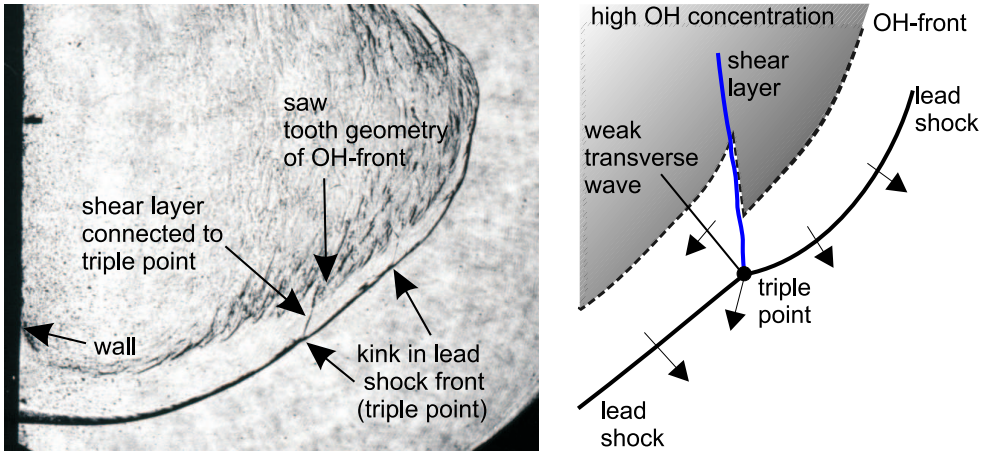

a) b)

Figure 5.20: a) Shear layers and kinks in lead shock front as seen on schlieren images indicative to weak transverse wave structures , shot 202 (see Fig. 5.21). b) Schematic of weak triple point configuration and corresponding saw tooth geometry observed on PLIF images.

critical regime. On the schlieren-PLIF overlay images, the geometry of keystones of higher fluorescence can be clearly matched to the curved outline of the lead shock (Fig. 5.21).

The chemiluminescence images show that the front luminosity persists for larger distances than in the sub-critical regime. The cone-like region of higher luminescence appears to have a shallower angle and the intensity seems to drop rather abruptly for larger distances from the end plate. For these distances, only a few bright regions of higher intensity along the reaction front are seen.

5.4.1.3 Super-critical experiments

All super-critical experiments within the critical regime are marked by a re-initiation event. The term itself is misleading since no failure of the entire detonation need precede the re-initiation. It is more a local re-coupling of shock and reaction front.

Prior to a re-ignition event, the shocked but unburned reactants are located in a region best described as a thick spherical shell. The inner radius corresponds to the distance from the tube exit plane center to the reaction front, the outer radius to the distance to the lead shock front. The shell thickness varies and is largest close to the

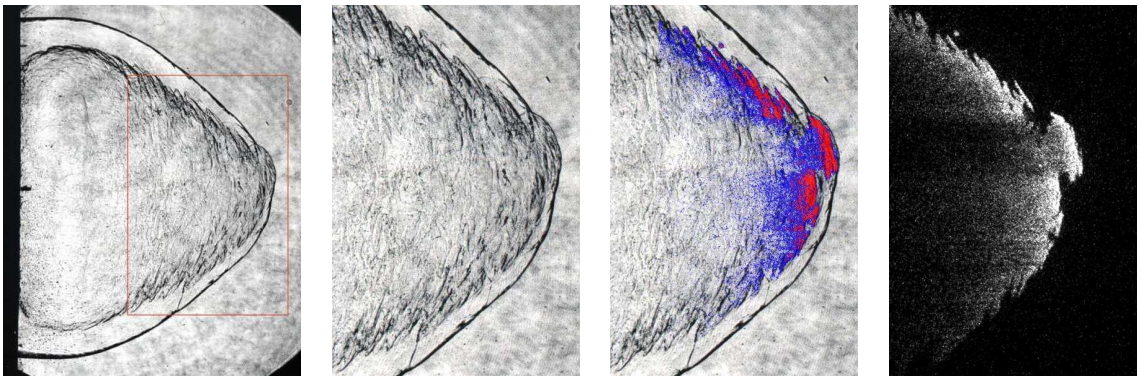

Figure 5.21: Keystones of higher fluorescence are observed where reaction front is coupled to shock front, see also Fig. 5.22b. Shot 202, 0.22 H_2 + 0.11 O_2 + 0.67 Ar, P_0=100 kPa, T_0=294 K. Schlieren image height: 125 mm. Cropped region height: 80 mm. PLIF image height 70 mm.

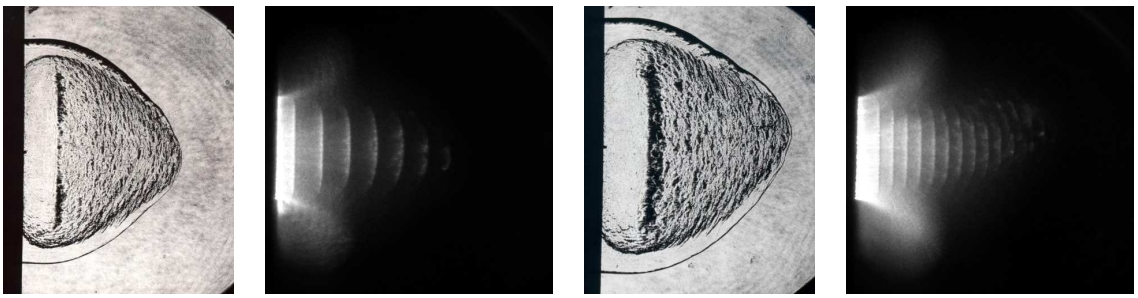

a) b) c) d)

Figure 5.22: Asymmetric diffraction process. a) and b) Shot 135, 0.217 H_2 + 0.108 O_2 + 0.675 Ar, P_0=100 kPa, T_0=294 K. Schlieren image height: 125 mm. Chemiluminescence image height: 109 mm. c) and d) Shot 149, 0.22 H_2 + 0.11 O_2 + 0.67 Ar, P_0=100 kPa, T_0=295 K. Schlieren image height: 125 mm. Chemiluminescence image height: 109 mm.

wall. Both radii increase with time since shock and reaction front are progressing outward. In a re-initiation event, a detonation advances transversely through the shocked reactants in the azimuthal and polar direction and completes the reaction in the shell-like region (Fig. 5.25b, schlieren image). A growing mushroom-like region of the re-coupled leading shock is created (Fig. 5.24).

On schlieren images, the transverse detonation resulting from a re-initiation event is best visualized if located on the very top or bottom, since the three-dimensional masking effect is then smallest. The outline of the lead shock changes at the point of the transverse detonation from very smooth in the still decoupled part to corrugated

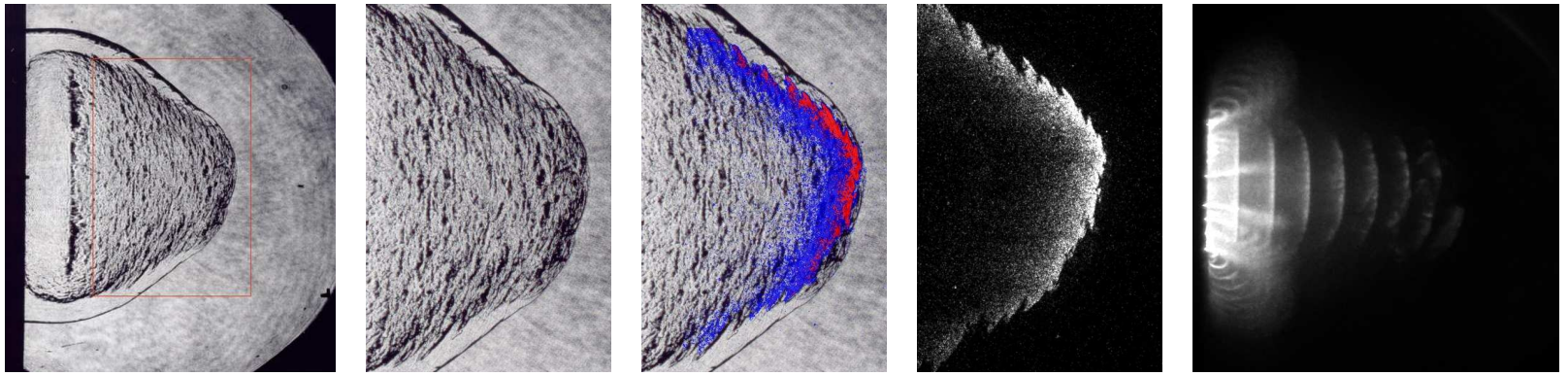

a) Shot 138, 0.223 H_2 + 0.112 O_2 + 0.665 Ar, P_0=100 kPa.
Schlieren image height: 125 mm. Cropped region height: 80 mm. PLIF image height: 70 mm.
Chemiluminescence image height: 109 mm, multiple gates delay: 8×6μs. t(P3-PLIF)=208μs, t(P3-chem)=172μs.

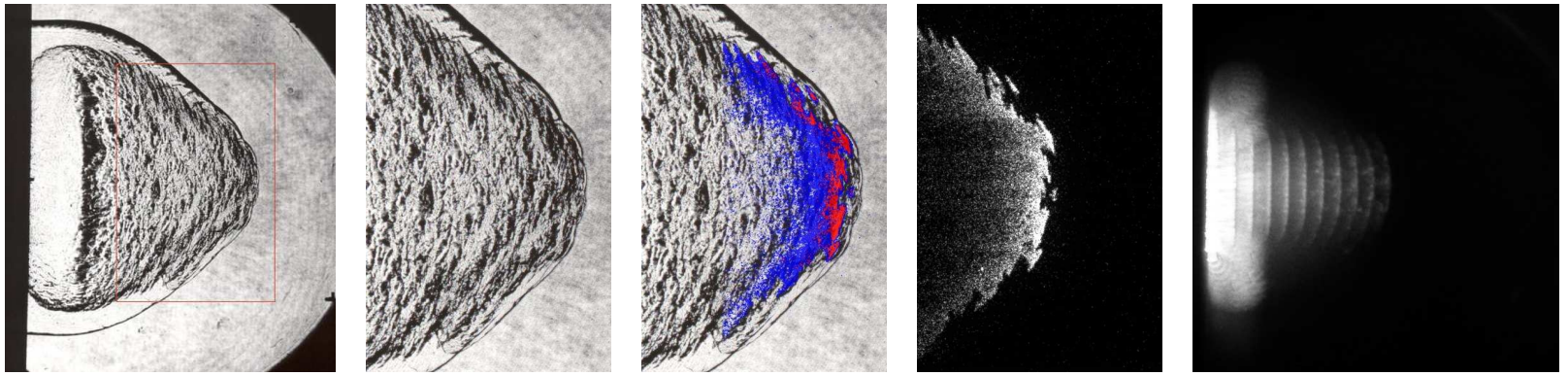

b) Shot 148, 0.22 H_2 + 0.11 O_2 + 0.67 Ar, P_0=100 kPa.
Schlieren image height: 125 mm. Cropped region height: 80 mm. PLIF image height: 70 mm.
Chemiluminescence image height: 109 mm, multiple gates delay: 10×3μs. t(P3-PLIF)=214μs, t(P3-chem)=172μs.

Figure 5.23: Observations in the critical regime for the Ar-diluted mixture.

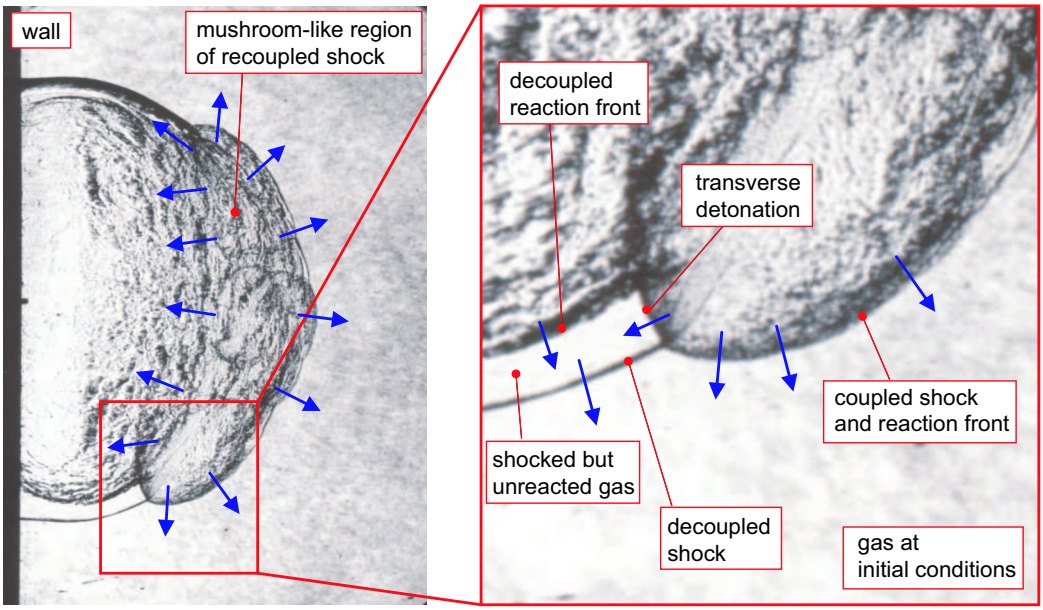

Figure 5.24: Re-initiation event and detailed view of transverse detonation, Shot 143, 0.5 H_2 + 0.5 N_2O, P_0=45 kPa, see also Fig. 5.31a.

in the re-initiated part (Fig. 5.24). An inflection point appears in the lead shock at the location of the transverse detonation. Multiple re-ignition events were observed to occur simultaneously at different locations (Fig. 5.26).

On chemiluminescence images, the transverse detonations appear, due to their high energy release rate, as bright bands comparable in intensity to the reaction front on the tube axis close to the tube exit plane. The intensity is lower in the early stages of the transverse detonation development, and it is difficult to locate exactly the origin of re-initiation. The location in the out of plane direction can only be inferred indirectly from a simultaneous schlieren image assuming axial symmetry, clearly an over-idealization in many cases.

For a large number of experiments the transverse detonation starts close to the edge of the coupled region at the leading reaction front and develops from there backward towards the wall (Fig. 5.23). For some experiments, the re-initiation event seems to take place closer to the wall and further off the tube axis. The transverse detonation spreads in a radial fashion, propagating into the shocked reactants towards the wall and also towards the leading front (Fig 5.26).

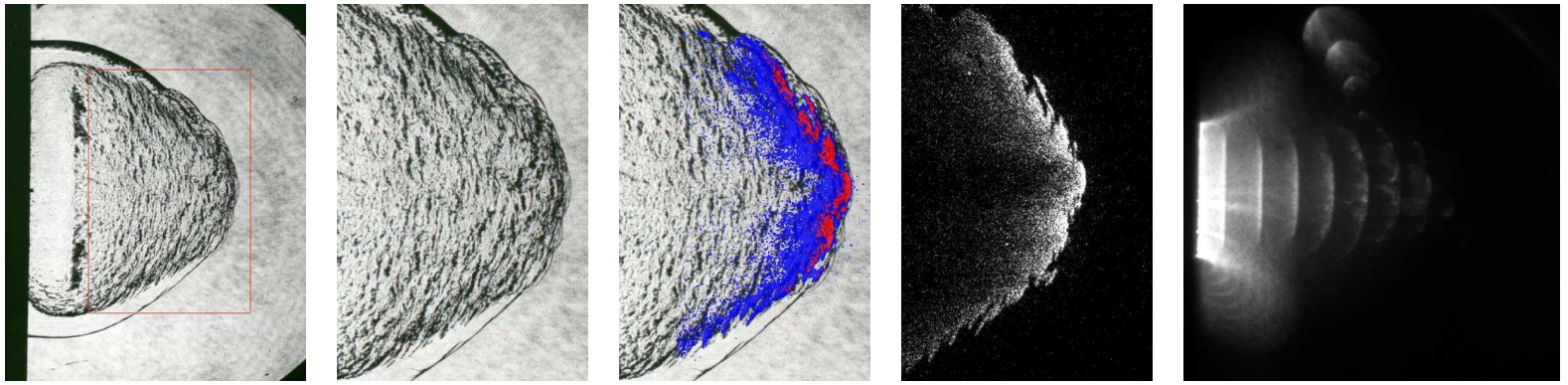

a) Shot 136, 0.22 H_2 + 0.11 O_2 + 0.67 Ar, P_0=100 kPa.
Schlieren image height: 125 mm. Cropped region height: 80 mm. PLIF image height: 70 mm.
Chemiluminescence image height: 109 mm, multiple gates delay: 9×6μs. t(P3-PLIF)=208μs, t(P3-chem)=172μs.

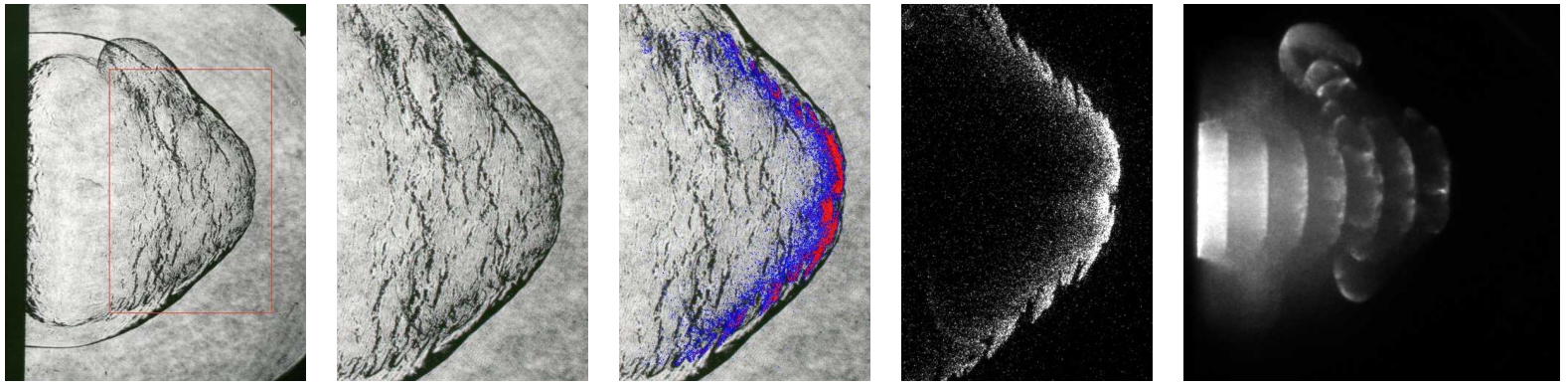

b) Shot 166, 0.333 H_2 + 0.167 O_2 + 0.5 Ar, P_0=57.5 kPa
Schlieren image height: 125 mm. Cropped region height: 80 mm. PLIF image height: 70 mm.
Chemiluminescence image height: 109 mm, multiple gates delay: 7×6μs. t(P3-PLIF)=193μs, t(P3-chem)=157μs.

Figure 5.25: Examples of re-initiation events for Ar-diluted mixtures.

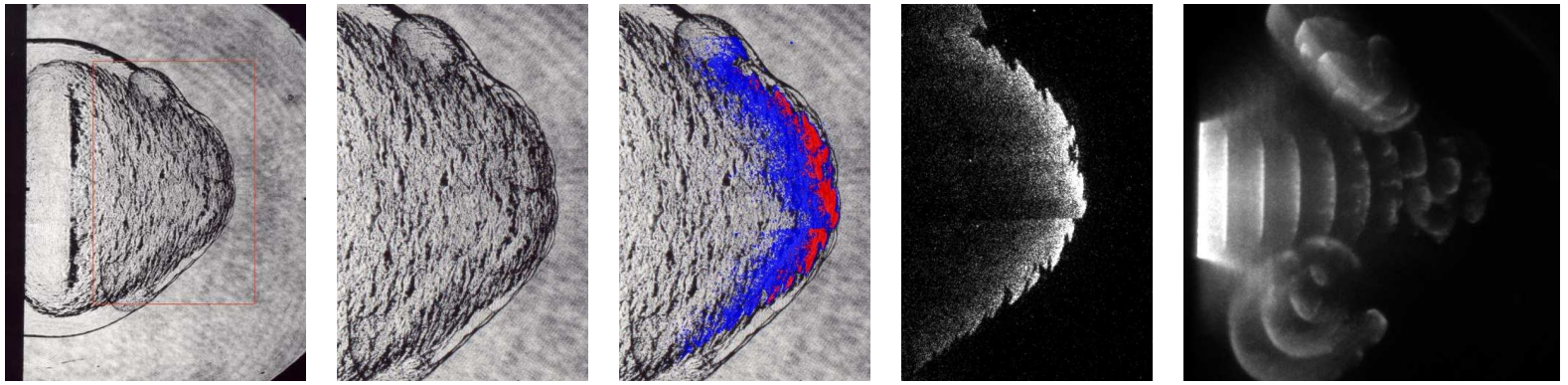

a) Shot 137, 0.22 H_2 + 0.11 O_2 + 0.67 Ar, P_0=100 kPa.
Schlieren image height: 125 mm. Cropped region height: 80 mm. PLIF image height: 70 mm.
Chemiluminescence image height: 109 mm, multiple gates delay: 9×6μs. t(P3-PLIF)=208μs, t(P3-chem)=172μs.

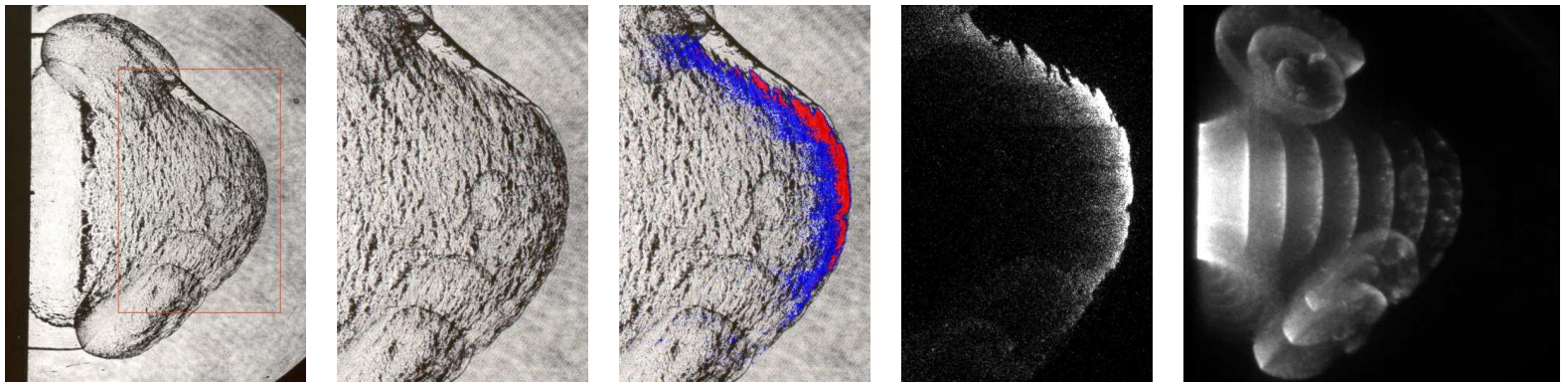

b) Shot 142, 0.24 H_2 + 0.12 O_2 + 0.64 Ar, P_0=100 kPa
Schlieren image height: 125 mm. Cropped region height: 80 mm. PLIF image height: 70 mm.
Chemiluminescence image height: 109 mm, multiple gates delay: 7×6μs. t(P3-PLIF)=208μs, t(P3-chem)=172μs.

Figure 5.26: Examples of re-initiation events for Ar-diluted mixtures.

On the PLIF images the transverse detonation appears as a clear step in the reaction front, as the reaction of shocked reactants get rapidly completed. For the case of the transverse detonation moving towards the wall this step is downwards when following the reaction front outline towards the wall. This can be seen in the PLIF image despite the low fluorescence intensity in the wings of the light sheet profile, Fig. 5.23a in the very top left corner. For the case of the transverse detonation propagating away from the wall, the step in the reaction front outline is correspondingly upwards, which can be seen in the PLIF image of Fig. 5.26a in the top left corner.

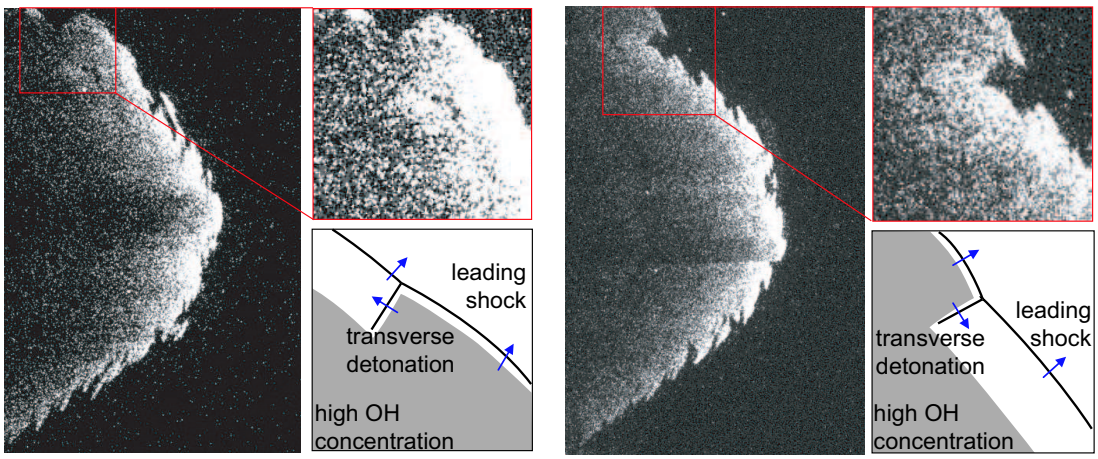

a) b)

Figure 5.27: Depending on the direction of the transverse detonation the step in the OH-front is downwards (a) or upwards (b). The clipped PLIF images are enhanced in contrast to clearly show the step in the reaction front. a) Shot 136 (see also Fig. 5.25a), b) Shot 137, (see also Fig. 5.26a).

Keystone-shaped structures of the leading reaction front are observed in most cases. The keystone of lower fluorescence seen on the PLIF image in Fig. 5.25b indicates two transverse waves traveling in opposite directions (Fig. 5.28). For the likely constellation of the corresponding triple-lines not being close to parallel the transverse waves have collided in a plane outside the light sheet plane, leading to a locally increased energy release rate. On the chemiluminescence image a very bright spot is observed which spatially correlates well with the keystone of lower fluorescence. This indicates that the previously mentioned spatial modulation in intensity along the reaction front observed on chemiluminescence images arises from the cellular structure

of the front.

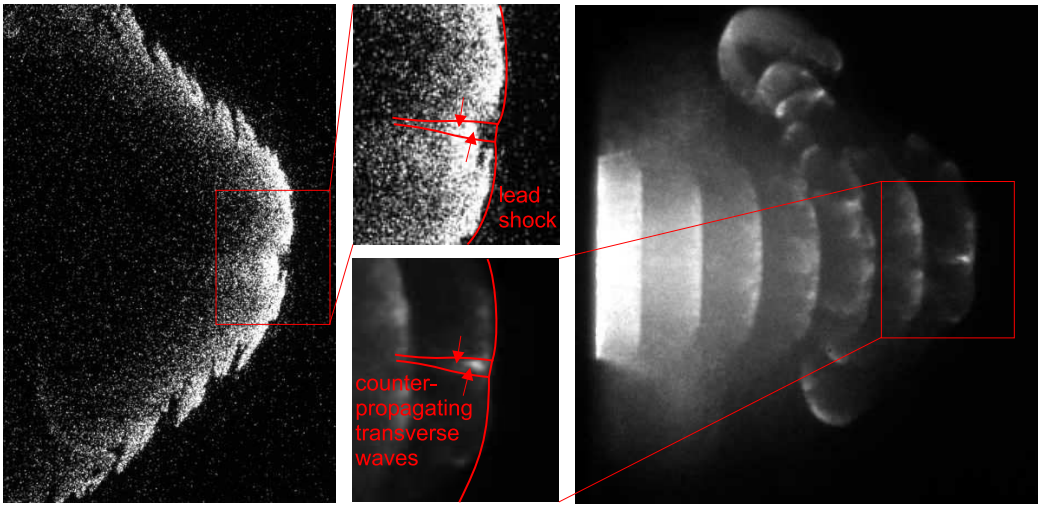

Figure 5.28: Collision of transverse wave at key-stone of lower fluorescence on the OH PLIF image (left). Out of the light sheet plane the transverse wave have collided as seen on the simultaneous chemiluminescence image (right). Shot 166, see also Fig. 5.25b.

5.4.2 H_2-N_2O mixtures

5.4.2.1 Sub-critical regime

The lead shock appears on schlieren images as a smooth front for regions distant from the tube axis just as for the Ar-diluted mixtures. The reaction front decouples from the shock in the area close to the wall right after the detonation exits the tube and appears to stay coupled longest close to the tube axis. For later times, the shock is, aside from the parts at the wall, close to a hemispherical shape (Section 5.8 and Fig 5.29). The reaction front is smoother close to the axis than in the case of the Ar-diluted mixtures. The keystone-like geometries are observed only for early stages in the diffraction process. Saw tooth-like geometries of the reaction front seen, have rounder tips than in the case of the more regular Ar-diluted mixture. The chemiluminescence images show a very bright planer reaction front right after the tube exit, which decreases in radial extent and intensity fairly quickly. About 40 mm from the tube end plate, it is indistinguishable from the silhouette of the decoupled

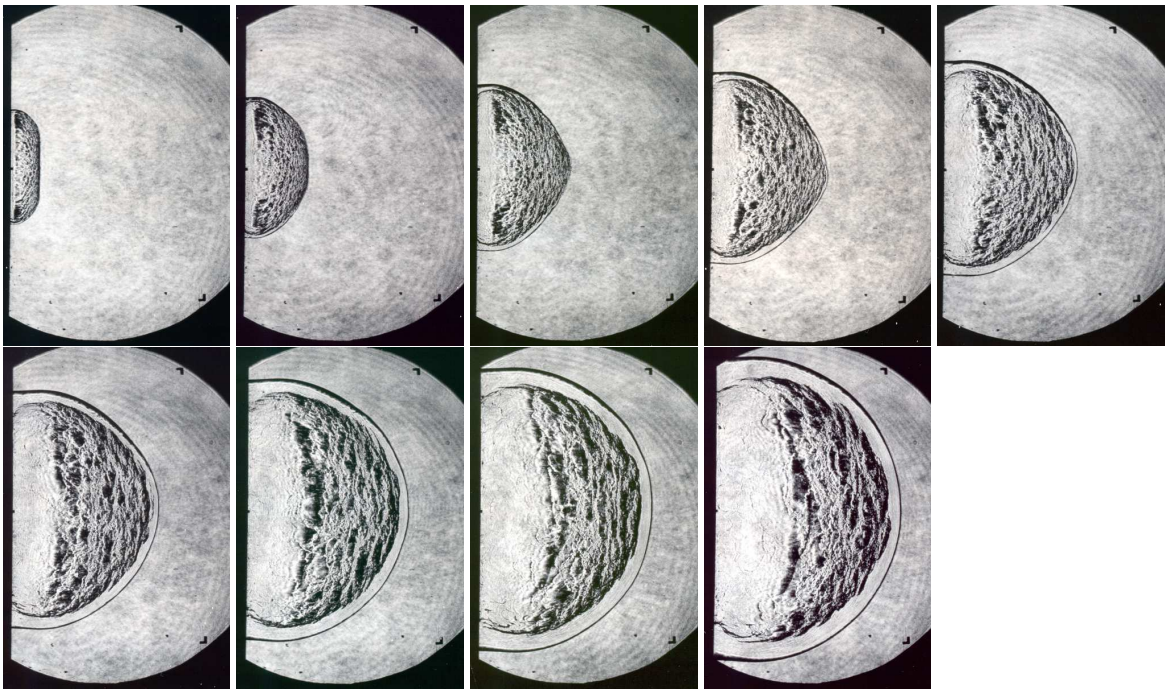

Figure 5.29: Schlieren images obtained from nine separate experiments using the same $0.5H_2$+$0.5N_2O$ mixture and initial conditions of P_0 = 40 kPa. The time increment between the point in time at which the schlieren image was taken is 6 μs. The shot numbers in the order shown are: 87, 86, 89, 84, 88, 82, 81, 80, 79.

reaction front.

5.4.2.2 Critical regime

The lead shock is less smooth than in the sub-critical regime. Shock kinks and small bumps are seen on the schlieren images. At the bumps, the reaction front location is more closely coupled to the shock than elsewhere on the shock outline (see Fig. 5.30b top right). For mixtures closer to the super-critical regime, the detonation front remains coupled slightly longer on the center line. This can be seen from the chemiluminescence images for a series of experiments with increasing pressure (Fig. 5.30).

5.4.2.3 Super-critical experiments

The re-ignition events observed for the H_2-N_2O mixtures appear to be similar to the ones for the Ar-diluted mixtures. Single and multiple re-initiation locations are

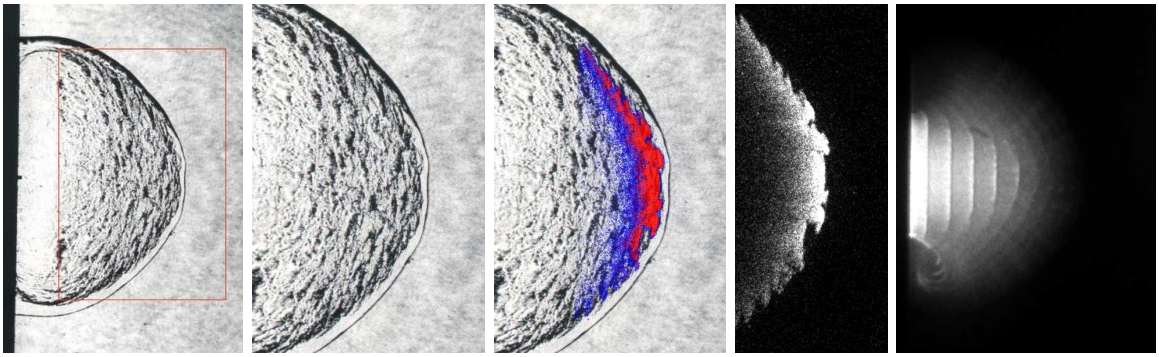

a) Shot 144, 0.5 H_2 + 0.5 N_2O, P_0=40 kPa, multiple gates delay: 10×3μs.

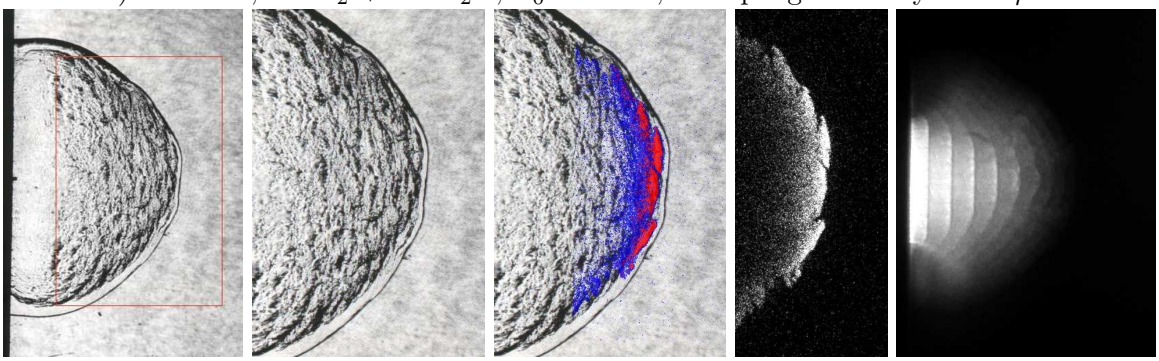

b) Shot 145, 0.5 H_2 + 0.5 N_2O, P_0=42.5 kPa, multiple gates delay: 9×3μs.

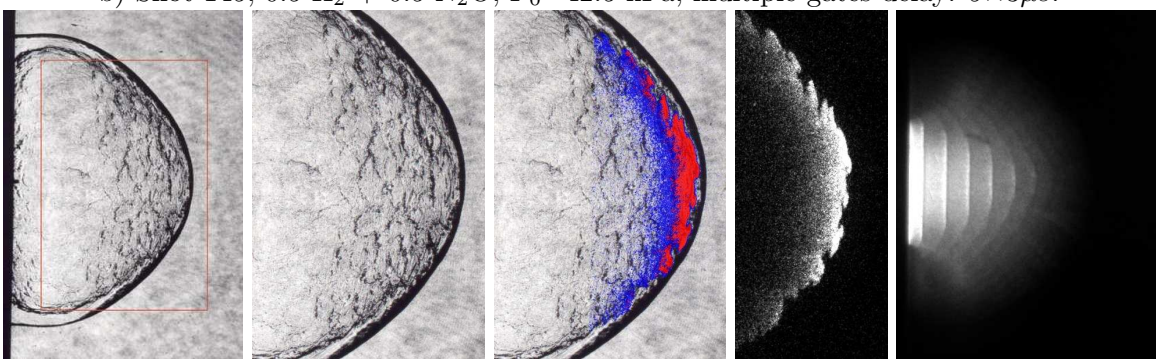

c) Shot 171, 0.5 H_2 + 0.5 N_2O, P_0=45 kPa, multiple gates delay: 11×3μs.

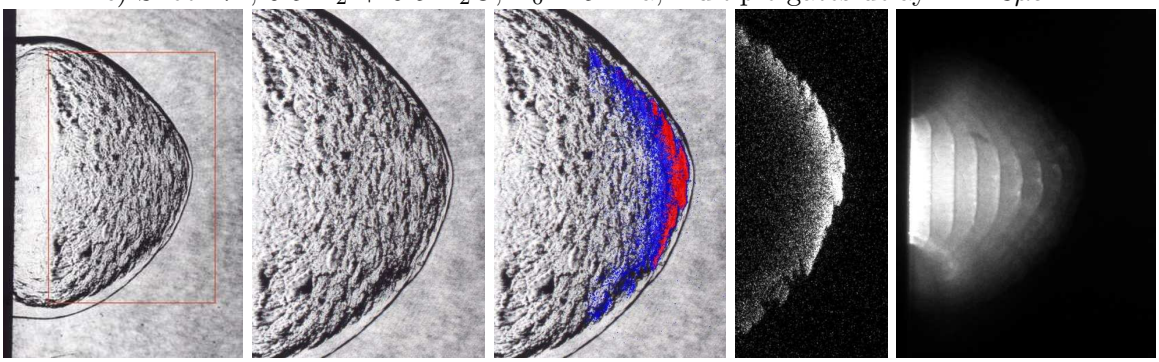

d) Shot 146, 0.5 H_2 + 0.5 N_2O, P_0=47.5 kPa, multiple gates delay: 9×3μs.

Figure 5.30: Series of images of sub-critical experiments for increasing initial pressure. Image heights from left: Schlieren 110 mm, cropped schlieren 80 mm, overlay 80 mm, PLIF 70 mm, Chemiluminescence 109 mm.

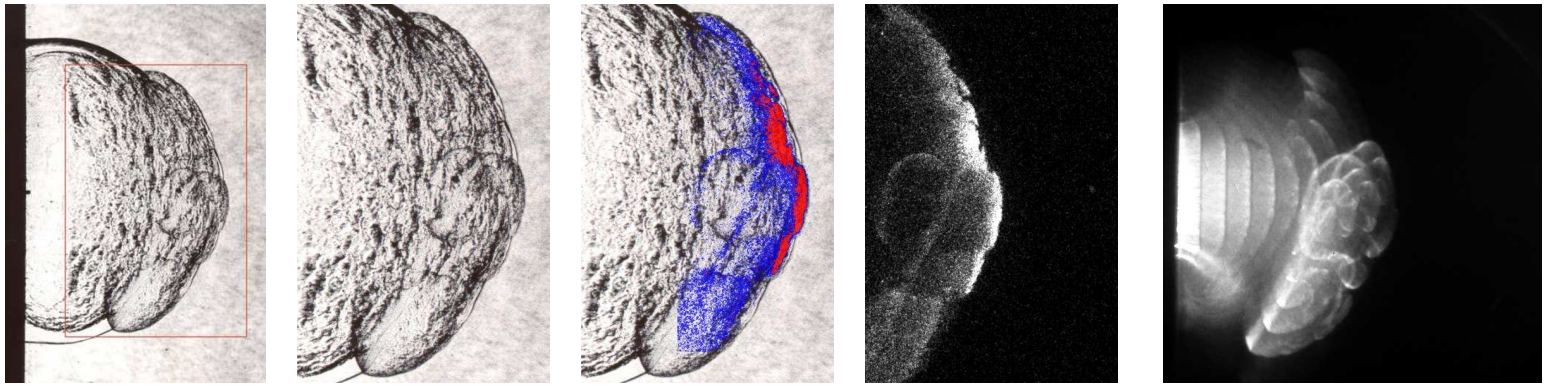

a) Shot 143, 0.5 H_2 + 0.5 N_2O, P_0=45 kPa.
Schlieren image height: 112 mm. Cropped region height: 80 mm. PLIF image height: 70 mm.
Chemiluminescence image height: 109 mm, multiple gates delay: 9×6μs. t(P3-PLIF)=208μs, t(P3-chem)=172μs.

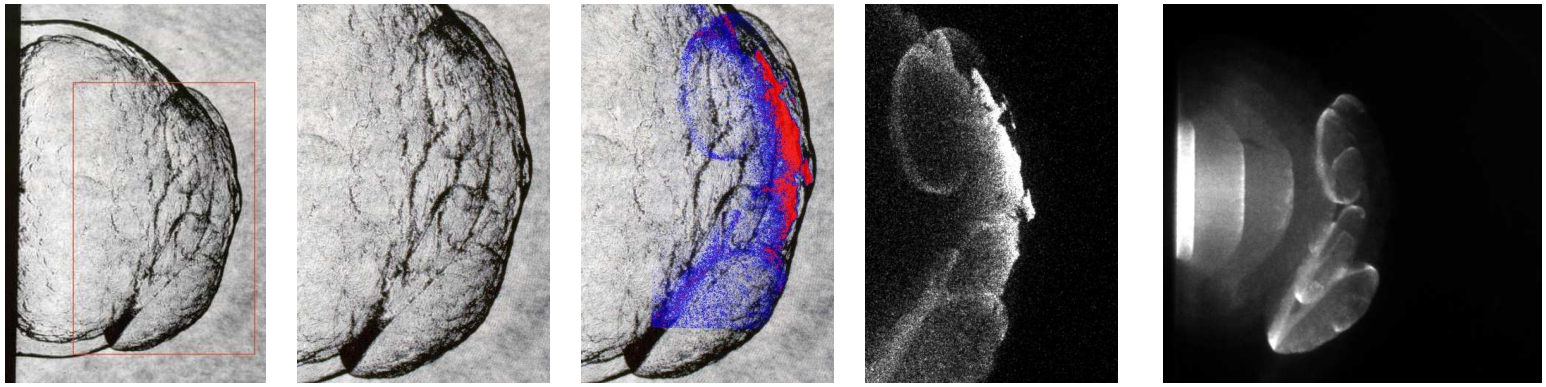

b) Shot 172, 0.5 H_2 + 0.5 N_2O, P_0=47.5 kPa.
Schlieren image height: 112 mm. Cropped region height: 80 mm. PLIF image height: 70 mm.
Chemiluminescence image height: 109 mm, multiple gates delay: 7×6μs. t(P3-PLIF)=208μs, t(P3-chem)=172μs.

Figure 5.31: Examples of re-initiation events for H_2-N_2O mixture.

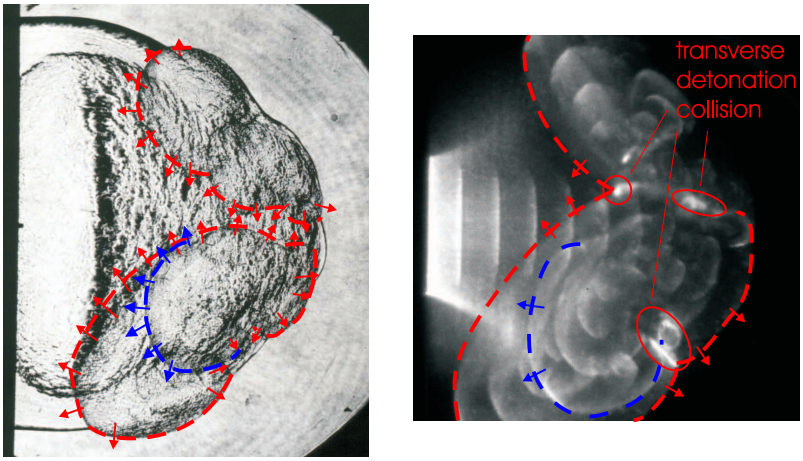

Figure 5.32: Collision process of transverse detonations resulting in very bright regions and kinks in the transverse detonation outline, schlieren image (left) and multiple exposure chemiluminescence image (right). Shot 150, 0.223 H_2 + 0.112 O_2 + 0.665 Ar, P_0=100 kPa, T_0=295 K. Schlieren image timing: t_{TEP}=48.5 μs. Multiple exposure image timing: t_{TEP}=0.6 μs, 10×6μs. Schlieren image height 127 mm, Chemiluminescence image height 109 mm (same scale). The schlieren image is taken simultaneously with the 9th exposure gate of the chemiluminescence, approximately 6μs before the transverse detonation collision. Marked on both images are the outlines and propagation direction of the transverse detonation. On the chemiluminescence image the outline of the tenth exposure gate is marked, coinciding with the collision process. Red and blue outlines are most likely on opposite sides of the diffracting shock. For three-dimensionality of diffraction process see Section. 5.5.

observed. In the case of multiple re-ignition, the collision point of transverse detonations appeared very clearly on chemiluminescence images (Fig. 5.32). For most experiments the transverse detonations originated from the point where the reaction front is being just decoupled. This can be best observed on the chemiluminescence images (Fig. 5.31). In some cases the transverse detonation seems to develop and fail again, e.g., shot 143, Fig. 5.31a, and Fig. 5.33a and b. On the top half of the chemiluminescence image the coupled bright part of the reaction front is seen to decrease in diameter for the first 15 μs. Since the first gate is set to approximately 3 μs after the detonation has exited the tube, this corresponds to the first five exposure gates, which form the cone-shaped outline of the higher fluorescence region. For the next 12 μs (four exposure gates), a transverse detonation develops on the top half of Fig. 5.33a. This is visible on the chemiluminescence image as a bright contour moving upwards and on the schlieren image as a kink and change in roughness of the shock outline. The schlieren image is taken simultaneously with the ninth exposure gate. On the last exposure gate, the brightness of the transverse detonation drops dramatically in intensity, indicating failure of the transverse detonation. The intensity is so low that it is hard to observe on the normalized image.

In Fig. 5.33b, the contrast of the image is enhanced to show the possible failure of the transverse detonation. The location of the leading reaction front is indicated in Fig. 5.33a and b by small line segments, identical on both images. The reaction front was detected manually through appropriate setting of the contrast level. The transverse detonation does not, on close inspection of the schlieren image shortly before failure, appear to be perpendicular to the decoupled shock. Contrast this with the transverse detonation seen on the bottom of the image in Fig. 5.31b. The failing transverse detonation in Fig. 5.31b is inclined such that the part closer to the decoupled shock is ahead. The chemiluminescence profile after the detonation failure shows a very low-luminosity but strikingly large-scale single saw tooth-shaped feature, which could be the remnant of the transverse detonation.

The phenomena of a failing transverse detonation is also observed for shot 102 (Fig. 5.33c and d). The detonation appears to fail between 36 and 40 μs after exiting

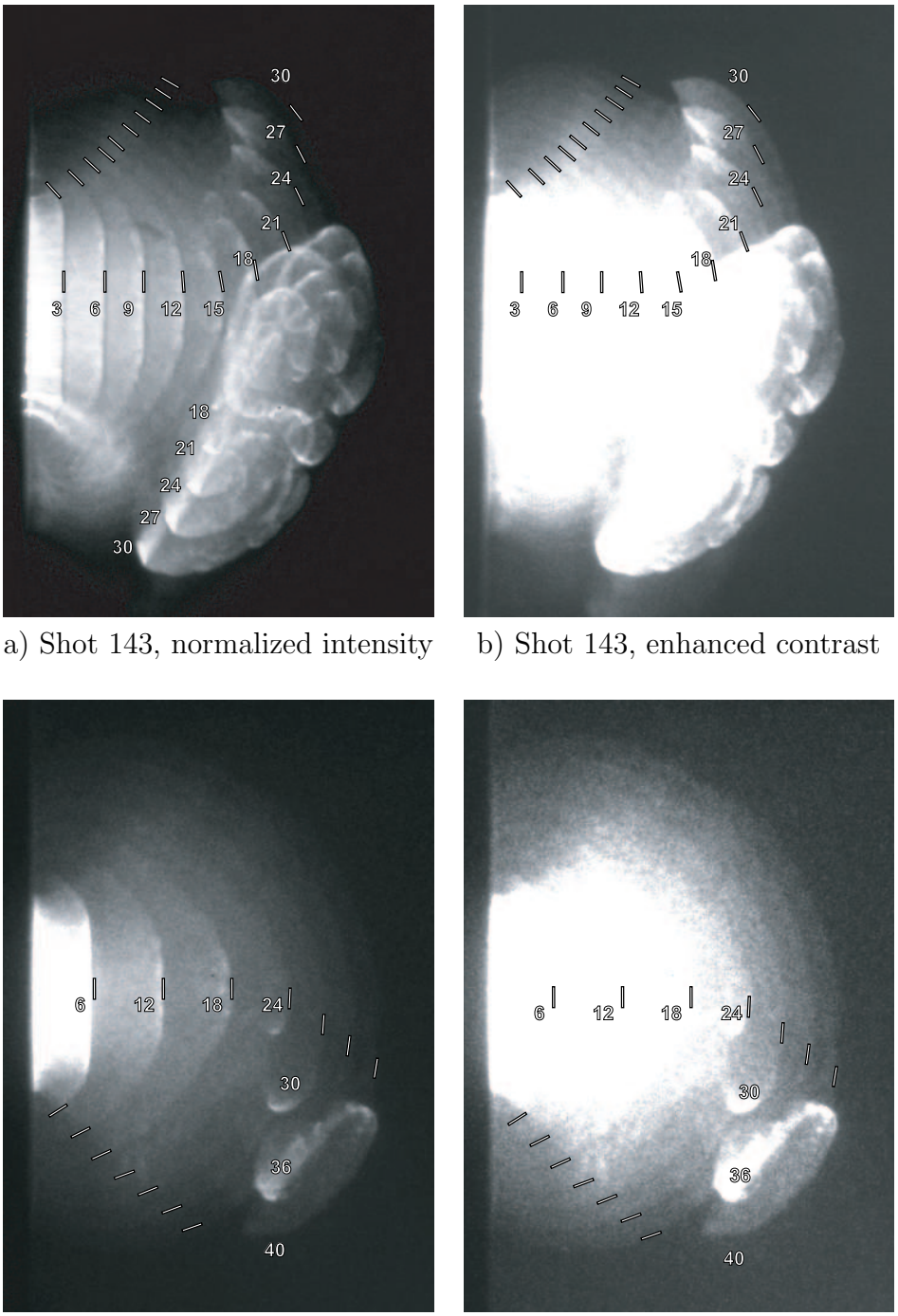

a) Shot 143, normalized intensity b) Shot 143, enhanced contrast

c) Shot 102, normalized intensity d) Shot 102, enhanced contrast

Figure 5.33: Chemiluminescence images indicating a possibly failing transverse detonation. Line segments mark the reaction front at different times. The numbers are the corresponding times in micro seconds from the detonation exiting the tube. a) and b): Shot 143, 0.5 H_2 + 0.5 N_2O, P_0=45 kPa, Multiple gates delay: $10\times3\mu s$. c) and d): Shot 102, 0.5 H_2 + 0.5 N_2O, P_0=45 kPa, Multiple gates delay: $7\times6\mu s$.

the tube, and the chemiluminescence image shows, on the last exposure, a large-scale saw tooth. The bright region seen left of the failed transverse detonation on the last exposure could be a second transverse detonation traveling in the other direction. Transverse detonations were found in other cases to also propagate towards the tube axis, e.g. shot 116, Fig. M.92, Appendix M. Further experimental studies are necessary to prove conclusively that the observed phenomena is a failing transverse detonation. It was observed only for the two experiments discussed here.

5.5 Three-dimensional image construction of transverse detonation

In order to obtain further insight into the transverse detonation and its position with respect to the shock, a stereoscopic image construction of the transverse detonation was performed. This is discussed in the next section.

A few general considerations about stereoscopic imaging are given at the beginning of the section since they are crucial for an understanding of the limitations of this imaging technique. In order to reconstruct the three-dimensional (3-D) position of a single particle, the images of two cameras are sufficient, as long as their line of sight is not collinear. Neglecting the issues of blurring and digitization of the image, a 3-D ray pair corresponding to the particle images can be assigned to each image. The ray pair intersects in the ideal case, and the intersection point determines the 3-D particle location. Due to the digital nature of the image and errors in the camera parameters and calibration, the calculated ray pair does not intersect. Instead, the ray pair is skew (Fig. 5.34a). In this case, the closest point E to both rays is often taken as the reconstructed 3-D position. This point is located half-way between the line describing the shortest distance d between both rays. Sub-pixel resolution and careful calibration can minimize that distance. This is analog to assigning a certain diameter to each ray, such that the cylindrical thereafter rays intersect. The minimum diameter is d in which case the cylinders are just touching.

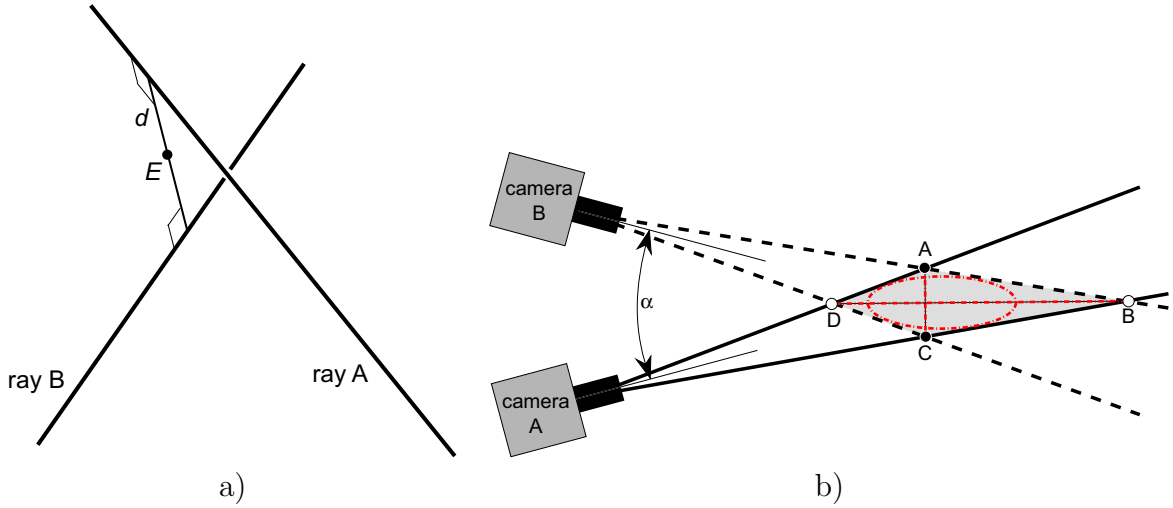

a) b)

Figure 5.34: a) Illustration of skew ray pair from camera A and B at a distance d apart and location of center point E. b) Principle of stereoscopic imaging of two particle located at A and C and their corresponding ghost images located at B and D. The shaded area corresponds to the possible location of all points 3-D reconstructed from both cameras imaging a line between A and C.

If two ideal point particles are in the field of view and both ray pairs assigned to each particle are within one plane, the ray pairs intersect more than twice. This leads to ghost particles in the reconstruction process (Fig. 5.34). The principal rays of both cameras are at an angle α to each other. Assuming the actual positions of the particles are at point A and C, ghost particles occur during the image reconstruction at positions B and D. In this case, it is not possible to retrieve the actual 3-D position with two cameras, and the particles could be either located at A and C or B and D. If an ideal line connecting points A and C is imaged, the possible line locations, besides the correct one, which are reconstructed from the ray tracing, are not just the straight line connecting B and D. Any line or 2-D object within the tetragon ABCD could result in the same set of images as long as each tetragon side is in contact with the object at least once, as indicated by the ellipse fitted in the shaded region (Fig 5.34). The region describing the possible locations of the imaged object has a large extent in the direction of the principle rays for both small α and α close to 180°.

This 3-D reconstruction technique is used to visualize the transverse detonation as defined by the volume in space with high luminosity. We do not attempt to

resolve the spatial variations, since for a complex geometry, this is not possible with only two cameras. Instead, the 3-D location is reconstructed of those points with chemiluminescence exceeding a certain level. The reconstruction technique is based on gradients, in contrast to the techniques based on target points as used, for example, in 3-D particle image velocimetry (Nishino et al., 1989). This is advantageous in the present case since the transverse detonation appears as a relatively thin band, limiting the possible error in the depth of scene. As shown in Fig 5.34, a large distance between points A and C results in a very large distance between B and C. This issue is addressed further below as an actual example of 3-D reconstruction is discussed, illustrating the limitations and step-by-step reconstruction procedure.

5.5.1 Experimental setup

The ICCD camera B previously used for multiple gates chemiluminescence images was positioned horizontally at a 15° angle to the optical axis of the schlieren system. Camera A, previously used for the detecting the laser induced fluorescence signal, was placed in a 25° angle to camera B at the same distance of 1350 mm from the tube center axis (Fig. 5.35). The angle of 25° was the maximum that could be achieved without blocking the field of view by the frame of the test section window. The height of the field of view was 125 mm for both cameras and 105 mm camera lenses were used, as described in Chapter 2. A WG305-UV high pass filter was placed in front of each camera, since the camera lenses used on both cameras had significantly different transmission characteristics in the ultraviolet. This ensures a similar spectral response of both camera systems. The chemiluminescence intensity is wavelength dependent and the different spectral camera responses could lead to different imaging characteristics of both cameras. The wavelength range detected by both cameras was from 305 nm to approximately 800 nm. Both cameras were gated simultaneously (within 5 ns); the gate width for most images was set to 200 ns, and the aperture f-numbers was varied between 16 and 32. The excimer laser was not used in these experiments and the schlieren image was obtained 50 ns after the ICCD

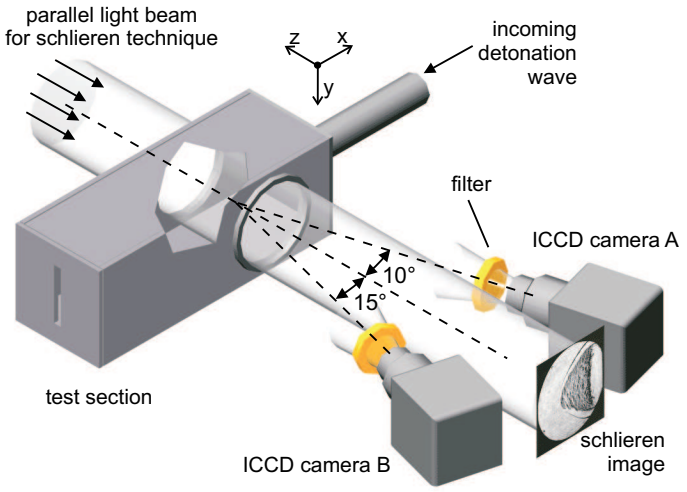

Figure 5.35: Experimental setup for stereoscopic imaging.

camera gates were closed.

5.5.2 Camera calibration

The purpose of the camera calibration is to determine the 3-D ray which corresponds to a specific pixel coordinate on the camera image. Two images of a calibration target were taken for each camera (Fig. 5.36). The plane checkerboard target with a pattern length of 10 mm was placed vertically close to the test section side wall facing the cameras. These images correspond to Fig. 5.36a and c. The plane in which the target is placed corresponds to $z = -60$ mm in the coordinate system. The coordinate system origin is at the center point of the exit plane, and the x axis coincides with the tube axis (Fig. 5.35 and 5.37a). The second target position corresponds to $z = 60$ mm, at the rear of the volume of interest (Fig. 5.36b and d). The general idea about the 3-D ray construction method applied here is the following: the 3-D ray corresponding to a specific pixel of a camera image is found by reconstructing the absolute coordinates of the points corresponding to that pixel in both target planes. Only the x and y coordinates within the target plane have to be determined since the z coordinate is already given by the target plane itself. The ray is then described by the absolute coordinates of two points, one of them in each target plane. This calibration process is done for both cameras independently.

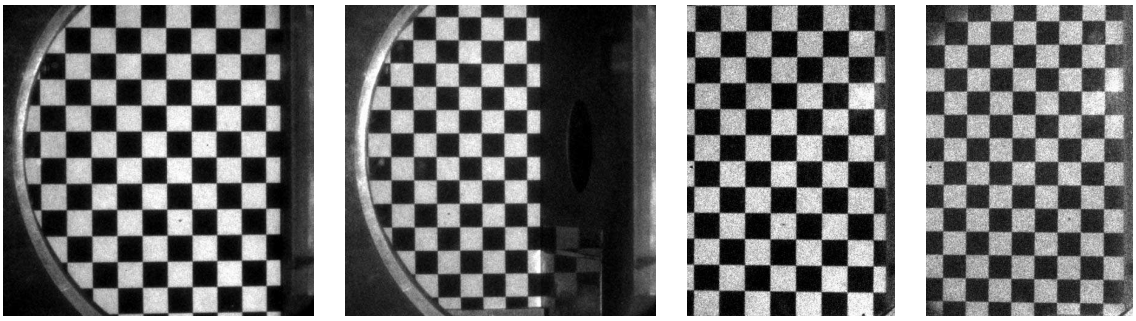

a) Camera B, $z = 60$ mm. b) Camera B, $z = -60$ mm. c) Camera A, $z = 60$ mm. d) Camera A, $z = -60$ mm.

Figure 5.36: Normalized calibration images for left (camera B) and right (camera A) view. The variable z is the distance of the checkerboard target plane from the tube axis, whereas negative values for z indicate the target being placed between camera and tube axis.

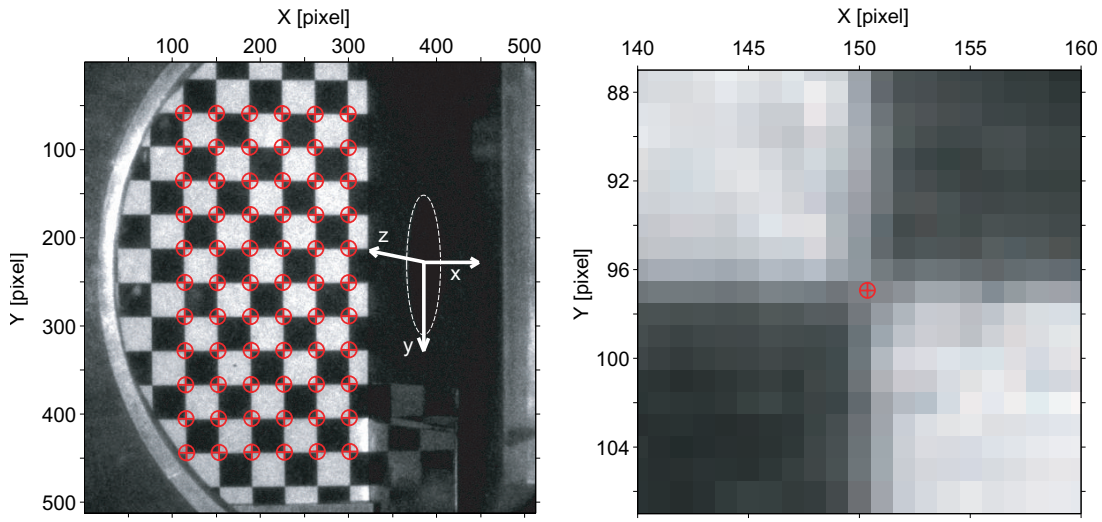

a) , b)

Figure 5.37: a) Corner detected image of target placed in $z = 60$ mm plane. Units of the photographic coordinate system (X,Y) are pixels. The absolute coordinate system axis are denoted x, y and z. The tube exit is indicated by the dashed ellipse b) Enlarged section of corner detected image to show sub-pixel accuracy of corner finding method.

In order to obtain the absolute coordinates, a point $P(x,y)$ corresponding to any photographic coordinate (X,Y) on the images, a transformation function has to be

determined. Here, the formulas given in Nishino et al. (1989) are used:

$$\begin{aligned} x &= (c_1 + c_2X + c_3Y)/(1 + c_7X + c_8Y), \\ y &= (c_4 + c_5X + c_6Y)/(1 + c_7X + c_8Y). \end{aligned} \tag{5.4}$$

The eight camera parameters c_i are valid for only one camera and one target position. The total calibration of the stereoscopic system consists of four sets of c_i parameters. Each set of calibration parameters was determined by a least squares fit of 66 pattern corner points for which the absolute coordinates (x,y) and photographic coordinates (X,Y) were known. The absolute coordinates of the corner points are directly given by the pattern of the checkerboard whereas the corresponding X and Y were found by digital image processing of the target image. A routine based on the Harris corner finding method, Harris and Stephens (1988), was used to extract the corner location for the set of 66 points (Fig. 5.37a). The corner finding method treats the pattern as a digitized saddle-point in intensity and detects the corner pattern (Fig.5.37b) with sub-pixel accuracy. Each set of c_i parameters together with Eqs. 5.4 defines the transformation of photographic coordinates into absolute coordinates for a specific set of target positions and camera location. The set of found parameters was saved in two 2×8 matrices $\mathbf{C_A}$ and $\mathbf{C_B}$, corresponding to camera A and B. The accuracy of the functional fit of Eqs. 5.4, can be tested by re-projection of the corner coordinates. For this calculation, Eqs. 5.4 is inverted and the set of 66 absolute (x,y)-coordinates of the pattern corners is mathematically projected onto the image plane. The inverse transformation is given by

$$\begin{aligned} X &= \frac{(c_4c_8 - c_6)x + (c_3 - c_8c_1)y + (c_6c_1 - c_4c_3)}{(c_7c_6 - c_8c_5)x + (c_2c_8 - c_3c_7)y - (c_2c_6 - c_3c_5)}, \\ Y &= \frac{(c_5 - c_7c_4)x + (c_1c_7 - c_2)y - (c_1c_5 - c_2c_4)}{(c_7c_6 - c_8c_5)x + (c_2c_8 - c_3c_7)y - (c_2c_6 - c_3c_5)}. \end{aligned} \tag{5.5}$$

The corner location in the image plane is then compared to the locations which were previously obtained from the image with the corner finding method. The distance in pixels between the calculated and corner extracted location is the re-projection

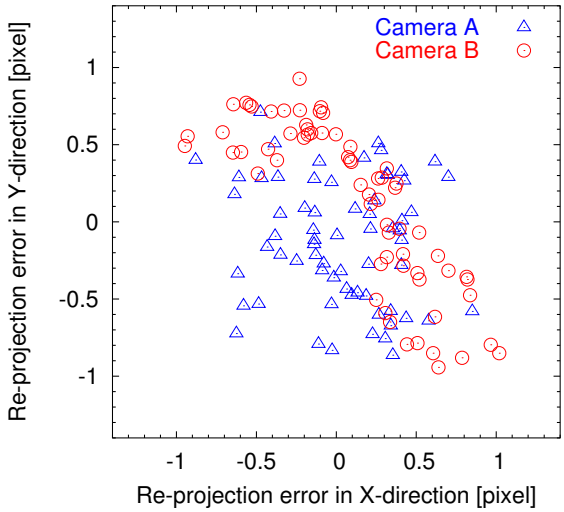

Figure 5.38: Re-projection error for camera target at $z = -60$ mm location.

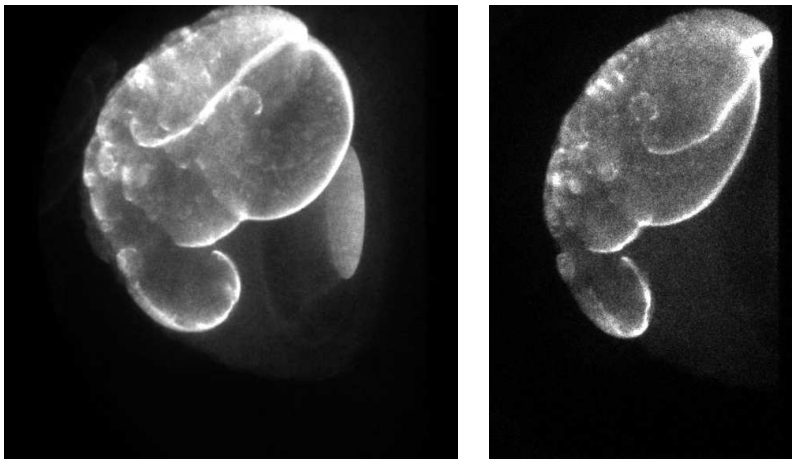

a) Camera B b) Camera A

Figure 5.39: Chemiluminescence images of camera A and B for shot 223, C_2H_6 + 3.5 O_2, P_0=42.5 kPa. Flow direction is right to left. Tube end plate is located to the right.

error (Fig. 5.38) and has an X and Y component. The maximum re-projection error is one pixel. The error can be attributed to lens aberrations and refraction through the thick glass window. Imperfections in the target and errors in the digital corner finding method represent additional possible error sources.

a) threshold: 0.72. b) threshold: 0.84. c) edge detected d) final

Figure 5.40: a) and b) Thresholded chemiluminescence images for two different threshold values. The images were prior to thresholding blurred by a Gaussian filter with a radius of 2 pixel. c) Laplacian of Gaussian edge detected image, which was blurred with a median filter prior to processing. d) Processed and filled edge detected image used for 3-D image reconstruction.

5.5.3 Image processing

The images for the stereoscopic reconstruction were obtained from a diffraction experiment with a C_2H_4-O_2 mixture, since the chemiluminescence intensity for this mixture type was highest among the mixtures studied. This enabled a short camera gate width and a small lens aperture, leading to a large depth of field of the imaging system. The transverse detonation appears as a bright band on the chemiluminescence images of Fig. 5.39. The purpose of the image processing is to make a 3-D representation of the transverse detonation. In order to do this, the transverse detonation must be extracted from the other features in the image. One possibility is to threshold the image, leading to a monochromatic (black and white) image. The white pixels would correspond to the transverse detonation. This technique did not isolate the bright band sufficiently from the background over the entire image, since the chemiluminescence intensity of the band was varying and a different threshold for different regions of the image would have been necessary. For lower threshold values (Fig.5.40a) the details of the brighter region on the image top were not resolved; for higher threshold values (Fig. 5.40b), the transverse detonation on the bottom was not fully detected. Blurring before the thresholding of the image did improve the results but another image processing method was needed to clearly extract the transverse detonation.

Since the transverse wave appears as a local intensity gradient on the images, this suggested using an edge detection routine in conjunction with the thresholded images. The image was filtered by a 5×5 pixel median filter prior the edge detection. The median filter is more appropriate than a Gaussian filter for edge detection. The median filter suppresses impulse noise while preserving strong gradients. The blurred image was then edge detected with the zero-crossing edge detector, also known as the Laplacian of Gaussian edge detector (LoG). The edge detector threshold was set manually. The edge-detected image included, besides the edges along the transverse detonation, the edges of the overall leading flame front and other undesired structures, seen in Fig. 5.40c. To minimize the manual deletion of these edges, the edge-detected image was multiplied pixel by pixel by the thresholded image. In a further step, end-points of edge segments with a distance smaller than 8 pixels were connected by straight lines in order to obtain a closed edge line enclosing the bright region. For some small regions, the outline had to be manually traced before the last step, the binary flood-fill operation, was performed. The final result (Fig. 5.40d) was an image that contained only information from the transverse detonation. In the 3-D reconstruction process, the transverse detonation location corresponds to the set of white pixels on the processed image.

5.5.4 Reconstruction process

The set of photographic coordinates X and Y corresponding to the white pixels of the processed images of camera A and B were stored in two separate matrices $\mathbf{P_A}$ (5127×2) and $\mathbf{P_B}$ (6345×2). The absolute coordinates of the points in the front and back target plane corresponding to $\mathbf{P_A}$ can be calculated via Eqs. 5.4 and the set of camera parameters $\mathbf{C_A}$. For the image taken by camera A this results in a set of 5127×6 coordinates representing the (x,y,z)-coordinates in the front and back target planes. The z-coordinate is either -60 mm or 60 mm, the location of the target planes. This set of point pair coordinates defines the 3-D ray to each white pixel and is stored for image A in $\mathbf{R_A}$ (5127×6) and, correspondingly for image B, in $\mathbf{R_B}$

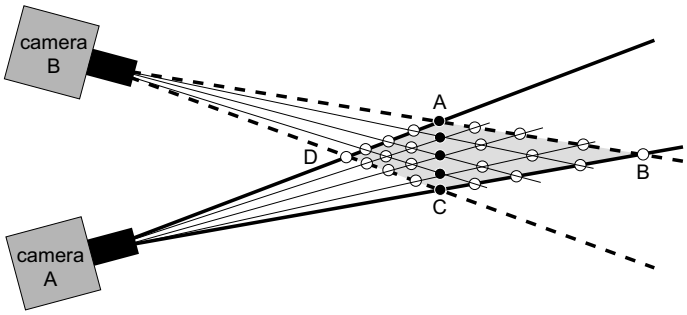

Figure 5.41: Closely spaced ray bundles lead in the reconstruction process to a point cloud.

(6345×6). The rays are saved in the two-point form as two points define a straight ray, which is represented parametrically through the test section. Up to this point, the data from both camera images were processed independently.

In order to decide which ray of $\mathbf{R_A}$ correlates with which ray of $\mathbf{R_B}$, the distance d (Fig. 5.34a) between every possible ray pair, one ray each from $\mathbf{R_A}$ and $\mathbf{R_B}$, was calculated and stored in a matrix $\mathbf{D}$ (5127×6345). Ideally, rays which correspond exactly to a single point in space would intersect, but do not because of various sources of errors and the digital nature of the images. All rays were found to be skew for the calculation precision of 16 significant digits used. This is referred to as "skewness" and is inevitably in 3-D image reconstruction from real 2-D images. The distance d between rays is a measure of both the correction to a given point in space and the skew errors. The maximum d calculated was 74 mm, which shows a very large, error and the two rays are very unlikely to arise from the same region of chemiluminescence. This ray pair is actually one ray on the very top of the image A and one from the very bottom of image B. The smallest distance d found was calculated to be 3 nm, which indicates that it is almost certain that these two rays arise from the same location in the test section. Note that even if $d = 0$ the rays do not have to arise from the same location in the test section, since, e.g., the ray from camera A could arise from point A and the ray from camera B arise from point C and both intersect ideally in point D (Fig. 5.41). The decision regarding which ray pairs are considered as correlating can be based on the distance matrix $\mathbf{D}$. All ray pairs for which d is below a certain threshold are correlated but may not necessarily

correspond to the same location in space. One ray from image A can be correlated with multiple rays of image B since the chemiluminescence intensity of the imaged volume is integrated over the line of sight of each camera and the intensity information is lost by the edge detection processes of the image. This is similar to the situation in particle tracking for which several particles are aligned and appear on one camera as a single point but multiple points on the other camera. For the example given at the beginning of this section, this means that the particle positions are reconstructed at all four locations, A, B, C, and D.

This effect influences the reconstruction process on two levels, depending on the distance between the ambiguous points. The case of a large distance between ambiguous points A and C is shown on Fig. 5.42. The transverse detonation image crosses the horizontal plane described by the cameras' principle rays more than once. From the context, it is obvious which section of the transverse detonation on image A corresponds to which one on image B. For the dashed plane shown in Fig. 5.42, it is clear that the left branch seen by camera B corresponds to the left branch seen by camera A. In the reconstruction, Fig. 5.42 right, the correct location is A and C - not B and D. If the locations were D and B, corresponding branches would occur on opposite sides on the images. To overcome this problem in the automated image reconstruction, the entire transverse detonation band was divided up on both images into three slightly overlapping segments (Fig. 5.43), which, by visual inspection, correspond to each other. The distance d between rays of different segments was set to a large number to avoid triggering spurious reconstruction points.

If the ambiguous points are close together (Fig. 5.41), a bundle of dense rays from one camera is detected to correlate with a bundle of rays from the other camera. The reconstructed locations will, in this case, correspond to a point cloud. The underlying effect is the same as discussed in the previous paragraph in the context of segmenting of the image, just on a smaller scale. The volume of the point cloud gets created in the reconstruction process regardless of whether the detected intensity arises from a plane or a volume. This effect is observed as the band of higher intensity that is several pixels wide.

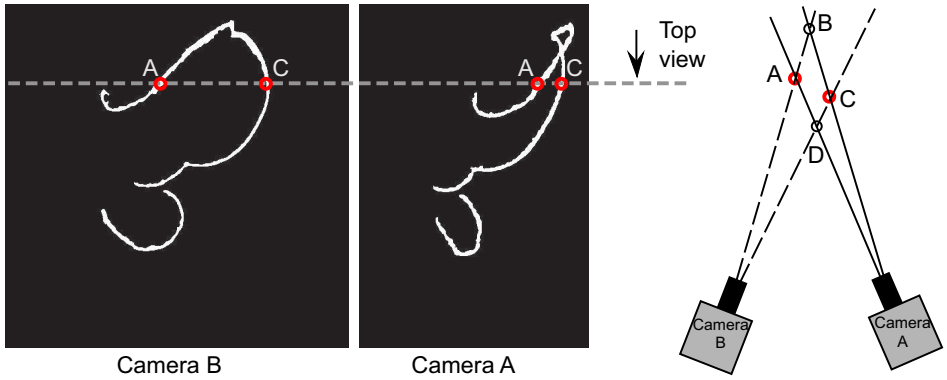

Figure 5.42: Effect of multiple intersections of the transverse detonation geometry with the camera plane. From the image context, it is obvious that the correct 3-D positions are A and C and not B and D as shown on the right.

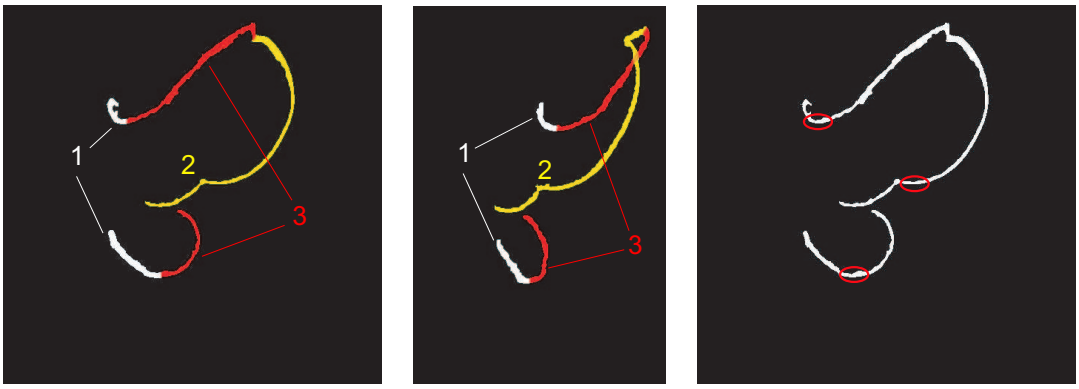

a) Camera B b) Camera A c)

Figure 5.43: a) and b): Manual sectioning of corresponding branches on both images. c) Regions in which the horizontal extent of detected pixel is large.

During the calculation of the distance matrix **D**, the absolute coordinates (x,y,z) of the center point E of the shortest line segment (Fig. 5.41a) between all rays from image A and all rays from image B were stored in a matrix **E** (5127×6345×3). The matrix **E** can be thought of as a look-up table for the locations of a chemiluminescence "event", given a specific ray pair. Together with **D**, this enables the plotting of point clouds which correspond to a certain maximum distance d_{err}. However, point clouds are difficult to interpret in 3-D plots. Iso-surfaces that correspond to a certain distance d_{err} are easier to view and interpret. In order to create iso-surfaces, the data has to be projected on an orthogonal grid.

The iso-surface is a closed surface for which all points inside this surface correspond

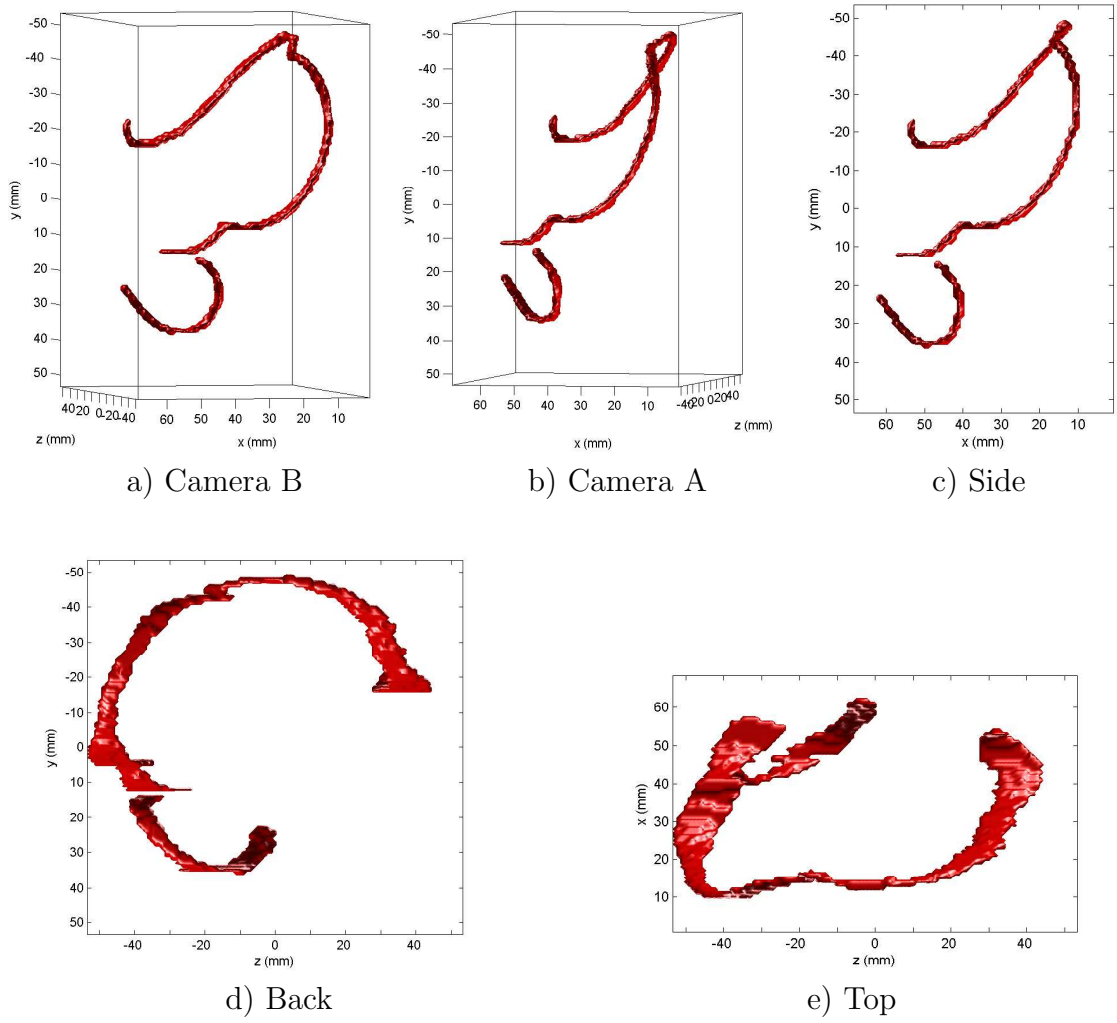

Figure 5.44: Reconstructed 3-D iso-surface corresponding to different view points.

to $d < d_{err}$. An orthogonal equidistant grid of vertex length 0.5 mm was introduced to cover the volume of interest (70 mm×120 mm×120 mm) in the test section. To each vertex point (x,y,z), the scalar value of d is attached. Initially, all vertices are set to a large value of $d = 100$ mm. Subsequently for all points of the unstructured point cloud, the value of d of that point was compared to the value of d at the closest vertex corner. If the d value of the point was smaller than the one at the vertex corner, the vertex corner value was overwritten by the point value. This process gives the 3-D distribution of the minimum d found within the cubic volume around the vertex on an orthogonal grid. The iso-surface for $d_{err} = 0.1$ mm was found to give reliable results. The thickness of the reconstructed region (Fig. 5.44) corresponds visually to

the thickness of the bright region of the transverse detonation seen on the original images (Fig. 5.39). Iso-surfaces for a much smaller value of d appeared punctured with openings while, for larger values of d, the extent in the field of view direction becomes very large. The 3-D image was manually post-processed in regions in which the horizontal extent of detected pixel was large (Fig. 5.43c). In these regions, the iso-surface extended a large amount in the depth of scene direction and was cropped manually. A larger angle between the two cameras or a third camera would minimize this limitation.

On the top view of the reconstructed transverse detonation, one can identify the manually cropped regions as the boundary is very straight, e.g. (x,y,z)=(50mm,-15mm,40mm). In the regions where the band of higher luminosity on the chemiluminescence images is close to being horizontal, one can observe the larger extent in the z direction, which corresponds to the viewing direction of the cameras (Fig. 5.44d).

5.5.5 Reconstruction of shock surface

In order to allow for a determination of the transverse detonation location with respect to the leading shock, the simultaneously obtained schlieren image was edge detected. Thereby, only the region of the completely decoupled shock, which was assumed to be axisymmetric, was edge detected (Fig. 5.45a). The derived shock surface is therefore not closed but open in the very front where no axis symmetry could be assumed. The shock surface was then plotted on the same coordinate system, which enabled to locate the position of the transverse detonation location with respect to the shock surface shown as grid, Fig. 5.45b, c and d.

Discounting some artifacts arising from the relatively small angle between the cameras, the transverse detonation can be clearly located just below the decoupled shock. In some locations, the reconstructed iso-surface of the transverse detonation is found outside the reconstructed shock surface, which can probably be explained by the large uncertainty of the iso-surface in the z direction. Other possible error sources include those mentioned earlier with regard to the calibration process and image processing.

The reconstructed transverse detonation is divided into two discontiguous parts. The upper part of the transverse detonations has two kinks at (x, y, z)=(40,5,-40) and (15,-45,-15) (see Fig. 5.44c). These kinks indicate that at these points transverse detonations join, which originated from different re-ignition points (Fig. 5.32). Three independent points of re-ignition seem to have caused the geometry of the upper part of the transverse detonation. The lower part of the transverse detonation seems to originate from a single re-ignition event as it appears smooth.

The image 3-D re-construction process clearly revealed the three-dimensional nature of the transverse detonation. The transverse detonation progresses into the shocked but unreacted fluid, which is located under the decoupled shock wave. To allow for smaller errors in the re-constructed transverse detonation geometry, especially in the z-direction, a larger angle in between the two cameras or a third camera is needed. If only one camera is available and the optical access is large enough a mirror could be used to allow for a second image from point B' besides the one from point B (Fig. 5.46). As the path length to the imaged object varies, probably a small f-number is needed with this setup for both images to be in focus. The back window in the current setup reflects some of the chemiluminescence intensity (Fig. 5.47), but the optical access is too small and the reflected light intensity is too low to allow for a 3-D re-construction based on these reflections.

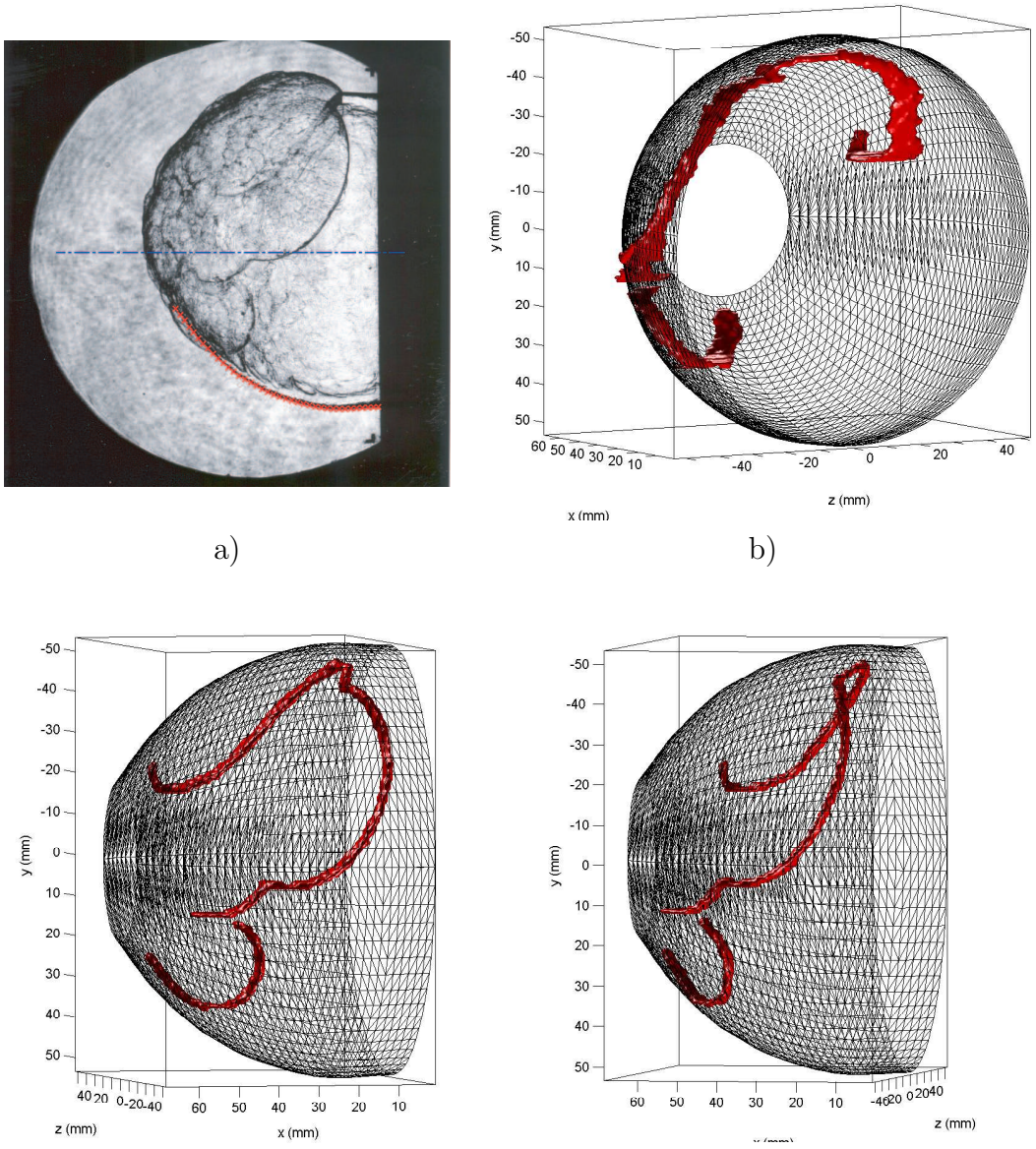

Figure 5.45: a) Edge-detected leading shock and assumed axis of symmetry. Flow direction left to right. b) View from rear of the wave through the tube exit plane. c) View corresponding to camera B. d) View corresponding to camera A, tube exit plane located on the right.

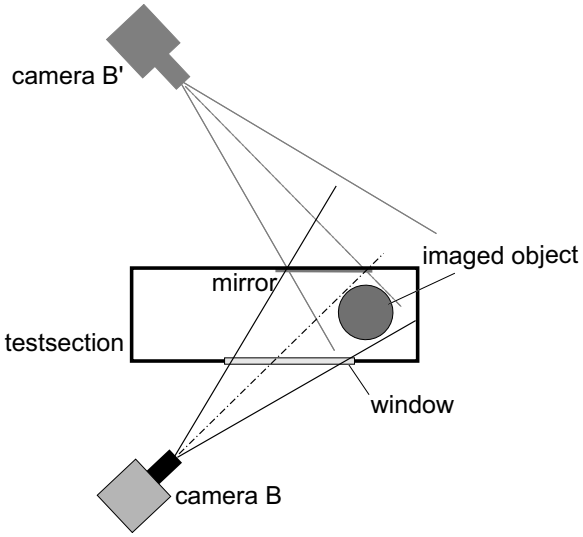

Figure 5.46: Possible setup for 3-D image re-construction by using a mirror to obtain a second image from point B'.

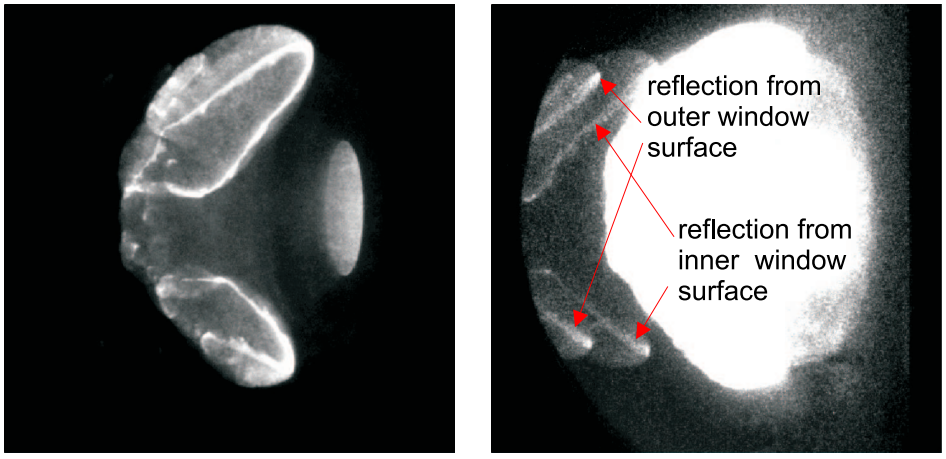

Figure 5.47: Reflections of chemiluminescence in back windows. Shot 217, 0.222 C_2H_6 + 0.778 O_2, P_0=42.5 kPa, T_0=295 K. Left: Intensity normalized image. Right: High contrast version of same image to allow for illustrations of low intensity reflections.

5.6 Distance between shock and reaction front

The PLIF schlieren overlay images were used to obtain the distance between the leading shock front seen on the schlieren images and the reaction front close to the tube axis. The data presented in the following paragraphs are acquired within 10 mm above and below the tube axis. Note that the distance between the shock and reaction front seen on the overlay images does not necessarily correspond to the induction zone length for the shock velocity at the instant the images were taken, since the process is transient and the reaction front is convected with the flow. Due to the cellular structure of the reaction front seen on the PLIF images and the slightly curved front on the schlieren images, the distance between both is not constant but varies along the front. The points detected along the reaction front were spaced approximately 1 mm; the points detected along the shock front were spaced approximately 0.25 mm. The smallest distance between a specific edge point of the reaction front and all points of the shock front was calculated. The dataset for one processed image consists of the average distance over the approximately 20 data points along with the minimum and maximum distance. A total of 80 images from experiments in Ar-diluted H_2-O_2 mixtures and H_2-N_2O mixtures was processed in this fashion.

The distance appearing on the overlay is a projected distance, as the leading shock front seen as the dark line on the schlieren images could arise from a different plane than the light sheet and consequently the PLIF image. As long as the shock is axisymmetric, the leading shock is close to the light sheet plane, which is oriented vertically through the tube axis. In case of re-ignition events where the lead shock is highly asymmetric, the error introduced is much larger. Images for which the leading shock appeared highly asymmetric on the schlieren images were not processed. In these cases the PLIF images showed a lower signal-to-noise ratio and were often not suited for edge detection.

The error corresponding to the maximum time delay of 80 ns between acquiring the PLIF and schlieren image results in a spatial uncertainty of 180 μm for the fastest CJ detonation velocities. The error in the overlay process was estimated

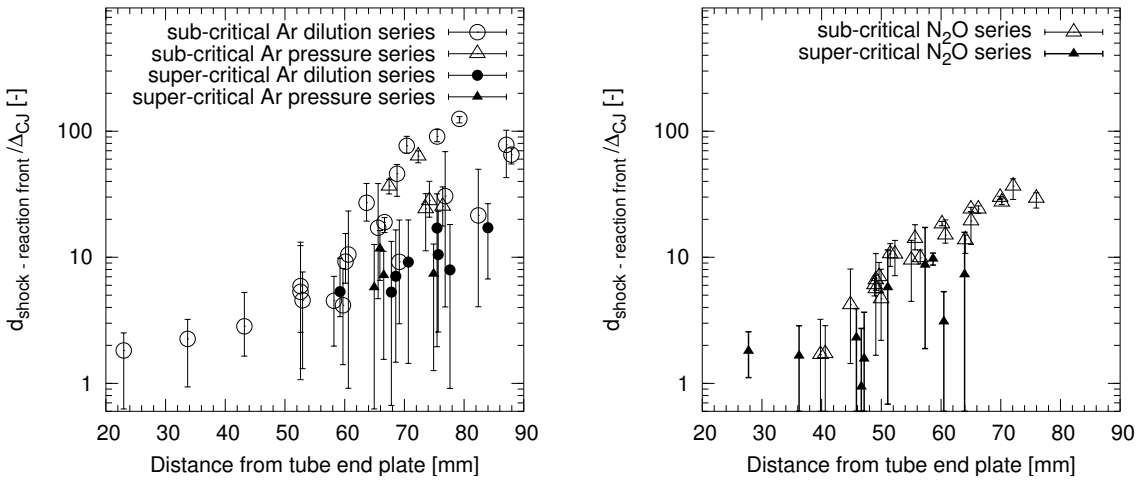

Figure 5.48: Normalized distances between shock and reaction front as measured from schlieren-PLIF overlays as a function of distance to tube end plate. a) H_2-O_2-Ar mixtures, b) H_2-O_2 mixtures.

to be 300 μm and the error in the reaction front detection was estimated to be 240 μm, which corresponds to two pixels. The total uncertainty for each data point measured is calculated by adding up the individual errors mentioned and amounts to approximately 0.7 mm.

The average distance measured between the shock and reaction front for both mixture types is shown as a distance x_{TEP} of the lead shock from the tube exit plane in Fig. 5.48; each data point corresponds to one experiment. The measured distance is normalized by the induction zone length at CJ conditions to allow for a comparison between experiments. The error bars shown do not correspond to the uncertainty of 0.7 mm in the measurement technique but to the minimum and maximum in distance measured for that specific overlay image. The CJ induction zone length for the Ar-diluted mixtures is approximately 0.1 mm and, for the H_2-N_2O mixtures, approximately 0.15 mm. The uncertainty of 0.7 mm corresponds on the plots shown to an uncertainty of about 7 and 4.5, respectively.

For both mixtures, the distance between the shock and reaction front is small – less than 3 Δ_{CJ} for $x_{TEP} < 45$ mm in all experiments. Note that these distances are smaller than the uncertainty in the measurement technique. For $x_{TEP} > 50$ mm,

the maximum distances measured for sub-critical experiments in H_2-O_2-Ar mixtures increase quickly with distance up to 100 Δ_{CJ} for $x_{TEP} = 80$ mm. There is a large spread in measured distances; the smallest distance measured for $x_{TEP} = 80$ mm was 20 Δ_{CJ}. The distances measured for the super-critical cases were smaller and increase from 5 Δ_{CJ} at $x_{TEP} = 60$ mm to about 20 Δ_{CJ} at $x_{TEP} = 80$ mm.

For the sub-critical cases in the N_2-O_2 mixtures, the distance between the shock and reaction front increased slightly faster with distances than in the Ar-diluted mixtures. A smaller spread in values is observed for a fixed x_{TEP} in N_2O mixtures compared to the Ar-diluted cases. Only a few distances in the super-critical cases could be measured. In general they were smaller than the sub-critical cases – less than 10 Δ_{CJ}. The distance between the shock and reaction front is connected to the lead shock velocity. When the reaction is close to the coupled shock, this leads to a higher velocity. Results of reaction front velocity measurements are shown in the next section.

5.7 Axial velocity decay

The velocity of the shock and reaction front is a good discriminant for them being coupled or not. In case of decoupling, the energy release rate is decreased, leading to an increase in induction zone length and a decrease in the velocity. Multiple exposure chemiluminescence images were used to determine x-t diagrams and velocity profiles of the leading front of the diffracting detonation. Comparison of PLIF and chemiluminescence images show that the leading front appearing in the chemiluminescence images coincides with the reaction front. The reaction front is trailing close to the wall and is not perpendicular to the wall, which can be seen on chemiluminescence and schlieren images (Fig.5.49). This is a consequence of the flow-field close to the tube exit and wall as a vortex structure gets formed, which reduces the flow speed at the wall close to the tube exit (Arienti (2002)). The lead shock is not strong enough to produce detectable luminescence. The reaction front is quenching close to the wall due to the strong expansion right after passing the sharp corner.

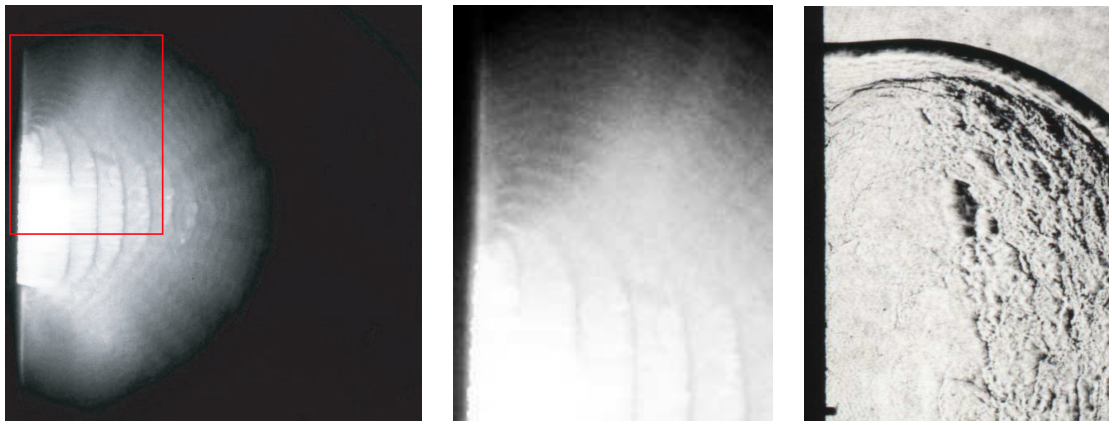

a) b) c)

Figure 5.49: a) Multiple gates chemiluminescence image in sub-critical regime. 0.5 H_2 + 0.5 N_2O, P_0 = 40 kPa. Multiple gates delay: 14×3μs. Shot 151. The chemiluminescence image is overexposed and shown to illustrate the kink in the reaction front close to the wall, which can be also seen on the schlieren image. b) Detail of (a) as marked. c) Corresponding schlieren image of same experiment.

The shock front is always times perpendicular to the wall as seen on the corresponding schlieren image (Fig.5.49c). This is due to the requirement that the flow adjacent to the wall moves parallel to the wall. The chemiluminescence emission is much lower in the regions where the shock has separated from the reaction zone than where the shock and reaction zone are coupled. The region behind the planar part of the detonation front (Fig. 5.50a) is a strong source of chemiluminescence emission. Re-ignition events can be clearly localized since they are also characterized by high emission intensity (Fig. 5.50b and c). Note that the intensity on each pixel is accumulated over successive exposure gates and some regions may appear brighter than they would in a single exposure image.

The bright isolated regions of chemiluminescence on the tube axis clearly define the motion of the reaction behind the shock and can be used to determine the axial velocity. In order to derive the axial velocity, a 20-pixel-wide horizontal stripe, centered on the tube axis, was extracted from each chemiluminescence image (Fig.5.51). The stripe width corresponds to 4.5 to 5 mm, depending on the field of view of the camera (118 or 109 mm). The pixel counts were then averaged in the vertical direction to obtain an one-dimensional intensity profile (Fig.5.51). The averaging is

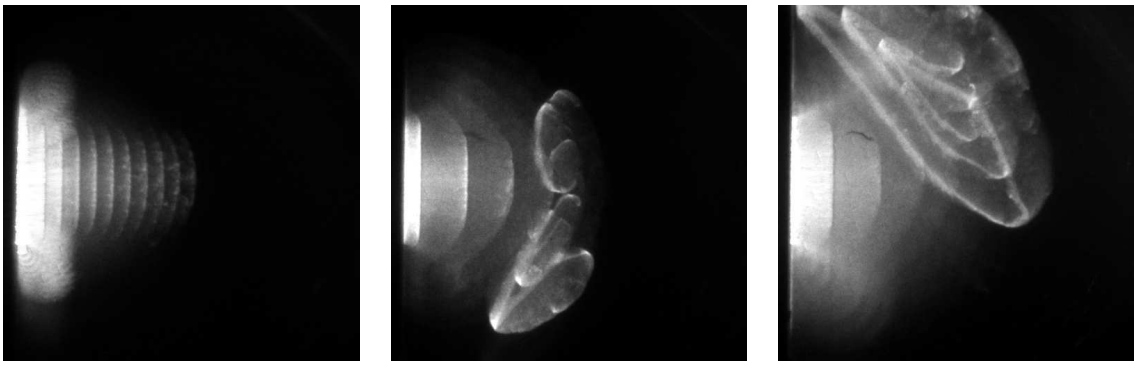

a) b) c)

Figure 5.50: Multiple gates chemiluminescence images. a) 0.22 H_2 + 0.11 O_2 + 0.67 Ar, P_0=100 kPa, multiple gates delay: 10×3μs, shot 148. b) 0.5 H_2 + 0.5 N_2O, P_0=47.5 kPa, multiple gates delay: 6×6μs, shot 172. c) 0.333 CH_4 + 0.667 O_2, P_0=120 kPa, multiple gates delay: 7×6μs, shot 195.

necessary in order to obtain a smoother intensity profile. The intensity profile clearly shows the local intensity fall-offs, which correspond to the chemiluminescence front location at each camera gate. In order to determine the position of the front, the intensity profile was differentiated with respect to distance by taking the difference quotient of adjacent data points. The location of the maximum negative gradient was taken as the location of the chemiluminescence front. Using the time delay Δt between gates, an x-t diagram of the axial chemiluminescence front and a velocity profile are obtained (Fig. 5.52). The derived velocity is an average in between consecutive camera gates. The distance coordinate of a velocity data point was set to the center position between the distance coordinates of the corresponding x-t data point pair. The error bars are shown on the x-t diagrams but are hardly visible and correspond to an uncertainty in location for the shock front of ± one pixel. For the velocity plots, this leads to a total uncertainty in Δx of four pixels. This corresponds to an uncertainty of ±150 m/s for the smallest Δt of 3 μ used. For larger values of Δt, the uncertainty decreases correspondingly. A summary of x-t diagrams and velocity profiles of all experiments is shown in Appendix L.

The particular method of obtaining the velocity profile does, however, have several limitations:

- The spatial resolution of the velocity profile is limited by the fact that using a

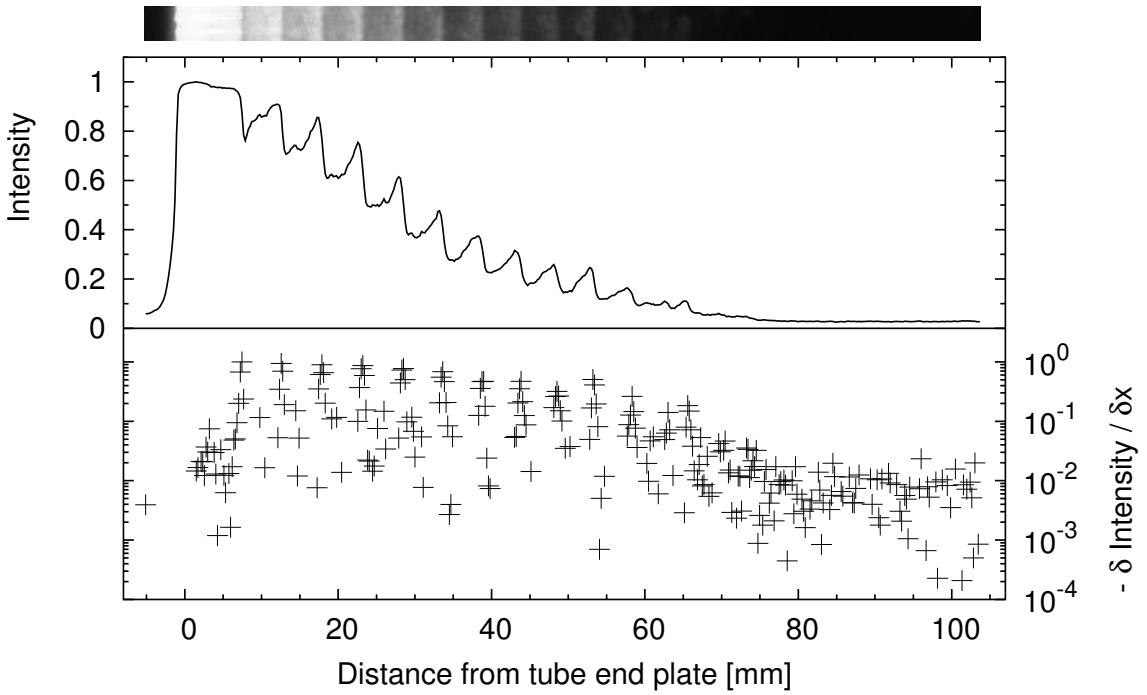

Figure 5.51: Example of chemiluminescence image analysis to determine front location, shot 148. Top: Extracted 20-pixel-wide stripe, Bottom: Averaged normalized intensity profile and negative normalized local derivative.

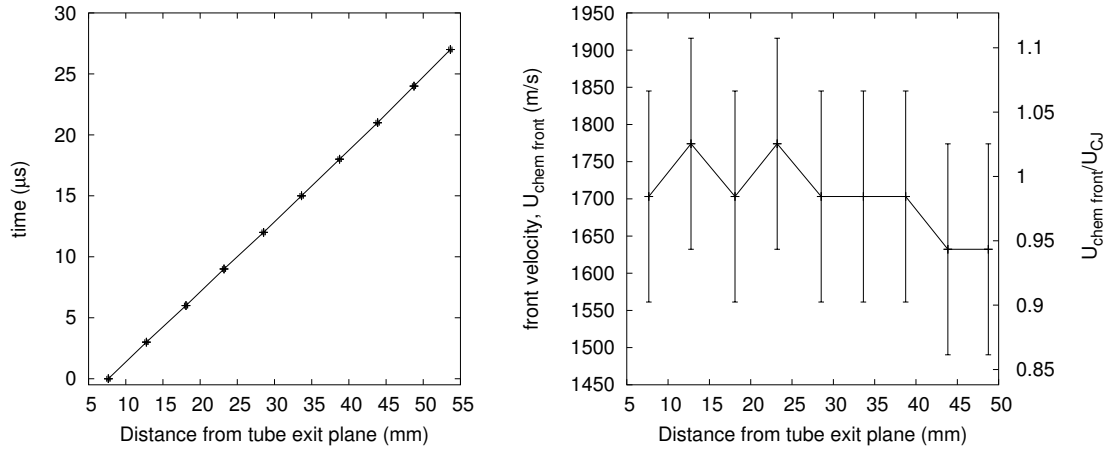

a) b)

Figure 5.52: a) x-t diagram obtained from multiple exposure chemiluminescence image. b) Corresponding velocity profile.

small Δt may lead to regions on the image being over-exposed. Over-exposed regions can lead to an error in determining the front location, since the luminosity gradients are not fully resolved. For smaller Δt, the uncertainty in the derived velocity also increases. With a streak camera, a higher spatial resolution of the velocity profile could be achieved. With a burst image, the accumulation of intensity limits the total number of gates. Regions close to the tube exit plane tend to get over-exposed, while the dynamic range in low-intensity regions is insufficient. The chemiluminescence intensity of failing detonation waves far from the tube exit plane tends to be very low and is sometimes difficult to detect. This could be compensated for by increasing the gate width for later camera gates. On the other hand, that would distort the qualitative link between energy release luminescence intensity, which is useful in interpreting the diffraction process from those images. For all experiments, the gate width within one burst series was kept constant.

- The integrating effect of the chemiluminescence technique has to be considered when interpreting the images. For the planar part of the diffracting detonation just exiting the tube, the intensity arising from the reaction front within that plane is integrated over the entire depth of the field. The leading front of a curved surface with a similar local luminescence would appear less bright. A large radius of curvature leads to a more distinct luminosity front. In return, this effect can be used to judge how planar the front is, as long as it is approximately aligned with the optical axis.

- The vertical averaging over the stripe can influence the determination of the front location for a curved front. For an ideal front of curvature radius 15 mm, the maximum horizontal displacement of the front location is 0.21 mm, which corresponds to one pixel. This assumes that the curvature center is on the center line of the stripe. For a curvature radius larger than 15 mm, the stripe is thin enough that the displacement is smaller than 1 pixel. The radius necessary for a horizontal displacement of one pixel is very sensitive to the location of

the curvature center. Assuming that the curvature center is on the stripe top or bottom, the curvature radius which corresponds to one pixel displacement is 59 mm.

- In case of a re-initiation event, the transverse detonation propagates sideways and backward into the shocked reactants. The luminosity of the transverse detonation is superposed on the regions containing the information about the front location from previous exposure gates (Fig. 5.50b). It is difficult, sometimes impossible, to unambiguously identify the origin of the luminosity, since the image contains no direct information about the chronology of the event. Events in which the luminosity front changes direction are difficult to interpret on multiple exposure images. A re-coupling event can also lead to a luminescence front that is not propagating along the tube axis. It can cross the horizontal averaging stripe at an angle. This leads to difficulties in locating the steepest gradient as described previously in the context of curvature. This results in erratic larger front velocities, since the velocity is not measured normal to the front. For this reason velocity profiles of re-ignition events are difficult to obtain with this technique. To avoid this, the camera timing parameters set prior to the experiment were chosen to stop recording shortly after a re-ignition. Since the re-ignition event is stochastic in nature, this is difficult to achieve. Using a narrow channel and studying cylindrical diffraction as done by previous researchers would overcome this problem since events are staggered spatially with respect to their chronology. To overcome this problem for the case of spherical diffraction, separate images have to be obtained with a high-speed camera or a streak camera.

- The lens distortion in the horizontal direction was measured by placing a target with equidistant stripes on the tube axis and was found to be less than one pixel over the field of view for the camera lens used for the chemiluminescence images. Lens distortion effects are therefore negligible.

- If the camera is placed at a distance d_{cam} (1.5 m) from the tube axis, the ray

defining the extremity of the front makes a varying angle β with respect to the tube axis (Fig. 5.53). The distance to the tube end plate x_{cam} is 25 mm, whereas the field of view is 109 mm for most experiments. As shown in Fig. 5.53, the image of the leading luminescence front can arise from a region behind or in front of the actual intercept of the front with the tube axis. Assuming that the leading luminosity arises from near the tube axis can lead to a displacement d between the apparent and actual location. The displacement is largest on the left and right edge of the field of view and is always positive, meaning that the distance to the tube end plate appears larger. The size of the error depends on the specific geometry of the imaged object and d_{cam}. Large planar regions of the front, occurring right after the detonation exits the tube, introduce a much larger error than fronts which are curved on the tube axis. In order to keep the angle β in the region up to approximately 50 mm from the tube end plate as close as possible to 90°, the camera was actually tilted by 1° with respect to the perpendicular of the tube axis. As an estimate, the displacement d_e in the tube exit plane was calculated to be 0.3 mm (1.5 pixel). Note that the displacement d changes gradually from the tube exit plane towards 0 at 25 mm distance from the tube exit plane. At this distance, the rays collected by the camera are perpendicular to the tube axis. The error this displacement introduces into velocity measurements has to be calculated by taking the difference in d between two exposure gates. This effect influences the determination of the absolute position of the front much more strongly than the determination of the velocity. Assuming, for example, a linear decrease in d with time and the wave velocity and camera settings as in shot 148, Fig. 5.52, the error in velocity measurements is only 38 m/s.

Several facts further decrease the influence of this effect. The steepest gradient in luminosity, used for determining the front location, seldom coincides with the leading point in luminosity. This is due to the integrating nature of the chemiluminescence images as the most intensity is collected from rays crossing close to the intersection of the reaction front and the tube axis. Also, the camera

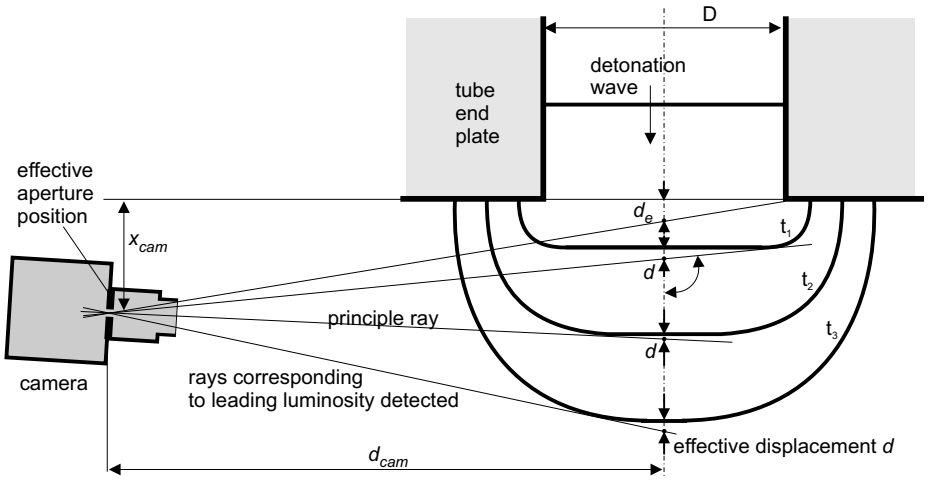

Figure 5.53: Sketch of apparent displacement between actual luminescence front on tube axis and leading luminescence front on image. Sketch is not drawn to scale.

aperture is finite, which blurs the luminescence gradients detected from outside the focal plane, which was set to be close to the tube axis. In summary, the oblique nature of the front has small effect on the velocity calculation. The detonation velocity will be slightly under-predicted for distances up to 25 mm from the tube end plate and over-predicted after that point.

Immediately after the detonation wave exits the tube, the detonation front on the tube axis is not influenced by the abrupt area change. The acoustic corner disturbance signal reaches the tube axis for the mixtures considered at a distance x_{TEP} from the tube exit plane of at least 39–45 mm, depending on the mixture composition (Section 5.3). On the basis of this calculation, the reaction front velocity on the tube center line is therefore expected to be close to the value for the detonation traveling inside the tube. This was measured by pressure transducer time of arrival data to be within 3% of the calculated CJ velocity (Section 5.2). Despite the previously discussed uncertainties, the velocity of the reaction front derived from multiple burst images was within 5% of the calculated CJ velocity for x_{TEP}<29 mm in all experiments conducted (Fig 5.54). For detonation velocities close to the CJ velocity, the reaction front virtually coincides with the leading shock front. This is due to the small induction zone length compared to the image resolution.

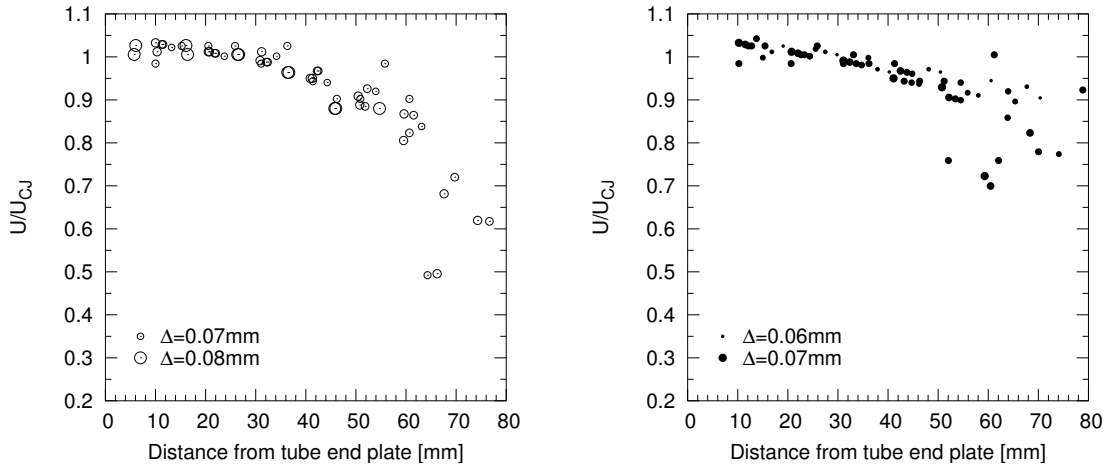

a) Ar dilution series, sub-critical cases. b) Ar dilution series, super-critical cases.

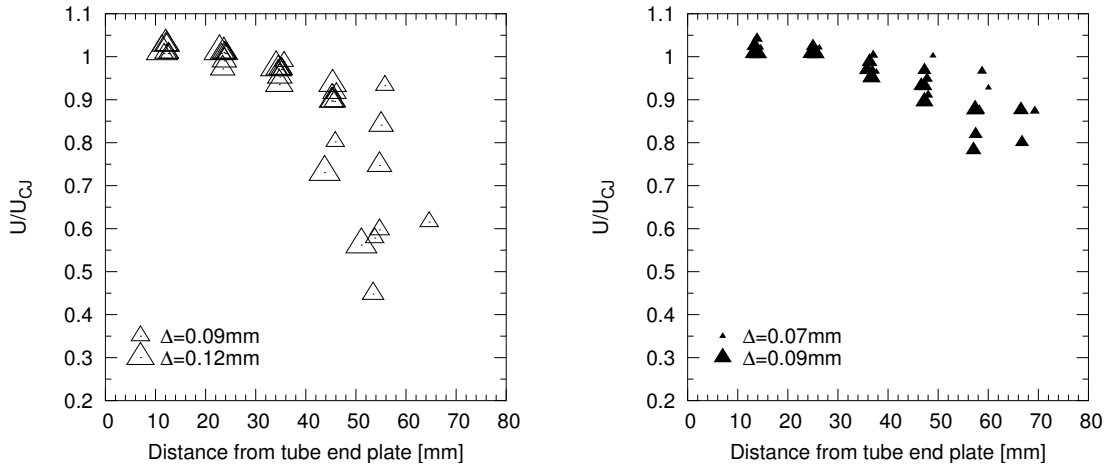

c) Ar pressure series, sub-critical cases. d) Ar series, super-critical cases.

Figure 5.54: Summary plots of all reaction front velocities obtained from multiple burst images as a function of distance from tube exit plane for H_2-O_2-Ar mixtures.

The size of the symbols shown in Fig. 5.54 scales with the size of the induction zone length at CJ conditions. Velocity measurements obtained from experiments with less sensitive mixtures correspond to larger symbols.

For the sub-critical cases of the H_2-O_2-Ar diluent series, the axial velocity is decaying slowly for x_{TEP} <44 mm and is greater than 90% of U_{CJ}. The measured velocities are found within a band of width 0.07 U_{CJ}. In the region 44 mm<x_{TEP}<56 mm, a large spread in velocity is observed. The velocity decays fairly rapidly down to approximately 0.5 U_{CJ} for some experiments while remaining at values close to 0.9 U_{CJ} for others. The most rapid decay is observed for the mixtures with the largest in-

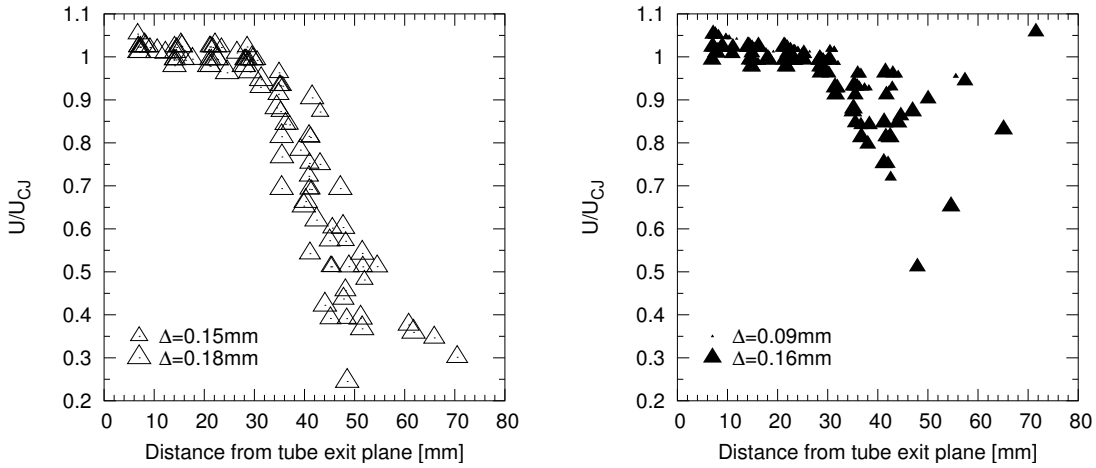

a) N_2O series, sub-critical cases. b) N_2O series, super-critical cases.

Figure 5.55: Summary plots of all reaction front velocities obtained from multiple burst images as a function of distance from tube exit plane for H_2-N_2O mixtures.

duction zone length. For the sub-critical cases of the Ar dilution series, conducted at higher pressure than the Ar pressure series, the inital slow decay rate is similar to the pressure series, but lasts longer in terms of distance from the tube exit plane. Velocities measured are above 0.8 U_{CJ} up to a distance of over 60 mm. Within 20 mm from that distance, the velocity declines to 50-60% of its CJ value.

For the super-critical cases of the Ar series, the velocity is up to 52 mm larger than 0.9 U_{CJ}. The spread in velocities measured is very small for the argon dilution series and within 0.05 U_{CJ}. For larger distances, velocities of 0.7–1 U_{CJ} are measured. The velocity data obtained at large distances from the tube end plate are not close to the CJ value since the re-initiation event has happened off axis or the last exposure took place before the re-ignition event in order to avoid overlay issues. One must also keep in mind the fact that the velocity data are averages. A time delay between gates of 3 μs corresponds to a distance of 7 mm for the fastest CJ velocities of approximately 2400 m/s measured for a N_2-O_2 mixture. The velocity is averaged in this case over a region from 3.5 mm behind to 7 mm ahead of the location shown on the plots.

The sub-critical cases of the N_2O series show a slow decay in reaction front velocity up to a distance of 34 mm for which the minimum velocity measured was 0.94 U_{CJ}. After that distance, a drastic fall-off in velocity for all sub-critical shots is measured.

Within 17 mm, the reaction front slows down to 0.25–0.55 U_{CJ}. Compared to the decays observed for the Ar-diluted mixtures, the spread in velocities measured within the strong fall-off is remarkably small. For the super-critical cases of the N_2O series, the velocity profiles for $x_{TEP} < 32$ mm are essentially unaltered from the sub-critical cases. The temporary decrease in velocity for $x_{TEP} > 34$ mm is inconsistent for the super-critical mixtures. The two points appearing for $U/U_{CJ}<0.7$ could be identified as cases where the re-initiation has taken place off the tube axis. The lowest data point corresponds to the last exposure of shot 172 (Fig. 5.8b). This illustrates the limitations of the center line velocity analysis to capture re-initiation events such as in Fig. 5.50b. Subsequently, the velocity increases and was measured to be up to 1.05 U_{CJ} at $x_{TEP} = 70$ mm. The dip in velocity for 30 mm $< x_{TEP} <$ 60 mm is observed for individual velocity profiles, e.g., shots 124 and 107, and is not just an effect of the presentation of many shots together.

5.8 Shape of diffracting detonation wave

Due to the strongly varying intensity along the luminescence front, it was not possible to accurately track the front over the entire outline. Instead, the schlieren images were used to locate the shock front location. This was done by an edge-tracking routine written in `MATLAB`. The accuracy was on the order of one pixel (0.06 mm), based on the steepest local gradient on the schlieren image. A sub-critical mixture was used to obtain a coherent time series of the diffracting detonation wave. Repeated experiments with identical mixture composition and a varying delay of the schlieren image trigger had to be conducted since only one schlieren image could be obtained per experiment. It was not possible to construct a coherent time series of diffraction experiments in the super-critical regime since the re-initiation location varies from shot to shot. One time series was obtained for $2H_2+O_2+7Ar$ mixture at $P_0 = 1$ bar and one for H_2+N_2O at $P_0 = 0.4$ bar. The sequence of derived shock shapes is shown in Fig. 5.56. The planar part of the front persists for the Ar-diluted mixture until approximately 40 mm from the tube exit plane. The curvature on the tube

axis seems to increase for larger distances more gradually for the Ar-diluted mixtures than for the H_2-N_2O mixture. For the H_2-N_2O mixture, the planar part of the shock front disappeared completely for $x_{TEP} > 30$ mm. It is tempting to try to use these outlines to examine propagation of the corner signal along the front. To do this, we need to consider determining the location of the interaction point through the front curvature variations. Defining the point on the shock outline at which the planar part of the front ends was found to be highly subjective as one can see from visual inspection of Fig. 5.56. For that reason, attempts were not made to quantify the disturbance propagation angle based on the location of the interaction point between the undisturbed front and acoustic corner signal.

In the case of the H_2-O_2-Ar mixture, the curvature near the tube axis appears stronger for $x_{TEP} > 50$ mm than in the regions 20–45 mm off the tube axis. For the H_2-N_2O mixture, the curvature varies little along the shock and the outline tends to resemble a half-circle. In the vicinity of the tube end plate, the shock was found to be perpendicular to the wall for all mixtures.

5.8.1 Shock and OH front velocities at wall and on tube axis

In order to illustrate the evolution of shock front geometry, the shock outlines were normalized by the wall shock location (Fig. 5.57). This shows that the shape of the shock is close to being self-similar for times larger than 42 μs for the Ar-diluted mixture and 29 μs for the H_2-N_2O mixture.

For most of the schlieren images used to construct the shock outlines simultaneous PLIF images where acquired. Shock and reaction front location were determined (Fig. 5.58, 5.59) along the tube axis and along the wall. This allows for determining simultaneously the lead shock location and the reaction front location. Due to the low fluorescence signal intensity close to the wall, the PLIF images could be used to determine only the reaction front location close to the tube axis. In order to detect the reaction front close to the wall, the reaction front was manually traced from the schlieren images. Close to the wall, the reaction front is, for most images,

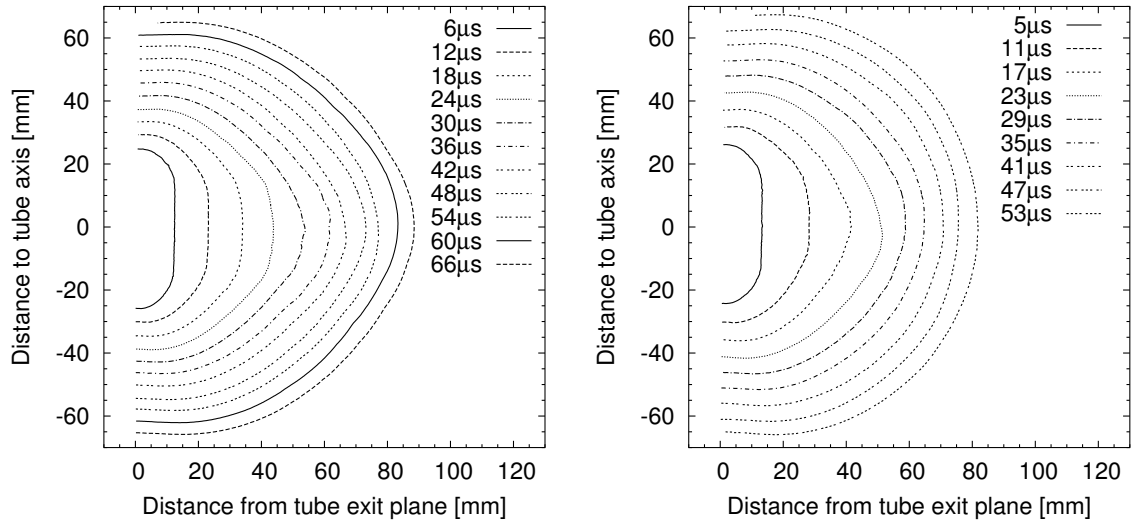

a) $2H_2+O_2+7Ar$, $P_0 = 1$ bar b) H_2+N_2O, $P_0 = 0.4$ bar.

Figure 5.56: Edge-detected leading shock front from multiple schlieren images taken at various points in time. The time given in the legend is measured from the point in time at which the detonation reached the tube exit plane. It is calculated from the delay between the detonation wave reaching pressure transducer P_3 to the point in time the image was taken, which was set prior to the experiment, and the assumption of CJ velocity within the tube.

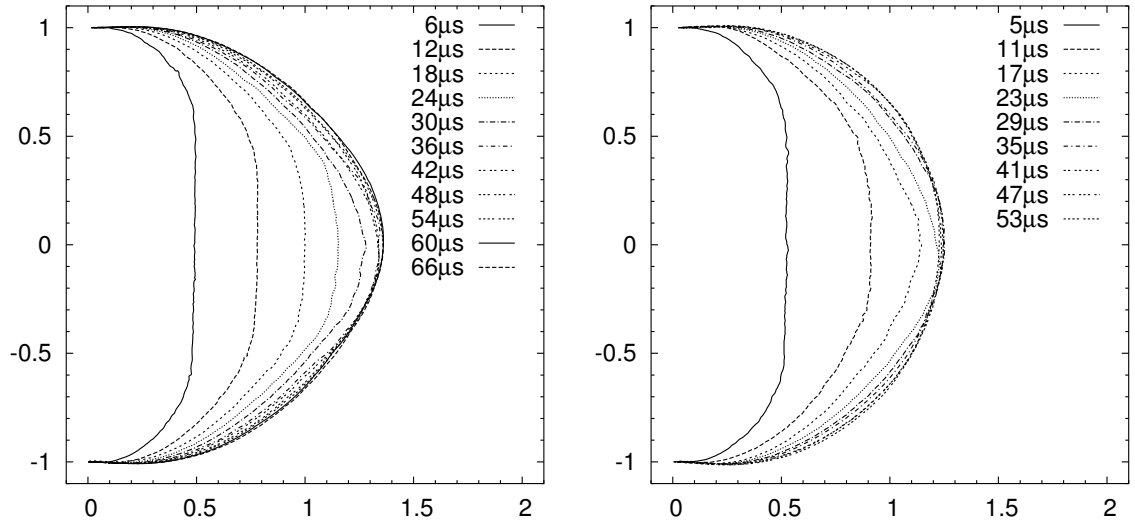

a) $2H_2+O_2+7Ar$, $P_0 = 1$ bar b) H_2+N_2O, $P_0 = 0.4$ bar.

Figure 5.57: Edge-detected leading shock front from multiple schlieren images taken at various times normalized to the shock location at the wall. The time given in the legend is measured from the point in time at which the detonation reached the tube exit plane. It is calculated from the delay between the detonation wave reaching pressure transducer P_3 to the point in time the image was taken, which was set prior to the experiment, and the assumption of CJ velocity within the tube.

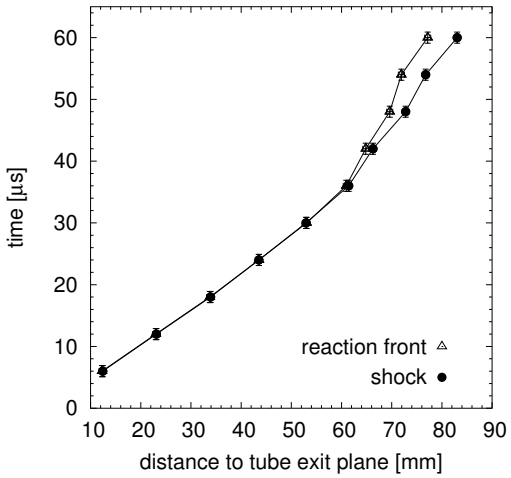

a) $2H_2+O_2+7Ar$, $P_0 = 1$ bar, on tube axis.

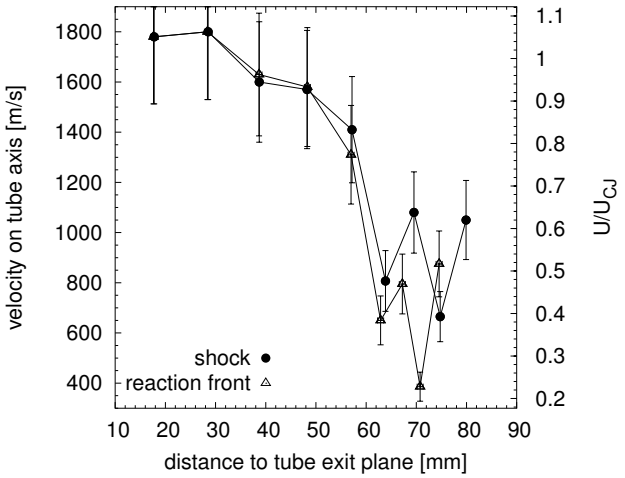

b) $2H_2+O_2+7Ar$, $P_0 = 1$ bar, on tube axis.

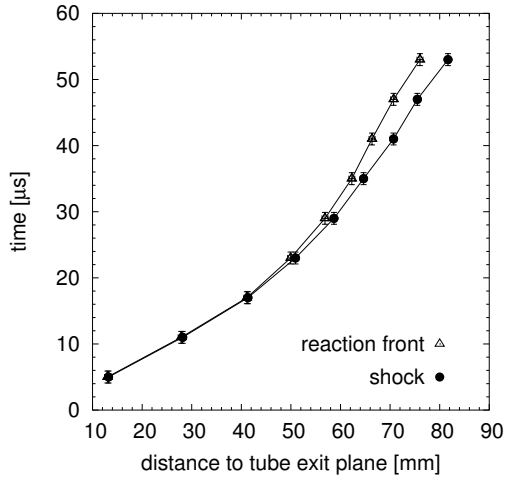

c) H_2+N_2O, $P_0 = 0.4$ bar, on tube axis.

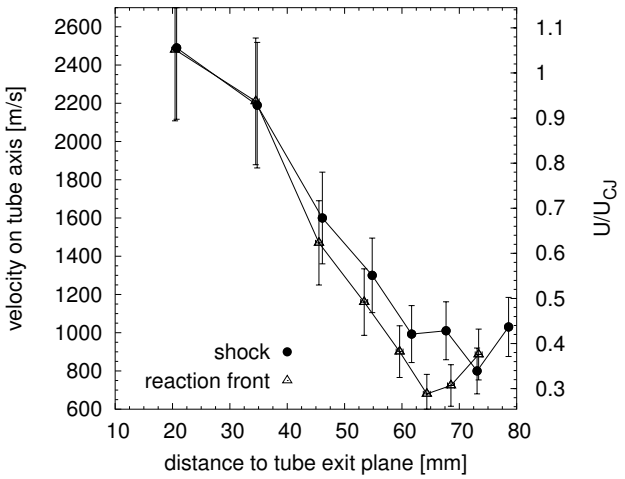

d) H_2+N_2O, $P_0 = 0.4$ bar, on tube axis.

Figure 5.58: Location of the shock and reaction front on tube axis and corresponding velocity profile.

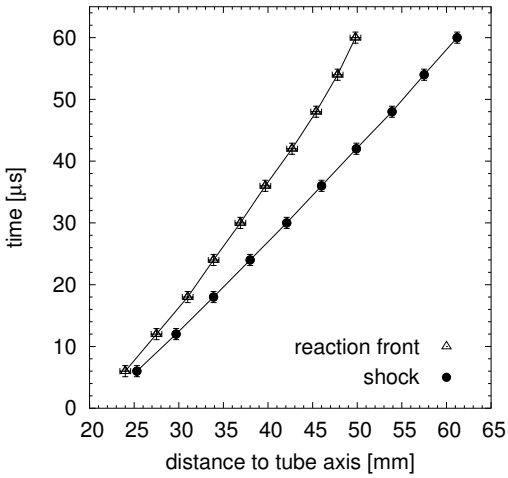

a) $2H_2+O_2+7Ar$, $P_0 = 1$ bar, close to wall.

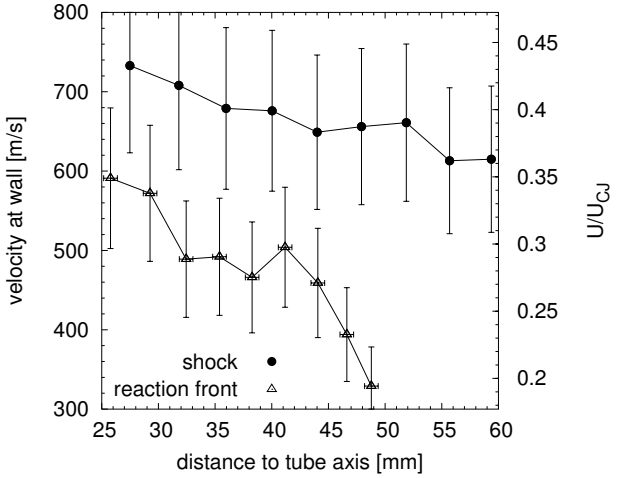

b) $2H_2+O_2+7Ar$, $P_0 = 1$ bar, close to wall.

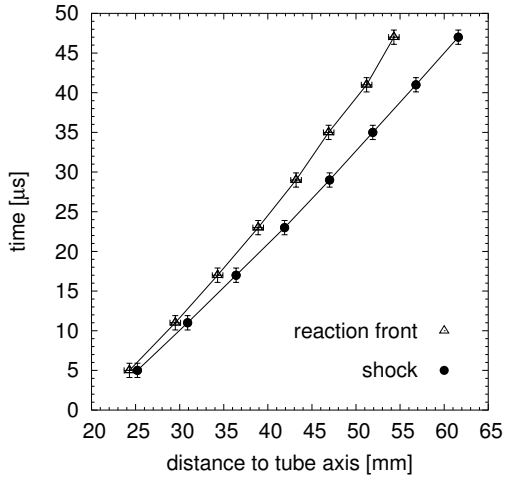

c) H_2+N_2O, $P_0 = 0.4$ bar, close to wall.

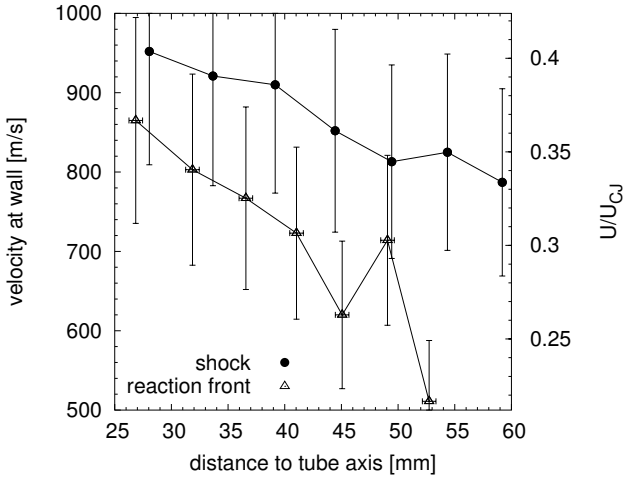

d) H_2+N_2O, $P_0 = 0.4$ bar, close to wall.

Figure 5.59: Location of the shock and reaction front close to the wall and corresponding velocity profile.

sufficiently spatially separated from the wall shock to be detected. Schlieren-PLIF overlay images of decoupled shock waves and reaction fronts taken close to the tube axis showed structures on the schlieren images which are identical to those seen close to the wall. This gives confidence in the manually-tracked reaction front close to the wall from schlieren images alone. The location of the shock and reaction front were determined by averaging the location of the edge-detected points within a 5-mm wide stripe. The stripe was either centered on the tube axis or oriented vertically close to the wall. For the front location at the wall, the average between the top part and bottom portion is presented. Note that due to the cellular structure, a large spread in the reaction front location is observed. This was discussed above (Section 5.6) in the context of measured shock-reaction front distance. The uncertainty in shock location due to the curvature of the shock within the stripe which was averaged over, was found to be at maximum 0.2 mm. The larger error in the presented x-t diagrams and velocity profiles for both shock and reaction front arises from the fact that the images were obtained from multiple experiments.

The time delay is based on the time of arrival of the detonation wave at pressure transducer P_3, located 298 mm upstream from the tube exit plane. Velocity measurements indicate a shot-to-shot variation of the detonation velocity of approximately 1%. The uncertainty caused by the spatial extent of the pressure transducer is neglected since this effect on the pressure trace is assumed to be the same for detonations in the same mixture. The shot-to-shot variation over all the experiments was measured to be 2.5% (Fig. 5.3). Since the experiments within one series were conducted consecutively within 30 minutes of one another, the facility temperature and the initial mixture temperature measured varied by only 2°C compared to a 6°C variation over all experiments. This could contribute to the smaller shot-to-shot variations within a consecutive series. A change in detonation velocity of 1% corresponds, for the Ar-diluted mixture, to a variation in time for the wave propagating from P_3 to the tube exit plane of 1.8 μs. In terms of the computed front velocities, this would translate to an error of 29%.

The small differences in detonation velocity and other fluctuations in initial con-

ditions to the diffraction process may be amplified during the diffraction process and increase the shot-to-shot variations. These variations are nearly impossible to quantify and are also evident from the asymmetry of some shock outlines, Fig. 5.56b, t = 23μs. The error bars on data shown in the plots of Fig. 5.58 and 5.59 reflect the uncertainties in location arising from the tracking process of the front and the error in time based on the discussion above of 1% perturbation in velocity within the detonation tube. The shot-to-shot uncertainty results in the large error bars for the velocities.

The x-t diagrams on the tube axis (Fig. 5.58a and c) indicate coupling between shock and reaction front location until a distance of $x_{TEP} \approx 60$ mm for the Ar-diluted mixture and $x_{TEP} \approx 40$ mm in the case of the H_2-N_2O mixture. The velocity close to the tube exit plane is within 6% of the calculated CJ velocity and then decreases with distance as the shock decouples. In the plots for the velocity profiles, the center position between two front locations is used. Due to the time increments of 6 μs used in both series and the larger CJ velocity in the case of the H_2-N_2O mixture, the spatial resolution was smaller for that case.

The x-t diagrams for the wall shock and reaction front suggest a decoupling for both cases at the first obtained data point, 5 mm from the sharp corner the detonation wave diffracted around (Fig. 5.59a and c). The distance between the shock and reaction front appears to increase with distance from the tube axis in a stronger than linear fashion, an effect also observed on the velocity profiles. While the shock velocity is close to 0.4 U_{CJ} for both mixtures and drops by only 15% over 30 mm, the reaction front velocity seems to decrease much more strongly from approximately 0.35 close to the corner to approximately 0.2 U_{CJ} at a distance of 50 mm from the tube axis.

5.8.2 Local shock and OH front velocities

Shock trajectories are rays, which are perpendicular to the shock surface at each instant in time, as the local propagation direction is normal to the shock. The deter-

mination of the exact local lead shock velocity at points distant from the tube axis and wall is challenging as the shock trajectories are not straight lines, but curved (Fig. 5.60). The distance over which the shock front travels corresponds in a given time instant to the length of the curved shock trajectory. All methods discussed here for deriving the shock velocity are based on determining a distance d between two shock outlines for each point along the shock outline. The rays are approximated as piecewise linear segments between the shock outlines. The time delay $\Delta t = 6$ μs between adjacent shock outlines and the velocity can be determined.

One possible method of constructing the rays is to obtain the direction of the ray as the normal to the shock outline. The ray is then linearly extended in the propagation direction of the shock until the intersection with the next shock outline. The length of each ray segment is taken as the distance d. This method is labeled as "forward" normal in Fig. 5.60a. The boundary condition of the ray being normal to the shock outline is not necessarily matched at the outer shock surface. Similarly, constructing the ray segments as normals to the shock outline opposite to the propagation direction of the shock does not necessarily lead to the ray segment being normal to the inner shock outline (see "backward" normal in Fig. 5.60a). Another approach closely related to using the normals to the shock outline is using the "closest point method". The ray segment length d is approximated as the distance to the closest point of the next shock outline. Note that in the case of the "normal" method, a forward and backward tracing is possible (Fig. 5.60a and b). The closest point on outline B to point P_A is point P_B (Fig. 5.60b). It is not P_A but a different point Q_B that is the closest point on the outline A to point P_B. Since the circle of radius d and center Q_b for the "closest point" method are tangent to the smoothed outline A, the ray segment is approximately normal to the outline A. The "backward closest point" method is therefore equivalent to the "forward normal" method. Correspondingly the "forward closest point" method is identical to the "backward normal" method. For constructing the ray normals to experimentally obtained data, smoothing and averaging over several adjacent points is necessary. Depending on the smoothing method and number of points used for the averaging, the actual result with corresponding

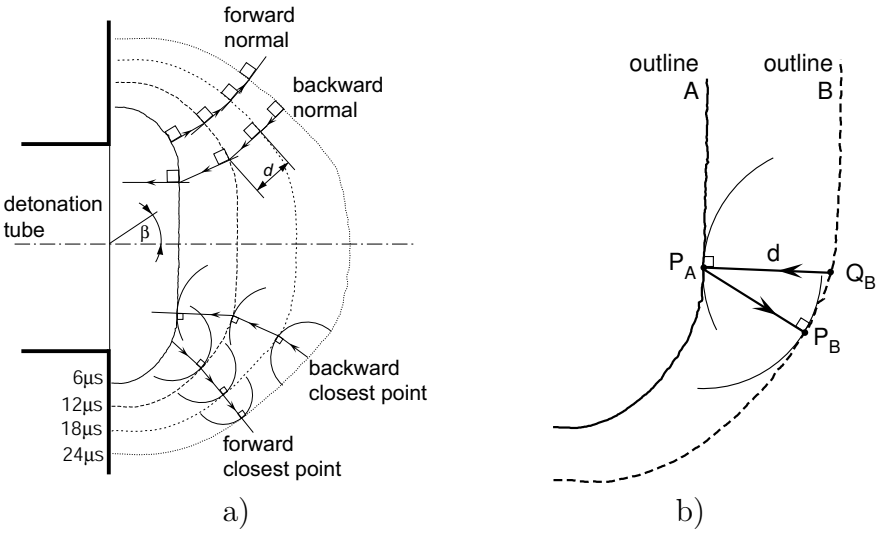

Figure 5.60: a) Sketch illustrating different techniques for obtaining the local shock velocity from a time sequence of shock outlines. The outlines correspond to the ones shown in Fig. 5.56a. b) Detail of closest point approximation for forward and backward tracking.

closest point and normal method can differ slightly. The closest point method was found to lead to less noise in the resulting velocity profiles.

The difference between the results obtained from the forward and backward closest point method is largest for the front portions with a large change in shock curvature. In these regions, the expansion wave is interacting with the detonation front. When plotting the results as a function of the angle β to the tube axis, the difference between the forward and backward closest point method was found for the Ar-diluted mixture to be at the shift in β by 5° (Fig. 5.61a). In the remaining plots the forward closest point method is used. The data shown in Fig. 5.61a are averaged over an angle segment of 3° assuming axial symmetry. The original data set before the smoothing process is shown in Fig. 5.61c. The point in time given in the plots for each velocity profile is halfway between the points in time at which the two corresponding shock outlines were obtained. The velocity is the average velocity between the two points in time at which the schlieren images were taken.

In the case of the H_2-O_2-Ar mixture, the shock velocity profile shows a plateau corresponding to the CJ value close to the tube axis. As time progresses, the width of the plateau decreases since the expansion head is moving towards the tube axis. The

shock velocity decays for the early times almost linearly with the angle β from the CJ value right at the expansion head to approximately 0.4 U_{CJ} at the wall (β=90°). For times later than 20 μs, a strong fall-off in shock velocity is observed with increasing angle β. The velocity decreases from 0.9 U_{CJ} on the tube axis to 0.55 U_{CJ} at $\beta = 30°$. For angles of $\beta > 30°$, the fall-off in shock velocity is modest. The velocity is below 0.6 U_{CJ} over the entire shock surface for times later than 40 μs.

In the case of the H_2-N_2O mixture, the plateau observed for early times is not as flat as in the Ar-diluted case. This could arise from the fact that the shock outlines used for the velocity determination are from separate experiments. The details of the shock outline close to the expansion head might vary slightly from shot to shot leading to errors in the velocity profiles. Furthermore, the values obtained for the shock velocity might also be influenced by the closest point approximation, especially close to the expansion head. In these positions of the front, the changes in curvature are large, the ideal shock trajectory ray significantly curved, and the errors introduced by the linear segment approximation substantial. The closest point approximation leads to the smallest value of d and, correspondingly, to a smaller velocity than a more realistic curved ray segment approximation. For this reason, shock velocities larger than U_{CJ} are more likely explained by the shot-to-shot variations. Up to 14 μs, the shock velocity is decreasing approximately linearly with β outside the plateau, reaching approximately 0.4 U_{CJ} at the wall. After the expansion head has reached the tube axis, the velocity on the tube axis is decreasing but the linearity in the decrease with the angle persists. For times later than 26 μs, the shock velocity is below 0.6 U_{CJ} over the entire shock surface.

For the sub-critical cases, a clear contact surface between shocked but unreacted material on one side and reacting or reacted gas on the other side can be observed on the schlieren images. The simultaneously obtained PLIF images show that the contact surface seen on schlieren images coincides with the front of OH radicals. The term “reaction front” is, at this point inappropriate, since it would imply chemical reaction taking place. This is not necessarily the case since, as will be shown in Chapter 6, the OH-front can also be convected along without a strong exothermic

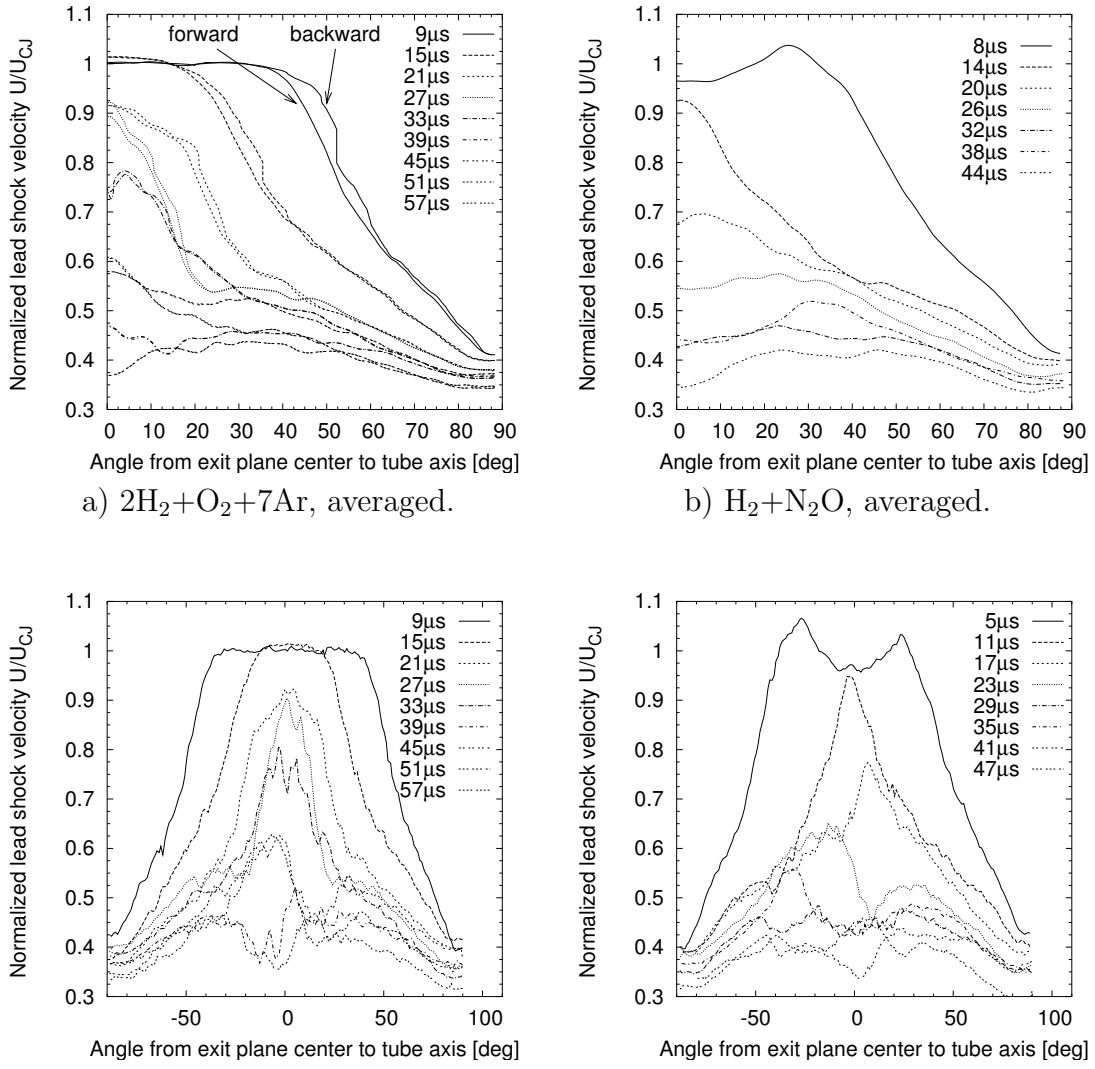

a) $2H_2+O_2+7Ar$, averaged.

b) H_2+N_2O, averaged.

c) $2H_2+O_2+7Ar$, raw data.

d) H_2+N_2O, raw data.

Figure 5.61: a) Averaged velocity profiles assuming axis symmetry for forward and backward closest point method, $2H_2+O_2+7Ar$, $P_0 = 1$ bar. Legend gives point in time after detonation exited the tube. b) Averaged velocity profiles assuming axis symmetry for forward and backward closest point method, H_2+N_2O $P_0 = 0.4$ bar. Legend gives point in time after detonation exited the tube. c) Normalized velocity obtained with forward closest point technique for $2H_2+O_2+7Ar$, $P_0 = 1$ bar, from shock outlines shown in Fig. 5.56a. d) Normalized velocity obtained with forward closest point technique for H_2+N_2O $P_0 = 0.4$ bar, from shock outlines shown in Fig. 5.56b.

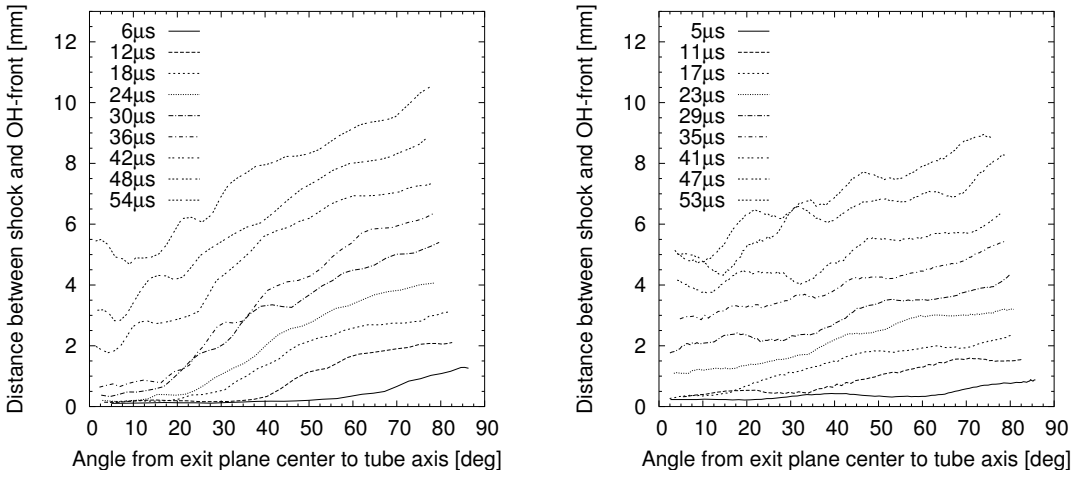

a) $2H_2+O_2+7Ar$, $P_0 = 1$ bar. b) H_2+N_2O $P_0 = 0.4$ bar.

Figure 5.62: Distance between shock and OH front for several times instances.

reaction taking place. The distance between the contact surface seen on schlieren images and leading shock front is, therefore, close to the distance between the OH-front and the lead shock. By obtaining the closest point on the lead shock outline to each point on the contact surface, the distance between the shock and the OH front was determined over the angle β. In order to achieve a smoother profile of the distance x_{OH} between the shock and the OH front, the data are averaged over an angle of 3° (Fig. 5.62). The plateau regions with lead shock velocities close to the CJ value seen in Fig. 5.61a and b correspond to the plateau region of very small values of x_{OH}, which were measured to be below 0.4 mm. For these regions, the values given for x_{OH} are an upper bound for the actual distance between the shock and the reaction front since the length scales are below the resolution of the system. Outside the plateau region, the distance x_{OH} is increasing with increasing β.

Chapter 6

Comparison of Induction Time and Residence Time

For an understanding of the diffraction process, it is important to know the induction time τ_i, of a shocked fluid particle since that determines when the chemical energy release will take place. The induction time is a strong function of shock velocity which, in turn, is a function of time after the detonation exits the tube and of the location on the shock front. By comparing τ_i to the residence time τ_r of the unreacted fluid particle just ahead of the OH-front, we can estimate the extent of reaction in the region between the shock and the OH-front. The residence time is the time that has elapsed since a given fluid particle passed through the shock wave. In order to compute the induction and residence time, we take a simplified quasi-one-dimensional view of the fluid motion and neglect the influence of transverse waves.

If the induction time of a particle at the OH-front is much longer than its residence time, this particle will not react within the observable time scale of the diffraction process and the OH-front is just convected with the post-shock fluid velocity. In this case, the shock wave has decoupled from the reaction, and the energy release rate behind the shock has decreased almost to zero. Unreacted fluid will accumulate behind a decaying leading shock wave. If the residence time of a particle at the OH-front is equal to or smaller than the induction time, significant chemical energy is released in the vicinity of the OH-front. From the experimental data, both low- and high-energy release rate regimes are mapped for the two mixtures discussed in

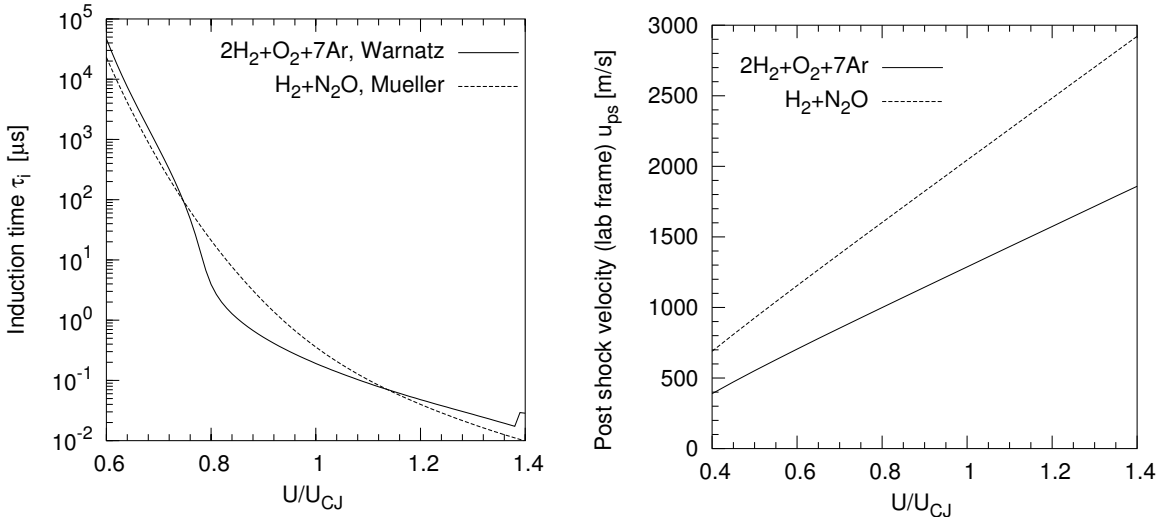

Figure 6.1: (a) Induction time τ_i and (b) post-shock fluid velocity in lab frame as a function of normalized shock velocity for two mixtures: $2H_2$+O_2+7Ar, P_0 = 1 bar and H_2-N_2O P_0 = 0.4 bar.

Section 5.8.2: $2H_2$+O_2+7Ar, P_0 = 1 bar and H_2+N_2O P_0 = 0.4 bar.

The induction time τ_i was calculated as a function of shock velocity by first determining the post-shock conditions via solving the shock jump conditions assuming a frozen mixture composition. Second, the induction time was determined as the adiabatic constant volume explosion time at post-shock conditions using the CV-code (Shepherd, 1986). The chemical reaction mechanisms of Konnov and Warnatz for the H_2-O_2-Ar mixtures gave similar results. In the following, the Warnatz mechanism is used for the H_2-O_2-Ar mixture and the Mueller mechanism for the H_2-N_2O mixture (Fig. 6.1a).

In Section 6.1, the Taylor-Sedov blast solution is used to estimate the error in the simplified calculation of the residence time. In Section 6.2, the induction time τ_i for particles at the OH-front is derived. The time scales τ_i and τ_r are compared in Section 6.3 in order to estimate where the adiabatic explosion at the OH-front is taking place.

6.1 Residence time

The shock velocity and distance between the shock and OH-front x_{OH} were measured experimentally over the shock outline in 6 μs time increments (Section 5.8.2). In order to calculate the residence time of a particle at the OH-front from x_{OH}, the velocity history of the particle has to be known. We use the Taylor-Sedov similarity solution for a spherical blast wave to estimate the particle path behind the decaying shock wave. The Taylor-Sedov blast solution is a non-reactive similarity solution of a strong spherical shock wave resulting from an instantaneous release of a large amount of energy E at time $t = 0$ and radius $r = 0$. The perfect gas in which the wave is propagating is initially uniform and at rest. In the strong shock limit ($(U_{shk}/c)^2 \gg 1$), the post-shock conditions are a function of the ratio of heat capacities γ only. The fluid velocity $u(r)$ is, in its normalized form u/u_{ps}, only a function of the dimensionless distance behind the shock front r/R, where R is the position of the shock front (Fig. 6.2a). The velocity gradient for $r/R > 0.85$ is approximately twice that for $r/R < 0.85$, and approximately constant for both intervals. The Taylor-Sedov solution parameters E and ρ_0 were chosen such that the velocity decay rate matches, as well as possible, the experimentally measured one (Fig. 6.2b). The experimentally measured velocity decay rate was slightly smaller than the Taylor-Sedov value. This is due to the non-spherical geometry of the diffracting wave. In the experiment, the leading shock is also influenced by the chemical reaction, which is neglected in the Taylor-Sedov solution. Furthermore, the Taylor-Sedov solution uses the strong shock approximation for the jump conditions. For the wall shock Mach number of $Ma \approx 2$, this introduces further errors.

The particle paths for five particles initially located equidistant between $r = 0.04$ m and 0.08 m were calculated based on the Taylor-Sedov velocity field behind the shock wave (Fig. 6.3a). With increasing time, particles are convected further behind the shock and the velocity is decreasing, as seen from the steeper slope of the particle path in the x-t diagram. The corresponding velocity history shows that the particle travels at the post-shock velocity immediately behind the shock wave

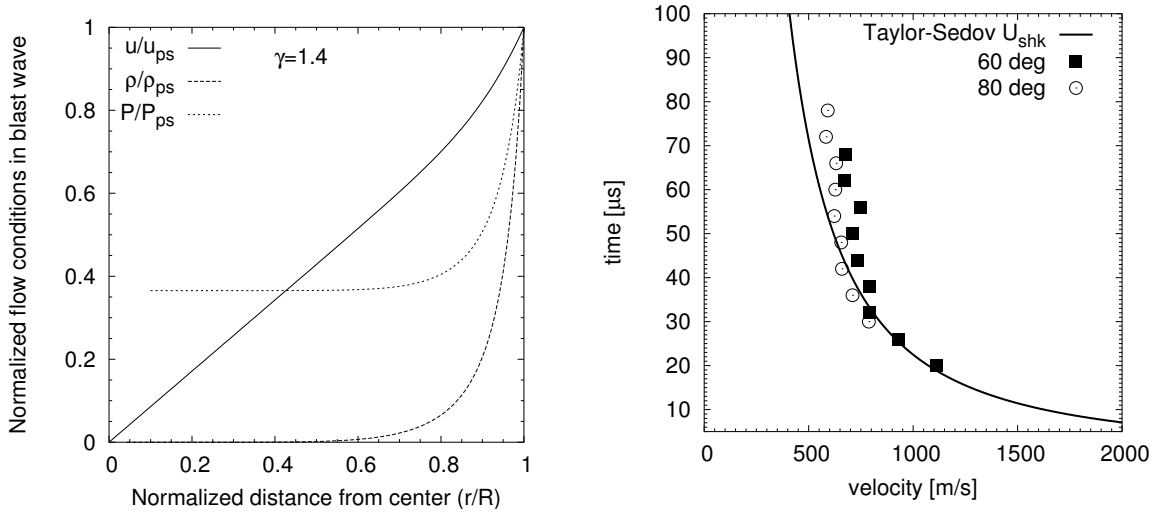

Figure 6.2: a) Taylor-Sedov blast solution in similarity coordinates of velocity profile behind spherically expanding shock wave. The parameter $\gamma = 1.4$ corresponds to the $2H_2+O_2+7Ar$ case. R is the location of the shock front, the velocity u, density ρ, and pressure P are normalized by their post-shock values. b) Shock velocity vs. time from Taylor-Sedov blast solution (solid line) and experimentally measured velocities (squares) for different angles β to tube axis (Fig. 5.60), H_2-O_2-Ar case.

(Fig. 6.3b). The velocity of a given fluid particle decreases faster with time than the post-shock velocity. The velocity of particle 1, which was processed by a shock wave traveling close to the CJ-velocity (1693 m/s), is for any given point in time at most 110 m/s smaller than the post-shock velocity u_{ps} (Fig. 6.3b). The lowest lead shock velocity of $U/U_{CJ} \approx 0.4$ was measured in the diffraction experiment close to the wall. The corresponding lowest post-shock velocity u_{ps}, in the case of the H_2-O_2-Ar mixture, is 400 m/s without the strong shock assumption (Fig. 6.1b). Approximating the particle velocity u_P at all times with the post-shock velocity u_{ps} would lead to an error of approximately 25% at most. The approximation is better for times close to the point in time when the particle passed through the shock wave, as the u_P departs gradually from u_{ps} for larger times (Fig. 6.4a).

At time t_2, the distance x_P between the shock front and a particle P can be written as (Fig. 6.4b)

$$x_P = \int_{t_1}^{t_2} (U_{shk} - u_P)\, \mathrm{d}t, \tag{6.1}$$

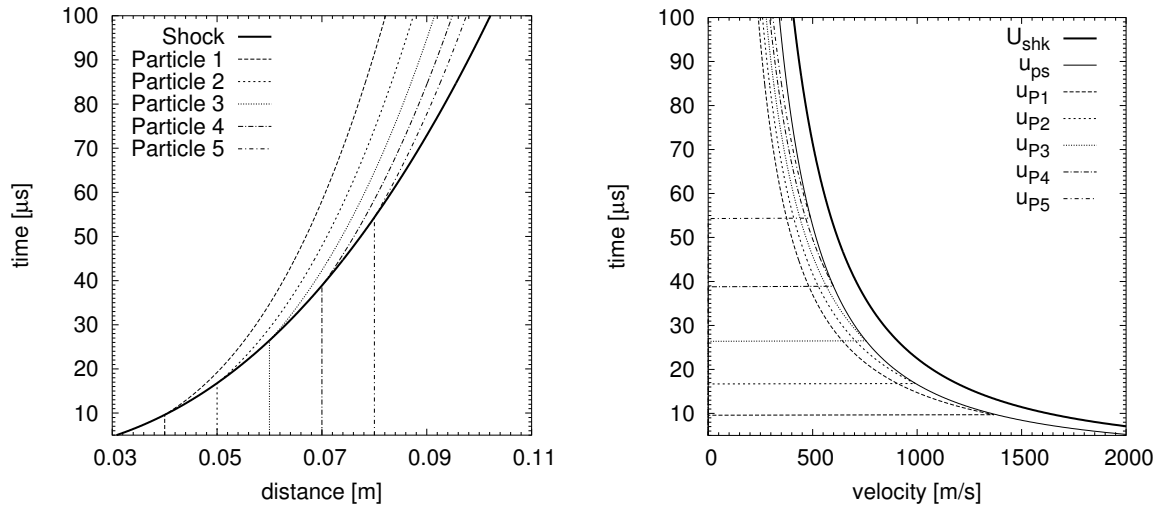

Figure 6.3: a) Particle path in x-t diagram for five particles, initially located between $r = 0.04$ m and $r = 0.08$ m, based on Taylor-Sedov solution shown in Fig. 6.2. b) Velocity of five particles shown in (a) as a function of time.

where t_1 is the time the particle passed through the shock wave and the residence time $\tau_r = t_2 - t_1$. Approximating the particle velocity $u_P(t)$ by the post-shock velocity $u_{ps}(t)$ leads to

$$\begin{aligned} x_P &= \int_{t_1}^{t_2} (U_{shk} - u_{ps})\,\mathrm{d}t \\ &= \int_{t_1}^{t_2} w_{ps}\,\mathrm{d}t\,. \end{aligned} \tag{6.2}$$

This is equivalent to transforming to shock-fixed coordinates and approximating the particle velocity w_P with the post-shock velocity w_{ps}. The approximation of $w_P(t) \approx w_{ps}(t)$ introduces, in the shock-fixed frame, an error larger than the 25% mentioned above for $u_P(t) \approx u_{ps}(t)$ in the lab fixed frame. In the shock-fixed frame, the post-shock velocity w_{ps} is 290 m/s for $U/U_{CJ} \approx 0.4$ (Fig. 6.5a). The difference between the particle and post-shock velocity is, nevertheless, the same in both frames as $u_{ps} - u_P = w_{ps} - w_P \approx 110$ m/s (Fig. 6.5a). The error in the approximation $w_P(t) \approx w_{ps}(t)$ for calculating x_P via Eq. 6.2 is, at most, 38% (Fig. 6.4a). The error introduced is

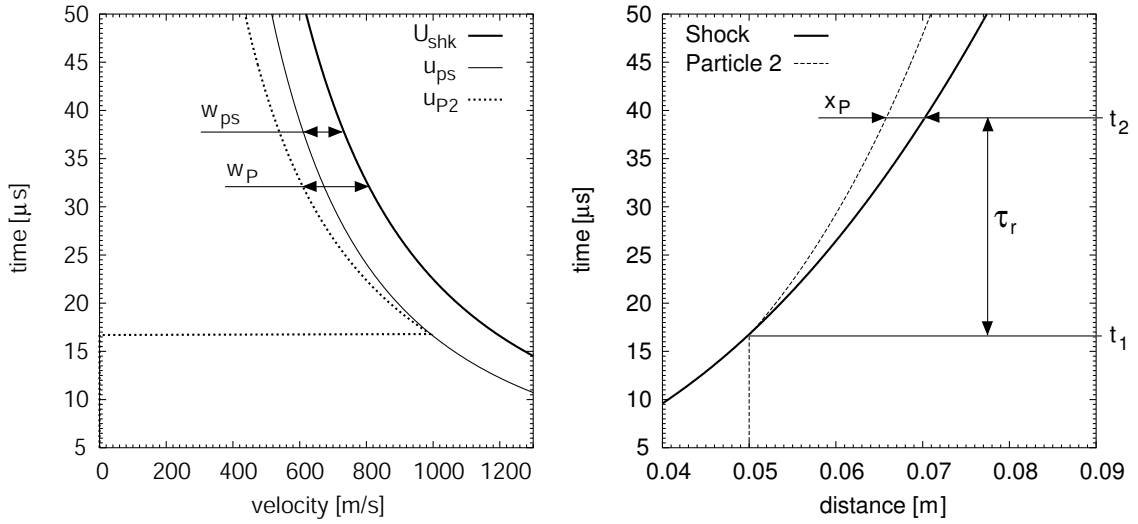

Figure 6.4: a) Post-shock and particle velocity in lab frame (u_{ps}, u_P) and shock-fixed frame (w_{ps}, w_P) based on Taylor-Sedov solution (see Fig. 6.2). b) Residence time τ_r of a particle at time t_2 at OH-front.

smallest for short time intervals t_2-t_1. Since $w_{ps}(t) < w_P(t)$, the particle velocity w_P is underestimated by this approximation.

The post-shock velocity w_{ps} depends on the shock strength in the range of lead shock velocities of interest (Fig 6.5). For the Ar-diluted mixture, w_{ps} decreases from 400 m/s at CJ conditions to 290 m/s at $U/U_{CJ} = 0.4$. For the H_2-N_2O mixture, the corresponding decrease in post-shock velocity is 10%. Neglecting this variation and assuming a steady state post-shock velocity w_{ps}, the residence time can be written as

$$\tau_r(t_2) = x_P(t_2)/w_{ps}(t_2). \tag{6.3}$$

Note that the steady state assumption causes a smaller error for w_{ps} than it would for u_{ps} (Fig. 6.5). The residence time of a particle at the OH-front can be approximated using this simplified formula by setting $x_P = x_{OH}$, the distance from the OH-front to the lead shock front. With the approximations $w_{ps} \approx u_{ps}$ and $u_{ps}(t) \approx u_{ps}(t_2)$, the residence time calculated via Eq. 6.3 is an upper bound for the actual particle residence time. The particle velocity for the Taylor-Sedov solution, $w_{ps}(t_2)$ is, for the duration of the diffraction experiment, at most 45% smaller than $w_P(t)$.

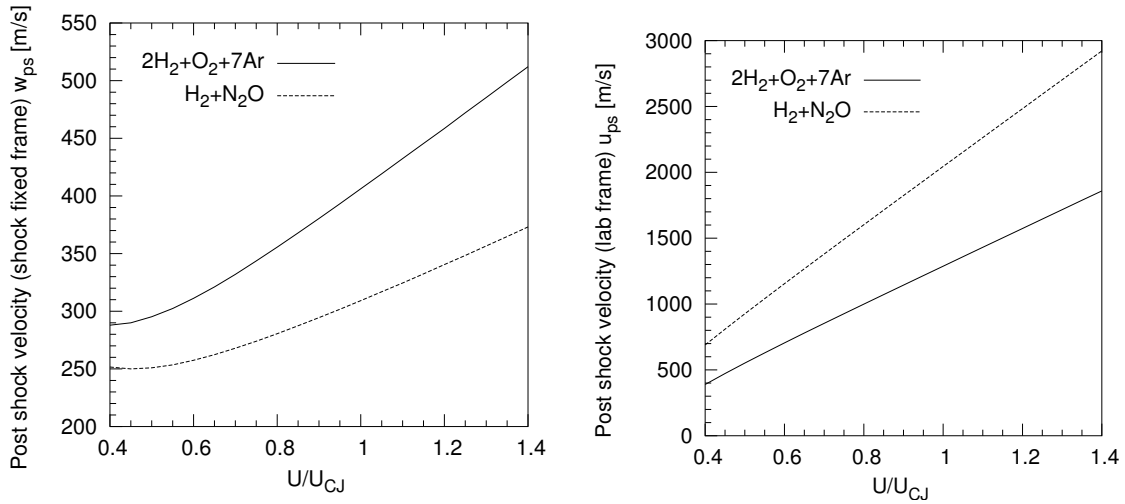

Figure 6.5: Post-shock fluid velocity w_{ps} in shock-fixed frame (a) and lab fixed frame (b) as a function of normalized shock velocity for two mixtures: $2H_2$+O_2+7Ar, $P_0 = 1$ bar and H_2-N_2O $P_0 = 0.4$ bar.

The estimated residence time of a particle (Eq. 6.3) is at most a factor of 1.8 larger than the actual residence time based on the Taylor-Sedov blast solution. In order to determine the flow field in the diffraction experiment precisely, either a numerical simulation is necessary or a quantitative experimental measurement of the density profile between shock and reaction front is necessary. This was done with a Mach-Zehnder interferometer for a cylindrical blast wave by Edwards et al. (1981). For the current analysis, the estimation of τ_r via Eq. 6.3 is sufficient as it is compared to τ_i, which changes by four orders of magnitude as a function of the angle β (Section 6.2). The region where $\tau_r \ll \tau_i$ is well defined irrespective of the errors in the approximation of τ_r.

To calculate τ_r, the post-shock velocity and the distance between the shock and OH-front have to be known for the same instant in time. The time passed since the detonation wave exited the tube is denoted as t_{TEP} and is given in the legend of all plots of experimental data in this chapter.

The shock velocities for an angle β, as described in Section 5.8.2, are average velocities defined in between measurements of the shock location. The time associated with each average velocity measurement is assumed to be the midpoint between

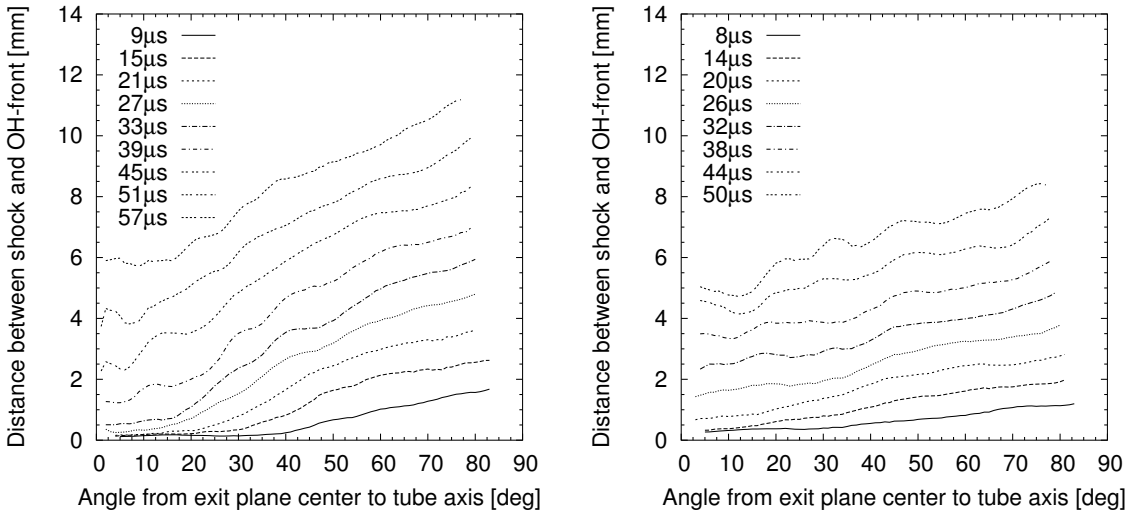

a) $2H_2$+O_2+7Ar, P_0 = 1 bar. b) H_2-N_2O P_0 = 0.4 bar.

Figure 6.6: Distance x_{OH} between shock and OH-front for several times t_{TEP} in the diffraction process measured from the time after the detonation has exited the tube. x_{OH} is interpolated to match the times of the velocity measurement.

the two times corresponding to the two shock outlines. In order to determine the distance x_{OH} between the shock and the OH-front for these intermediate times, the x_{OH}-profiles shown in Fig. 5.62 were linearly interpolated in time for each angle β (Fig. 5.60). Using the interpolated x_{OH}-profiles and the post-shock velocities corresponding to the momentary shock velocity, the residence time was calculated via Eq. 6.3 (Fig. 6.7). The increase of x_{OH} with β (Fig. 6.7) for the Ar-diluted mixture shows that, near the tube axis, the OH-front stays coupled to the shock front for a longer time than near the wall. This has also been observed when comparing the shape of the shock outlines (Section 5.8) and is a direct consequence of the low activation energy of the Ar-diluted mixtures.

The residence time profiles are qualitatively similar to the x_{OH}-profiles, as the post-shock velocity does not change by more than 30% over the range of lead shock velocities. At early times t_{TEP}, the values of τ_r are fairly constant close to the tube axis. This region corresponds to the plateau observed in the profiles of the shock velocity and x_{OH}. Note that the values for $\tau_r < 1$ μs are derived from values for x_{OH} which are close to the resolution of the distance measurements. Therefore, $\tau_r = 1$ μs represents an upper bound for the actual residence time of these values.

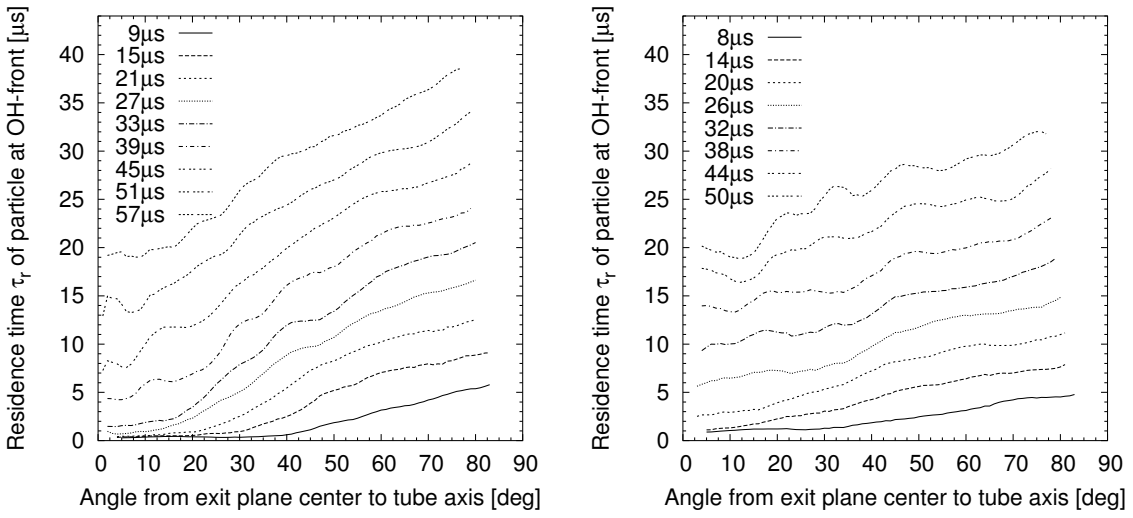

a) $2H_2$+O_2+7Ar, P_0 = 1 bar. b) H_2-N_2O P_0 = 0.4 bar.

Figure 6.7: Residence time τ_r of particle at the OH-front assuming steady post-shock velocity corresponding to the instantaneous lead shock velocity. The instantaneous shock velocity is the shock velocity determined at the specific point in time given in the legend.

For both mixtures studied, the residence times are increasing approximately linearly with the angle β for late times at which no plateau region is observed.

For fluid particles at the OH-front closest to the wall, τ_r is for all times approximately 0.6 t_{TEP} (Fig. 6.7). If the reaction front close to the wall decoupled completely from the shock immediately after exiting the tube and the OH-front did not progress relative to the surrounding fluid, then τ_r would be approximately t_{TEP}. The particle processed by the wall shock right at the tube exit has an extremely large induction time (Fig. 6.1a) and will not react.

One possibility is that the fluid particles at the OH-front do not react in an adiabatic explosion process, but the reaction front propagates as a flame behind the shock front. This would lead to a shorter distance between the shock and the OH-front and correspondingly smaller values of τ_r as the flame progresses into the shocked but unreacted fluid. To investigate this possibility, the OH-front velocity in the lab frame u_{OH} was determined in the same fashion as the shock velocity (Fig. 6.8a). The OH-front velocity profile is wrinkled and less smooth than the shock velocity profile and was averaged over an angle of β =3°. For early times and near the tube axis,

the OH-front velocity u_{OH} has a plateau with values close to the CJ-velocity. In this region the distance between the shock and the OH-front is small (Fig. 5.60a).

If u_{OH} is larger than the velocity u_P of a particle at the OH-front, particles pass through the OH-front. In this case, the OH-front is progressing relative to the surrounding fluid and is not just convected passively. From the Taylor-Sedov blast wave solution, the post-shock velocity u_{ps} is at all times an upper bound for the particle velocity u_P (Fig. 6.3b). It follows that if $u_{OH} > u_{ps}$, $u_{OH} > u_P$ is also true for all particles behind the front, specifically those at the OH-front. To compare both velocities, the velocity $u_{OH} - u_{ps}$ is shown for the Ar-diluted case in Fig. 6.8b. The velocity $u_{OH} - u_P$ is the relative velocity with which a particle passes through the OH-front, $u_{OH} - u_{ps}$ is a lower bound for this velocity. Whenever $u_{OH} - u_{ps} > 0$, particles pass through the OH-front implying that combustion is taking place at the front.

Near the tube axis at early times, the particles pass through the OH-front with a relative velocity of approximately 400 m/s (Fig. 6.8b). This is equal to w_{ps} for $u_{shk}/U_{CJ} = 1$ (Fig. 6.5a), as $u_{OH} \approx u_{shk}$ in this region. The oscillations in the obtained velocity profile of $u_{OH} - u_{ps}$ are caused by the wrinkled geometry of the OH-front. Despite the oscillations in the velocity profile, it is clear that close to the wall and times up to 40 μs, particles are passing through the OH-front with a velocity of at least 100 m/s. Note that the velocity plotted in Fig. 6.8b is a lower bound for the velocity with which a particle passes through the OH-front. For later times, the $u_{OH} - u_{ps}$ is smaller but slightly positive when averaged over β over a 10° interval. Only for these very late times in the diffraction process the chemical reaction is possibly entirely quenched. For earlier times, the OH-front progresses with a velocity of at least 100 m/s into the shocked but unreacted fluid.

6.2 Induction time

A particle passing through the diffracting shock wave experiences a temperature increase which corresponds to the shock strength at the instant the particle passes

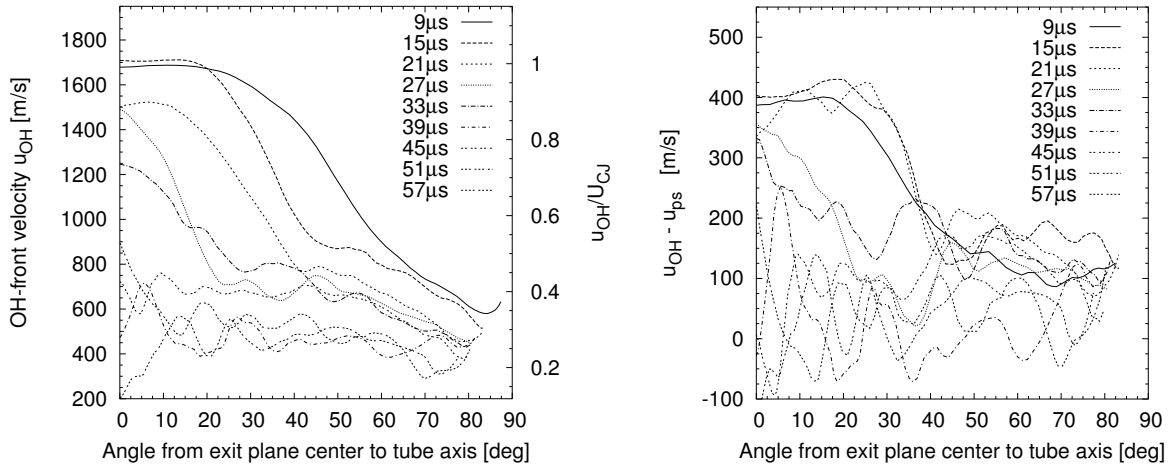

a) b)

Figure 6.8: a) Velocity of OH-front u_{OH} as a function of angle to the tube center axis for several time instances after the detonation exited the tube, $2H_2+O_2+7Ar$, $P_0 = 1$ bar. b) Comparison of u_{OH} and u_{ps}. The quantity $u_{OH} - u_{ps}$ is a lower bound for the relative velocity of a particle passing through the OH-front.

through the shock wave. After passing through the shock, the particle convects away from the shock wave. Although the shock wave decays further, in the frame of reference of the particle, the temperature remains approximately constant as shown in Fig. 6.9a. The plateau in temperature is also seen in two-dimensional numerical simulations of the diffraction process (Fig. 6.10). The temperature of the fluid particles is approximately constant until the chemical energy is released, causing a rapid increase in temperature.

Fluid particles which pass through the shock wave at a later point in time experience a lower temperature increase (particle B in Fig. 6.9a), since the shock is decaying. From an Eulerian viewpoint, the temperature increases with increasing distance from the shock wave. The particles shocked earlier have a longer residence time and are convected further from the shock (Fig. 6.9b). However, the temperature profile of a fluid particle (Lagrangian viewpoint) is what is relevant to determining the combustion time. Consider the unreacted fluid element just ahead of the OH-front. In order to estimate the induction time of this particle, the temperature history is needed. Assuming that the particle is at a constant temperature after passing through the shock until it reaches the OH-front, the induction time corresponds to the shock

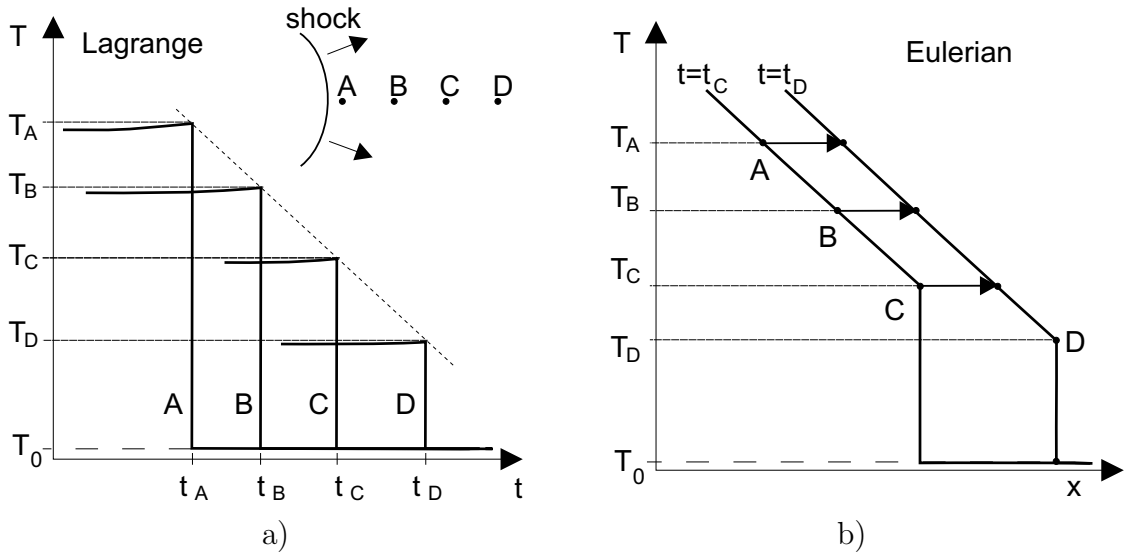

Figure 6.9: Sketch of temperature profiles for Lagrangian (a) and Eulerian (b) view for decaying shock wave. The four particles A-D are placed in line, whereas A is closest to the incoming shock wave, the sketch in (a).

strength at the particular time when the particle passed through the shock. Since the shock strength varies with time and over the shock surface, the initial location and the particle path must be known.

The time since a particle at the OH-front passed through the shock wave is equal to its residence time τ_r, as discussed in Section 6.1. We assume that the particle path is at all times perpendicular to the shock outline and is approximated as linear rays originating from the tube exit center. Each particle path corresponds to a specific value of β. In view of Fig. 5.60a, this seems to be a reasonable assumption. From the normalized shock velocity profiles (Fig. 5.61a and c), the time history of the velocity profile corresponding to each β was obtained as a spline fit. From the spline fits $U(t)$ for each β, the shock velocities for the time when the particle got shocked could be determined as $U(t_{TEP} - \tau_r)$ (Fig. 6.11). The velocity $U(t_{TEP} - \tau_r)$ is the shock velocity when the particle which is momentarily (at time t_{TEP}) at the OH-front has passed through the shock wave. The difference between $U(t_{TEP} - \tau_r)$ and $U(t_{TEP})$, the momentary shock velocity, is an increasing function of the local shock decay rate and the residence time.

The induction time τ_i (Fig. 6.12) for the particles at the OH-front is calculated

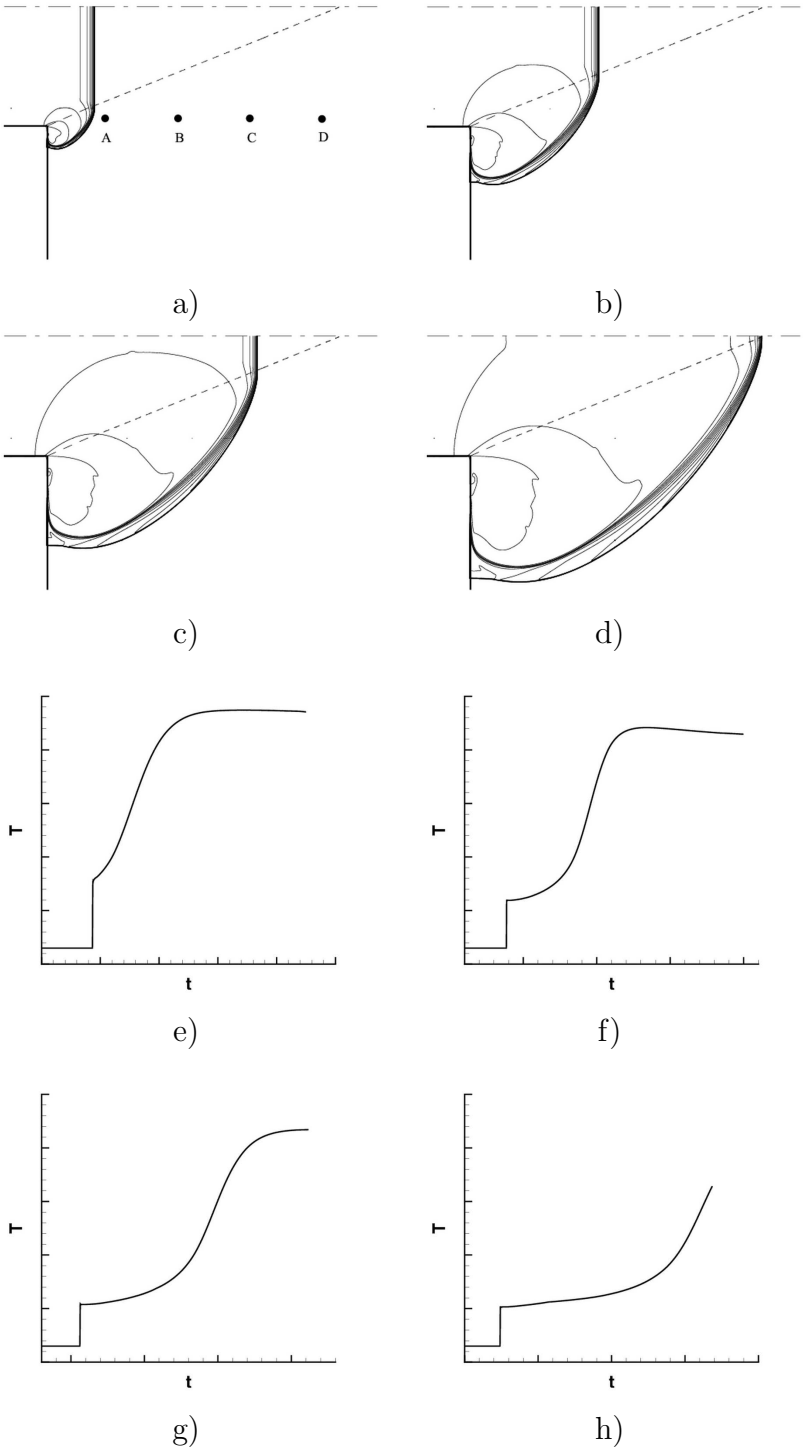

Figure 6.10: Simulation (Arienti, 2002) of detonation diffraction under sub-critical condition, showing density contours (a-d) at four times and the temperature profiles (e-h) of four particles, placed initially off axis as shown in (a). The temperature and time given in the plots are non-dimensionalized.

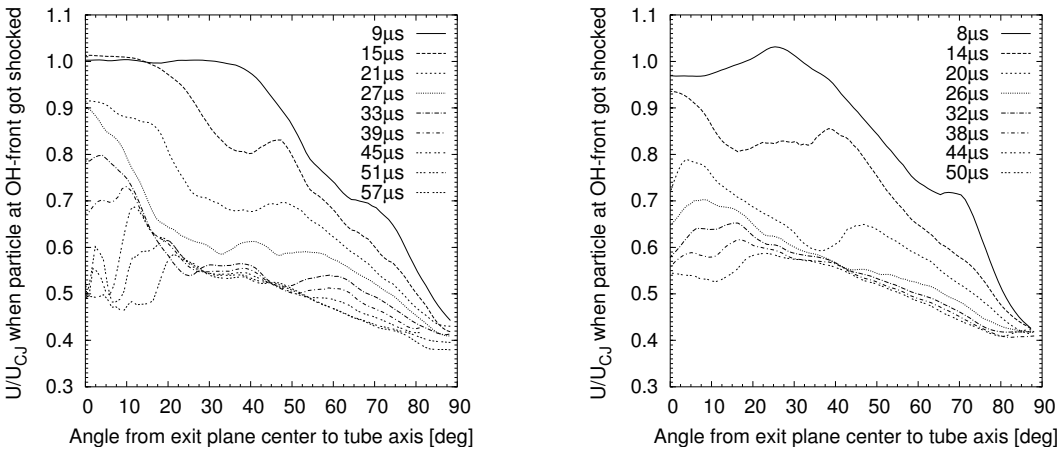

a) $2H_2$+O_2+7Ar, P_0=1 bar. b) H_2+N_2O, P_0=0.4 bar.

Figure 6.11: Shock velocity at the time when the particle currently at OH-front passed through the shock wave.

from the shock velocity profiles (Fig. 6.11) and the steady flow induction time as a function of shock velocity (Fig. 6.1a). The induction time τ_i increases for the Ar-diluted mixture by three orders of magnitude within 10° for a specific angle β, which depends on t_{TEP}. For the H_2-N_2O mixture, the increase is less rapid over the angle β. In order to estimate where particles along the OH-front react and where the reaction is quenched, we must compare τ_i to τ_r for particles at the OH-front. This is done in the next section.

6.3 Comparison of induction time and residence time

The calculated residence times and induction times are shown in Fig. 6.13. Physically, the residence time for an unreacted fluid element cannot be longer than the induction time. Within the resolution of the measurement, this is the case. The induction time is rapidly increasing with angle enabling an accurate determination of the points at which $\tau_i \gg \tau_r$, irrespective of the uncertainty in τ_r. The comparison of τ_i and τ_r indicates when complete reaction is occurring. This estimate neglects possible effects of mass diffusion and heat conduction.

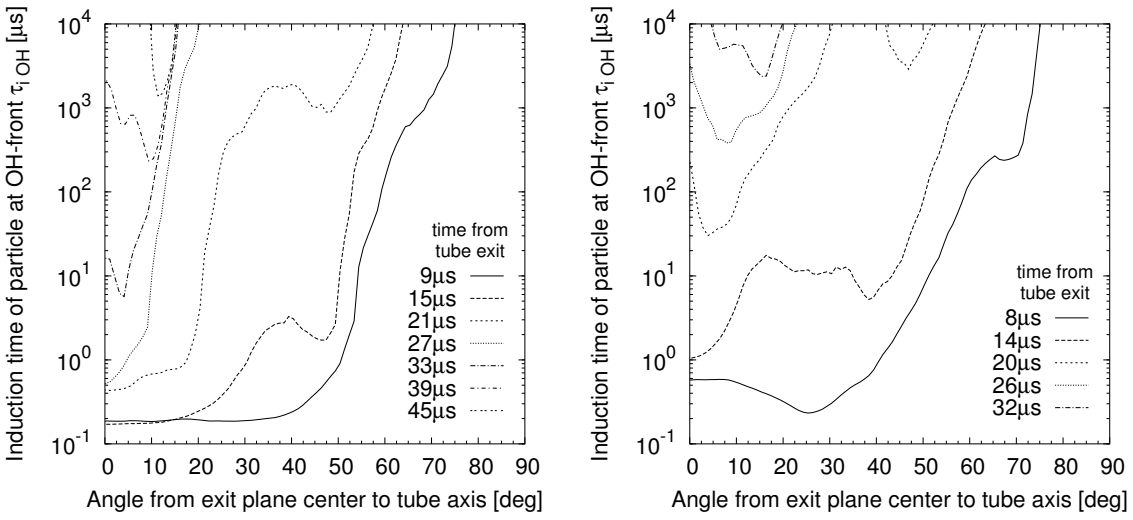

a) $2H_2$+O_2+7Ar, P_0=1 bar. b) H_2+N_2O, P_0=0.4 bar.

Figure 6.12: Induction time of particle at OH-front.

For the Ar-diluted case, the reaction appears to be quenched for angles larger than approximately 50° up to $t_{TEP}\sim$ 15μs. For t_{TEP}= 20μs, this angle decreased to 21°, and for t_{TEP}= 27μs, only particles at the OH-front close to the tube axis react completely. At t_{TEP}= 33μs, the reaction appears to be quenched over the entire shock outline. For the H_2-N_2O mixture, the reaction is quenched at t_{TEP}=8μs for β >45°. Shortly after t_{TEP}=14μs, the reaction appears quenched over the entire OH-front since τ_i is at least one order of magnitude larger than τ_r. These results agree well with the observations presented in Chapter 5. For the Ar-diluted mixture with low activation energy, the reaction is quenched at a later point in time than for the higher activation energy mixture. The activation energy at the CJ-point seems to be the controlling quantity.

Once the shock velocity has decreased significantly, the activation energy θ for the Ar-diluted mixture rapidly increases (Fig. 6.14a) as the slow three-body reactions become dominant in the consumption of H atoms over the fast chain branching reaction (Shepherd, 1986). For the H_2-N_2O mixture, the increase in θ is more modest with decreasing lead shock velocity (Fig. 6.14a). The activation energy θ for $0.7 < U/U_{CJ} < 0.82$ is actually larger for the Ar-diluted mixture than for the H_2-N_2O mixture. This indicates a fast decoupling process of shock and reaction front

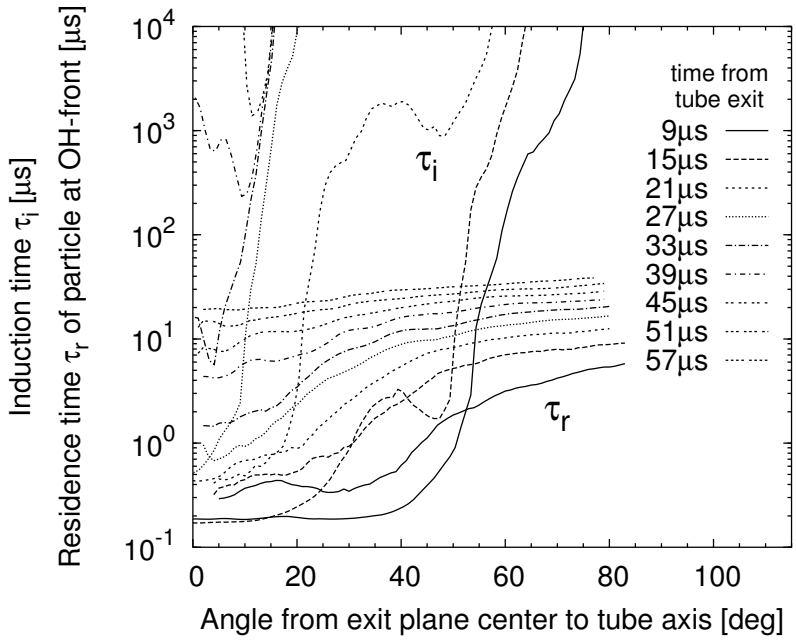

a) $2H_2+O_2+7Ar$, P_0=1 bar.

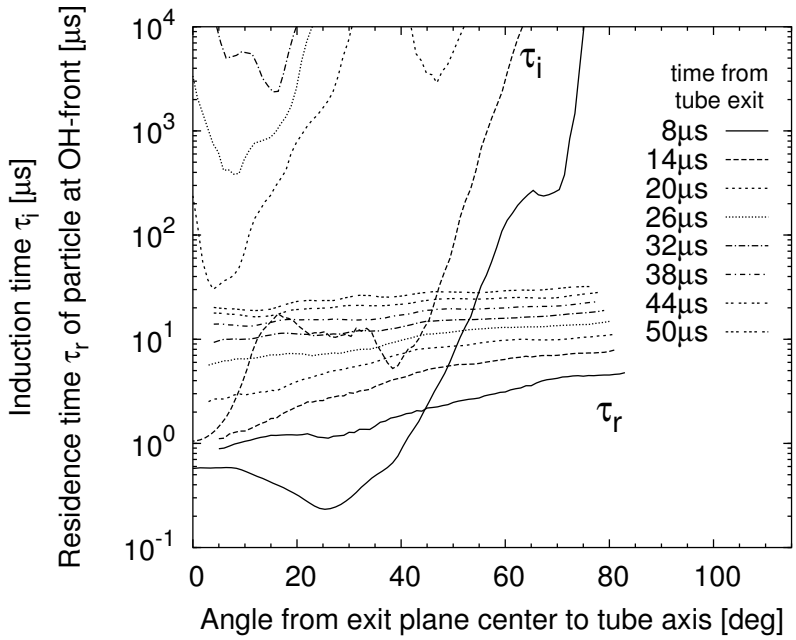

b) H_2+N_2O, P_0=0.4 bar.

Figure 6.13: Comparison of induction time and residence time of particle at OH-front.

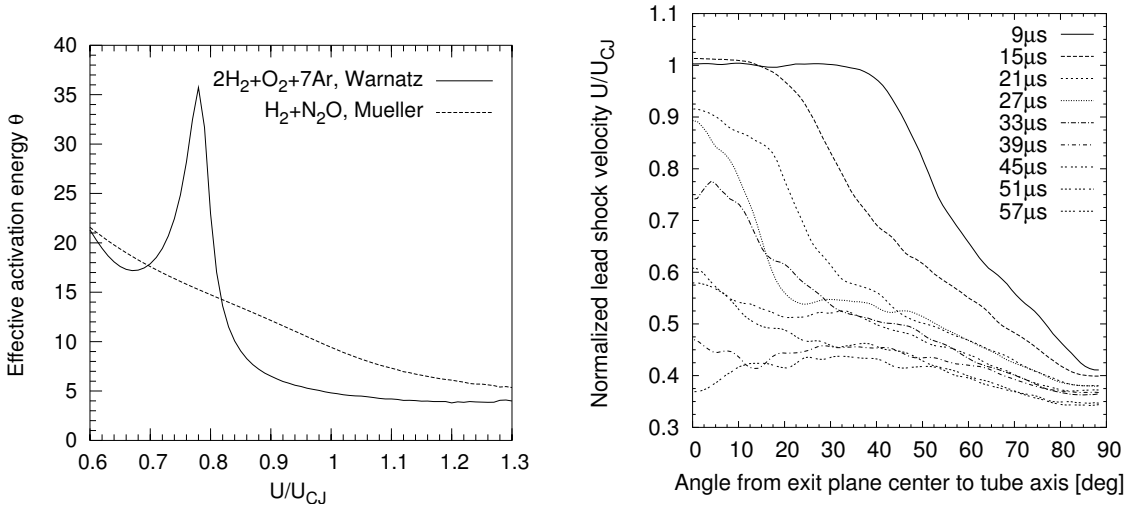

a) b)

Figure 6.14: a) Activation energy θ as function of normalized lead shock velocity. b) Shock velocity profile for $2H_2$+O_2+7Ar, P_0=1 bar.

for decaying waves in this velocity range. This agrees with the shock velocity profiles (Fig. 6.14b) which show the shock velocity decaying very quickly for the velocity range of $0.6 < U/U_{CJ} < 0.8$, most strikingly for t_{TEP}=21 μs and 27 μs. The decoupling process appears to be very localized, as the induction time increases faster once the wave velocity is below approximately $U/U_{CJ} \sim 0.8$. For the H_2-N_2O mixture, the velocity profile is approximately linear with β (Fig. 5.61c) for all times. In this case, the decoupling close to the tube axis happens earlier as the activation energy at CJ conditions is higher than for the Ar-diluted mixture at CJ conditions. The quenching process of the reaction is less localized in space, and the dividing line between the coupled and decoupled region is "fuzzier".

Chapter 7

Conclusions

The present study consists of two parts. In the first part, a planar laser induced fluorescence (PLIF) model for detonations is developed and compared to experimentally obtained fluorescence profiles of fully developed detonations. In the second part, detonation diffraction by an abrupt area change was studied, revealing the quantitative differences between mixtures of various activation energies.

PLIF of the OH radical has only recently been successfully applied to visualizing the OH distribution in detonations. Up to now, the results have only been qualitative due to the challenges in linking the OH radical concentration to the fluorescence signal. For the conclusive interpretation of the experimentally obtained PLIF images, two key questions were outstanding, both of which were answered by the model: Does the location of the fluorescence front seen on PLIF images coincide with the actual OH-concentration front? What is responsible for the strong decay in fluorescence intensity behind the detonation front? The one-dimensional PLIF model predicts the fluorescence intensity profile for a given distribution of thermodynamic conditions and background composition, which were computed with the one-dimensional ZND model. The predicted fluorescence profile was found to be in good agreement with the experimental results. The three-level model takes into account light sheet energy absorption (self-absorption by OH and broad band by H_2O and CO_2), broadening and shifting effects on the pumped absorption line, and collisional quenching.

The self-absorption of light sheet energy by OH was identified to be responsible for the strong decrease in fluorescence intensity behind the front. This implies that

the strong fall-off in fluorescence intensity further behind the front will persist for higher laser output intensities as long as the system operates in the linear fluorescence regime. The absorption effects can be reduced by choosing a weaker transition line for the excitation. This leads to a lower fluorescence signal but a more uniform proportionality constant between fluorescence signal and OH-concentration over the profile. For the current system, this was not achievable since a higher peak fluorescence signal is needed to overcome the noise arising from chemiluminescence.

Depending on the mixture, a shift of up to 0.1 mm between the OH-front and the fluorescence front is predicted by the model. This is caused by the strong increase of the collisional quenching during the sharp rise in OH-concentration. For the current work, the results are not affected by this as the scale of the observed structures is larger and the OH-front virtually coincides with the fluorescence front seen on the PLIF images. For future work, care has to be taken when interpreting fluorescence structures at smaller spatial scales since the imaging system performance also has to be considered. As shown in this study, the effective resolution is not only limited by the digital nature of the ICCD but also the modulation transfer function of the imaging system.

In the detonation diffraction experiment, two mixture types, highly diluted H_2-O_2-Ar and H_2-N_2O, were studied in the sub-critical, critical, and super-critical regimes. The mixtures have normalized effective activation energies at CJ conditions of $\theta = 4.5$ and 9.4 respectively, and represent extreme cases in classification of cellular regularity. Different modes have been identified and quantified. Most striking (Fig. 7.1) were the sub-critical and critical regime, for which the detonation wave fails to transition into the unconfined half-space. For the first time, the reaction front has been directly visualized for a diffracting detonation using PLIF of the OH radical, clearly showing the details of the reaction front.

In the sub-critical case, sawtooth-like geometries in the OH-front are observed where the shock wave decoupled from the reaction front. These are remnants of keystone-shaped features characteristic of the cellular structure of fully developed detonations, present before the detonation reaches the abrupt area change. In the sub-

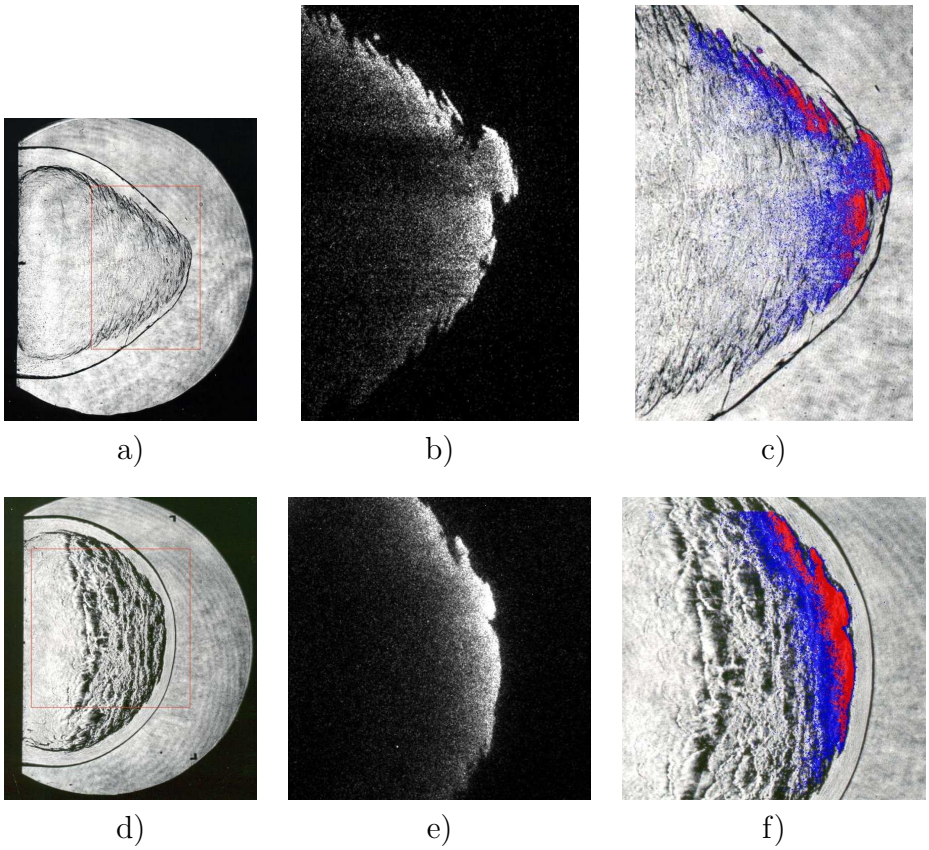

Figure 7.1: Observations for sub-critical experimental outcome in the critical regime. a),b), and c) 0.22 H_2 + 0.11 O_2 + 0.67 Ar, P_0=100 kPa, θ = 4.5, shot 202. d), e), and f) 0.5 H_2+ 0.5N_2O, P_0=40 kPa, θ = 9.4, shot 80. (a) and (d) are schlieren images (150 mm height), (b) and (d) are the simultaneously obtained corresponding OH PLIF images, (c) and (f) are false color overlays as indicated by boxed region in schlieren images.

critical case, these structures are passive and much larger in scale than in propagating detonations. In the critical case, the keystone-shaped structures are regenerated by localized explosions. In the super-critical case, the keystones persist and are active as the cellular structure evolves.

For the low-activation-energy mixture and sub-critical outcomes, the reaction front velocity on the center line decays slower than in the high-activation-energy case. In some sub-critical cases, the reaction front was attached to the lead shock up to 2.3 tube diameters from the tube end plate (Fig. 7.1c). The reaction front velocity was above 0.8 U_{CJ} up to approximately 1.5 tube diameters (d) from the end plate. For the H_2-

N_2O mixture, the reaction front velocity decreased to approximately 0.6 U_{CJ} after a distance of 1.1 d. The whole reaction front decoupled rapidly for the H_2-N_2O mixtures, leading shortly after the tube exit to a self-similar shock shape (Fig. 7.1d). The rapid decay of the reaction front velocity can be attributed to the higher activation energy of the H_2-N_2O mixture, which leads to large changes in the induction time for small changes in lead shock strength.

A simplified analysis comparing the residence time and the induction time of particles at the OH-front showed that the reaction in the sub-critical case is rapidly quenched with increasing distance from the tube axis. The decoupling is due to rapid increase of induction time relative to residence time as the wave decays. The sawtooth geometries of the OH-front are convected along with the post-shock flow field, but the energy release rate must be comparatively small at the OH-front in these regions. Measurements of the OH-front velocity and shock velocity in the sub-critical case indicate that fluid particles are slowly passing through the OH-front during most of the diffraction event. The reaction at the OH-front seems entirely quenched close to the wall only and for late times in the diffraction process ($t_{TEP}>$ 40μs for the H_2-O_2-Ar mixture).

The shock velocity for the Ar-diluted case decreases more rapidly than in the H_2-N_2O case once the lead shock velocity has reached a velocity below 0.8 U_{CJ}. A sudden decrease is observed for the sub-critical H_2-O_2-Ar case when the lead shock drops below 0.8 U_{CJ}. This can be explained by the rapid increase in the normalized activation energy with decreasing shock velocity for the Ar-diluted mixture. At $U_{shk} = 0.8U_{CJ}$, the normalized activation energy for the Ar-diluted mixture is 35, much higher than the value of $\theta = 16$ for the H_2-N_2O mixture. Clearly, it is important to consider the variation of activation energy with shock velocity and not just the value at CJ conditions.

To reveal the three-dimensional structure of the transverse detonations in the super-critical regime, a stereoscopic image of the high-luminosity region was constructed. This clearly showed the location of the transverse detonation just below the shock surface, which corresponds to the region of high chemiluminescence and high

energy release as the transverse detonation travels into the shocked but unreacted gas.

Skews' construction for the propagation of the corner signal into the front was found to be applicable only for the higher activation energy mixture in the sub-critical case. In these cases, the predicted distance at which the corner disturbance signals collide on the tube axis correlates well with the distance at which the reaction front velocity drops significantly. This is due to the fact that, for the higher activation energy the reaction front decouples very quickly outside the conical area which is not influenced by the corner signal. For the mixture with a lower activation energy, the coupling of reaction front and shock persists longer as changes in the shock velocity have a weaker influence on the induction time.

Future work

In the case of a re-ignition event, the transverse detonation was found in some cases to propagate both toward the wall and toward the tube axis. If the re-ignition "bubble" originated from the interaction point of the coupled and uncoupled region, the transverse detonation wave would always be found propagating toward the wall. The evolution leading to the re-ignition event was difficult to capture with the diagnostics used in this experiment as it occurs at varying locations. To understand the phenomena that lead to the re-ignition event, a high-speed, high-resolution image sequence would be helpful. Multiple gate chemiluminescence images indicated that the transverse detonation can fail in rare cases. Possible failure mechanisms are not clear at this point. From the practical viewpoint of safety and hazard analysis, it is important to examine the mechanisms of re-ignition and failure and the influence of confinement geometry and wave interactions.

Bibliography

R. Akbar. *Mach Reflection of Gaseous Detonations*. PhD thesis, California Institute of Technology, Pasadena, California, August 1997. 17, 20

M.G. Allen, K.R. McManus, D.M. Sonnenfroh, and P.H. Paul. Planar laser-induced-fluorescence imaging measurements of OH and hydrocarbon fuel fragments in high-pressure spray-flame combustion. *Applied Optics*, 27:6287–6300, 1995. 52

P. Andresen, A. Bath, W. Groger, H.W. Lulf, G. Meijer, and J.J. terMeulen. Laser-induced fluorescence with tunable excimer lasers as a possible method for instantaneous temperature field measurements at high pressures: checks with an atmospheric flame. *Applied Optics*, 27(2):365–378, 1988. 53

M. Arienti. *A numerical and analytical study of Detonation Diffraction*. PhD thesis, California Institute of Technology, 2002. xv, 12, 148, 182

J.M. Austin, F. Pintgen, and J.E. Shepherd. Reaction zones in highly unstable detonation. In *30th (Int.) Symposium on Combust.*, pages 2735–2742, Chicago, USA, 2004. The Combustion Institute. 12, 62

Joanna Austin. *The Role of Instability in Gaseous Detonation*. PhD thesis, California Institute of Technology, Pasadena, California, June 2003. 10, 15, 70, 73

P. Beaud, P.P. Radi, D. Franzke, H.M. Frey, B. Mischler, A.P. Tzannis, and T. Gerber. Picosecond investigation of the collisional deactivation of OH A^2-Σ^+(v'=1, n'=4,12) in an athmospheric flame. *Applied Optics*, 37:3354–3367, 1998. 49, 50, 66

W.G. Bessler, C. Schultz, V. Sick, and J.W. Daily. A versatile modeling tool for nitric oxide LIF spectra. In *Proceedings of the Third Joint Meeting of the U.S. Sections of The Combustion Institute*, Chicago, 2003. Paper PI05. 41, 52

H.J. Catrakis and P.E. Dimotakis. Mixing in turbulent jets: scalar measures and isosurface geometry. *Journal of Fluid Mechanics*, 317:369–406, 1996. 80, 85

D.L. Chapman. On the rate of explosions in gases. *Phil. Mag. 47*, 5th series, No. 284:90–104, 1899. 1

N.T. Clemens. Flow imaging. In J.P. Hornak, editor, *Encyclopedia of Imaging Science and Technology*, pages 390–420. John Wiley and Sons, New York, 2002. 73

D.R. Crosley. Rotational and translation effects in collisions of electronically excited diatomic hydrides. *Journal of Physical Chemistry*, 93:6273–6282, 1989. 49

G. Damköhler. Der einfluss der turbulenz auf die flammengeschwindigkeit in gasgemischen. *Zeitschrift für Elektrochemie*, 46(11):601–652, 1940. 85

P. Deasgroux, L. Gasnot, J.F. Pauwels, and L.R. Sochet. Correction of LIF temperature measurements for laser absorption and fluorescence trapping in a flame. *Applied Physics B*, 61:401–407, 1995. 67

Yu.N. Denisov and Ya.K. Troshin. Pulsating and spinning detonation of gaseous mixtures in tubes. *Dokl. Akad. Nauk.*, 125:110–113, 1959. 4

W. Döring. über den detonationsvorgang in gasen. *Analen der Physik*, Band 43: 421–436, 1943. 2

J.W. Eaton. Octave, 1998. GNU Octave is a high-level language, primarily intended for numerical computations. GNU General Public License (GPL) as published by the Free Software Foundation, http://www.octave.org. 54

C. Eckbreth. *Laser Diagnostics for Combustion Temperature and Species*. Gordon and Breach Publishers, 1996. ISBN 90-5699-532-4. 31, 34, 35, 53

C. Eckett. *Numerical and Analytical Studies of the Dynamics of Gaseous Detonations*. PhD thesis, California Institute of Technology, 2000. xi, 5, 12, 63, 64, 65

D.H. Edwards, G. Hooper, and G.O. Thomas. Two-dimensional nozzle-generated reactive blast wave. *Journal of Physics D: Applied Physics*, 14:833–840, 1981. 176

D.H. Edwards, G.O. Thomas, and M.A. Nettleton. The diffraction of a planar detonation wave at an abrupt area change. *Journal of Fluid Mechanics*, 95:79–96, 1979. 14

Grant F. Fowles. *Introduction to Modern Optics*. Holt, Rinehart and Winston Inc., 1968. 35

F. Gouldin. An application of fractals to modeling premixed turbulent flames. *Combustion and Flame*, 68:249–266, 1987. 85, 86

C.G. Harris and M. Stephens. A combined corner and edge detector. In *In Proc. of the 4th Alvey Vision Conference*, pages 147–151, Manchester, UK, 1988. 134

F. Hildenbrandt and C. Schulz. Measurements and simulation of in-cylinder UV-absorption in spark ignition and diesel engines. *Applied Physics B*, 73:173–180, 2001. 48

J.B. Jeffries, K. Kohse-Höinghaus, G.P. Smith, R.A. Copeland, and D.R. Crosley. Rotational-level-dependent quenching of OH A^2-Σ^+ at flame temperatures. *Chemical Physics Letters*, 152:160–166, 1988. 49

R.J. Jensen, R.D. Guettler, and J.L. Lyman. The ultraviolet absorption spectrum of hot carbon dioxide. *Chemical Physics Letters*, 4:356–360, 1997. 48

E. Jouguet. Sur la propagation des reactions chimiques dans les gaz. *J. Mathematique*, page 347, 1905. 1

M.J. Kaneshige. *Gaseous detonation initiation and stabilization by hypervelocity projectiles*. PhD thesis, California Institute of Technology, Pasadena, California, January 1999. 19

R.J. Kee, F.M. Rupley, and J.A. Miller. CHEMKIN-II: A FORTRAN chemical kinetics package for the analysis of gas-phase chemical kinetics. Technical Report SAND89-8009, Sandia National Laboratory, 1989. 72

W.J. Kessler, M.G. Allen, and S.J. Davis. Rotational level dependent collisional broadening and line shift of the $A^2\Sigma^+ - X^2\Pi$ (1,0) band of OH in hydrogen-air combustion gases. *J. Quantitative Spectroscopy and Radiative Transfer*, 49:107–117, 1993. 36, 37, 40, 41, 42

D.A.V. Kliner and R.L. Farrow. Measurement of ground-state OH rotational energy-transfer rates. *Journal of Chemical Physics*, 110(1):412–422, 1999. 66

R. Knystautas, J.H. Lee, and C.M. Guirao. The critical tube diameter for detonation failure in hydrocarbon-air mixtures. *Combustion and Flame*, 48(1):63–83, 1982. 14

M. Köllner, P. Monkhouse, and J. Wolfrum. Time-resolved LIF of OH($A^2\sigma^+, \nu' = 1$ and $\nu' = 0$) in atmospheric-pressure flames using picosecond excitation. *Chemical Physics Letters*, 168:355–360, 1990. 49

A.A. Konnov. Detailed reaction mechanisms for small hydrocarbons combustion. release 0.5, 2000. http://homepages.vub.ac.be/ akonnov/. 55, 208

K.K. Kuo. *Principles of Combustion*. Wiley & Sons, New York, 1986. 2

H.I. Lee and D. Scott Stewart. Calculation of linear detonation instability: One-dimensional instability of plane detonation. *Journal of Fluid Dynamics*, 216:103–132, 1990. 10, 12

J.H.S. Lee. Dynamic parameters of gaseous detonations. *Annual Review of Fluid Mechanics*, 16:311–336, 1984. 7

J.C. Libouton, A. Jacques, and P.J. Van Tiggelen. Cinétique, structure et entretien des ondes de détonation. *Actes du Colloque International Berthelot-Vieille-Mallard-Le Chatelier*, 2:437–442, 1981. Bordeaux. 73

H.M. Lin, M. Seaver, K.Y. Tang, A.E.W. Knight, and C.S. Parmenter. The role of intermolecular potential well depths in collision-induced state changes. *Journal of Chemical Physics*, 70:5442–5457, 1979. 207

J. Luque and D.R. Crosley. LIFBASE: Database and spectral simulation program (version 1.5). Technical Report MP-99-009, SRI International, 1999. 44

V.V. Mitrofanov and R.I. Soloukhin. The diffraction of multifront detonation waves. *Soviet Physics-Doklady*, 9(12):1055–1058, 1965. 14

P. Monkhouse and S. Selle. Energy transfer in the A^2-Σ^+ state of OH following v'=1 excitation in a low pressure CH_4/O_2-flame. *Applied Physics B*, 66:645–651, 1998. 51

M.A. Mueller, R.A. Yetter, and F.L. Dryer. Kinetic modeling of the $CO/H_2O/O_2/NO/SO_2$ system: Implications for high-pressure fall-off in the SO_2+O(+M)=SO_3(+M) reaction. *Int. J. Chem. Kinetics*, 32(6):317–339, 2000. 72

S.B. Murray and J.H. Lee. On the transformation of planar detonation to cylindrical detonation. *Combustion and Flame*, 52:269–189, 1983. 94

K. Nishino, N. Kasagi, and M. Hirata. Three-dimensional particle tracking velocimetry based on automated digital image processing. *Journal of Fluids Engineering, Transactions of the ASME*, 111:384–391, 1989. 131, 134

P.C. Palma, T.J. McIntyre, and A.F.P. Houwing. PLIF thermometry in shock tunnel flows using a raman-shifted tunable excimer laser. *Shock Waves*, 8:275–284, 1998. 34

E.G. Pantow, M. Fischer, and T. Kratzel. Decoupling and recoupling of detonation waves associated with sudden diffraction. *Shock Waves*, 6:119–129, 1996. 14

W.P. Partridge and N.M. Laurendeau. Formulation of a dimensionless overlap fraction to account for spectrally distributed interactions in fluorescence studies. *Applied Optics*, 34(15):2645–2647, 1995. 34

P.H. Paul. A model for temperature-dependent collisional quenching of OH A^2-Σ^+. *Journal of Quantitative Spectroscopy and Radiative Transfer*, 51(3):511–524, 1994. xxxvi, 51, 205, 206

P.H. Paul. Vibrational energy transfer and quenching of OH A^2-Σ^+(v'=1) measured at high temperatures in a shock tube. *Journal of Physical Chemistry*, 99:8472–8476, 1995. 205

S.S. Penner. *Quantitative Molecular Spectroscopy and Gas Emissivities*. Addison-Wesley Publishing Company, Inc, Reading, Massachusetts, USA, 1959. 46

F. Pintgen. *Laser-Optical Visualization of Detonation Structures*. Diplomarbeit, Lehrstuhl für Thermodynamik: Technische Universität München / Graduate Aeronautical Laboratories: California Institute of Technology, Munich, Germany, December 2000. 9, 20, 24, 27, 44, 62, 70

F. Pintgen, J.M. Austin, and J.E. Shepherd. Detonation front structure: Variety and characterization. In G.D. Roy, S.M. Frolov, R.J. Santoro, and S.A. Tsyganov, editors, *Confined Detonations and Pulse Detonation Engines*, pages 105–116. Torus Press, Moscow, 2003a. 6, 11, 70, 73

F. Pintgen, C.A. Eckett, J.M. Austin, and J.E. Shepherd. Direct observations of reaction zone structure in propagating detonations. *Combustion and Flame*, 133(3): 211–229, 2003b. 6, 70, 79

F. Pintgen and J.E. Shepherd. Simultaneous soot foil and PLIF imaging of propagating detonations. In *19th International Colloquium on the Dynamics of Explosions and Reactive Systems*, Hakone, Japan, 2003. ICDERS. 7

F. Pintgen and J.E. Shepherd. Detonation sensitivity of partially-oxidized aviation kerosene. Explosion Dynamics Laboratory Report FM2003.007, California Institute of Technology, February 2004. 11

E.C. Rea, A.Y. Chang, and R.K. Hanson. Shock-tube study of pressure broadening of the A^2-Σ^+ X2-Π (0,0) band of OH by Ar and N2. *Journal of Quantitative Spectroscopy and Radiative Transfer*, 37(2):117–127, 1987. 36, 37, 42

E.C. Rea, A.Y. Chang, and R.K. Hanson. Collisional broadening of the A^2-Σ^+ X2-Π (0,0) band of OH by H_2O and CO2 in atmospheric pressure flames. *Journal of Quantitative Spectroscopy and Radiative Transfer*, 41(1):29–42, 1989. 36, 37

W.C. Reynolds. The element potential method for chemical equilibrium analysis: Implementation in the interactive program STANJAN, version 3. Technical report, Dept. of Mechanical Engineering, Stanford, CA, 1986. 2, 41, 91

L.S. Rothman, A. Barbe, D.C. Benner, L.R. Brown, C. Camy-Peyret, M.R. Carleer, K. Chance, C. Clerbaux, V. Dana, V.M. Devi, A. Fayt, J.-M. Flaud, R.R. Gamache, A. Goldman, D. Jacquemart, K.W. Jucks, W.J. Lafferty, J.-Y. Mandin, S.T. Massie, V. Nemtchinov, D.A. Newnham, A. Perrin, C.P. Rinsland, J. Schroeder, K.M. Smith, M.A.H. Smith, K. Tang, R.A. Toth, J. Vander Auwera, P. Varanasi, and K. Yoshino. The HITRAN molecular spectroscopic database: Edition of 2000 including updates of 2001. *Journal of Quantitative Spectroscopy & Radiative Transfer*, 82:5–44, 2003. 47, 48, 54

H. Schardin. Das toeplersche schlierenverfahren. *VDI-Forschungsheft*, 367, 1934. 109

E. Schultz. *Detonation Diffraction Through an Abrupt Area Expansion*. PhD thesis, California Institute of Technology, 2000. 14, 18, 98

C. Schulz, J.B. Jeffries, J.D. Koch, D.F. Davidson, J. Wolfrum, and R.K. Hanson. Impact of UV absorption by CO_2 and H_2O on NO LIF in high pressure combustion.

In *29th (Int.) Symposium on Combust.*, pages 2735–2742, Sapporo, Japan, 2002a. The Combustion Institute. xxxvi, 48, 203, 204

C. Schulz, J.D. Koch, D.F. Davidson, J.B. Jeffries, and R.K. Hanson. Ultraviolet absorption spectra of shock-heated carbon dioxide and water between 900 and 3050 k. *Chemical Physics Letter*, 355:82–88, 2002b. 48

K.I. Shchelkin and Y.K. Troshin. *Gasdynamics of Detonations*. Mono Book Corp., Baltimore, 1965. 4

J.E. Shepherd. Chemical kinetics of hydrogen-air-diluent detonations. In J.R. Bowen and J.C. Leyer, editors, *Dynamics of Explosion*, volume 106 of *Prog. in Astronautics and Aeronautics*, pages 263–293. AIAA, 1986. 2, 11, 54, 63, 72, 171, 184

J.E. Shepherd, I.O. Moen, S.B. Murray, and P.A. Thibault. Analysis of the cellular structure of detonations. In *21st (Int.) Symposium on Combust.*, pages 1649–1658. The Combustion Institute, 1986. 14

B. Shirinzadeh, D.M. Bakalyar, and C.C. Wang. Measurement of collision-induced shift and broadening of the ultraviolet transitions of OH. *Journal of Chemical Physics*, 82(1):2877–2890, 1985. 36, 37, 42

M. Short and J.J. Quirk. On the nonlinear stability and detonability limit of a detonation wave for a model three-step chain-branching reaction. *J. Fluid Mech.*, 339:89–119, 1997. 10, 12

S. Singh, D. Lieberman, and J.E. Shepherd. Combustion behind shock waves. Paper 03F-29 Western States Section/Combustion Institute, October 2003. 70, 86

B.W. Skews. The shape of a diffracting shock wave. *Journal of Fluid Mechanics*, 29:297–304, 1967. 97

G.J. Smallwood, Ö.L. Glder, D.R. Snelling, B.M. Deschamps, and I. Gökalp. Characterization of flame front surfaces in turbulent premixed methane/air combustion. *Combustion and Flame*, 101:461–470, 1995. 86

G.P. Smith, D.M. Golden, M. Frenklach, N.W. Moriarty, B. Eiteneer, M. Goldenberg, C.T. Bowman, R.K. Hanson, S. Song, V.V. Lissianski W.C. Gardiner, and Z. Qin. GRI-Mech 3.0. http://www.me.berkeley.edu/gri_mech, 2004. 208

M.D. Smooke, Y. Xu, R.M. Zurn, P. Lin, J.H. Frank, and M.B. Long. Computational and experimental study of OH and CH radicals in axisymmetric laminar diffusion flames. *24th Symposium (International) on Combustion*, pages 813–821, 1992. 40

G.B. Steel and A.K. Oppenheim. Experimental study of the wave structure of marginal detonation in a rectangular tube. Technical Report AS66-4, University of California Berkley, 1966. 60

D. Stepowski and M.J. Cottereau. Time resolved study of rotational energy transfer in A^2-Σ^+(v'=0) state of OH in a flame by laser induced fluorescence. *The Journal of Chemical Physics*, 74:6674–6679, 1981. 49

R.A. Strehlow. Gas phase detonations: Recent developments. *Combustion and Flame*, 12:81–101, 1968. 10, 13, 70

M. Tamura, P.A. Berg, J.E. Harrington, J. Luque, J.B. Jeffries, G.P. Smith, and D.R. Crosley. Collisional quenching for CH(A), OH(A) and NO(A) in low pressure hydrocarbon flames. *Combustion and Flame*, 114:502–514, 1998. xxxvi, 51, 205, 207

G.O. Thomas, D.H. Edwards, J.H. Lee, R. Knystautas, I.O. Moen, and Y.M. Wei. Detonation diffraction by divergent channels. volume 106 of *Prog. in Astronautics and Aeronautics*, pages 144–154. 1986. 94

A.A. Vasil'ev. Characteristic regimes of multifront-detonation propagation along a convex surface. *Combustion, Explosion, and Shock Waves*, 35(5):543–548, 1999. 14

B.V. Voitsekhovskii, V.V. Mitrofanov, and M.E. Topchian. The structure of a detonation front in gases. Technical Report TD-MT-64-527 (AD 633821), Wright-Patterson AFB, 1966. 4

J. von Neumann. Progress report on theory of detonation waves. Technical report, Office of Scientific Research and Development, OSDR Rep. No. 549, Proj. Rep. No. 238, 1942. 2

D.R. White. Turbulent structure of gaseous detonations. *The Physics of Fluids*, 4/4:465–480, 1961. 3

Y.B. Zel'dovich. On the theory of the propagation of detonation in gaseous systems. NACA TM, No. 1261, ursprgl. JETP10 (1940), 1950. 2

G. Zizak, G.A. Petrucci, C.L. Stevenson, and J.D. Winefordner. Ground state saturated population distribution of OH in an acetylene-air flame measured by two optical double resonance pump-probe approaches. *Applied Optics*, 30(36):5270–5275, 1991. 66

Appendix A

Model for UV Absorption by CO_2 and H_2O

The calculation of light sheet attenuation by CO_2 and H_2O is based on the absorption cross sections from the analytical expressions given in Schulz et al. (2002a). The analytical expression given below results in an optimum fit error of less than 10% to the absorption data measured in shock-heated CO_2 and H_2O at temperatures ranging from 900 to 3050 K, Schulz et al. (2002a).

The absorption cross section, $\sigma(\lambda, T)$, is given is units of 10^{-19} cm^2, the temperature, T, in 1000 K, and the wavelength, λ, in 100 nm

$$\ln \sigma(\lambda, T) = a + b\lambda, \tag{A.1}$$

$$a = c_1 + c_2 T + c3/T, \tag{A.2}$$

$$b = d_1 + d_2 T + d_3/T. \tag{A.3}$$

The parameters for the wavelength region 200 - 320 nm are given in the Table A. Parameters for lower wavelength regions can be found in Schulz et al. (2002a).

	CO_2	H_2O
c_1	17.2456	40.5890
c_2	-3.1813	-7.1598
c_3	0.8836	-4.4701
d_1	-7.0094	-20.4788
d_2	1.6142	4.0009
d_3	-3.1777	0.4555

Table A.1: Parameters for analytical expression of absorption cross section function, Schulz et al. (2002a)

Appendix B

Quenching Models for the OH Radical

Two temperature dependent models and empirical expression from the literature are used to evaluate the quenching coefficients of the OH radical; the "harpooned model" by Paul (1994) and the empirical model by Tamura et al. (1998). Both supply an analytical expression to evaluate the quenching cross section of OH $A^2\text{-}\Sigma^+$ (v'=0) for a variety of collision partners. Experimental measurements of the quenching cross section of OH $A^2\text{-}\Sigma^+$ (v'=0) and (v'=1) (Paul, 1995) showed that the quenching cross section for both vibrational levels is for most colliders within 20%, which makes it a reasonable estimation to use the quenching cross section for the v'=1 case. Note that the quenching cross sections measured vary up to 15% for the same vibrational level depending on the researcher measuring it and the measuring technique (Paul, 1995), Tamura et al. (1998).

B.1 Harpooned model

Based on the harpooned model Paul (1994) suggests the following analytical expression for the absorption cross section OH $A^2\text{-}\Sigma^+$ (v'=0):

$$\sigma(T) = P_A C_0 \left\{ \left((1+h_c)\exp(-h_c) \right) + \left(C_1 ({h_c}^{2/\alpha}) \gamma(2-2/\alpha, h_c) \right) \right\}, \quad \text{(B.1)}$$

$$h_c = C_2\, 300/T, \quad \text{(B.2)}$$

where the temperature T is in units of K, P_a, C_0 in units of $\mathring{A}^2$, C_1, C_2 and α are curve fit constants given in Table B.1 and γ is the lower incomplete gamma function defined as

$$\gamma(a,x) = \int_0^x t^{a-1} e^t dt. \quad \text{(B.3)}$$

colliding species	P_A	C_0	C_1	C_2	α
KR	0.238	14.641	1.501	5.572	6.00
XE	0.698	18.686	1.515	4.013	6.00
H	1.038	13.743	1.347	1.399	4.00
O	1	13.959	1.451	2.064	5.20
CO	0.846	14.536	1.664	6.206	4.60
H2	0.330	12.848	1.350	3.079	3.50
O2	0.537	14.892	1.327	3.866	3.95
NO	1.003	27.157	1.800	1.269	3.90
CO2	0.770	15.418	1.391	8.205	3.22
H2O	1.120	15.955	2.251	4.302	3.12
N2O	1.026	16.490	1.677	6.815	4.60
NH3	1.285	30.244	2.632	1.320	3.90
CH4	0.826	16.561	1.109	3.591	3.050
C2H2	1.620	20.267	1.656	3.866	4.510
C2H4	1.809	23.769	0.833	2.706	2.205
C2H6	1.560	17.210	1.083	6.070	3.105
C3H6	1.850	32.362	1.716	1.291	4.405

Table B.1: Parameters for analytical expression of collisional cross section of OH $A^2\text{-}\Sigma^+$ for harpooned model, Paul (1994).

B.2 Empirical expression for quenching cross section by Tamura

Tamura et al. (1998) gives the following two-parameter expression for the collisional quenching cross section σ:

$$\sigma(T) = \sigma_\infty \ \exp(\epsilon/kT), \tag{B.4}$$

where the units of temperature T are in K and the fitting parameter ϵ/k for each colliding species is given in Table B.2. Lin et al. (1979) developed this functional form based on two theoretical concepts correlating the rate constants and cross sections for a number of colliding gases. For the LIF model suggested here, only the quenching rates for the colliders N_2 and OH itself are evaluated with Eq. B.4 and all other with Eq. B.2.

colliding species	σ_∞ [$\mathring{A}^2$]	ϵ/k [K]
N_2	0.4	624
O_2	8	243
H_2O	20	434
H_2	4,5	224
CO_2	11	488
CO	12	397
CH_4	11	320
H	14.5	84
OH	20	384

Table B.2: Parameters for analytical expression given in Eq. B.4 of collisional cross section of OH A^2-Σ^+ from Tamura et al. (1998).

Appendix C

Example Evaluations of PLIF Model for a Variety of Mixtures

In this Chapter the plots of predicted fluorescence profiles and quenching rates are given for a variety of mixtures. They are based on the PLIF model and one dimensional ZND-model as discussed in detail in Chapter 3. The initial temperature and pressure for all mixtures presented is 300 K and 20 kPa respectively. All plots correspond to a detonation wave at CJ conditions. The predicted fluorescence is plotted in arbitrary units, normalized to the peak OH number density. For the mixtures considered, the Konnov (Konnov, 2000) and GRI (Smith et al., 2004) mechanisms gave similar results.

C.1 $2H_2$-O_2-12Ar

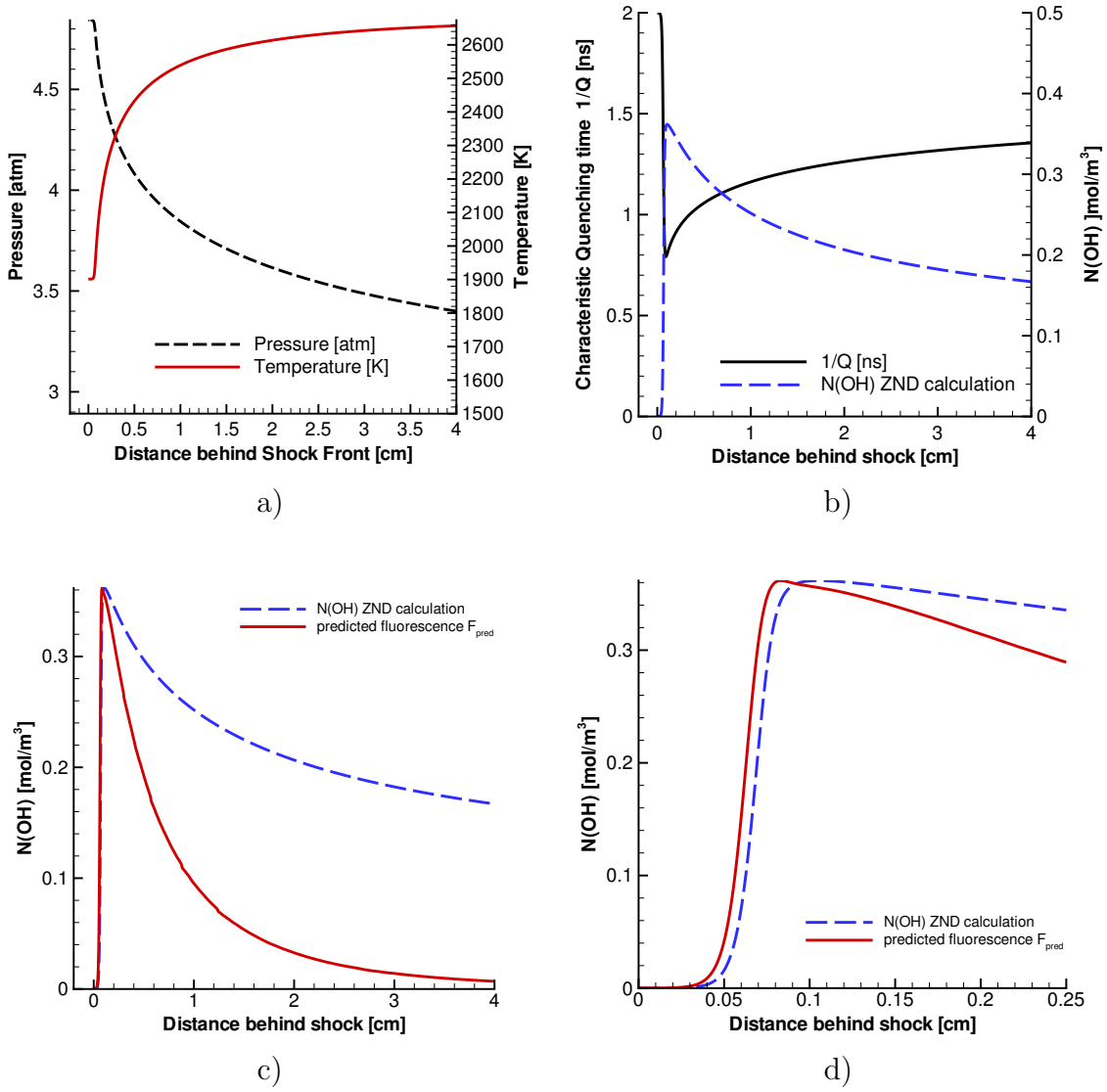

Figure C.1: a) Thermodynamic conditions b) Characteristic quenching time and OH mole fraction. c) OH number density and predicted fluorescence profile. d) Close up of the OH number density and predicted fluorescence profile at the end of the induction zone. $2H_2$-O_2-12Ar, T_0=300 K, p_0=20 kPa, Konnov mechanism

C.2 $2H_2$-O_2-17Ar

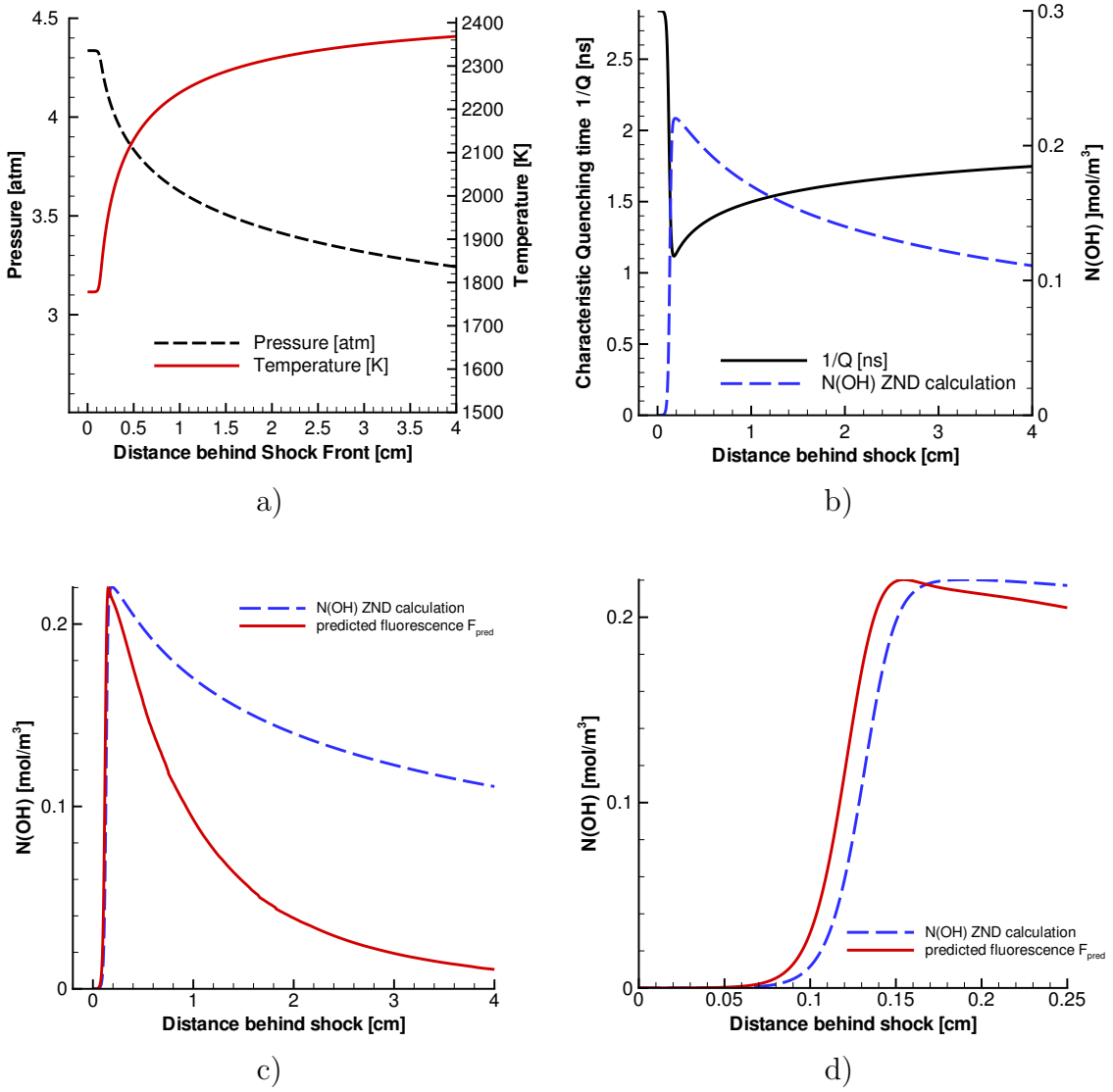

Figure C.2: a) Thermodynamic conditions b) Characteristic quenching time and OH mole fraction. c) OH number density and predicted fluorescence profile. d) Close up of the OH number density and predicted fluorescence profile at the end of the induction zone. $2H_2$-O_2-17Ar, T_0=300 K, p_0=20 kPa, Konnov mechanism

C.3 $2H_2$-O_2-$5.5N_2$

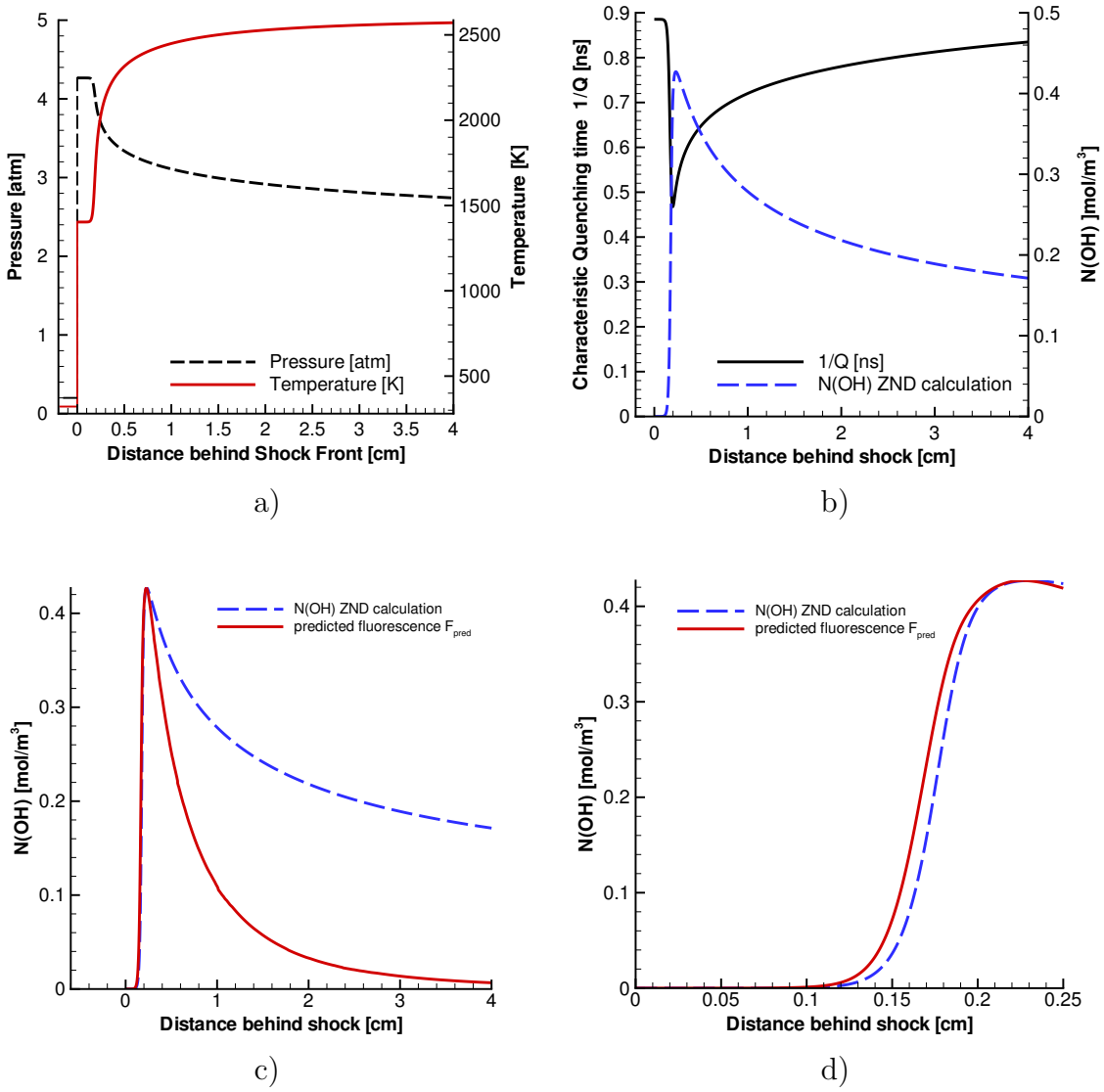

Figure C.3: a) Thermodynamic conditions b) Characteristic quenching time and OH mole fraction. c) OH number density and predicted fluorescence profile. d) Close up of the OH number density and predicted fluorescence profile at the end of the induction zone. $2H_2$-O_2-$5.5N_2$, T_0=300 K, p_0=20 kPa, Konnov mechanism

C.4 CH_4-$2O_2$

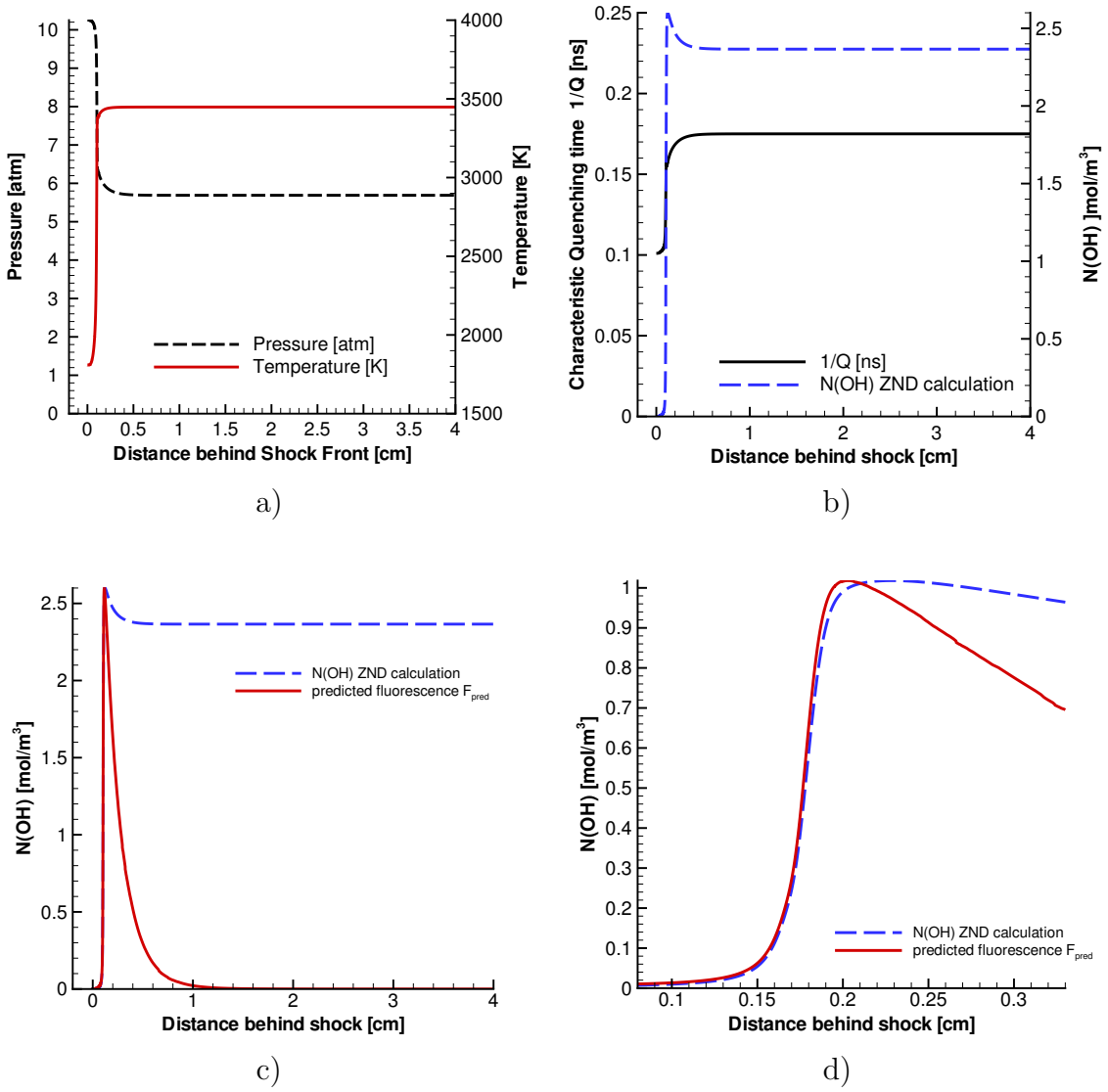

Figure C.4: a) Thermodynamic conditions b) Characteristic quenching time and OH mole fraction. c) OH number density and predicted fluorescence profile. d) Close up of the OH number density and predicted fluorescence profile at the end of the induction zone. CH_4-$2O_2$, T_0=300 K, p_0=20 kPa, Konnov mechanism

C.5 CH_4-$2O_2$-$3N_2$

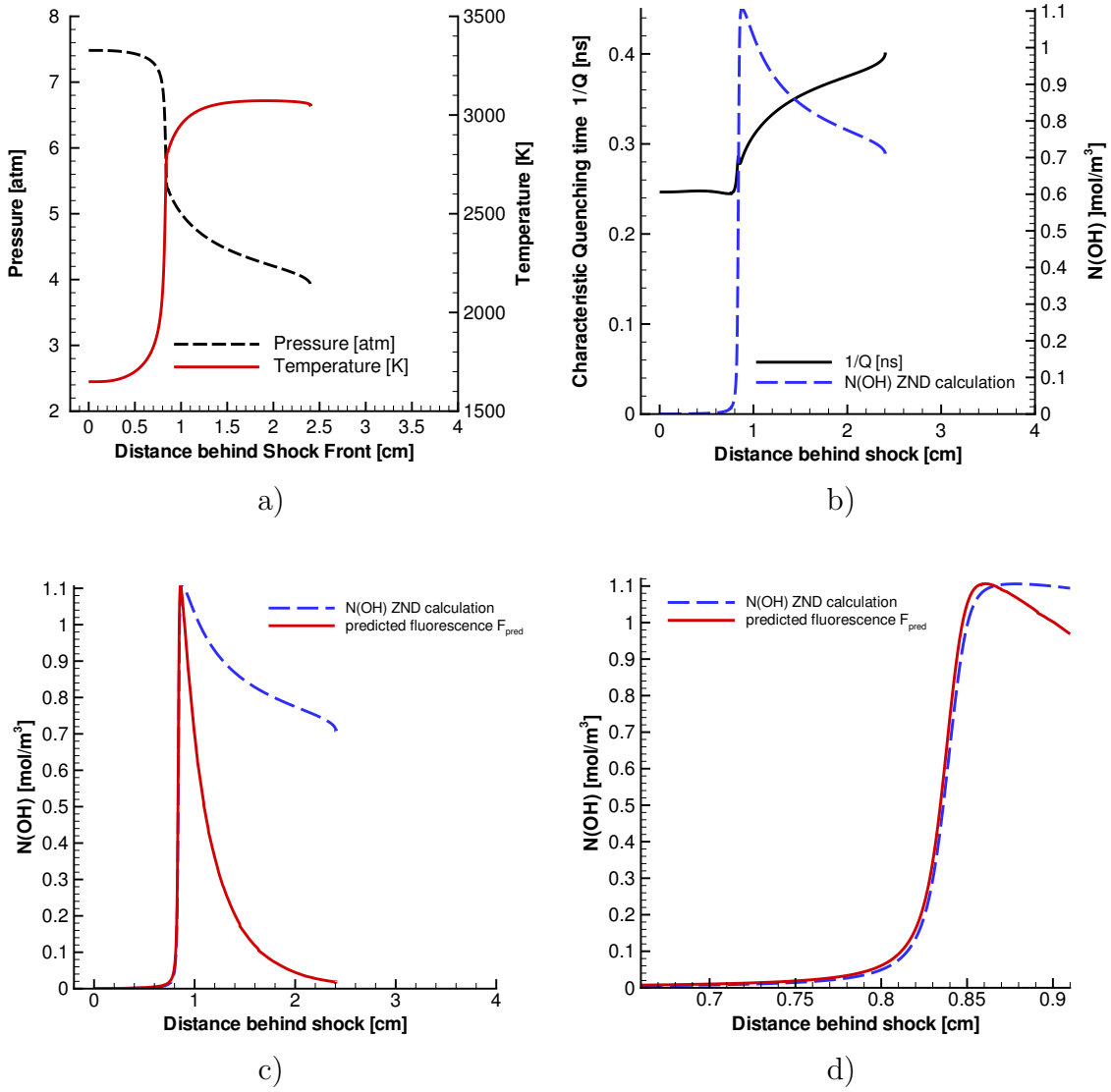

Figure C.5: a) Thermodynamic conditions b) Characteristic quenching time and OH mole fraction. c) OH number density and predicted fluorescence profile. d) Close up of the OH number density and predicted fluorescence profile at the end of the induction zone. CH_4-$2O_2$-$3N_2$, T_0=300 K, p_0=20 kPa, Konnov mechanism

C.6 C_2H_4-3O_2-8N_2

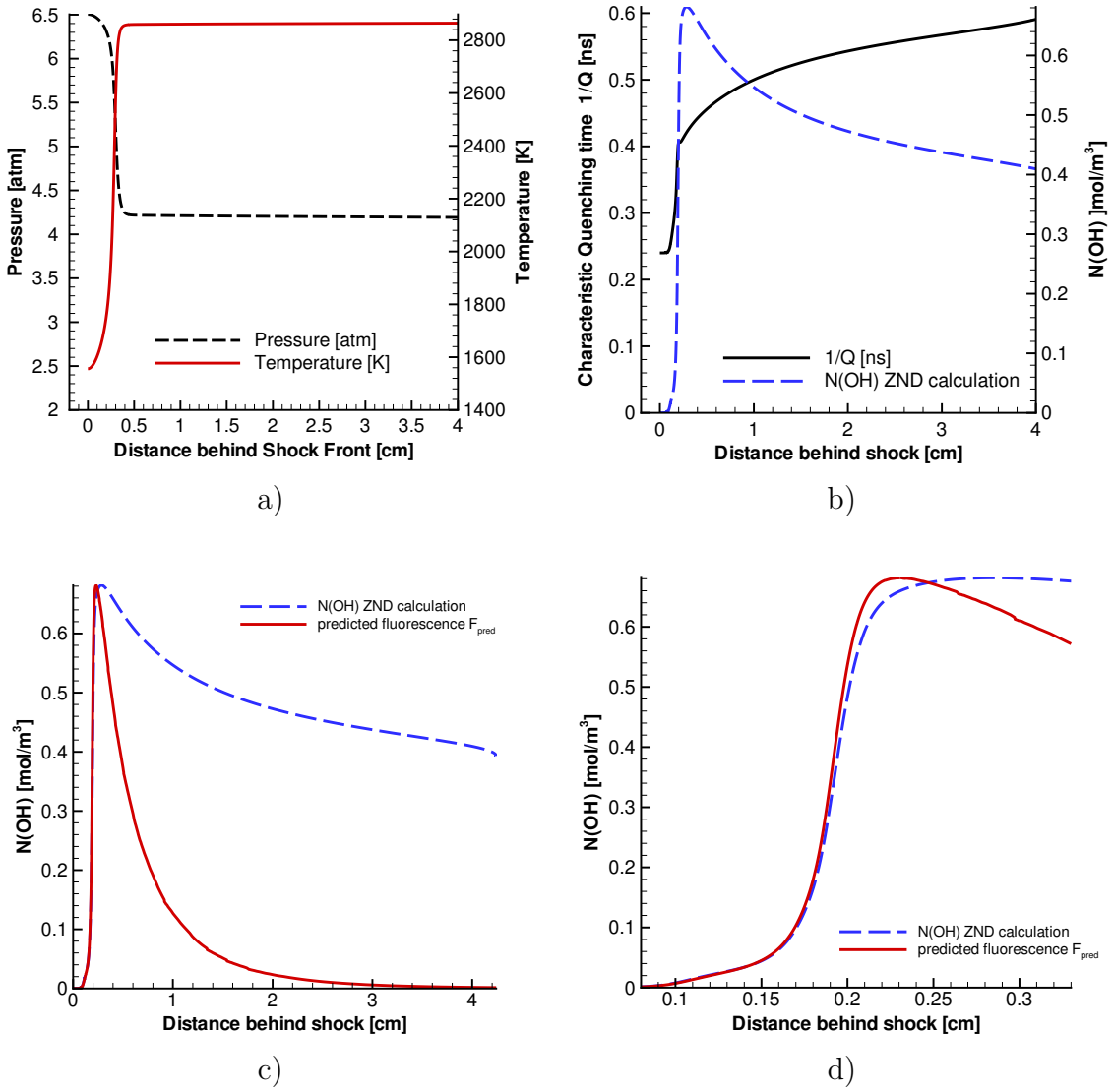

Figure C.6: a) Thermodynamic conditions b) Characteristic quenching time and OH mole fraction. c) OH number density and predicted fluorescence profile. d) Close up of the OH number density and predicted fluorescence profile at the end of the induction zone. C_2H_4-3O_2-8N_2, T_0=300 K, p_0=20 kPa, Konnov mechanism

C.7 C_3H_8-$5O_2$-$9N_2$

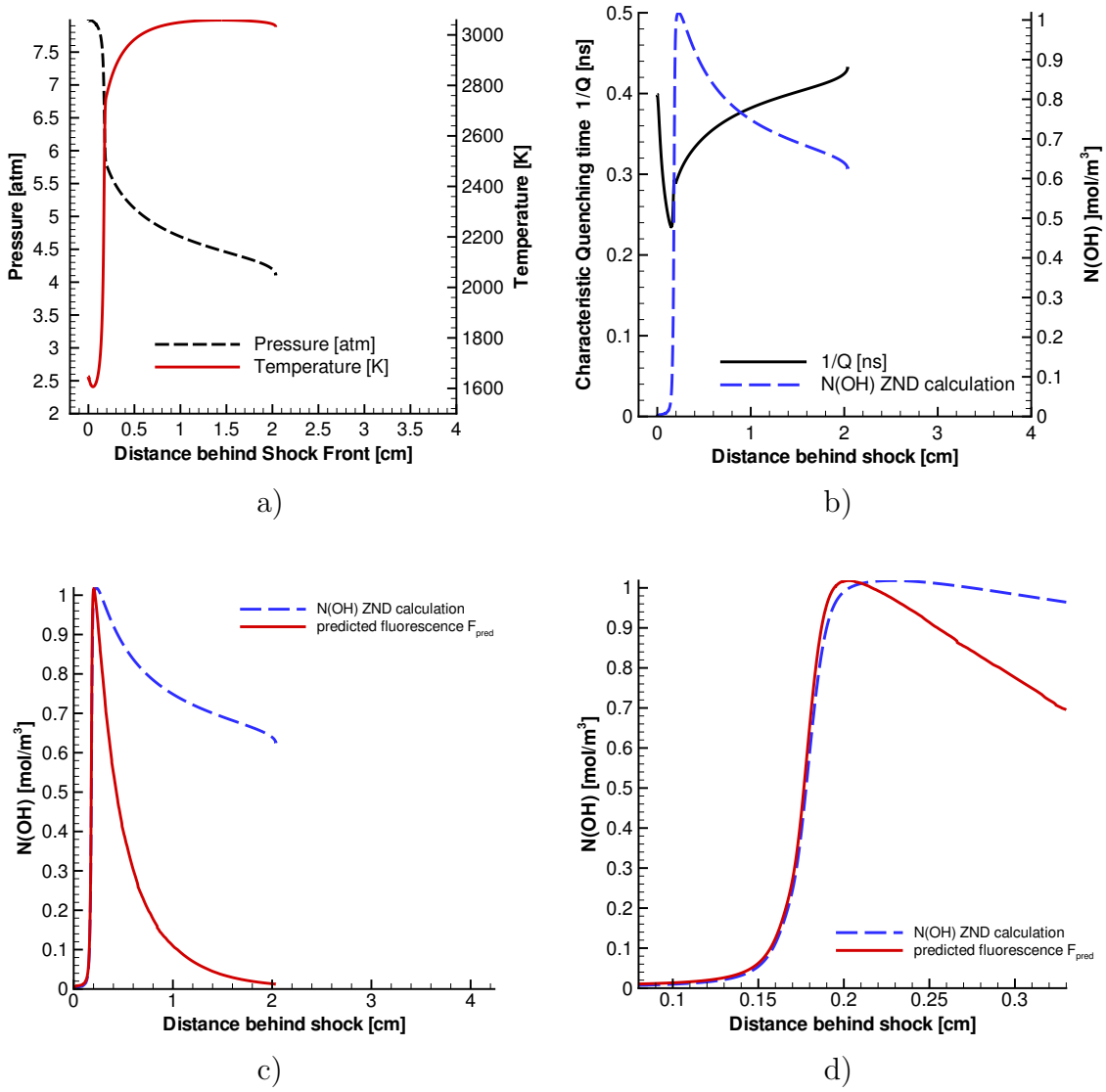

Figure C.7: a) Thermodynamic conditions b) Characteristic quenching time and OH mole fraction. c) OH number density and predicted fluorescence profile. d) Close up of the OH number density and predicted fluorescence profile at the end of the induction zone. C_3H_8-$5O_2$-$9N_2$, T_0=300 K, p_0=20 kPa, Konnov mechanism

C.8 N_2O-O_2-$2N_2$

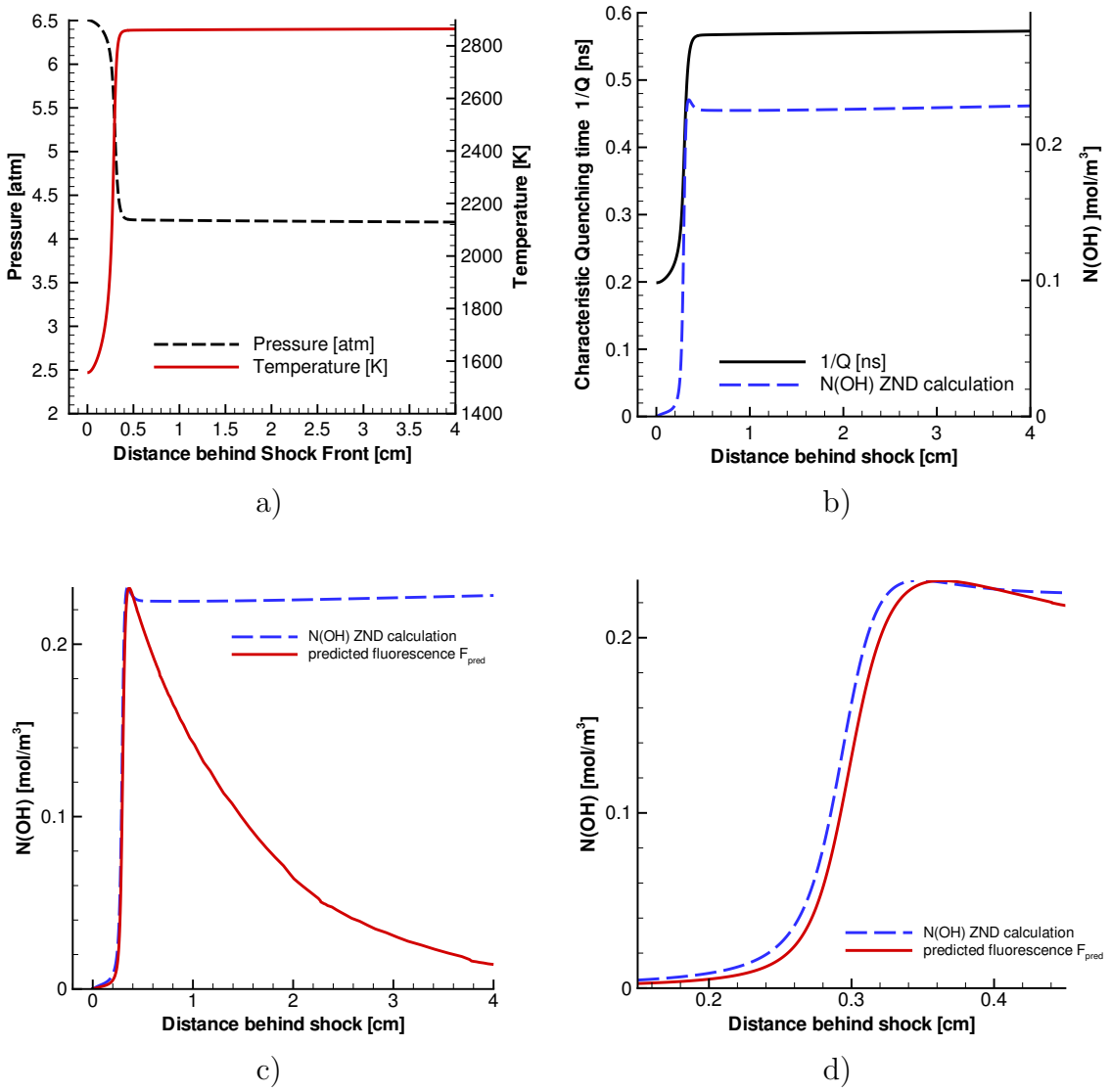

Figure C.8: a) Thermodynamic conditions b) Characteristic quenching time and OH mole fraction. c) OH number density and predicted fluorescence profile. d) Close up of the OH number density and predicted fluorescence profile at the end of the induction zone. N_2O-O_2-$2N_2$, T_0=300 K, p_0=20 kPa, Dryer mechanism

Appendix D

Evaluation of Mixture Properties for Shock Strength Unsteadiness Based on ZND model

The properties relevant to the shock decay considerations of Section 3.8 are evaluated for three types of mixtures, standing as examples on the scale of regularity. The shock decay time t_d through the cell cycle is needed as an input in order to estimate the effects of the decaying lead shock on the induction zone, as done for the Ar- diluted mixture in Section 3.8.

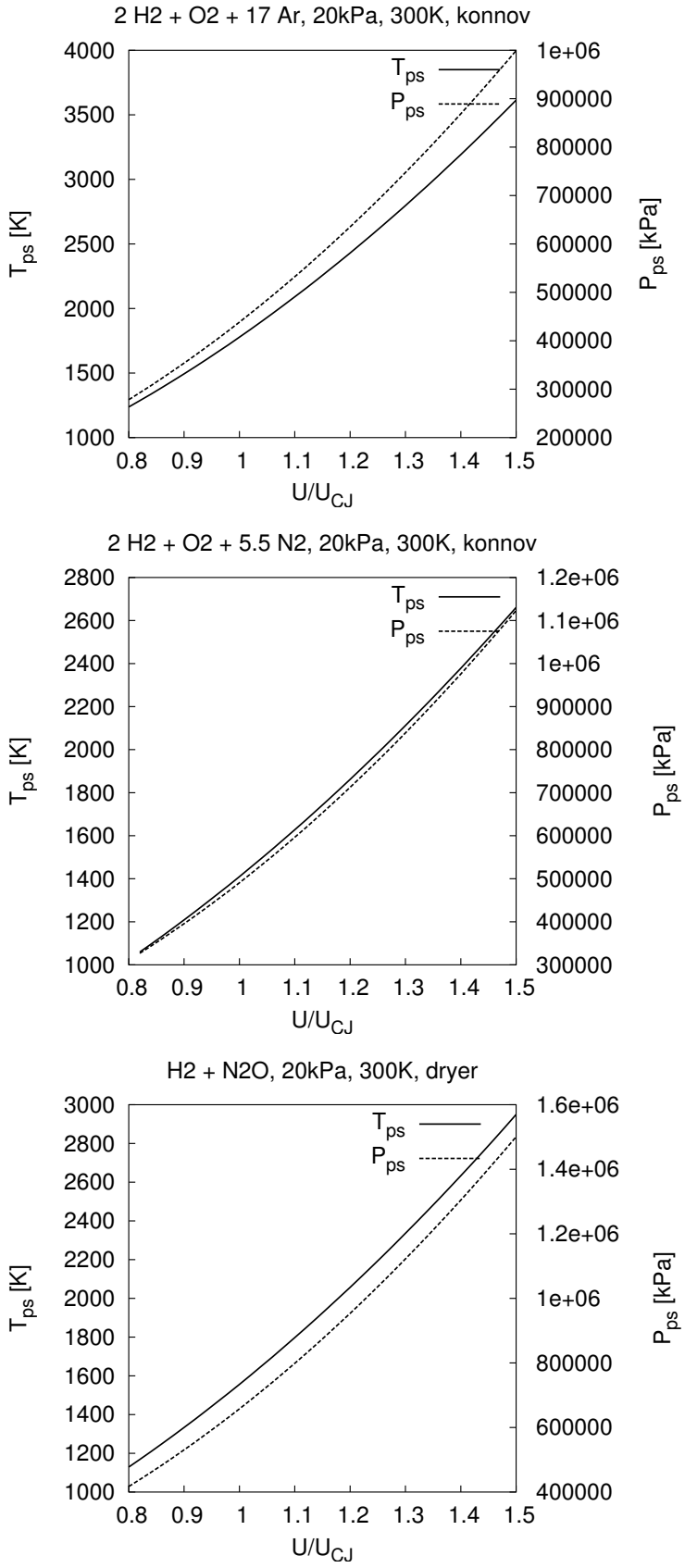

Figure D.1: Post shock conditions

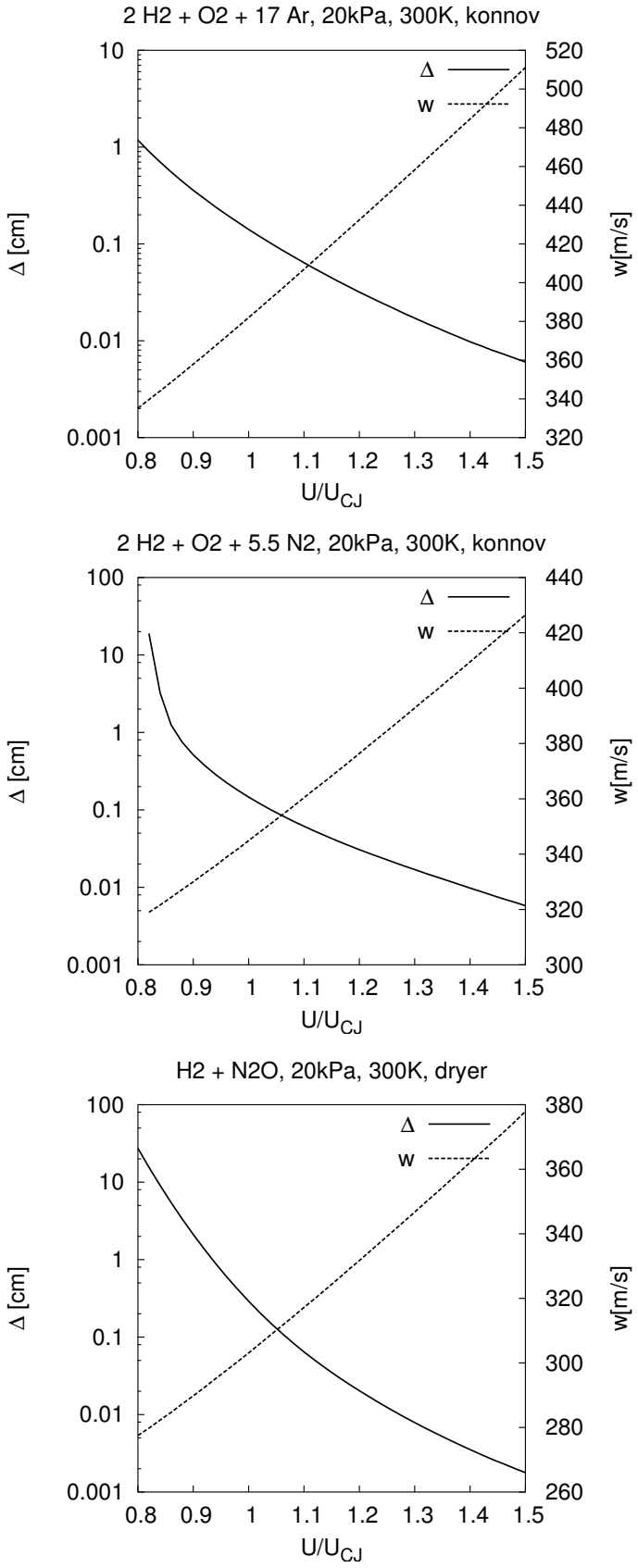

Figure D.2: Induction zone length and post shock velocity

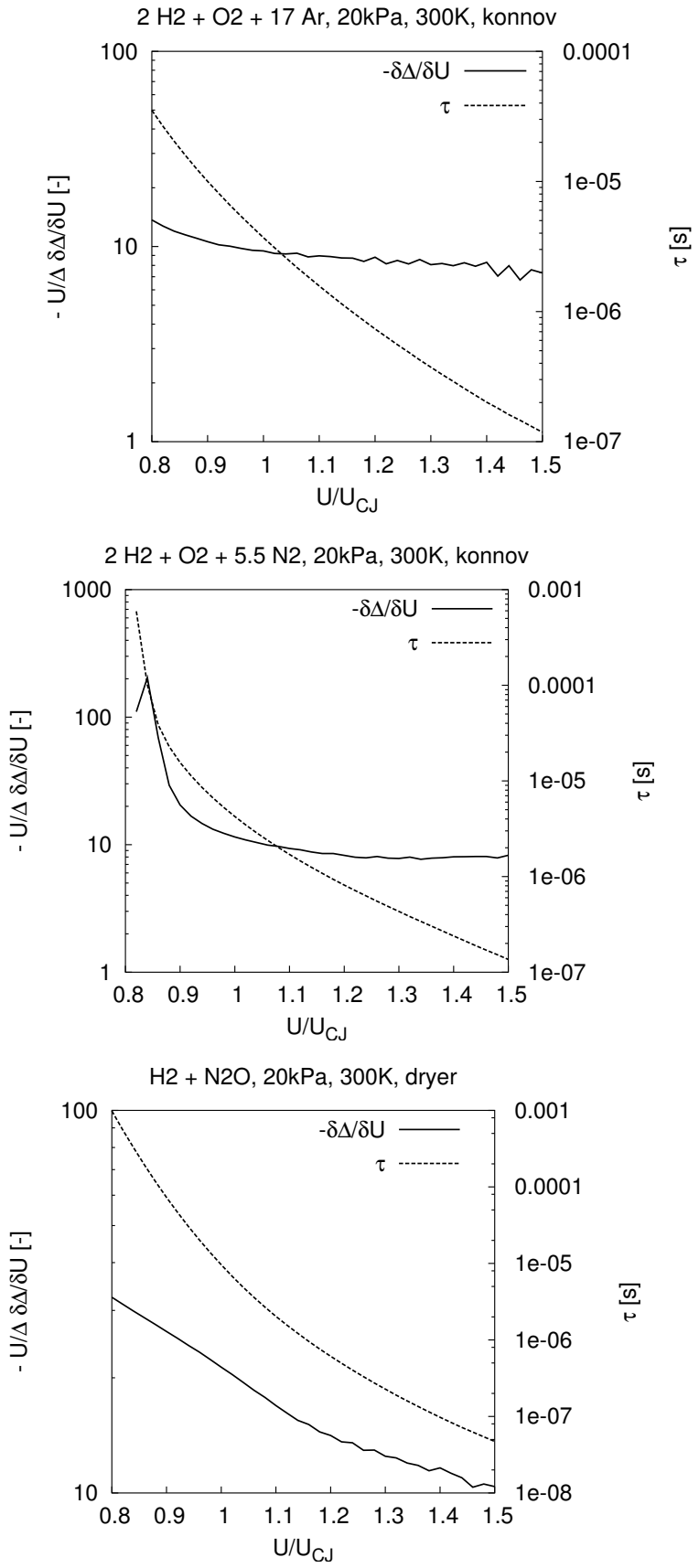

Figure D.3: $U/\Delta\,\partial\Delta/\partial U$ (y1 axis) and induction time τ (y2 axis).

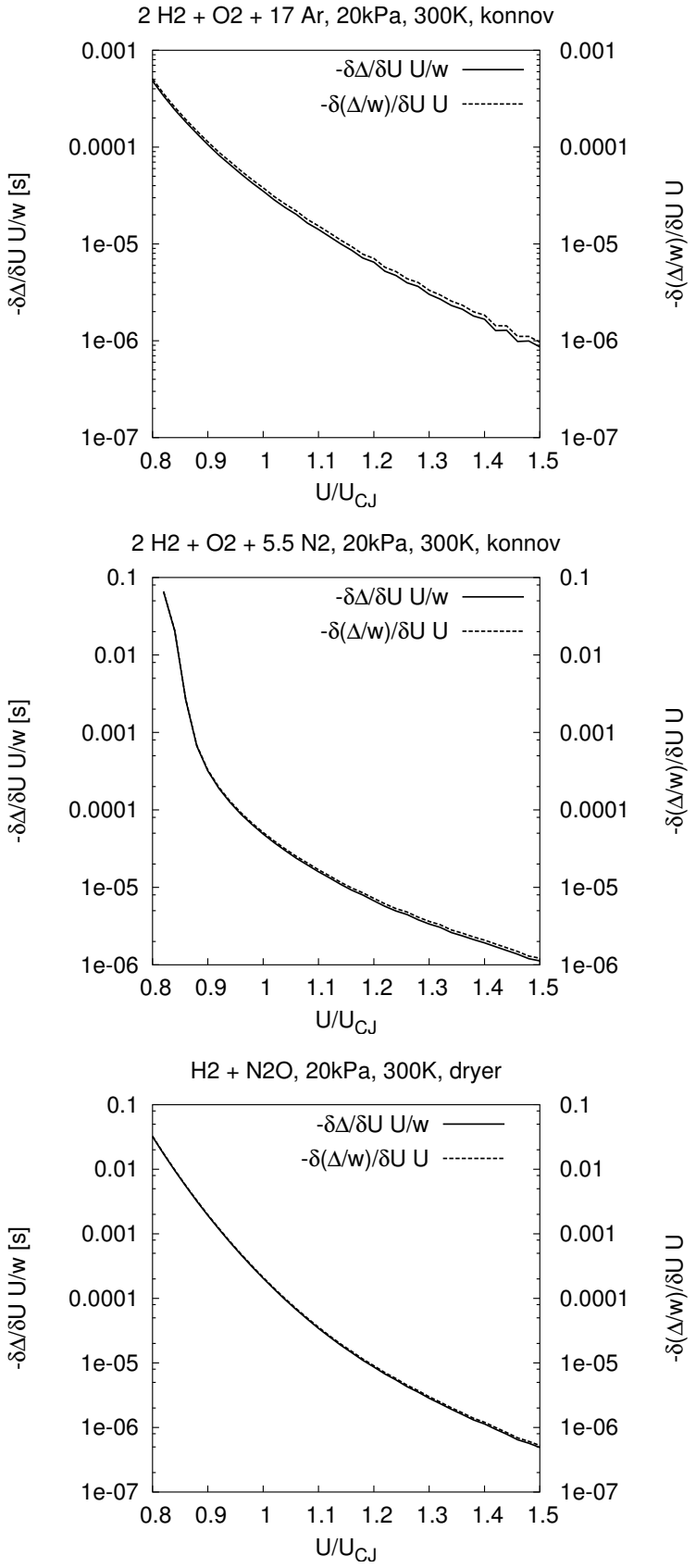

Figure D.4: Absolute change in induction time with relative change in U, $\mathcal{T}$.

Appendix E

Overview of Experiments from Detonation Diffraction Experiment

E.1 H_2-O_2-Ar mixtures

shot	mixture composition	P_0	T_0	img.hght.(mm)			burst	$\Delta t_{TEP}(\mu s)$			gate (ns)		f#		fil-
no.	by mol fraction	(kPa)	(K)	P	S	C	para.	P	S	C	P	C	P	C	ter
1	$0.333H_2$+$0.167O_2$+0.500Ar	100	295	-	-	-	-	-	-	-	0	0	0	0	-
2	$0.267H_2$+$0.133O_2$+0.600Ar	100	295	-	-	-	-	-	-	-	0	0	0	0	-
3	$0.233H_2$+$0.117O_2$+0.650Ar	100	295	-	-	-	-	-	-	-	0	0	0	0	-
4	$0.200H_2$+$0.100O_2$+0.700Ar	100	295	-	-	-	-	-	-	-	0	0	0	0	-
5	$0.167H_2$+$0.083O_2$+0.750Ar	100	295	-	-	-	-	-	-	-	0	0	0	0	-
6	$0.187H_2$+$0.093O_2$+0.720Ar	100	295	-	-	-	-	-	-	-	0	0	0	0	-
7	$0.173H_2$+$0.087O_2$+0.740Ar	100	295	-	-	-	-	-	-	-	0	0	0	0	-
8	$0.160H_2$+$0.080O_2$+0.760Ar	100	295	-	-	-	-	-	-	-	0	0	0	0	-
16	$0.182H_2$+$0.091O_2$+0.727Ar	100	297	50	-	-	-	13.5	-	-	50	0	4.5	0	313
17	$0.187H_2$+$0.093O_2$+0.720Ar	100	297	50	-	-	-	14.5	-	-	60	0	4.5	0	313
18	$0.187H_2$+$0.093O_2$+0.720Ar	100	296	48	-	-	-	21.5	-	-	60	0	4.5	0	313
19	$0.187H_2$+$0.093O_2$+0.720Ar	100	297	48	-	-	-	21.5	-	-	60	0	4.5	0	313
20	$0.187H_2$+$0.093O_2$+0.720Ar	100	296	48	-	-	-	21.5	-	-	70	0	4.5	0	313
21	$0.200H_2$+$0.100O_2$+0.700Ar	100	297	48	-	-	-	24.2	-	-	60	0	4.5	0	313
22	$0.200H_2$+$0.100O_2$+0.700Ar	100	298	48	-	-	-	30.2	-	-	60	0	4.5	0	313
23	$0.200H_2$+$0.100O_2$+0.700Ar	100	298	48	-	-	-	36.2	-	-	60	0	4.5	0	313
24	$0.200H_2$+$0.100O_2$+0.700Ar	100	298	48	-	-	-	42.2	-	-	60	0	4.5	0	313
25	$0.200H_2$+$0.100O_2$+0.700Ar	100	298	48	-	-	-	48.2	-	-	60	0	4.5	0	313
26	$0.200H_2$+$0.100O_2$+0.700Ar	100	298	48	-	-	-	54.2	-	-	60	0	4.5	0	313
27	$0.200H_2$+$0.100O_2$+0.700Ar	100	298	48	-	-	-	14.2	-	-	60	0	4.5	0	313
28	$0.200H_2$+$0.100O_2$+0.700Ar	100	298	48	-	-	-	11.2	-	-	60	0	4.5	0	313
29	$0.213H_2$+$0.107O_2$+0.680Ar	100	295	-	-	-	-	-	-	-	60	0	4.5	0	-
30	$0.213H_2$+$0.107O_2$+0.680Ar	100	296	50	150	-	-	34.6	34.6	-	60	0	4.5	0	313
31	$0.213H_2$+$0.107O_2$+0.680Ar	100	296	50	150	-	-	43.7	44.4	-	60	0	4.5	0	313
32	$0.213H_2$+$0.107O_2$+0.680Ar	100	296	50	150	-	-	53.7	54.4	-	50	0	4.5	0	313

Table E.1: H_2-O_2-Ar mixtures. Experimental set up parameters for Detonation diffraction experiments.

shot no.	mixture composition by mol fraction	P_0 (kPa)	T_0 (K)	img.hght.(mm) P	S	C	burst para.	$\Delta t_{TEP}(\mu s)$ P	S	C	gate (ns) P	C	f# P	C	filter
33	$0.213H_2$+$0.107O_2$+0.680Ar	100	296	50	-	-	-	53.7	-	-	50	0	16	0	UG5
34	$0.213H_2$+$0.107O_2$+0.680Ar	100	297	50	-	-	-	53.7	-	-	50	0	22	0	UG5
35	$0.227H_2$+$0.113O_2$+0.660Ar	100	294	50	150	-	-	56.1	56.1	-	50	0	8.5	0	313
36	$0.227H_2$+$0.113O_2$+0.660Ar	100	294	50	150	-	-	56.1	56.1	-	50	0	8	0	313
37	$0.227H_2$+$0.113O_2$+0.660Ar	100	295	50	150	-	-	56.1	56.1	-	40	0	22	0	UG5
38	$0.227H_2$+$0.113O_2$+0.660Ar	100	295	50	150	-	-	61.1	62.1	-	40	0	22	0	UG5
39	$0.227H_2$+$0.113O_2$+0.660Ar	100	295	50	150	-	-	61.1	61.1	-	40	0	22	0	UG5
40	$0.227H_2$+$0.113O_2$+0.660Ar	100	295	50	150	-	-	61.1	61.1	-	40	0	22	0	UG5
41	$0.233H_2$+$0.117O_2$+0.650Ar	100	296	50	-	-	-	62.2	-	-	40	0	22	0	UG5
42	$0.227H_2$+$0.113O_2$+0.660Ar	100	296	50	150	-	-	61.1	61.9	-	40	0	22	0	UG5
43	$0.227H_2$+$0.113O_2$+0.660Ar	100	296	50	150	-	-	61.1	61.9	-	40	0	22	0	UG5
44	$0.233H_2$+$0.117O_2$+0.650Ar	100	296	50	-	-	-	62.2	-	-	40	0	22	0	UG5
45	$0.230H_2$+$0.115O_2$+0.655Ar	100	296	50	150	-	-	61.7	61.7	-	40	0	22	0	UG5
46	$0.227H_2$+$0.113O_2$+0.660Ar	100	293	-	-	-	-	-	-	-	0	0	0	0	-
47	$0.227H_2$+$0.113O_2$+0.660Ar	100	294	-	-	-	-	-	-	-	0	0	0	0	-
62	$0.200H_2$+$0.100O_2$+0.700Ar	100	294	-	-	-	-	-	-	-	0	0	0	0	-
63	$0.200H_2$+$0.100O_2$+0.700Ar	100	294	-	-	-	-	-	-	-	0	0	0	0	-
64	$0.200H_2$+$0.100O_2$+0.700Ar	100	294	50	150	-	-	14.2	15.3	-	40	0	4.5	0	313
65	$0.200H_2$+$0.100O_2$+0.700Ar	100	295	50	150	-	-	20.2	21.3	-	40	0	22	0	UG11
66	$0.200H_2$+$0.100O_2$+0.700Ar	100	294	-	150	-	-	-	27.3	-	0	0	0	0	-
67	$0.200H_2$+$0.100O_2$+0.700Ar	100	295	50	150	-	-	32.2	32.3	-	30	0	22	0	UG11
68	$0.200H_2$+$0.100O_2$+0.700Ar	100	295	50	150	-	-	38.2	38.3	-	30	0	22	0	UG11
69	$0.200H_2$+$0.100O_2$+0.700Ar	100	295	50	150	-	-	44.2	44.3	-	30	0	16	0	UG11
70	$0.200H_2$+$0.100O_2$+0.700Ar	100	296	50	150	-	-	50.2	50.3	-	30	0	16	0	UG11
71	$0.200H_2$+$0.100O_2$+0.700Ar	100	296	50	150	-	-	56.2	56.3	-	30	0	16	0	UG11

Table E.2: H_2-O_2-Ar mixtures. Experimental set up parameters for Detonation diffraction experiments.

shot	mixture composition	P_0	T_0	img.hght.(mm)			burst	$\Delta t_{TEP}(\mu s)$			gate (ns)		f#		fil-
no.	by mol fraction	(kPa)	(K)	P	S	C	para.	P	S	C	P	C	P	C	ter
72	$0.200H_2+0.100O_2+0.700Ar$	100	296	50	150	-	-	62.2	62.3	-	30	0	16	0	UG11
73	$0.200H_2+0.100O_2+0.700Ar$	100	296	50	150	-	-	8.2	8.3	-	30	0	16	0	UG11
74	$0.200H_2+0.100O_2+0.700Ar$	100	296	50	150	-	-	2.2	2.3	-	30	0	16	0	UG11
126	$0.200H_2+0.100O_2+0.700Ar$	100	294	70	150	109	$1\times6\mu s$	38.2	38.3	2.3	40	200	5.6	8	313
127	$0.200H_2+0.100O_2+0.700Ar$	100	294	70	150	109	$6\times7\mu s$	32.2	32.3	-3.7	40	300	16	2.8	UG11
128	$0.200H_2+0.100O_2+0.700Ar$	100	295	70	150	109	$6\times6\mu s$	26.2	26.3	-3.7	40	300	16	2.8	UG11
129	$0.200H_2+0.100O_2+0.700Ar$	100	295	70	150	109	$9\times6\mu s$	26.2	26.3	-3.7	40	300	16	2.8	UG11
130	$0.213H_2+0.107O_2+0.680Ar$	100	295	70	-	109	$9\times6\mu s$	28.7	-	-1.2	40	300	16	2.8	UG11
131	$0.213H_2+0.107O_2+0.680Ar$	100	296	-	-	109	$9\times6\mu s$	-	-	-1.2	0	300	0	2.8	-
132	$0.213H_2+0.107O_2+0.680Ar$	100	296	70	150	109	$9\times6\mu s$	28.7	28.8	-1.2	40	300	16	2.8	UG11
133	$0.217H_2+0.108O_2+0.675Ar$	100	296	70	150	109	$9\times6\mu s$	29.3	29.4	-0.6	40	300	16	2.8	UG11
134	$0.217H_2+0.108O_2+0.675Ar$	100	296	70	150	109	$9\times6\mu s$	29.3	29.3	-0.6	40	300	16	2.8	UG11
135	$0.217H_2+0.108O_2+0.675Ar$	100	294	70	150	109	$9\times6\mu s$	35.3	35.3	-0.6	40	300	22	2.8	UG11
136	$0.220H_2+0.110O_2+0.670Ar$	100	295	70	150	109	$9\times6\mu s$	35.9	36.0	0.0	40	300	16	2.8	UG11
137	$0.220H_2+0.110O_2+0.670Ar$	100	295	70	150	109	$9\times6\mu s$	35.9	36.0	0.0	40	300	16	2.8	UG11
138	$0.223H_2+0.112O_2+0.665Ar$	100	296	70	150	109	$8\times6\mu s$	45.5	45.5	0.6	40	300	16	2.8	UG11
139	$0.223H_2+0.112O_2+0.665Ar$	100	296	70	150	109	$9\times6\mu s$	36.5	36.5	0.6	40	300	16	2.8	UG11
140	$0.227H_2+0.113O_2+0.660Ar$	100	296	70	150	109	$9\times6\mu s$	37.1	37.2	1.2	40	300	22	2.8	UG11
141	$0.233H_2+0.117O_2+0.650Ar$	100	296	70	-	109	$7\times6\mu s$	38.2	-	2.3	40	250	22	2.8	UG11
142	$0.240H_2+0.120O_2+0.640Ar$	100	296	70	150	109	$7\times6\mu s$	39.3	39.4	3.5	30	250	16	2.8	UG11
148	$0.220H_2+0.110O_2+0.670Ar$	100	295	70	150	109	$10\times3\mu s$	41.9	42.0	0.0	30	300	22	2.8	UG11
149	$0.220H_2+0.110O_2+0.670Ar$	100	295	70	150	109	$19\times3\mu s$	44.9	45.0	0.0	30	300	22	2.8	UG11
150	$0.223H_2+0.112O_2+0.665Ar$	100	295	70	150	109	$10\times6\mu s$	48.5	48.5	0.6	30	250	22	2.8	UG11
154	$0.333H_2+0.167O_2+0.500Ar$	55	296	70	-	109	$9\times6\mu s$	42.5	-	0.7	30	300	22	2.8	UG11
155	$0.333H_2+0.167O_2+0.500Ar$	45	296	-	-	-	-	-	-	-	0	0	0	0	-

Table E.3: H_2-O_2-Ar mixtures. Experimental set up parameters for Detonation diffraction experiments.

shot no.	mixture composition by mol fraction	P_0 (kPa)	T_0 (K)	img.hght.(mm) P	S	C	burst para.	$\Delta t_{TEP}(\mu s)$ P	S	C	gate (ns) P	C	f# P	C	filter
156	$0.333H_2$+$0.167O_2$+0.500Ar	45	296	70	150	109	9×6μs	41.9	42.0	0.0	30	300	22	2.8	UG11
157	$0.333H_2$+$0.167O_2$+0.500Ar	47.5	296	70	150	109	11×6μs	48.1	48.1	0.2	30	350	22	2.8	UG11
158	$0.333H_2$+$0.167O_2$+0.500Ar	50	296	70	-	109	11×6μs	48.3	-	0.4	30	350	22	2.8	UG11
159	$0.333H_2$+$0.167O_2$+0.500Ar	50	296	-	-	-	-	-	-	-	0	0	0	0	-
160	$0.333H_2$+$0.167O_2$+0.500Ar	50	295	70	150	109	10×6μs	42.3	42.3	0.4	35	400	22	2.8	UG11
161	$0.333H_2$+$0.167O_2$+0.500Ar	52.5	295	70	150	109	10×6μs	42.4	42.5	0.5	35	150	32	2.8	UG11
162	$0.333H_2$+$0.167O_2$+0.500Ar	53.75	296	70	150	109	10×6μs	42.5	42.5	0.6	35	0	32	2.8	UG11
163	$0.333H_2$+$0.167O_2$+0.500Ar	55	296	70	150	109	10×6μs	42.5	42.6	0.7	35	0	22	2.8	UG11
164	$0.333H_2$+$0.167O_2$+0.500Ar	55	296	70	150	109	10×6μs	42.5	42.6	0.7	35	300	22	2.8	UG11
165	$0.333H_2$+$0.167O_2$+0.500Ar	57.5	296	70	150	109	10×6μs	42.7	42.7	0.8	35	300	22	2.8	UG11
166	$0.333H_2$+$0.167O_2$+0.500Ar	57.5	296	70	150	109	7×6μs	36.7	36.7	0.8	35	300	22	2.8	UG11
167	$0.333H_2$+$0.167O_2$+0.500Ar	60	297	70	150	109	7×6μs	30.8	30.9	0.9	35	300	16	2.8	UG11
168	$0.333H_2$+$0.167O_2$+0.500Ar	62.5	296	70	150	109	6×6μs	30.9	31.0	1.1	35	300	16	2.8	UG11
169	$0.333H_2$+$0.167O_2$+0.500Ar	65	296	70	150	109	7×6μs	31.1	31.1	1.2	35	300	16	2.8	UG11
170	$0.333H_2$+$0.167O_2$+0.500Ar	70	296	70	150	109	6×6μs	31.3	31.4	1.4	35	300	16	2.8	UG11
200	$0.220H_2$+$0.110O_2$+0.670Ar	100	293	-	150	109	2×43μs	-	42.0	0.0	0	0	0	16	-
201	$0.220H_2$+$0.110O_2$+0.670Ar	100	294	70	150	109	80×1μs	41.9	42.0	0.0	30	200	22	2.8	UG11
202	$0.220H_2$+$0.110O_2$+0.670Ar	100	294	70	150	109	1×0μs	47.9	48.0	0.0	30	48000	16	16	UG11
203	$0.220H_2$+$0.110O_2$+0.670Ar	100	294	70	150	109	1×0μs	59.9	60.0	6.0	30	54000	16	16	UG11

Table E.4: H_2-O_2-Ar mixtures. Experimental set up parameters for Detonation diffraction experiments.

E.2 H_2-O_2-N_2mixtures

shot	mixture composition	P_0	T_0	img.hght.(mm)			burst	$\Delta t_{TEP}(\mu s)$			gate (ns)		f#		fil-
no.	by mol fraction	(kPa)	(K)	P	S	C	para.	P	S	C	P	C	P	C	ter
14	$0.500H_2+0.250O_2+0.250N_2$	100	296	-	-	-	-	-	-	-	0	0	0	0	-
15	$0.500H_2+0.250O_2+0.250N_2$	100	296	-	-	-	-	-	-	-	0	0	0	0	-
48	$0.540H_2+0.270O_2+0.190N_2$	100	294	-	-	-	-	-	-	-	0	0	0	0	-
49	$0.540H_2+0.270O_2+0.190N_2$	100	295	-	150	-	-	-	62.5	-	0	0	0	0	-
50	$0.527H_2+0.263O_2+0.210N_2$	100	295	50	150	-	-	29.0	29.0	-	40	0	22	0	UG11
51	$0.527H_2+0.263O_2+0.210N_2$	100	295	50	150	-	-	39.0	39.0	-	40	0	22	0	UG11
52	$0.520H_2+0.260O_2+0.220N_2$	100	296	50	150	-	-	38.2	38.2	-	40	0	22	0	UG11
53	$0.520H_2+0.260O_2+0.220N_2$	100	295	50	150	-	-	38.2	38.2	-	40	0	22	0	UG11
54	$0.507H_2+0.253O_2+0.240N_2$	100	297	50	150	-	-	36.7	36.7	-	40	0	22	0	UG11
55	$0.507H_2+0.253O_2+0.240N_2$	100	294	50	150	-	-	36.7	36.7	-	40	0	4.5	0	313
56	$0.507H_2+0.253O_2+0.240N_2$	100	295	50	150	-	-	36.7	36.7	-	40	0	16	0	UG11
57	$0.507H_2+0.253O_2+0.240N_2$	100	296	50	150	-	-	31.7	31.6	-	40	0	16	0	UG11
58	$0.520H_2+0.260O_2+0.220N_2$	100	296	50	150	-	-	38.2	38.2	-	40	0	16	0	UG11

Table E.5: H_2-O_2-N_2mixtures. Experimental set up parameters for Detonation diffraction experiments.

E.3 H_2-N_2Omixtures

shot	mixture composition	P_0	T_0	img.hght.(mm)			burst	$\Delta t_{TEP}(\mu s)$			gate (ns)		f#		fil-
no.	by mol fraction	(kPa)	(K)	P	S	C	para.	P	S	C	P	C	P	C	ter
59	$0.500H_2$+$0.500N_2O$	70	296	150	150	-	-	34.8	34.9	-	40	0	16	0	UG11
60	$0.500H_2$+$0.500N_2O$	40	296	50	150	-	-	33.5	33.6	-	40	0	16	0	UG11
61	$0.500H_2$+$0.500N_2O$	55	296	50	150	-	-	34.3	35.3	-	40	0	16	0	UG11
75	$0.500H_2$+$0.500N_2O$	45	294	73	150	-	-	39.8	39.9	-	40	0	4.5	0	313
76	$0.500H_2$+$0.500N_2O$	45	295	73	150	-	-	27.8	27.9	-	40	0	4.5	0	313
77	$0.500H_2$+$0.500N_2O$	45	295	73	150	-	-	15.8	15.9	-	40	0	4.5	0	313
78	$0.500H_2$+$0.500N_2O$	40	295	73	150	-	-	39.5	39.6	-	40	0	4.5	0	313
79	$0.500H_2$+$0.500N_2O$	40	295	73	150	-	-	51.5	51.7	-	40	0	16	0	UG11
80	$0.500H_2$+$0.500N_2O$	40	296	73	150	-	-	45.5	45.7	-	40	0	16	0	UG11
81	$0.500H_2$+$0.500N_2O$	40	296	73	150	-	-	39.5	39.6	-	40	0	16	0	UG11
82	$0.500H_2$+$0.500N_2O$	40	296	73	150	-	-	33.5	33.6	-	50	0	16	0	UG11
83	$0.500H_2$+$0.500N_2O$	40	296	73	150	-	-	27.5	27.6	-	40	0	16	0	UG11
84	$0.500H_2$+$0.500N_2O$	40	296	73	150	-	-	21.5	21.6	-	40	0	16	0	UG11
85	$0.500H_2$+$0.500N_2O$	40	296	73	150	-	-	15.5	15.5	-	40	0	11	0	UG11
86	$0.500H_2$+$0.500N_2O$	40	296	73	150	-	-	9.5	9.5	-	40	0	11	0	UG11
87	$0.500H_2$+$0.500N_2O$	40	296	-	150	-	-	-	3.5	-	0	0	0	0	-
88	$0.500H_2$+$0.500N_2O$	40	296	73	150	-	-	27.5	27.4	-	40	0	16	0	UG11
89	$0.500H_2$+$0.500N_2O$	40	296	73	150	-	-	15.5	15.4	-	40	0	16	0	UG11
90	$0.500H_2$+$0.500N_2O$	40	294	-	-	118	$3\times10\mu$s	-	-	9.6	0	59	0	22	-
91	$0.500H_2$+$0.500N_2O$	40	294	-	-	-	-	-	-	-	0	0	0	0	-
92	$0.500H_2$+$0.500N_2O$	40	294	-	-	118	$1\times0\mu$s	-	-	3.6	0	400	0	8	-
93	$0.500H_2$+$0.500N_2O$	40	294	-	-	118	$4\times12\mu$s	-	-	9.6	0	400	0	8	-
94	$0.500H_2$+$0.500N_2O$	40	295	-	-	-	$9\times6\mu$s	-	-	-	0	300	0	8	-
95	$0.500H_2$+$0.500N_2O$	40	295	-	-	-	-	-	-	-	0	0	0	0	-
96	$0.500H_2$+$0.500N_2O$	40	295	-	-	118	$3\times6\mu$s	-	-	0.6	0	200	0	22	-

Table E.6: H_2-N_2Omixtures. Experimental set up parameters for Detonation diffraction experiments.

shot	mixture composition	P_0	T_0	img.hght.(mm)			burst	$\Delta t_{TEP}(\mu s)$			gate (ns)		f#		fil-
no.	by mol fraction	(kPa)	(K)	P	S	C	para.	P	S	C	P	C	P	C	ter
97	$0.500H_2$+$0.500N_2O$	40	295	-	-	118	7×3μs	-	-	0.6	0	130	0	8	-
98	$0.500H_2$+$0.500N_2O$	42.5	295	-	-	118	9×3μs	-	-	0.8	0	180	0	8	-
99	$0.500H_2$+$0.500N_2O$	42.5	295	-	-	118	9×6μs	-	-	3.8	0	220	0	5.6	-
100	$0.500H_2$+$0.500N_2O$	45	295	-	-	118	7×3μs	-	-	0.9	0	130	0	8	-
101	$0.500H_2$+$0.500N_2O$	45	295	-	-	118	9×6μs	-	-	3.9	0	220	0	5.6	-
102	$0.500H_2$+$0.500N_2O$	45	296	-	-	118	7×6μs	-	-	3.9	0	100	0	8	-
103	$0.500H_2$+$0.500N_2O$	47.5	296	-	-	118	7×6μs	-	-	4.0	0	220	0	5.6	-
104	$0.500H_2$+$0.500N_2O$	47.5	296	-	-	118	7×3μs	-	-	1.0	0	130	0	8	-
105	$0.500H_2$+$0.500N_2O$	47.5	296	-	-	118	7×3μs	-	-	1.0	0	200	0	8	-
106	$0.500H_2$+$0.500N_2O$	45	294	-	150	109	7×3μs	-	21.8	0.9	0	130	0	8	-
107	$0.500H_2$+$0.500N_2O$	45	294	-	150	109	8×3μs	-	24.8	0.9	0	130	0	5.6	-
108	$0.500H_2$+$0.500N_2O$	45	295	-	150	109	8×3μs	-	24.8	0.9	0	200	0	5.6	-
109	$0.500H_2$+$0.500N_2O$	45	295	-	150	109	8×3μs	-	24.8	0.9	0	200	0	5.6	-
110	$0.500H_2$+$0.500N_2O$	45	295	-	150	109	9×3μs	-	21.8	0.9	0	200	0	5.6	-
111	$0.500H_2$+$0.500N_2O$	45	295	-	150	109	8×3μs	-	21.8	0.9	0	200	0	5.6	-
112	$0.500H_2$+$0.500N_2O$	47.5	296	-	150	109	7×3μs	-	19.0	1.0	0	200	0	5.6	-
113	$0.500H_2$+$0.500N_2O$	47.5	296	-	150	109	7×3μs	-	19.0	1.0	0	200	0	5.6	-
114	$0.500H_2$+$0.500N_2O$	50	296	-	150	109	7×3μs	-	19.1	1.1	0	200	0	5.6	-
115	$0.500H_2$+$0.500N_2O$	50	296	-	150	109	7×3μs	-	19.1	1.1	0	200	0	5.6	-
116	$0.500H_2$+$0.500N_2O$	55	296	-	150	109	7×3μs	-	19.3	1.4	0	200	0	5.6	-
117	$0.500H_2$+$0.500N_2O$	55	296	-	150	109	7×3μs	-	19.3	1.4	0	180	0	5.6	-
118	$0.500H_2$+$0.500N_2O$	60	296	-	150	109	7×3μs	-	19.5	1.6	0	150	0	5.6	-
119	$0.500H_2$+$0.500N_2O$	60	296	-	150	109	6×3μs	-	16.5	1.6	0	150	0	5.6	-
120	$0.500H_2$+$0.500N_2O$	65	297	-	150	-	-	-	13.8	-	0	0	0	0	-
121	$0.500H_2$+$0.500N_2O$	65	297	-	150	109	5×3μs	-	13.7	1.7	0	200	0	8	-

Table E.7: H_2-N_2Omixtures. Experimental set up parameters for Detonation diffraction experiments.

shot	mixture composition	P_0	T_0	img.hght.(mm)			burst	$\Delta t_{TEP}(\mu s)$			gate (ns)		f#		fil-
no.	by mol fraction	(kPa)	(K)	P	S	C	para.	P	S	C	P	C	P	C	ter
122	$0.500H_2$+$0.500N_2O$	65	297	-	150	109	$6\times3\mu$s	-	16.7	1.7	0	200	0	8	-
123	$0.500H_2$+$0.500N_2O$	70	297	-	150	109	$5\times3\mu$s	-	13.8	1.9	0	200	0	8	-
124	$0.500H_2$+$0.500N_2O$	70	297	-	150	109	$5\times6\mu$s	-	25.8	1.9	0	200	0	8	-
125	$0.500H_2$+$0.500N_2O$	80	297	-	150	109	$4\times3\mu$s	-	11.1	2.2	0	200	0	8	-
143	$0.500H_2$+$0.500N_2O$	45	296	70	150	109	$10\times3\mu$s	24.8	24.8	0.9	30	200	16	5.6	UG11
144	$0.500H_2$+$0.500N_2O$	40	296	70	150	109	$10\times3\mu$s	24.5	24.6	0.7	30	200	16	5.6	UG11
145	$0.500H_2$+$0.500N_2O$	42.5	296	70	150	109	$9\times3\mu$s	24.7	24.7	0.8	30	200	22	5.6	UG11
146	$0.500H_2$+$0.500N_2O$	47.5	297	70	150	109	$9\times3\mu$s	24.9	25.0	1.1	30	200	22	5.6	UG11
147	$0.500H_2$+$0.500N_2O$	50	297	70	150	109	$9\times3\mu$s	25.1	25.1	1.2	30	200	22	5.6	UG11
151	$0.500H_2$+$0.500N_2O$	40	295	70	150	109	$14\times3\mu$s	33.5	33.6	0.7	30	200	16	4	UG11
152	$0.500H_2$+$0.500N_2O$	42.5	295	70	150	109	$9\times6\mu$s	36.7	36.7	0.8	30	200	16	5.6	UG11
153	$0.500H_2$+$0.500N_2O$	43.75	296	70	150	109	$9\times6\mu$s	36.8	36.8	0.9	30	200	22	5.6	UG11
171	$0.500H_2$+$0.500N_2O$	45	297	70	150	109	$11\times3\mu$s	27.8	27.9	0.9	35	150	16	5.6	UG11
172	$0.500H_2$+$0.500N_2O$	47.5	297	70	150	109	$6\times6\mu$s	27.9	28.0	1.1	35	150	16	0	UG11
173	$0.500H_2$+$0.500N_2O$	47.5	297	70	150	109	$6\times6\mu$s	30.9	31.0	1.1	35	150	22	0	UG11
174	$0.500H_2$+$0.500N_2O$	46.25	297	70	150	109	$11\times3\mu$s	30.9	31.0	1.0	35	150	4.5	0	313
204	$0.500H_2$+$0.500N_2O$	47.5	295	70	150	109	$1\times0\mu$s	42.9	43.0	1.1	30	42000	16	32	UG11
205	$0.500H_2$+$0.500N_2O$	47.5	295	-	150	109	$1\times0\mu$s	-	43.0	1.1	0	42000	0	32	-
206	$0.500H_2$+$0.500N_2O$	45	295	70	150	109	$1\times0\mu$s	42.8	42.8	0.9	25	42000	16	32	UG11
207	$0.500H_2$+$0.500N_2O$	47.5	296	70	150	109	$1\times0\mu$s	42.9	42.9	1.1	25	42000	16	32	UG11

Table E.8: H_2-N_2Omixtures. Experimental set up parameters for Detonation diffraction experiments.

E.4 CH_4-O_2mixtures

shot no.	mixture composition by mol fraction	P_0 (kPa)	T_0 (K)	img.hght.(mm) P	S	C	burst para.	$\Delta t_{TEP}(\mu s)$ P	S	C	gate (ns) P	C	f# P	C	filter
9	$0.333CH_4$+$0.667O_2$	100	295	-	-	-	-	-	-	-	0	0	0	0	-
10	$0.333CH_4$+$0.667O_2$	50	294	-	-	-	-	-	-	-	0	0	0	0	-
11	$0.333CH_4$+$0.667O_2$	50	295	-	-	-	-	-	-	-	0	0	0	0	-
12	$0.333CH_4$+$0.667O_2$	60	295	-	-	-	-	-	-	-	0	0	0	0	-
13	$0.333CH_4$+$0.667O_2$	50	295	-	-	-	-	-	-	-	0	0	0	0	-
187	$0.333CH_4$+$0.667O_2$	50	294	70	150	109	7×6μs	31.0	31.0	1.1	35	130	22	16	UG11
188	$0.333CH_4$+$0.667O_2$	55	295	70	150	109	8×6μs	31.2	31.2	1.3	20	180	16	16	UG11
189	$0.333CH_4$+$0.667O_2$	60	296	70	150	109	8×6μs	31.4	31.4	1.5	20	180	4.5	16	313
190	$0.333CH_4$+$0.667O_2$	65	296	70	-	109	8×6μs	31.6	-	1.7	75	180	16	16	UG11
191	$0.333CH_4$+$0.667O_2$	70	297	70	150	109	8×6μs	31.8	31.8	1.9	20	180	16	16	UG11
192	$0.333CH_4$+$0.667O_2$	80	298	0	-	109	8×6μs	-10.0	-	-9.8	0	180	0	22	313
193	$0.333CH_4$+$0.667O_2$	90	298	70	-	109	8×6μs	32.4	-	2.5	20	180	16	22	UG11
194	$0.333CH_4$+$0.667O_2$	100	299	70	150	109	8×6μs	32.6	32.6	2.7	20	130	16	16	UG11
195	$0.333CH_4$+$0.667O_2$	120	299	70	150	109	7×6μs	33.0	33.1	3.2	20	130	16	16	UG11
196	$0.333CH_4$+$0.667O_2$	110	299	70	150	109	6×6μs	32.8	32.9	3.0	20	130	16	16	UG11
197	$0.333CH_4$+$0.667O_2$	115	300	-	150	109	6×6μs	-	32.9	3.1	0	130	0	16	-
198	$0.333CH_4$+$0.667O_2$	120	298	-	150	109	6×6μs	-	33.1	3.2	0	130	0	16	-
199	$0.333CH_4$+$0.667O_2$	125	301	-	150	109	6×6μs	-	33.2	3.2	0	130	0	16	-

Table E.9: CH_4-O_2mixtures. Experimental set up parameters for Detonation diffraction experiments.

E.5 C_2H_6-O_2mixtures

shot	mixture composition	P_0	T_0	img.hght.(mm)			burst	$\Delta t_{TEP}(\mu s)$			gate (ns)		f#		fil-
no.	by mol fraction	(kPa)	(K)	P	S	C	para.	P	S	C	P	C	P	C	ter
175	$0.222C_2H_6$+$0.778O_2$	30	297	70	150	109	6×6μs	31.6	31.6	-1.3	35	150	22	16	UG11
176	$0.222C_2H_6$+$0.778O_2$	32.5	297	70	150	109	14×3μs	31.8	31.8	-1.1	35	150	22	11	UG11
177	$0.222C_2H_6$+$0.778O_2$	35	297	70	150	109	7×6μs	32.0	32.0	2.1	30	200	22	16	UG11
178	$0.222C_2H_6$+$0.778O_2$	40	297	70	150	109	7×6μs	32.3	32.3	2.4	30	200	22	16	UG11
179	$0.222C_2H_6$+$0.778O_2$	37.5	298	70	150	109	7×6μs	26.1	26.1	2.2	30	200	22	16	UG11
180	$0.222C_2H_6$+$0.778O_2$	37.5	297	70	150	109	11×6μs	26.1	26.2	2.2	30	200	22	16	UG11
181	$0.222C_2H_6$+$0.778O_2$	36.25	297	70	150	109	11×6μs	32.0	32.1	2.2	30	200	22	16	UG11
182	$0.222C_2H_6$+$0.778O_2$	36.25	298	70	150	109	9×6μs	32.1	32.1	2.2	20	200	4.5	16	313
183	$0.222C_2H_6$+$0.778O_2$	37.5	298	70	150	109	9×6μs	32.1	32.2	2.2	20	180	4.5	16	313
184	$0.222C_2H_6$+$0.778O_2$	38.25	298	70	150	109	9×6μs	32.2	32.2	2.3	20	180	4.5	16	313
185	$0.222C_2H_6$+$0.778O_2$	42.5	298	70	150	109	9×6μs	32.4	32.5	2.6	20	180	4.5	16	313
186	$0.222C_2H_6$+$0.778O_2$	45	299	70	150	109	10×3μs	32.6	32.6	2.7	20	180	4.5	16	313
208	$0.222C_2H_6$+$0.778O_2$	40	295	-	150	-	-	-	62.3	-	50	200	16	16	-
209	$0.222C_2H_6$+$0.778O_2$	40	296	140	150	140	-	20.4	20.2	20.4	30	200	32	16	313
210	$0.222C_2H_6$+$0.778O_2$	42.5	296	140	150	140	-	26.9	26.4	25.9	150	200	32	16	313
211	$0.222C_2H_6$+$0.778O_2$	42.5	297	140	150	140	-	29.9	29.4	28.9	200	200	32	16	313
212	$0.222C_2H_6$+$0.778O_2$	42.5	297	140	150	140	-	27.9	27.4	26.9	200	200	32	16	313
213	$0.222C_2H_6$+$0.778O_2$	42.5	298	140	150	140	-	28.9	28.4	27.9	200	200	32	16	313
214	$0.222C_2H_6$+$0.778O_2$	42.5	298	140	150	140	-	28.9	28.4	27.9	200	200	32	16	313
215	$0.222C_2H_6$+$0.778O_2$	42.5	294	140	150	140	-	28.6	28.4	28.6	200	200	32	16	313
216	$0.222C_2H_6$+$0.778O_2$	42.5	295	140	150	140	-	28.6	28.4	28.6	200	200	32	16	313
217	$0.222C_2H_6$+$0.778O_2$	42.5	295	140	150	140	-	28.6	28.4	28.6	200	200	32	16	313
218	$0.222C_2H_6$+$0.778O_2$	42.5	296	140	150	140	-	28.6	28.4	28.6	200	200	32	16	313
219	$0.222C_2H_6$+$0.778O_2$	42.5	296	140	150	140	-	28.6	28.4	28.6	200	200	32	16	313
220	$0.222C_2H_6$+$0.778O_2$	42.5	297	140	150	140	-	28.6	28.4	28.6	200	200	32	16	313

Table E.10: C_2H_6-O_2mixtures. Experimental set up parameters for Detonation diffraction experiments.

shot	mixture composition	P_0	T_0	img.hght.(mm)			burst	$\Delta t_{TEP}(\mu s)$			gate (ns)		f#		fil-
no.	by mol fraction	(kPa)	(K)	P	S	C	para.	P	S	C	P	C	P	C	ter
221	$0.222C_2H_6$+$0.778O_2$	42.5	297	140	150	140	-	28.6	28.4	28.6	200	200	32	16	313
222	$0.222C_2H_6$+$0.778O_2$	42.5	297	140	150	140	-	30.6	30.4	28.6	200	200	32	16	313
223	$0.222C_2H_6$+$0.778O_2$	42.5	298	140	150	140	-	33.6	33.4	28.6	200	200	32	16	313
224	$0.222C_2H_6$+$0.778O_2$	42.5	298	140	150	140	-	32.6	32.4	28.6	200	200	32	16	313
225	$0.222C_2H_6$+$0.778O_2$	42.5	297	-	-	-	-	-	-	-	0	0	0	0	-
226	$0.222C_2H_6$+$0.778O_2$	42.5	297	140	150	140	$2\times5\mu$s	28.6	28.4	28.6	200	200	32	16	313
227	$0.222C_2H_6$+$0.778O_2$	42.5	298	140	150	140	-	32.6	32.4	28.6	200	200	32	16	313
228	$0.222C_2H_6$+$0.778O_2$	42.5	298	140	150	140	$3\times2\mu$s	32.6	28.4	28.6	200	200	32	16	313
229	$0.222C_2H_6$+$0.778O_2$	42.5	298	140	150	140	$3\times3\mu$s	32.6	26.4	26.6	200	200	32	16	313

Table E.11: C_2H_6-O_2mixtures. Experimental set up parameters for Detonation diffraction experiments.

Appendix F

Mixture Parameters

F.1 H_2-O_2-Ar mixtures, pressure series

Mixture	P_0 [kPa]	U_{CJ} [m/s]	P_{CJ} [MPa]	T_{CJ} [K]	w [m/s]	P_{vN} [MPa]	T_{vN} [K]	c_{vN} [m/s]	Δ [mm]	D/Δ [-]	θ [-]
$0.333H_2+0.167O_2+0.500Ar$	45	1895.1	0.800	3265	412	1.36	1975	948	0.114	334	4.6
$0.333H_2+0.167O_2+0.500Ar$	47.5	1897.2	0.847	3273	412	1.44	1978	948	0.107	355	4.6
$0.333H_2+0.167O_2+0.500Ar$	50	1899.1	0.893	3280	413	1.52	1982	949	0.101	376	4.6
$0.333H_2+0.167O_2+0.500Ar$	52.5	1900.9	0.939	3287	413	1.60	1985	950	0.096	397	4.6
$0.333H_2+0.167O_2+0.500Ar$	53.75	1901.8	0.962	3290	413	1.64	1986	950	0.093	407	4.6
$0.333H_2+0.167O_2+0.500Ar$	55	1902.7	0.985	3294	413	1.68	1988	950	0.091	417	4.6
$0.333H_2+0.167O_2+0.500Ar$	57.5	1904.3	1.031	3300	413	1.76	1990	951	0.087	438	4.6
$0.333H_2+0.167O_2+0.500Ar$	60	1905.9	1.078	3306	414	1.84	1993	952	0.083	460	4.6
$0.333H_2+0.167O_2+0.500Ar$	62.5	1907.5	1.124	3312	414	1.92	1996	952	0.079	480	4.6
$0.333H_2+0.167O_2+0.500Ar$	65	1909.0	1.171	3318	414	2.00	1998	953	0.076	502	4.6
$0.333H_2+0.167O_2+0.500Ar$	70	1911.7	1.264	3328	414	2.16	2003	954	0.070	543	4.6
$0.333H_2+0.167O_2+0.500Ar$	100	1925.1	1.827	3380	416	3.13	2026	959	0.048	798	4.9

Table F.1:

F.2 H_2-O_2-Ar mixtures, dilution series

Mixture	P_0 [kPa]	U_{CJ} [m/s]	P_{CJ} [MPa]	T_{CJ} [K]	w [m/s]	P_{vN} [MPa]	T_{vN} [K]	c_{vN} [m/s]	Δ [mm]	D/Δ [-]	θ [-]
$0.267H_2+0.133O_2+0.600Ar$	100	1810.7	1.775	3261	411	3.02	2058	929	0.057	663	4.8
$0.240H_2+0.120O_2+0.640Ar$	100	1765.1	1.744	3199	409	2.97	2063	918	0.064	593	4.5
$0.233H_2+0.117O_2+0.650Ar$	100	1753.6	1.734	3182	409	2.95	2064	915	0.066	575	4.5
$0.230H_2+0.115O_2+0.655Ar$	100	1747.7	1.730	3173	408	2.94	2064	913	0.067	566	4.8
$0.227H_2+0.113O_2+0.660Ar$	100	1741.9	1.724	3164	408	2.94	2064	912	0.068	556	4.5
$0.223H_2+0.112O_2+0.665Ar$	100	1736.0	1.719	3154	408	2.93	2063	910	0.070	546	4.5
$0.220H_2+0.110O_2+0.670Ar$	100	1730.1	1.714	3144	408	2.92	2063	909	0.071	537	4.6
$0.217H_2+0.108O_2+0.675Ar$	100	1724.1	1.708	3134	407	2.91	2062	907	0.072	527	4.5
$0.213H_2+0.107O_2+0.680Ar$	100	1718.1	1.702	3124	407	2.90	2062	906	0.074	516	4.5
$0.200H_2+0.100O_2+0.700Ar$	100	1693.6	1.677	3080	406	2.86	2057	899	0.080	473	4.5
$0.187H_2+0.093O_2+0.720Ar$	100	1668.1	1.647	3029	405	2.81	2049	892	0.089	429	4.9
$0.182H_2+0.091O_2+0.727Ar$	100	1658.5	1.635	3009	404	2.80	2045	890	0.092	413	4.9
$0.173H_2+0.087O_2+0.740Ar$	100	1641.2	1.612	2972	404	2.76	2037	885	0.099	383	4.9
$0.167H_2+0.083O_2+0.750Ar$	100	1627.0	1.592	2940	403	2.73	2029	881	0.106	360	4.9
$0.160H_2+0.080O_2+0.760Ar$	100	1612.3	1.571	2905	402	2.70	2019	876	0.113	336	4.9

Table F.2:

F.3 H_2-O_2-N_2 mixtures

Mixture	P_0 [kPa]	U_{CJ} [m/s]	P_{CJ} [MPa]	T_{CJ} [K]	w [m/s]	P_{vN} [MPa]	T_{vN} [K]	c_{vN} [m/s]	Δ [mm]	D/Δ [-]	θ [-]
$0.540H_2+0.270O_2+0.190N_2$	100	2489.6	1.802	3511	449	3.17	1714	1116	0.070	543	6.8
$0.527H_2+0.263O_2+0.210N_2$	100	2458.5	1.794	3491	444	3.15	1708	1102	0.072	528	6.8
$0.520H_2+0.260O_2+0.220N_2$	100	2443.0	1.790	3481	441	3.14	1704	1096	0.074	514	6.9
$0.507H_2+0.253O_2+0.240N_2$	100	2412.7	1.782	3460	436	3.13	1698	1082	0.077	494	6.9
$0.500H_2+0.250O_2+0.250N_2$	100	2397.6	1.777	3449	434	3.12	1695	1076	0.078	487	6.9

Table F.3:

F.4 H_2-N_2O mixtures

Mixture	P_0 [kPa]	U_{CJ} [m/s]	P_{CJ} [MPa]	T_{CJ} [K]	w [m/s]	P_{vN} [MPa]	T_{vN} [K]	c_{vN} [m/s]	Δ [mm]	D/Δ [-]	θ [-]
$0.500H_2+0.500N_2O$	40	2353.4	0.975	3478	309	1.82	1789	887	0.178	213	9.4
$0.500H_2+0.500N_2O$	42.5	2356.0	1.038	3488	309	1.93	1792	888	0.168	226	9.4
$0.500H_2+0.500N_2O$	43.75	2357.3	1.070	3492	310	1.99	1794	888	0.164	232	9.4
$0.500H_2+0.500N_2O$	45	2358.5	1.102	3497	310	2.05	1795	889	0.160	238	9.4
$0.500H_2+0.500N_2O$	46.25	2359.7	1.133	3501	310	2.11	1796	889	0.155	245	9.4
$0.500H_2+0.500N_2O$	47.5	2360.8	1.165	3506	310	2.17	1798	889	0.152	250	9.4
$0.500H_2+0.500N_2O$	50	2363.1	1.228	3514	310	2.29	1800	890	0.145	262	9.5
$0.500H_2+0.500N_2O$	55	2367.2	1.355	3529	310	2.53	1805	891	0.133	286	9.5
$0.500H_2+0.500N_2O$	60	2371.0	1.483	3543	310	2.77	1810	892	0.122	311	9.5
$0.500H_2+0.500N_2O$	65	2374.4	1.611	3557	311	3.00	1814	893	0.114	333	9.5
$0.500H_2+0.500N_2O$	70	2377.6	1.739	3569	311	3.24	1817	894	0.107	355	9.6
$0.500H_2+0.500N_2O$	80	2383.4	1.996	3591	311	3.73	1824	896	0.095	400	9.6

Table F.4:

F.5 CH_4-O_2 mixtures

Mixture	P_0 [kPa]	U_{CJ} [m/s]	P_{CJ} [MPa]	T_{CJ} [K]	w [m/s]	P_{vN} [MPa]	T_{vN} [K]	c_{vN} [m/s]	Δ [mm]	D/Δ [-]	θ [-]
$0.333CH_4+0.667O_2$	50	2361.6	1.426	3598	274	2.69	1872	828	0.436	87	11.0
$0.333CH_4+0.667O_2$	55	2365.8	1.573	3615	274	2.97	1877	829	0.391	97	11.0
$0.333CH_4+0.667O_2$	60	2369.7	1.722	3630	275	3.25	1881	830	0.354	107	11.0
$0.333CH_4+0.667O_2$	65	2373.3	1.870	3645	275	3.53	1885	830	0.323	118	10.9
$0.333CH_4+0.667O_2$	70	2376.6	2.019	3658	275	3.81	1889	831	0.297	128	10.9
$0.333CH_4+0.667O_2$	80	2382.6	2.318	3683	275	4.38	1896	833	0.255	149	10.8
$0.333CH_4+0.667O_2$	90	2387.8	2.619	3705	275	4.95	1901	834	0.224	170	10.7
$0.333CH_4+0.667O_2$	100	2392.6	2.920	3724	276	5.52	1907	835	0.198	192	10.7
$0.333CH_4+0.667O_2$	110	2396.8	3.223	3742	276	6.09	1912	836	0.178	213	10.6
$0.333CH_4+0.667O_2$	115	2398.8	3.374	3750	276	6.38	1914	837	0.169	225	10.6
$0.333CH_4+0.667O_2$	120	2400.7	3.526	3758	276	6.67	1916	837	0.162	235	10.6
$0.333CH_4+0.667O_2$	125	2402.5	3.678	3766	276	6.96	1918	838	0.154	247	10.5

Table F.5:

F.6 C_2H_6-O_2 mixtures

Mixture	P_0 [kPa]	U_{CJ} [m/s]	P_{CJ} [MPa]	T_{CJ} [K]	w [m/s]	P_{vN} [MPa]	T_{vN} [K]	c_{vN} [m/s]	Δ [mm]	D/Δ [-]	θ [-]
$0.222C_2H_6+0.778O_2$	30	2317.4	0.972	3574	233	1.86	1871	753	0.131	290	10.1
$0.222C_2H_6+0.778O_2$	32.5	2321.0	1.056	3588	233	2.03	1875	754	0.122	311	10.1
$0.222C_2H_6+0.778O_2$	35	2324.3	1.141	3602	233	2.19	1879	754	0.114	333	10.2
$0.222C_2H_6+0.778O_2$	36.25	2325.9	1.183	3608	233	2.27	1880	755	0.110	345	10.2
$0.222C_2H_6+0.778O_2$	37.5	2327.4	1.225	3614	233	2.35	1882	755	0.107	355	10.2
$0.222C_2H_6+0.778O_2$	38.25	2328.3	1.251	3618	233	2.40	1883	755	0.105	362	10.2
$0.222C_2H_6+0.778O_2$	40	2330.3	1.310	3626	233	2.51	1885	756	0.100	380	10.2
$0.222C_2H_6+0.778O_2$	42.5	2333.1	1.395	3637	233	2.68	1889	756	0.095	400	10.2
$0.222C_2H_6+0.778O_2$	45	2335.6	1.480	3648	233	2.84	1891	757	0.090	422	10.3

Table F.6:

Appendix G

Plots of Mixture Parameters

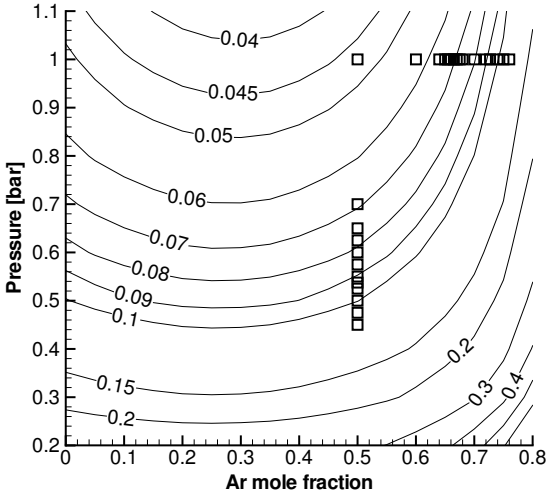

Figure G.1: $2H_2+O_2+\beta Ar$; Induction zone length [mm], Warnatz mechanism.

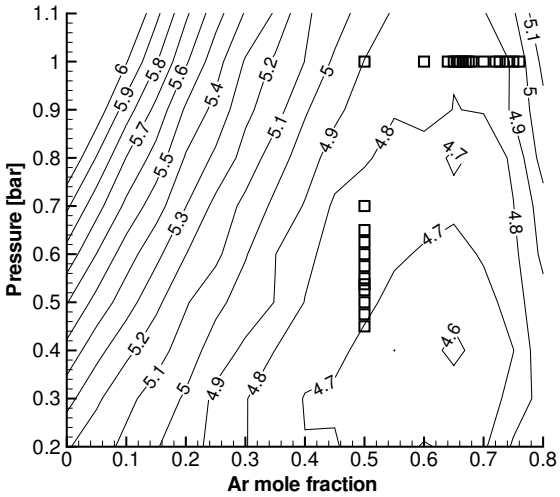

Figure G.2: $2H_2+O_2+\beta Ar$; Effective activation energy, Warnatz mechanism.

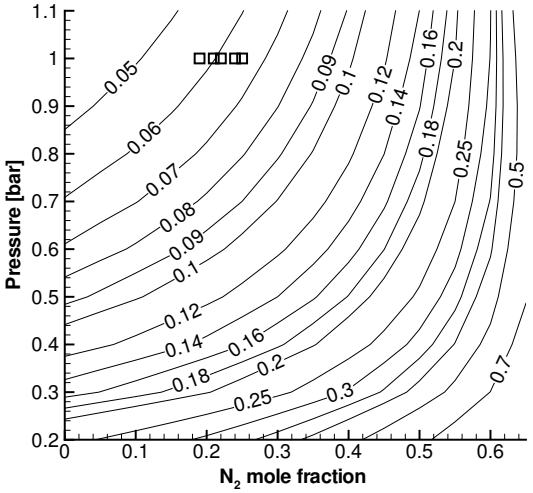

Figure G.3: $2H_2+O_2+\beta N_2$; Induction zone length [mm], Konnov mechanism

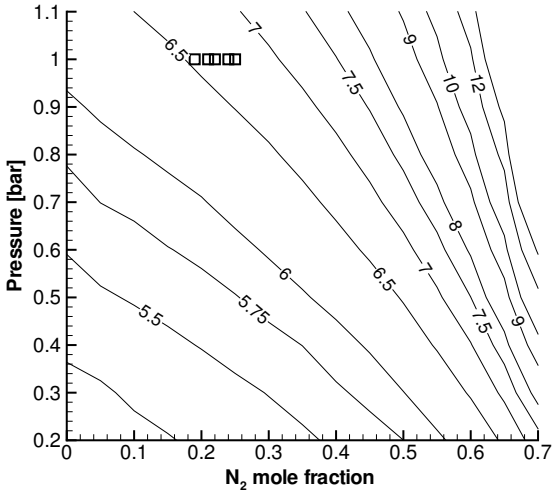

Figure G.4: $2H_2+O_2+\beta N_2$; Effective activation energy, Konnov mechanism.

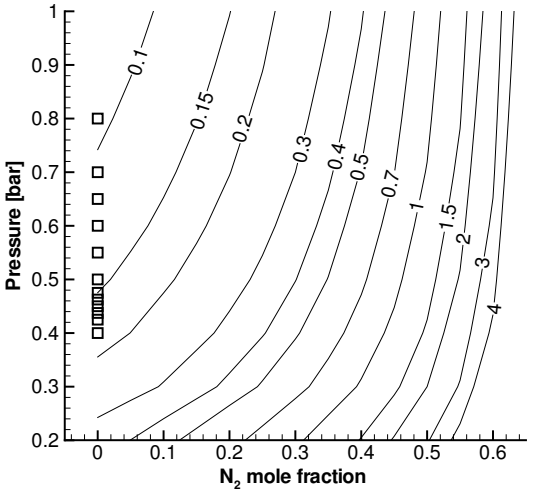

Figure G.5: $H_2+N_2O+\beta N_2$; Induction zone length [mm], Mueller mechanism

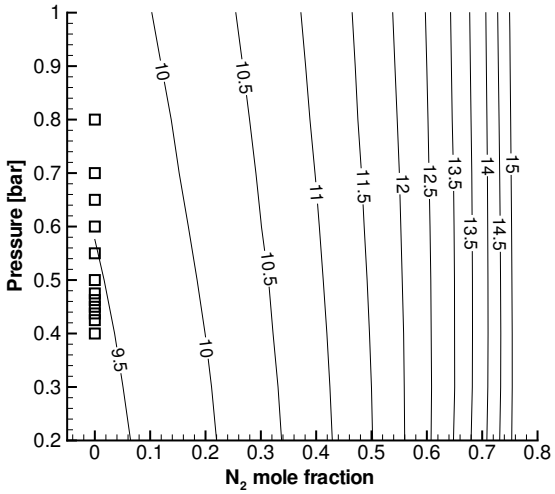

Figure G.6: $H_2+N_2O+\beta N_2$; Effective activation energy, Mueller mechanism.

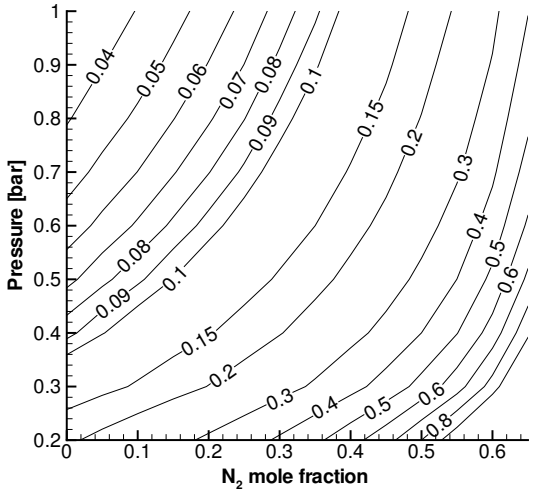

Figure G.7: $C_2H_4+3O_2+\beta N_2$; Induction zone length [mm], Konnov mechanism

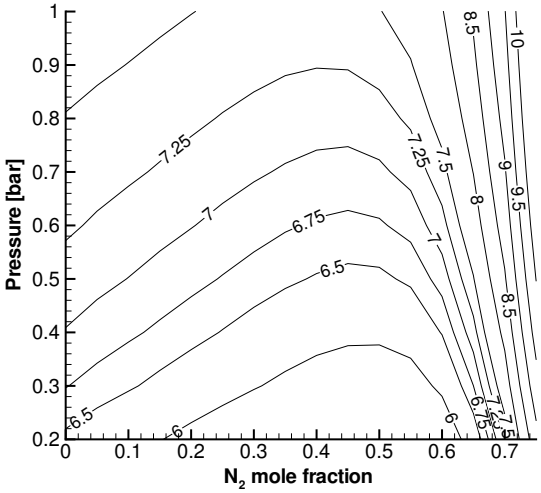

Figure G.8: $C_2H_4+3O_2+\beta N_2$; Effective activation energy, Konnov mechanism.

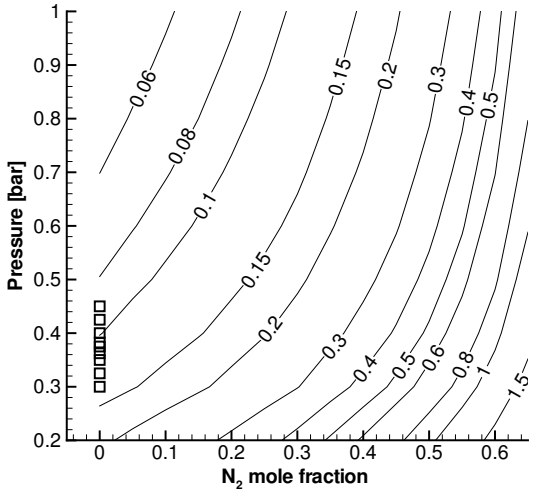

Figure G.9: $C_2H_6+3.5O_2+\beta N_2$; Induction zone length [mm], Konnov mechanism

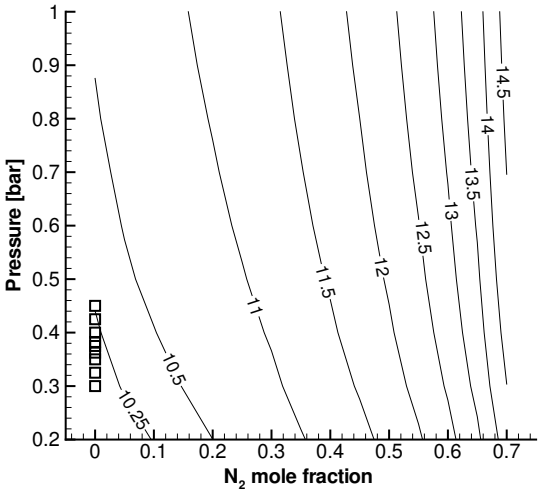

Figure G.10: $C_2H_6+3.5O_2+\beta N_2$; Effective activation energy, Konnov mechanism.

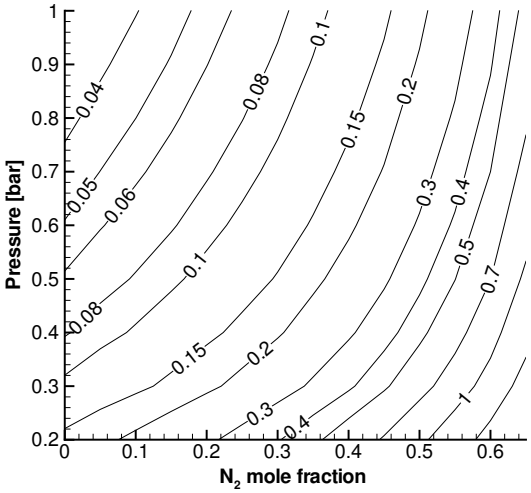

Figure G.11: $C_3H_8+5O_2+\beta N_2$; Induction zone length [mm], Konnov mechanism

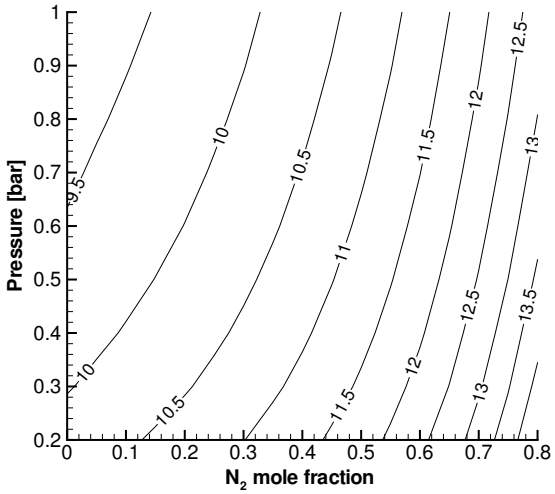

Figure G.12: $C_3H_8+5O_2+\beta N_2$; Effective activation energy, Konnov mechanism.

Appendix H

Mixture Regime Documentation

Contour plots of induction zone length Δ and reduced activation energy θ for all mixtures investigated experimentally. Open square symmbols represents the conditions of experiments. Multiple experiments are contucted for identical conditions, so the number of squares does not reflect the number of experiments.

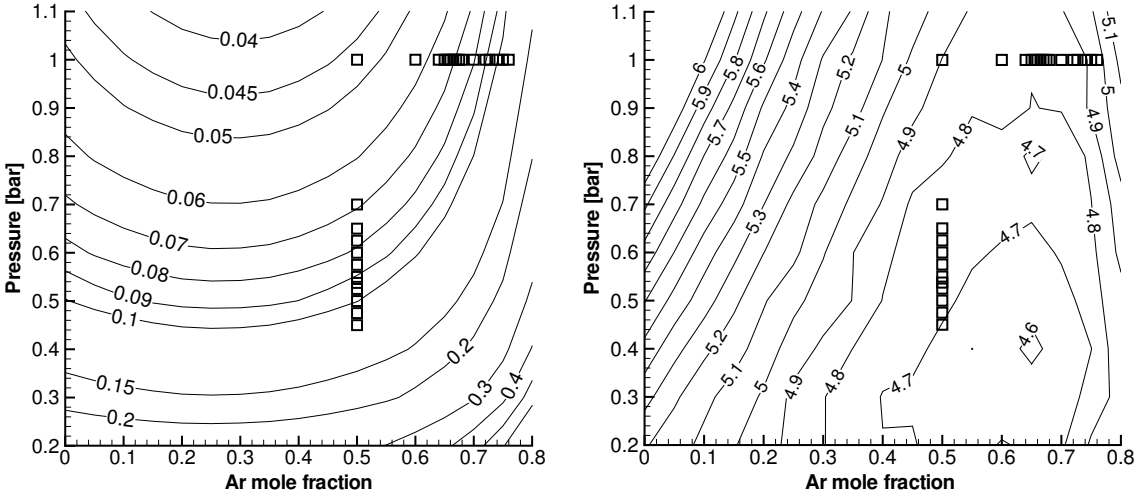

a) Δ [mm] b) θ

Figure H.1: $2H_2+O_2+\beta$AR, Warnatz mechnism. a) Induction zone length Δ [mm]. b) Reduced activation energy θ.

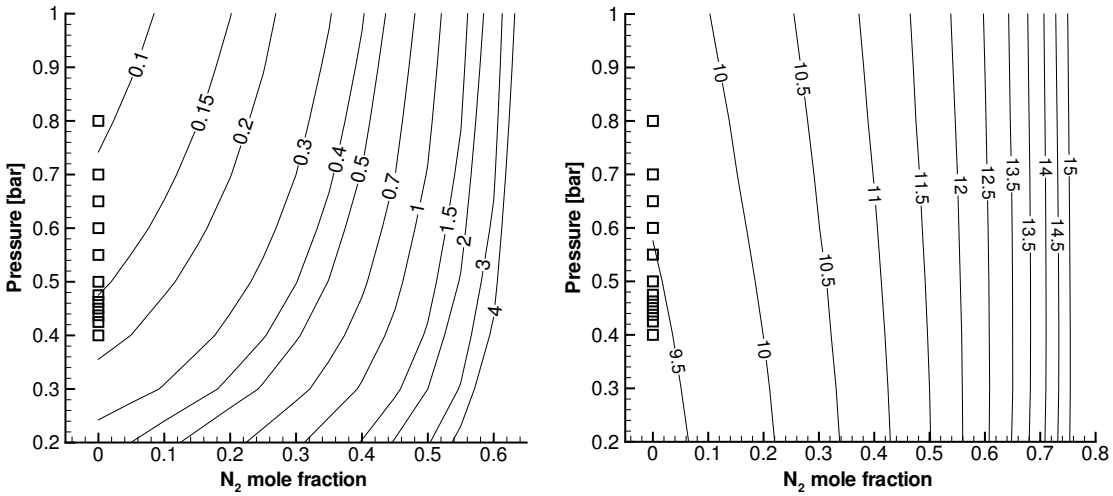

a) Δ [mm] b) θ

Figure H.2: H_2+N_2O+βN_2, Mueller mechnism. a) Induction zone length Δ [mm]. b) Reduced activation energy θ.

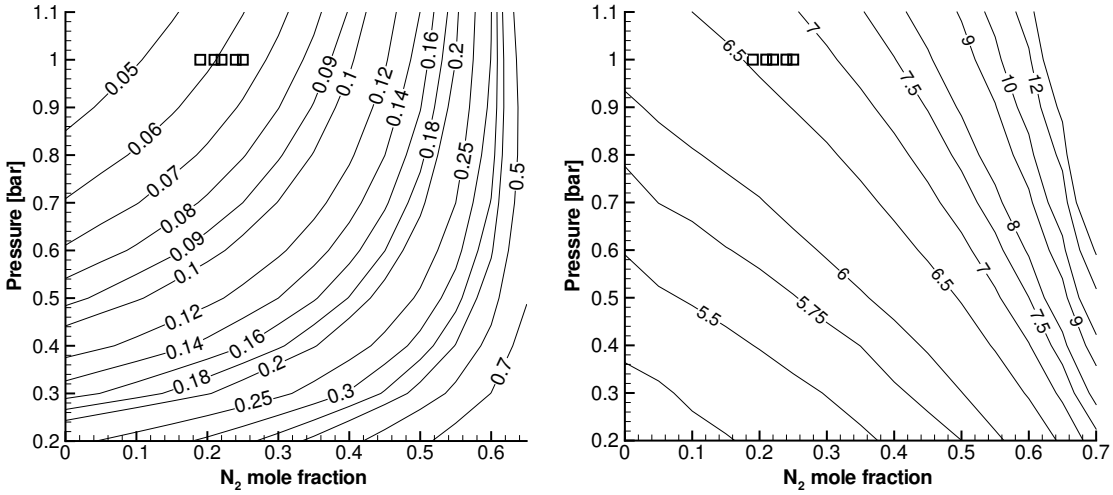

a) Δ [mm] b) θ

Figure H.3: $2H_2$+O_2+βN_2, Konnov mechnism. a) Induction zone length Δ [mm]. b) Reduced activation energy θ.

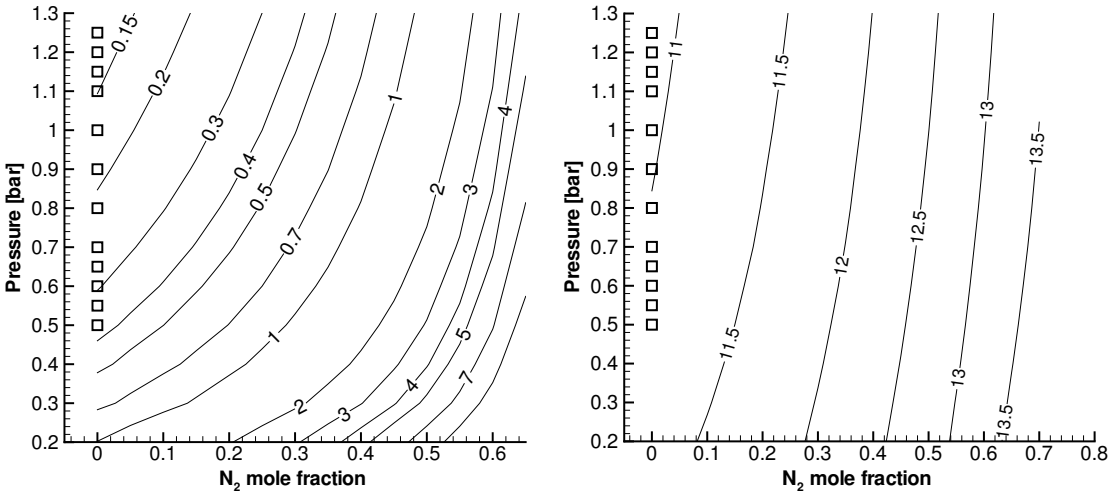

a) Δ [mm] b) θ

Figure H.4: CH_4+2O_2+βN_2, GRI mechnism. a) Induction zone length Δ [mm]. b) Reduced activation energy θ.

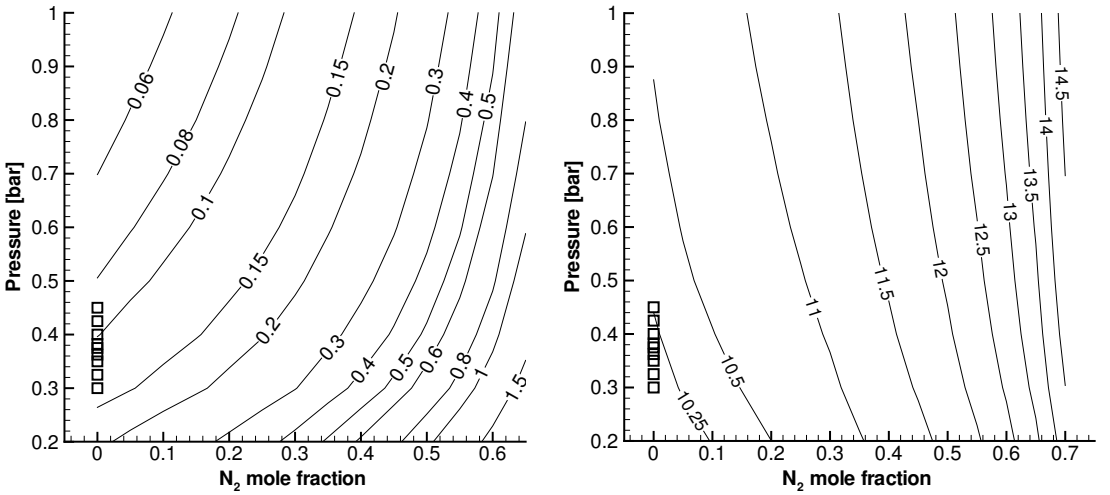

a) Δ [mm] b) θ

Figure H.5: C_2H_6+3.5O_2+βN_2, GRI mechnism. a) Induction zone length Δ [mm]. b) Reduced activation energy θ.

Appendix I

Maximum Pressure

The maximum pressure P_{max} plotted below, was derived from the pressure histories of pressure transducers P_4, P_5 and P_6, all located in the test section. The pressure P_{max} is defined as the largest pressure within 100 μs after the first pressure rise and is not the over all maximum pressure.

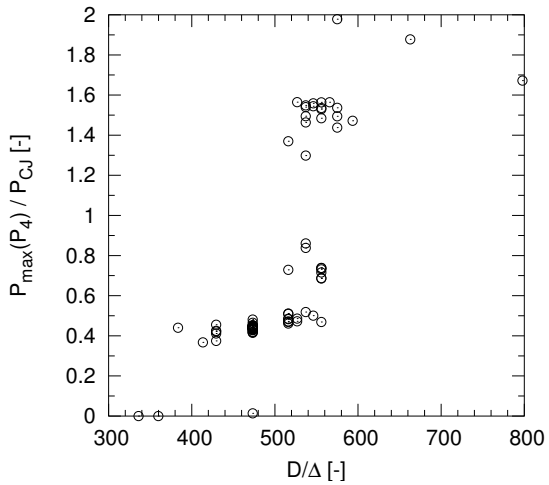

Figure I.1: Maximum pressure at P_4, Ar dilution series.

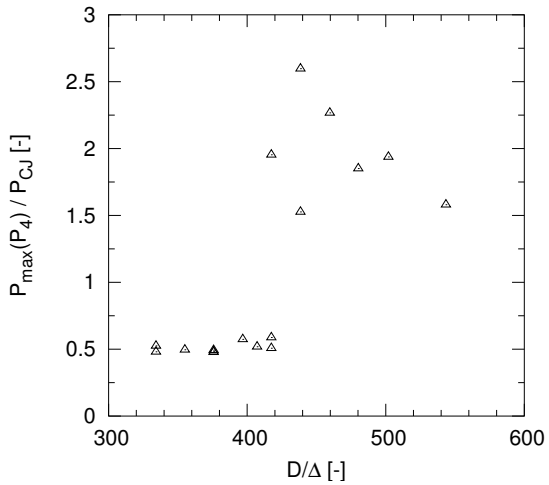

Figure I.2: Maximum pressure at P_4, Ar pressure series.

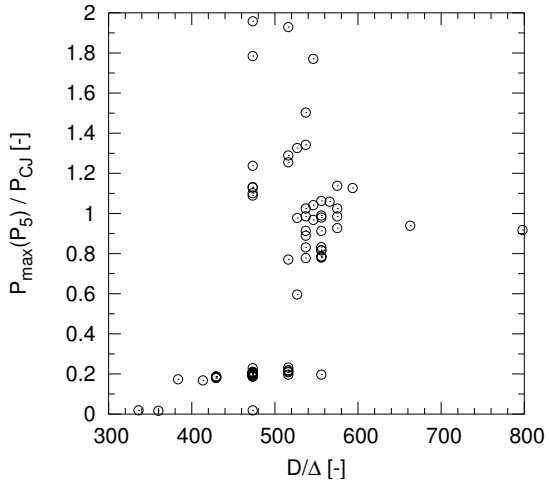

Figure I.3: Maximum pressure at P_5, Ar dilution series.

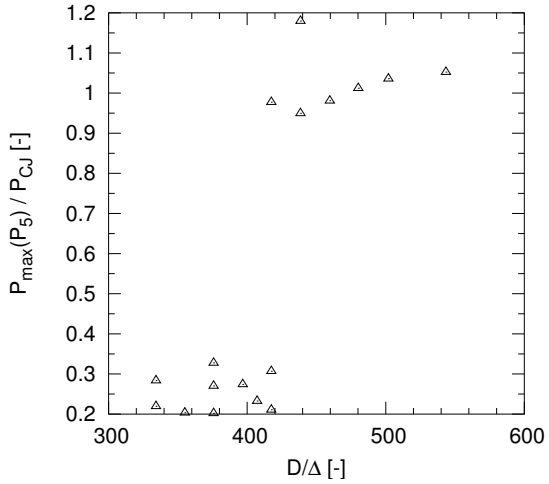

Figure I.4: Maximum pressure at P_5, Ar pressure series.

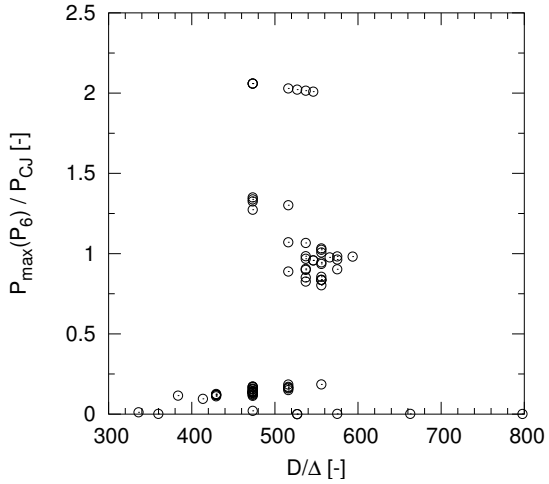

Figure I.5: Maximum pressure at P_6, Ar dilution series.

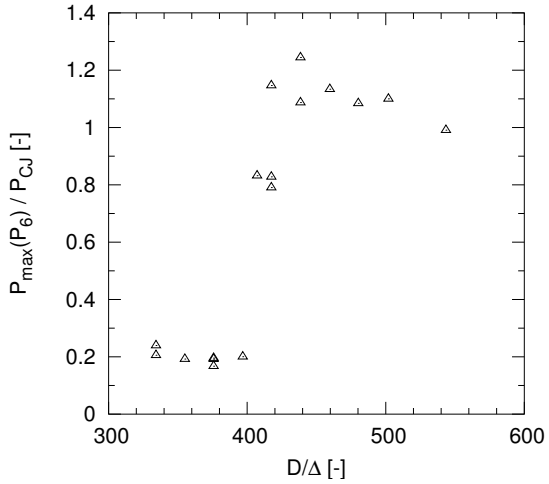

Figure I.6: Maximum pressure at P_6, Ar pressure series.

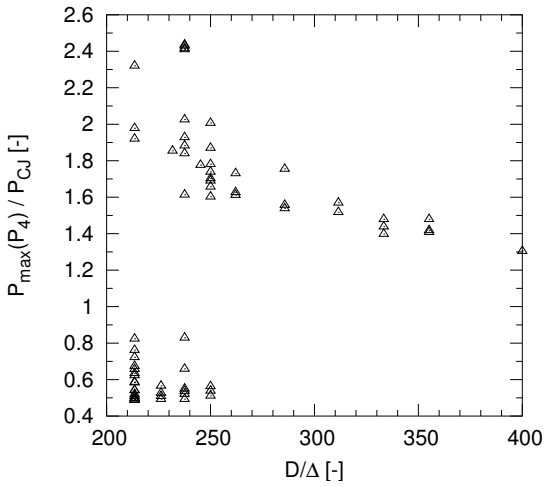

Figure I.7: Maximum pressure at P_4, N_2O series.

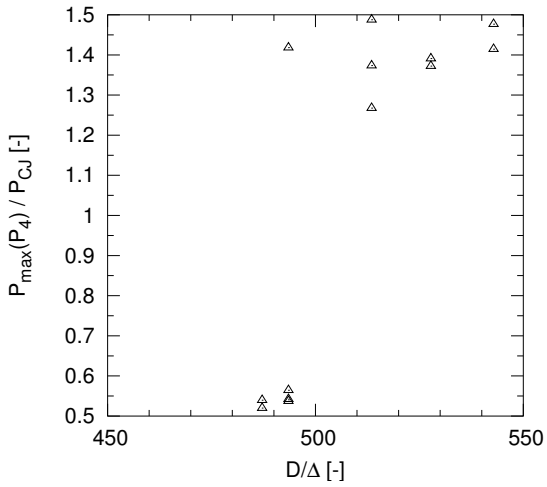

Figure I.8: Maximum pressure at P_4, N_2 series.

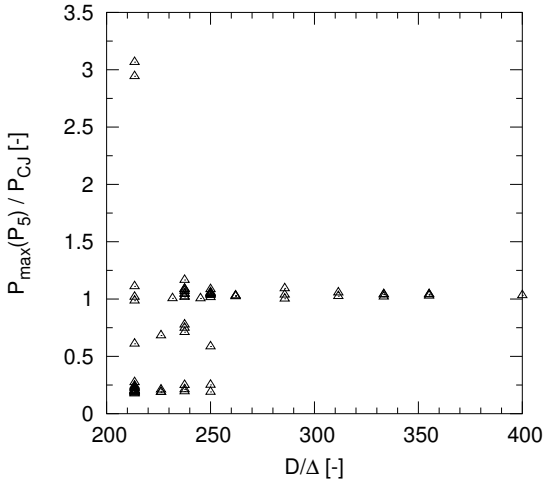

Figure I.9: Maximum pressure at P_5, N_2O series.

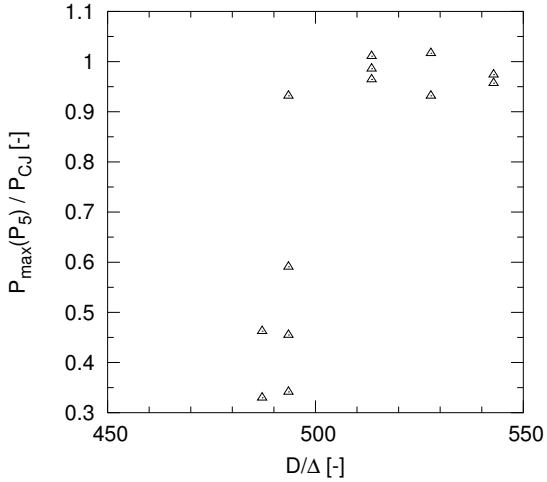

Figure I.10: Maximum pressure at P_5, N_2 series.

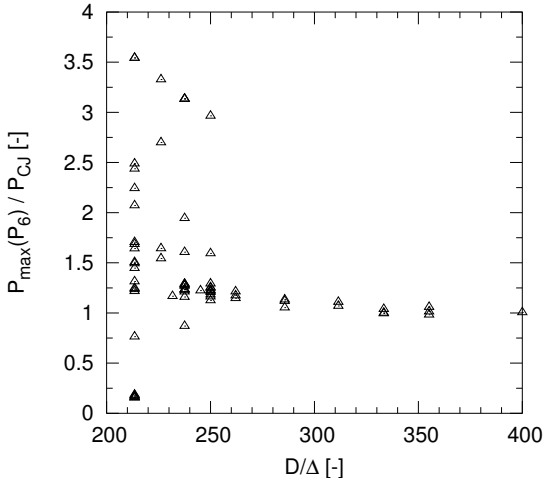

Figure I.11: Maximum pressure at P_6, N_2O series.

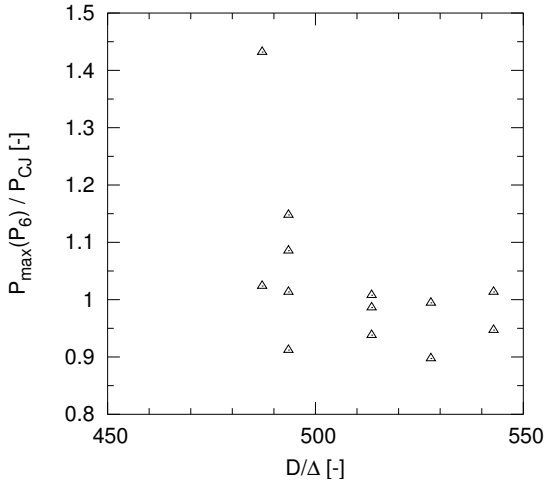

Figure I.12: Maximum pressure at P_6, N_2 series.

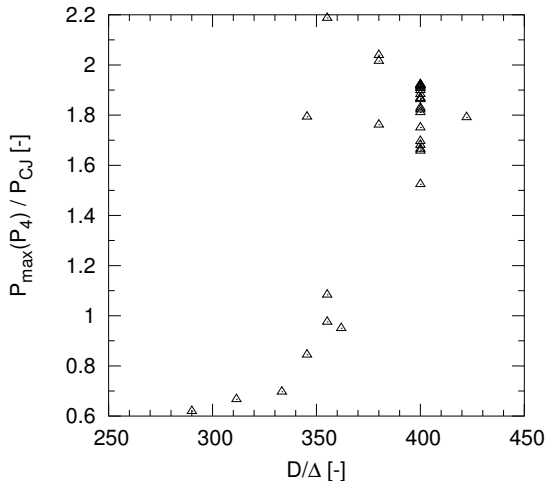

Figure I.13: Maximum pressure at P_4, C_2H_6 series.

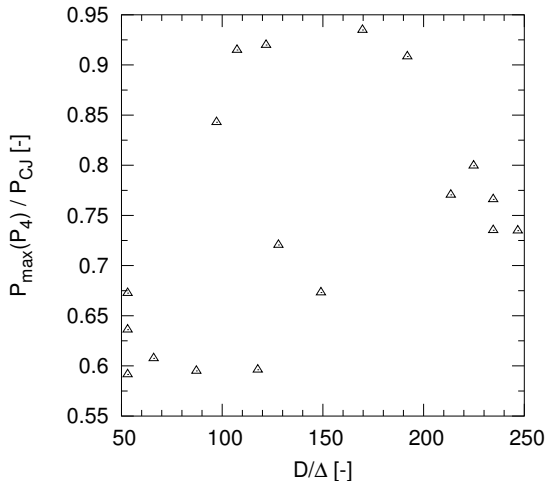

Figure I.14: Maximum pressure at P_4, CH_4 series.

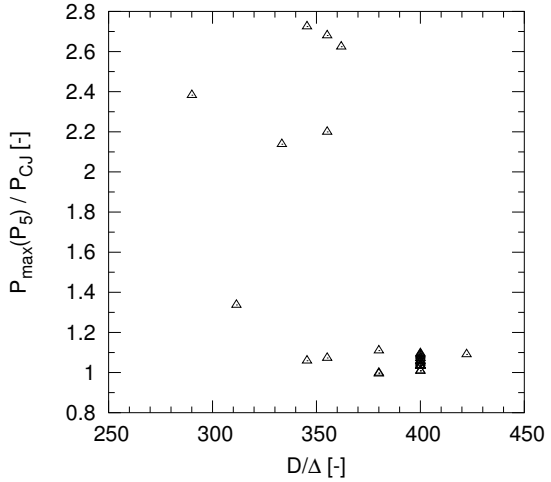

Figure I.15: Maximum pressure at P_5, C_2H_6 series.

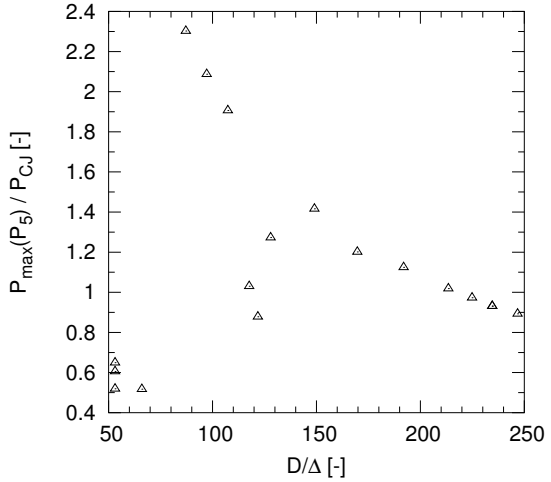

Figure I.16: Maximum pressure at P_5, CH_4 series.

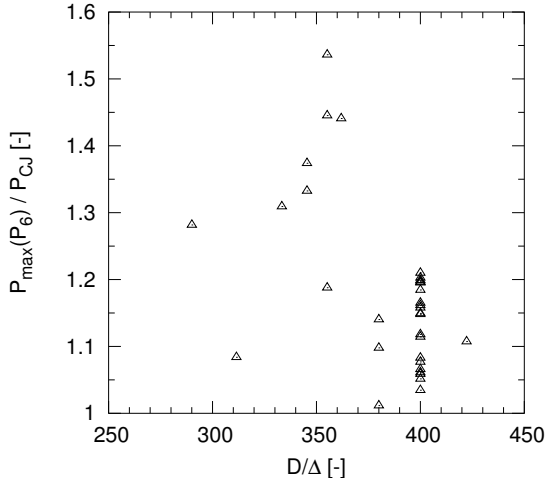

Figure I.17: Maximum pressure at P_6, C_2H_6 series.

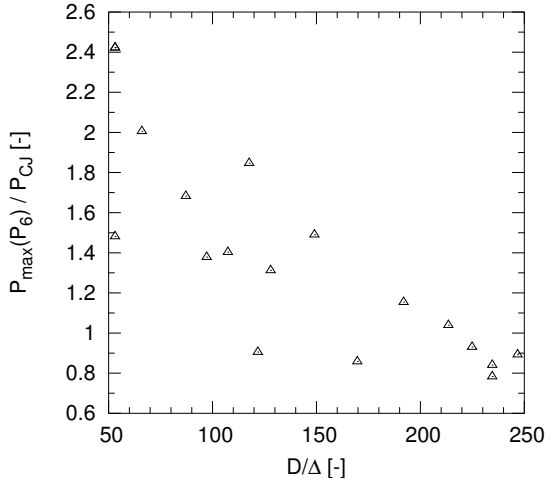

Figure I.18: Maximum pressure at P_6, CH_4 series.

Appendix J

Corner Signal Propagation

The distance x_c from the tube exit plane to the point at which the acoustic signal of the corner disturbance reaches the tube axis is here calculated for the diameter tube D =38 mm as in the experiment. The disturbance propagation angle α can be calculated from that via $2\tan\alpha = D/x_c$. The distance x_c was calculated in two ways as described in Chapter 5:

- Using the post shock (von Neumann) conditions at CJ conditions. In the plots labeled as "post shock".
- Using the conditions at that distance behind the shock, which lead to the minimum distance x_c, as calculated from a one dimensional ZND profile of the detonation front at CJ conditions. In the plots these data-points are labeled as "minimum".

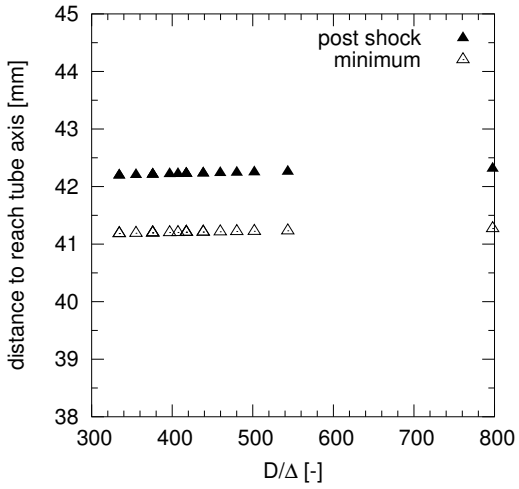

Figure J.1: Corner disturbance signal. Ar pressure series.

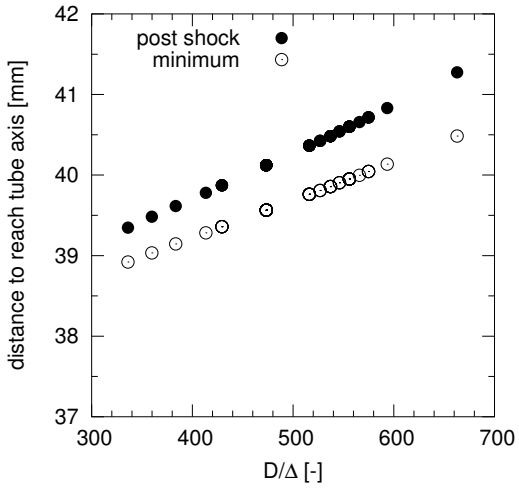

Figure J.2: Corner disturbance signal. Ar dilution series.

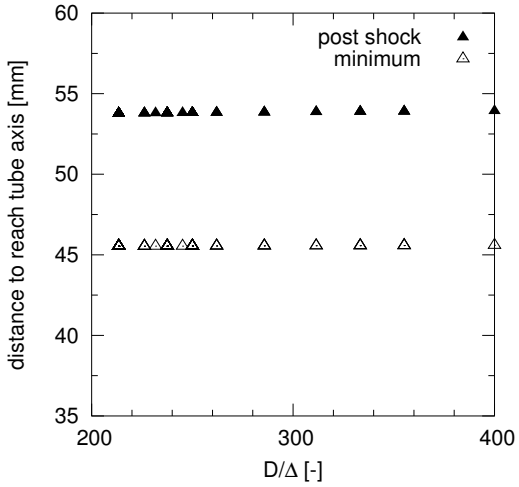

Figure J.3: Corner disturbance signal. N_2O series.

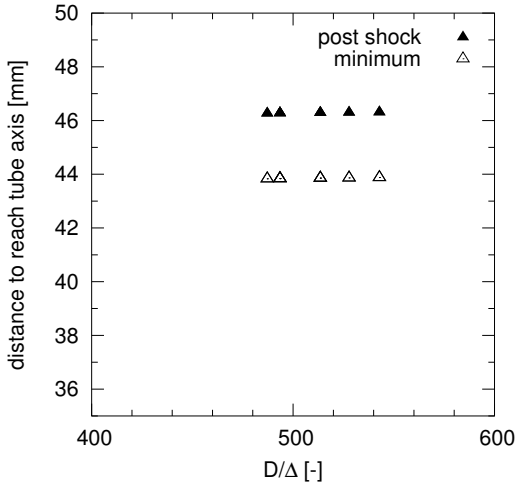

Figure J.4: Corner disturbance signal. N_2 series.

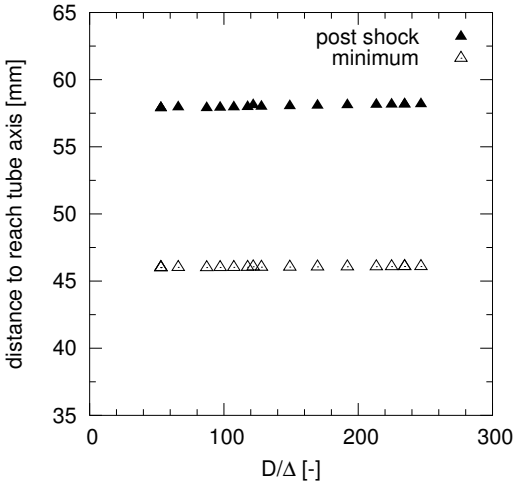

Figure J.5: Corner disturbance signal. CH_4 series.

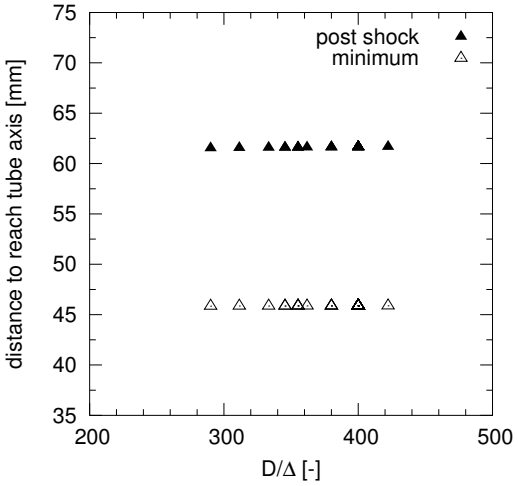

Figure J.6: Corner disturbance signal. C_2H_6 series.

Appendix K

Pressure Traces from Detonation Diffraction Experiments

In this Chapter the pressure traces of the detonation diffraction experiments are shown. Six PCB 113A26 piezoelectric pressure transducers were mounted in the top side of the detonation tube and test section. The position of the pressure transducers with respect to the spark plug position are given in Table K.1. Transducer P1, P2 and P3 are in the detonation tube. Transducer P4, P5 and P6 are in the test-section, Fig. 2.3. The apparent pressure spikes seen in some pressure histories are erratic and caused by loose pressure transducer cables, e.g. shot 108, P2, at 2.2 ms.

transducer number	location (m)		
	shot 1–54	shot 55–61	shot 62–228
P1	0.400	0.400	0.400
P2	0.800	0.800	0.800
P3	1.200	1.200	1.200
P4	1.540	1.510	1.500
P5	1.754	1.724	1.714
P6	2.015	1.975	1.965

Table K.1: Position of the pressure transducers with respect to the spark-plug. Since the test section location was varied with respect to the detonation tube the location of pressure transducers P4, P5 and P6 depends on the shot number.

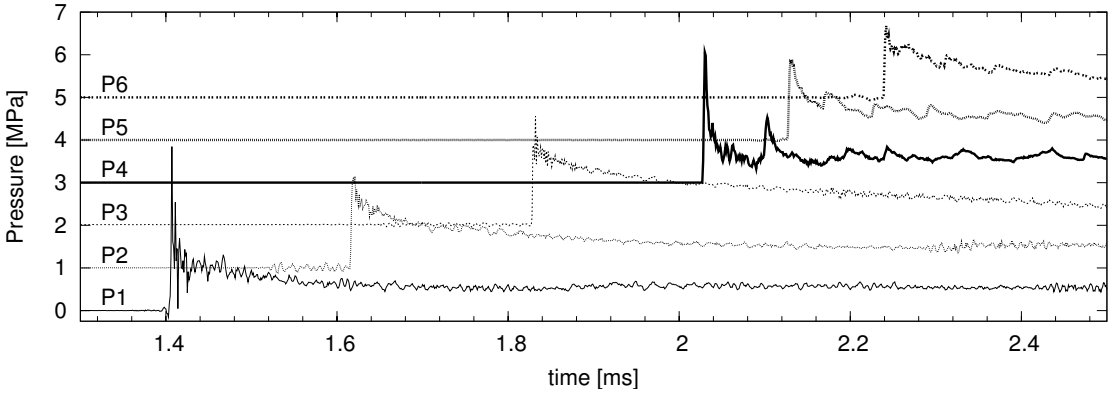

Figure K.1: Shot 1, 0.333 H_2 + 0.167 O_2 + 0.5 Ar, P_0=100 kPa, T_0=295 K. U(P_1-P_2)/U_{CJ} = 0.985, U(P_2-P_3)/U_{CJ} = 0.980.

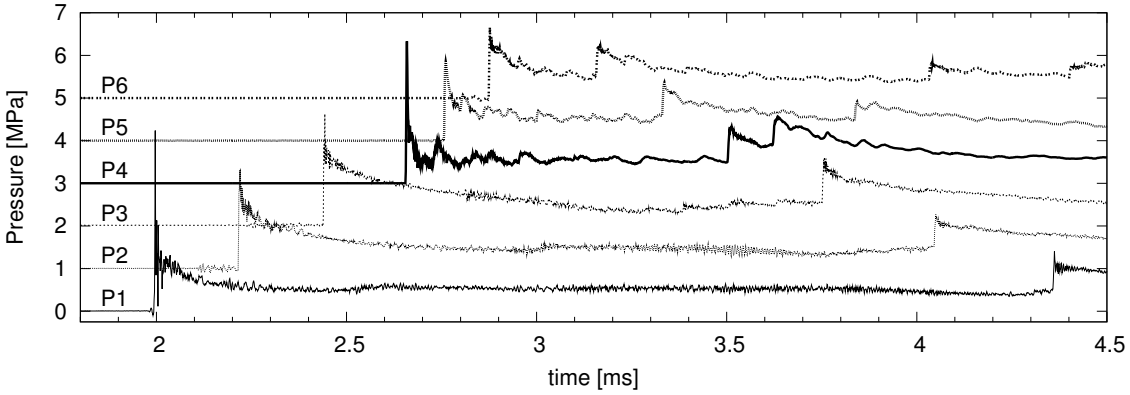

Figure K.2: Shot 2, 0.267 H_2 + 0.133 O_2 + 0.6 Ar, P_0=100 kPa, T_0=295 K. U(P_1-P_2)/U_{CJ} = 1.000, U(P_2-P_3)/U_{CJ} = 0.991.

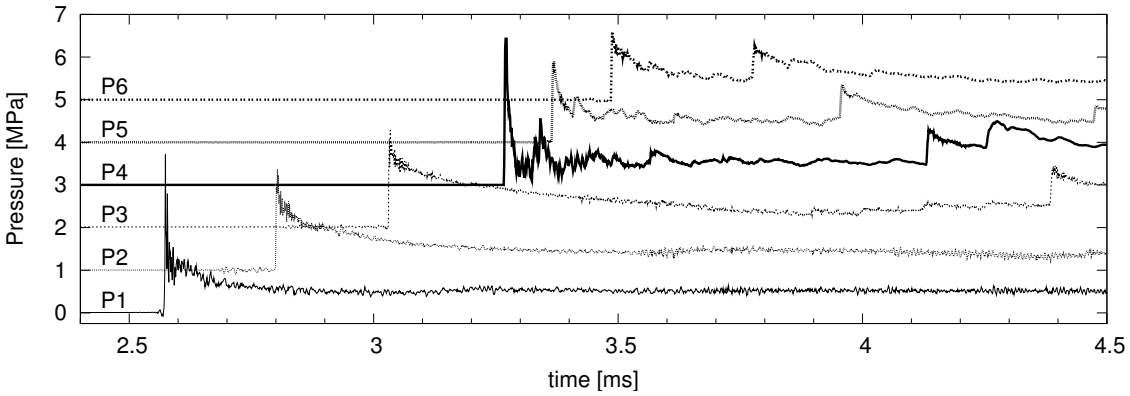

Figure K.3: Shot 3, 0.233 H_2 + 0.117 O_2 + 0.65 Ar, P_0=100 kPa, T_0=295 K. U(P_1-P_2)/U_{CJ} = 0.996, U(P_2-P_3)/U_{CJ} = 0.988.

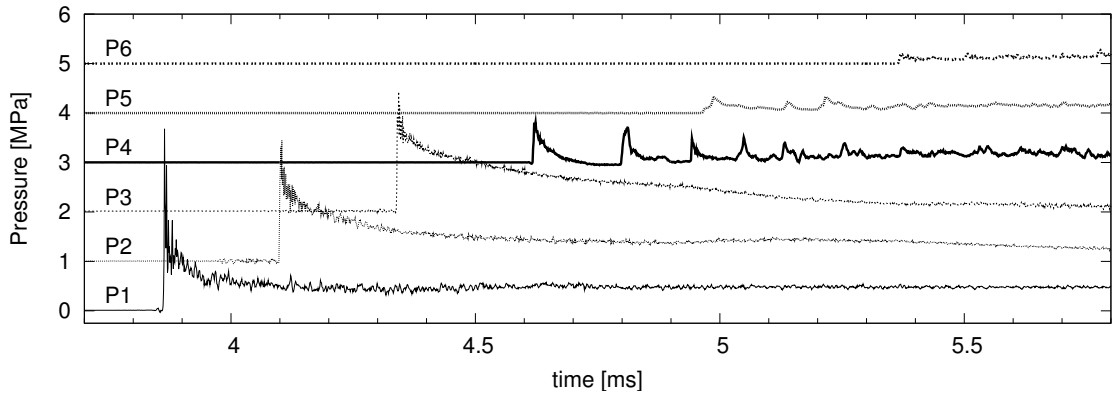

Figure K.4: Shot 4, 0.2 H_2 + 0.1 O_2 + 0.7 Ar, P_0=100 kPa, T_0=295 K. U(P_1-P_2)/U_{CJ} = 0.992, U(P_2-P_3)/U_{CJ} = 0.984.

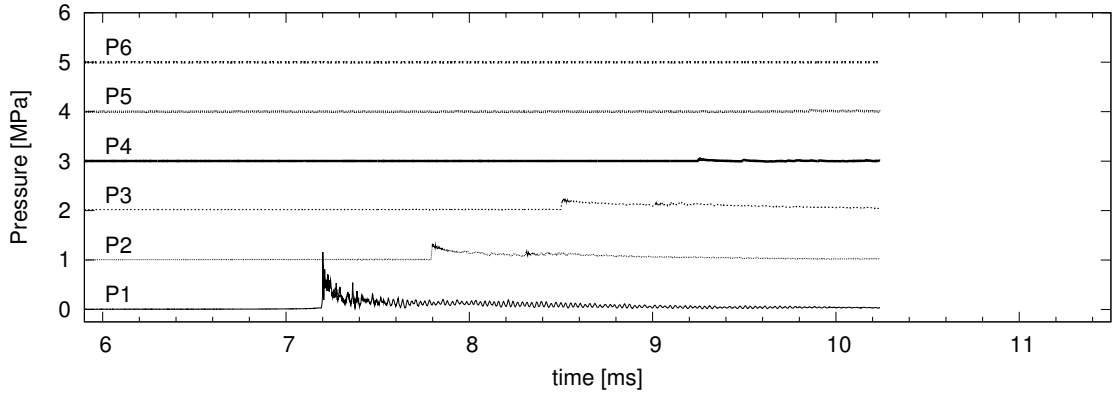

Figure K.5: Shot 5, 0.167 H_2 + 0.083 O_2 + 0.75 Ar, P_0=100 kPa, T_0=295 K. U(P_1-P_2)/U_{CJ} = 0.411, U(P_2-P_3)/U_{CJ} = 0.347.

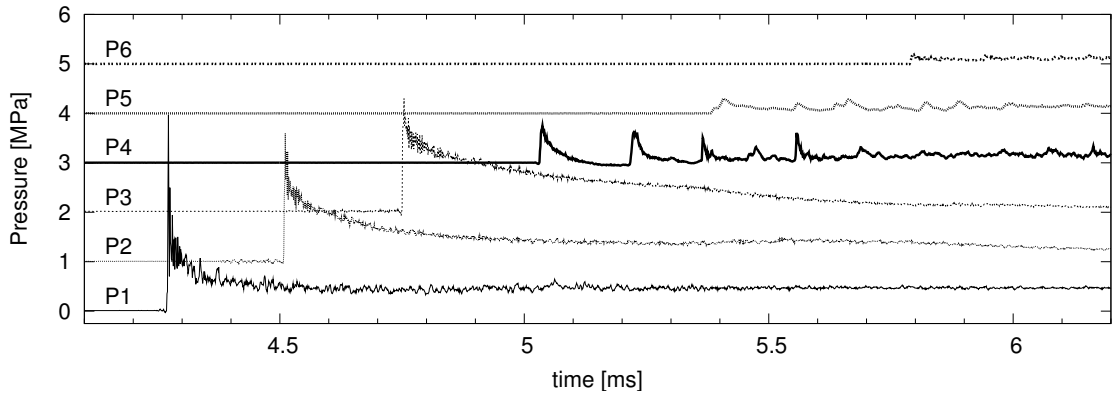

Figure K.6: Shot 6, 0.187 H_2 + 0.093 O_2 + 0.72 Ar, P_0=100 kPa, T_0=295 K. U(P_1-P_2)/U_{CJ} = 1.003, U(P_2-P_3)/U_{CJ} = 0.987.

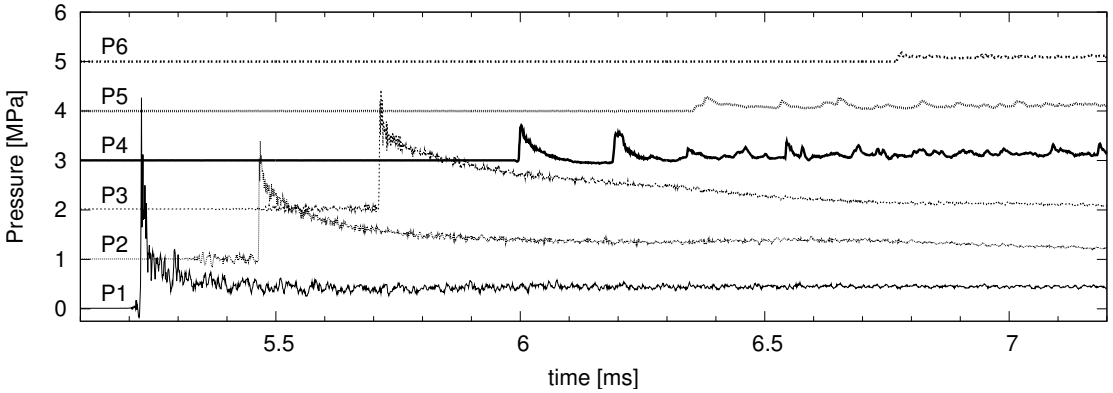

Figure K.7: Shot 7, 0.173 H_2 + 0.087 O_2 + 0.74 Ar, P_0=100 kPa, T_0=295 K. U(P_1-P_2)/U_{CJ} = 1.007, U(P_2-P_3)/U_{CJ} = 0.991.

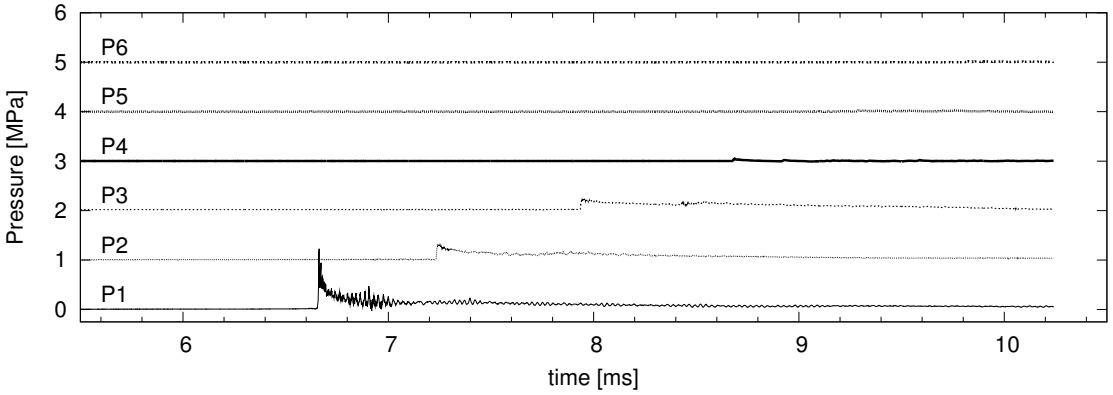

Figure K.8: Shot 8, 0.16 H_2 + 0.08 O_2 + 0.76 Ar, P_0=100 kPa, T_0=295 K. U(P_1-P_2)/U_{CJ} = 0.429, U(P_2-P_3)/U_{CJ} = 0.352.

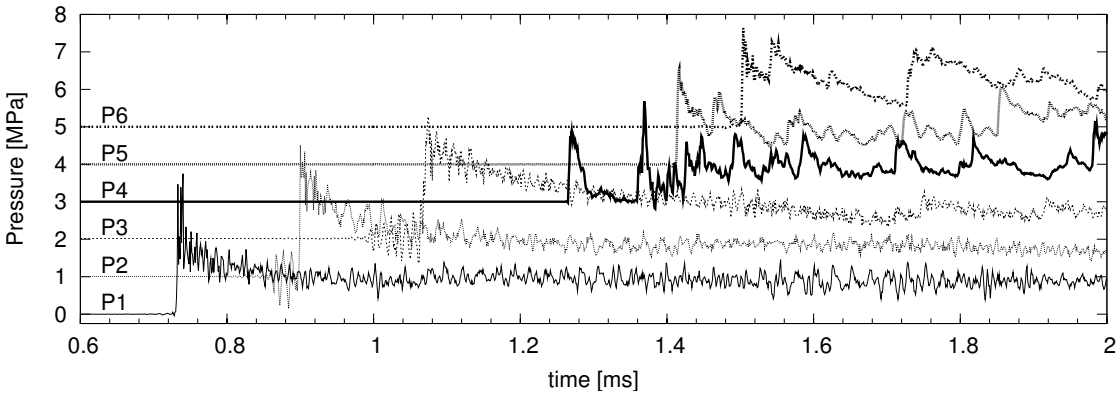

Figure K.9: Shot 9, 0.333 CH_4 + 0.667 O_2, P_0=100 kPa, T_0=295 K. U(P_1-P_2)/U_{CJ} = 1.001, U(P_2-P_3)/U_{CJ} = 1.013.

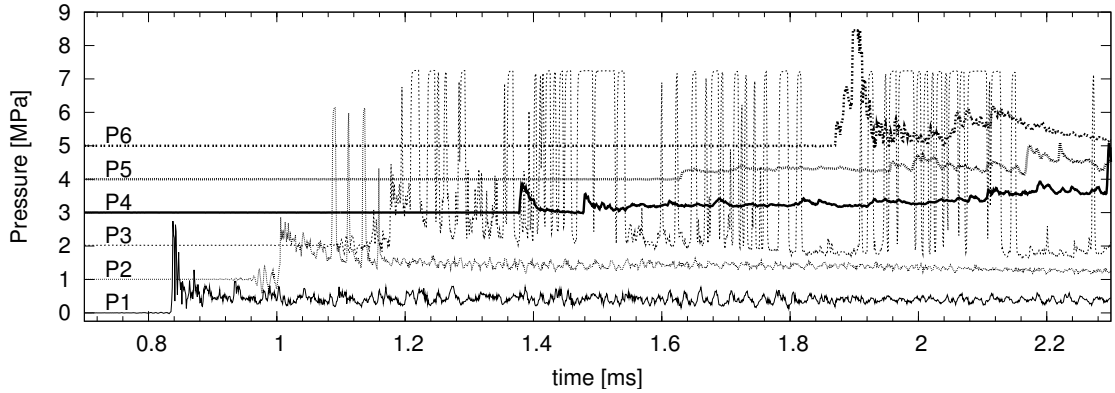

Figure K.10: Shot 10, 0.333 CH_4 + 0.667 O_2, P_0=50 kPa, T_0=294 K. $U(P_1\text{-}P_2)/U_{CJ}$ = 1.008, $U(P_2\text{-}P_3)/U_{CJ}$ = 1.168.

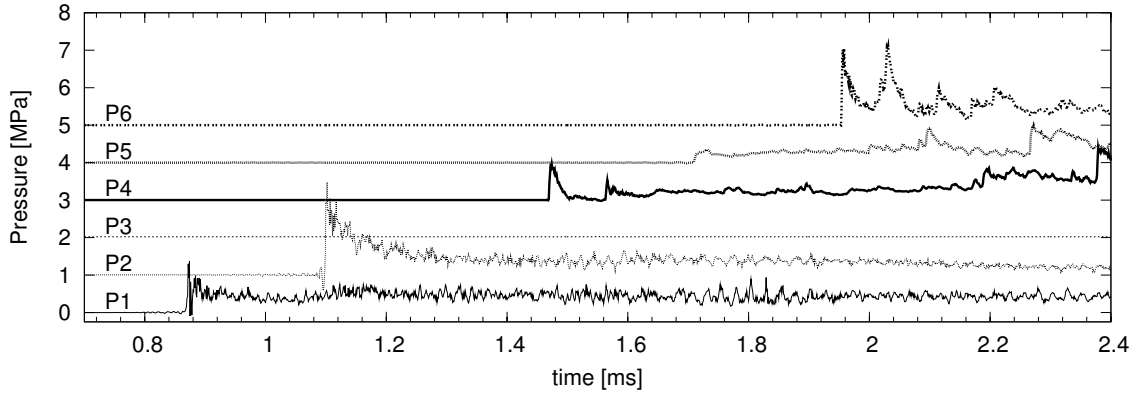

Figure K.11: Shot 11, 0.333 CH_4 + 0.667 O_2, P_0=50 kPa, T_0=295 K. $U(P_1\text{-}P_2)/U_{CJ}$ = 0.743, $U(P_2\text{-}P_3)/U_{CJ}$ = 0.001.

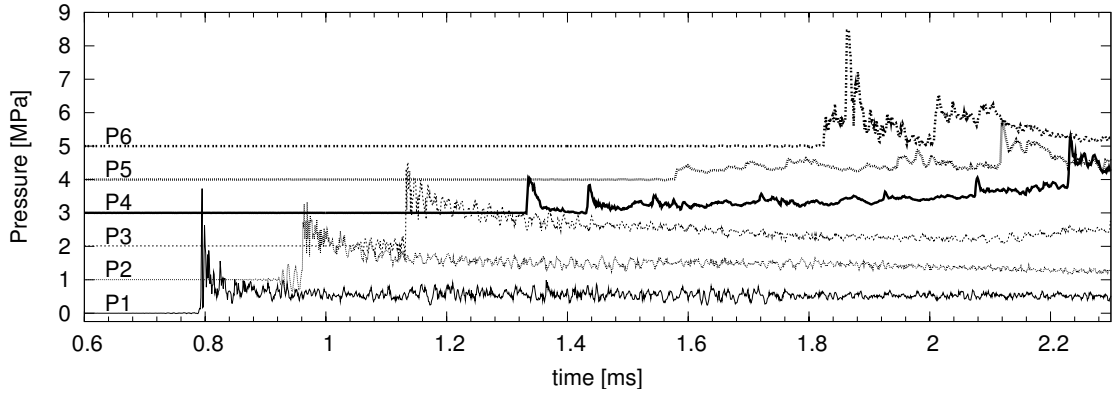

Figure K.12: Shot 12, 0.333 CH_4 + 0.667 O_2, P_0=60 kPa, T_0=295 K. $U(P_1\text{-}P_2)/U_{CJ}$ = 1.005, $U(P_2\text{-}P_3)/U_{CJ}$ = 0.987.

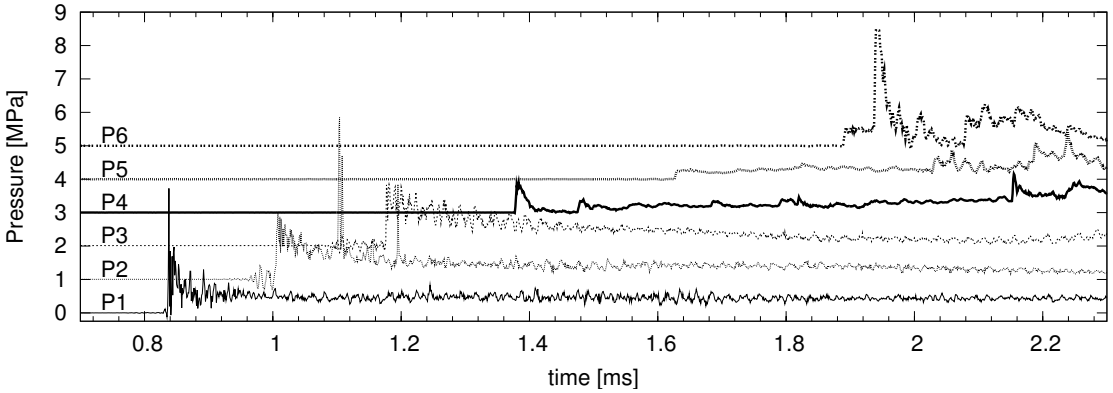

Figure K.13: Shot 13, 0.333 CH_4 + 0.667 O_2, P_0=50 kPa, T_0=295 K. $U(P_1\text{-}P_2)/U_{CJ}$ = 1.002, $U(P_2\text{-}P_3)/U_{CJ}$ = 0.991.

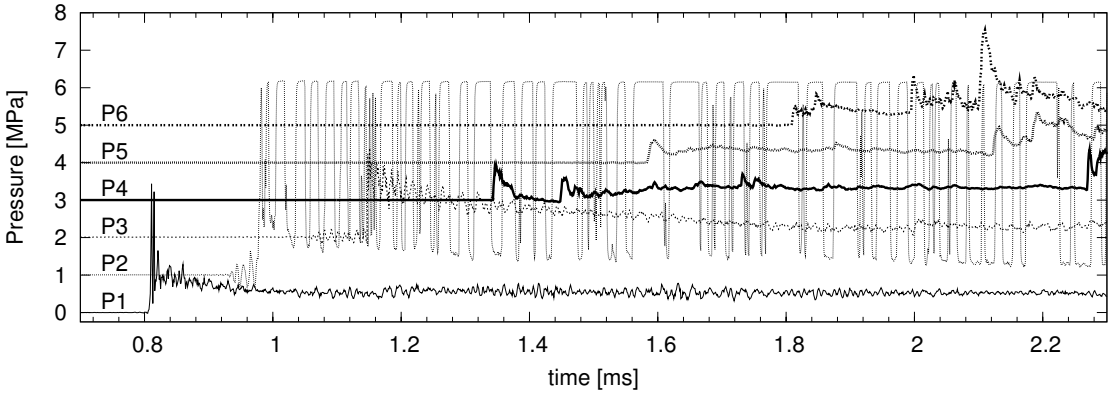

Figure K.14: Shot 14, 0.5 H_2 + 0.25 O_2 + 0.25 N_2, P_0=100 kPa, T_0=296 K. $U(P_1\text{-}P_2)/U_{CJ}$ = 0.993, $U(P_2\text{-}P_3)/U_{CJ}$ = 0.981.

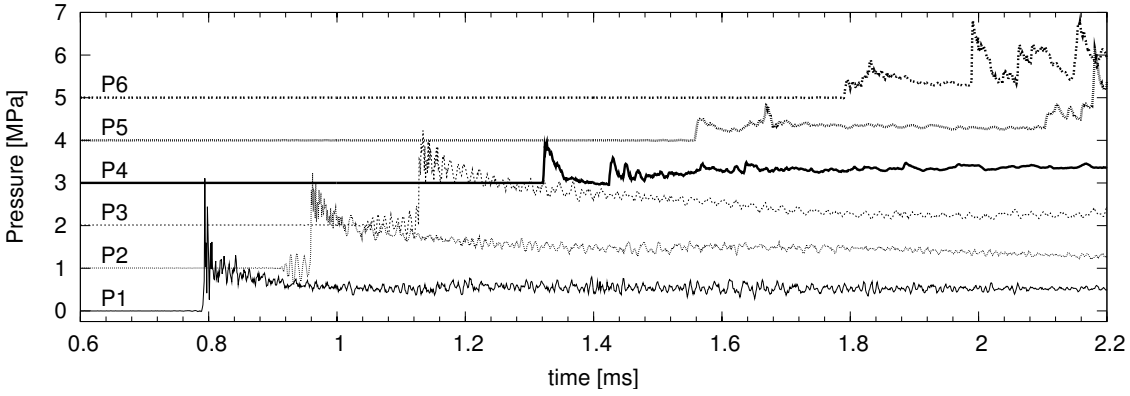

Figure K.15: Shot 15, 0.5 H_2 + 0.25 O_2 + 0.25 N_2, P_0=100 kPa, T_0=296 K. $U(P_1\text{-}P_2)/U_{CJ}$ = 1.005, $U(P_2\text{-}P_3)/U_{CJ}$ = 0.993.

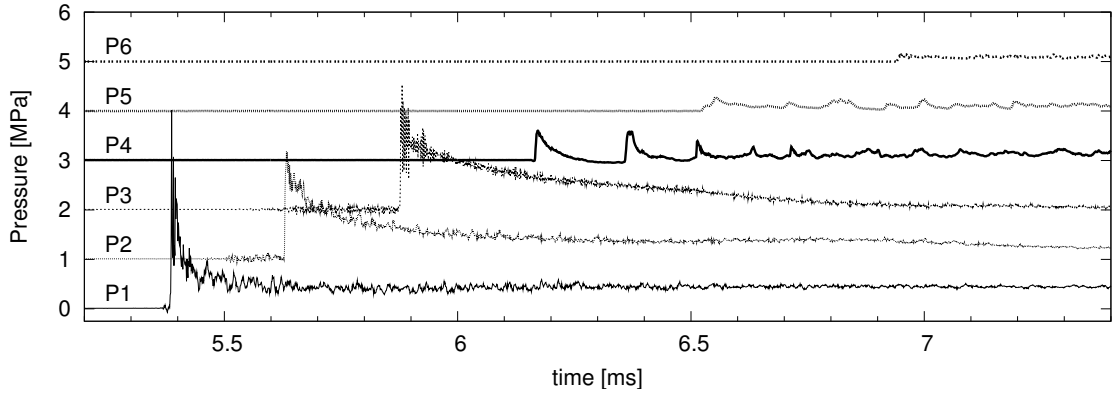

Figure K.16: Shot 16, 0.182 H_2 + 0.091 O_2 + 0.727 Ar, P_0=100 kPa, T_0=297 K. $U(P_1\text{-}P_2)/U_{CJ} = 0.988$, $U(P_2\text{-}P_3)/U_{CJ} = 0.973$.

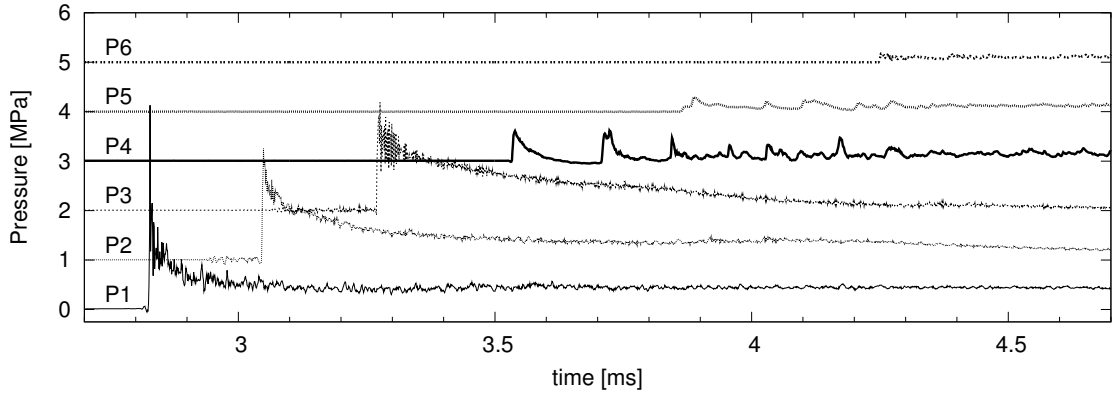

Figure K.17: Shot 17, 0.187 H_2 + 0.093 O_2 + 0.72 Ar, P_0=100 kPa, T_0=297 K. $U(P_1\text{-}P_2)/U_{CJ} = 1.085$, $U(P_2\text{-}P_3)/U_{CJ} = 1.070$.

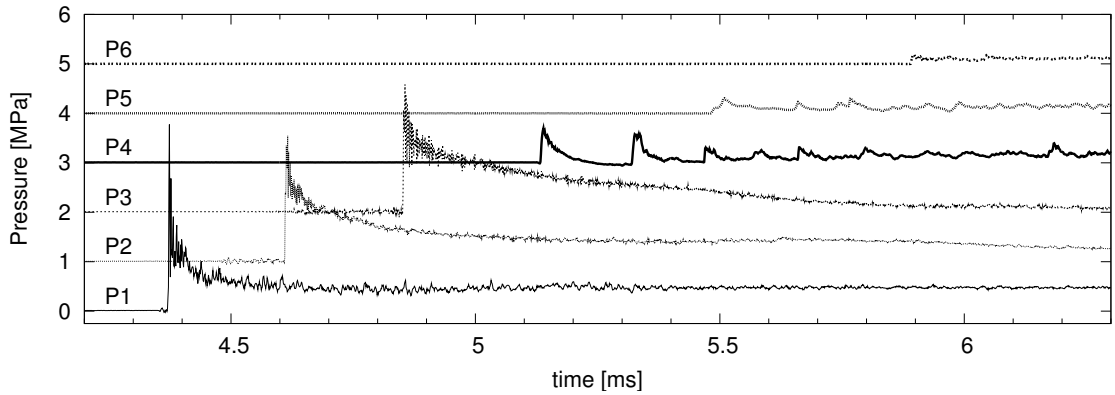

Figure K.18: Shot 18, 0.187 H_2 + 0.093 O_2 + 0.72 Ar, P_0=100 kPa, T_0=296 K. $U(P_1\text{-}P_2)/U_{CJ} = 1.008$, $U(P_2\text{-}P_3)/U_{CJ} = 0.991$.

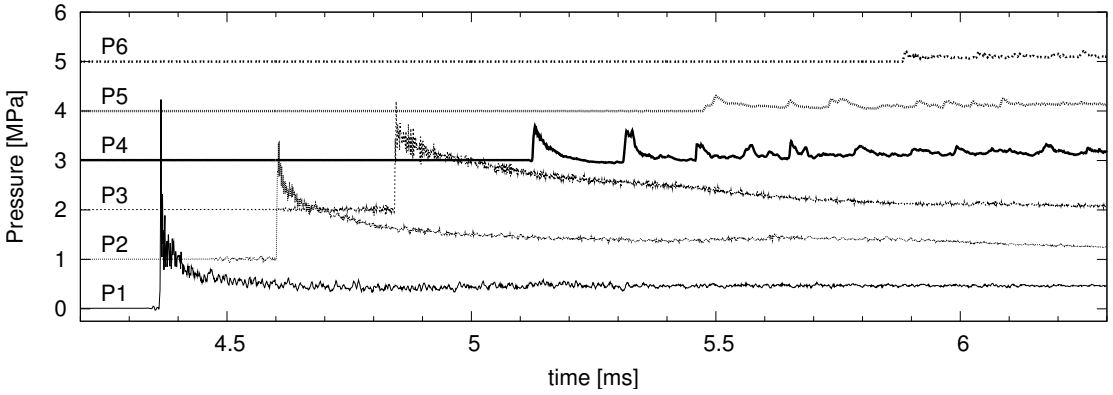

Figure K.19: Shot 19, 0.187 H_2 + 0.093 O_2 + 0.72 Ar, P_0=100 kPa, T_0=297 K. $U(P_1\text{-}P_2)/U_{CJ} = 0.999$, $U(P_2\text{-}P_3)/U_{CJ} = 0.995$.

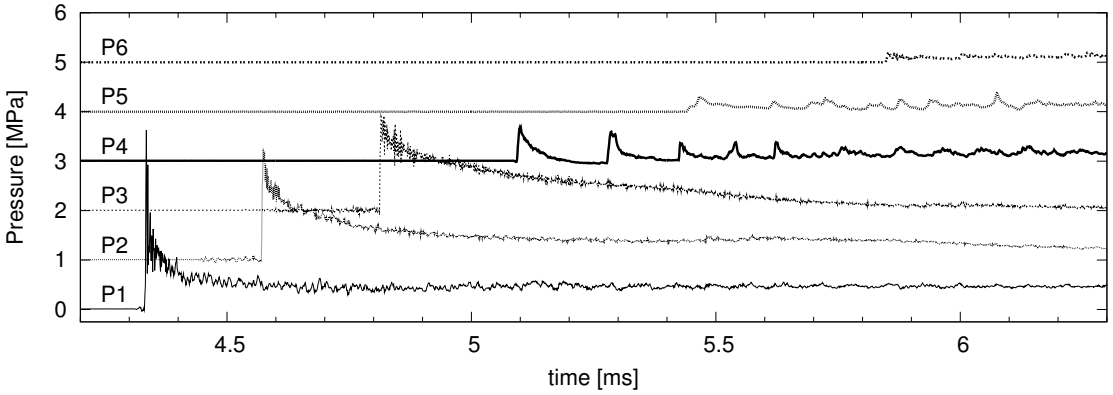

Figure K.20: Shot 20, 0.187 H_2 + 0.093 O_2 + 0.72 Ar, P_0=100 kPa, T_0=296 K. $U(P_1\text{-}P_2)/U_{CJ} = 1.003$, $U(P_2\text{-}P_3)/U_{CJ} = 0.991$.

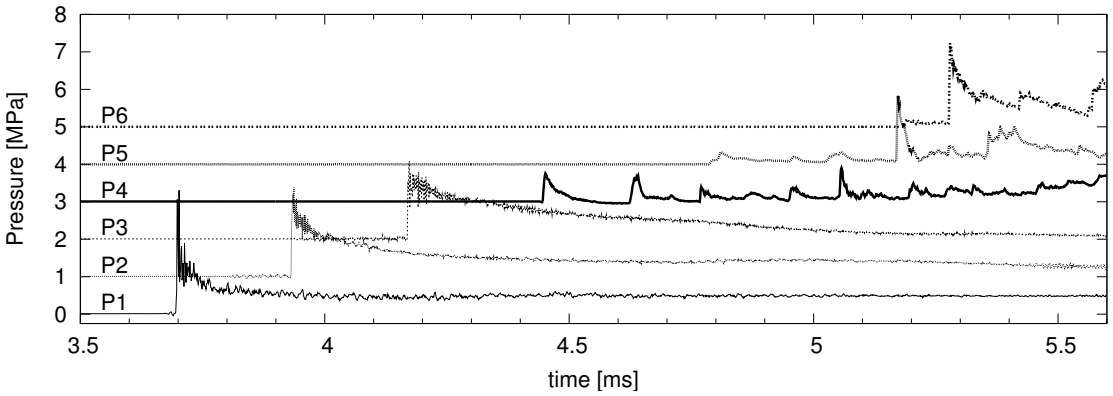

Figure K.21: Shot 21, 0.2 H_2 + 0.1 O_2 + 0.7 Ar, P_0=100 kPa, T_0=297 K. $U(P_1\text{-}P_2)/U_{CJ} = 1.009$, $U(P_2\text{-}P_3)/U_{CJ} = 0.992$.

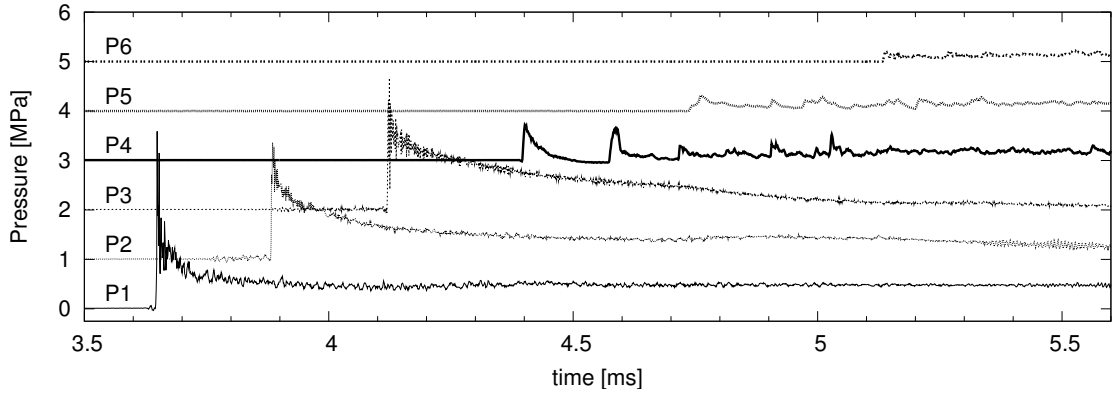

Figure K.22: Shot 22, 0.2 H_2 + 0.1 O_2 + 0.7 Ar, P_0=100 kPa, T_0=298 K. U(P_1-P_2)/U_{CJ} = 1.005, U(P_2-P_3)/U_{CJ} = 0.992.

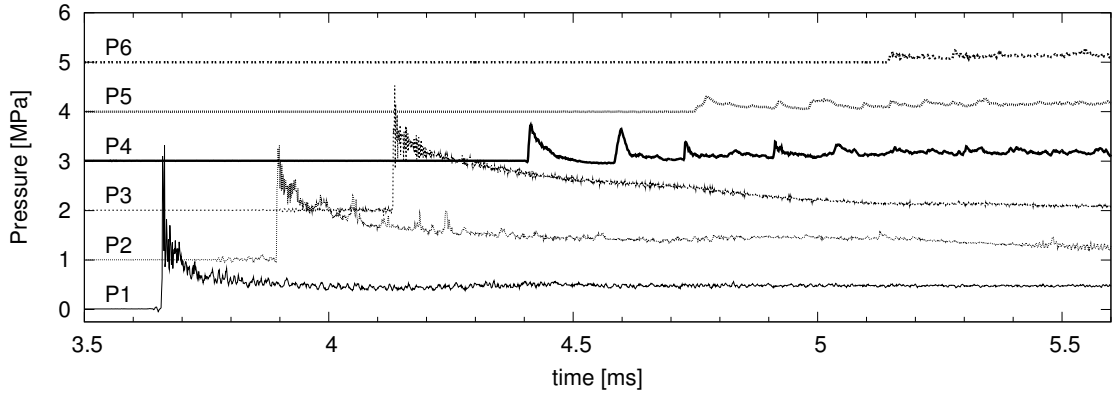

Figure K.23: Shot 23, 0.2 H_2 + 0.1 O_2 + 0.7 Ar, P_0=100 kPa, T_0=298 K. U(P_1-P_2)/U_{CJ} = 1.005, U(P_2-P_3)/U_{CJ} = 0.988.

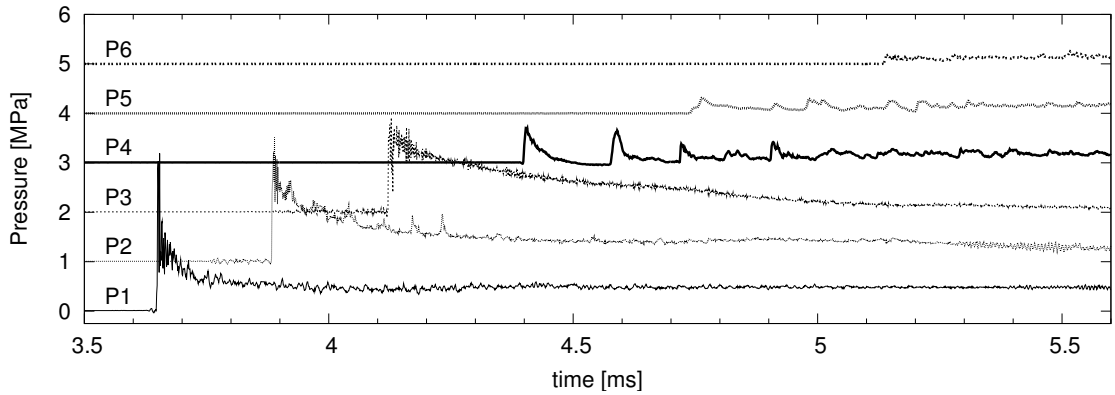

Figure K.24: Shot 24, 0.2 H_2 + 0.1 O_2 + 0.7 Ar, P_0=100 kPa, T_0=298 K. U(P_1-P_2)/U_{CJ} = 1.005, U(P_2-P_3)/U_{CJ} = 0.992.

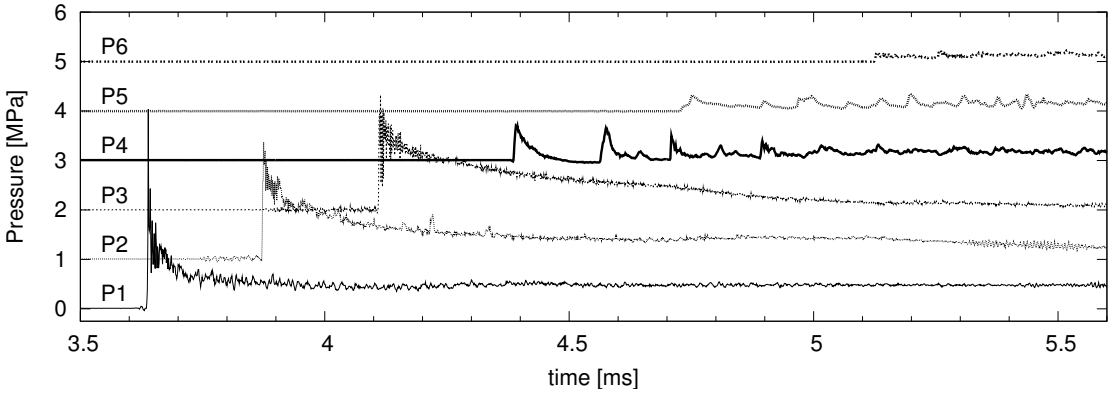

Figure K.25: Shot 25, 0.2 H_2 + 0.1 O_2 + 0.7 Ar, P_0=100 kPa, T_0=298 K. U(P_1-P_2)/U_{CJ} = 1.001, U(P_2-P_3)/U_{CJ} = 0.992.

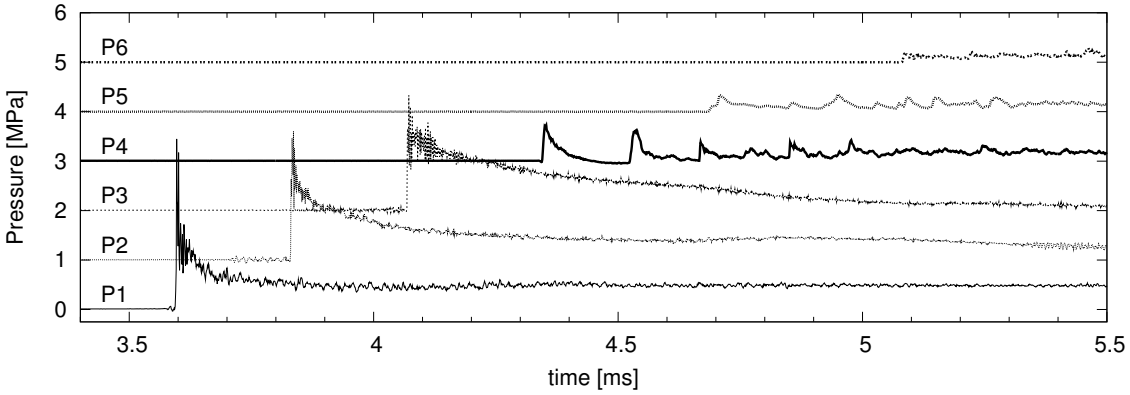

Figure K.26: Shot 26, 0.2 H_2 + 0.1 O_2 + 0.7 Ar, P_0=100 kPa, T_0=298 K. U(P_1-P_2)/U_{CJ} = 1.005, U(P_2-P_3)/U_{CJ} = 0.988.

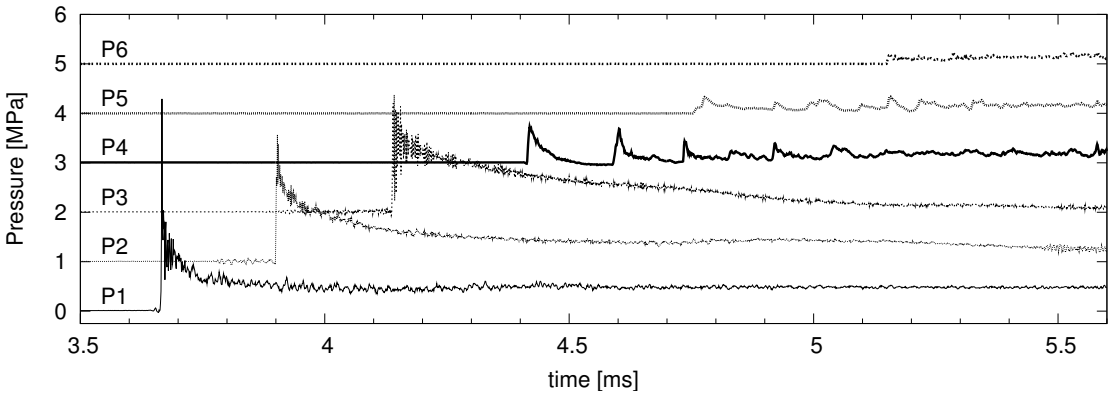

Figure K.27: Shot 27, 0.2 H_2 + 0.1 O_2 + 0.7 Ar, P_0=100 kPa, T_0=298 K. U(P_1-P_2)/U_{CJ} = 1.001, U(P_2-P_3)/U_{CJ} = 0.992.

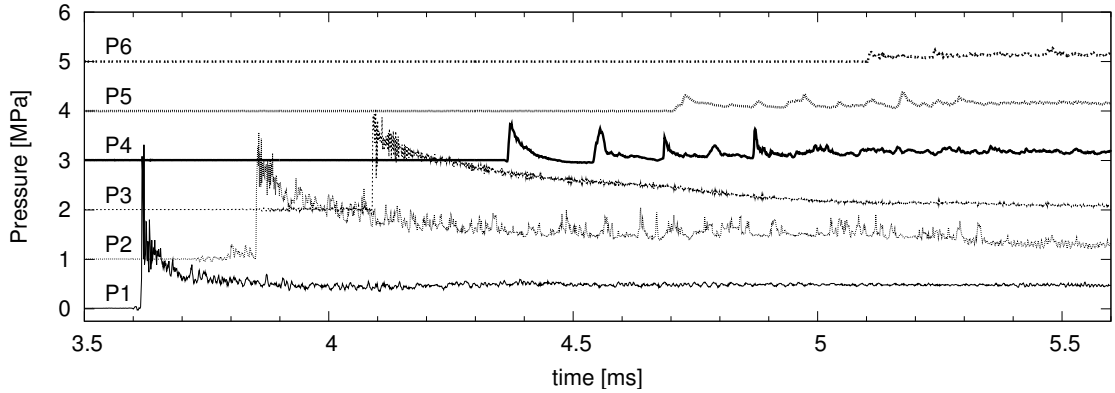

Figure K.28: Shot 28, 0.2 H_2 + 0.1 O_2 + 0.7 Ar, P_0=100 kPa, T_0=298 K. U(P_1-P_2)/U_{CJ} = 1.009, U(P_2-P_3)/U_{CJ} = 0.992.

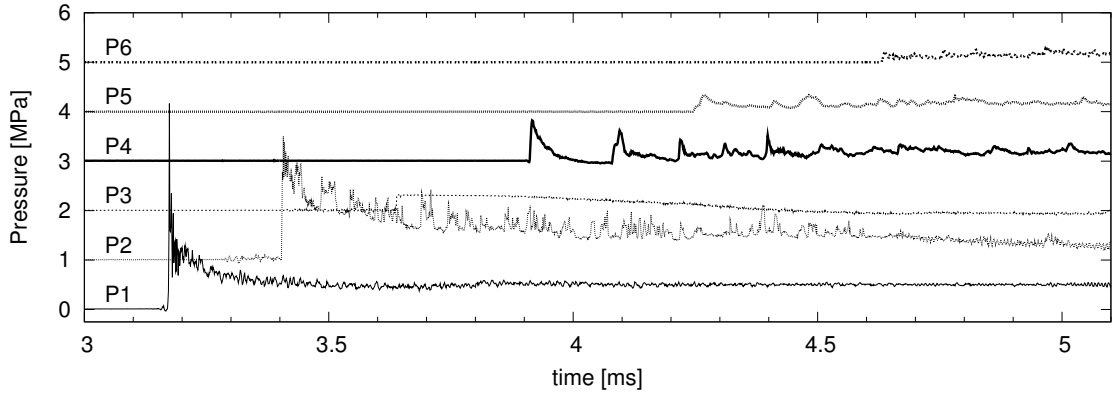

Figure K.29: Shot 29, 0.213 H_2 + 0.107 O_2 + 0.68 Ar, P_0=100 kPa, T_0=295 K. U(P_1-P_2)/U_{CJ} = 0.999, U(P_2-P_3)/U_{CJ} = 0.991.

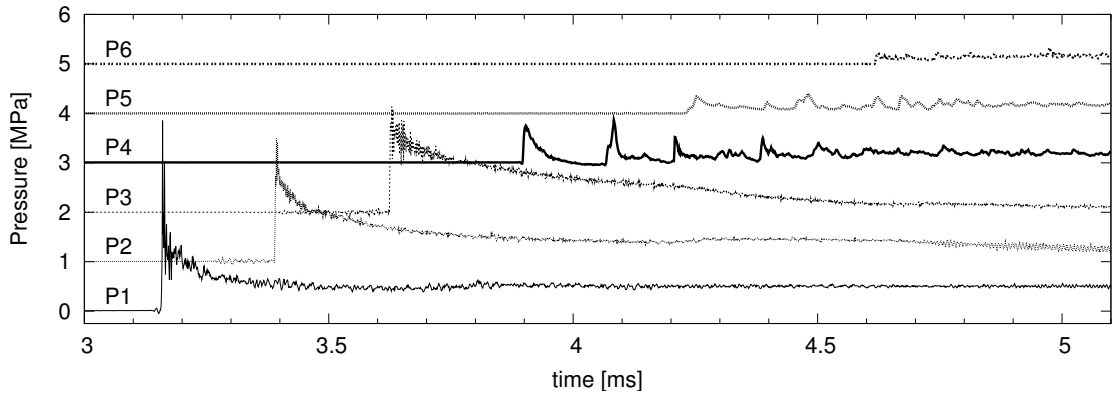

Figure K.30: Shot 30, 0.213 H_2 + 0.107 O_2 + 0.68 Ar, P_0=100 kPa, T_0=296 K. U(P_1-P_2)/U_{CJ} = 1.008, U(P_2-P_3)/U_{CJ} = 0.991.

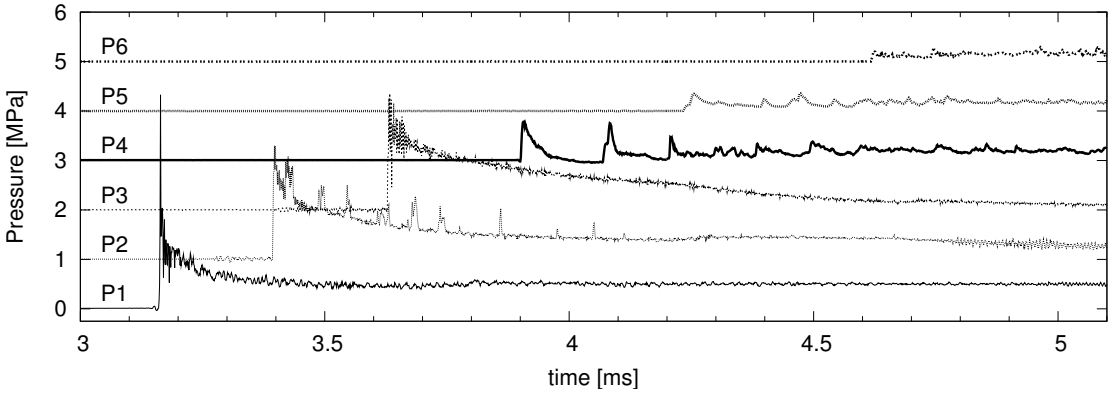

Figure K.31: Shot 31, 0.213 H_2 + 0.107 O_2 + 0.68 Ar, P_0=100 kPa, T_0=296 K. $U(P_1\text{-}P_2)/U_{CJ} = 0.999$, $U(P_2\text{-}P_3)/U_{CJ} = 0.991$.

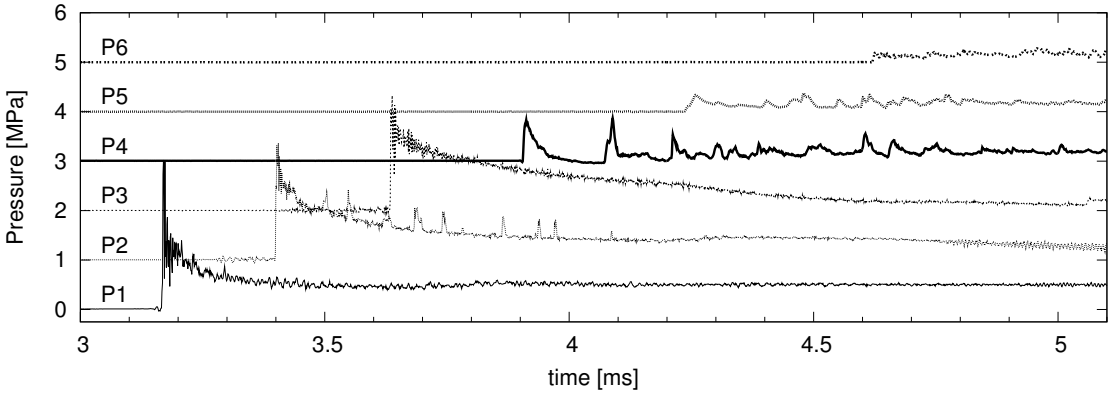

Figure K.32: Shot 32, 0.213 H_2 + 0.107 O_2 + 0.68 Ar, P_0=100 kPa, T_0=296 K. $U(P_1\text{-}P_2)/U_{CJ} = 1.003$, $U(P_2\text{-}P_3)/U_{CJ} = 0.991$.

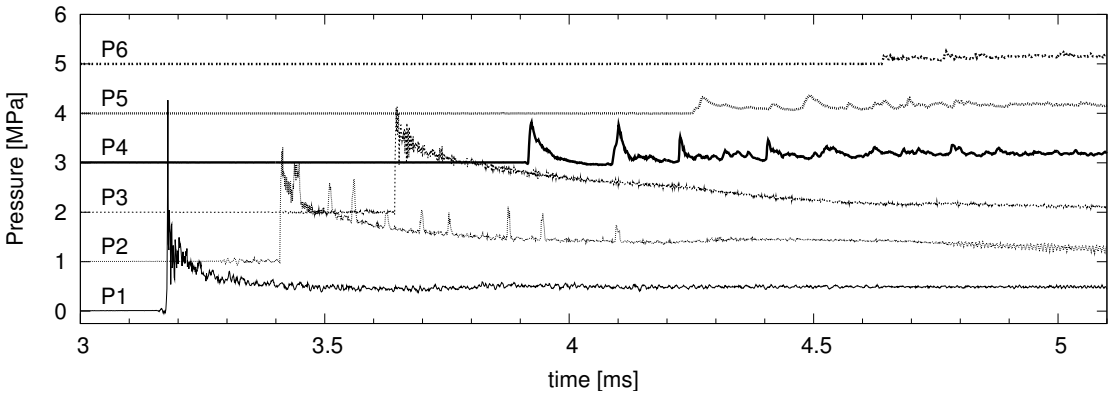

Figure K.33: Shot 33, 0.213 H_2 + 0.107 O_2 + 0.68 Ar, P_0=100 kPa, T_0=296 K. $U(P_1\text{-}P_2)/U_{CJ} = 0.999$, $U(P_2\text{-}P_3)/U_{CJ} = 0.991$.

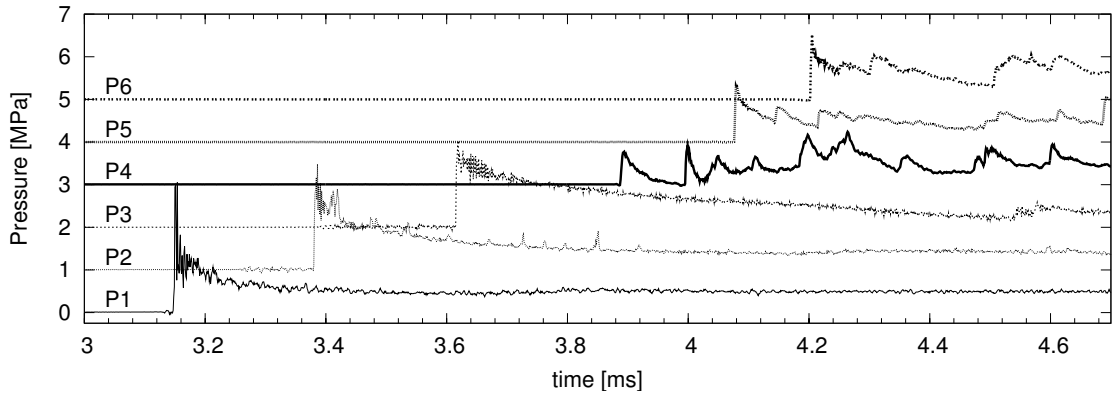

Figure K.34: Shot 34, 0.213 H_2 + 0.107 O_2 + 0.68 Ar, P_0=100 kPa, T_0=297 K. $U(P_1\text{-}P_2)/U_{CJ} = 0.999$, $U(P_2\text{-}P_3)/U_{CJ} = 0.991$.

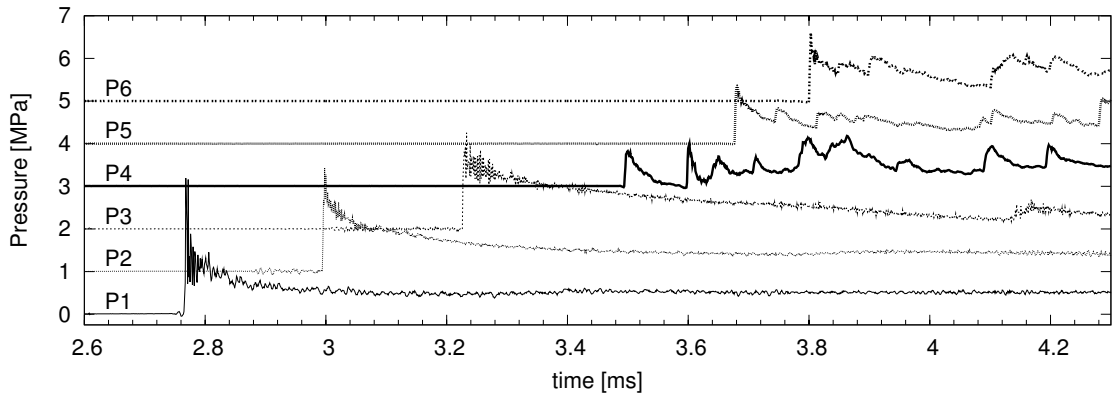

Figure K.35: Shot 35, 0.227 H_2 + 0.113 O_2 + 0.66 Ar, P_0=100 kPa, T_0=294 K. $U(P_1\text{-}P_2)/U_{CJ} = 1.003$, $U(P_2\text{-}P_3)/U_{CJ} = 0.990$.

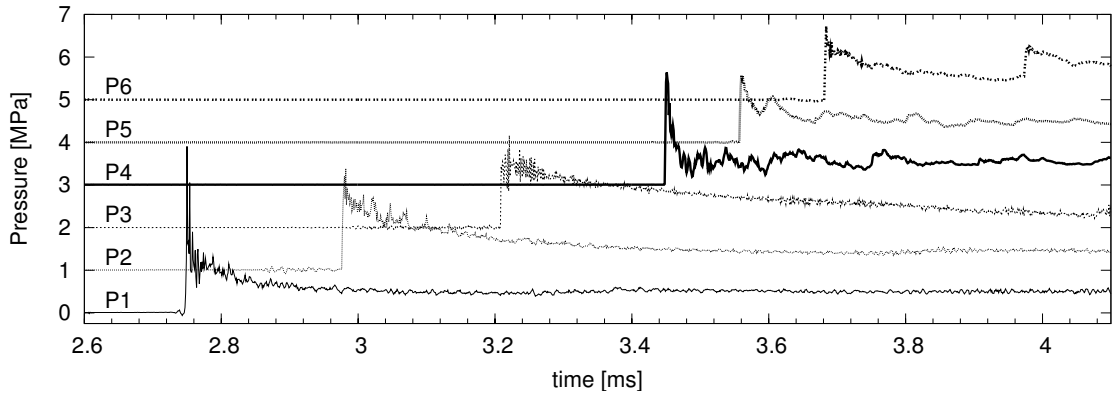

Figure K.36: Shot 36, 0.227 H_2 + 0.113 O_2 + 0.66 Ar, P_0=100 kPa, T_0=294 K. $U(P_1\text{-}P_2)/U_{CJ} = 0.998$, $U(P_2\text{-}P_3)/U_{CJ} = 0.990$.

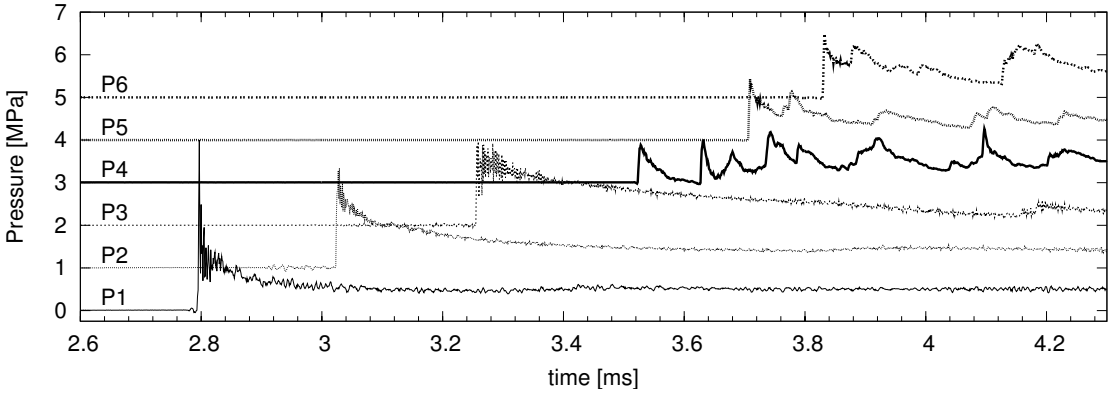

Figure K.37: Shot 37, 0.227 H_2 + 0.113 O_2 + 0.66 Ar, P_0=100 kPa, T_0=295 K. $U(P_1\text{-}P_2)/U_{CJ} = 0.998$, $U(P_2\text{-}P_3)/U_{CJ} = 0.990$.

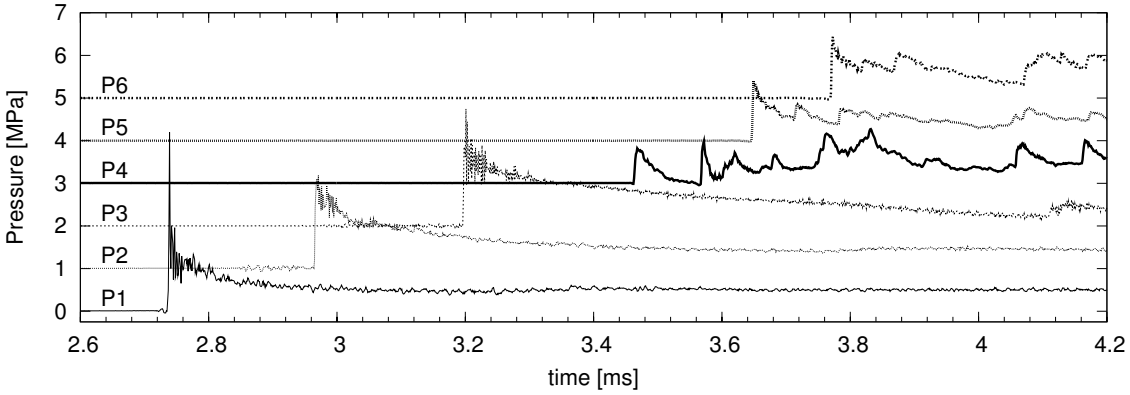

Figure K.38: Shot 38, 0.227 H_2 + 0.113 O_2 + 0.66 Ar, P_0=100 kPa, T_0=295 K. $U(P_1\text{-}P_2)/U_{CJ} = 1.003$, $U(P_2\text{-}P_3)/U_{CJ} = 0.990$.

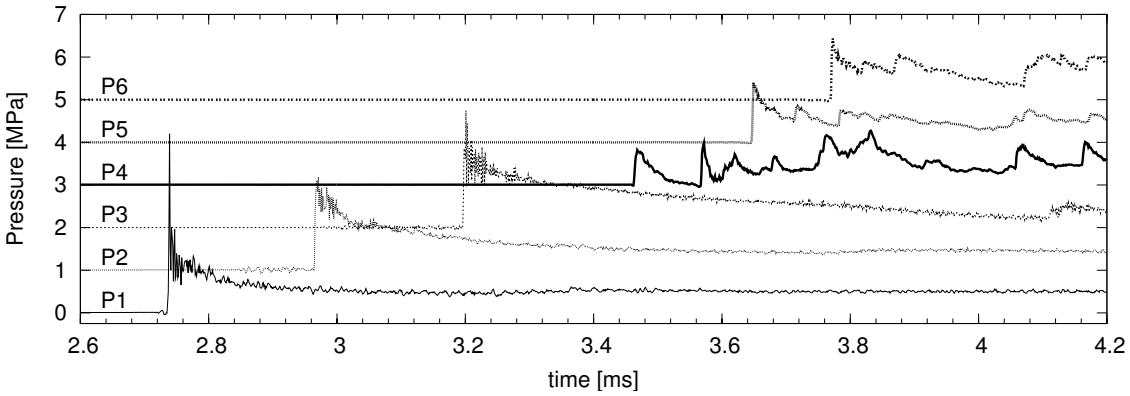

Figure K.39: Shot 39, 0.227 H_2 + 0.113 O_2 + 0.66 Ar, P_0=100 kPa, T_0=295 K. $U(P_1\text{-}P_2)/U_{CJ} = 1.003$, $U(P_2\text{-}P_3)/U_{CJ} = 0.990$.

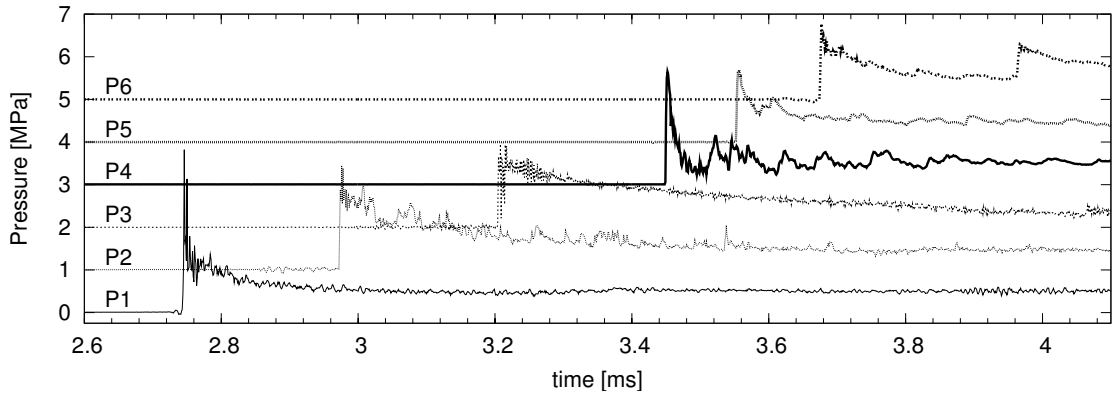

Figure K.40: Shot 40, 0.227 H_2 + 0.113 O_2 + 0.66 Ar, P_0=100 kPa, T_0=295 K. $U(P_1\text{-}P_2)/U_{CJ} = 1.003$, $U(P_2\text{-}P_3)/U_{CJ} = 0.990$.

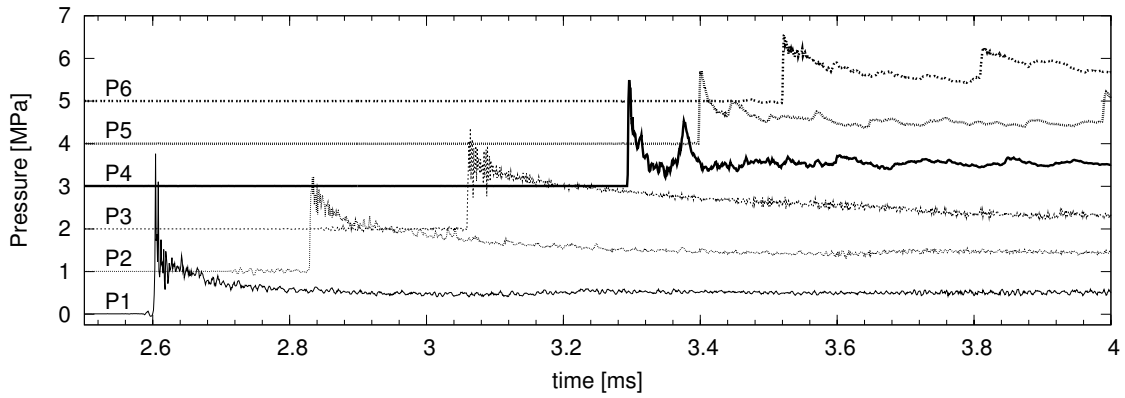

Figure K.41: Shot 41, 0.233 H_2 + 0.117 O_2 + 0.65 Ar, P_0=100 kPa, T_0=296 K. $U(P_1\text{-}P_2)/U_{CJ} = 1.005$, $U(P_2\text{-}P_3)/U_{CJ} = 0.988$.

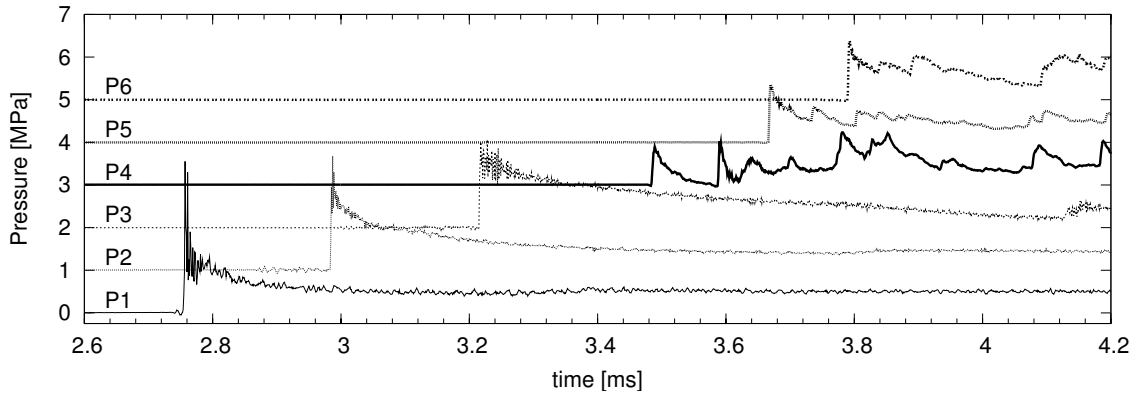

Figure K.42: Shot 42, 0.227 H_2 + 0.113 O_2 + 0.66 Ar, P_0=100 kPa, T_0=296 K. $U(P_1\text{-}P_2)/U_{CJ} = 1.003$, $U(P_2\text{-}P_3)/U_{CJ} = 0.990$.

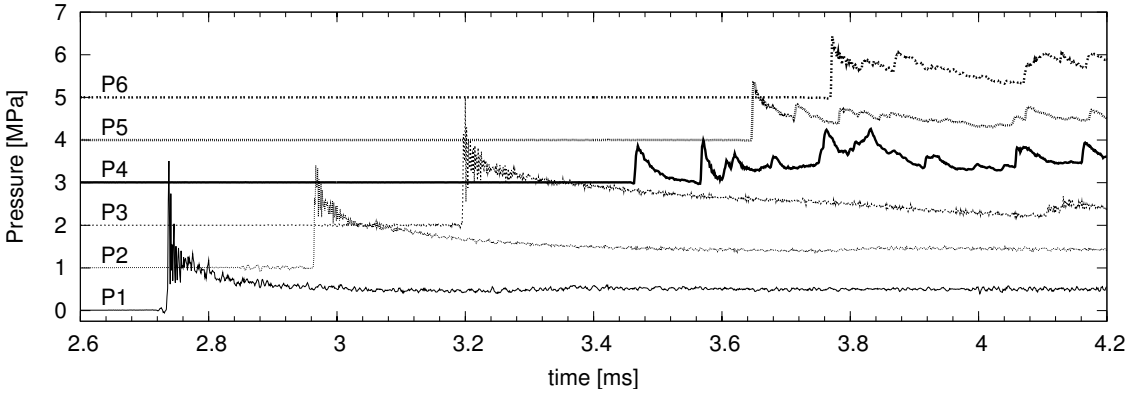

Figure K.43: Shot 43, 0.227 H_2 + 0.113 O_2 + 0.66 Ar, P_0=100 kPa, T_0=296 K. $U(P_1\text{-}P_2)/U_{CJ} = 1.003$, $U(P_2\text{-}P_3)/U_{CJ} = 0.990$.

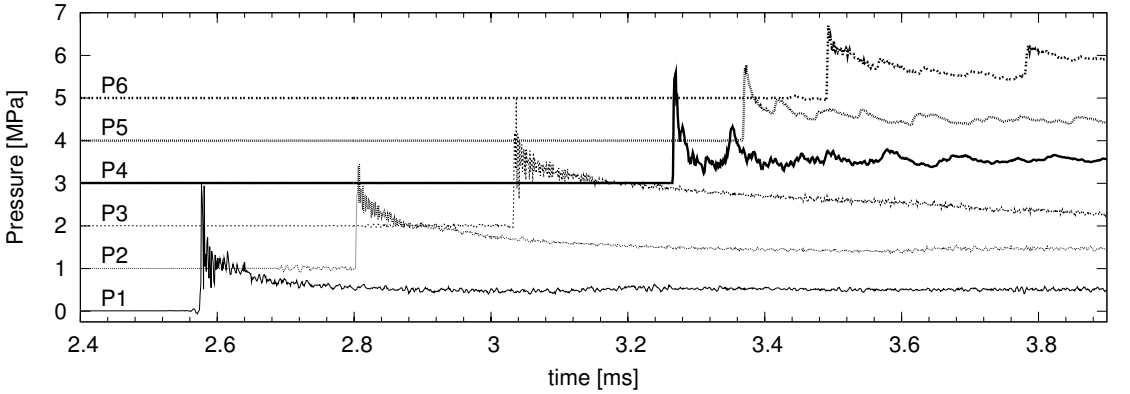

Figure K.44: Shot 44, 0.233 H_2 + 0.117 O_2 + 0.65 Ar, P_0=100 kPa, T_0=296 K. $U(P_1\text{-}P_2)/U_{CJ} = 1.001$, $U(P_2\text{-}P_3)/U_{CJ} = 0.992$.

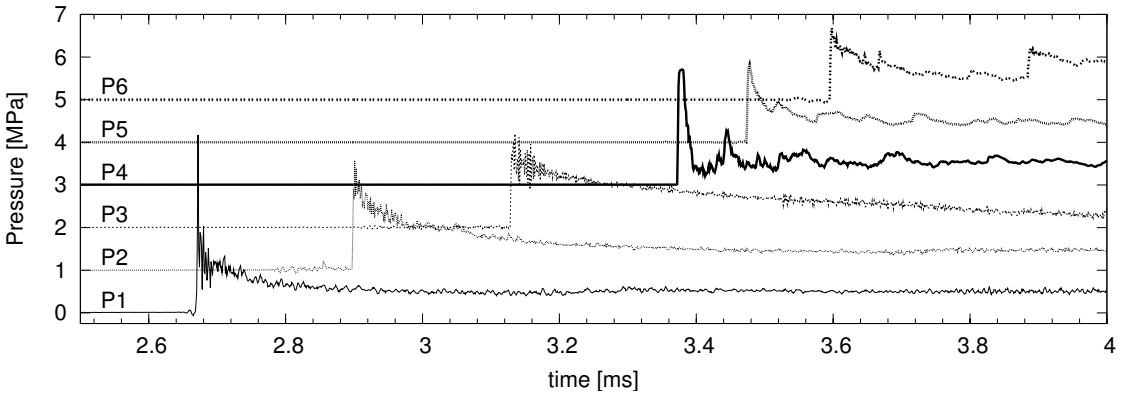

Figure K.45: Shot 45, 0.23 H_2 + 0.115 O_2 + 0.655 Ar, P_0=100 kPa, T_0=296 K. $U(P_1\text{-}P_2)/U_{CJ} = 1.004$, $U(P_2\text{-}P_3)/U_{CJ} = 0.991$.

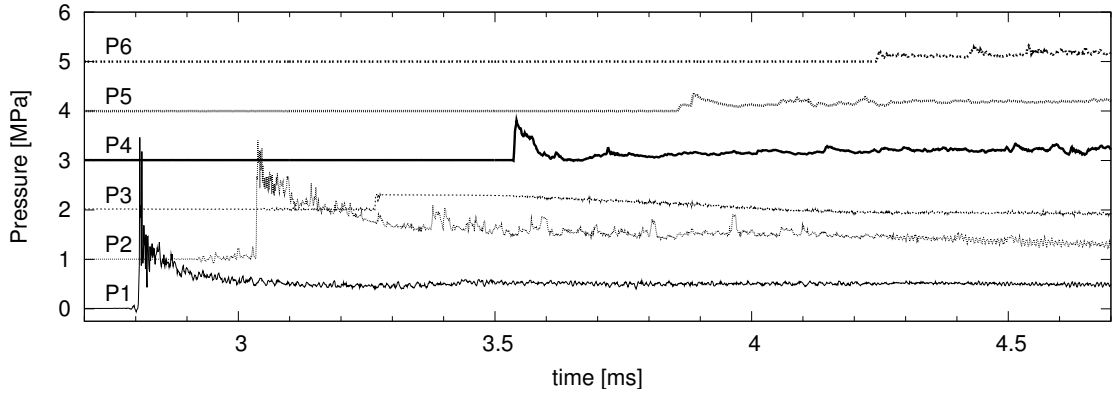

Figure K.46: Shot 46, 0.227 H_2 + 0.113 O_2 + 0.66 Ar, P_0=100 kPa, T_0=293 K. $U(P_1\text{-}P_2)/U_{CJ} = 1.007$, $U(P_2\text{-}P_3)/U_{CJ} = 0.002$.

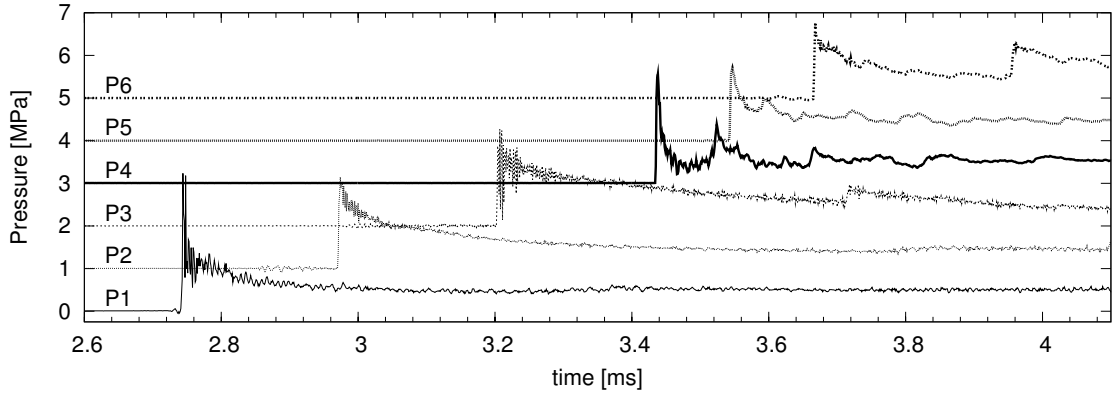

Figure K.47: Shot 47, 0.227 H_2 + 0.113 O_2 + 0.66 Ar, P_0=100 kPa, T_0=294 K. $U(P_1\text{-}P_2)/U_{CJ} = 1.003$, $U(P_2\text{-}P_3)/U_{CJ} = 0.990$.

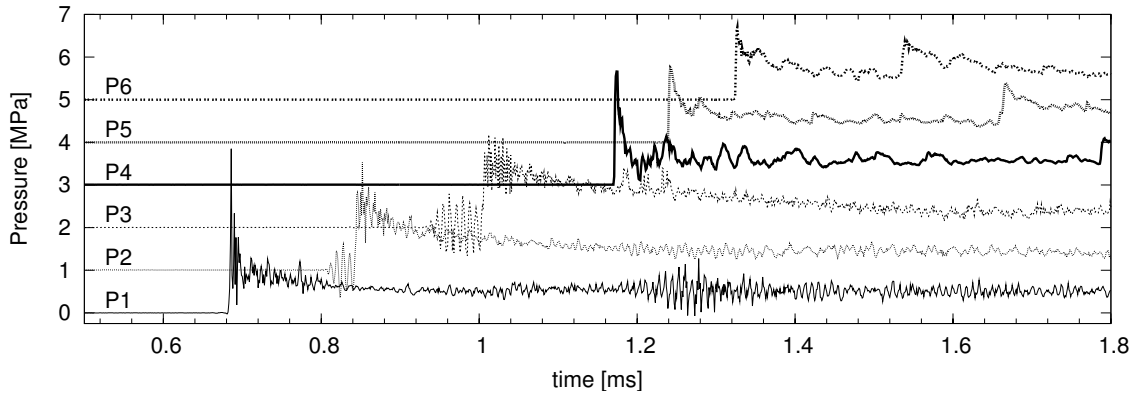

Figure K.48: Shot 48, 0.54 H_2 + 0.27 O_2 + 0.19 N_2, P_0=100 kPa, T_0=294 K. $U(P_1\text{-}P_2)/U_{CJ} = 1.004$, $U(P_2\text{-}P_3)/U_{CJ} = 0.998$.

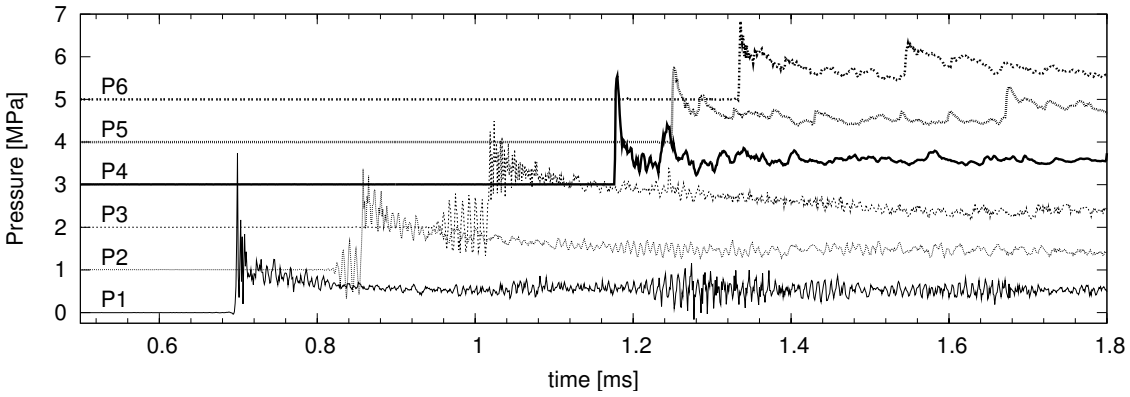

Figure K.49: Shot 49, 0.54 H_2 + 0.27 O_2 + 0.19 N_2, P_0=100 kPa, T_0=295 K. U(P_1-P_2)/U_{CJ} = 1.010, U(P_2-P_3)/U_{CJ} = 0.998.

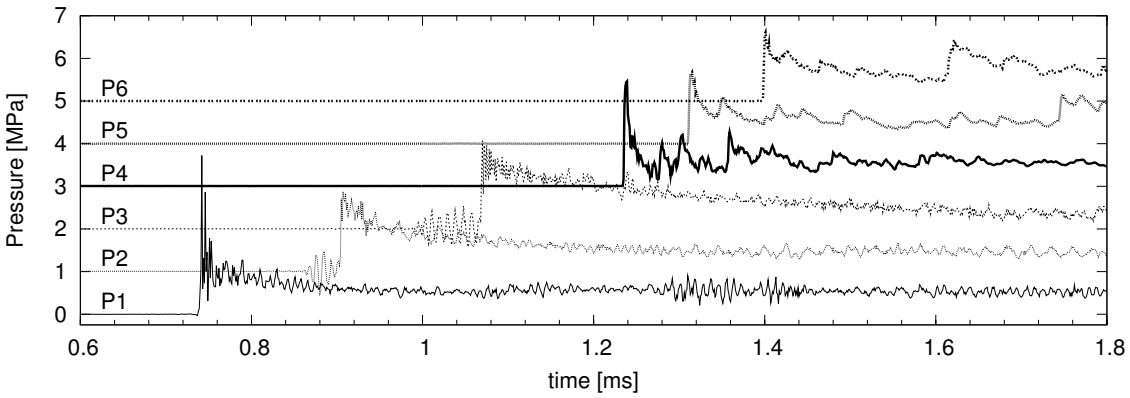

Figure K.50: Shot 50, 0.527 H_2 + 0.263 O_2 + 0.21 N_2, P_0=100 kPa, T_0=295 K. U(P_1-P_2)/U_{CJ} = 0.992, U(P_2-P_3)/U_{CJ} = 0.992.

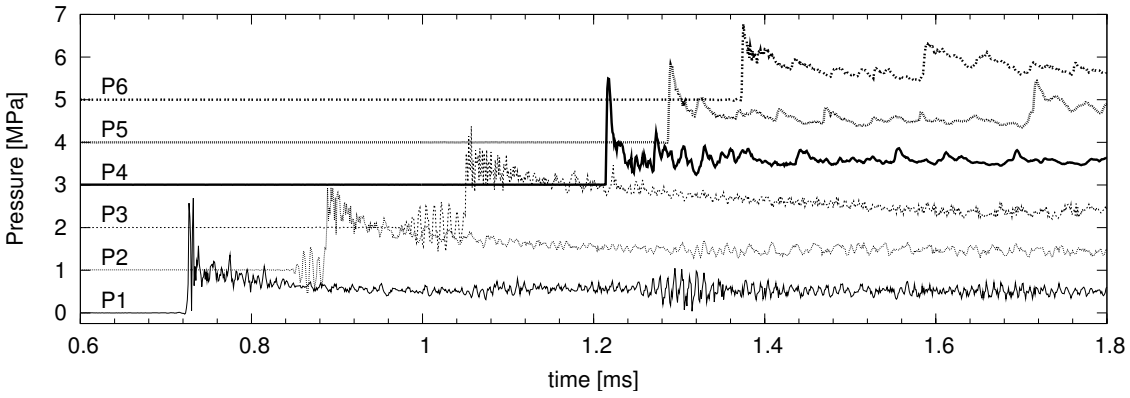

Figure K.51: Shot 51, 0.527 H_2 + 0.263 O_2 + 0.21 N_2, P_0=100 kPa, T_0=295 K. U(P_1-P_2)/U_{CJ} = 1.011, U(P_2-P_3)/U_{CJ} = 0.998.

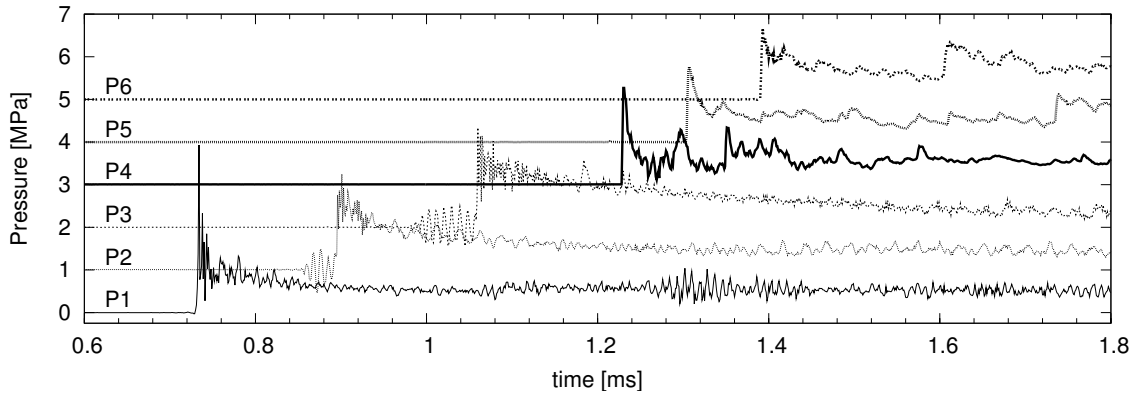

Figure K.52: Shot 52, 0.52 H_2 + 0.26 O_2 + 0.22 N_2, P_0=100 kPa, T_0=296 K. U(P_1-P_2)/U_{CJ} = 1.005, U(P_2-P_3)/U_{CJ} = 0.998.

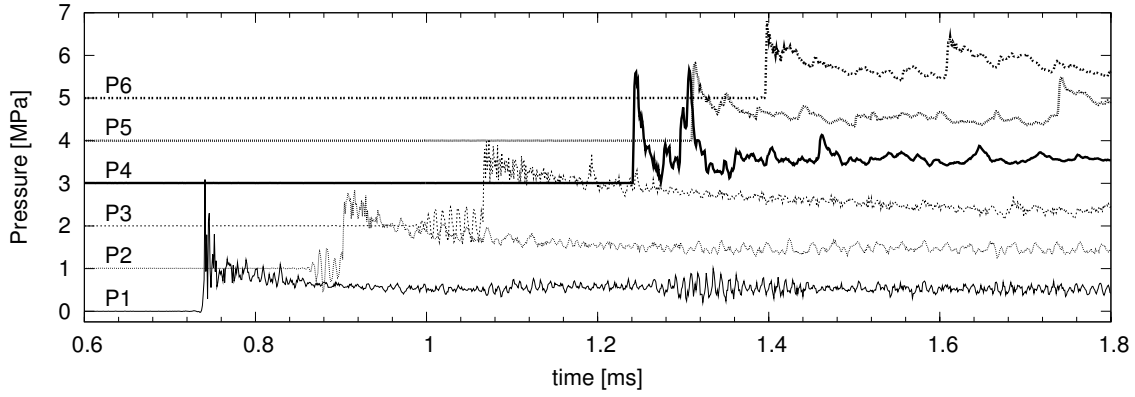

Figure K.53: Shot 53, 0.52 H_2 + 0.26 O_2 + 0.22 N_2, P_0=100 kPa, T_0=295 K. U(P_1-P_2)/U_{CJ} = 1.011, U(P_2-P_3)/U_{CJ} = 0.998.

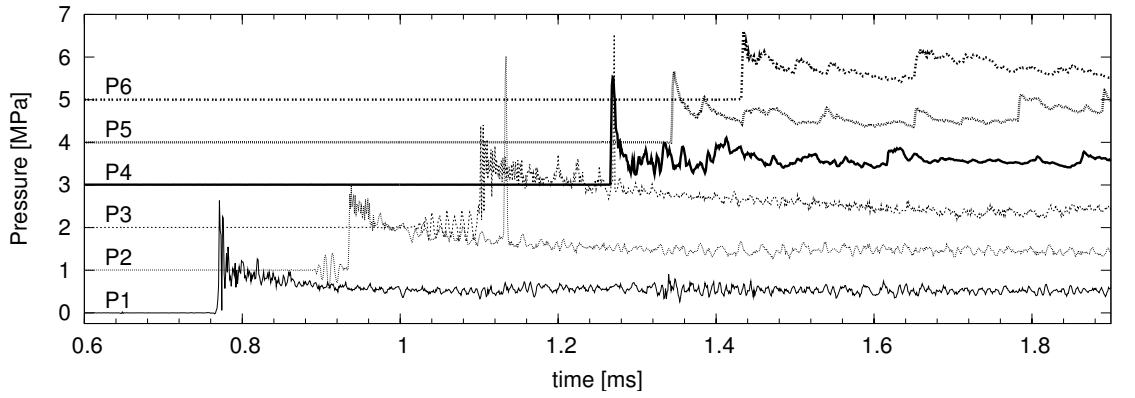

Figure K.54: Shot 54, 0.507 H_2 + 0.253 O_2 + 0.24 N_2, P_0=100 kPa, T_0=297 K. U(P_1-P_2)/U_{CJ} = 1.005, U(P_2-P_3)/U_{CJ} = 0.999.

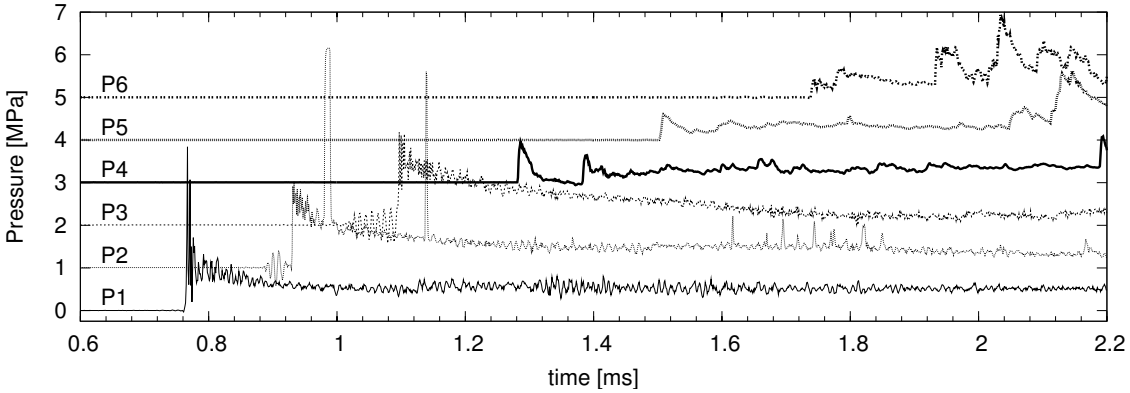

Figure K.55: Shot 55, 0.507 H_2 + 0.253 O_2 + 0.24 N_2, P_0=100 kPa, T_0=294 K. $U(P_1\text{-}P_2)/U_{CJ} = 1.005$, $U(P_2\text{-}P_3)/U_{CJ} = 0.999$.

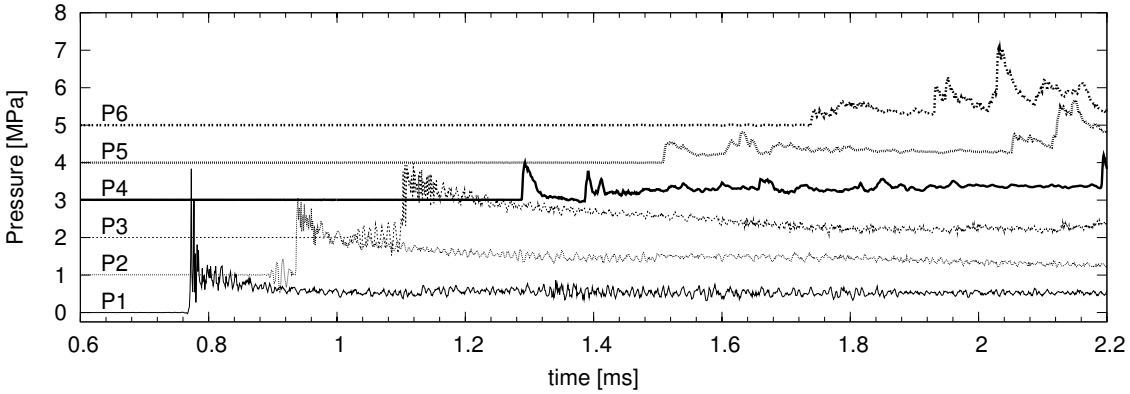

Figure K.56: Shot 56, 0.507 H_2 + 0.253 O_2 + 0.24 N_2, P_0=100 kPa, T_0=295 K. $U(P_1\text{-}P_2)/U_{CJ} = 1.005$, $U(P_2\text{-}P_3)/U_{CJ} = 0.999$.

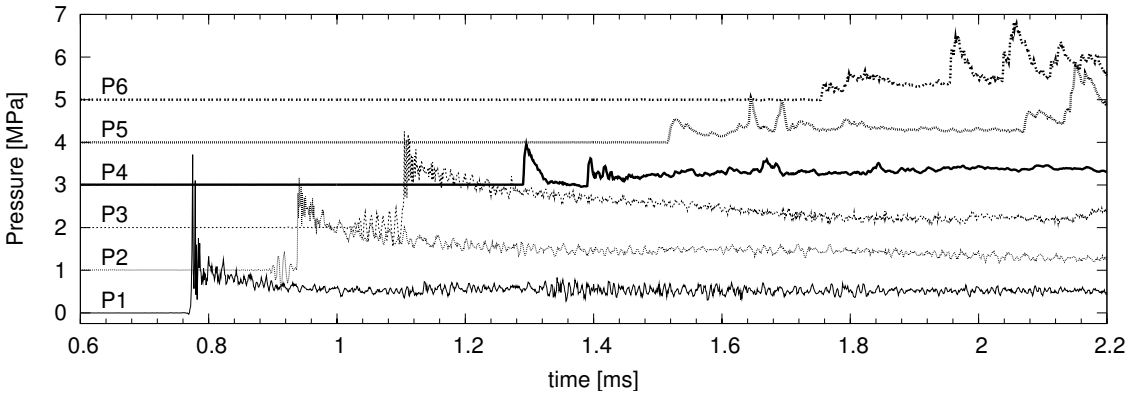

Figure K.57: Shot 57, 0.507 H_2 + 0.253 O_2 + 0.24 N_2, P_0=100 kPa, T_0=296 K. $U(P_1\text{-}P_2)/U_{CJ} = 1.005$, $U(P_2\text{-}P_3)/U_{CJ} = 0.999$.

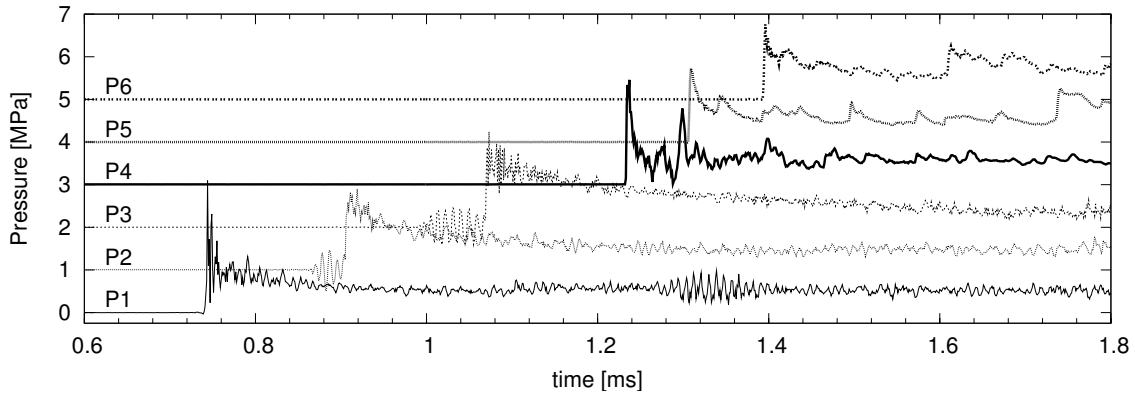

Figure K.58: Shot 58, 0.52 H_2 + 0.26 O_2 + 0.22 N_2, P_0=100 kPa, T_0=296 K. U(P_1-P_2)/U_{CJ} = 1.011, U(P_2-P_3)/U_{CJ} = 0.998.

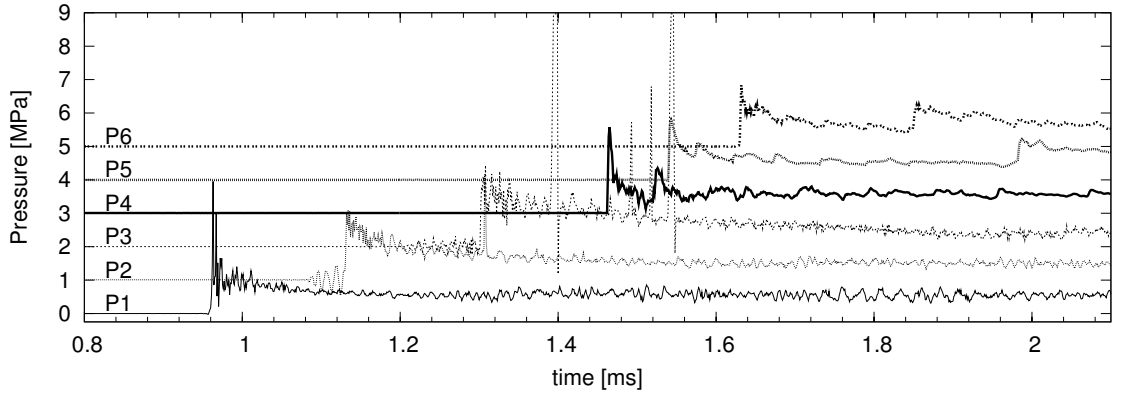

Figure K.59: Shot 59, 0.5 H_2 + 0.5 N_2O, P_0=70 kPa, T_0=296 K. U(P_1-P_2)/U_{CJ} = 0.990, U(P_2-P_3)/U_{CJ} = 0.990.

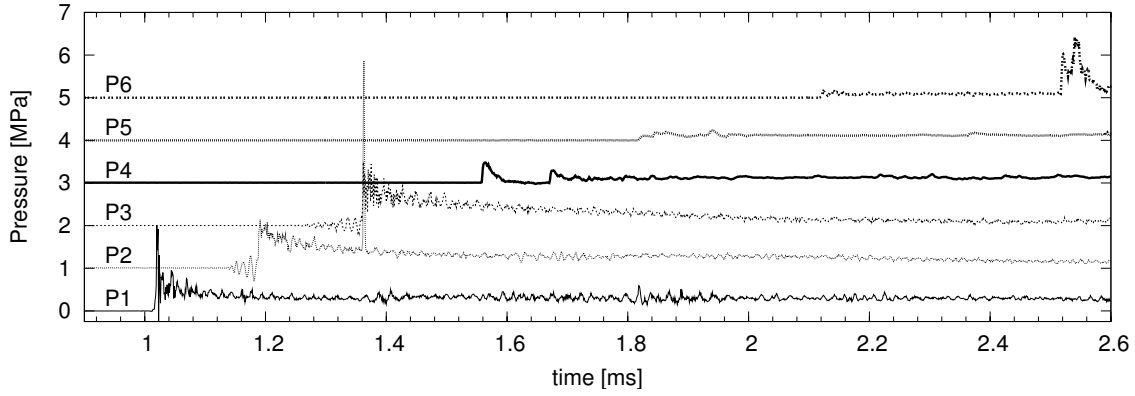

Figure K.60: Shot 60, 0.5 H_2 + 0.5 N_2O, P_0=40 kPa, T_0=296 K. U(P_1-P_2)/U_{CJ} = 0.994, U(P_2-P_3)/U_{CJ} = 0.994.

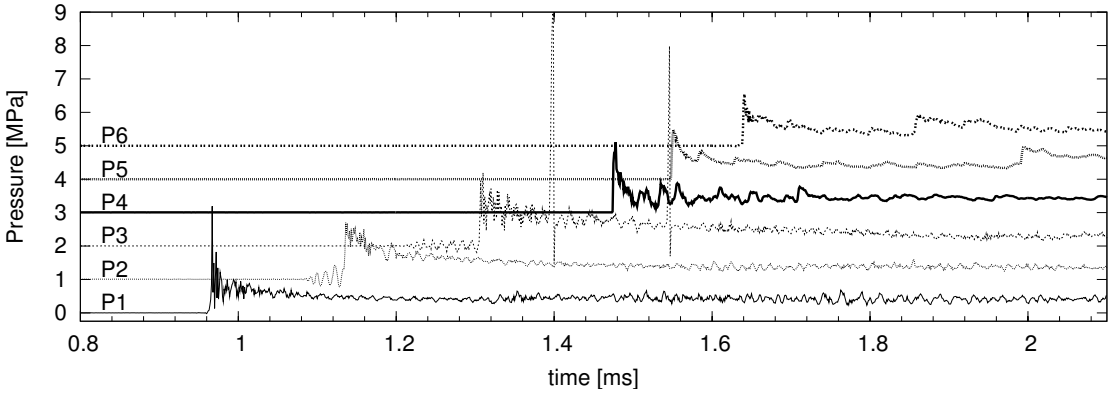

Figure K.61: Shot 61, 0.5 H_2 + 0.5 N_2O, P_0=55 kPa, T_0=296 K. $U(P_1\text{-}P_2)/U_{CJ}$ = 1.000, $U(P_2\text{-}P_3)/U_{CJ}$ = 0.988.

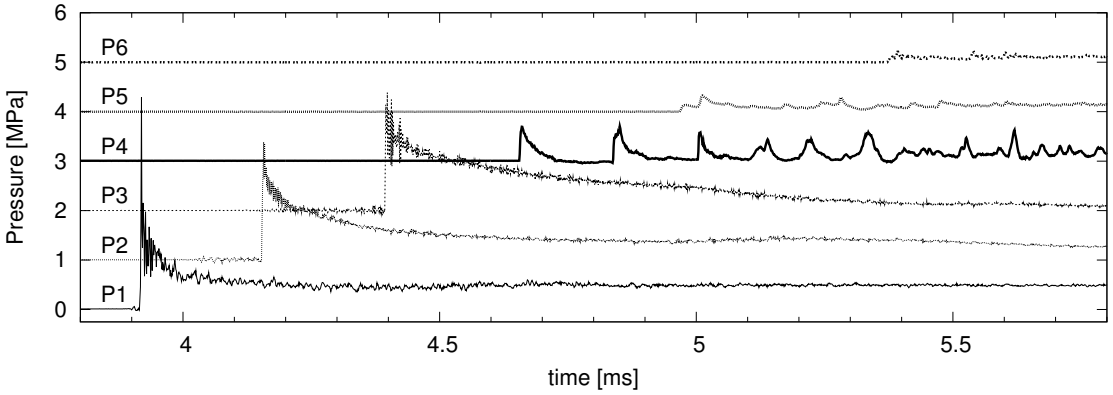

Figure K.62: Shot 62, 0.2 H_2 + 0.1 O_2 + 0.7 Ar, P_0=100 kPa, T_0=294 K. $U(P_1\text{-}P_2)/U_{CJ}$ = 1.001, $U(P_2\text{-}P_3)/U_{CJ}$ = 0.984.

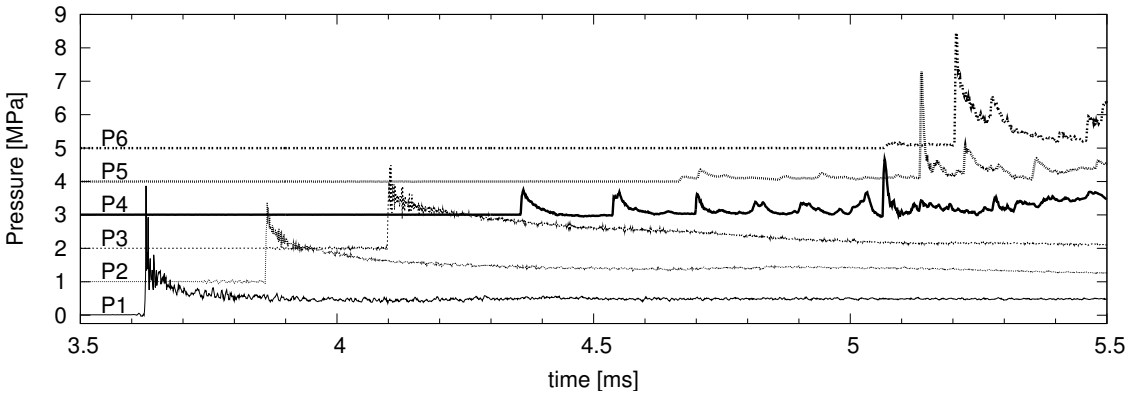

Figure K.63: Shot 63, 0.2 H_2 + 0.1 O_2 + 0.7 Ar, P_0=100 kPa, T_0=294 K. $U(P_1\text{-}P_2)/U_{CJ}$ = 1.009, $U(P_2\text{-}P_3)/U_{CJ}$ = 0.992.

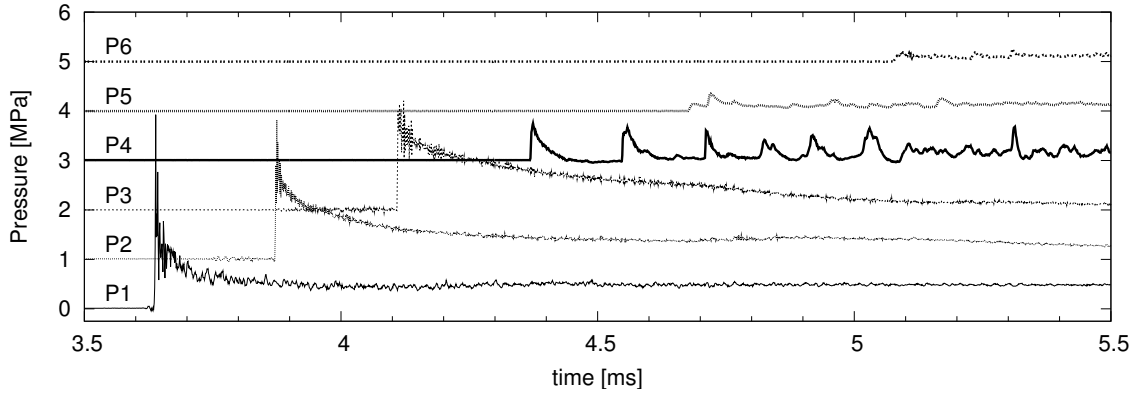

Figure K.64: Shot 64, 0.2 H_2 + 0.1 O_2 + 0.7 Ar, P_0=100 kPa, T_0=294 K. U(P_1-P_2)/U_{CJ} = 1.009, U(P_2-P_3)/U_{CJ} = 0.992.

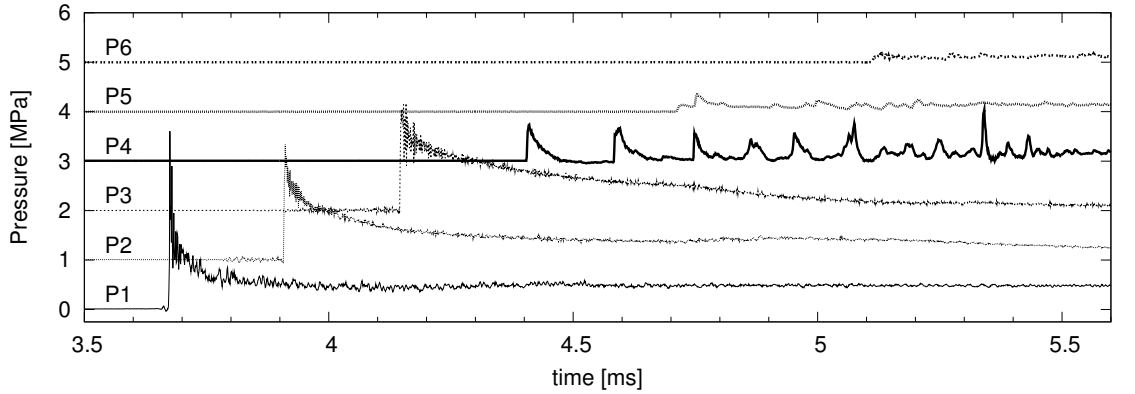

Figure K.65: Shot 65, 0.2 H_2 + 0.1 O_2 + 0.7 Ar, P_0=100 kPa, T_0=295 K. U(P_1-P_2)/U_{CJ} = 1.009, U(P_2-P_3)/U_{CJ} = 0.992.

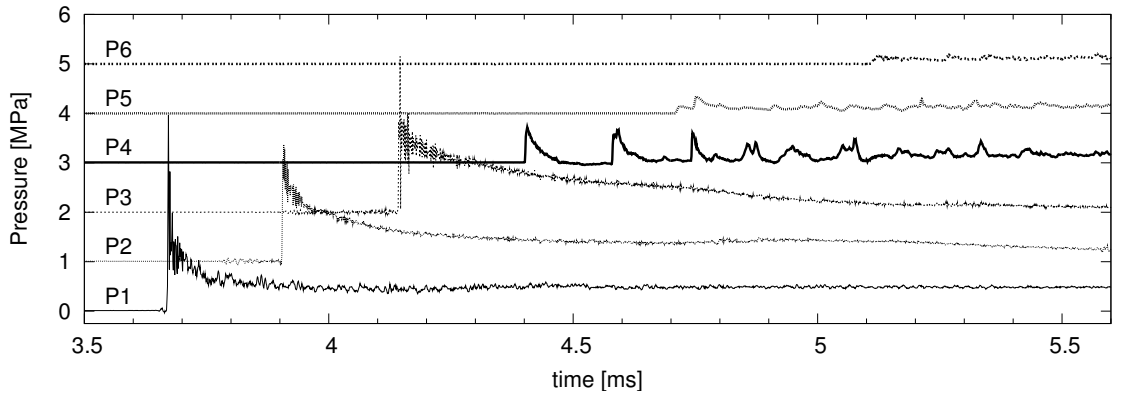

Figure K.66: Shot 66, 0.2 H_2 + 0.1 O_2 + 0.7 Ar, P_0=100 kPa, T_0=294 K. U(P_1-P_2)/U_{CJ} = 1.009, U(P_2-P_3)/U_{CJ} = 0.992.

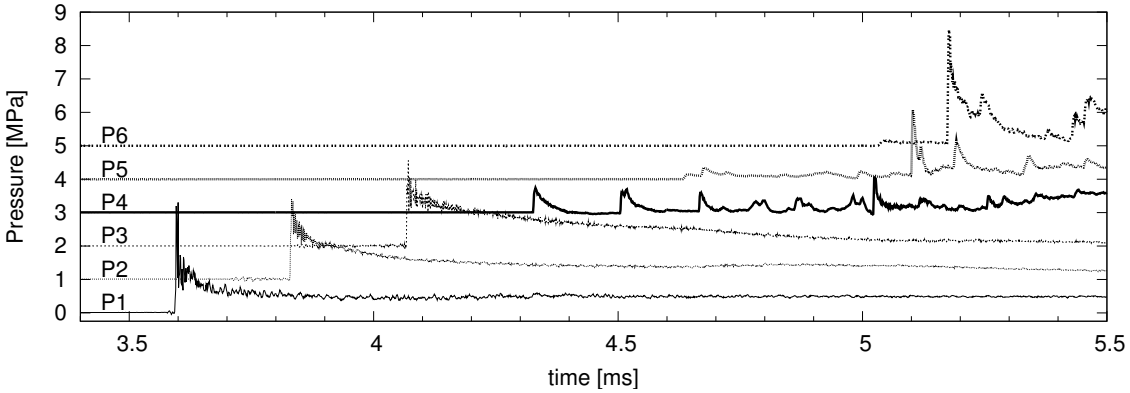

Figure K.67: Shot 67, 0.2 H_2 + 0.1 O_2 + 0.7 Ar, P_0=100 kPa, T_0=295 K. U(P_1-P_2)/U_{CJ} = 1.005, U(P_2-P_3)/U_{CJ} = 0.992.

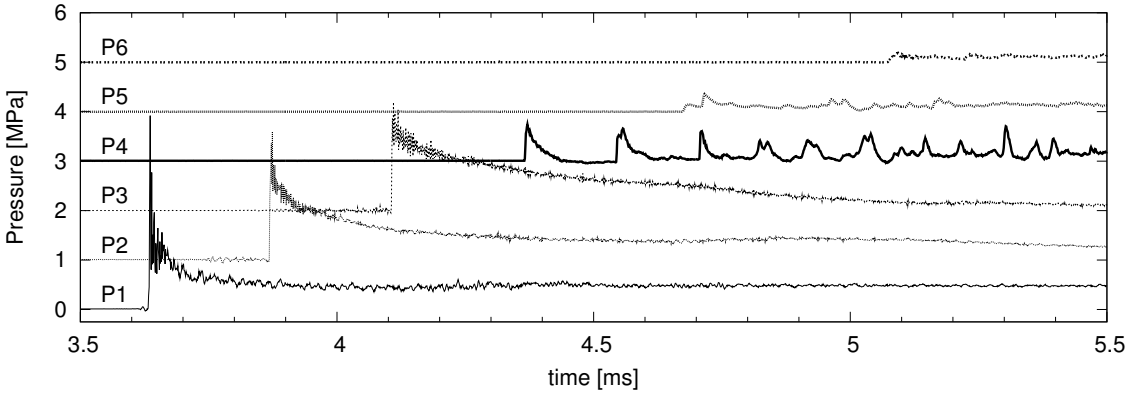

Figure K.68: Shot 68, 0.2 H_2 + 0.1 O_2 + 0.7 Ar, P_0=100 kPa, T_0=295 K. U(P_1-P_2)/U_{CJ} = 1.009, U(P_2-P_3)/U_{CJ} = 0.992.

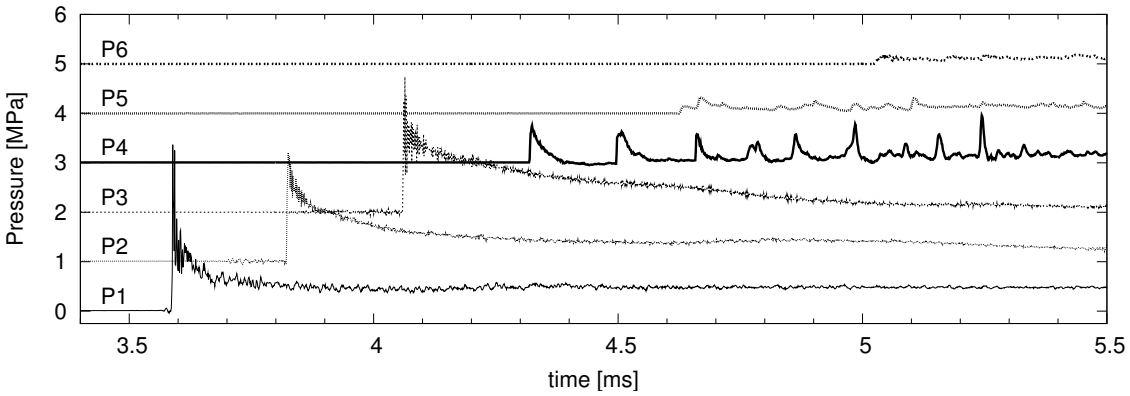

Figure K.69: Shot 69, 0.2 H_2 + 0.1 O_2 + 0.7 Ar, P_0=100 kPa, T_0=295 K. U(P_1-P_2)/U_{CJ} = 1.005, U(P_2-P_3)/U_{CJ} = 0.997.

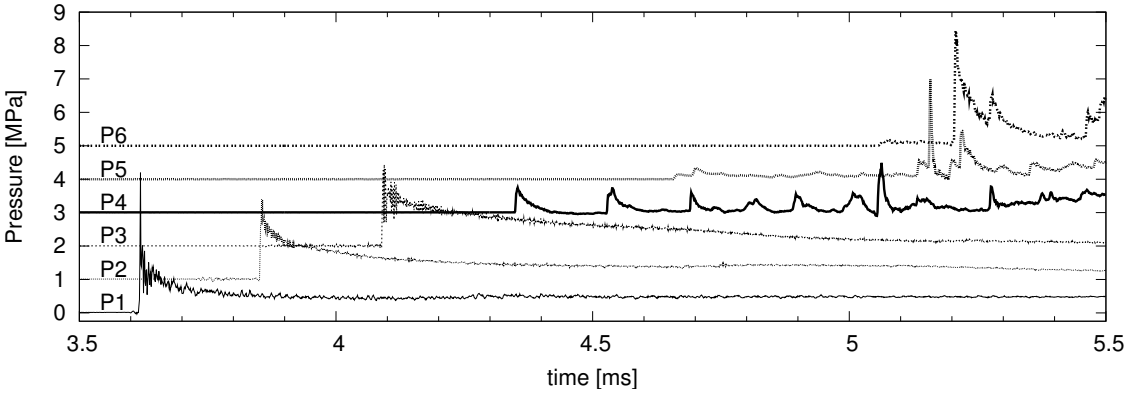

Figure K.70: Shot 70, 0.2 H_2 + 0.1 O_2 + 0.7 Ar, P_0=100 kPa, T_0=296 K. U(P_1-P_2)/U_{CJ} = 1.009, U(P_2-P_3)/U_{CJ} = 0.992.

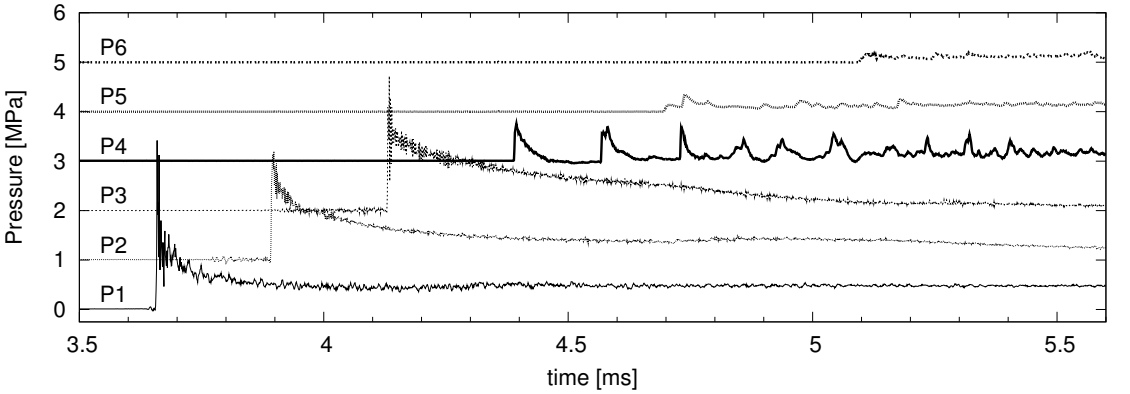

Figure K.71: Shot 71, 0.2 H_2 + 0.1 O_2 + 0.7 Ar, P_0=100 kPa, T_0=296 K. U(P_1-P_2)/U_{CJ} = 1.005, U(P_2-P_3)/U_{CJ} = 0.992.

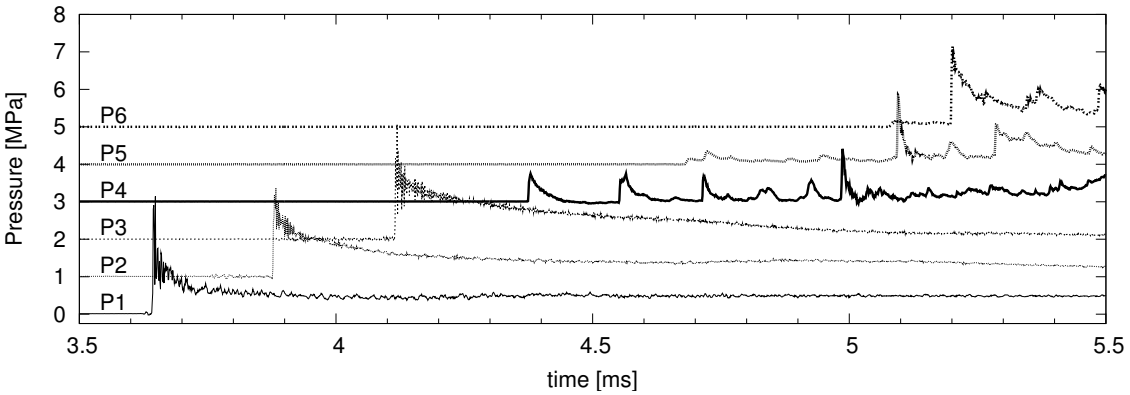

Figure K.72: Shot 72, 0.2 H_2 + 0.1 O_2 + 0.7 Ar, P_0=100 kPa, T_0=296 K. U(P_1-P_2)/U_{CJ} = 1.005, U(P_2-P_3)/U_{CJ} = 0.992.

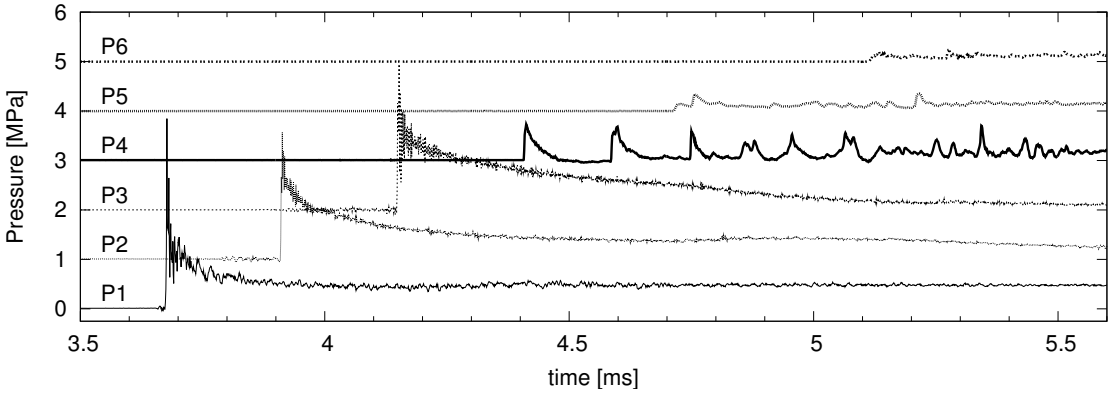

Figure K.73: Shot 73, 0.2 H_2 + 0.1 O_2 + 0.7 Ar, P_0=100 kPa, T_0=296 K. U(P_1-P_2)/U_{CJ} = 1.005, U(P_2-P_3)/U_{CJ} = 0.992.

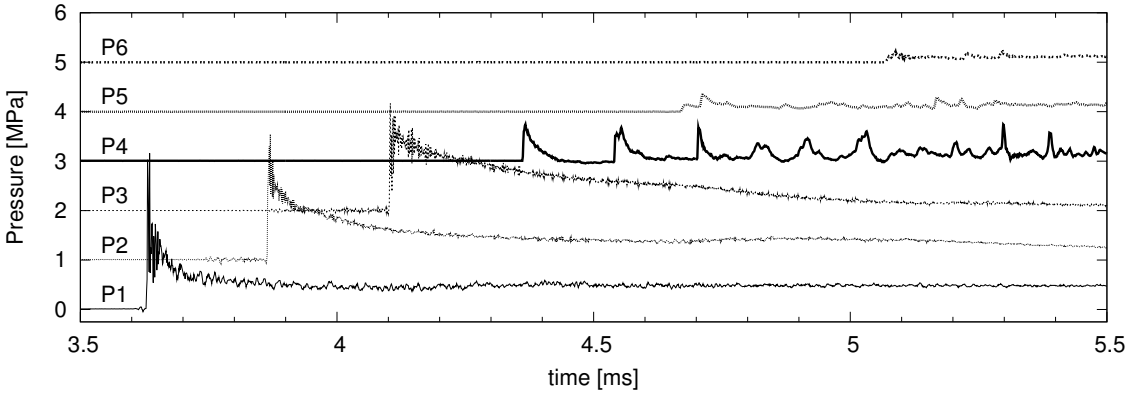

Figure K.74: Shot 74, 0.2 H_2 + 0.1 O_2 + 0.7 Ar, P_0=100 kPa, T_0=296 K. U(P_1-P_2)/U_{CJ} = 1.005, U(P_2-P_3)/U_{CJ} = 0.992.

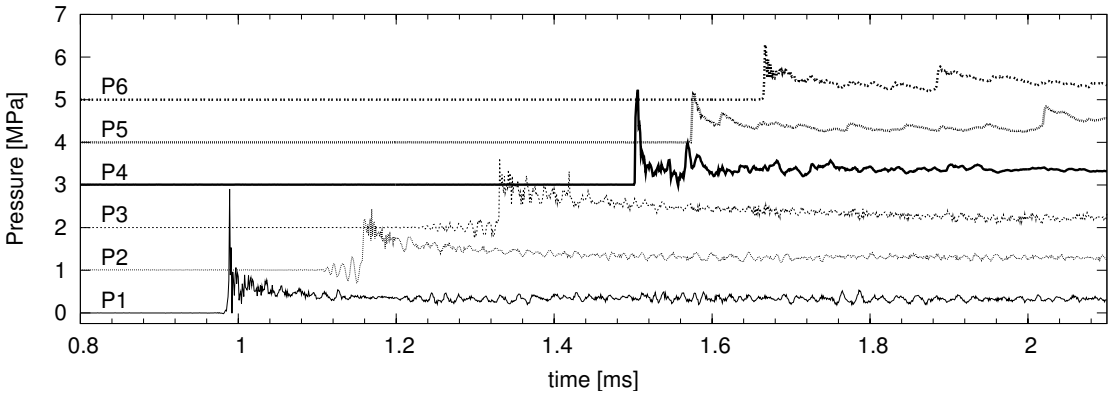

Figure K.75: Shot 75, 0.5 H_2 + 0.5 N_2O, P_0=45 kPa, T_0=294 K. U(P_1-P_2)/U_{CJ} = 0.998, U(P_2-P_3)/U_{CJ} = 0.980.

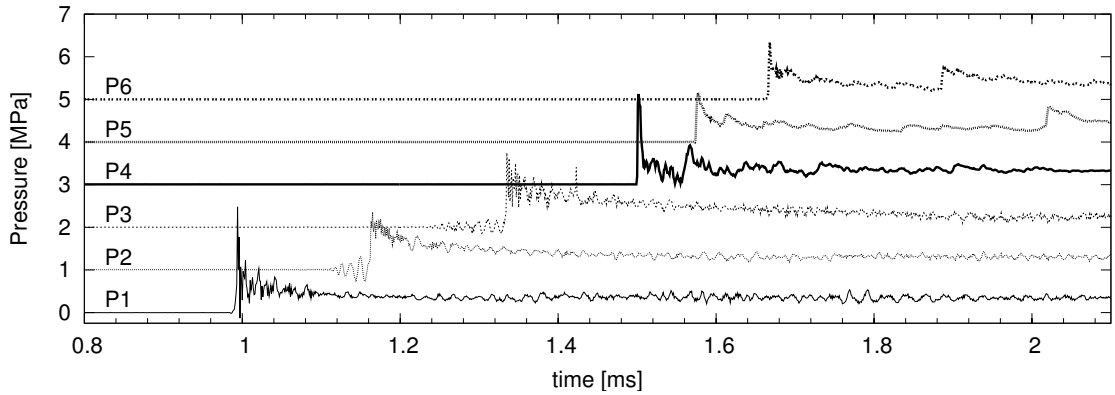

Figure K.76: Shot 76, 0.5 H_2 + 0.5 N_2O, P_0=45 kPa, T_0=295 K. $U(P_1\text{-}P_2)/U_{CJ}$ = 0.998, $U(P_2\text{-}P_3)/U_{CJ}$ = 0.986.

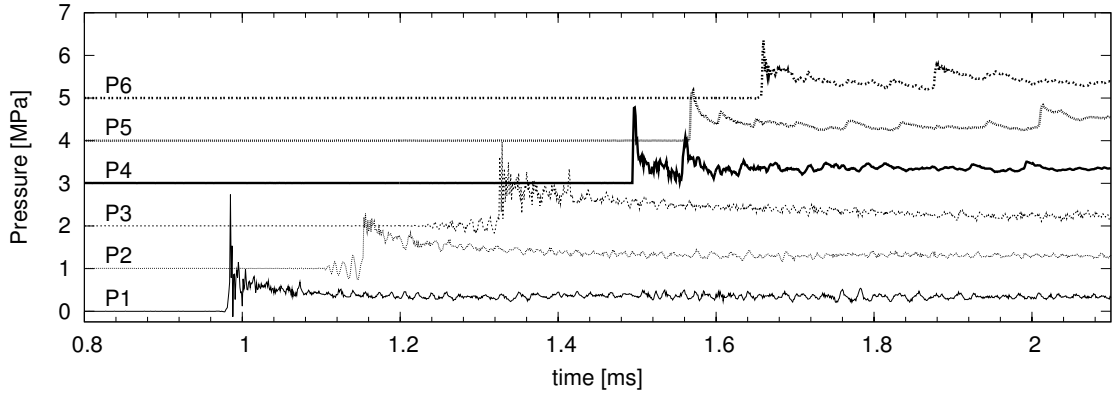

Figure K.77: Shot 77, 0.5 H_2 + 0.5 N_2O, P_0=45 kPa, T_0=295 K. $U(P_1\text{-}P_2)/U_{CJ}$ = 0.998, $U(P_2\text{-}P_3)/U_{CJ}$ = 0.986.

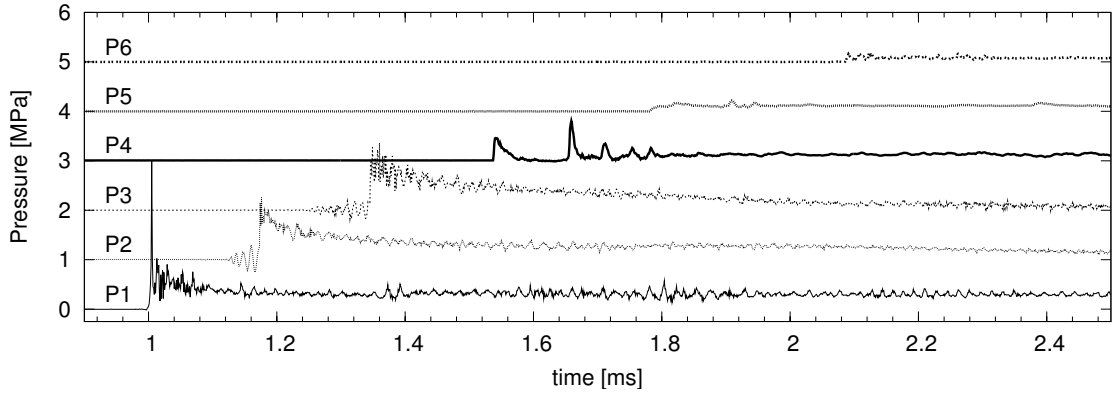

Figure K.78: Shot 78, 0.5 H_2 + 0.5 N_2O, P_0=40 kPa, T_0=295 K. $U(P_1\text{-}P_2)/U_{CJ}$ = 1.000, $U(P_2\text{-}P_3)/U_{CJ}$ = 0.988.

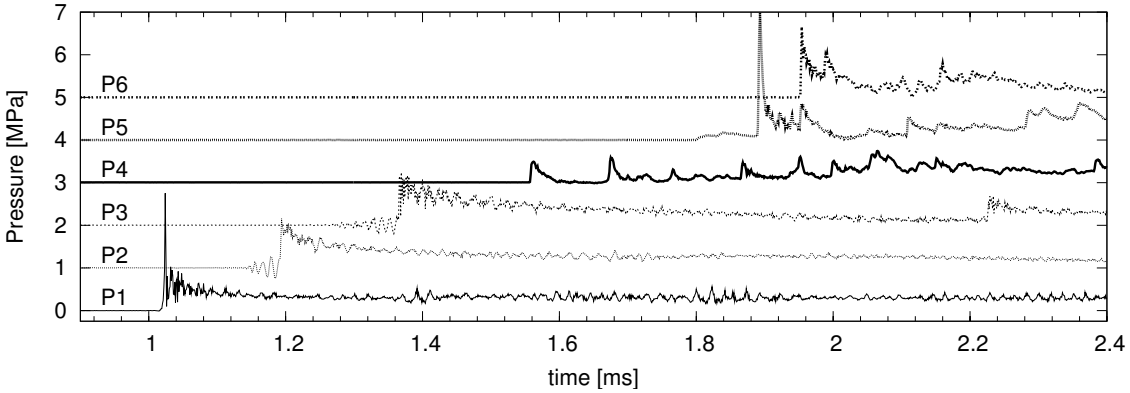

Figure K.79: Shot 79, 0.5 H_2 + 0.5 N_2O, P_0=40 kPa, T_0=295 K. $U(P_1\text{-}P_2)/U_{CJ}$ = 0.994, $U(P_2\text{-}P_3)/U_{CJ}$ = 0.982.

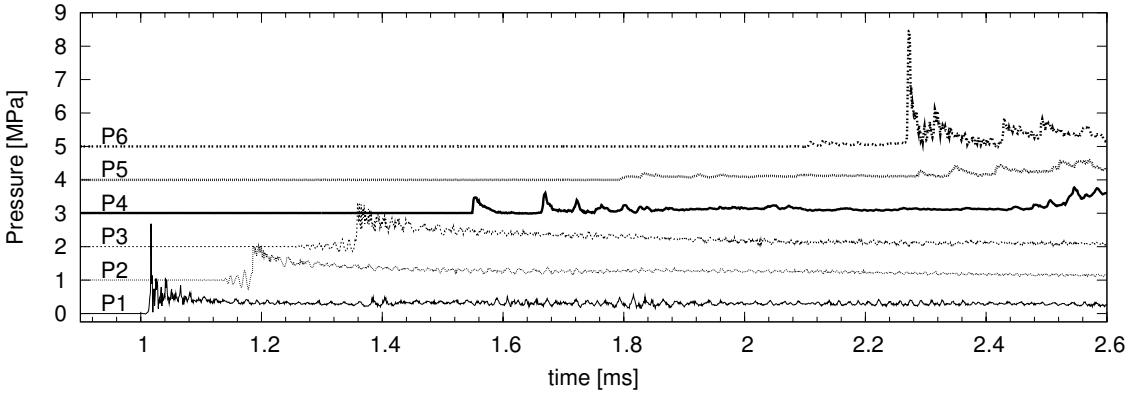

Figure K.80: Shot 80, 0.5 H_2 + 0.5 N_2O, P_0=40 kPa, T_0=296 K. $U(P_1\text{-}P_2)/U_{CJ}$ = 1.000, $U(P_2\text{-}P_3)/U_{CJ}$ = 0.988.

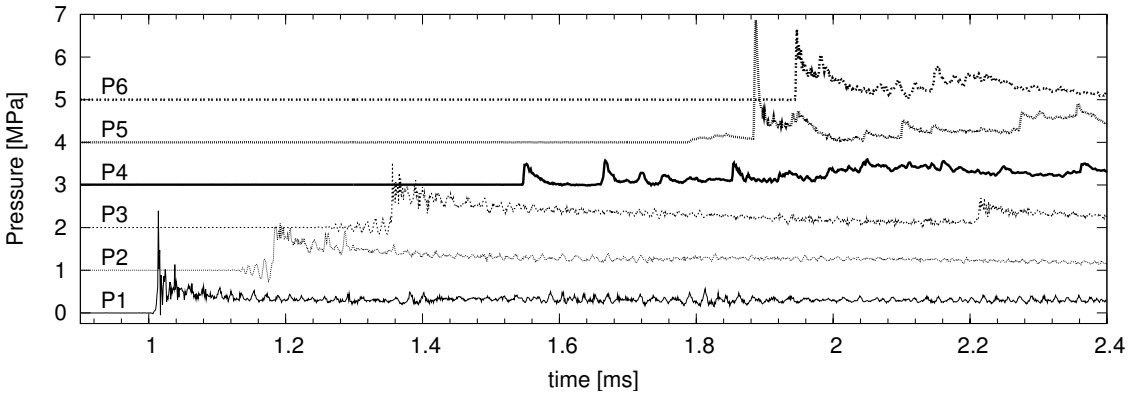

Figure K.81: Shot 81, 0.5 H_2 + 0.5 N_2O, P_0=40 kPa, T_0=296 K. $U(P_1\text{-}P_2)/U_{CJ}$ = 1.000, $U(P_2\text{-}P_3)/U_{CJ}$ = 0.982.

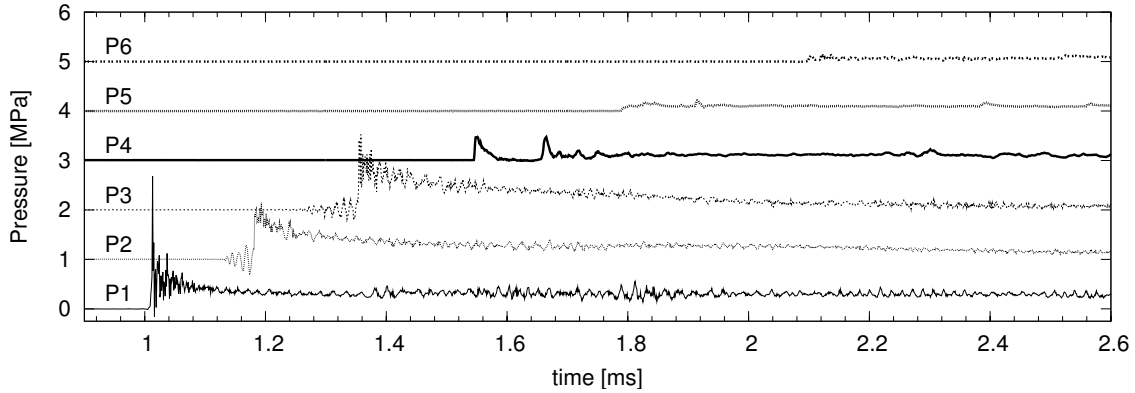

Figure K.82: Shot 82, 0.5 H_2 + 0.5 N_2O, P_0=40 kPa, T_0=296 K. $U(P_1\text{-}P_2)/U_{CJ}$ = 1.000, $U(P_2\text{-}P_3)/U_{CJ}$ = 0.982.

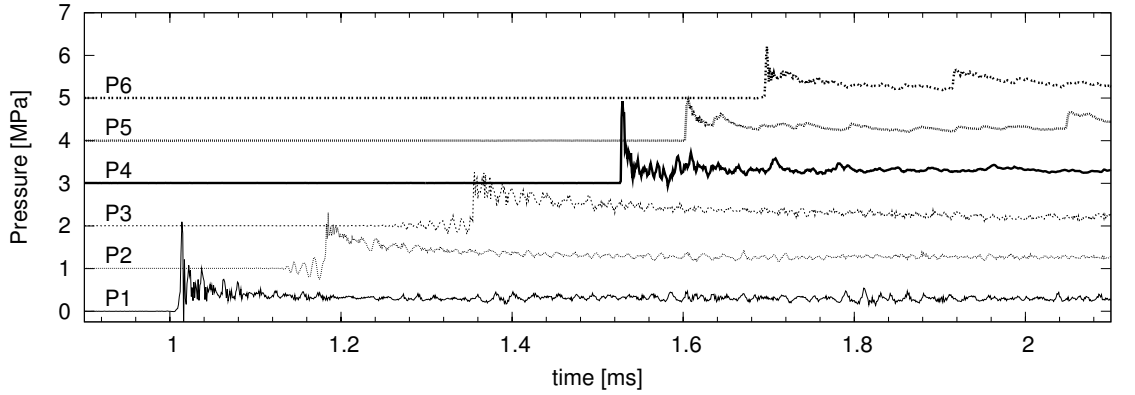

Figure K.83: Shot 83, 0.5 H_2 + 0.5 N_2O, P_0=40 kPa, T_0=296 K. $U(P_1\text{-}P_2)/U_{CJ}$ = 1.000, $U(P_2\text{-}P_3)/U_{CJ}$ = 0.988.

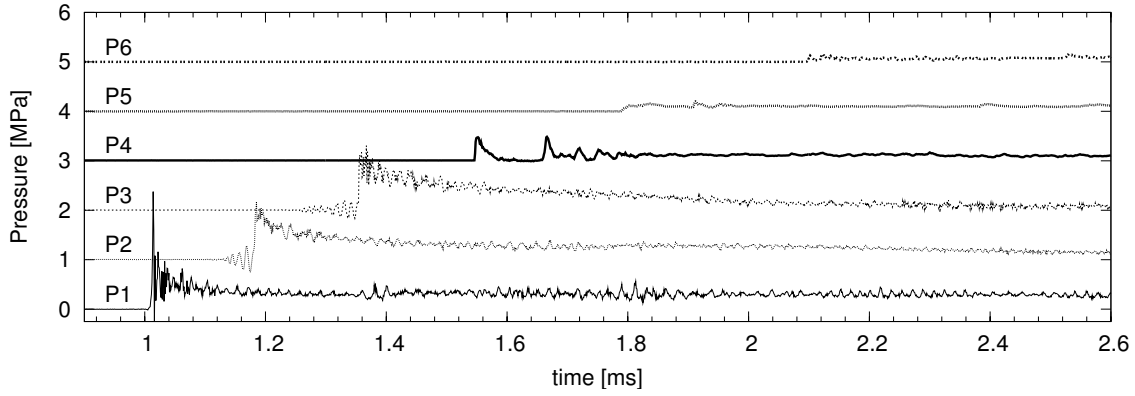

Figure K.84: Shot 84, 0.5 H_2 + 0.5 N_2O, P_0=40 kPa, T_0=296 K. $U(P_1\text{-}P_2)/U_{CJ}$ = 0.994, $U(P_2\text{-}P_3)/U_{CJ}$ = 0.988.

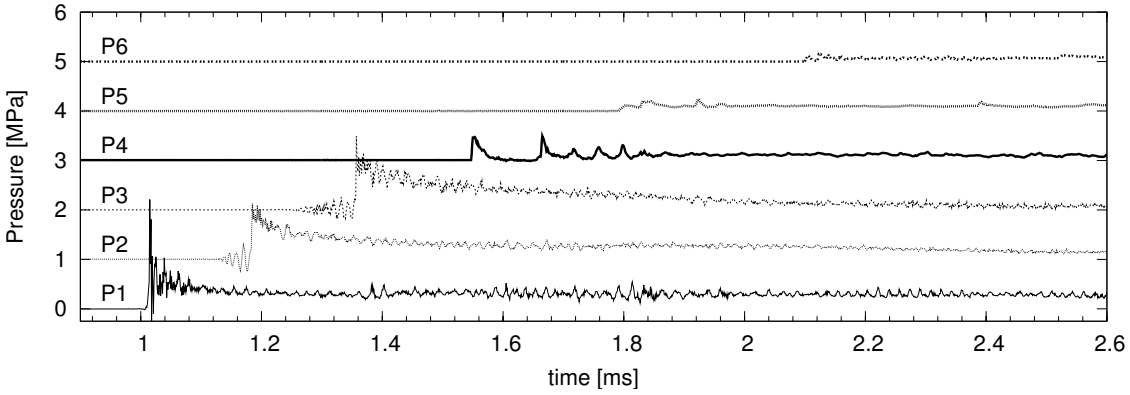

Figure K.85: Shot 85, 0.5 H_2 + 0.5 N_2O, P_0=40 kPa, T_0=296 K. $U(P_1\text{-}P_2)/U_{CJ}$ = 1.000, $U(P_2\text{-}P_3)/U_{CJ}$ = 0.982.

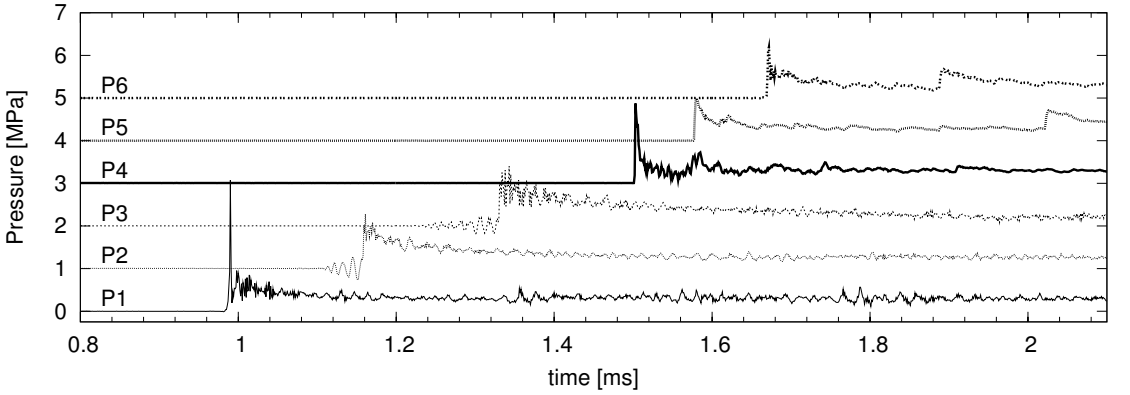

Figure K.86: Shot 86, 0.5 H_2 + 0.5 N_2O, P_0=40 kPa, T_0=296 K. $U(P_1\text{-}P_2)/U_{CJ}$ = 0.994, $U(P_2\text{-}P_3)/U_{CJ}$ = 0.988.

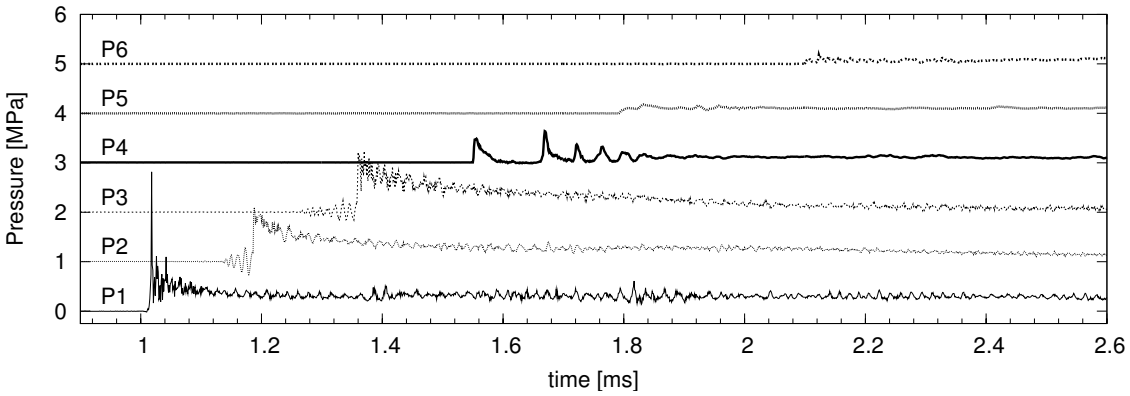

Figure K.87: Shot 87, 0.5 H_2 + 0.5 N_2O, P_0=40 kPa, T_0=296 K. $U(P_1\text{-}P_2)/U_{CJ}$ = 0.994, $U(P_2\text{-}P_3)/U_{CJ}$ = 0.988.

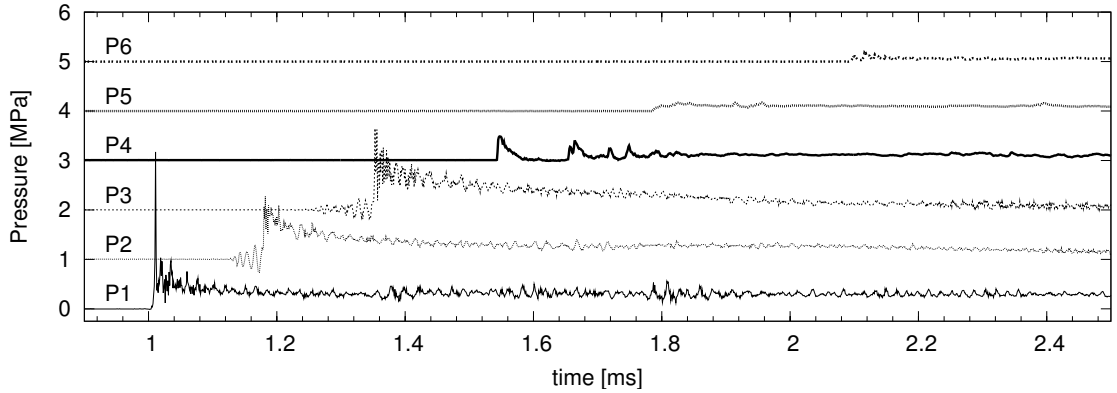

Figure K.88: Shot 88, 0.5 H_2 + 0.5 N_2O, P_0=40 kPa, T_0=296 K. $U(P_1\text{-}P_2)/U_{CJ}$ = 1.000, $U(P_2\text{-}P_3)/U_{CJ}$ = 0.988.

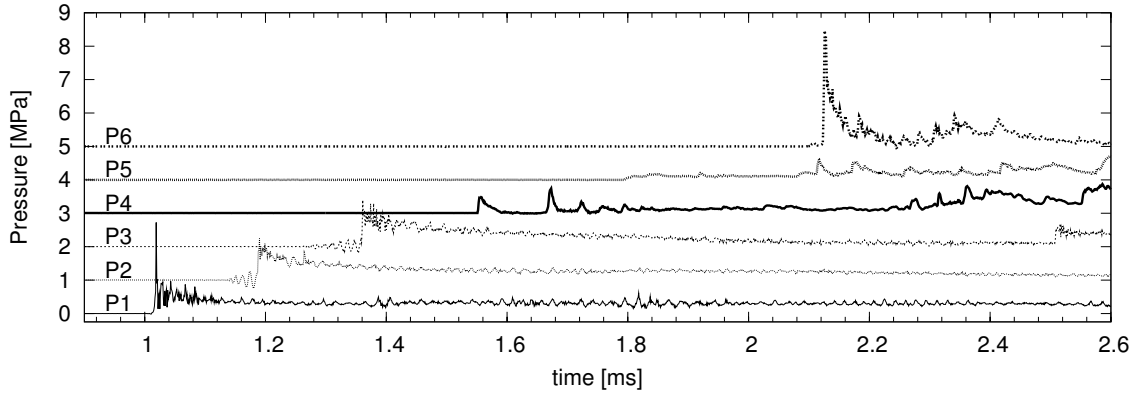

Figure K.89: Shot 89, 0.5 H_2 + 0.5 N_2O, P_0=40 kPa, T_0=296 K. $U(P_1\text{-}P_2)/U_{CJ}$ = 1.000, $U(P_2\text{-}P_3)/U_{CJ}$ = 0.988.

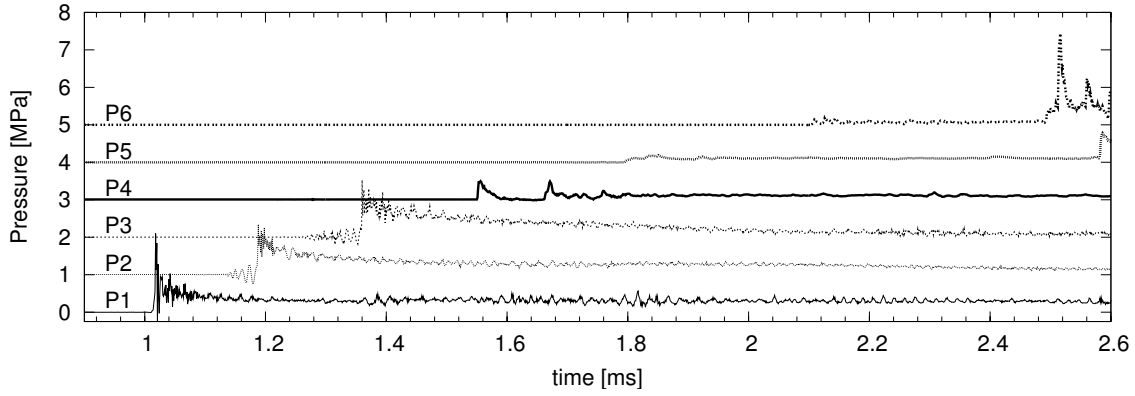

Figure K.90: Shot 90, 0.5 H_2 + 0.5 N_2O, P_0=40 kPa, T_0=294 K. $U(P_1\text{-}P_2)/U_{CJ}$ = 1.000, $U(P_2\text{-}P_3)/U_{CJ}$ = 0.982.

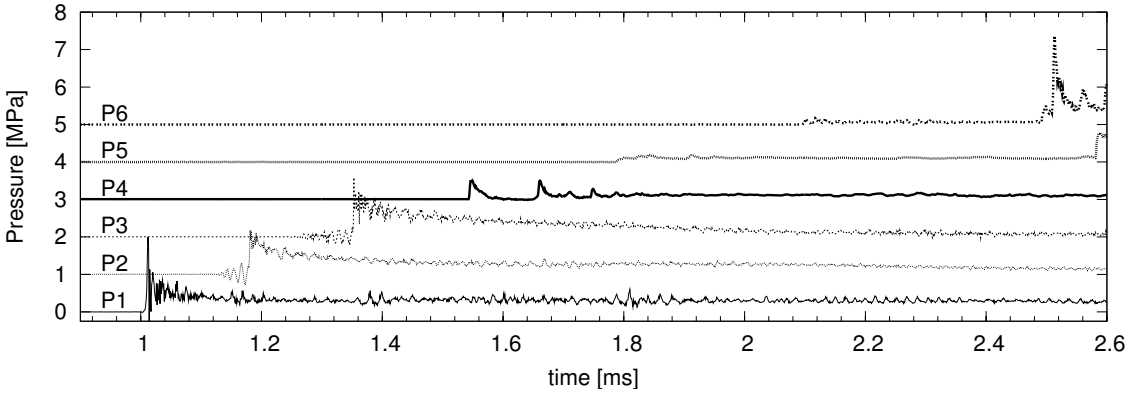

Figure K.91: Shot 91, 0.5 H_2 + 0.5 N_2O, P_0=40 kPa, T_0=294 K. $U(P_1\text{-}P_2)/U_{CJ}$ = 0.994, $U(P_2\text{-}P_3)/U_{CJ}$ = 0.988.

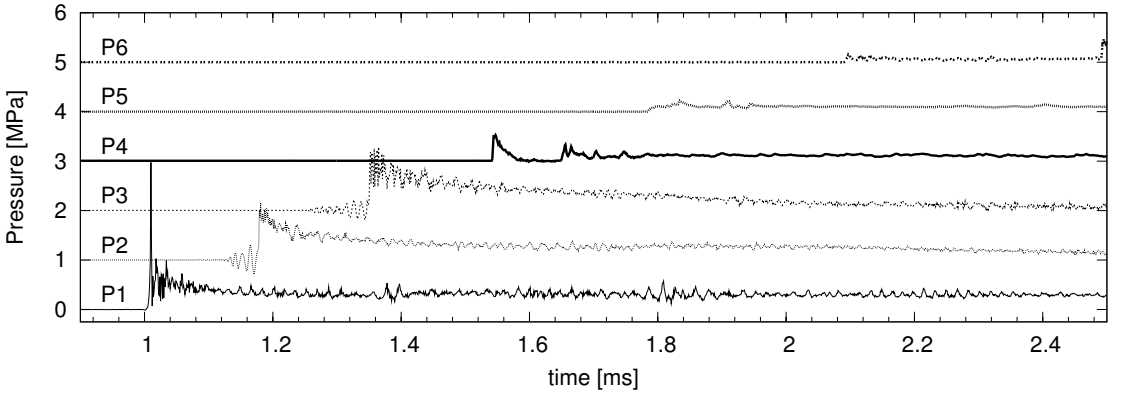

Figure K.92: Shot 92, 0.5 H_2 + 0.5 N_2O, P_0=40 kPa, T_0=294 K. $U(P_1\text{-}P_2)/U_{CJ}$ = 0.994, $U(P_2\text{-}P_3)/U_{CJ}$ = 0.988.

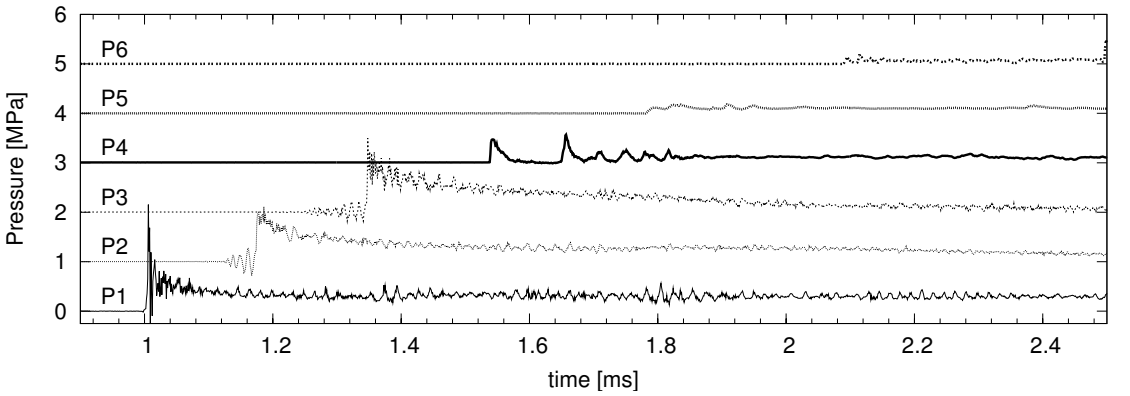

Figure K.93: Shot 93, 0.5 H_2 + 0.5 N_2O, P_0=40 kPa, T_0=294 K. $U(P_1\text{-}P_2)/U_{CJ}$ = 1.000, $U(P_2\text{-}P_3)/U_{CJ}$ = 0.982.

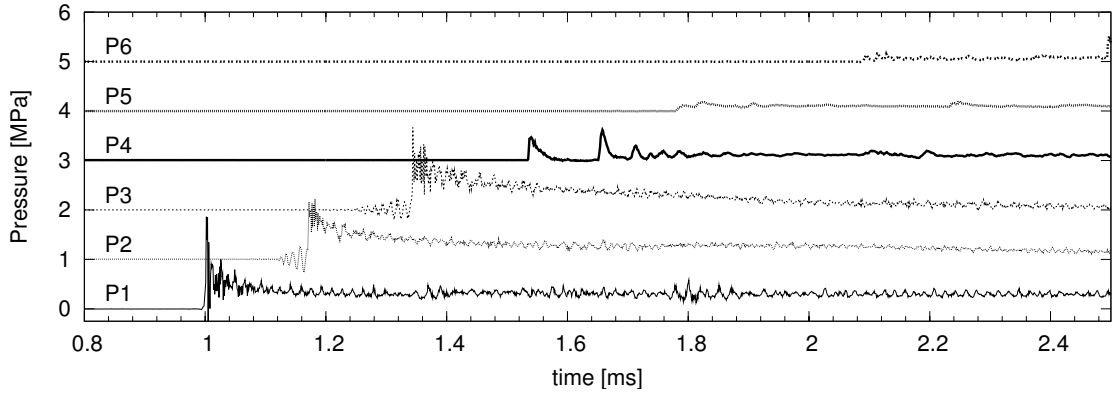

Figure K.94: Shot 94, 0.5 H_2 + 0.5 N_2O, P_0=40 kPa, T_0=295 K. $U(P_1\text{-}P_2)/U_{CJ}$ = 1.000, $U(P_2\text{-}P_3)/U_{CJ}$ = 0.982.

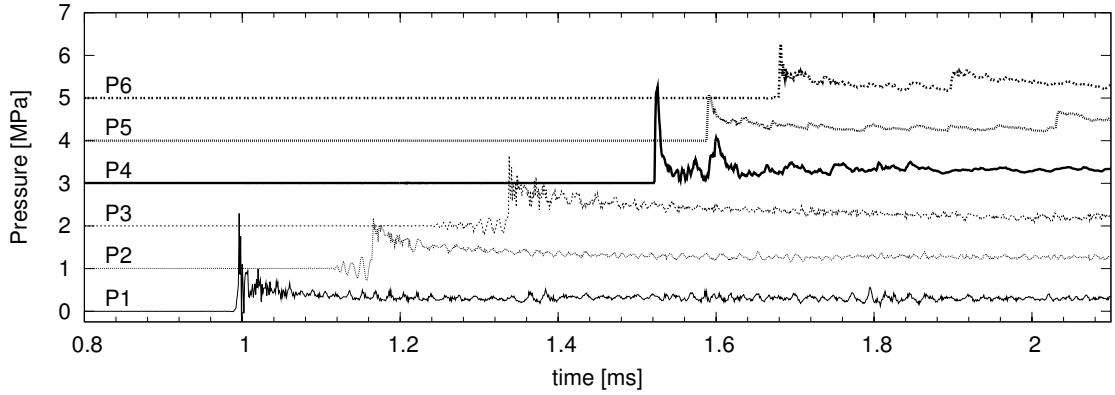

Figure K.95: Shot 95, 0.5 H_2 + 0.5 N_2O, P_0=40 kPa, T_0=295 K. $U(P_1\text{-}P_2)/U_{CJ}$ = 1.000, $U(P_2\text{-}P_3)/U_{CJ}$ = 0.982.

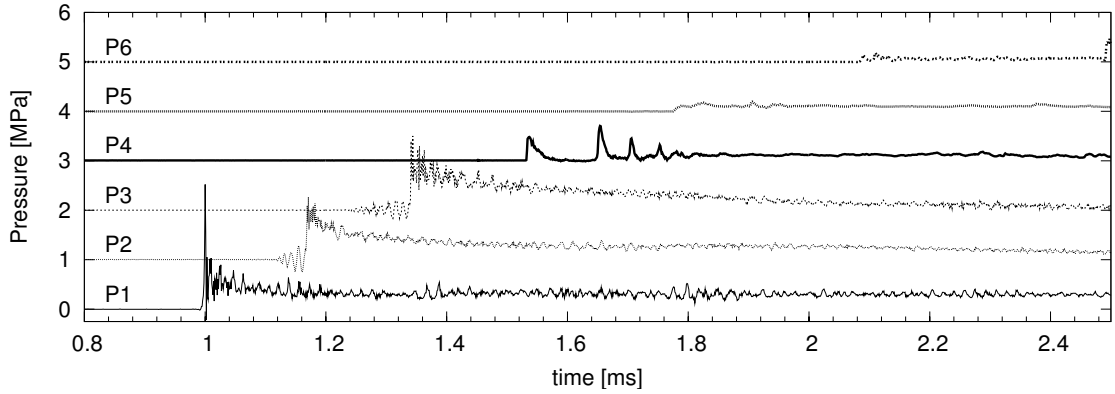

Figure K.96: Shot 96, 0.5 H_2 + 0.5 N_2O, P_0=40 kPa, T_0=295 K. $U(P_1\text{-}P_2)/U_{CJ}$ = 1.000, $U(P_2\text{-}P_3)/U_{CJ}$ = 0.982.

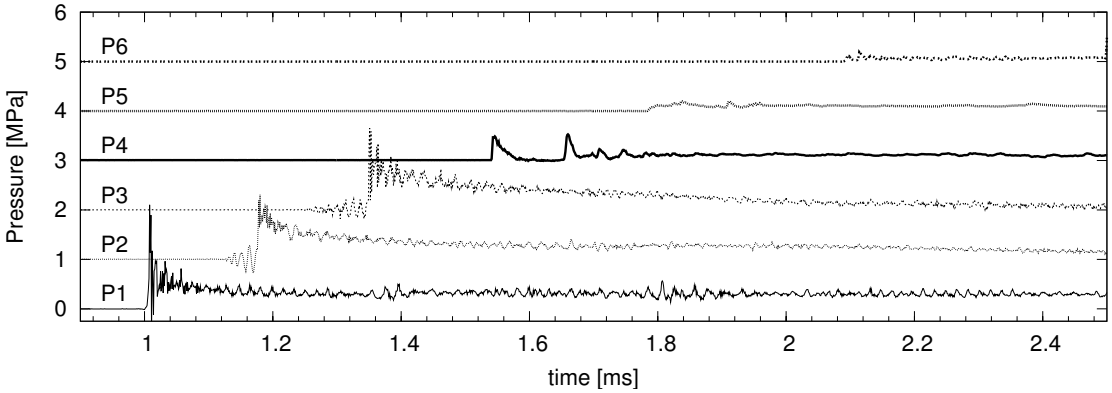

Figure K.97: Shot 97, 0.5 H_2 + 0.5 N_2O, P_0=40 kPa, T_0=295 K. $U(P_1\text{-}P_2)/U_{CJ}$ = 1.000, $U(P_2\text{-}P_3)/U_{CJ}$ = 0.982.

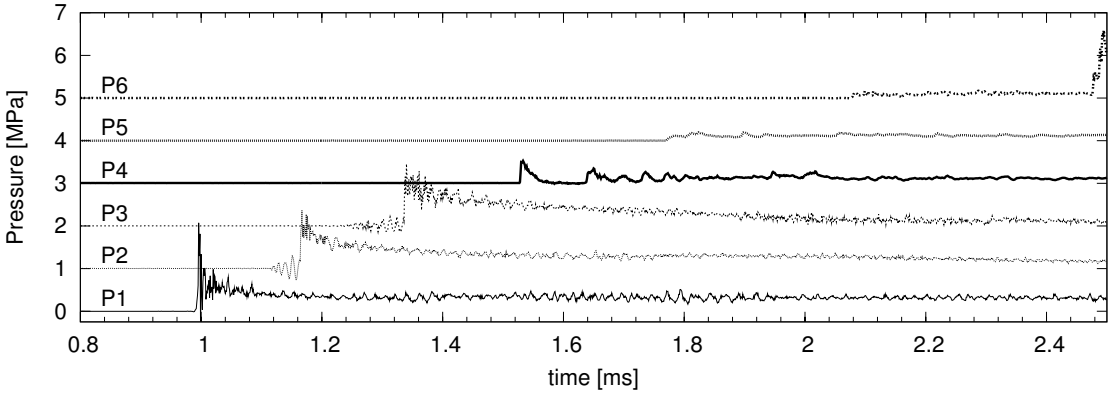

Figure K.98: Shot 98, 0.5 H_2 + 0.5 N_2O, P_0=42.5 kPa, T_0=295 K. $U(P_1\text{-}P_2)/U_{CJ}$ = 0.999, $U(P_2\text{-}P_3)/U_{CJ}$ = 0.987.

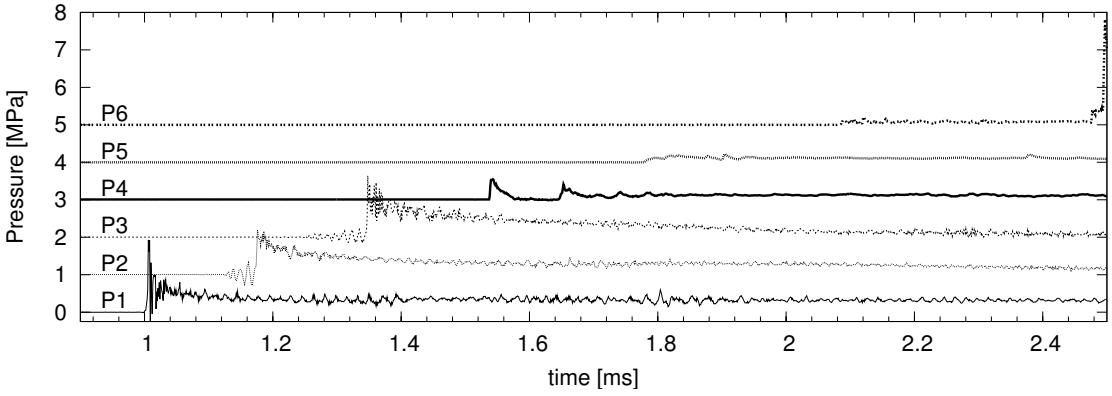

Figure K.99: Shot 99, 0.5 H_2 + 0.5 N_2O, P_0=42.5 kPa, T_0=295 K. $U(P_1\text{-}P_2)/U_{CJ}$ = 0.999, $U(P_2\text{-}P_3)/U_{CJ}$ = 0.987.

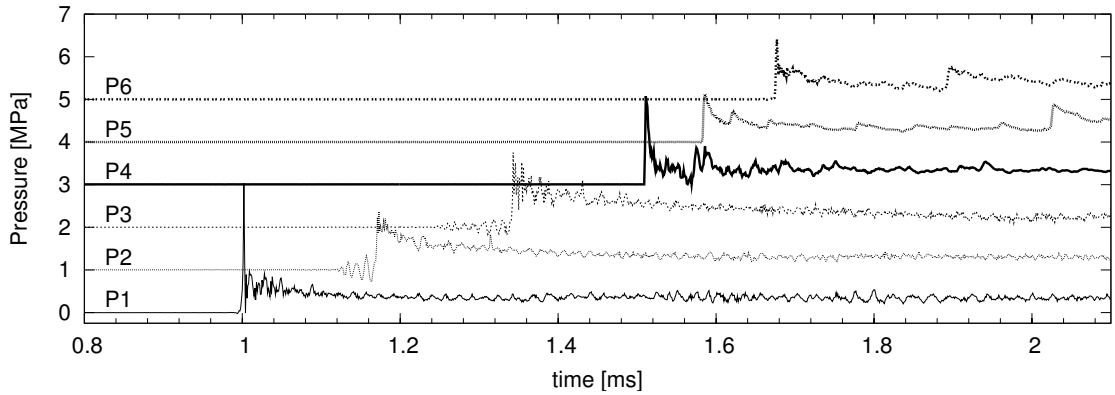

Figure K.100: Shot 100, 0.5 H_2 + 0.5 N_2O, P_0=45 kPa, T_0=295 K. $U(P_1\text{-}P_2)/U_{CJ}$ = 0.998, $U(P_2\text{-}P_3)/U_{CJ}$ = 0.986.

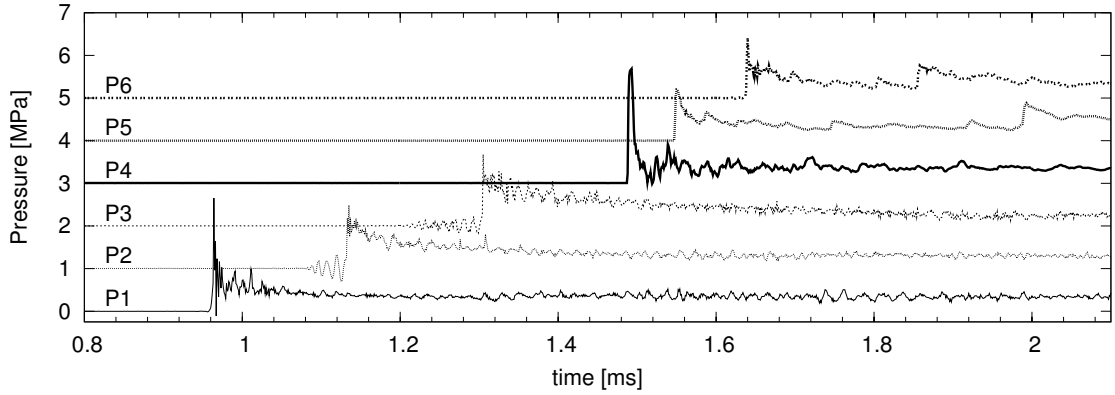

Figure K.101: Shot 101, 0.5 H_2 + 0.5 N_2O, P_0=45 kPa, T_0=295 K. $U(P_1\text{-}P_2)/U_{CJ}$ = 0.998, $U(P_2\text{-}P_3)/U_{CJ}$ = 0.986.

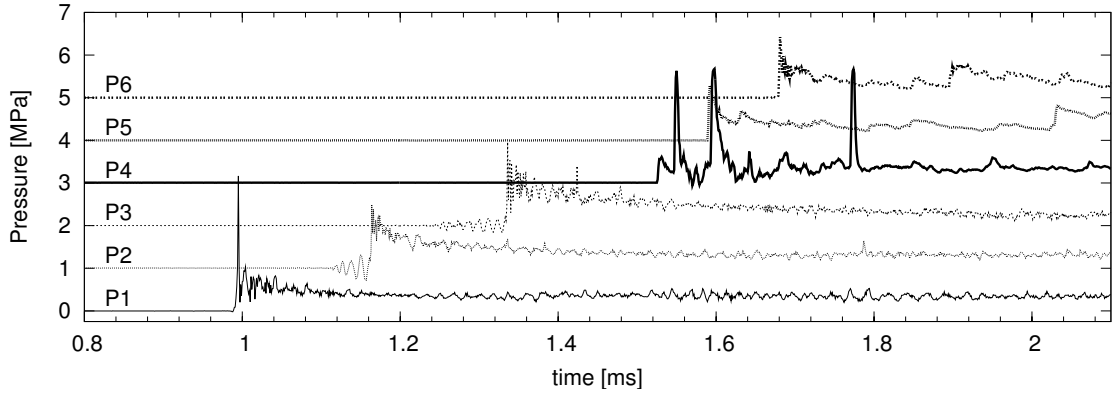

Figure K.102: Shot 102, 0.5 H_2 + 0.5 N_2O, P_0=45 kPa, T_0=296 K. $U(P_1\text{-}P_2)/U_{CJ}$ = 0.992, $U(P_2\text{-}P_3)/U_{CJ}$ = 0.986.

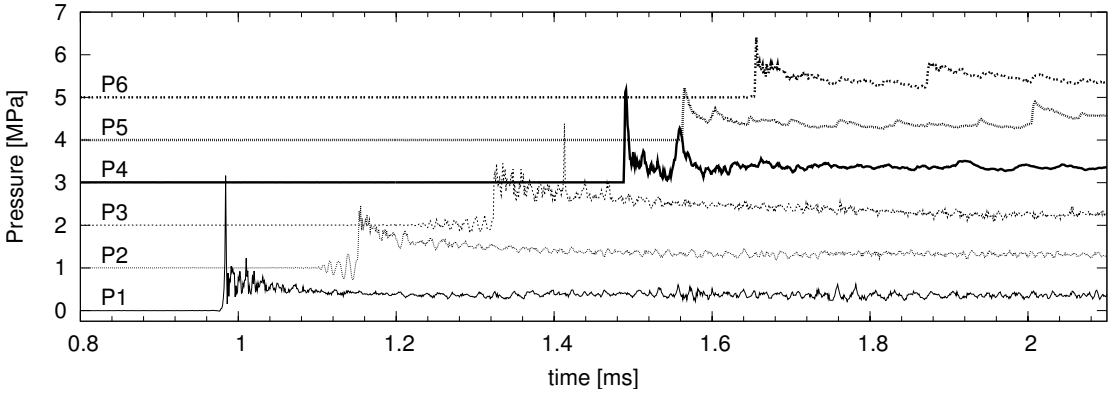

Figure K.103: Shot 103, 0.5 H_2 + 0.5 N_2O, P_0=47.5 kPa, T_0=296 K. U(P_1-P_2)/U_{CJ} = 0.997, U(P_2-P_3)/U_{CJ} = 0.985.

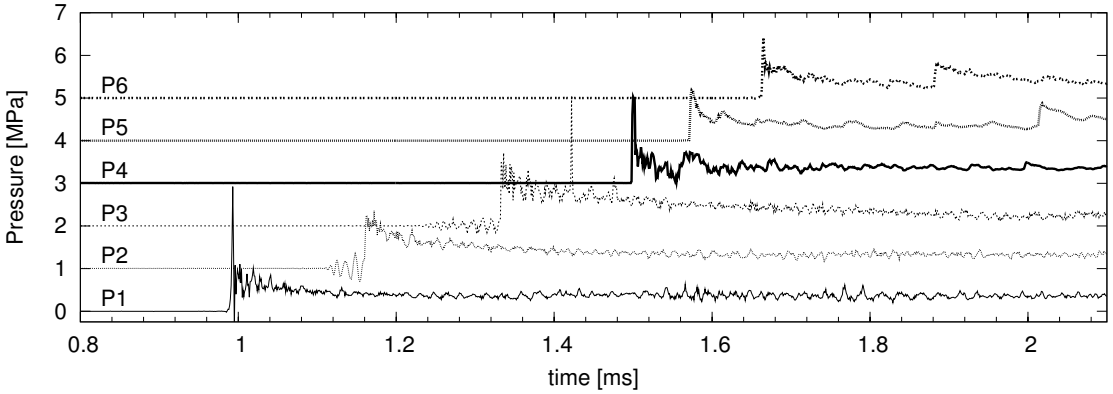

Figure K.104: Shot 104, 0.5 H_2 + 0.5 N_2O, P_0=47.5 kPa, T_0=296 K. U(P_1-P_2)/U_{CJ} = 0.997, U(P_2-P_3)/U_{CJ} = 0.985.

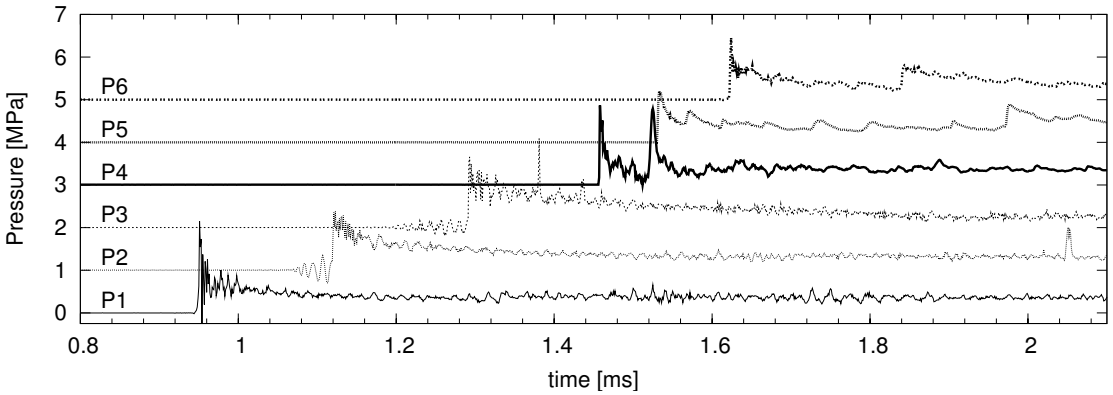

Figure K.105: Shot 105, 0.5 H_2 + 0.5 N_2O, P_0=47.5 kPa, T_0=296 K. U(P_1-P_2)/U_{CJ} = 0.997, U(P_2-P_3)/U_{CJ} = 0.985.

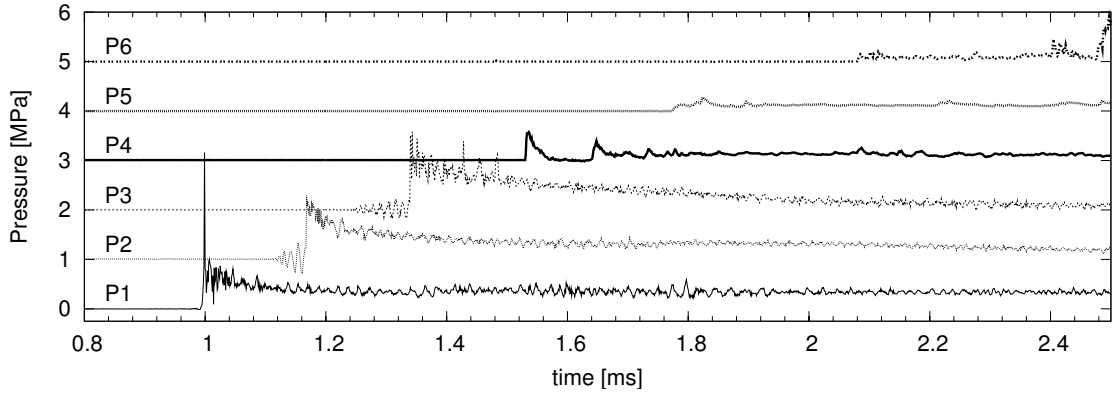

Figure K.106: Shot 106, 0.5 H_2 + 0.5 N_2O, P_0=45 kPa, T_0=294 K. $U(P_1\text{-}P_2)/U_{CJ}$ = 0.998, $U(P_2\text{-}P_3)/U_{CJ}$ = 0.986.

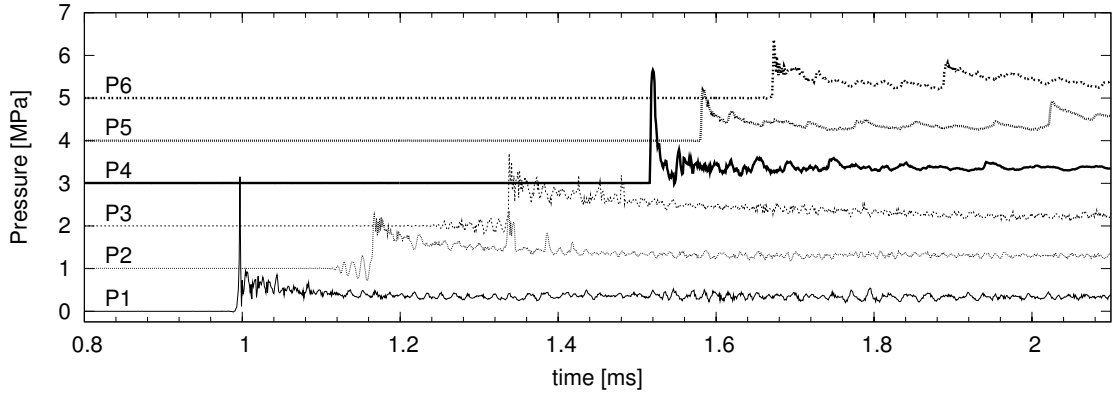

Figure K.107: Shot 107, 0.5 H_2 + 0.5 N_2O, P_0=45 kPa, T_0=294 K. $U(P_1\text{-}P_2)/U_{CJ}$ = 0.992, $U(P_2\text{-}P_3)/U_{CJ}$ = 0.986.

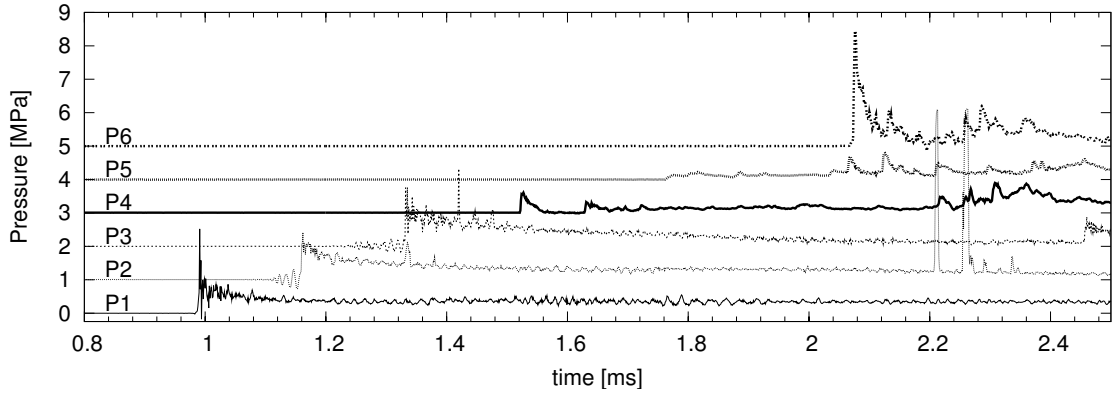

Figure K.108: Shot 108, 0.5 H_2 + 0.5 N_2O, P_0=45 kPa, T_0=295 K. $U(P_1\text{-}P_2)/U_{CJ}$ = 0.998, $U(P_2\text{-}P_3)/U_{CJ}$ = 0.986.

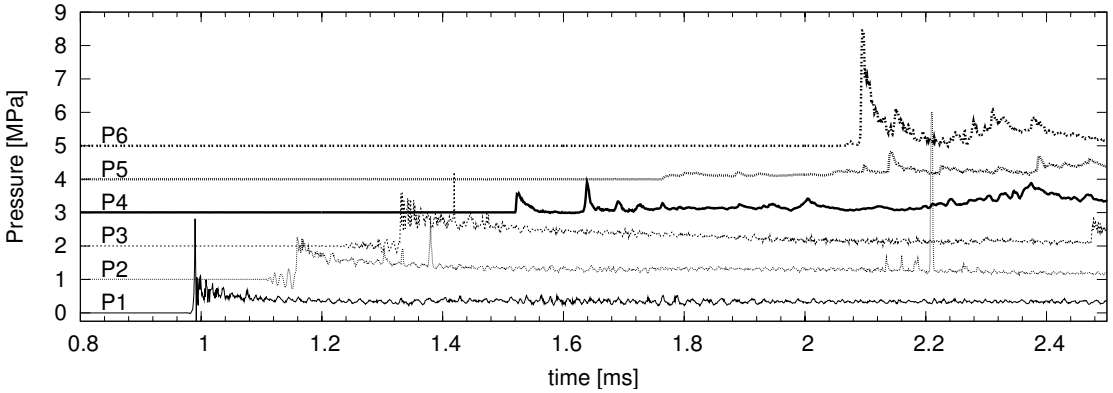

Figure K.109: Shot 109, 0.5 H_2 + 0.5 N_2O, P_0=45 kPa, T_0=295 K. $U(P_1\text{-}P_2)/U_{CJ}$ = 0.998, $U(P_2\text{-}P_3)/U_{CJ}$ = 0.986.

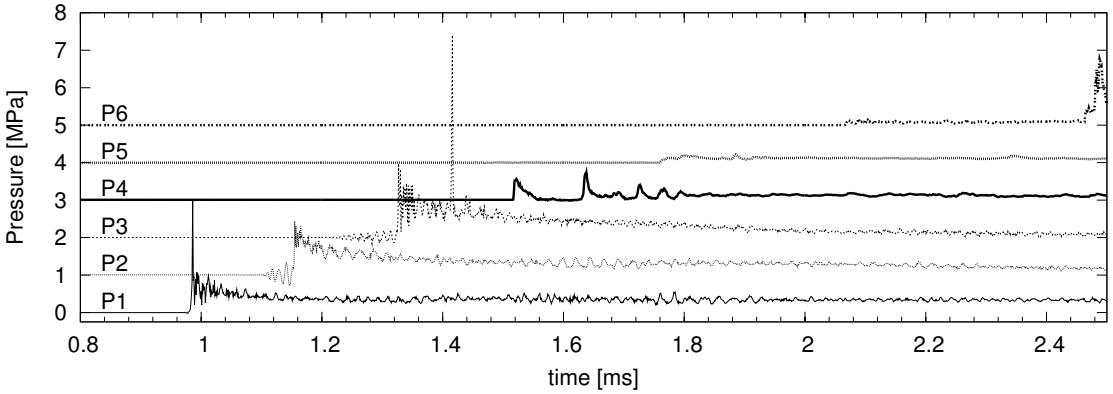

Figure K.110: Shot 110, 0.5 H_2 + 0.5 N_2O, P_0=45 kPa, T_0=295 K. $U(P_1\text{-}P_2)/U_{CJ}$ = 0.998, $U(P_2\text{-}P_3)/U_{CJ}$ = 0.992.

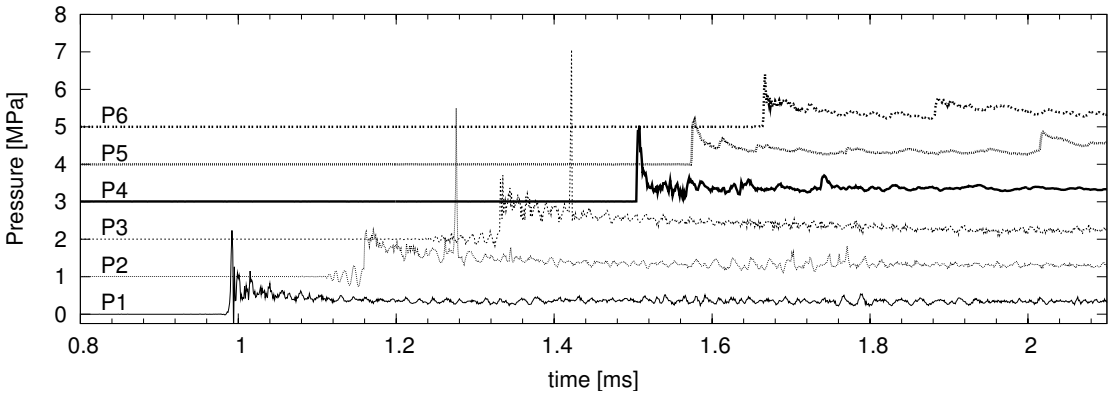

Figure K.111: Shot 111, 0.5 H_2 + 0.5 N_2O, P_0=45 kPa, T_0=295 K. $U(P_1\text{-}P_2)/U_{CJ}$ = 0.998, $U(P_2\text{-}P_3)/U_{CJ}$ = 0.986.

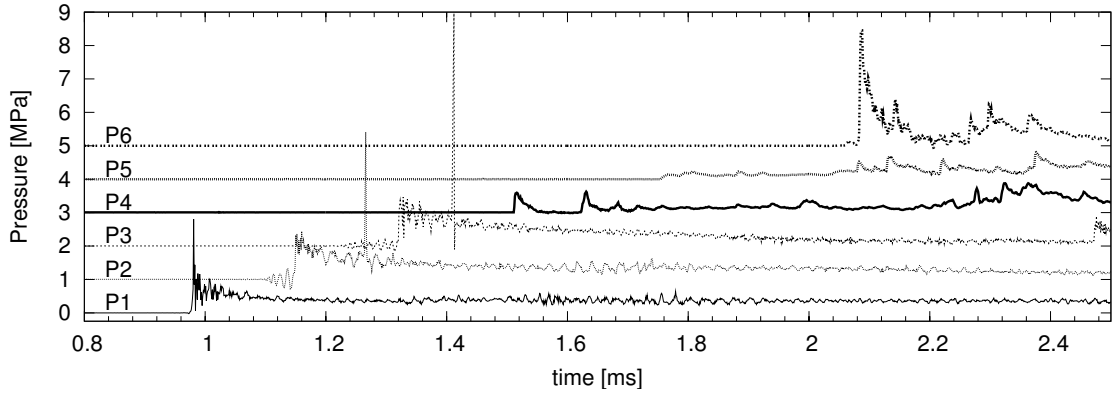

Figure K.112: Shot 112, 0.5 H_2 + 0.5 N_2O, P_0=47.5 kPa, T_0=296 K. $U(P_1\text{-}P_2)/U_{CJ}$ = 0.997, $U(P_2\text{-}P_3)/U_{CJ}$ = 0.991.

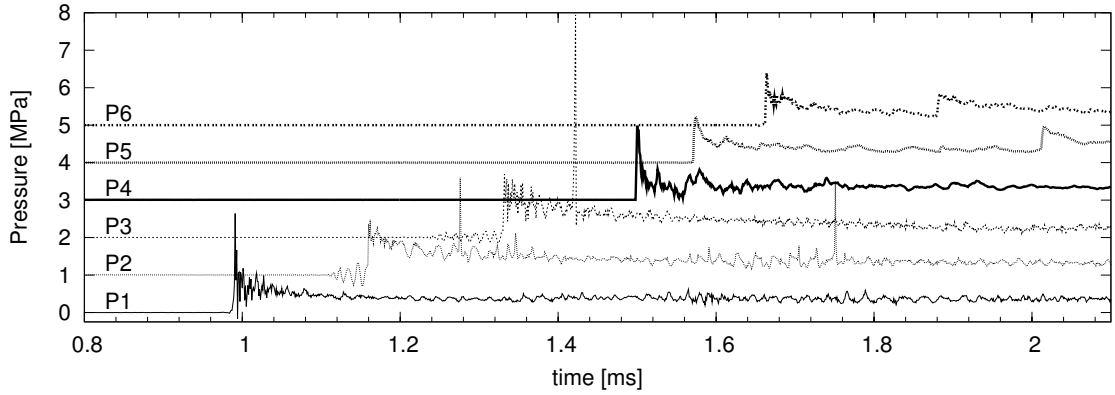

Figure K.113: Shot 113, 0.5 H_2 + 0.5 N_2O, P_0=47.5 kPa, T_0=296 K. $U(P_1\text{-}P_2)/U_{CJ}$ = 0.997, $U(P_2\text{-}P_3)/U_{CJ}$ = 0.991.

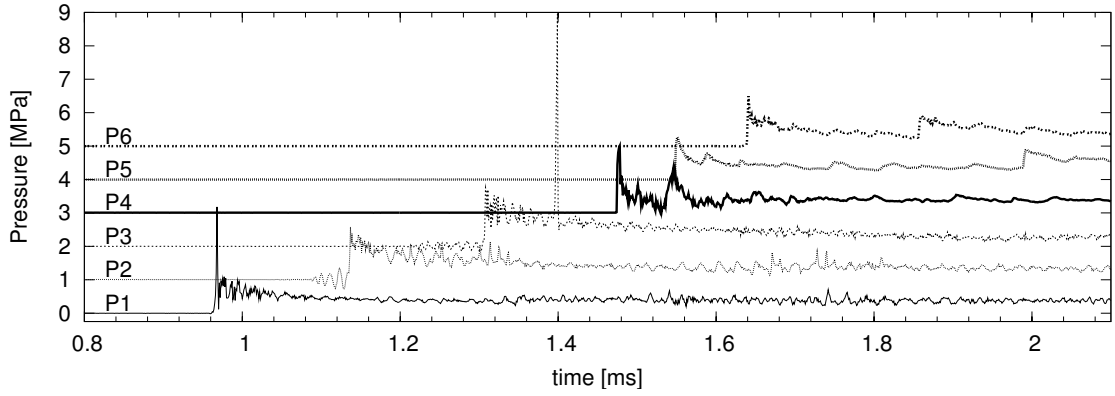

Figure K.114: Shot 114, 0.5 H_2 + 0.5 N_2O, P_0=50 kPa, T_0=296 K. $U(P_1\text{-}P_2)/U_{CJ}$ = 0.996, $U(P_2\text{-}P_3)/U_{CJ}$ = 0.984.

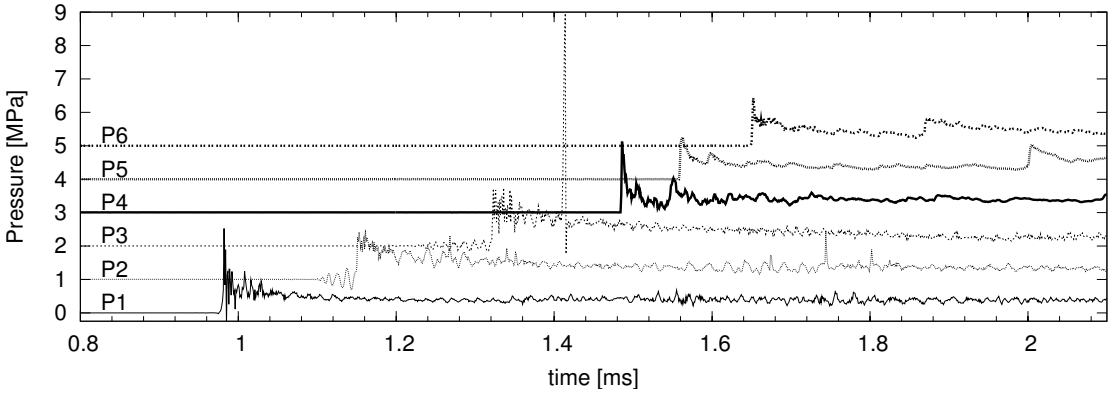

Figure K.115: Shot 115, 0.5 H_2 + 0.5 N_2O, P_0=50 kPa, T_0=296 K. $U(P_1\text{-}P_2)/U_{CJ}$ = 0.996, $U(P_2\text{-}P_3)/U_{CJ}$ = 0.990.

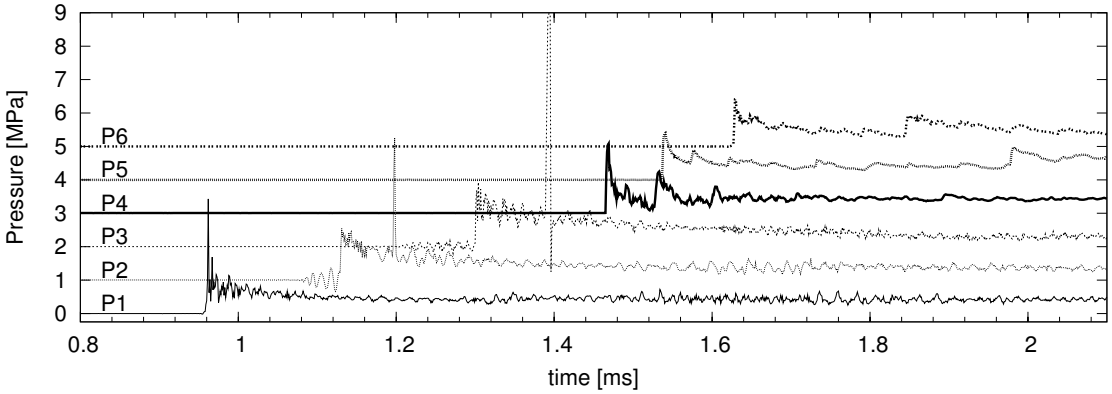

Figure K.116: Shot 116, 0.5 H_2 + 0.5 N_2O, P_0=55 kPa, T_0=296 K. $U(P_1\text{-}P_2)/U_{CJ}$ = 1.000, $U(P_2\text{-}P_3)/U_{CJ}$ = 0.988.

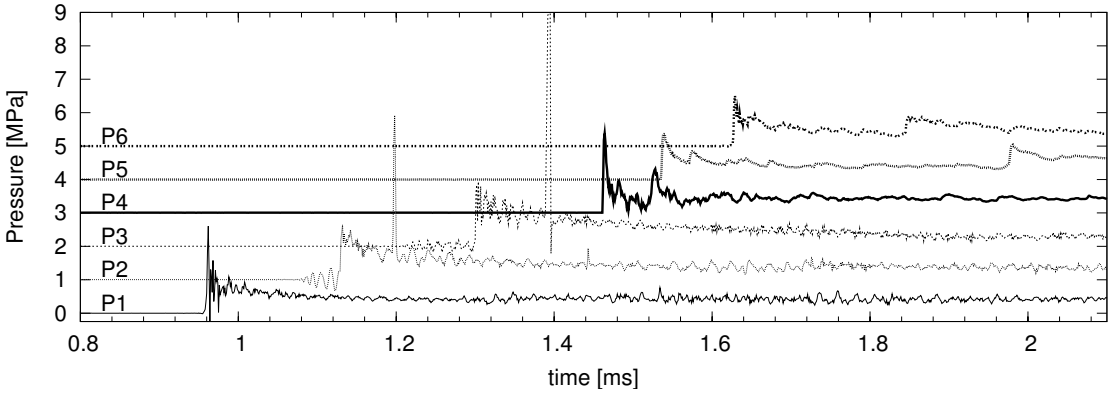

Figure K.117: Shot 117, 0.5 H_2 + 0.5 N_2O, P_0=55 kPa, T_0=296 K. $U(P_1\text{-}P_2)/U_{CJ}$ = 0.994, $U(P_2\text{-}P_3)/U_{CJ}$ = 0.988.

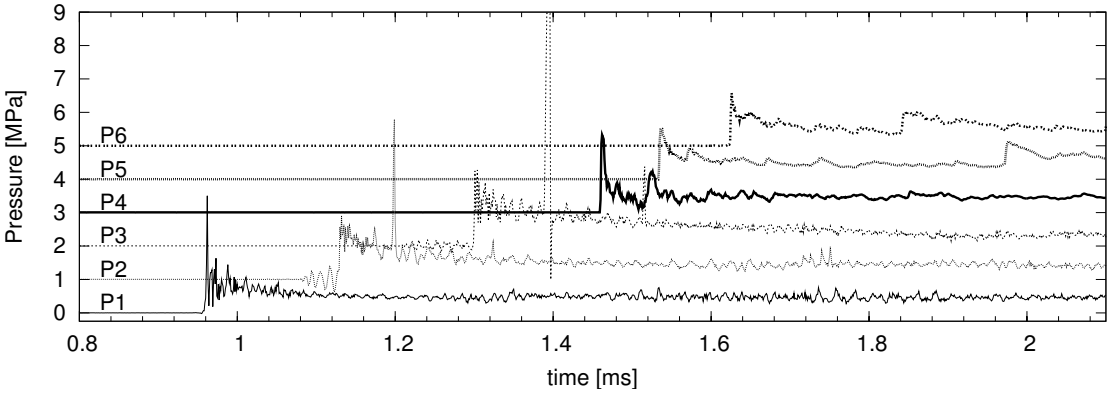

Figure K.118: Shot 118, 0.5 H_2 + 0.5 N_2O, P_0=60 kPa, T_0=296 K. $U(P_1\text{-}P_2)/U_{CJ}$ = 0.998, $U(P_2\text{-}P_3)/U_{CJ}$ = 0.992.

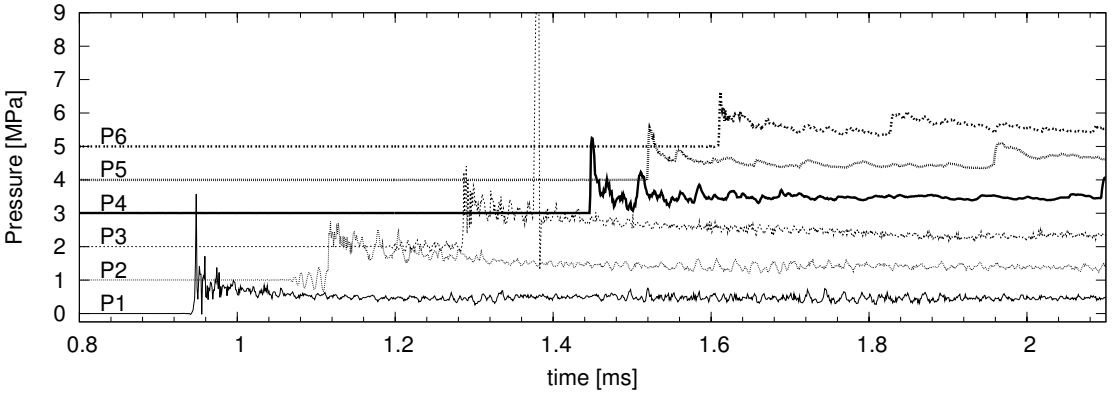

Figure K.119: Shot 119, 0.5 H_2 + 0.5 N_2O, P_0=60 kPa, T_0=296 K. $U(P_1\text{-}P_2)/U_{CJ}$ = 0.998, $U(P_2\text{-}P_3)/U_{CJ}$ = 0.992.

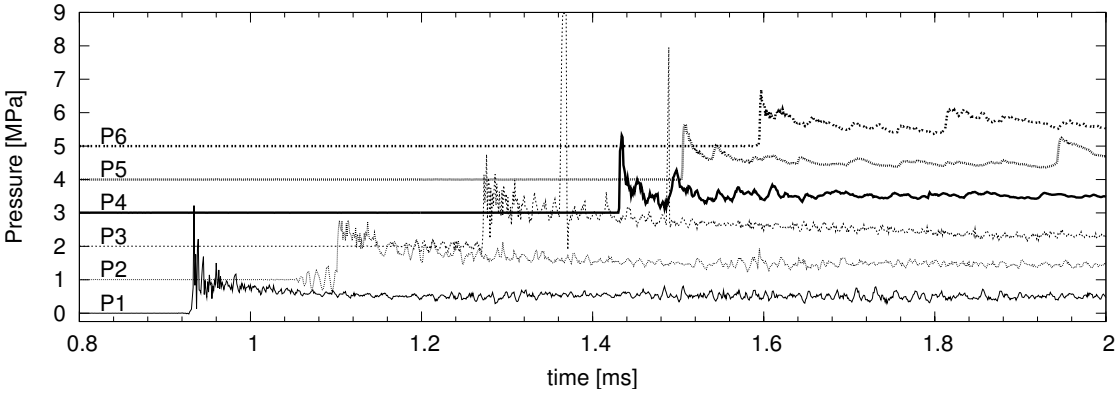

Figure K.120: Shot 120, 0.5 H_2 + 0.5 N_2O, P_0=65 kPa, T_0=297 K. $U(P_1\text{-}P_2)/U_{CJ}$ = 0.997, $U(P_2\text{-}P_3)/U_{CJ}$ = 0.991.

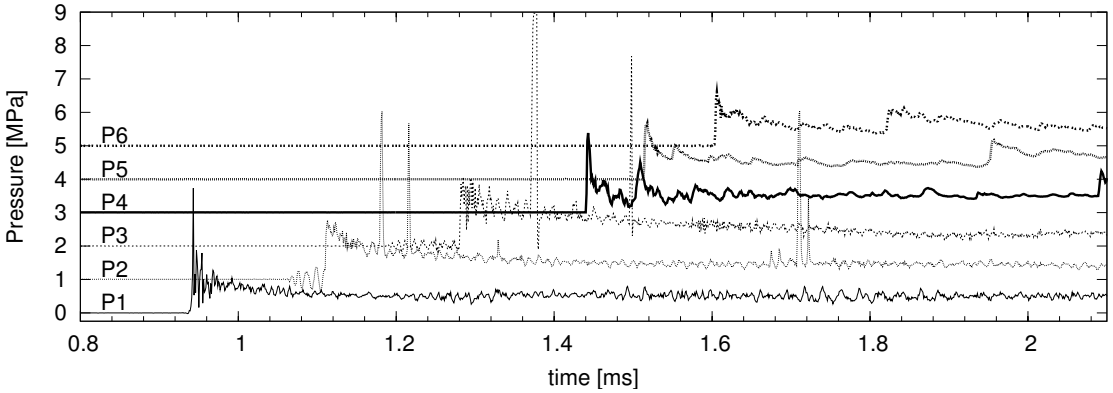

Figure K.121: Shot 121, 0.5 H_2 + 0.5 N_2O, P_0=65 kPa, T_0=297 K. U(P_1-P_2)/U_{CJ} = 0.997, U(P_2-P_3)/U_{CJ} = 0.991.

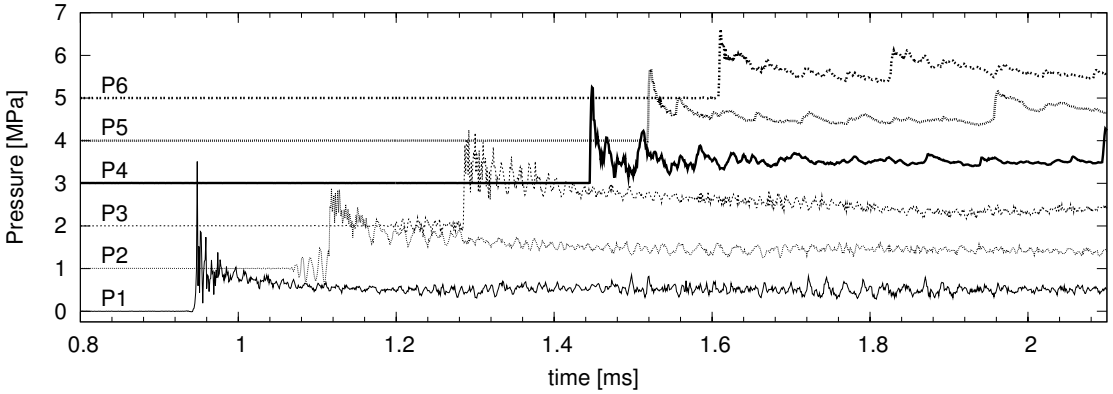

Figure K.122: Shot 122, 0.5 H_2 + 0.5 N_2O, P_0=65 kPa, T_0=297 K. U(P_1-P_2)/U_{CJ} = 0.997, U(P_2-P_3)/U_{CJ} = 0.991.

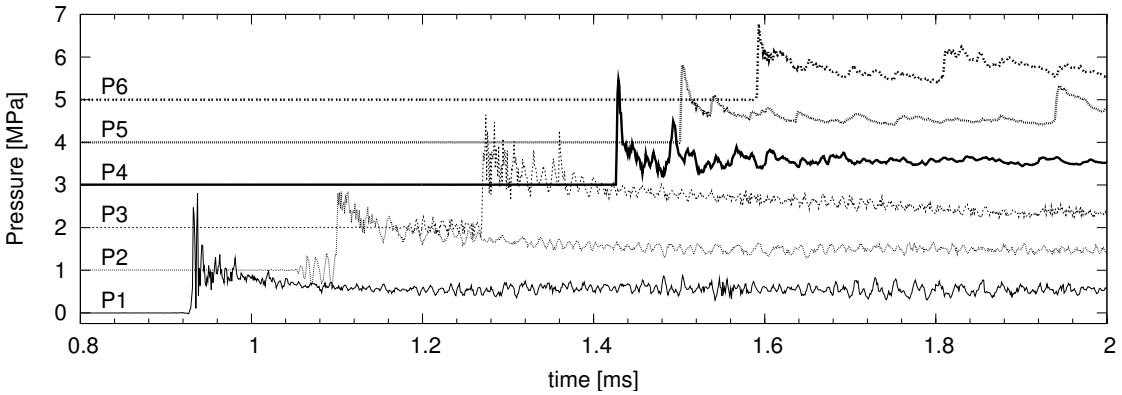

Figure K.123: Shot 123, 0.5 H_2 + 0.5 N_2O, P_0=70 kPa, T_0=297 K. U(P_1-P_2)/U_{CJ} = 0.995, U(P_2-P_3)/U_{CJ} = 0.990.

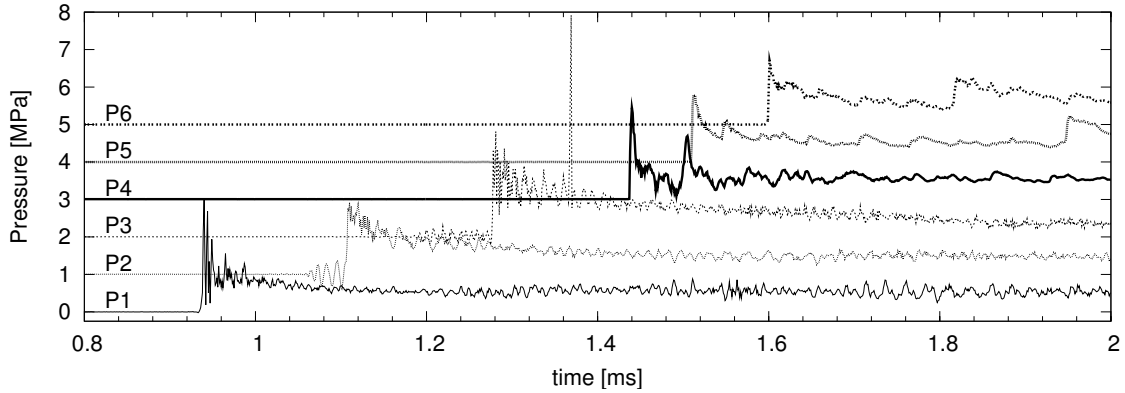

Figure K.124: Shot 124, 0.5 H_2 + 0.5 N_2O, P_0=70 kPa, T_0=297 K. $U(P_1\text{-}P_2)/U_{CJ}$ = 0.995, $U(P_2\text{-}P_3)/U_{CJ}$ = 0.990.

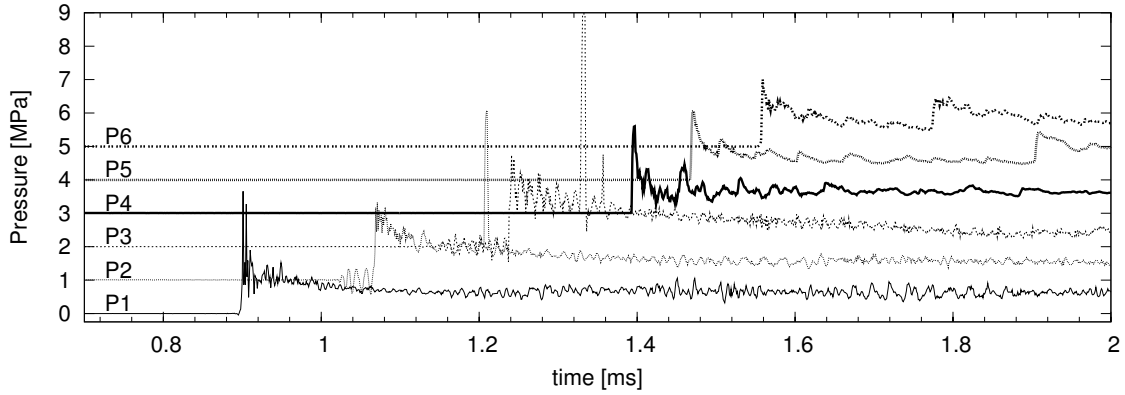

Figure K.125: Shot 125, 0.5 H_2 + 0.5 N_2O, P_0=80 kPa, T_0=297 K. $U(P_1\text{-}P_2)/U_{CJ}$ = 0.999, $U(P_2\text{-}P_3)/U_{CJ}$ = 0.987.

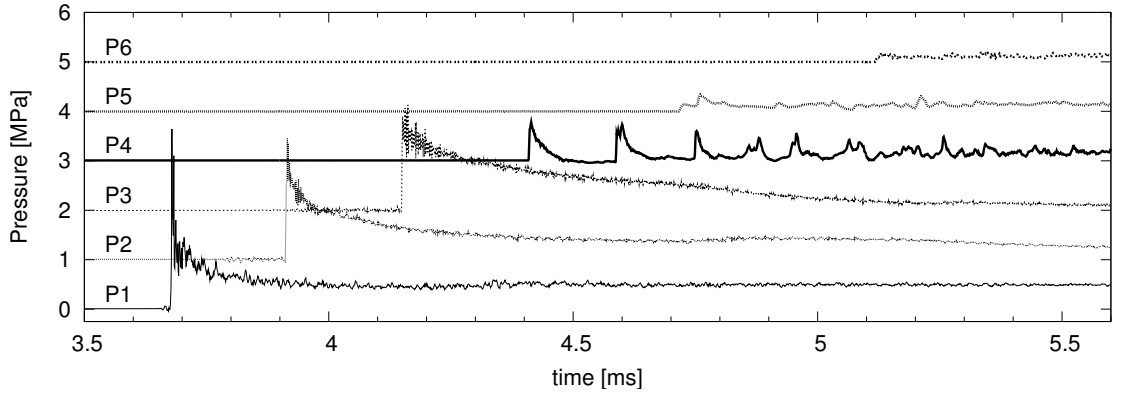

Figure K.126: Shot 126, 0.2 H_2 + 0.1 O_2 + 0.7 Ar, P_0=100 kPa, T_0=294 K. $U(P_1\text{-}P_2)/U_{CJ}$ = 1.009, $U(P_2\text{-}P_3)/U_{CJ}$ = 0.992.

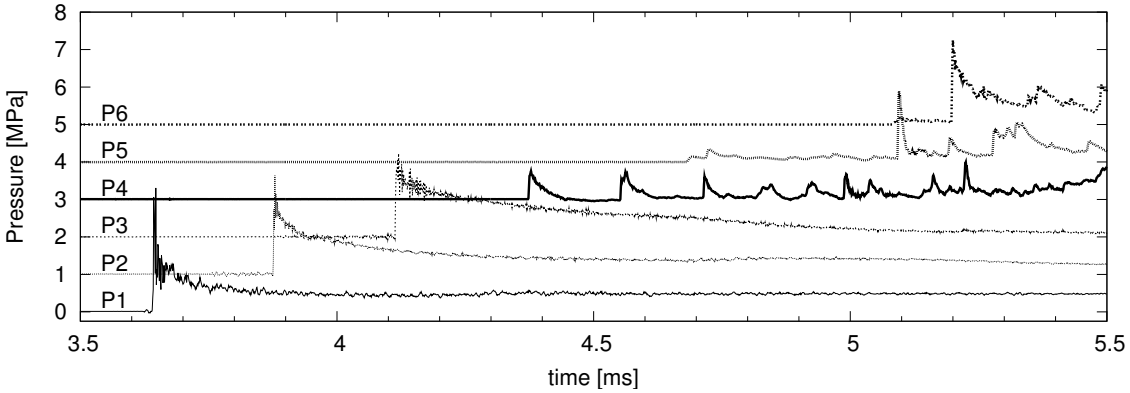

Figure K.127: Shot 128, 0.2 H_2 + 0.1 O_2 + 0.7 Ar, P_0=100 kPa, T_0=295 K. U(P_1-P_2)/U_{CJ} = 1.005, U(P_2-P_3)/U_{CJ} = 0.997.

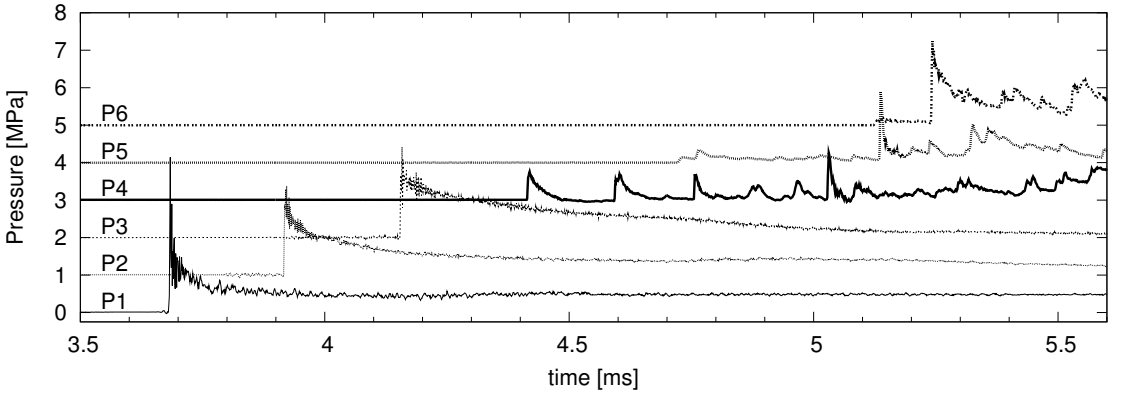

Figure K.128: Shot 129, 0.2 H_2 + 0.1 O_2 + 0.7 Ar, P_0=100 kPa, T_0=295 K. U(P_1-P_2)/U_{CJ} = 1.009, U(P_2-P_3)/U_{CJ} = 0.992.

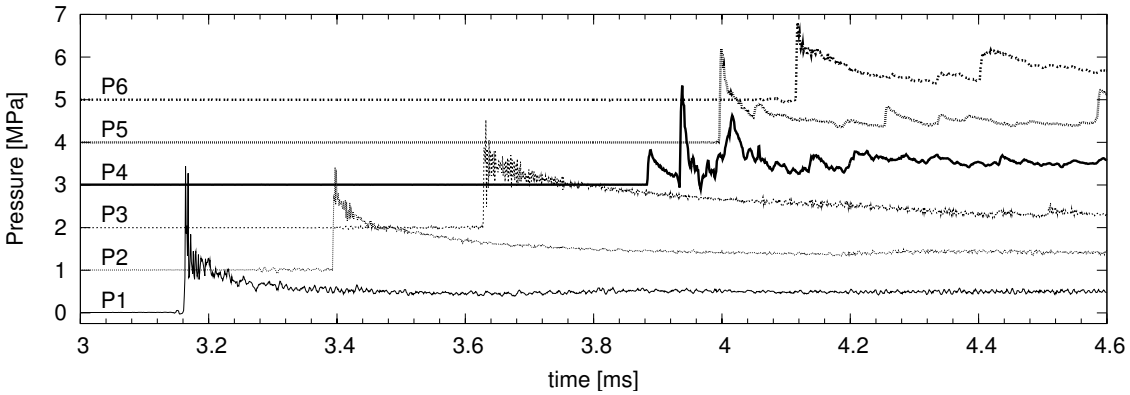

Figure K.129: Shot 130, 0.213 H_2 + 0.107 O_2 + 0.68 Ar, P_0=100 kPa, T_0=295 K. U(P_1-P_2)/U_{CJ} = 1.008, U(P_2-P_3)/U_{CJ} = 0.991.

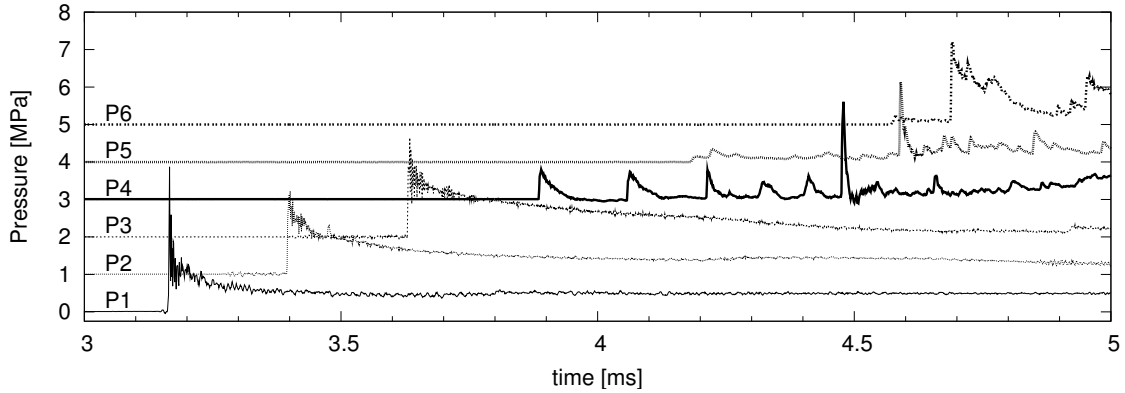

Figure K.130: Shot 131, 0.213 H_2 + 0.107 O_2 + 0.68 Ar, P_0=100 kPa, T_0=296 K. $U(P_1\text{-}P_2)/U_{CJ} = 1.008$, $U(P_2\text{-}P_3)/U_{CJ} = 0.995$.

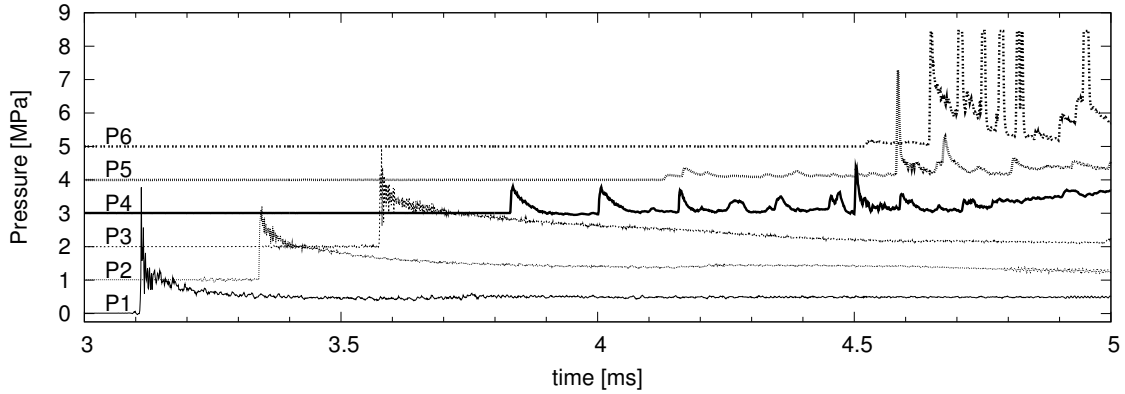

Figure K.131: Shot 132, 0.213 H_2 + 0.107 O_2 + 0.68 Ar, P_0=100 kPa, T_0=296 K. $U(P_1\text{-}P_2)/U_{CJ} = 1.008$, $U(P_2\text{-}P_3)/U_{CJ} = 0.991$.

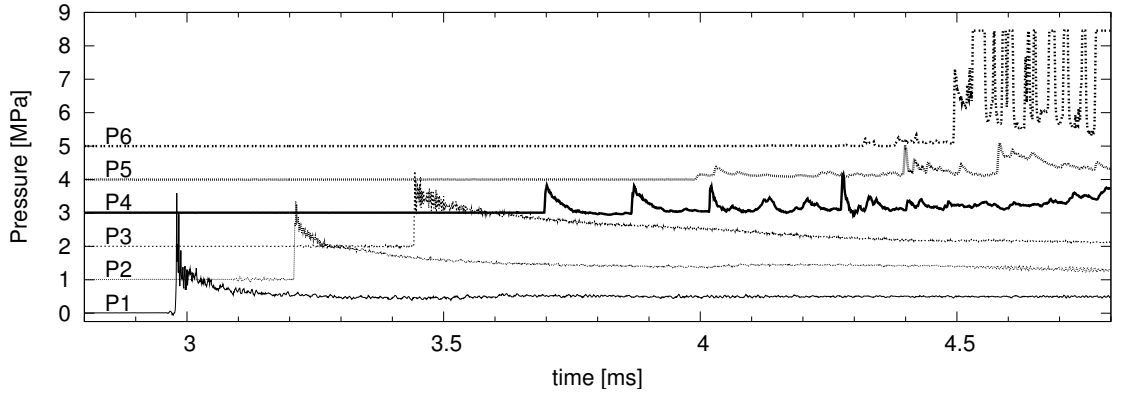

Figure K.132: Shot 133, 0.217 H_2 + 0.108 O_2 + 0.675 Ar, P_0=100 kPa, T_0=296 K. $U(P_1\text{-}P_2)/U_{CJ} = 1.009$, $U(P_2\text{-}P_3)/U_{CJ} = 0.991$.

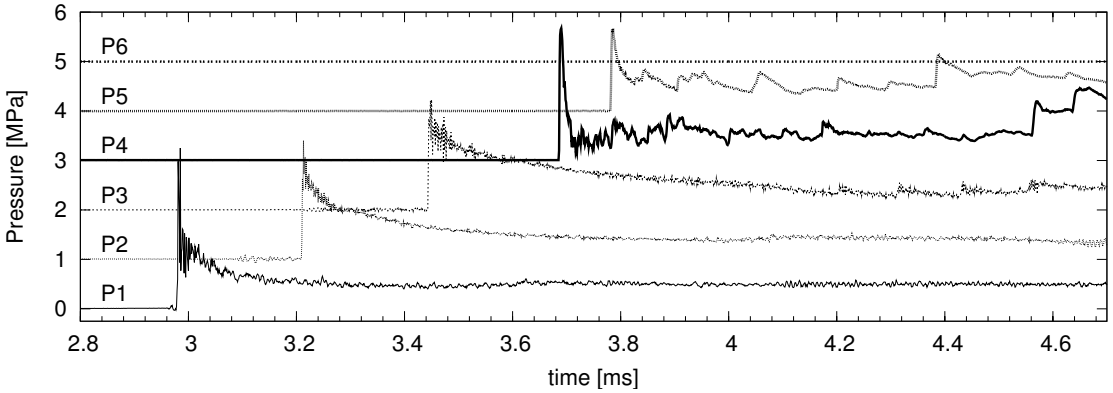

Figure K.133: Shot 134, 0.217 H_2 + 0.108 O_2 + 0.675 Ar, P_0=100 kPa, T_0=296 K. $U(P_1\text{-}P_2)/U_{CJ} = 1.004$, $U(P_2\text{-}P_3)/U_{CJ} = 0.996$.

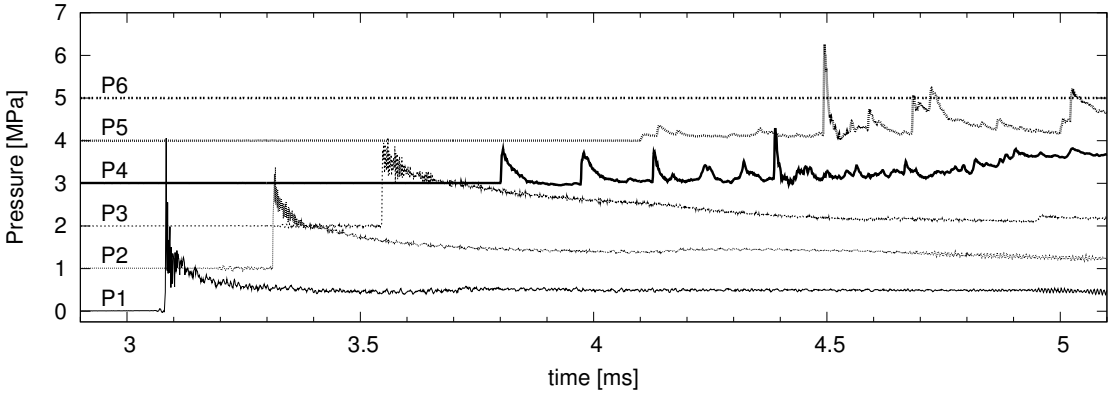

Figure K.134: Shot 135, 0.217 H_2 + 0.108 O_2 + 0.675 Ar, P_0=100 kPa, T_0=294 K. $U(P_1\text{-}P_2)/U_{CJ} = 1.009$, $U(P_2\text{-}P_3)/U_{CJ} = 0.991$.

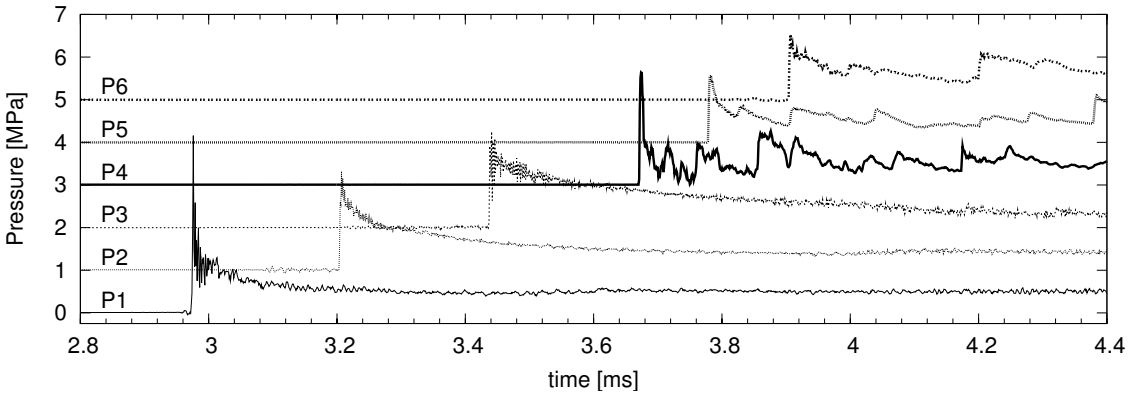

Figure K.135: Shot 136, 0.22 H_2 + 0.11 O_2 + 0.67 Ar, P_0=100 kPa, T_0=295 K. $U(P_1\text{-}P_2)/U_{CJ} = 1.010$, $U(P_2\text{-}P_3)/U_{CJ} = 0.988$.

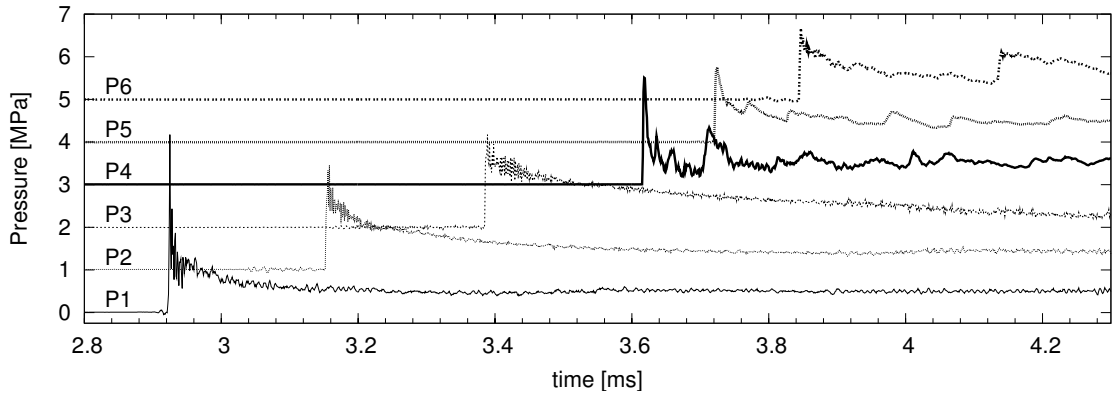

Figure K.136: Shot 137, 0.22 H_2 + 0.11 O_2 + 0.67 Ar, P_0=100 kPa, T_0=295 K. $U(P_1\text{-}P_2)/U_{CJ} = 1.010$, $U(P_2\text{-}P_3)/U_{CJ} = 0.992$.

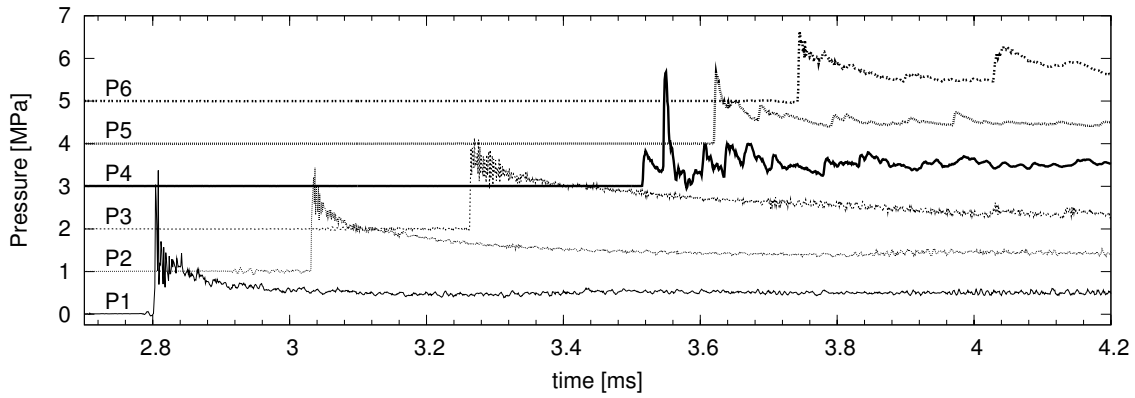

Figure K.137: Shot 138, 0.223 H_2 + 0.112 O_2 + 0.665 Ar, P_0=100 kPa, T_0=296 K. $U(P_1\text{-}P_2)/U_{CJ} = 1.006$, $U(P_2\text{-}P_3)/U_{CJ} = 0.993$.

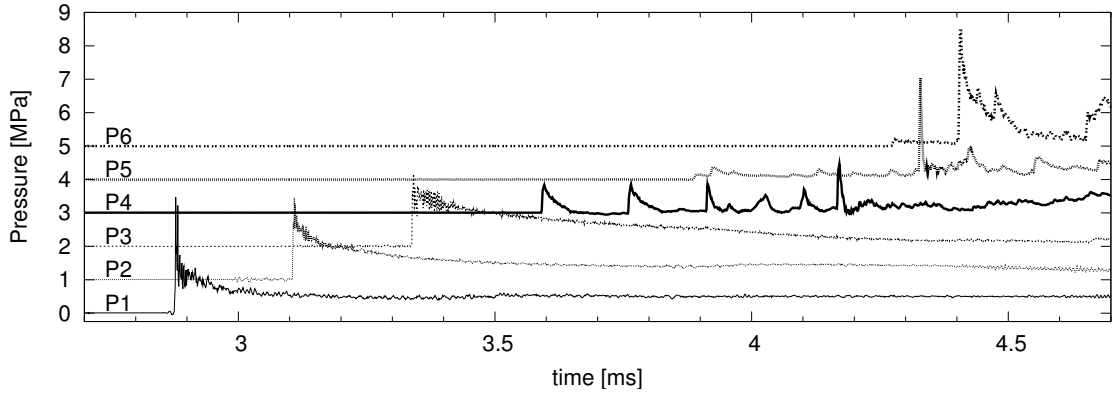

Figure K.138: Shot 139, 0.223 H_2 + 0.112 O_2 + 0.665 Ar, P_0=100 kPa, T_0=296 K. $U(P_1\text{-}P_2)/U_{CJ} = 1.006$, $U(P_2\text{-}P_3)/U_{CJ} = 0.989$.

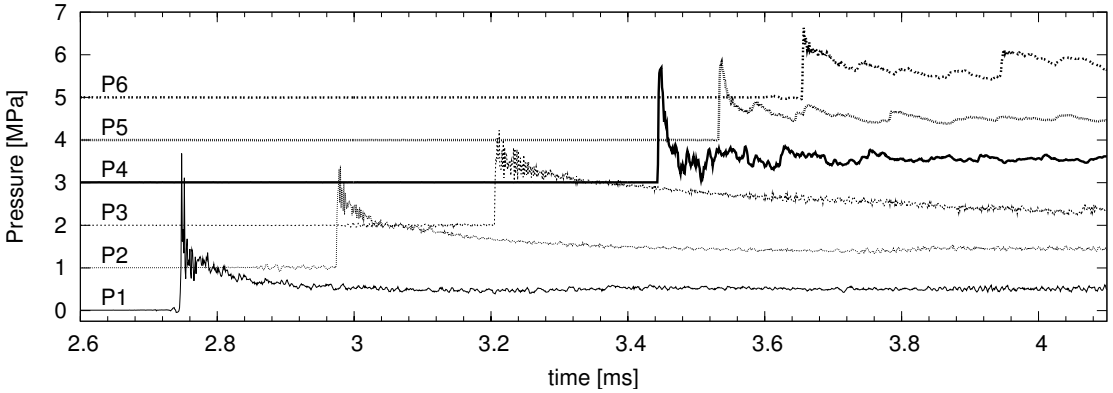

Figure K.139: Shot 140, 0.227 H_2 + 0.113 O_2 + 0.66 Ar, P_0=100 kPa, T_0=296 K. $U(P_1\text{-}P_2)/U_{CJ} = 1.007$, $U(P_2\text{-}P_3)/U_{CJ} = 0.994$.

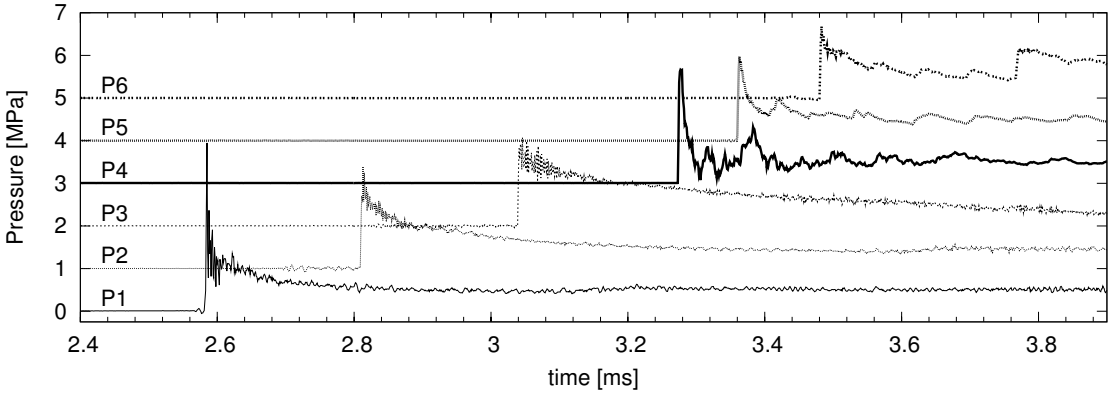

Figure K.140: Shot 141, 0.233 H_2 + 0.117 O_2 + 0.65 Ar, P_0=100 kPa, T_0=296 K. $U(P_1\text{-}P_2)/U_{CJ} = 1.009$, $U(P_2\text{-}P_3)/U_{CJ} = 0.992$.

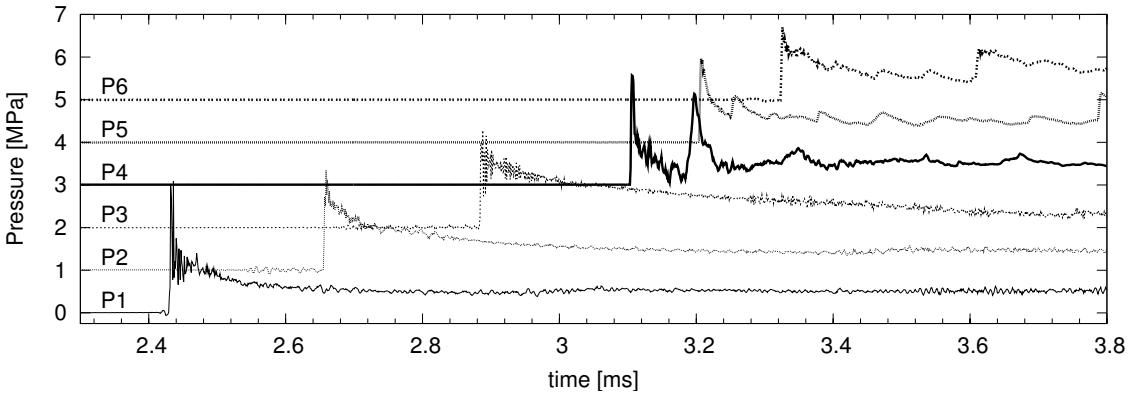

Figure K.141: Shot 142, 0.24 H_2 + 0.12 O_2 + 0.64 Ar, P_0=100 kPa, T_0=296 K. $U(P_1\text{-}P_2)/U_{CJ} = 1.007$, $U(P_2\text{-}P_3)/U_{CJ} = 0.990$.

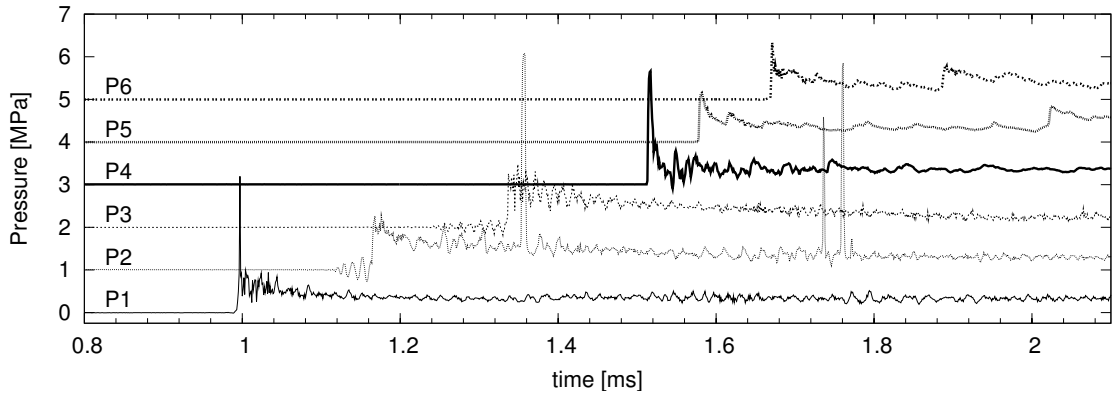

Figure K.142: Shot 143, 0.5 H_2 + 0.5 N_2O, P_0=45 kPa, T_0=296 K. $U(P_1\text{-}P_2)/U_{CJ}$ = 1.004, $U(P_2\text{-}P_3)/U_{CJ}$ = 0.986.

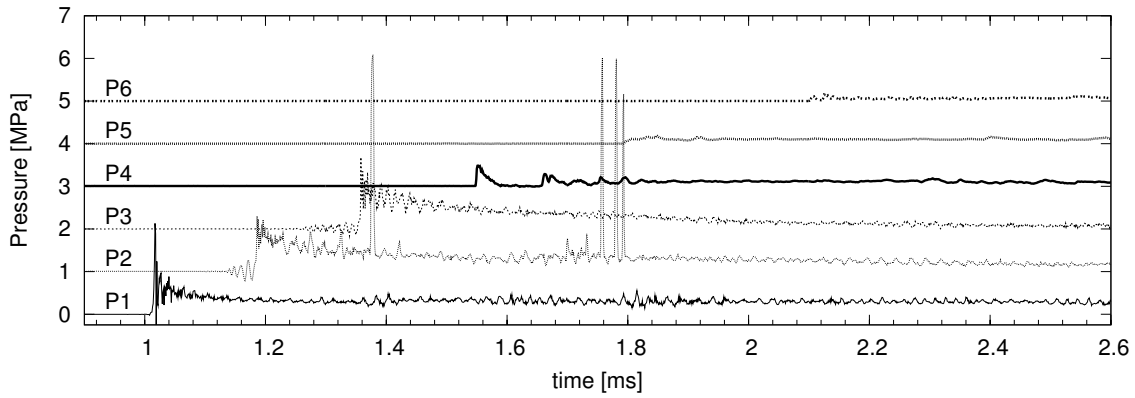

Figure K.143: Shot 144, 0.5 H_2 + 0.5 N_2O, P_0=40 kPa, T_0=296 K. $U(P_1\text{-}P_2)/U_{CJ}$ = 1.000, $U(P_2\text{-}P_3)/U_{CJ}$ = 0.982.

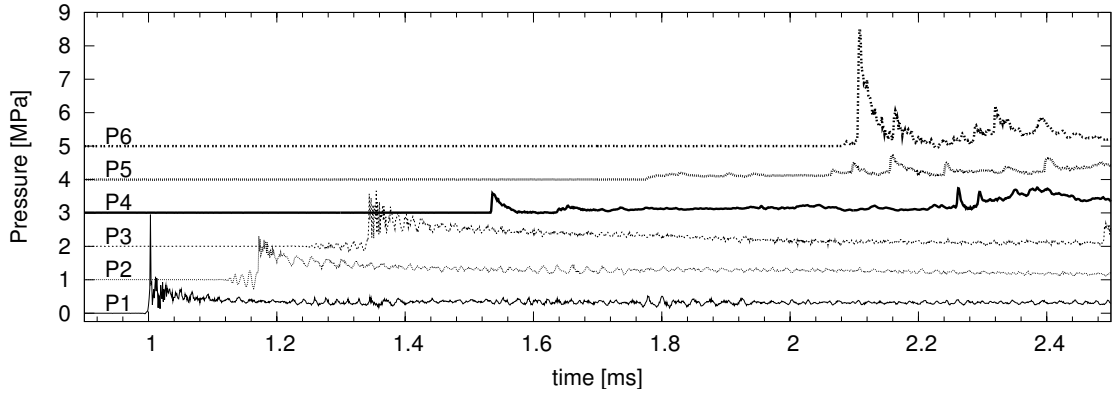

Figure K.144: Shot 145, 0.5 H_2 + 0.5 N_2O, P_0=42.5 kPa, T_0=296 K. $U(P_1\text{-}P_2)/U_{CJ}$ = 0.999, $U(P_2\text{-}P_3)/U_{CJ}$ = 0.993.

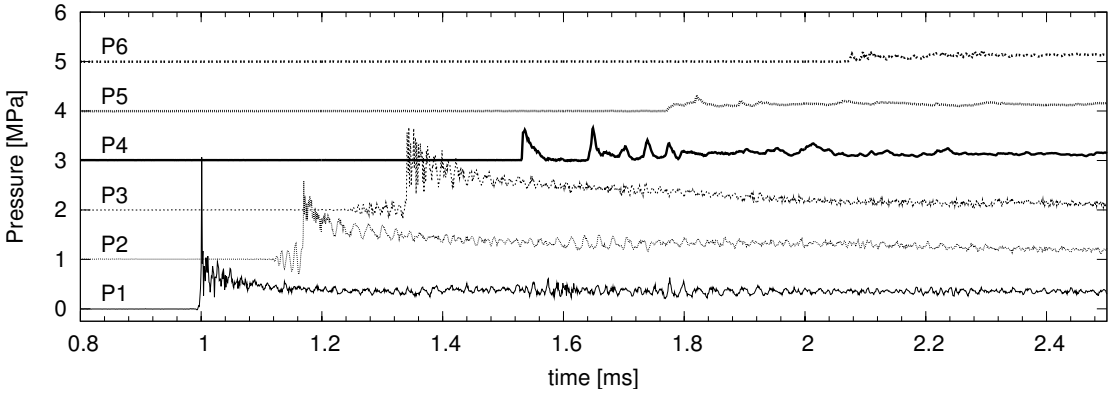

Figure K.145: Shot 146, 0.5 H_2 + 0.5 N_2O, P_0=47.5 kPa, T_0=297 K. $U(P_1\text{-}P_2)/U_{CJ}$ = 0.997, $U(P_2\text{-}P_3)/U_{CJ}$ = 0.991.

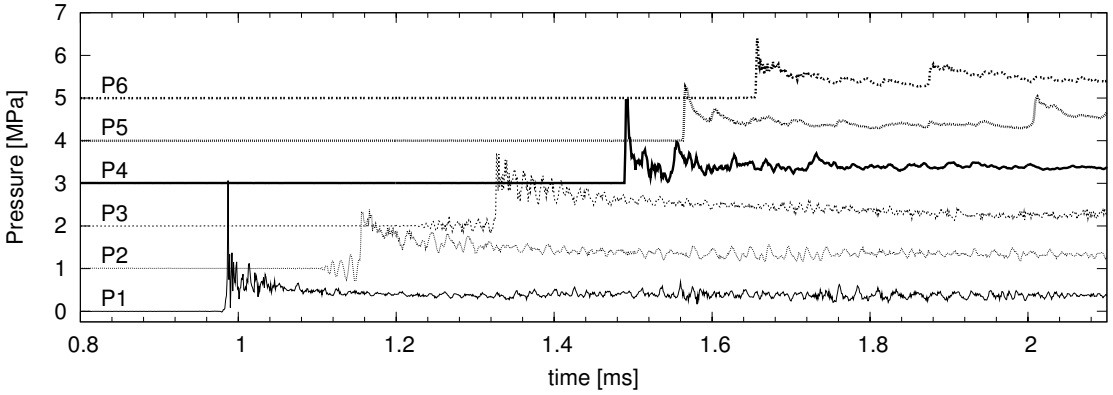

Figure K.146: Shot 147, 0.5 H_2 + 0.5 N_2O, P_0=50 kPa, T_0=297 K. $U(P_1\text{-}P_2)/U_{CJ}$ = 1.002, $U(P_2\text{-}P_3)/U_{CJ}$ = 0.984.

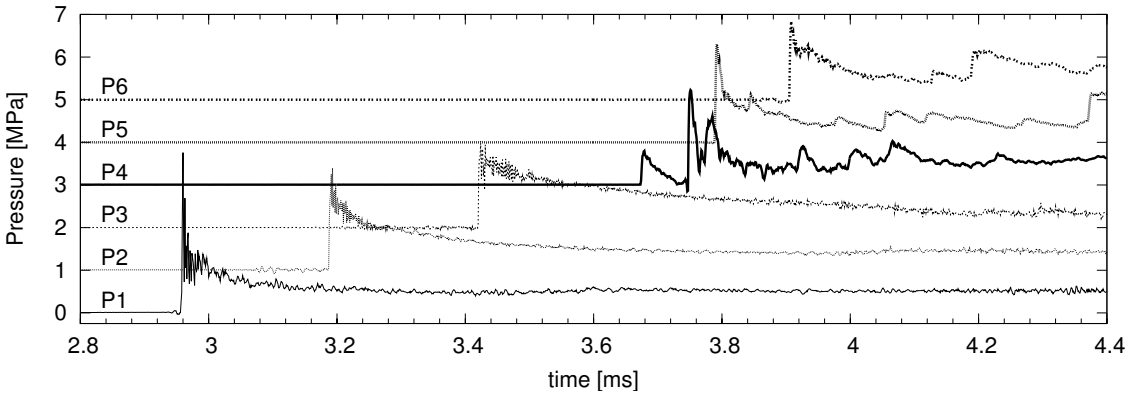

Figure K.147: Shot 148, 0.22 H_2 + 0.11 O_2 + 0.67 Ar, P_0=100 kPa, T_0=295 K. $U(P_1\text{-}P_2)/U_{CJ}$ = 1.010, $U(P_2\text{-}P_3)/U_{CJ}$ = 0.992.

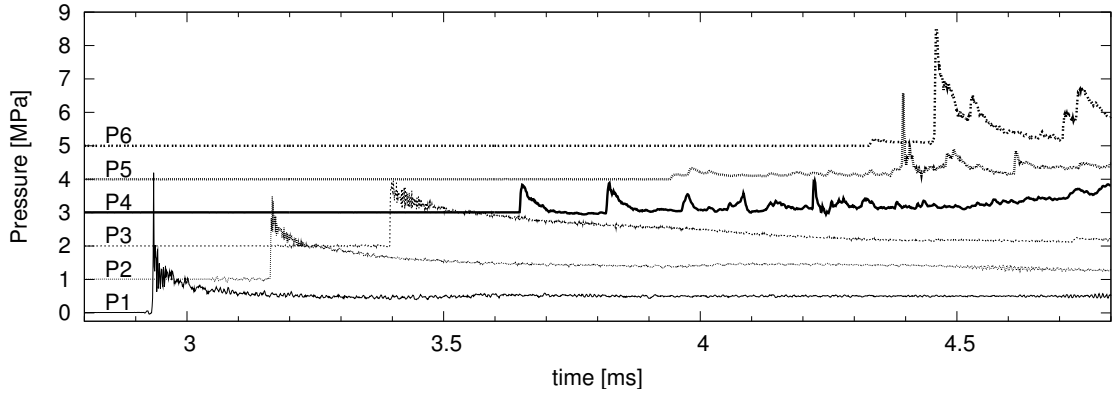

Figure K.148: Shot 149, 0.22 H_2 + 0.11 O_2 + 0.67 Ar, P_0=100 kPa, T_0=295 K. $U(P_1\text{-}P_2)/U_{CJ} = 1.010$, $U(P_2\text{-}P_3)/U_{CJ} = 0.992$.

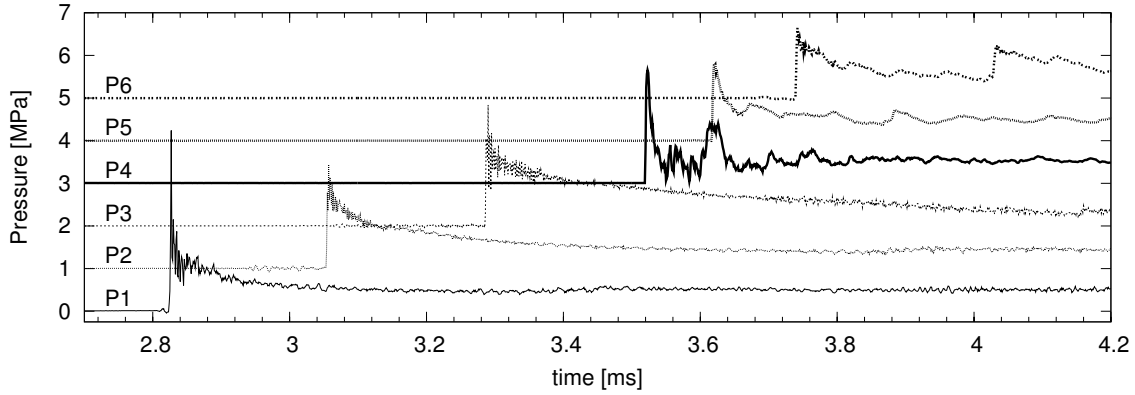

Figure K.149: Shot 150, 0.223 H_2 + 0.112 O_2 + 0.665 Ar, P_0=100 kPa, T_0=295 K. $U(P_1\text{-}P_2)/U_{CJ} = 1.006$, $U(P_2\text{-}P_3)/U_{CJ} = 0.993$.

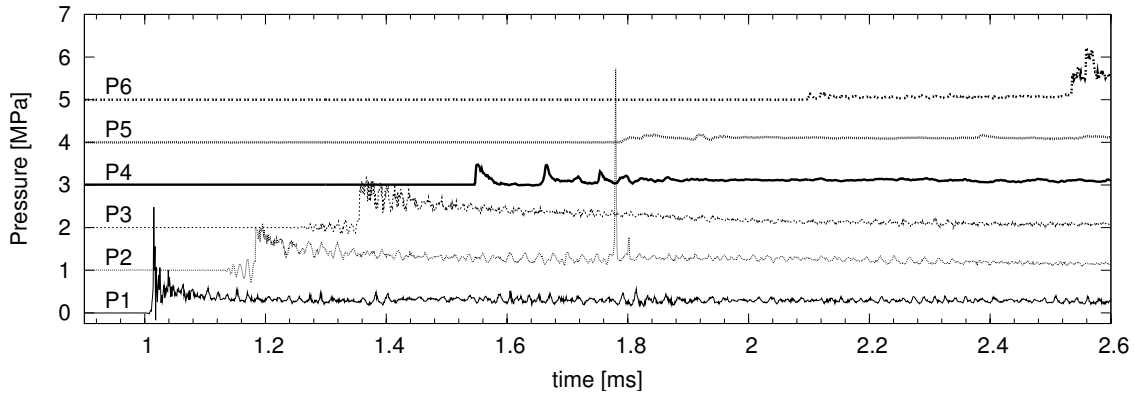

Figure K.150: Shot 151, 0.5 H_2 + 0.5 N_2O, P_0=40 kPa, T_0=295 K. $U(P_1\text{-}P_2)/U_{CJ} = 1.000$, $U(P_2\text{-}P_3)/U_{CJ} = 0.988$.

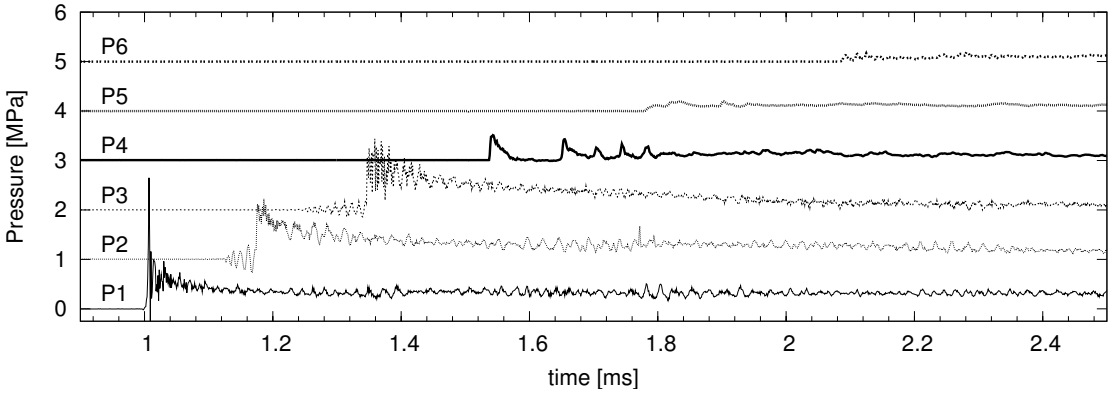

Figure K.151: Shot 152, 0.5 H_2 + 0.5 N_2O, P_0=42.5 kPa, T_0=295 K. $U(P_1\text{-}P_2)/U_{CJ}$ = 0.999, $U(P_2\text{-}P_3)/U_{CJ}$ = 0.987.

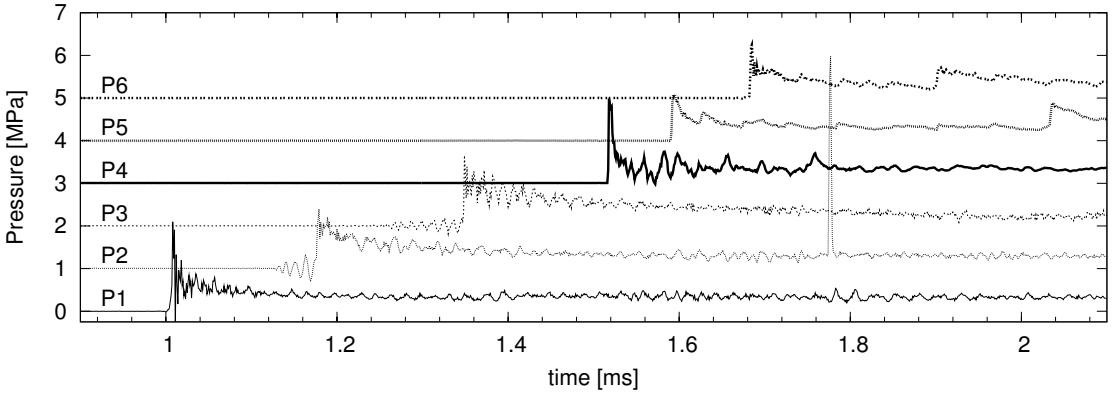

Figure K.152: Shot 153, 0.5 H_2 + 0.5 N_2O, P_0=43.75 kPa, T_0=296 K. $U(P_1\text{-}P_2)/U_{CJ}$ = 0.998, $U(P_2\text{-}P_3)/U_{CJ}$ = 0.987.

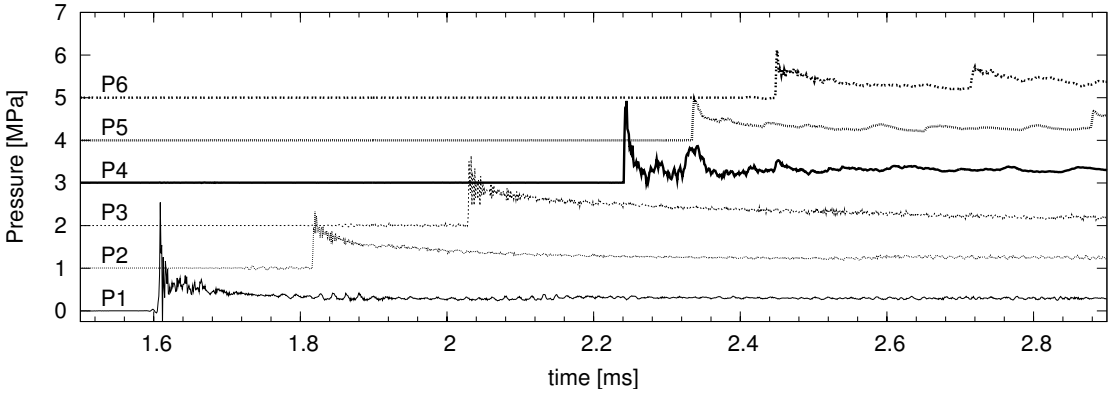

Figure K.153: Shot 154, 0.333 H_2 + 0.167 O_2 + 0.5 Ar, P_0=55 kPa, T_0=296 K. $U(P_1\text{-}P_2)/U_{CJ}$ = 1.001, $U(P_2\text{-}P_3)/U_{CJ}$ = 0.992.

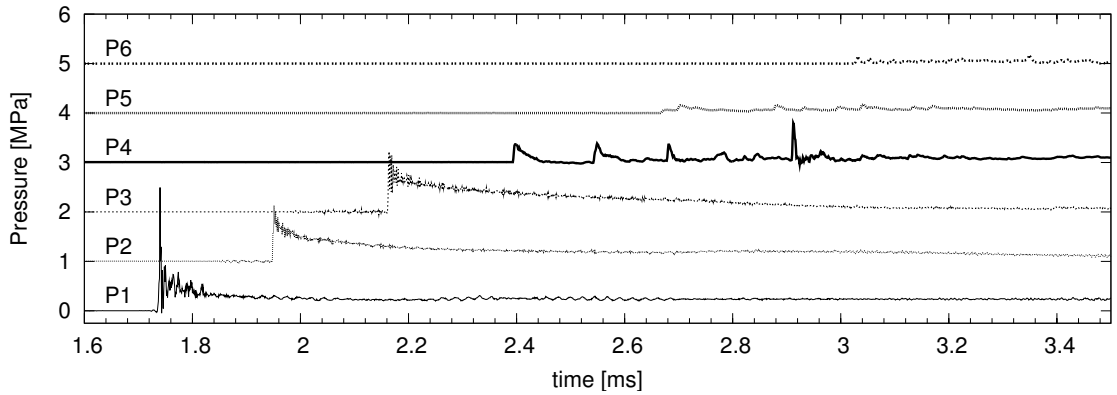

Figure K.154: Shot 155, 0.333 H_2 + 0.167 O_2 + 0.5 Ar, P_0=45 kPa, T_0=296 K. $U(P_1\text{-}P_2)/U_{CJ} = 1.000$, $U(P_2\text{-}P_3)/U_{CJ} = 0.986$.

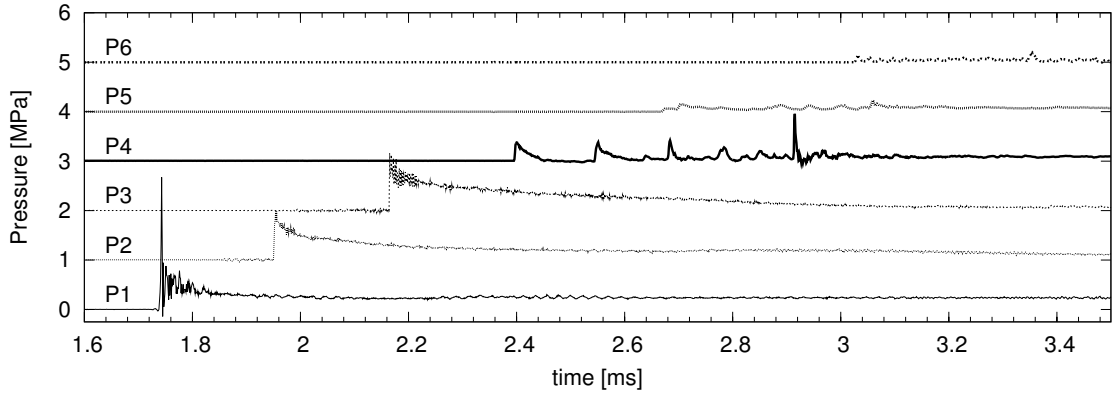

Figure K.155: Shot 156, 0.333 H_2 + 0.167 O_2 + 0.5 Ar, P_0=45 kPa, T_0=296 K. $U(P_1\text{-}P_2)/U_{CJ} = 1.000$, $U(P_2\text{-}P_3)/U_{CJ} = 0.991$.

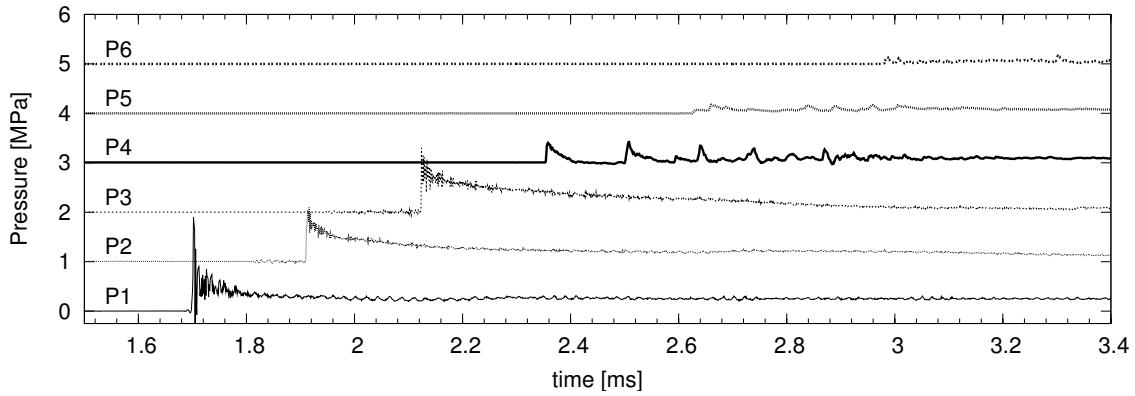

Figure K.156: Shot 157, 0.333 H_2 + 0.167 O_2 + 0.5 Ar, P_0=47.5 kPa, T_0=296 K. $U(P_1\text{-}P_2)/U_{CJ} = 1.004$, $U(P_2\text{-}P_3)/U_{CJ} = 0.990$.

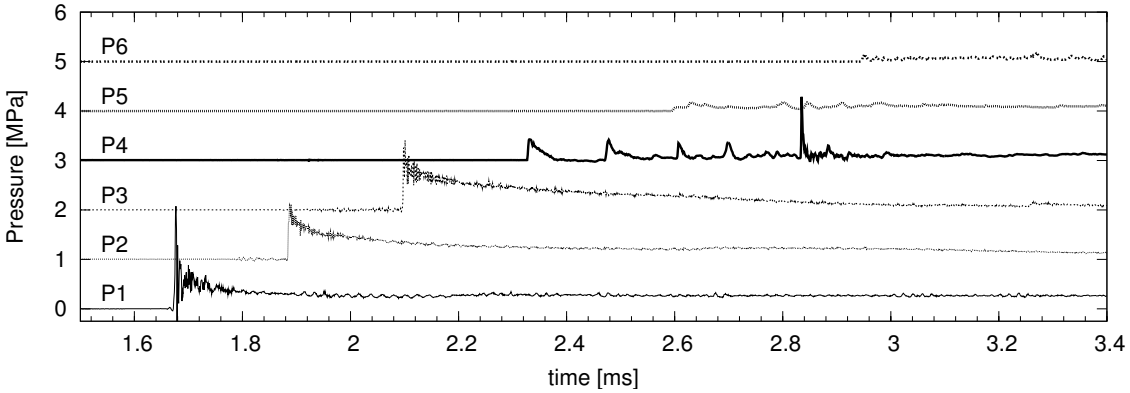

Figure K.157: Shot 158, 0.333 H_2 + 0.167 O_2 + 0.5 Ar, P_0=50 kPa, T_0=296 K. $U(P_1\text{-}P_2)/U_{CJ} = 1.003$, $U(P_2\text{-}P_3)/U_{CJ} = 0.989$.

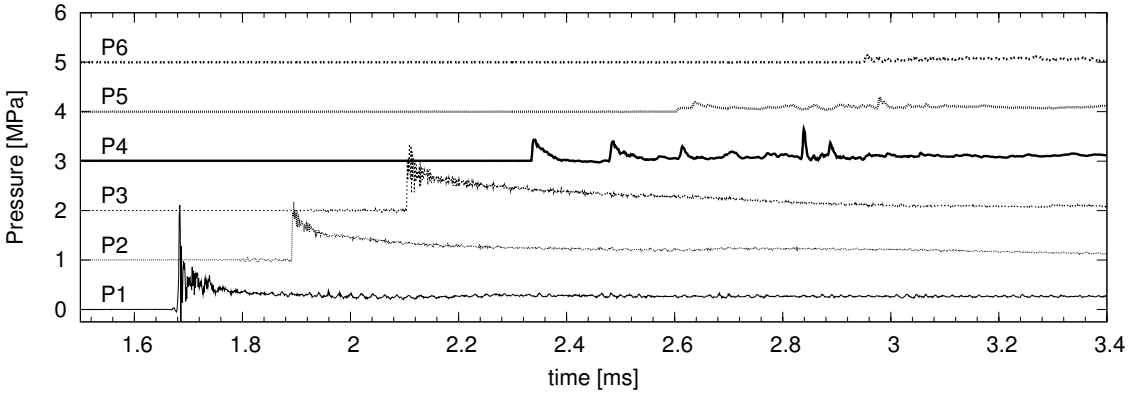

Figure K.158: Shot 159, 0.333 H_2 + 0.167 O_2 + 0.5 Ar, P_0=50 kPa, T_0=296 K. $U(P_1\text{-}P_2)/U_{CJ} = 1.003$, $U(P_2\text{-}P_3)/U_{CJ} = 0.989$.

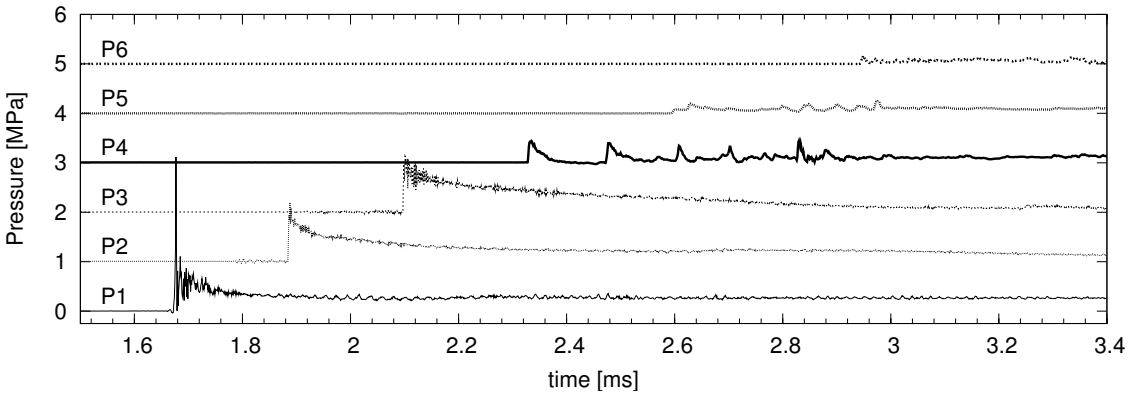

Figure K.159: Shot 160, 0.333 H_2 + 0.167 O_2 + 0.5 Ar, P_0=50 kPa, T_0=295 K. $U(P_1\text{-}P_2)/U_{CJ} = 0.998$, $U(P_2\text{-}P_3)/U_{CJ} = 0.994$.

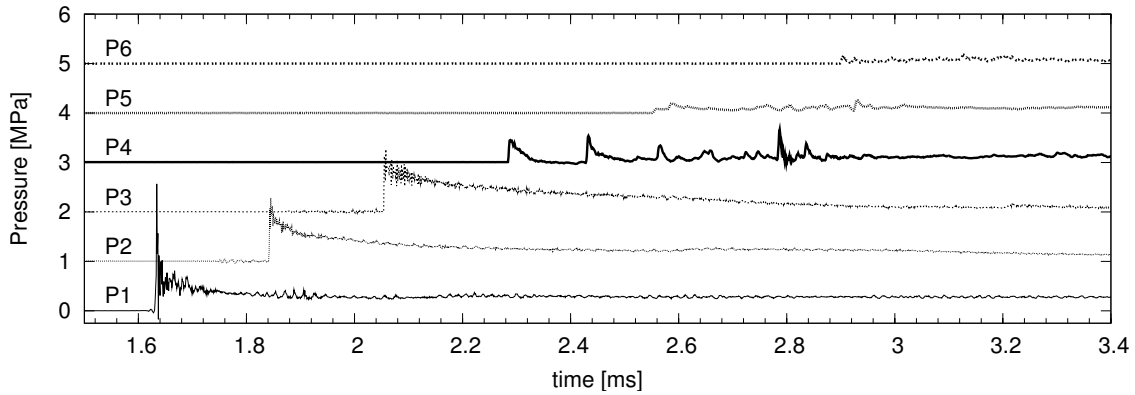

Figure K.160: Shot 161, 0.333 H_2 + 0.167 O_2 + 0.5 Ar, P_0=52.5 kPa, T_0=295 K. $U(P_1\text{-}P_2)/U_{CJ} = 1.002$, $U(P_2\text{-}P_3)/U_{CJ} = 0.993$.

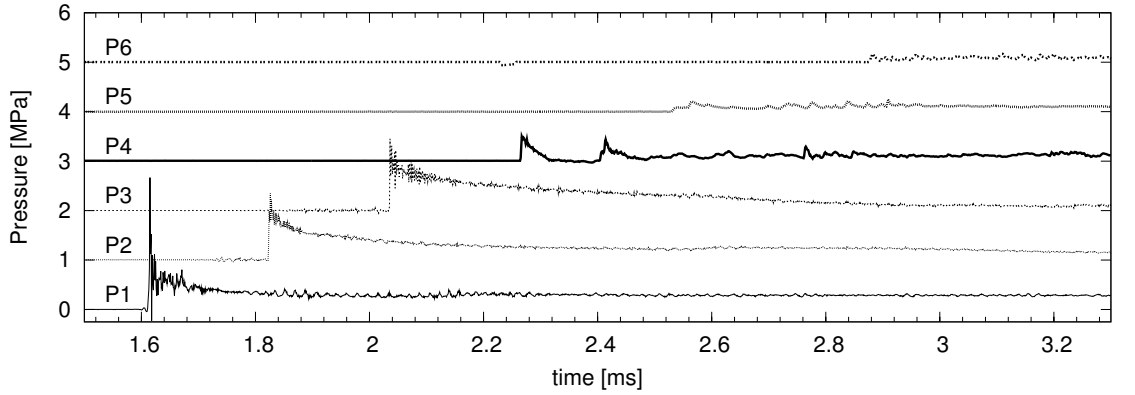

Figure K.161: Shot 162, 0.333 H_2 + 0.167 O_2 + 0.5 Ar, P_0=53.75 kPa, T_0=296 K. $U(P_1\text{-}P_2)/U_{CJ} = 1.002$, $U(P_2\text{-}P_3)/U_{CJ} = 0.992$.

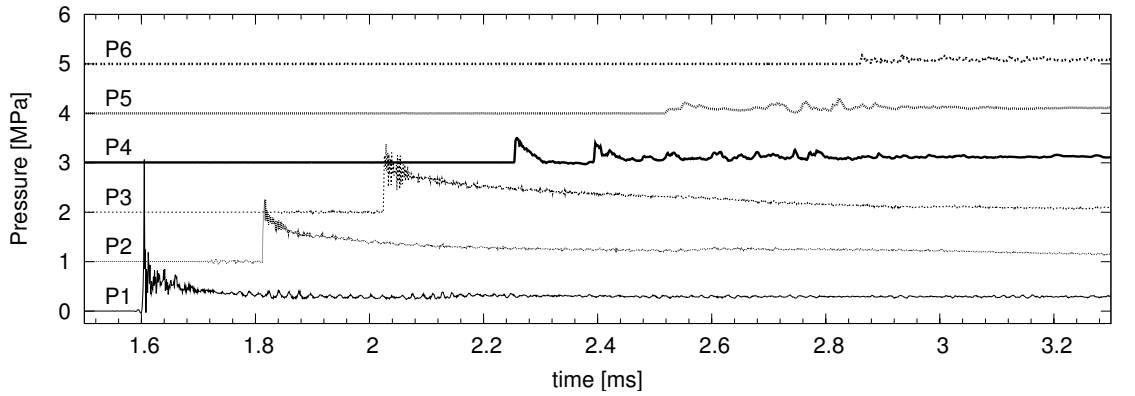

Figure K.162: Shot 163, 0.333 H_2 + 0.167 O_2 + 0.5 Ar, P_0=55 kPa, T_0=296 K. $U(P_1\text{-}P_2)/U_{CJ} = 1.006$, $U(P_2\text{-}P_3)/U_{CJ} = 0.992$.

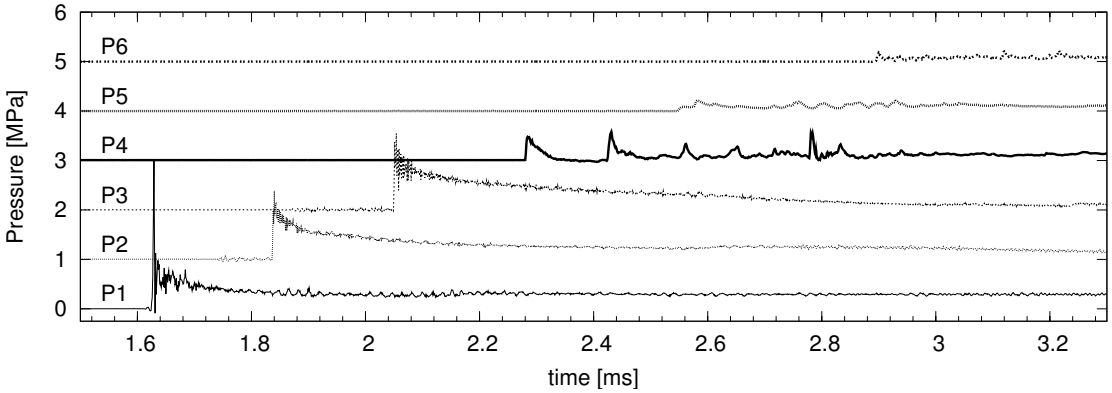

Figure K.163: Shot 164, 0.333 H_2 + 0.167 O_2 + 0.5 Ar, P_0=55 kPa, T_0=296 K. $U(P_1\text{-}P_2)/U_{CJ} = 0.996$, $U(P_2\text{-}P_3)/U_{CJ} = 0.987$.

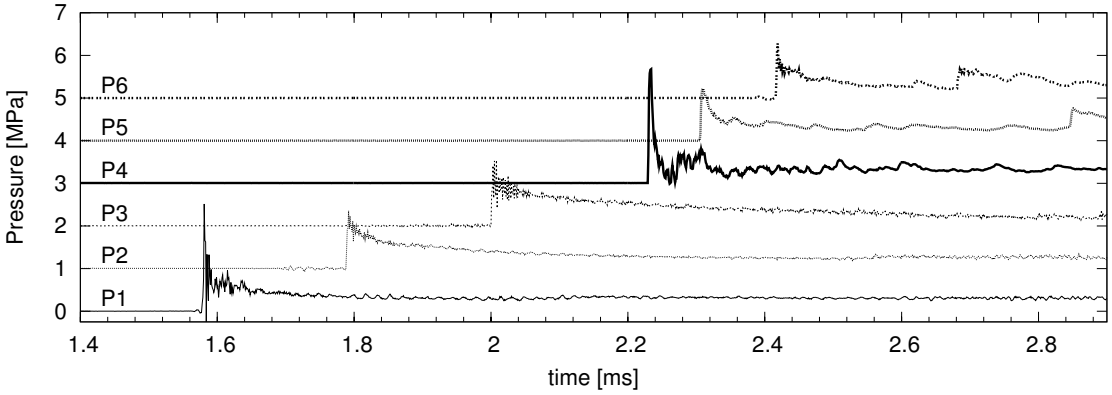

Figure K.164: Shot 165, 0.333 H_2 + 0.167 O_2 + 0.5 Ar, P_0=57.5 kPa, T_0=296 K. $U(P_1\text{-}P_2)/U_{CJ} = 1.000$, $U(P_2\text{-}P_3)/U_{CJ} = 0.995$.

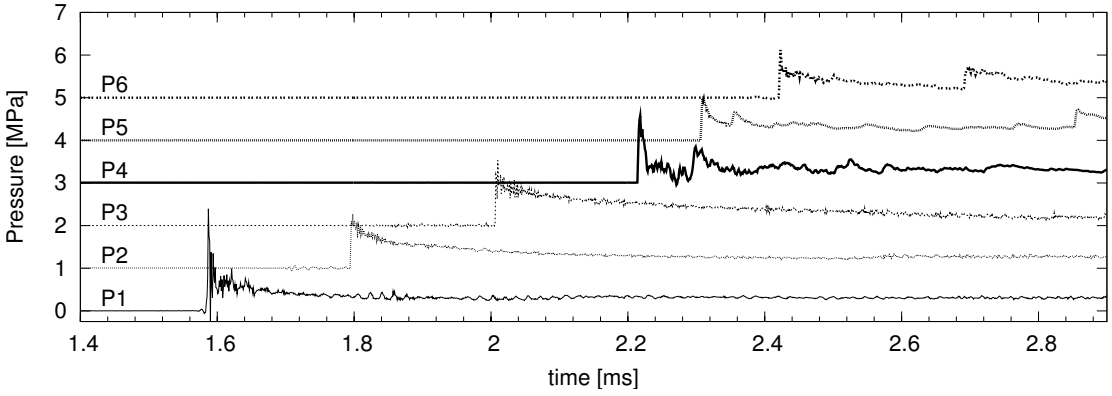

Figure K.165: Shot 166, 0.333 H_2 + 0.167 O_2 + 0.5 Ar, P_0=57.5 kPa, T_0=296 K. $U(P_1\text{-}P_2)/U_{CJ} = 1.005$, $U(P_2\text{-}P_3)/U_{CJ} = 0.991$.

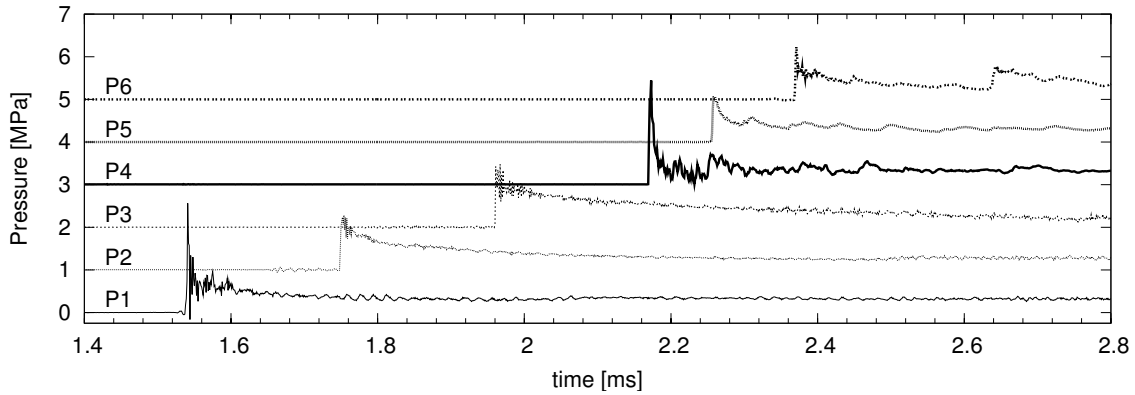

Figure K.166: Shot 167, 0.333 H_2 + 0.167 O_2 + 0.5 Ar, P_0=60 kPa, T_0=297 K. $U(P_1\text{-}P_2)/U_{CJ} = 0.999$, $U(P_2\text{-}P_3)/U_{CJ} = 0.995$.

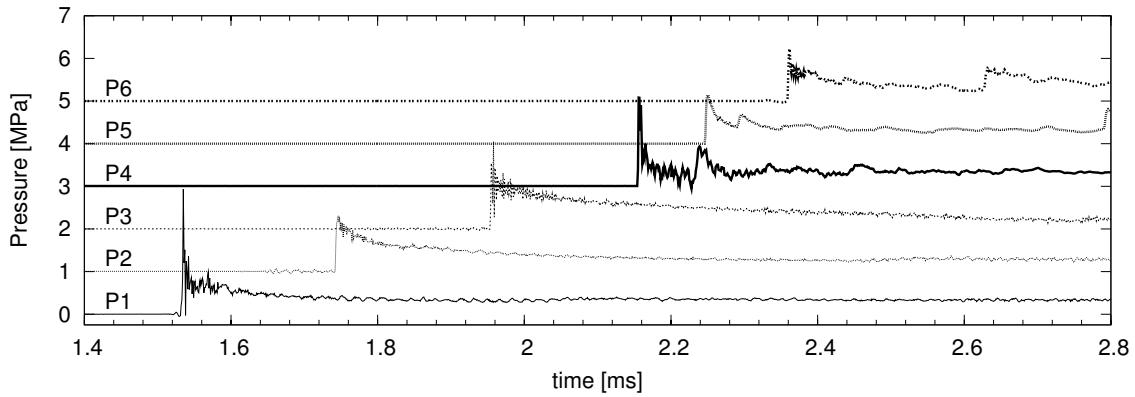

Figure K.167: Shot 168, 0.333 H_2 + 0.167 O_2 + 0.5 Ar, P_0=62.5 kPa, T_0=296 K. $U(P_1\text{-}P_2)/U_{CJ} = 1.003$, $U(P_2\text{-}P_3)/U_{CJ} = 0.989$.

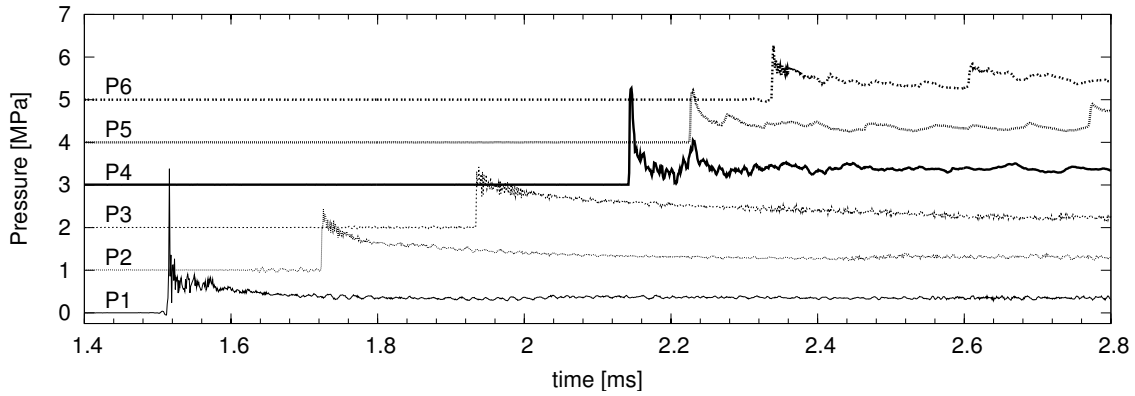

Figure K.168: Shot 169, 0.333 H_2 + 0.167 O_2 + 0.5 Ar, P_0=65 kPa, T_0=296 K. $U(P_1\text{-}P_2)/U_{CJ} = 1.003$, $U(P_2\text{-}P_3)/U_{CJ} = 0.993$.

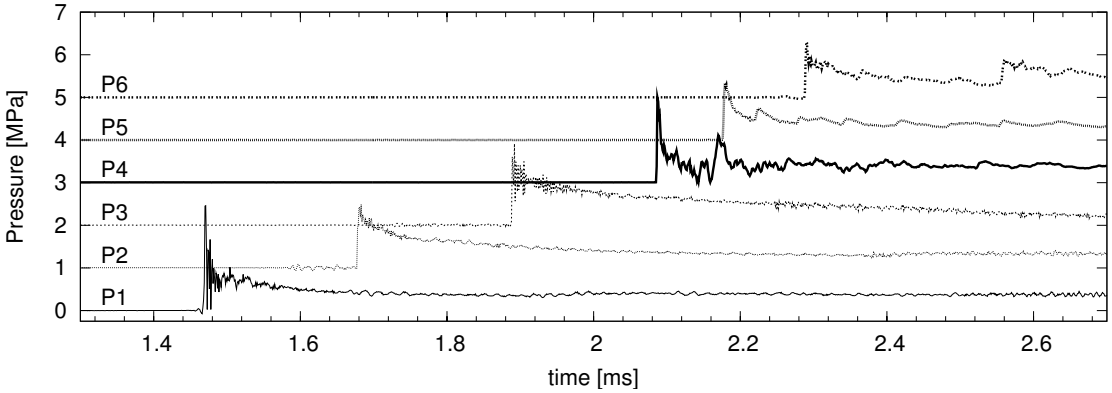

Figure K.169: Shot 170, 0.333 H_2 + 0.167 O_2 + 0.5 Ar, P_0=70 kPa, T_0=296 K. $U(P_1\text{-}P_2)/U_{CJ} = 1.001$, $U(P_2\text{-}P_3)/U_{CJ} = 0.992$.

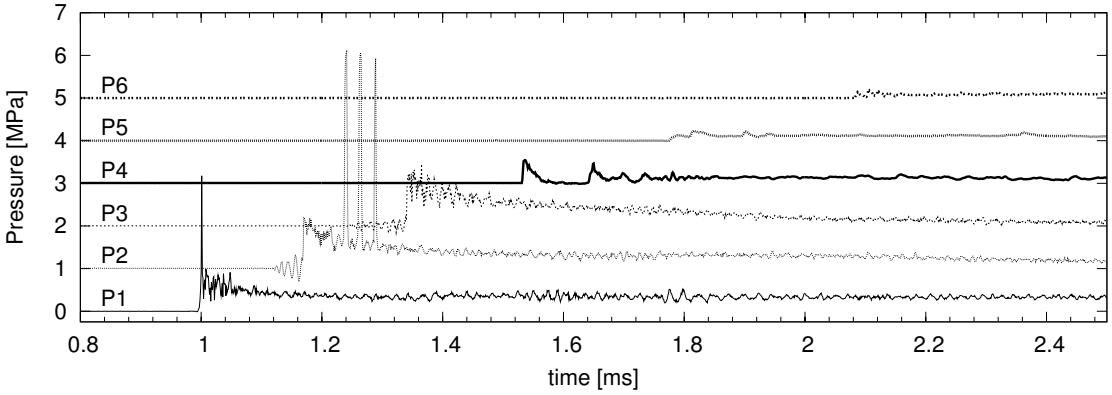

Figure K.170: Shot 171, 0.5 H_2 + 0.5 N_2O, P_0=45 kPa, T_0=297 K. $U(P_1\text{-}P_2)/U_{CJ} = 0.998$, $U(P_2\text{-}P_3)/U_{CJ} = 0.992$.

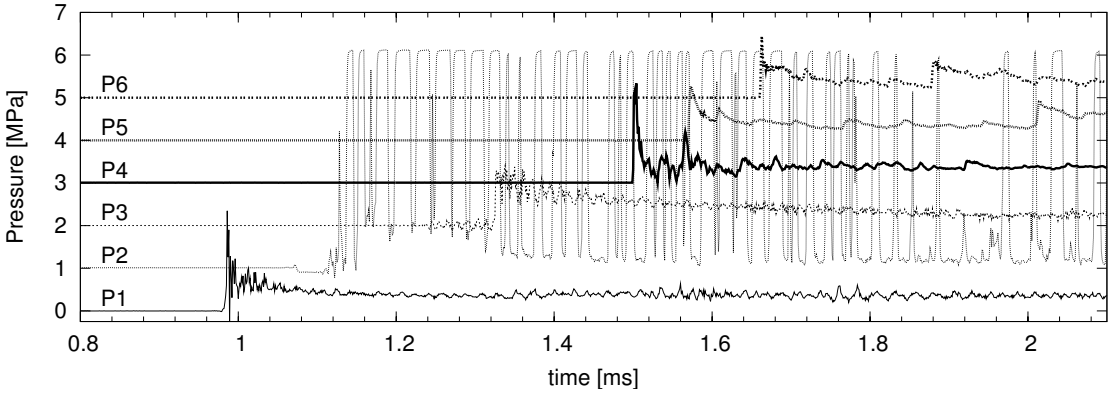

Figure K.171: Shot 172, 0.5 H_2 + 0.5 N_2O, P_0=47.5 kPa, T_0=297 K. $U(P_1\text{-}P_2)/U_{CJ} = 1.085$, $U(P_2\text{-}P_3)/U_{CJ} = 0.956$.

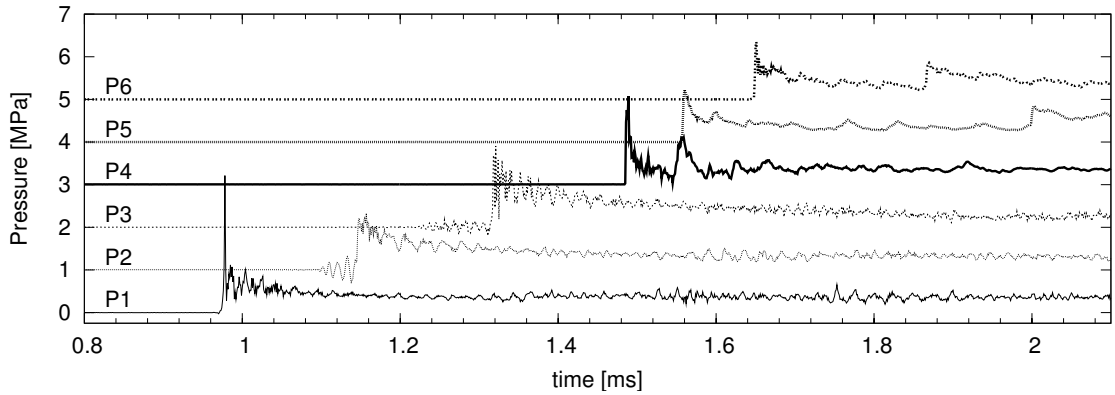

Figure K.172: Shot 173, 0.5 H_2 + 0.5 N_2O, P_0=47.5 kPa, T_0=297 K. $U(P_1\text{-}P_2)/U_{CJ}$ = 0.997, $U(P_2\text{-}P_3)/U_{CJ}$ = 0.985.

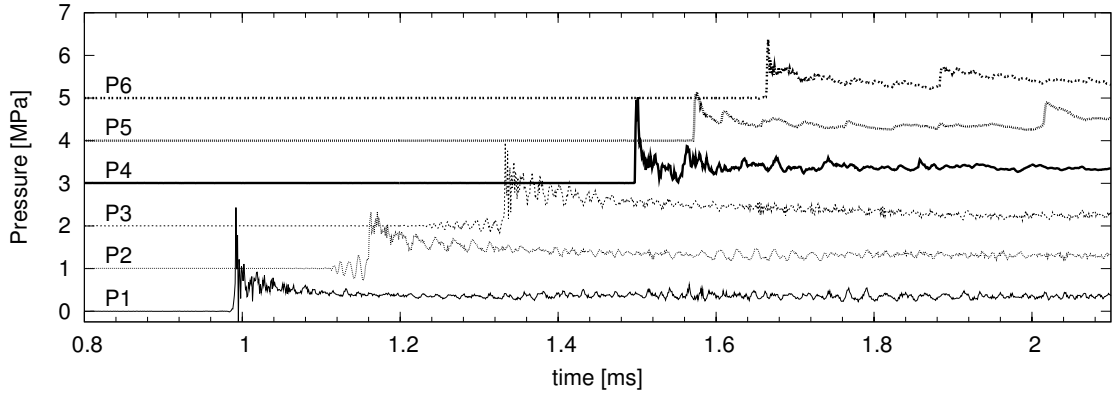

Figure K.173: Shot 174, 0.5 H_2 + 0.5 N_2O, P_0=46.25 kPa, T_0=297 K. $U(P_1\text{-}P_2)/U_{CJ}$ = 0.997, $U(P_2\text{-}P_3)/U_{CJ}$ = 0.986.

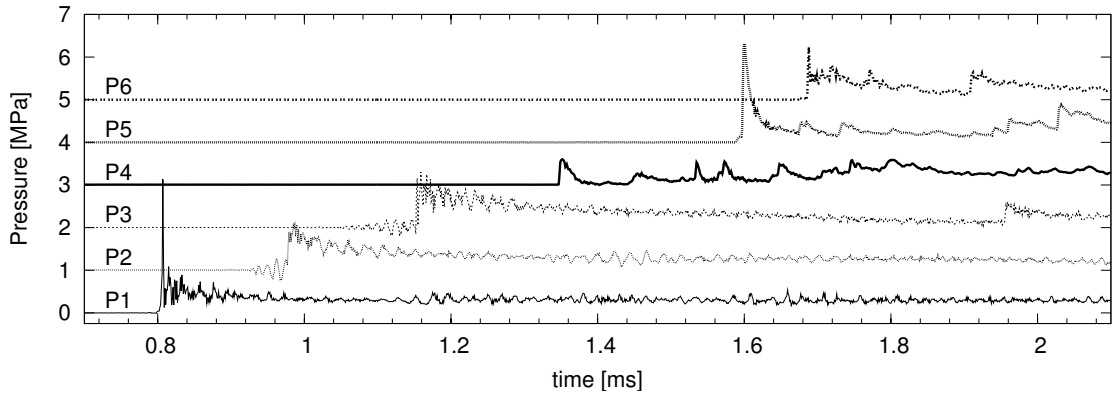

Figure K.174: Shot 175, 0.222 C_2H_6 + 0.778 O_2, P_0=30 kPa, T_0=297 K. $U(P_1\text{-}P_2)/U_{CJ}$ = 0.998, $U(P_2\text{-}P_3)/U_{CJ}$ = 0.986.

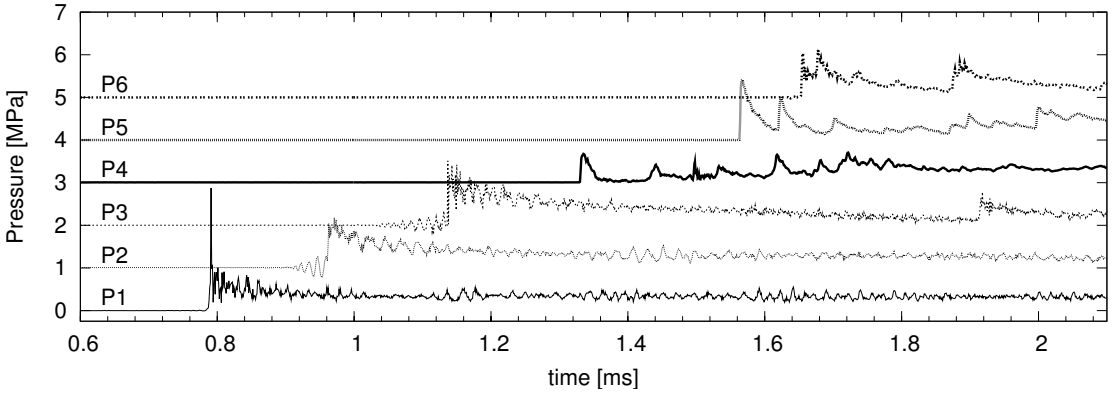

Figure K.175: Shot 176, 0.222 C_2H_6 + 0.778 O_2, P_0=32.5 kPa, T_0=297 K. U(P_1-P_2)/U_{CJ} = 0.996, U(P_2-P_3)/U_{CJ} = 0.985.

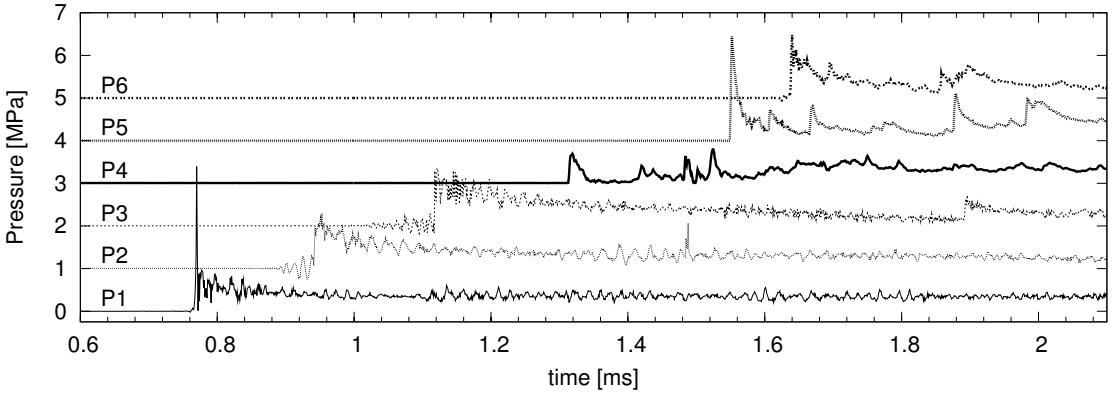

Figure K.176: Shot 177, 0.222 C_2H_6 + 0.778 O_2, P_0=35 kPa, T_0=297 K. U(P_1-P_2)/U_{CJ} = 0.989, U(P_2-P_3)/U_{CJ} = 0.978.

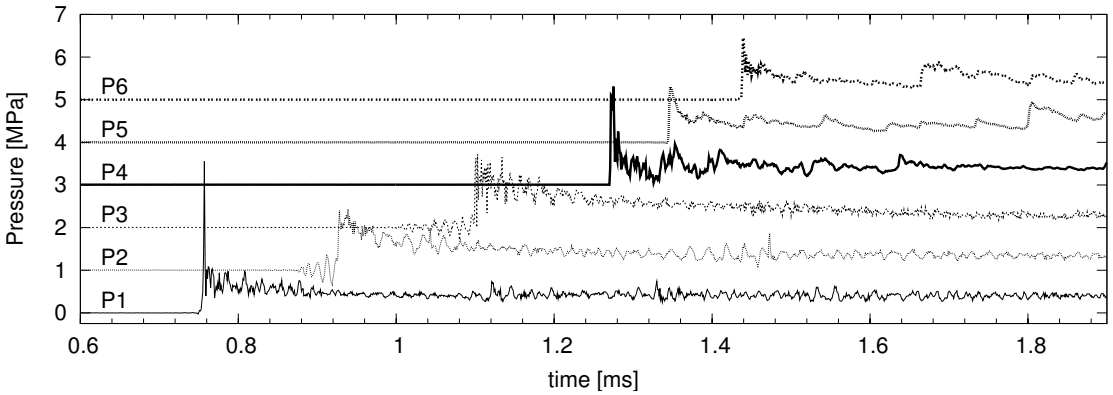

Figure K.177: Shot 178, 0.222 C_2H_6 + 0.778 O_2, P_0=40 kPa, T_0=297 K. U(P_1-P_2)/U_{CJ} = 1.004, U(P_2-P_3)/U_{CJ} = 0.992.

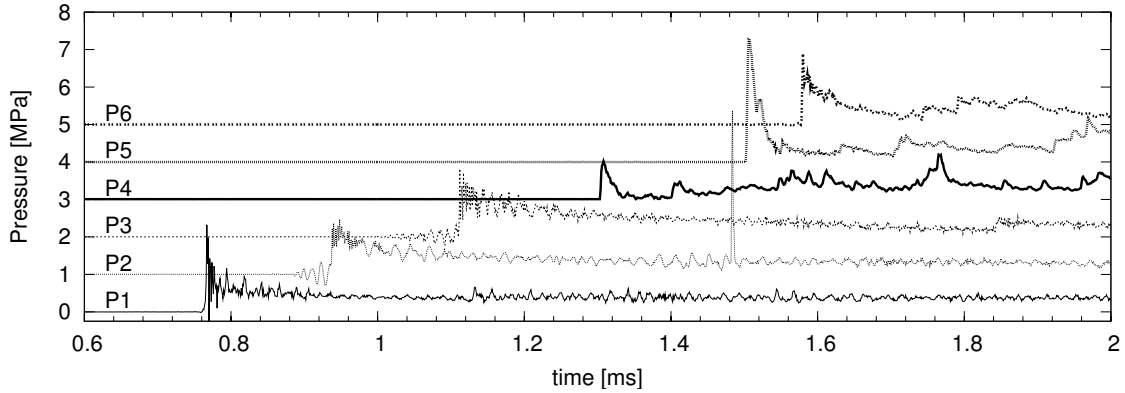

Figure K.178: Shot 179, 0.222 C_2H_6 + 0.778 O_2, P_0=37.5 kPa, T_0=298 K. U(P_1-P_2)/U_{CJ} = 0.999, U(P_2-P_3)/U_{CJ} = 0.988.

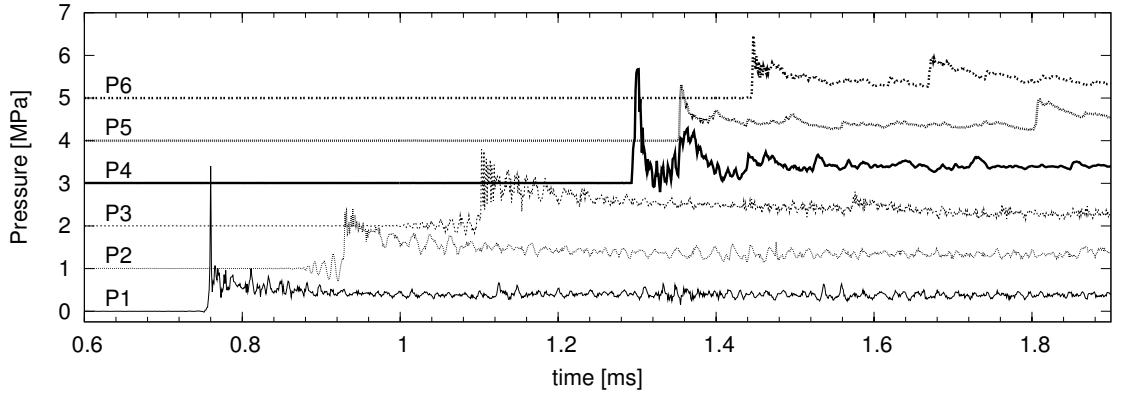

Figure K.179: Shot 180, 0.222 C_2H_6 + 0.778 O_2, P_0=37.5 kPa, T_0=297 K. U(P_1-P_2)/U_{CJ} = 0.999, U(P_2-P_3)/U_{CJ} = 0.993.

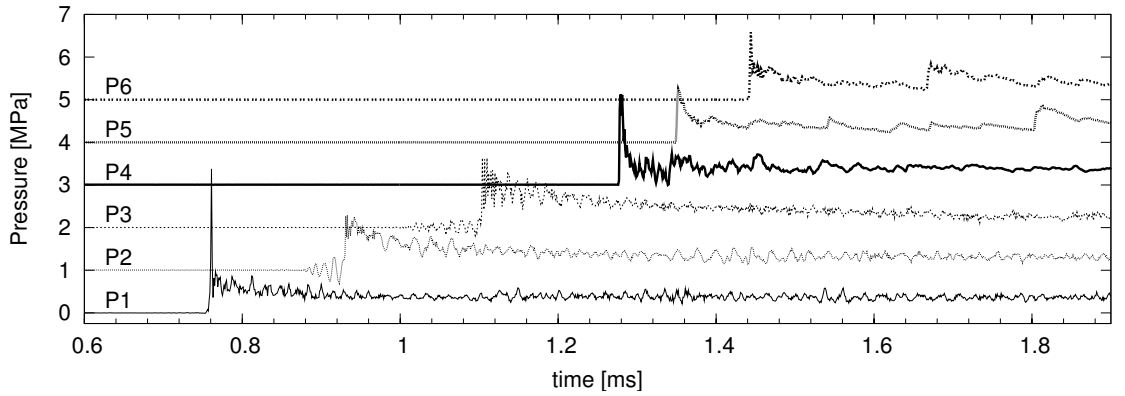

Figure K.180: Shot 181, 0.222 C_2H_6 + 0.778 O_2, P_0=36.25 kPa, T_0=297 K. U(P_1-P_2)/U_{CJ} = 1.006, U(P_2-P_3)/U_{CJ} = 0.994.

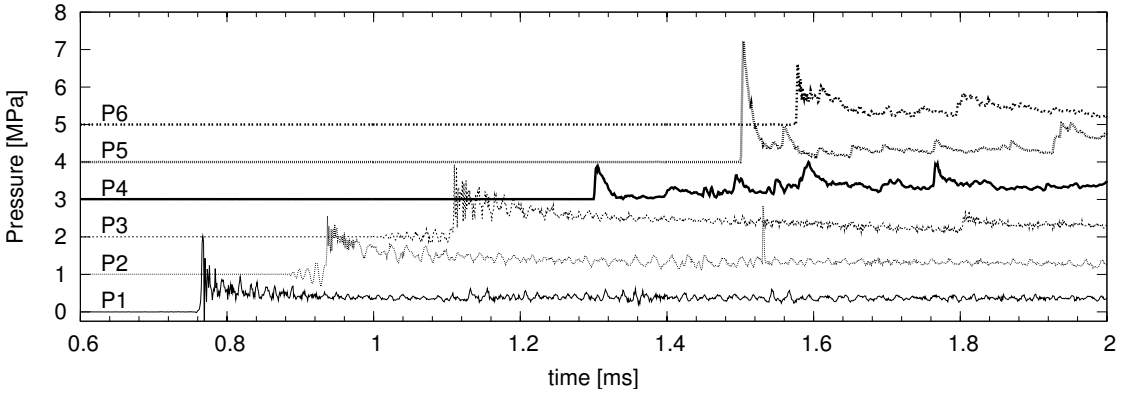

Figure K.181: Shot 182, 0.222 C_2H_6 + 0.778 O_2, P_0=36.25 kPa, T_0=298 K. U(P_1-P_2)/U_{CJ} = 1.006, U(P_2-P_3)/U_{CJ} = 0.988.

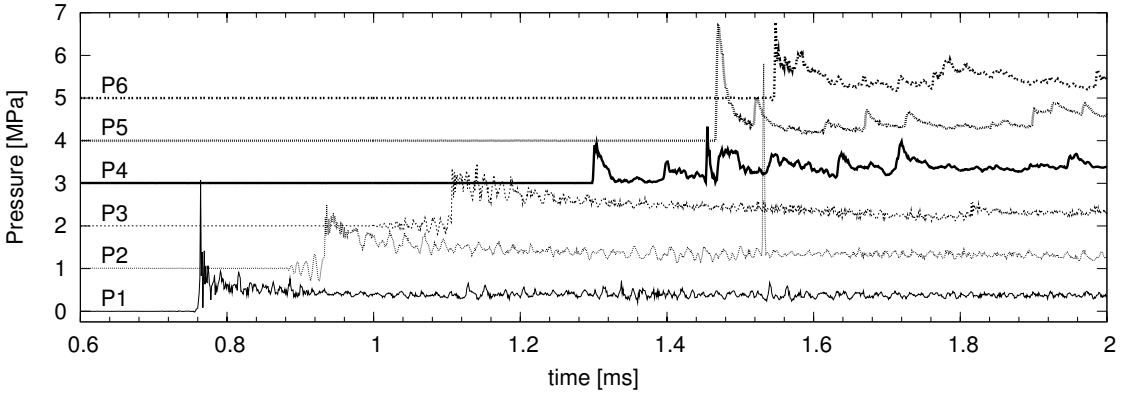

Figure K.182: Shot 183, 0.222 C_2H_6 + 0.778 O_2, P_0=37.5 kPa, T_0=298 K. U(P_1-P_2)/U_{CJ} = 1.005, U(P_2-P_3)/U_{CJ} = 0.993.

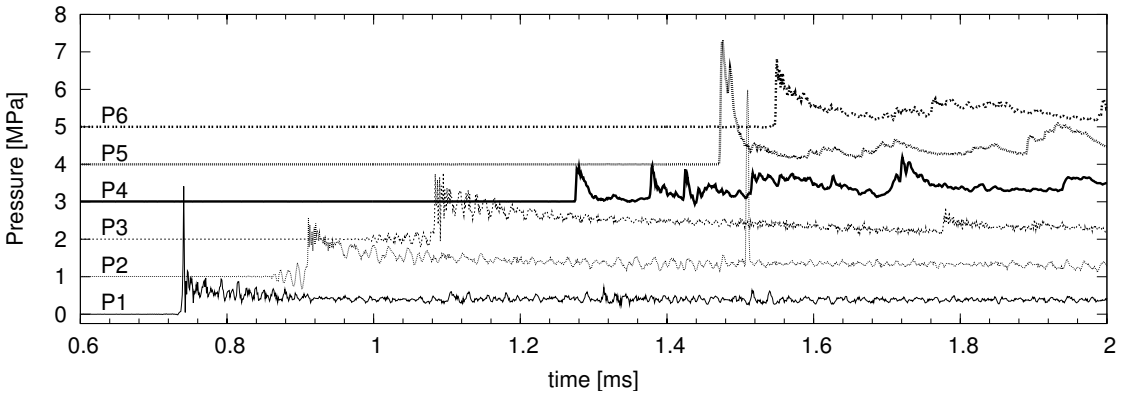

Figure K.183: Shot 184, 0.222 C_2H_6 + 0.778 O_2, P_0=38.25 kPa, T_0=298 K. U(P_1-P_2)/U_{CJ} = 0.999, U(P_2-P_3)/U_{CJ} = 0.999.

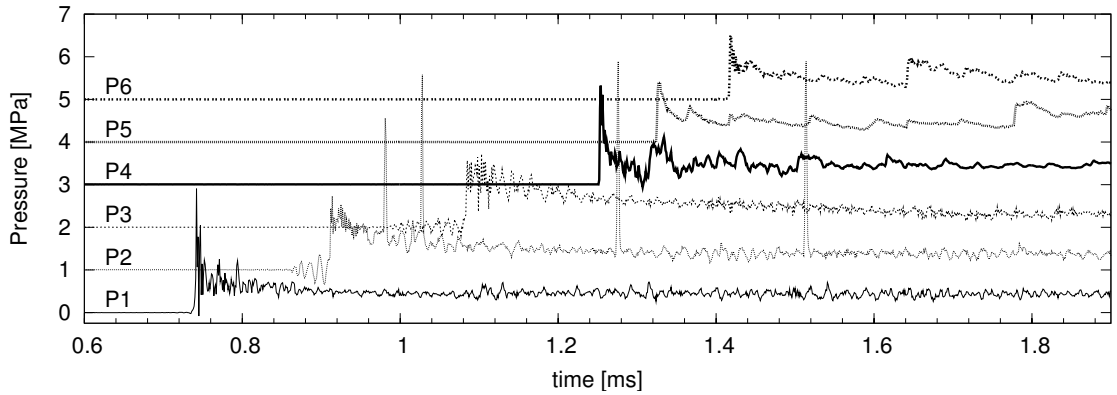

Figure K.184: Shot 185, 0.222 C_2H_6 + 0.778 O_2, P_0=42.5 kPa, T_0=298 K. U(P_1-P_2)/U_{CJ} = 1.003, U(P_2-P_3)/U_{CJ} = 0.997.

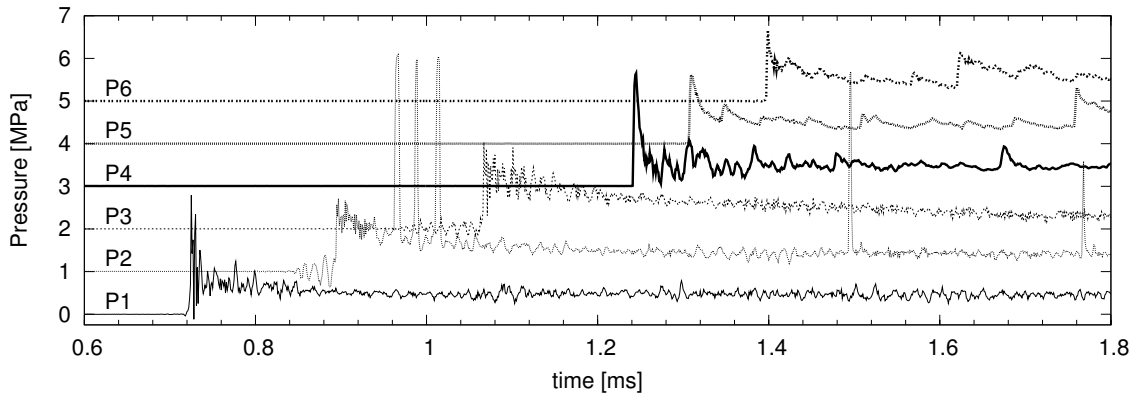

Figure K.185: Shot 186, 0.222 C_2H_6 + 0.778 O_2, P_0=45 kPa, T_0=299 K. U(P_1-P_2)/U_{CJ} = 1.002, U(P_2-P_3)/U_{CJ} = 0.996.

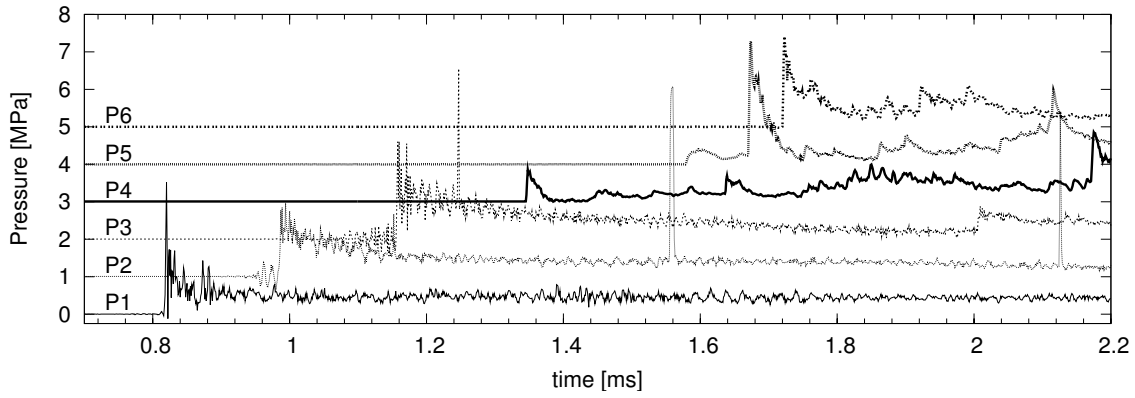

Figure K.186: Shot 187, 0.333 CH_4 + 0.667 O_2, P_0=50 kPa, T_0=294 K. U(P_1-P_2)/U_{CJ} = 1.008, U(P_2-P_3)/U_{CJ} = 0.991.

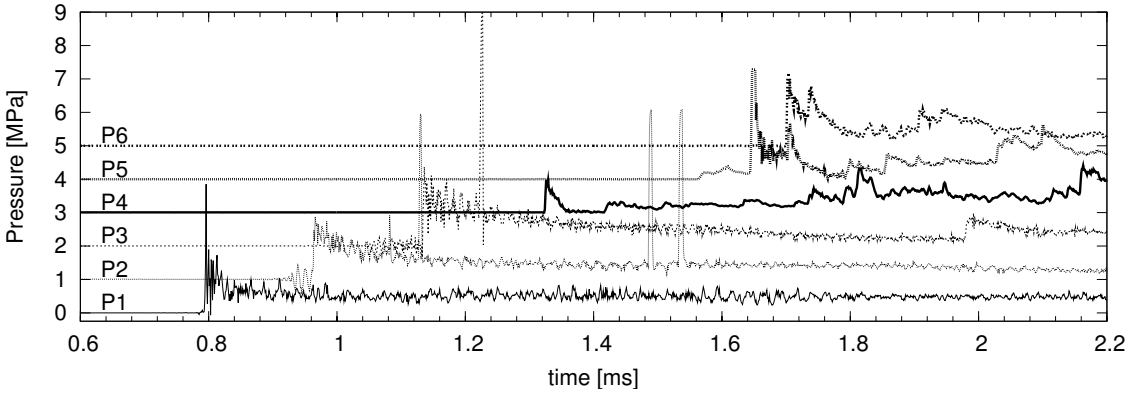

Figure K.187: Shot 188, 0.333 CH_4 + 0.667 O_2, P_0=55 kPa, T_0=295 K. U(P_1-P_2)/U_{CJ} = 1.000, U(P_2-P_3)/U_{CJ} = 0.995.

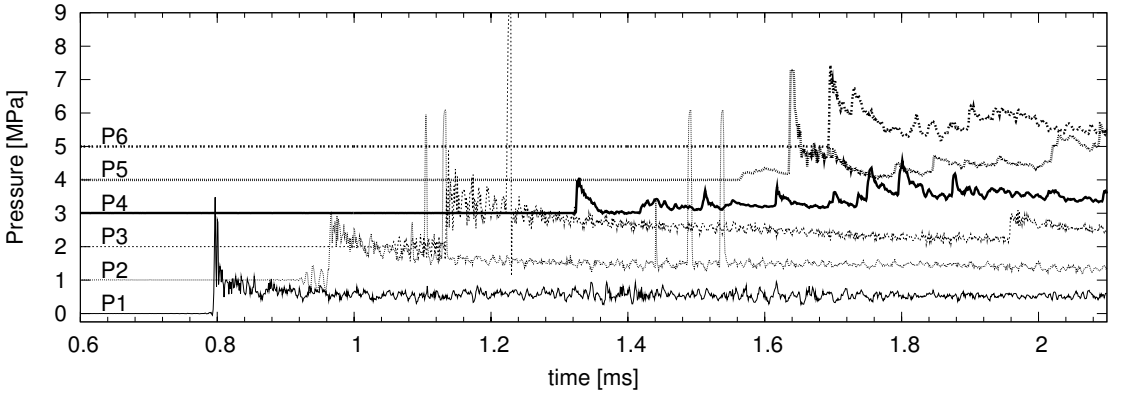

Figure K.188: Shot 189, 0.333 CH_4 + 0.667 O_2, P_0=60 kPa, T_0=296 K. U(P_1-P_2)/U_{CJ} = 0.999, U(P_2-P_3)/U_{CJ} = 0.987.

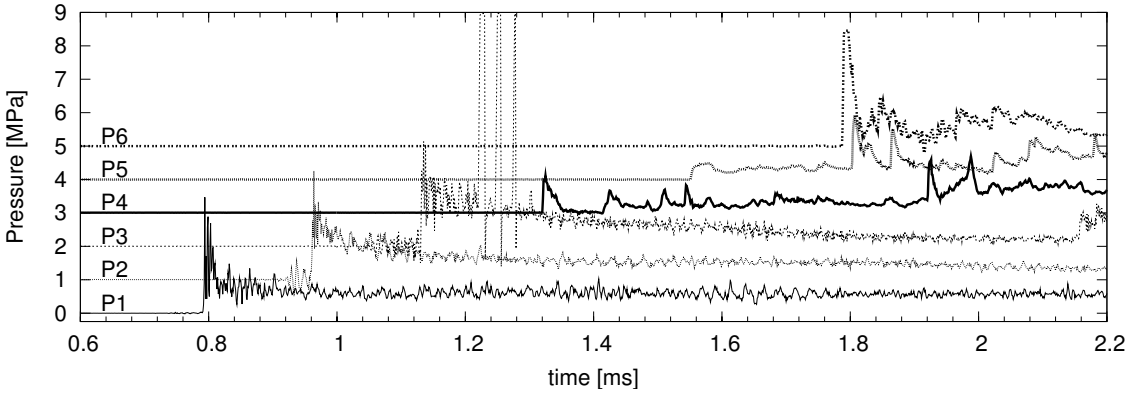

Figure K.189: Shot 190, 0.333 CH_4 + 0.667 O_2, P_0=65 kPa, T_0=296 K. U(P_1-P_2)/U_{CJ} = 1.003, U(P_2-P_3)/U_{CJ} = 0.991.

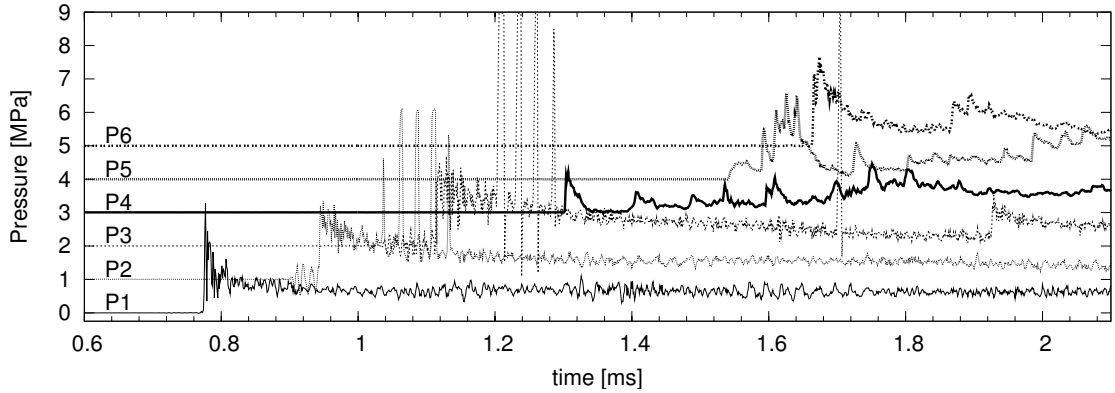

Figure K.190: Shot 191, 0.333 CH_4 + 0.667 O_2, P_0=70 kPa, T_0=297 K. $U(P_1\text{-}P_2)/U_{CJ}$ = 0.996, $U(P_2\text{-}P_3)/U_{CJ}$ = 1.026.

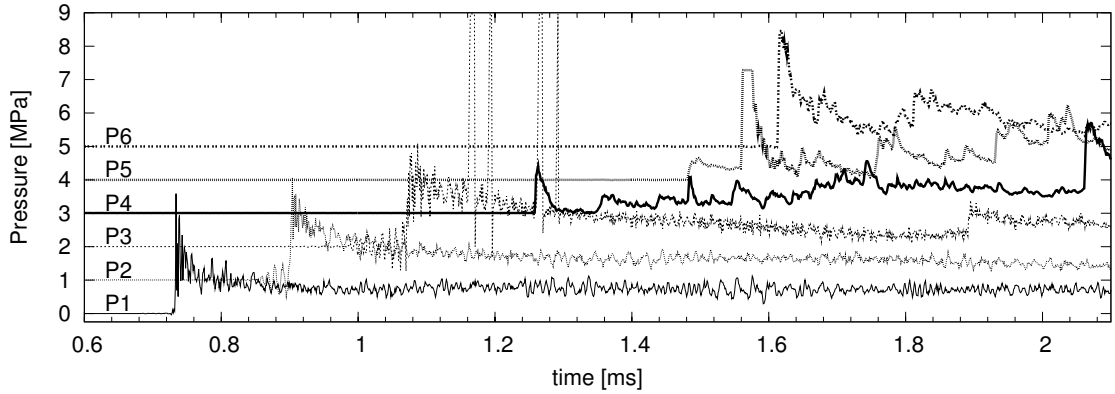

Figure K.191: Shot 192, 0.333 CH_4 + 0.667 O_2, P_0=80 kPa, T_0=298 K. $U(P_1\text{-}P_2)/U_{CJ}$ = 0.999, $U(P_2\text{-}P_3)/U_{CJ}$ = 0.976.

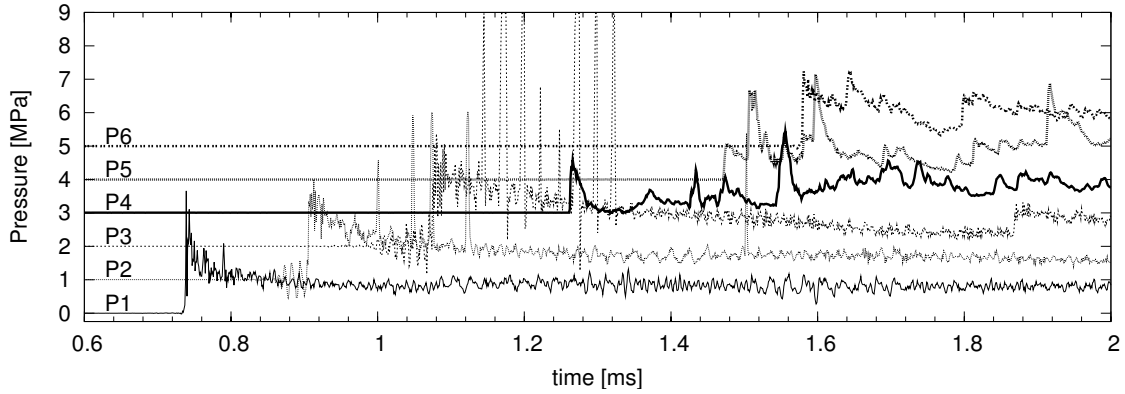

Figure K.192: Shot 193, 0.333 CH_4 + 0.667 O_2, P_0=90 kPa, T_0=298 K. $U(P_1\text{-}P_2)/U_{CJ}$ = 1.003, $U(P_2\text{-}P_3)/U_{CJ}$ = 0.974.

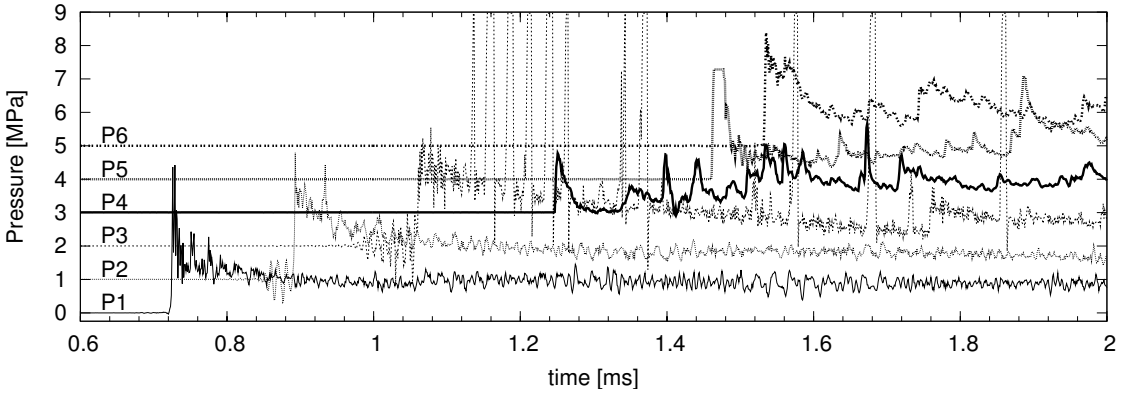

Figure K.193: Shot 194, 0.333 CH_4 + 0.667 O_2, P_0=100 kPa, T_0=299 K. U(P_1-P_2)/U_{CJ} = 1.001, U(P_2-P_3)/U_{CJ} = 0.995.

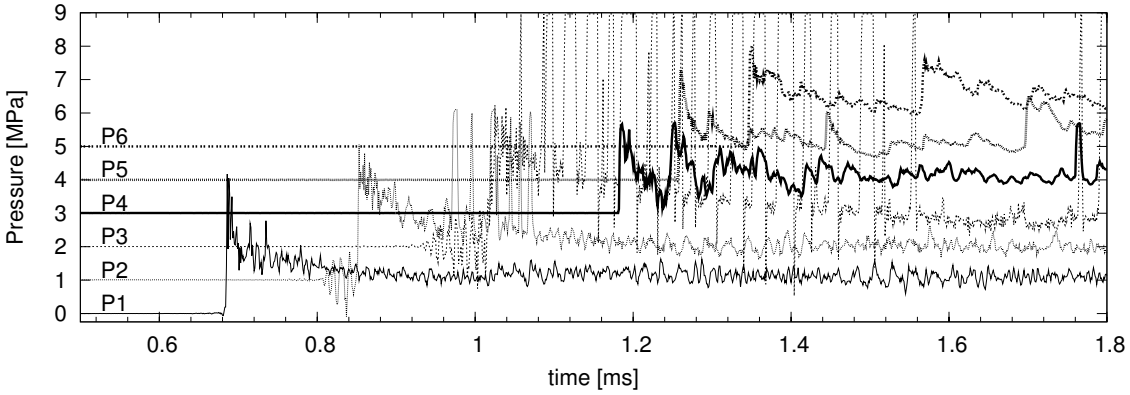

Figure K.194: Shot 195, 0.333 CH_4 + 0.667 O_2, P_0=120 kPa, T_0=299 K. U(P_1-P_2)/U_{CJ} = 1.004, U(P_2-P_3)/U_{CJ} = 0.992.

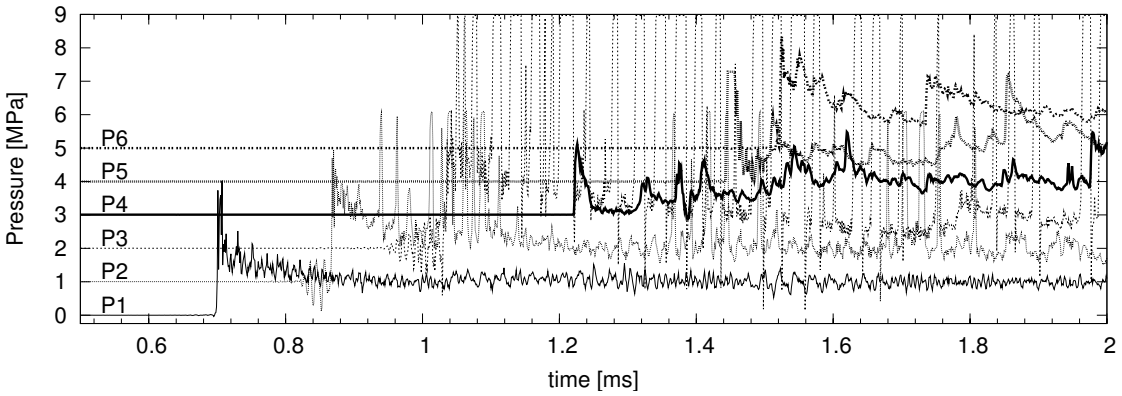

Figure K.195: Shot 196, 0.333 CH_4 + 0.667 O_2, P_0=110 kPa, T_0=299 K. U(P_1-P_2)/U_{CJ} = 0.999, U(P_2-P_3)/U_{CJ} = 0.993.

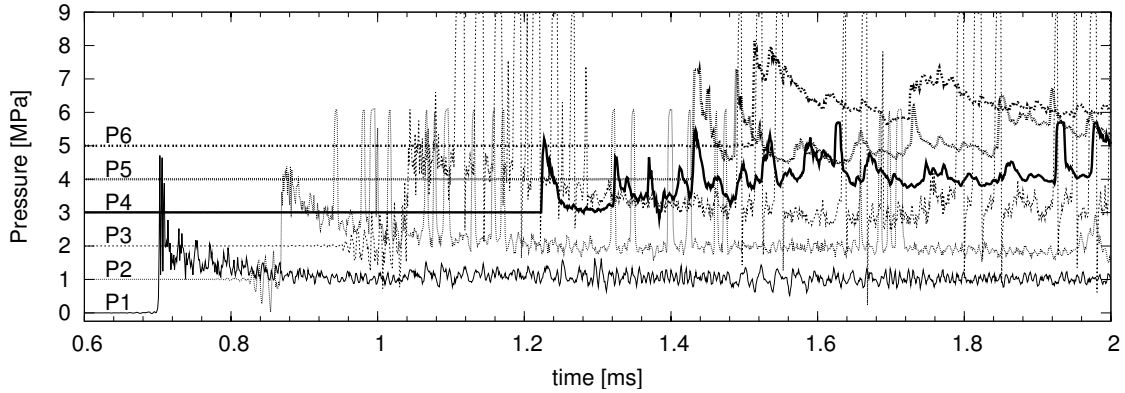

Figure K.196: Shot 197, 0.333 CH_4 + 0.667 O_2, P_0=115 kPa, T_0=300 K. U(P_1-P_2)/U_{CJ} = 0.998, U(P_2-P_3)/U_{CJ} = 0.964.

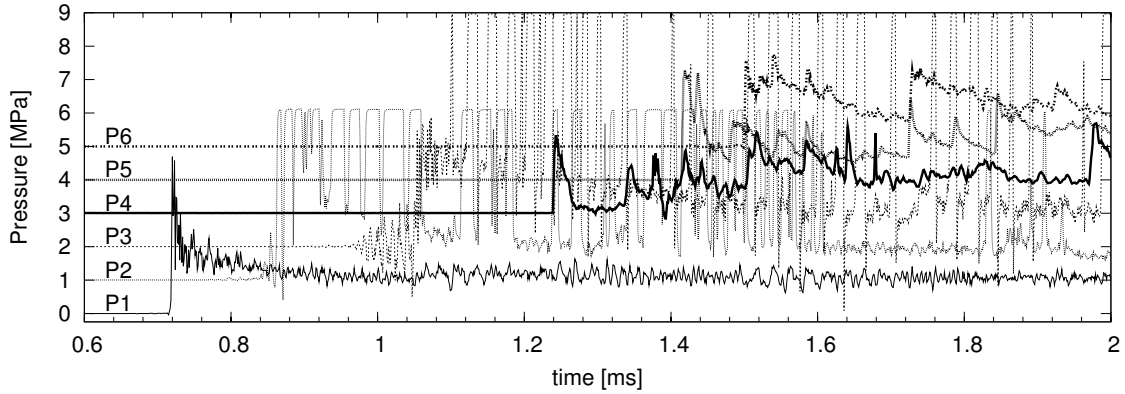

Figure K.197: Shot 198, 0.333 CH_4 + 0.667 O_2, P_0=120 kPa, T_0=298 K. U(P_1-P_2)/U_{CJ} = 1.157, U(P_2-P_3)/U_{CJ} = 0.872.

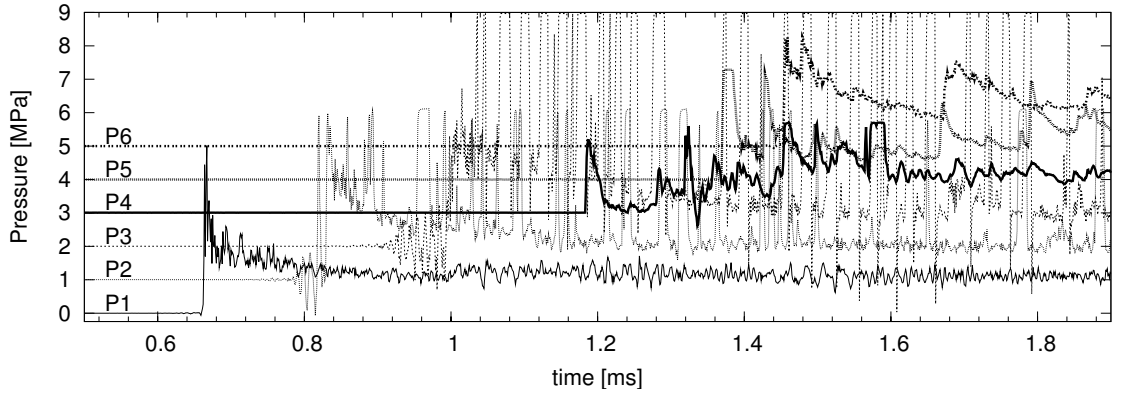

Figure K.198: Shot 199, 0.333 CH_4 + 0.667 O_2, P_0=125 kPa, T_0=301 K. U(P_1-P_2)/U_{CJ} = 1.074, U(P_2-P_3)/U_{CJ} = 0.930.

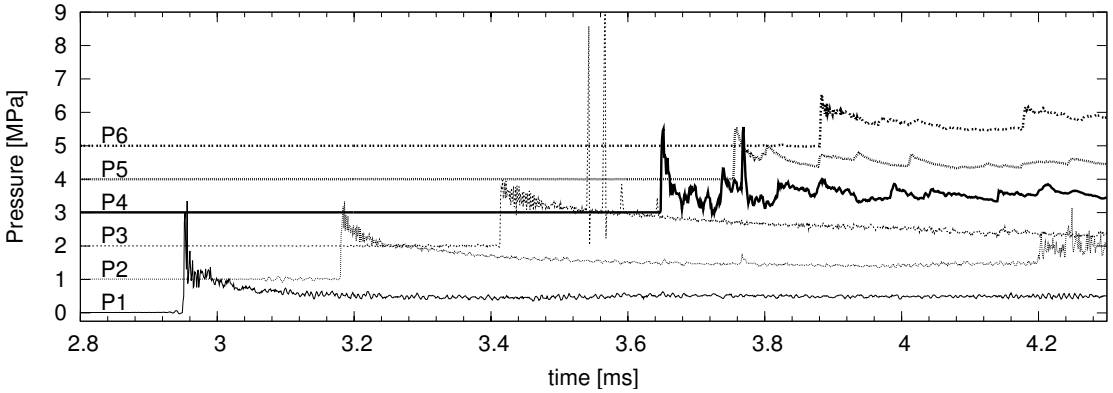

Figure K.199: Shot 200, 0.22 H_2 + 0.11 O_2 + 0.67 Ar, P_0=100 kPa, T_0=293 K. $U(P_1\text{-}P_2)/U_{CJ} = 1.010$, $U(P_2\text{-}P_3)/U_{CJ} = 0.992$.

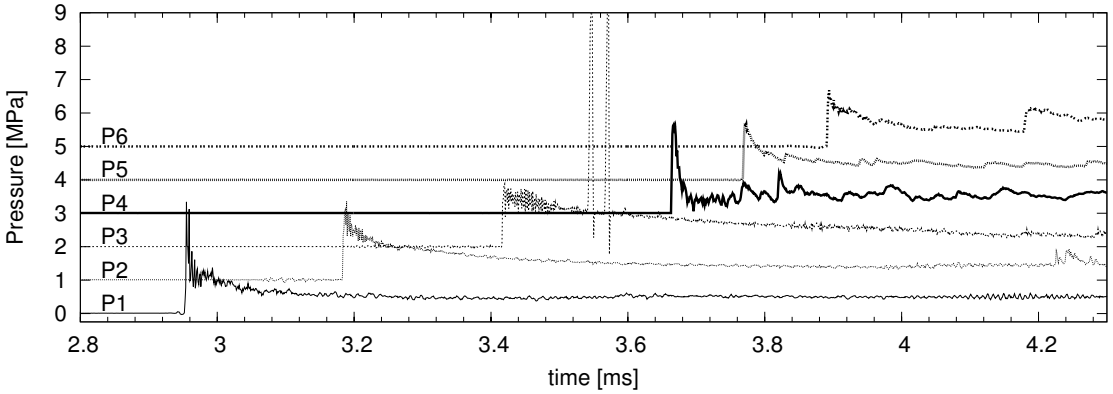

Figure K.200: Shot 201, 0.22 H_2 + 0.11 O_2 + 0.67 Ar, P_0=100 kPa, T_0=294 K. $U(P_1\text{-}P_2)/U_{CJ} = 1.005$, $U(P_2\text{-}P_3)/U_{CJ} = 0.992$.

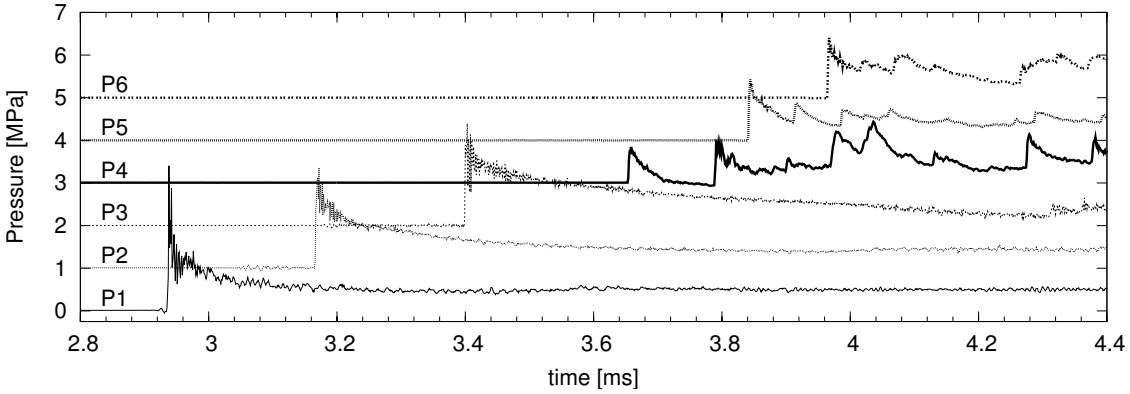

Figure K.201: Shot 202, 0.22 H_2 + 0.11 O_2 + 0.67 Ar, P_0=100 kPa, T_0=294 K. $U(P_1\text{-}P_2)/U_{CJ} = 1.005$, $U(P_2\text{-}P_3)/U_{CJ} = 0.992$.

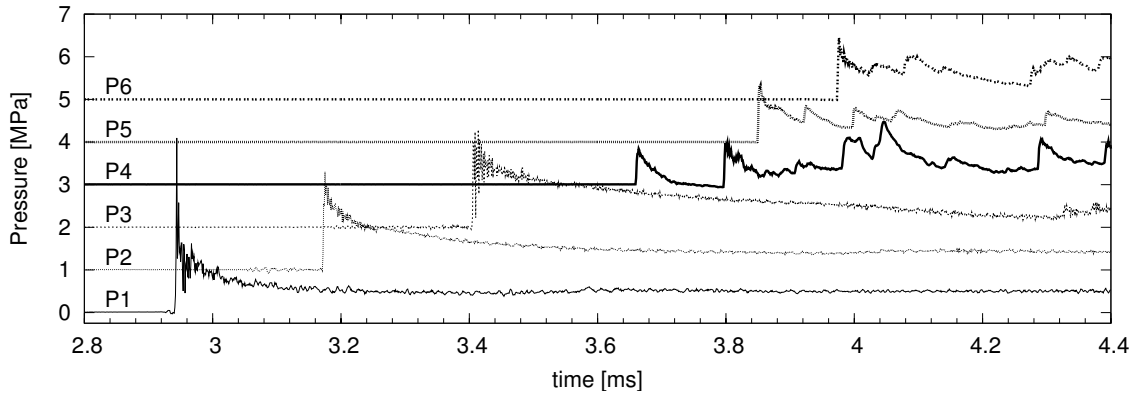

Figure K.202: Shot 203, 0.22 H_2 + 0.11 O_2 + 0.67 Ar, P_0=100 kPa, T_0=294 K. $U(P_1\text{-}P_2)/U_{CJ}$ = 1.005, $U(P_2\text{-}P_3)/U_{CJ}$ = 0.992.

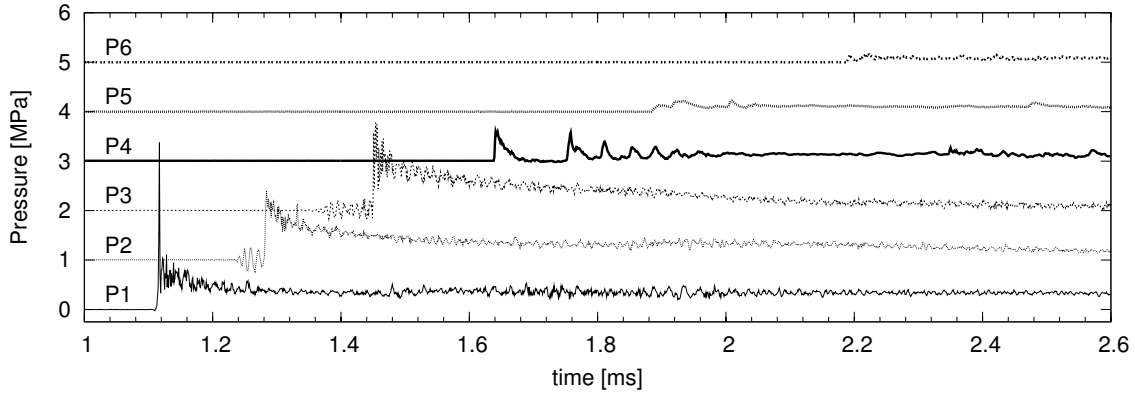

Figure K.203: Shot 204, 0.5 H_2 + 0.5 N_2O, P_0=47.5 kPa, T_0=295 K. $U(P_1\text{-}P_2)/U_{CJ}$ = 1.021, $U(P_2\text{-}P_3)/U_{CJ}$ = 1.003.

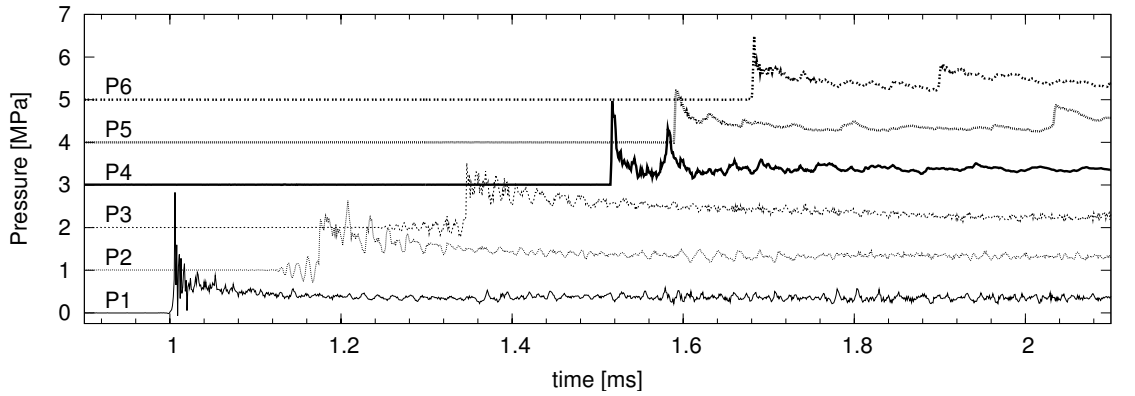

Figure K.204: Shot 205, 0.5 H_2 + 0.5 N_2O, P_0=47.5 kPa, T_0=295 K. $U(P_1\text{-}P_2)/U_{CJ}$ = 0.997, $U(P_2\text{-}P_3)/U_{CJ}$ = 0.985.

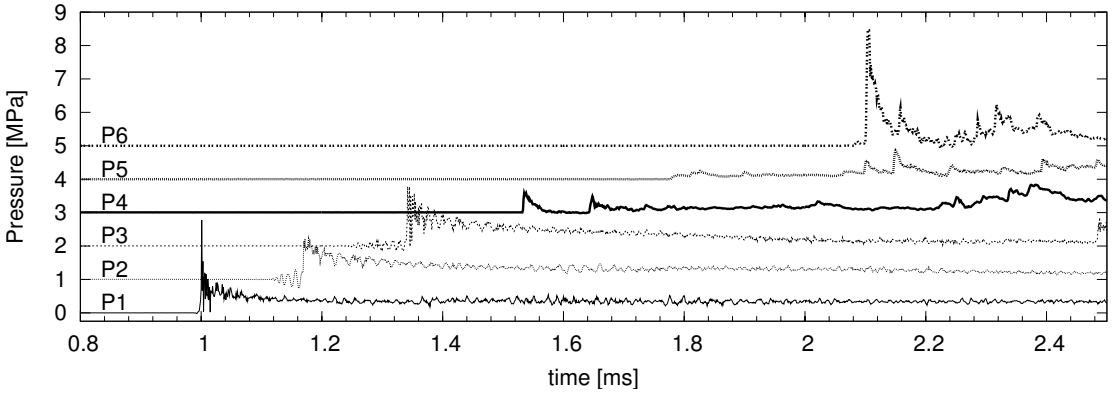

Figure K.205: Shot 206, 0.5 H_2 + 0.5 N_2O, P_0=45 kPa, T_0=295 K. U(P_1-P_2)/U_{CJ} = 0.998, U(P_2-P_3)/U_{CJ} = 0.992.

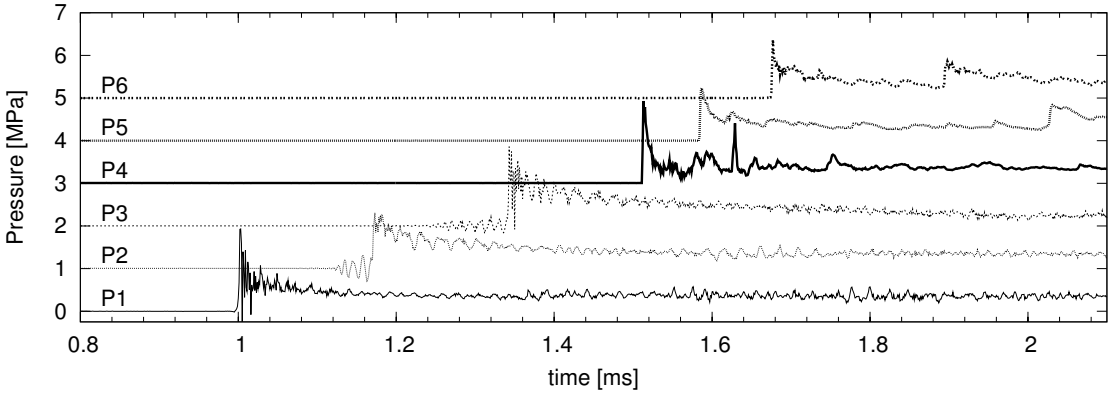

Figure K.206: Shot 207, 0.5 H_2 + 0.5 N_2O, P_0=47.5 kPa, T_0=296 K. U(P_1-P_2)/U_{CJ} = 0.997, U(P_2-P_3)/U_{CJ} = 0.991.

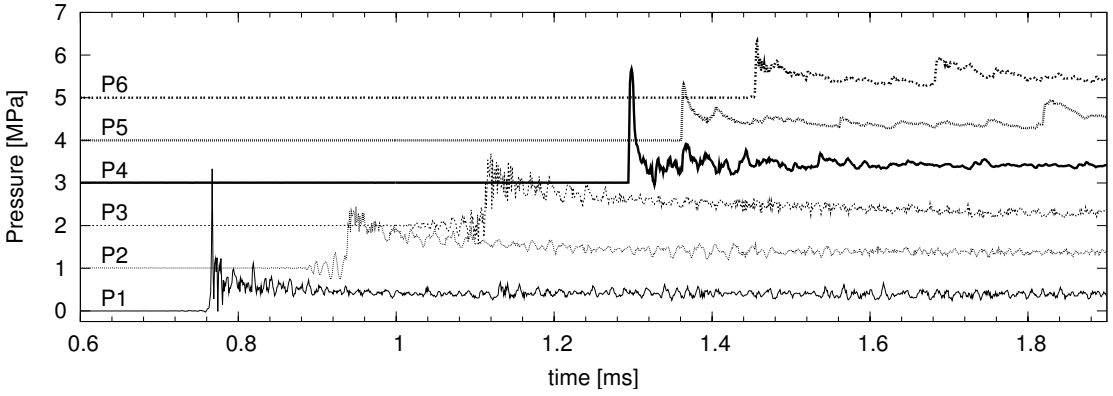

Figure K.207: Shot 208, 0.222 C_2H_6 + 0.778 O_2, P_0=40 kPa, T_0=295 K. U(P_1-P_2)/U_{CJ} = 0.998, U(P_2-P_3)/U_{CJ} = 0.981.

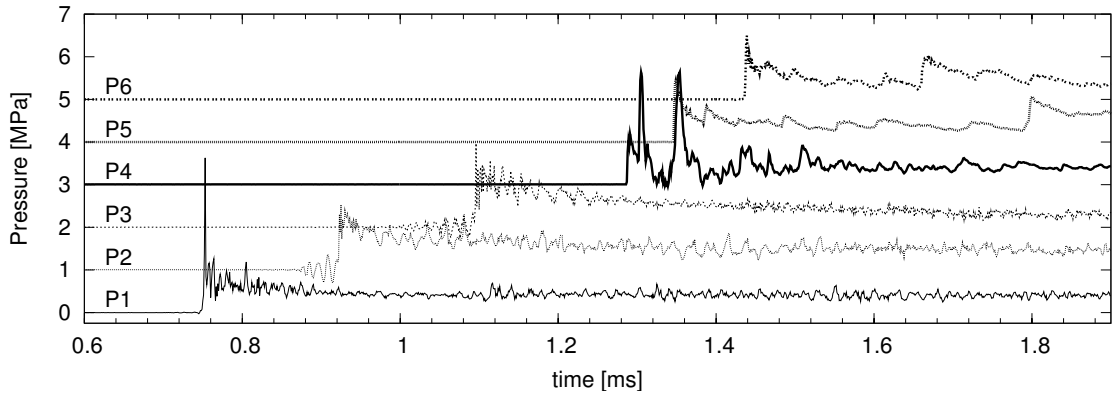

Figure K.208: Shot 209, 0.222 C_2H_6 + 0.778 O_2, P_0=40 kPa, T_0=296 K. U(P_1-P_2)/U_{CJ} = 1.004, U(P_2-P_3)/U_{CJ} = 0.992.

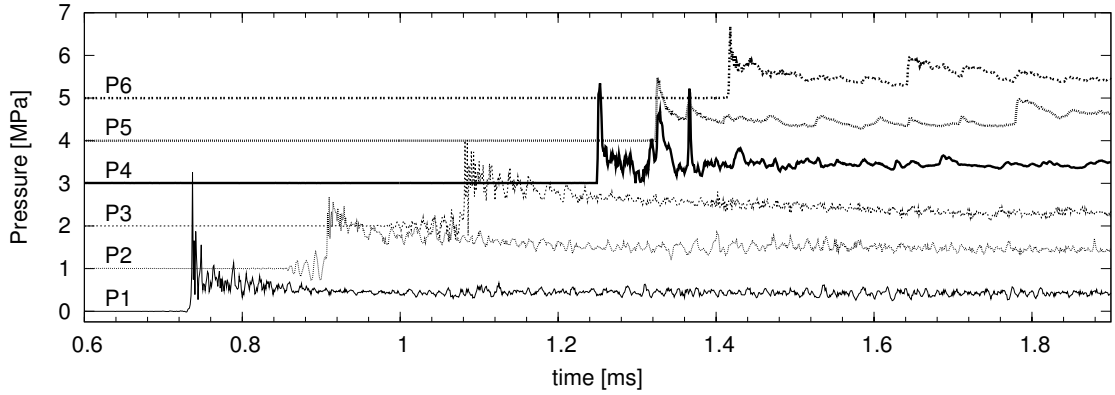

Figure K.209: Shot 210, 0.222 C_2H_6 + 0.778 O_2, P_0=42.5 kPa, T_0=296 K. U(P_1-P_2)/U_{CJ} = 0.997, U(P_2-P_3)/U_{CJ} = 0.985.

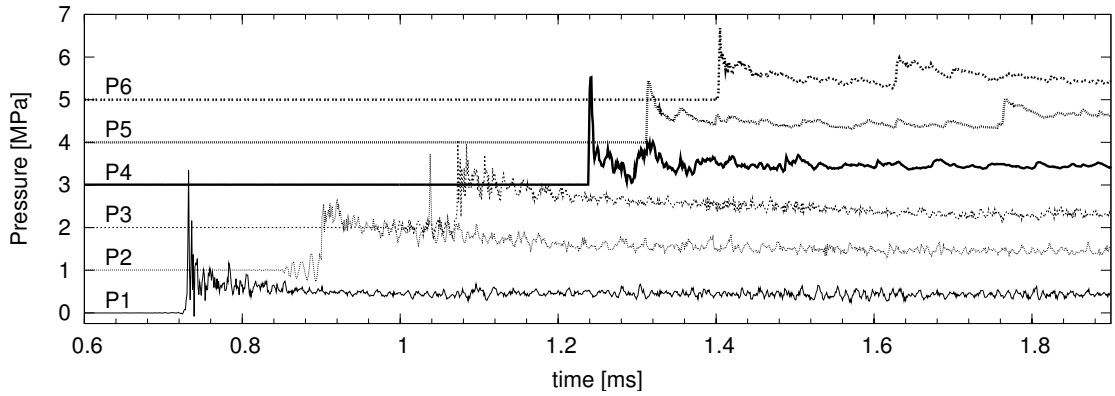

Figure K.210: Shot 211, 0.222 C_2H_6 + 0.778 O_2, P_0=42.5 kPa, T_0=297 K. U(P_1-P_2)/U_{CJ} = 1.008, U(P_2-P_3)/U_{CJ} = 0.997.

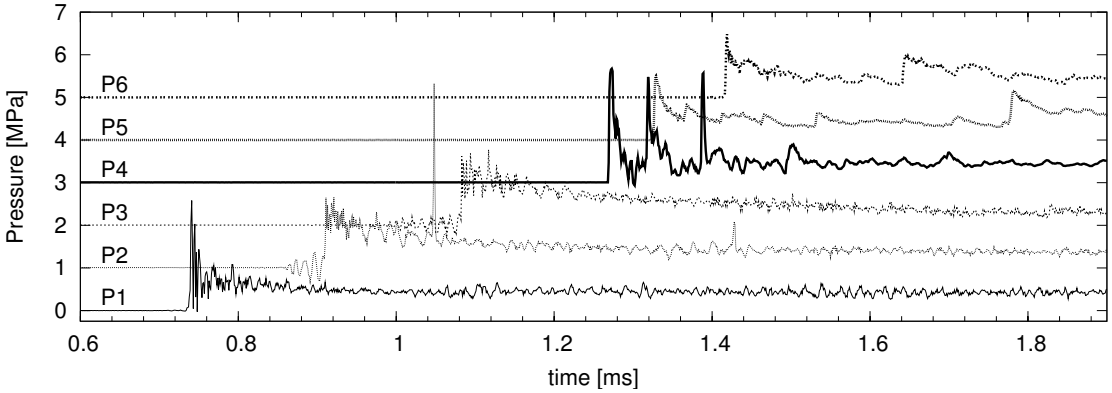

Figure K.211: Shot 212, 0.222 C_2H_6 + 0.778 O_2, P_0=42.5 kPa, T_0=297 K. U(P_1-P_2)/U_{CJ} = 1.008, U(P_2-P_3)/U_{CJ} = 0.991.

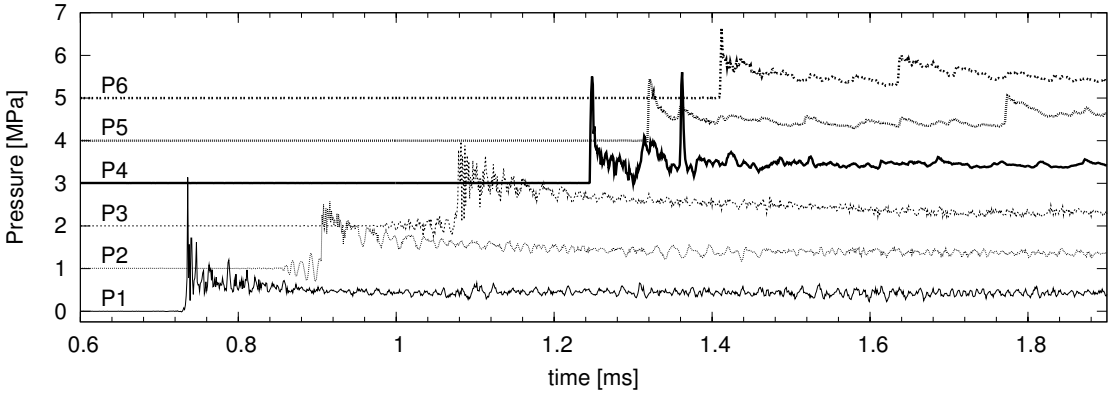

Figure K.212: Shot 213, 0.222 C_2H_6 + 0.778 O_2, P_0=42.5 kPa, T_0=298 K. U(P_1-P_2)/U_{CJ} = 1.003, U(P_2-P_3)/U_{CJ} = 0.997.

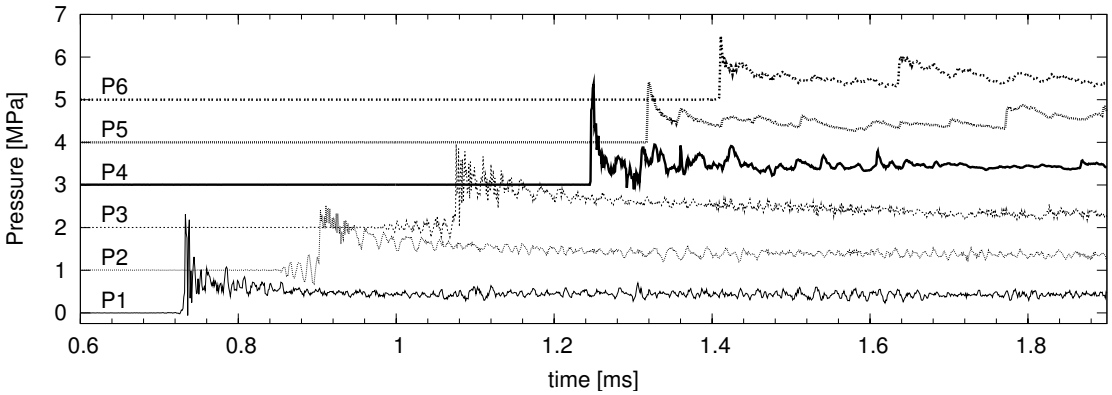

Figure K.213: Shot 214, 0.222 C_2H_6 + 0.778 O_2, P_0=42.5 kPa, T_0=298 K. U(P_1-P_2)/U_{CJ} = 1.008, U(P_2-P_3)/U_{CJ} = 0.991.

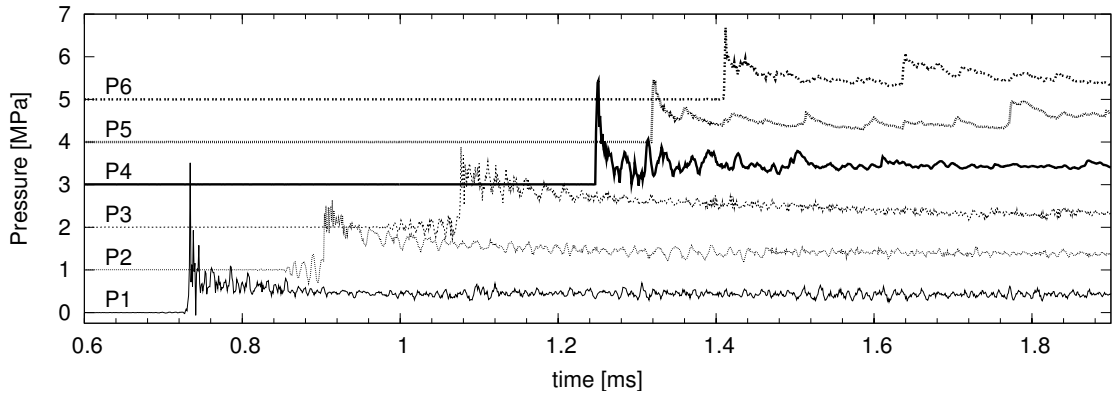

Figure K.214: Shot 215, 0.222 C_2H_6 + 0.778 O_2, P_0=42.5 kPa, T_0=294 K. U(P_1-P_2)/U_{CJ} = 1.003, U(P_2-P_3)/U_{CJ} = 0.997.

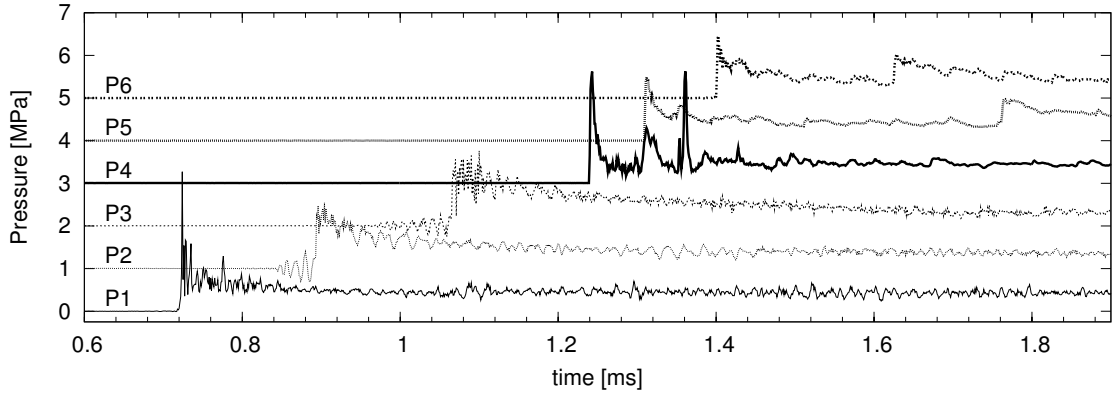

Figure K.215: Shot 216, 0.222 C_2H_6 + 0.778 O_2, P_0=42.5 kPa, T_0=295 K. U(P_1-P_2)/U_{CJ} = 1.003, U(P_2-P_3)/U_{CJ} = 0.997.

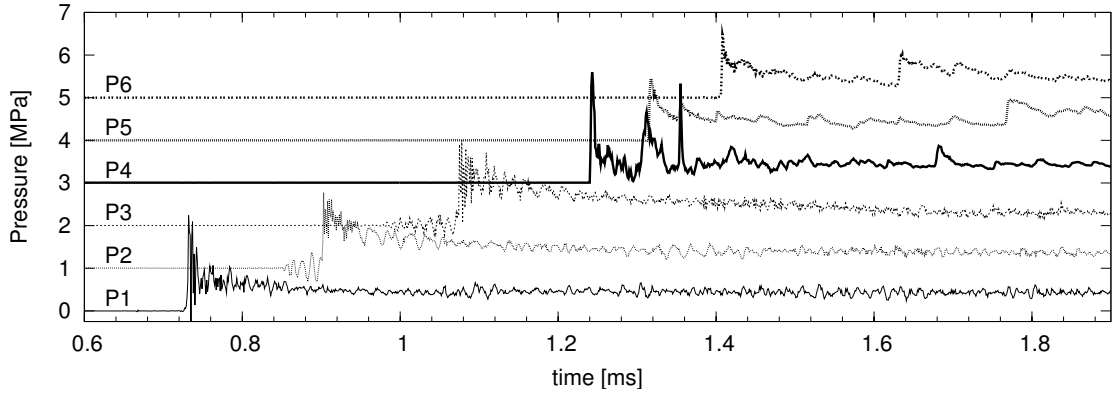

Figure K.216: Shot 217, 0.222 C_2H_6 + 0.778 O_2, P_0=42.5 kPa, T_0=295 K. U(P_1-P_2)/U_{CJ} = 1.003, U(P_2-P_3)/U_{CJ} = 0.991.

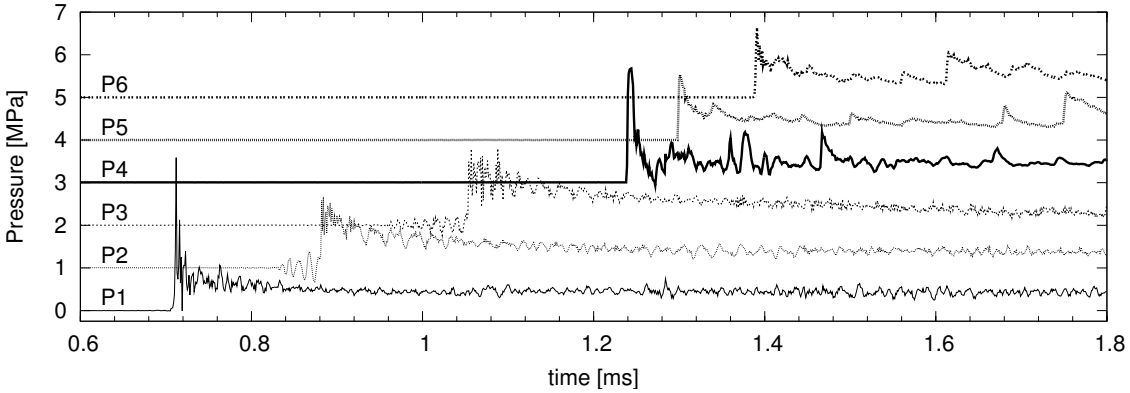

Figure K.217: Shot 218, 0.222 C_2H_6 + 0.778 O_2, P_0=42.5 kPa, T_0=296 K. U(P_1-P_2)/U_{CJ} = 1.003, U(P_2-P_3)/U_{CJ} = 0.997.

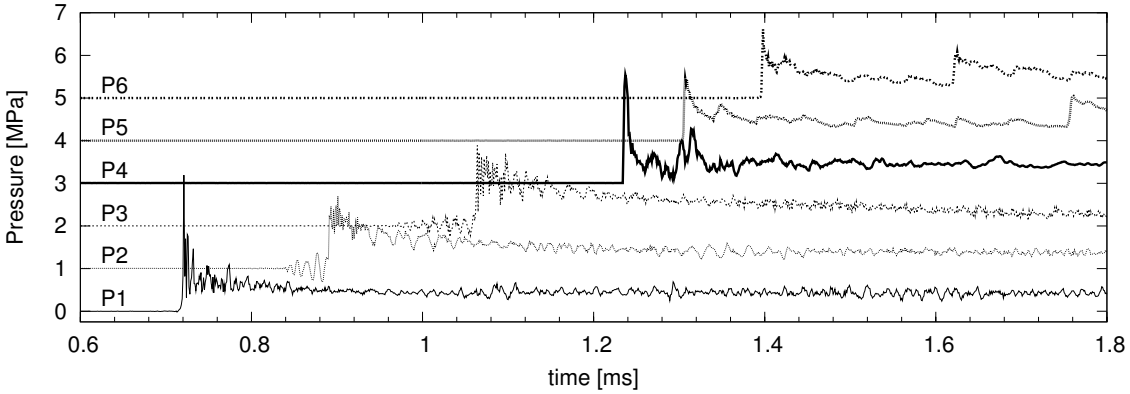

Figure K.218: Shot 219, 0.222 C_2H_6 + 0.778 O_2, P_0=42.5 kPa, T_0=296 K. U(P_1-P_2)/U_{CJ} = 1.003, U(P_2-P_3)/U_{CJ} = 0.997.

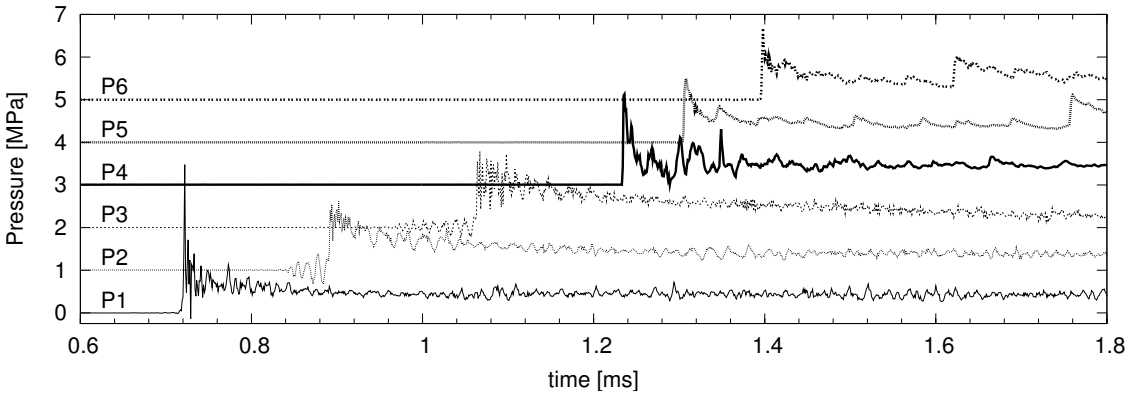

Figure K.219: Shot 220, 0.222 C_2H_6 + 0.778 O_2, P_0=42.5 kPa, T_0=297 K. U(P_1-P_2)/U_{CJ} = 1.003, U(P_2-P_3)/U_{CJ} = 0.997.

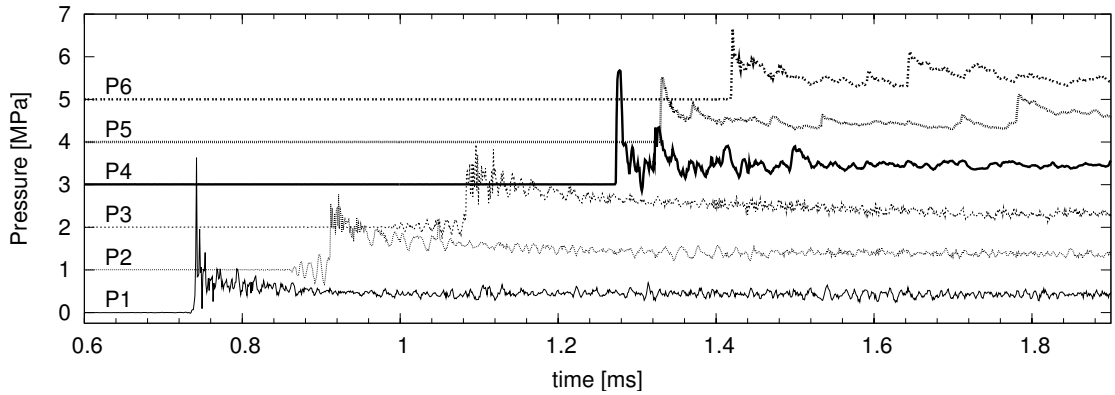

Figure K.220: Shot 221, 0.222 C_2H_6 + 0.778 O_2, P_0=42.5 kPa, T_0=297 K. U(P_1-P_2)/U_{CJ} = 1.003, U(P_2-P_3)/U_{CJ} = 0.997.

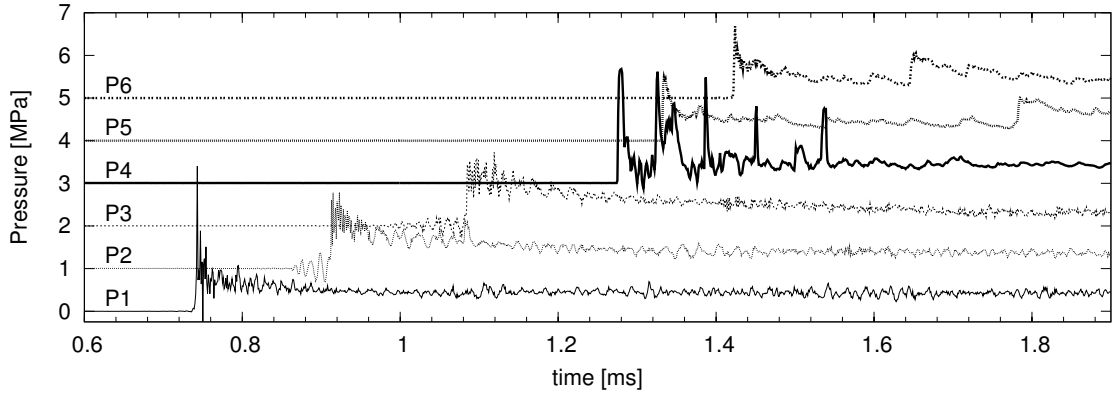

Figure K.221: Shot 222, 0.222 C_2H_6 + 0.778 O_2, P_0=42.5 kPa, T_0=297 K. U(P_1-P_2)/U_{CJ} = 1.003, U(P_2-P_3)/U_{CJ} = 0.997.

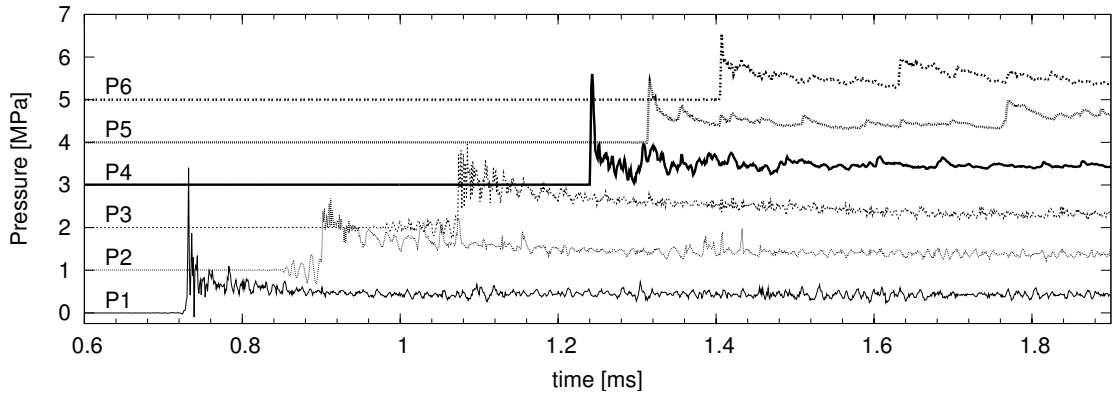

Figure K.222: Shot 223, 0.222 C_2H_6 + 0.778 O_2, P_0=42.5 kPa, T_0=298 K. U(P_1-P_2)/U_{CJ} = 1.008, U(P_2-P_3)/U_{CJ} = 0.991.

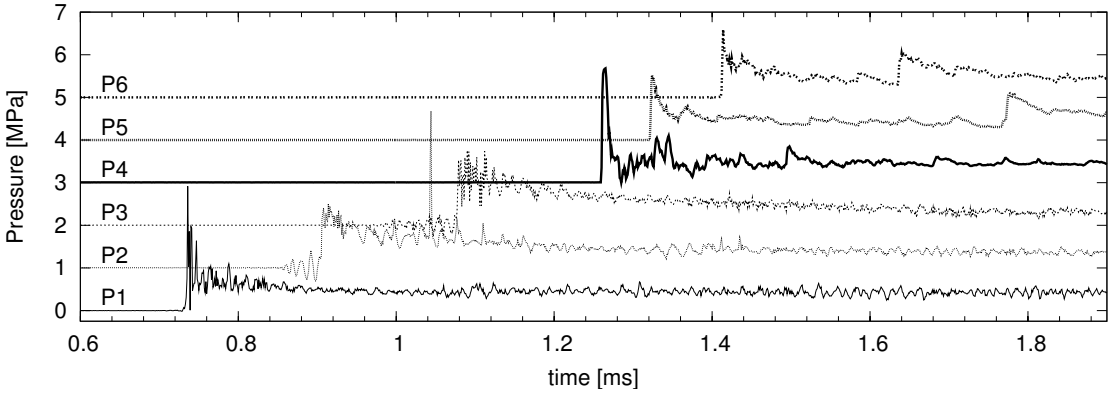

Figure K.223: Shot 224, 0.222 C_2H_6 + 0.778 O_2, P_0=42.5 kPa, T_0=298 K. U(P_1-P_2)/U_{CJ} = 1.003, U(P_2-P_3)/U_{CJ} = 0.997.

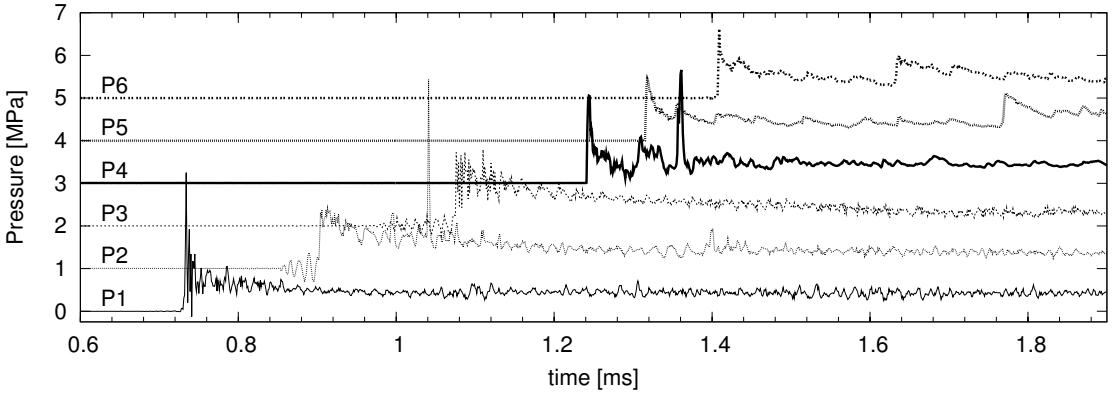

Figure K.224: Shot 225, 0.222 C_2H_6 + 0.778 O_2, P_0=42.5 kPa, T_0=297 K. U(P_1-P_2)/U_{CJ} = 1.008, U(P_2-P_3)/U_{CJ} = 0.991.

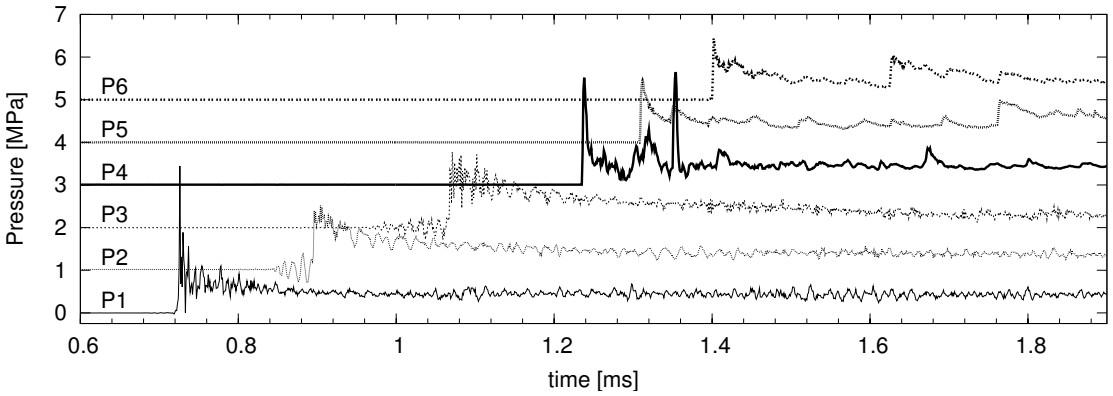

Figure K.225: Shot 226, 0.222 C_2H_6 + 0.778 O_2, P_0=42.5 kPa, T_0=297 K. U(P_1-P_2)/U_{CJ} = 1.003, U(P_2-P_3)/U_{CJ} = 0.997.

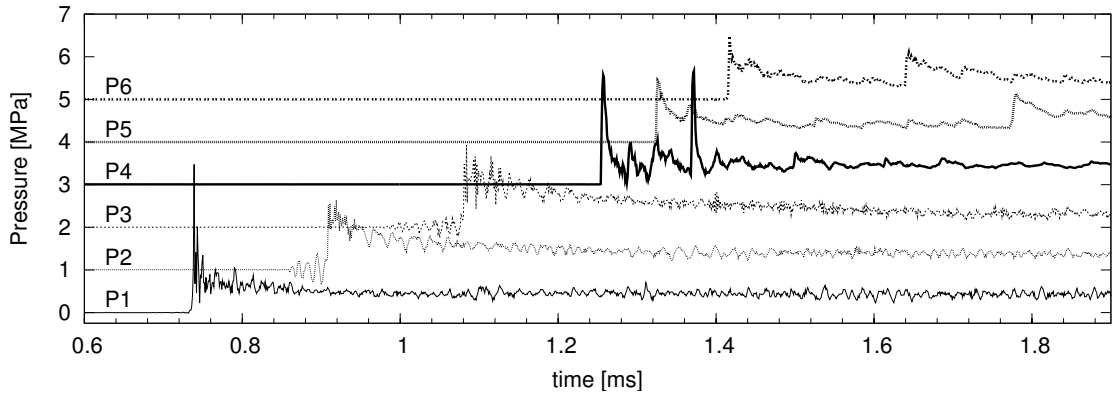

Figure K.226: Shot 227, 0.222 C_2H_6 + 0.778 O_2, P_0=42.5 kPa, T_0=298 K. U(P_1-P_2)/U_{CJ} = 1.003, U(P_2-P_3)/U_{CJ} = 0.997.

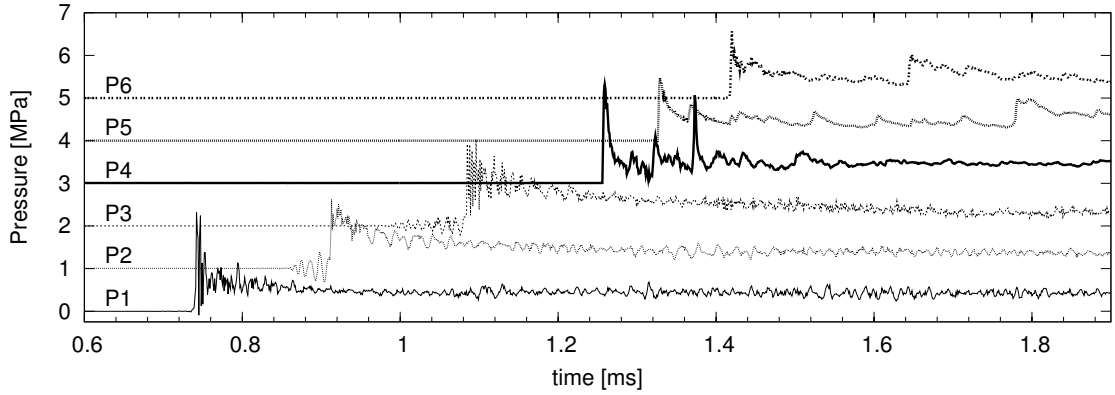

Figure K.227: Shot 228, 0.222 C_2H_6 + 0.778 O_2, P_0=42.5 kPa, T_0=298 K. U(P_1-P_2)/U_{CJ} = 1.003, U(P_2-P_3)/U_{CJ} = 0.991.

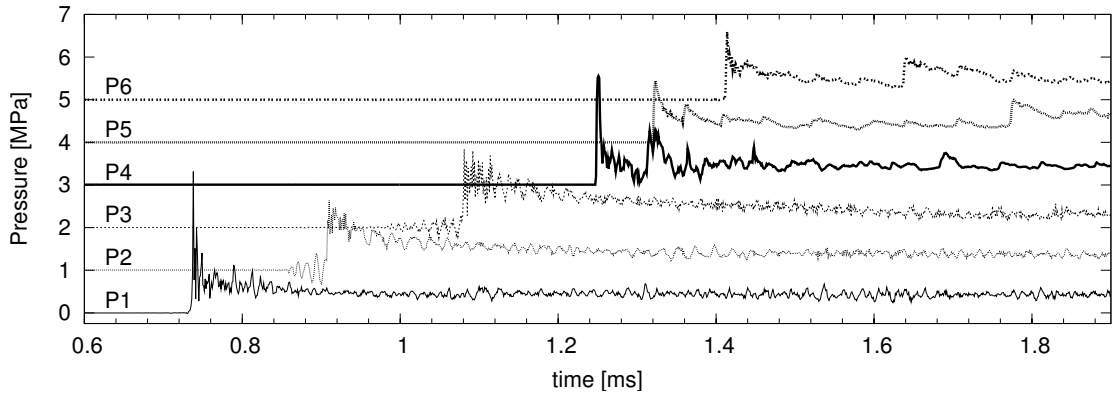

Figure K.228: Shot 229, 0.222 C_2H_6 + 0.778 O_2, P_0=42.5 kPa, T_0=298 K. U(P_1-P_2)/U_{CJ} = 0.000, U(P_2-P_3)/U_{CJ} = 0.000.

Appendix L

Multiple Exposure Image Analysis from Detonation Diffraction Experiments

The x -t diagrams and velocity profiles of the fluorescence front on the centerline are shown. They are obtained from the multiple exposure images as described in Chapter 5. The x-t diagram is shown for each shot on the left and the corresponding velocity profile on the right.

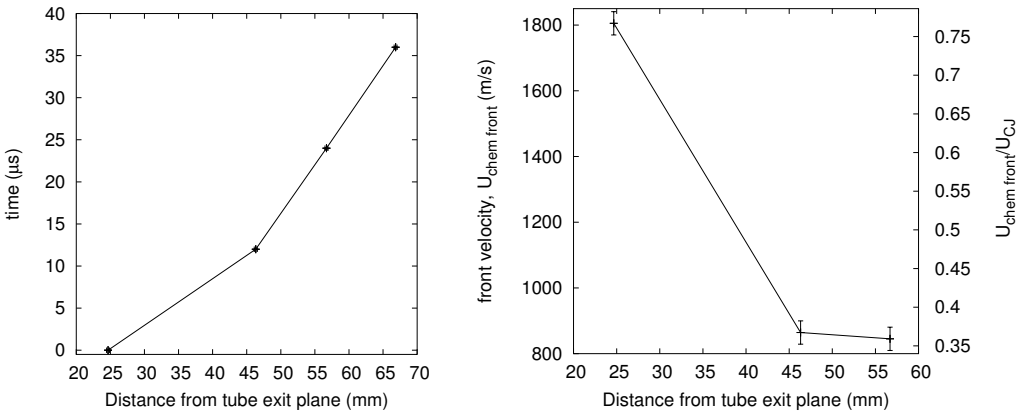

Figure L.1: Velocity profile. Shot 93, 0.5 H_2 + 0.5 N_2O, P_0=40 kPa, T_0=294 K.

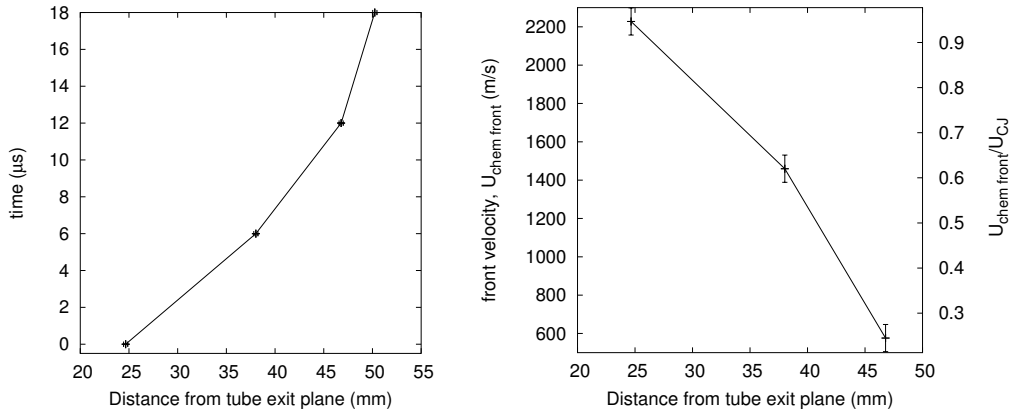

Figure L.2: Velocity profile. Shot 94, 0.5 H_2 + 0.5 N_2O, P_0=40 kPa, T_0=295 K.

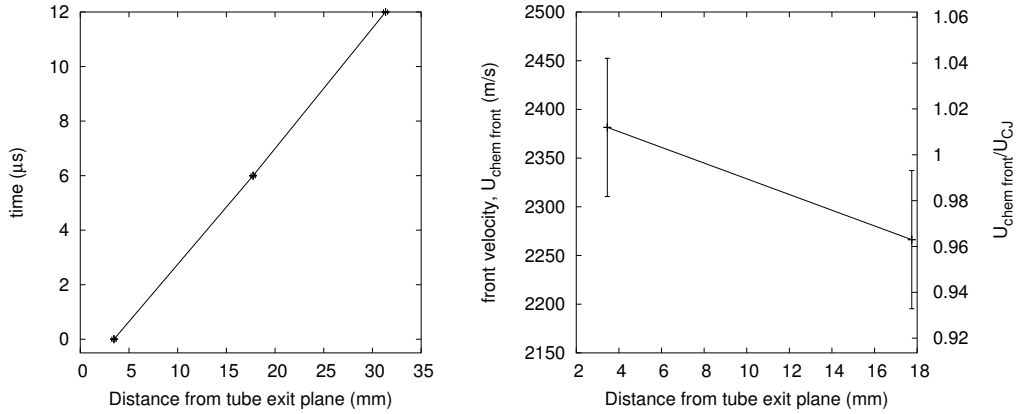

Figure L.3: Velocity profile. Shot 96, 0.5 H_2 + 0.5 N_2O, P_0=40 kPa, T_0=295 K.

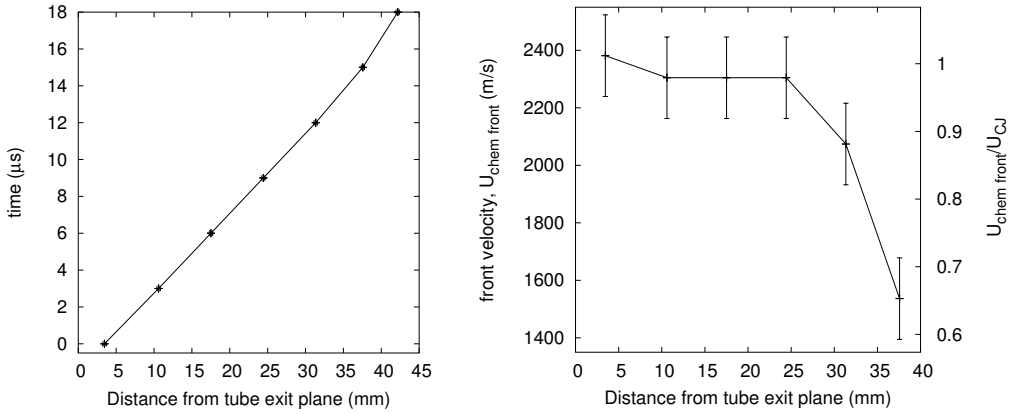

Figure L.4: Velocity profile. Shot 97, 0.5 H_2 + 0.5 N_2O, P_0=40 kPa, T_0=295 K.

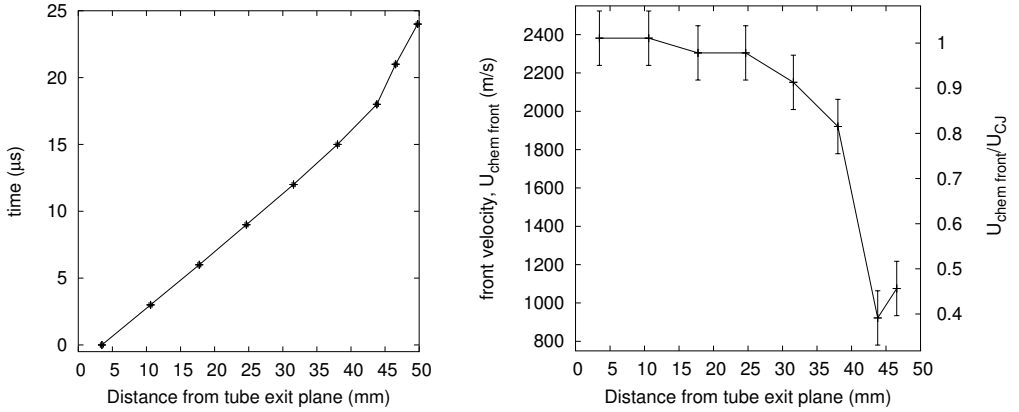

Figure L.5: Velocity profile. Shot 98, 0.5 H_2 + 0.5 N_2O, P_0=42.5 kPa, T_0=295 K.

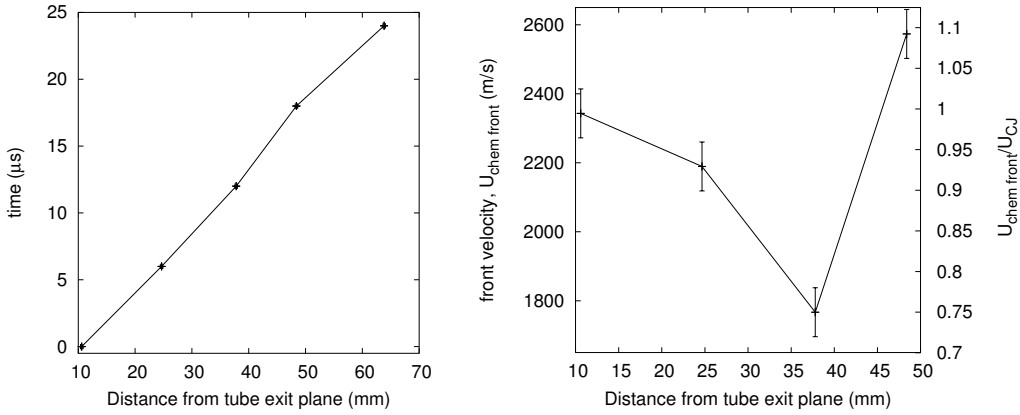

Figure L.6: Velocity profile. Shot 99, 0.5 H_2 + 0.5 N_2O, P_0=42.5 kPa, T_0=295 K.

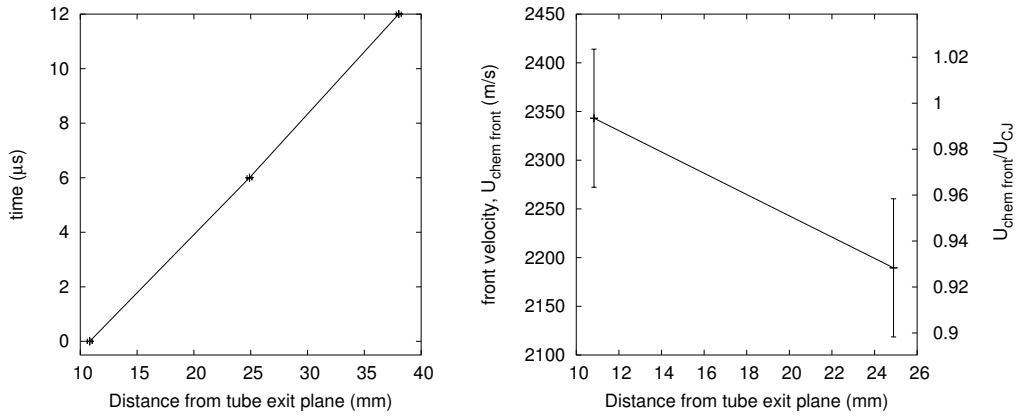

Figure L.7: Velocity profile. Shot 101, 0.5 H_2 + 0.5 N_2O, P_0=45 kPa, T_0=295 K.

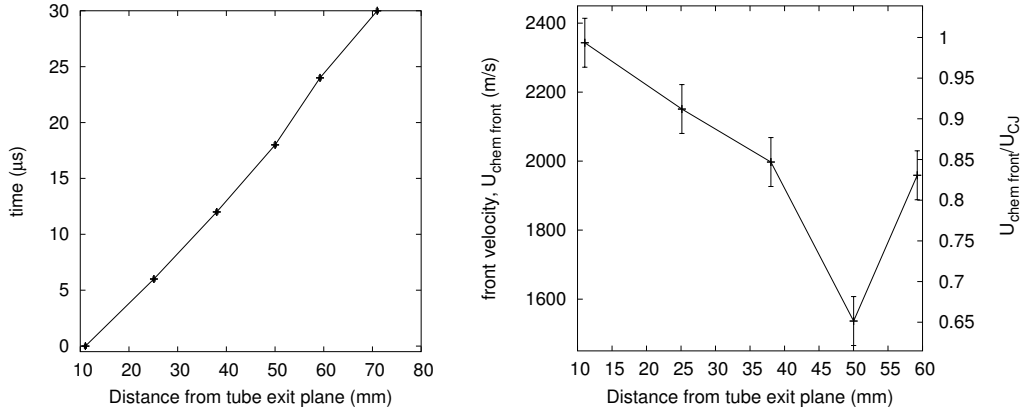

Figure L.8: Velocity profile. Shot 102, 0.5 H_2 + 0.5 N_2O, P_0=45 kPa, T_0=296 K.

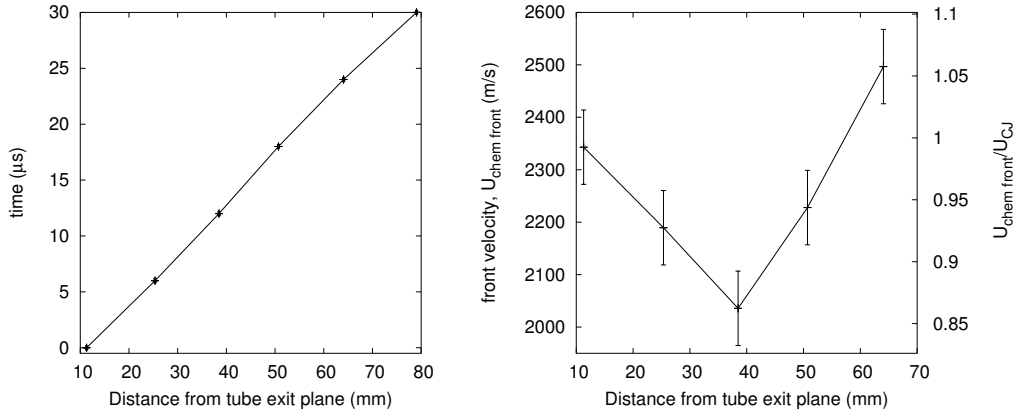

Figure L.9: Velocity profile. Shot 103, 0.5 H_2 + 0.5 N_2O, P_0=47.5 kPa, T_0=296 K.

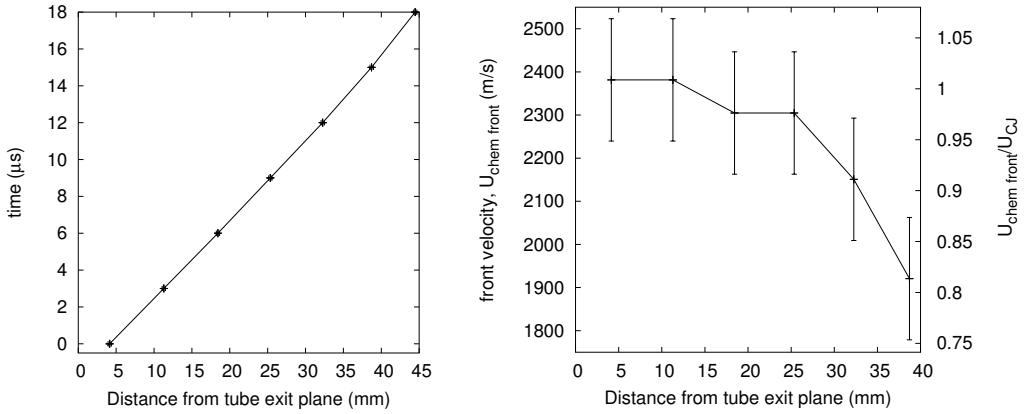

Figure L.10: Velocity profile. Shot 104, 0.5 H_2 + 0.5 N_2O, P_0=47.5 kPa, T_0=296 K.

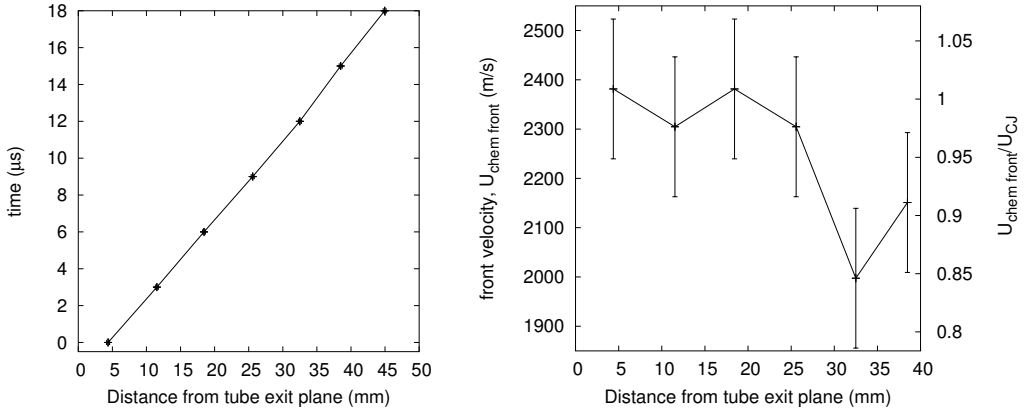

Figure L.11: Velocity profile. Shot 105, 0.5 H_2 + 0.5 N_2O, P_0=47.5 kPa, T_0=296 K.

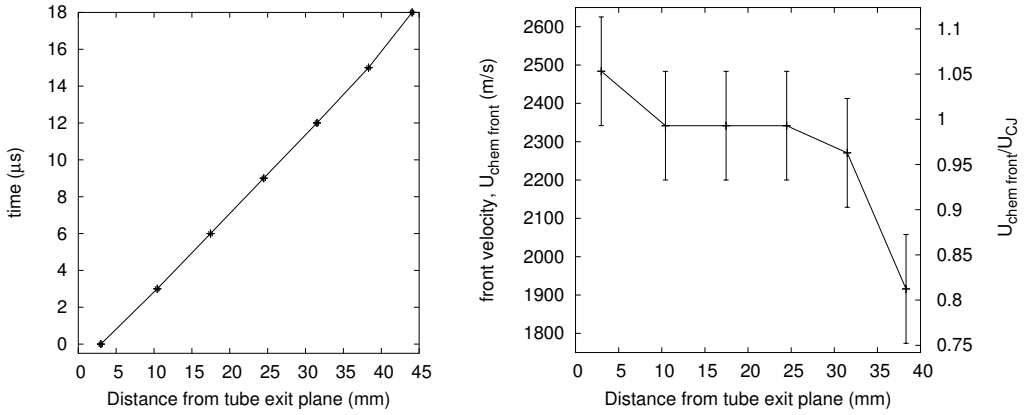

Figure L.12: Velocity profile. Shot 106, 0.5 H_2 + 0.5 N_2O, P_0=45 kPa, T_0=294 K.

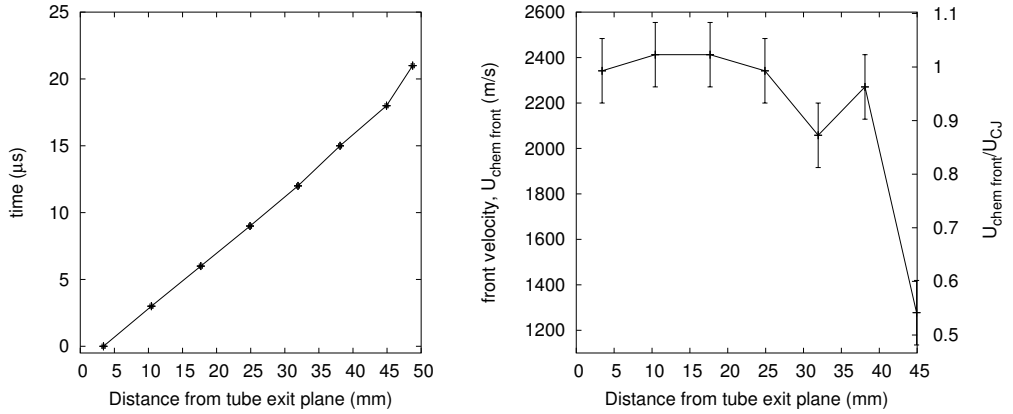

Figure L.13: Velocity profile. Shot 107, 0.5 H_2 + 0.5 N_2O, P_0=45 kPa, T_0=294 K.

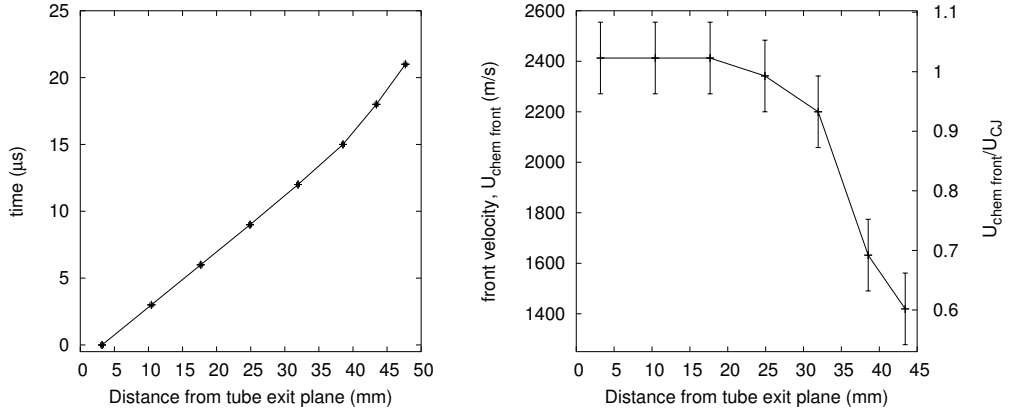

Figure L.14: Velocity profile. Shot 109, 0.5 H_2 + 0.5 N_2O, P_0=45 kPa, T_0=295 K.

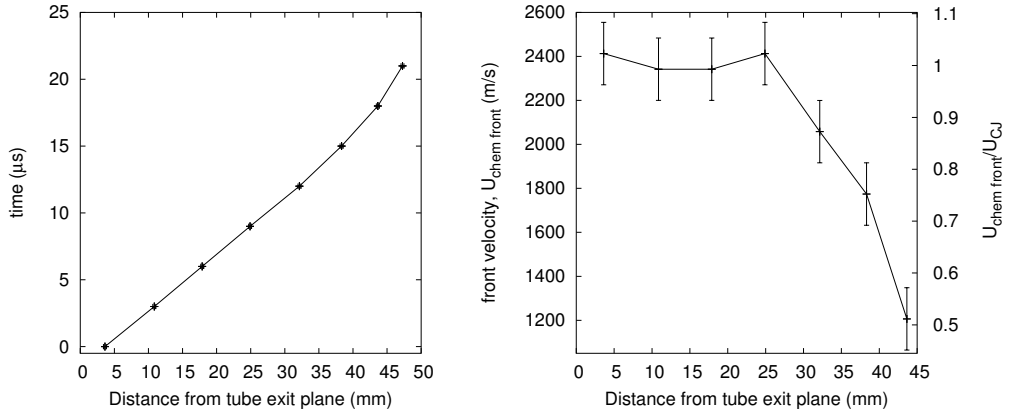

Figure L.15: Velocity profile. Shot 110, 0.5 H_2 + 0.5 N_2O, P_0=45 kPa, T_0=295 K.

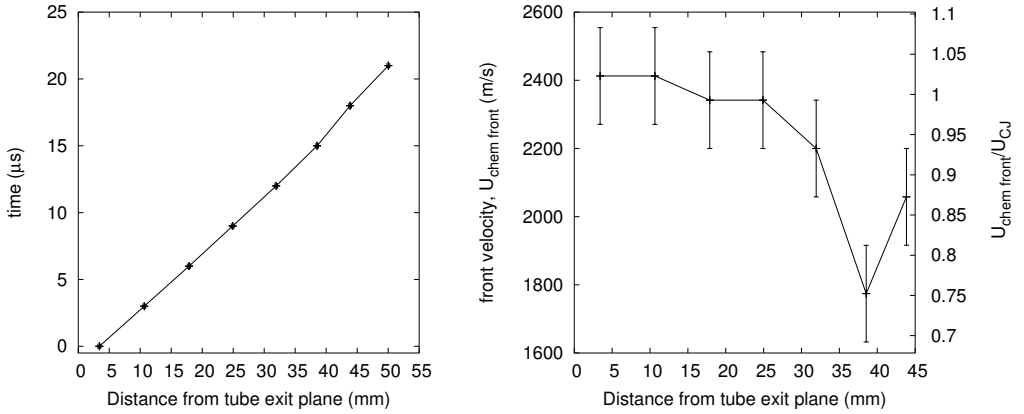

Figure L.16: Velocity profile. Shot 111, 0.5 H_2 + 0.5 N_2O, P_0=45 kPa, T_0=295 K.

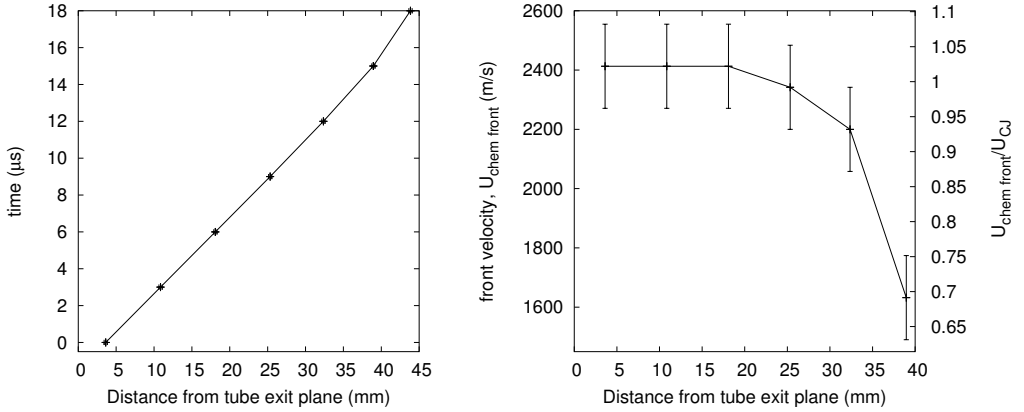

Figure L.17: Velocity profile. Shot 112, 0.5 H_2 + 0.5 N_2O, P_0=47.5 kPa, T_0=296 K.

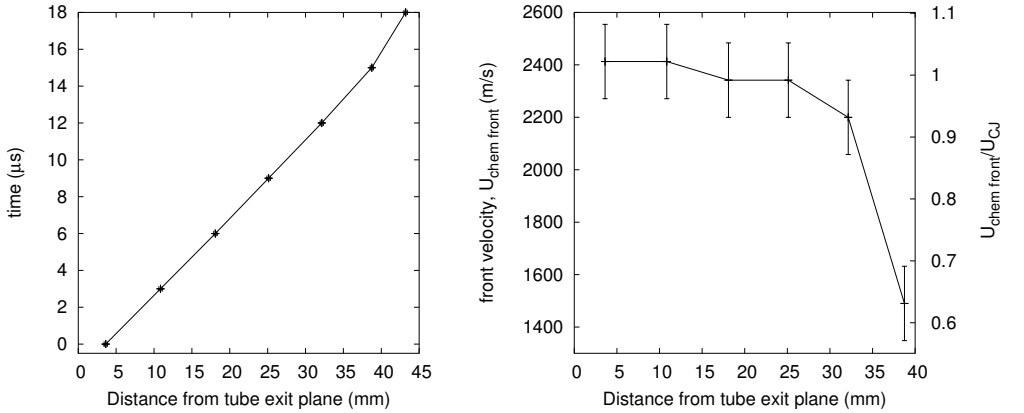

Figure L.18: Velocity profile. Shot 113, 0.5 H_2 + 0.5 N_2O, P_0=47.5 kPa, T_0=296 K.

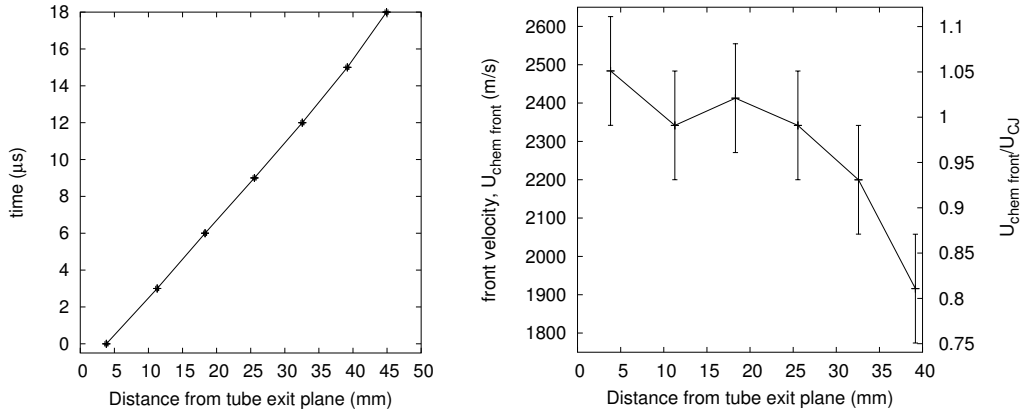

Figure L.19: Velocity profile. Shot 114, 0.5 H_2 + 0.5 N_2O, P_0=50 kPa, T_0=296 K.

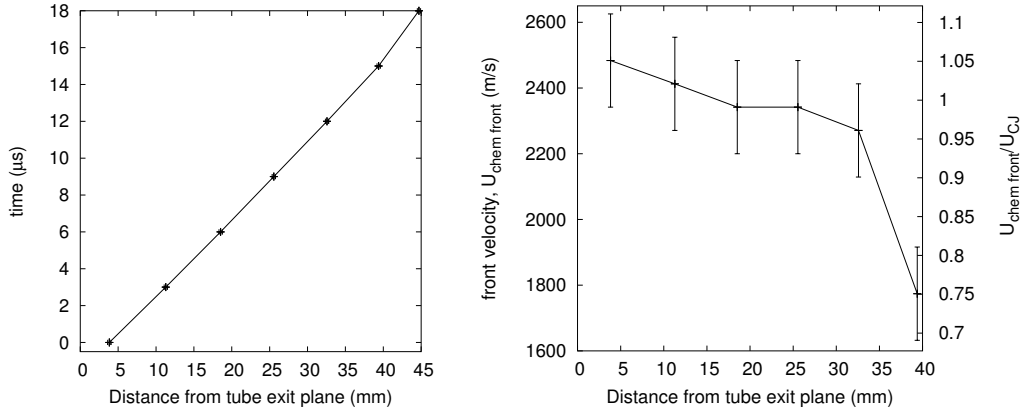

Figure L.20: Velocity profile. Shot 115, 0.5 H_2 + 0.5 N_2O, P_0=50 kPa, T_0=296 K.

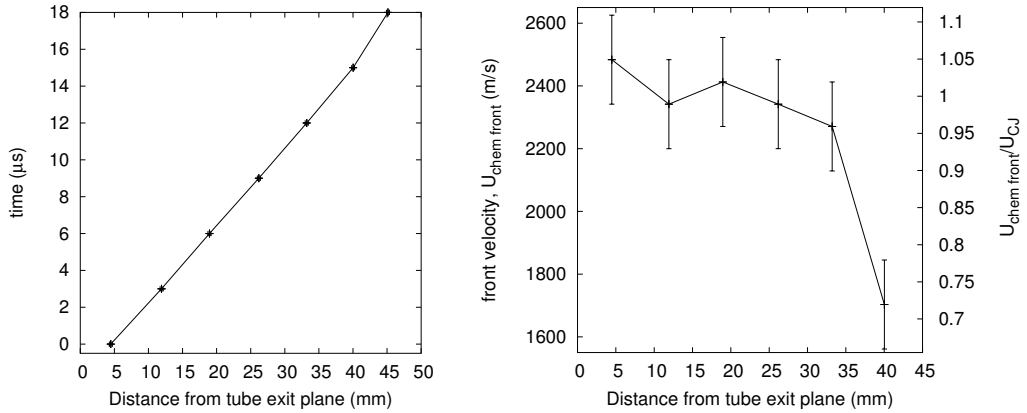

Figure L.21: Velocity profile. Shot 116, 0.5 H_2 + 0.5 N_2O, P_0=55 kPa, T_0=296 K.

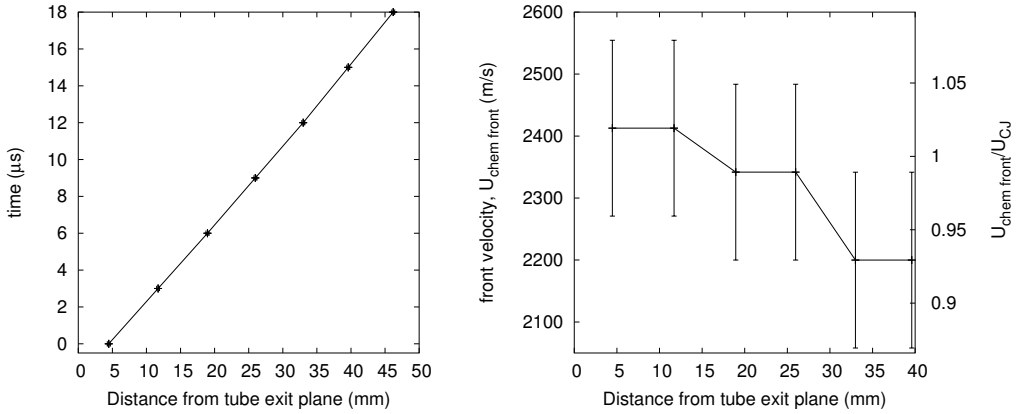

Figure L.22: Velocity profile. Shot 117, 0.5 H_2 + 0.5 N_2O, P_0=55 kPa, T_0=296 K.

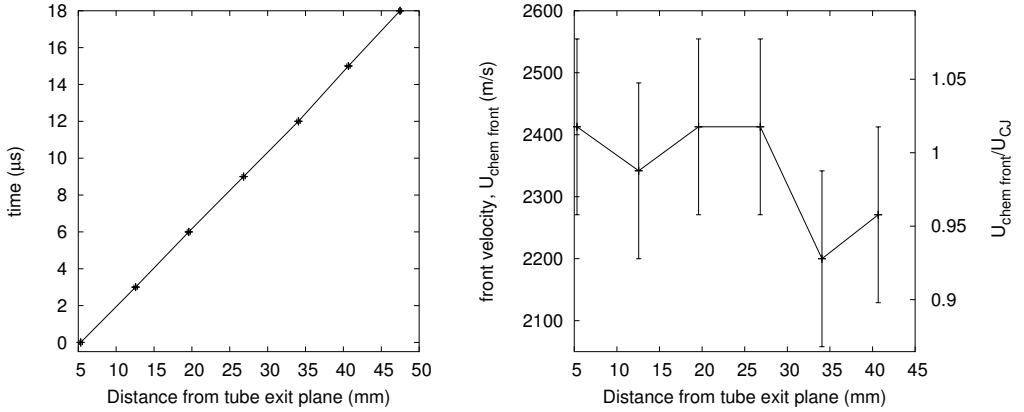

Figure L.23: Velocity profile. Shot 118, 0.5 H_2 + 0.5 N_2O, P_0=60 kPa, T_0=296 K.

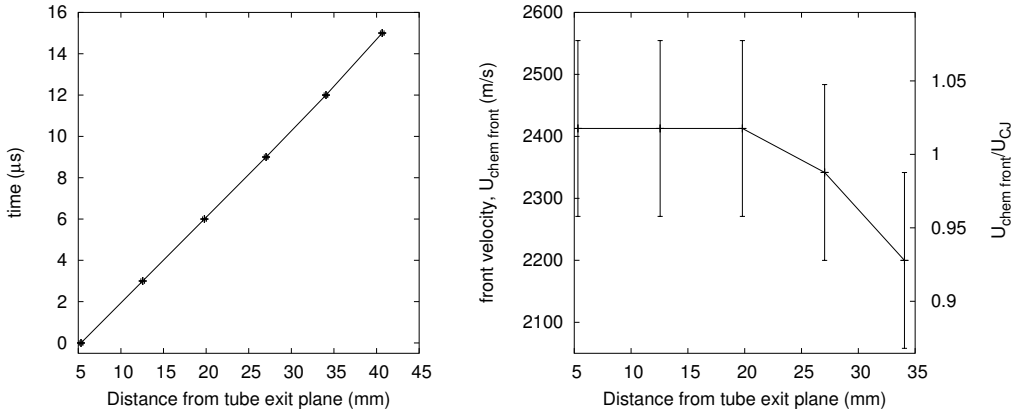

Figure L.24: Velocity profile. Shot 119, 0.5 H_2 + 0.5 N_2O, P_0=60 kPa, T_0=296 K.

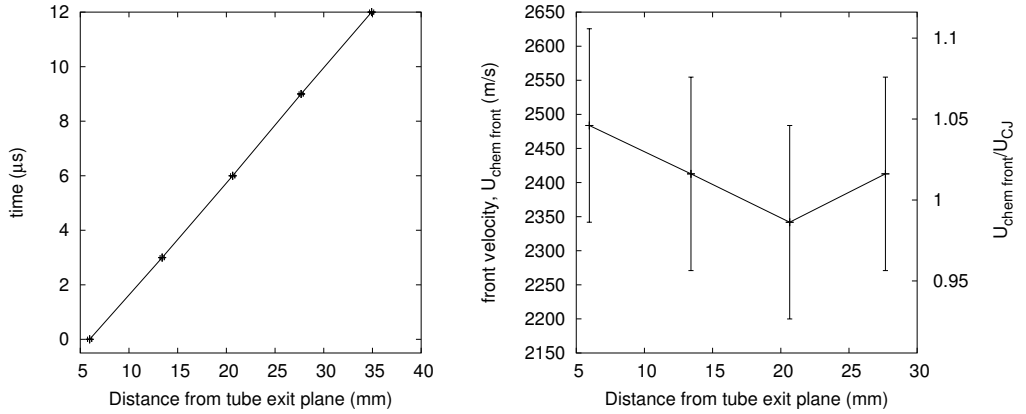

Figure L.25: Velocity profile. Shot 121, 0.5 H_2 + 0.5 N_2O, P_0=65 kPa, T_0=297 K.

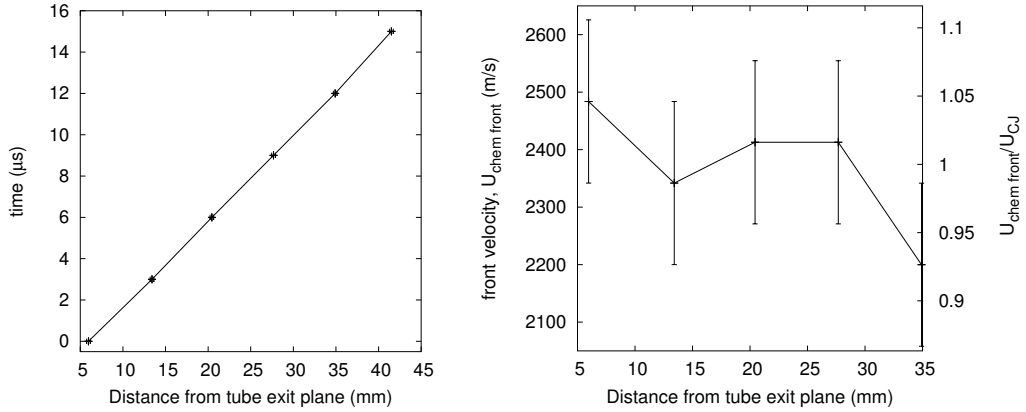

Figure L.26: Velocity profile. Shot 122, 0.5 H_2 + 0.5 N_2O, P_0=65 kPa, T_0=297 K.

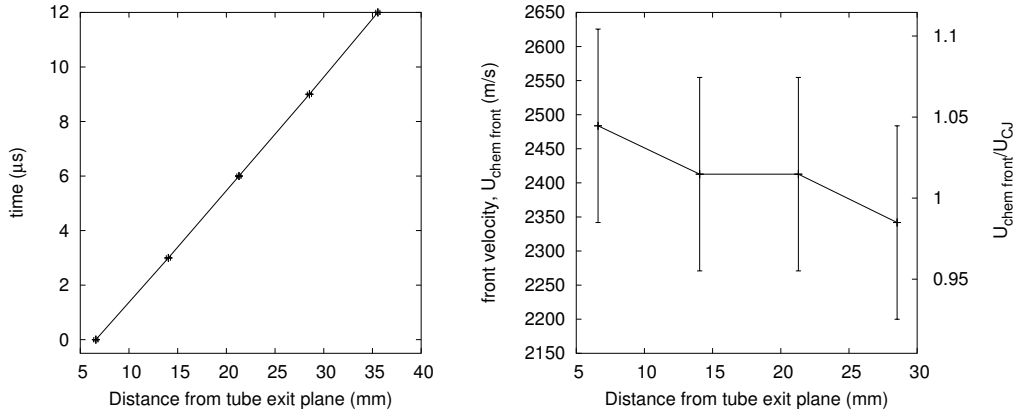

Figure L.27: Velocity profile. Shot 123, 0.5 H_2 + 0.5 N_2O, P_0=70 kPa, T_0=297 K.

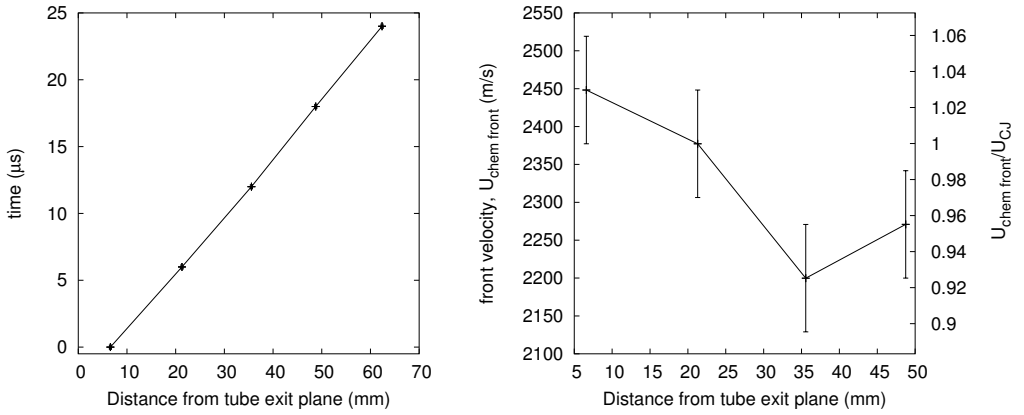

Figure L.28: Velocity profile. Shot 124, 0.5 H_2 + 0.5 N_2O, P_0=70 kPa, T_0=297 K.

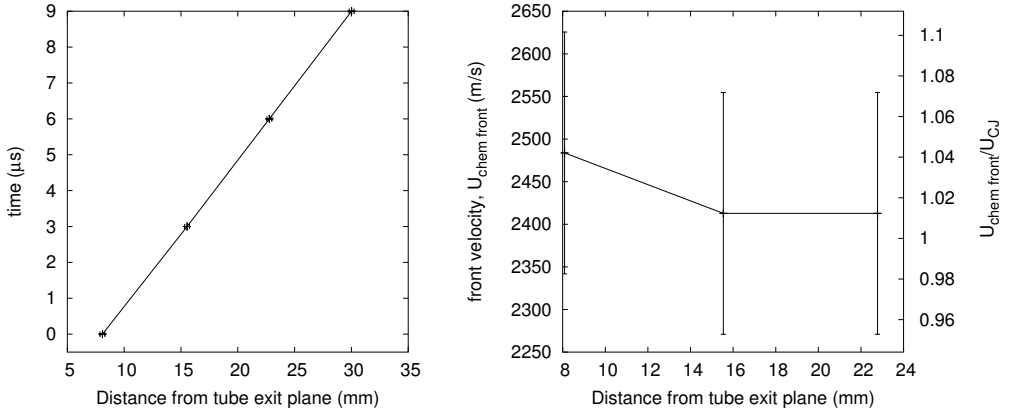

Figure L.29: Velocity profile. Shot 125, 0.5 H_2 + 0.5 N_2O, P_0=80 kPa, T_0=297 K.

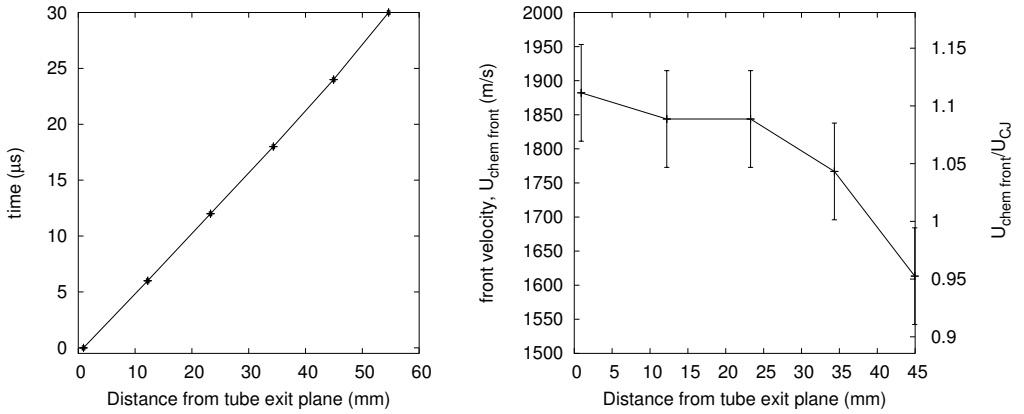

Figure L.30: Velocity profile. Shot 128, 0.2 H_2 + 0.1 O_2 + 0.7 Ar, P_0=100 kPa, T_0=295 K.

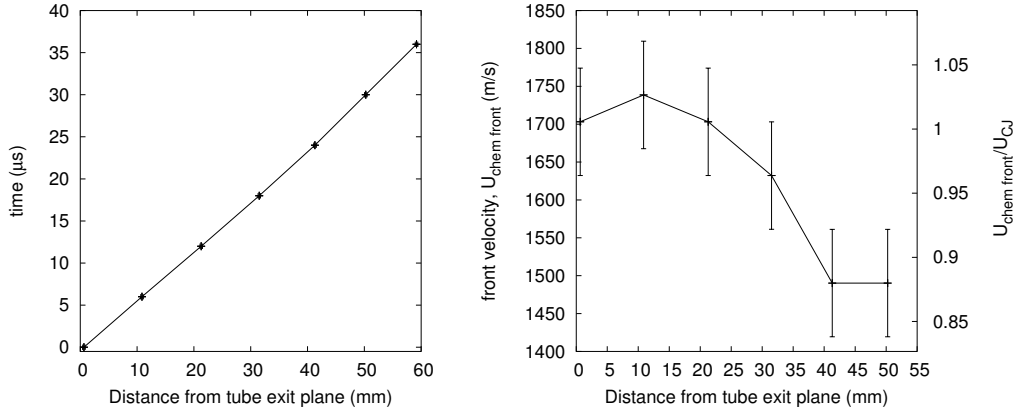

Figure L.31: Velocity profile. Shot 129, 0.2 H_2 + 0.1 O_2 + 0.7 Ar, P_0=100 kPa, T_0=295 K.

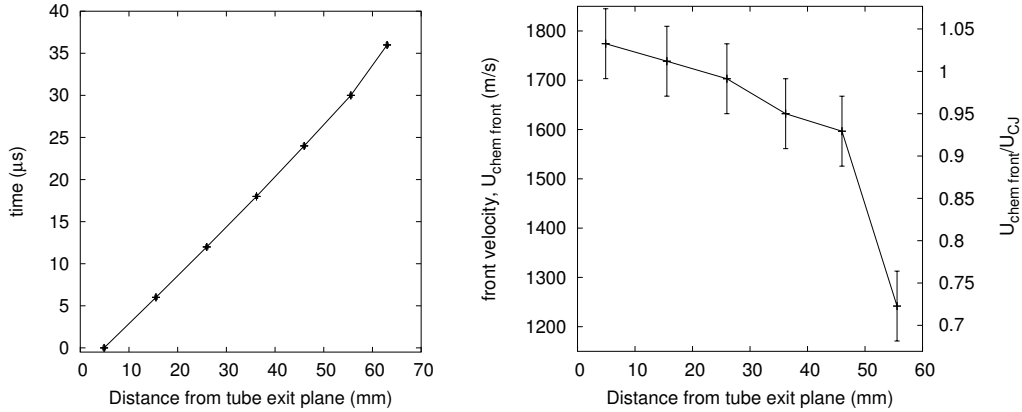

Figure L.32: Velocity profile. Shot 130, 0.213 H_2 + 0.107 O_2 + 0.68 Ar, P_0=100 kPa, T_0=295 K.

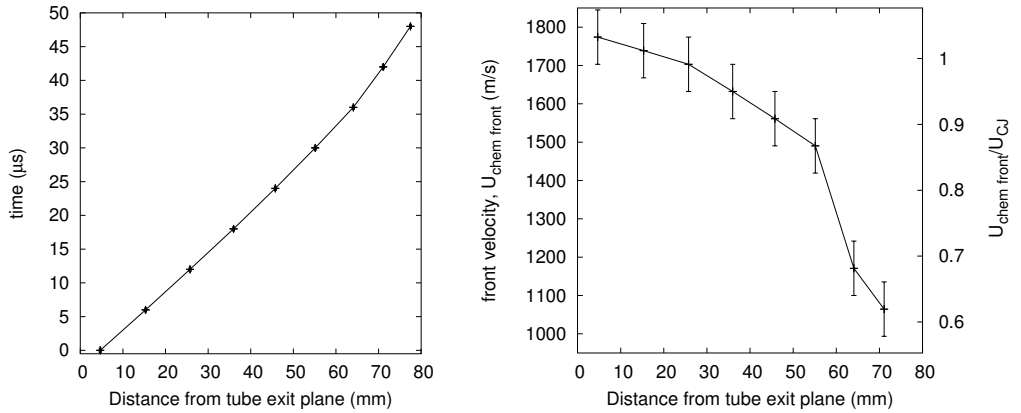

Figure L.33: Velocity profile. Shot 131, 0.213 H_2 + 0.107 O_2 + 0.68 Ar, P_0=100 kPa, T_0=296 K.

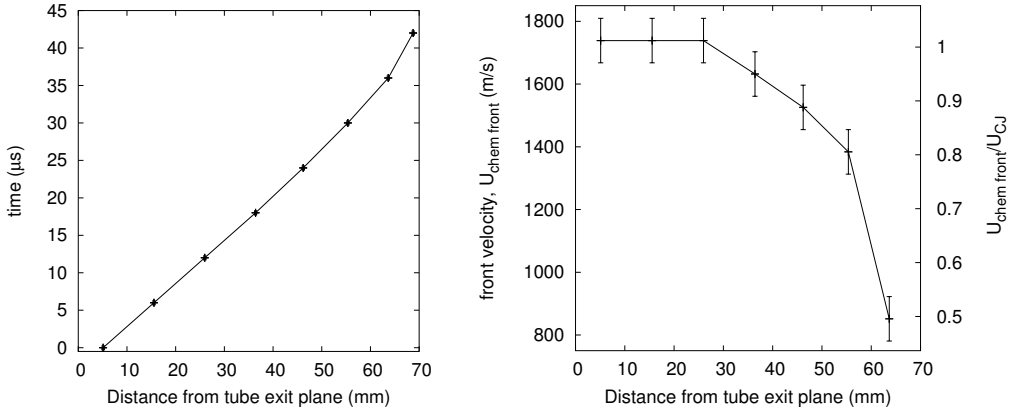

Figure L.34: Velocity profile. Shot 132, 0.213 H_2 + 0.107 O_2 + 0.68 Ar, P_0=100 kPa, T_0=296 K.

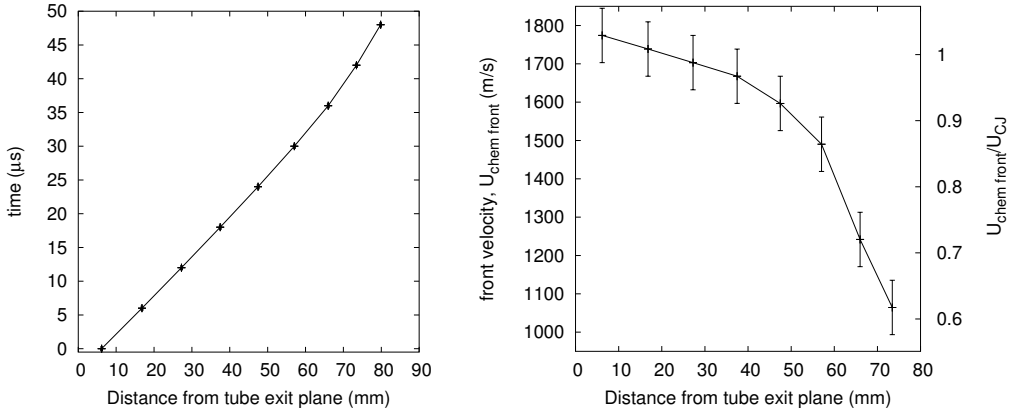

Figure L.35: Velocity profile. Shot 133, 0.217 H_2 + 0.108 O_2 + 0.675 Ar, P_0=100 kPa, T_0=296 K.

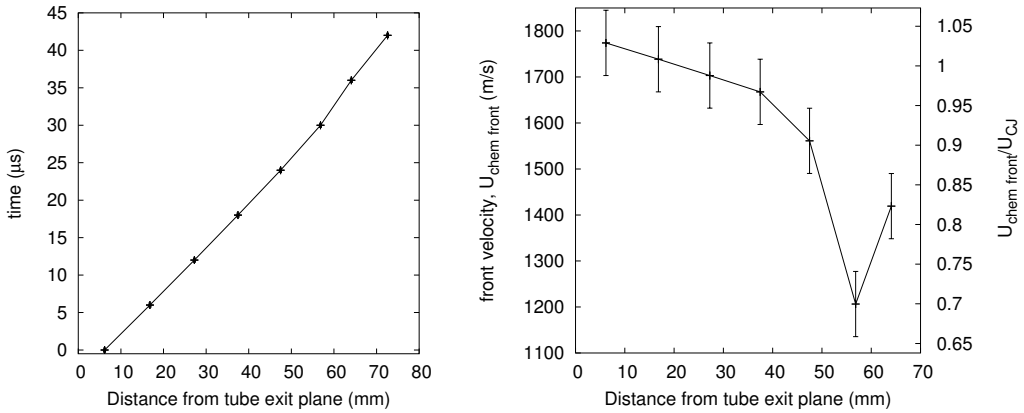

Figure L.36: Velocity profile. Shot 134, 0.217 H_2 + 0.108 O_2 + 0.675 Ar, P_0=100 kPa, T_0=296 K.

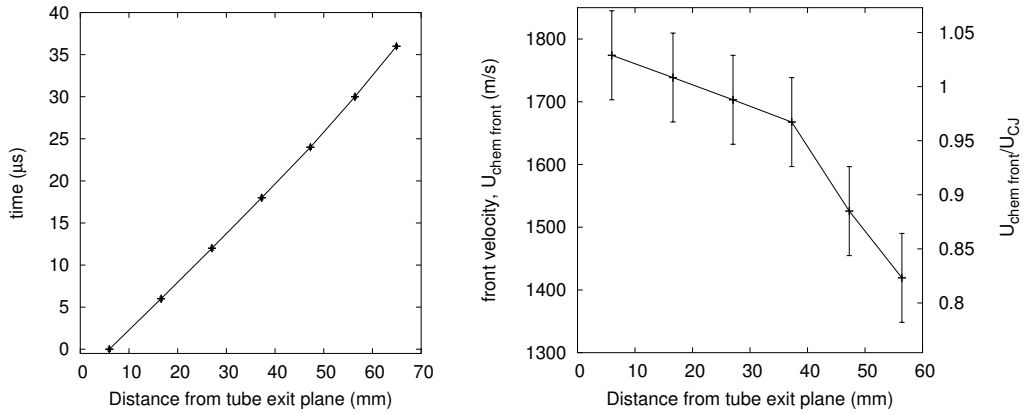

Figure L.37: Velocity profile. Shot 135, 0.217 H_2 + 0.108 O_2 + 0.675 Ar, P_0=100 kPa, T_0=294 K.

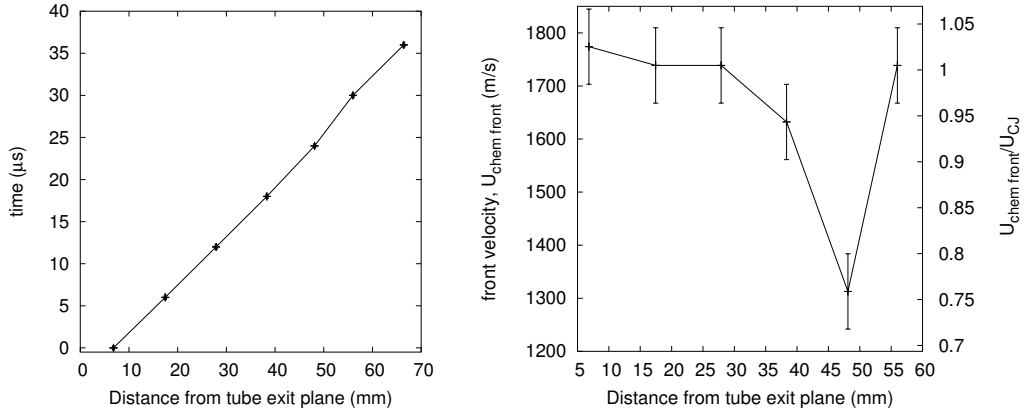

Figure L.38: Velocity profile. Shot 136, 0.22 H_2 + 0.11 O_2 + 0.67 Ar, P_0=100 kPa, T_0=295 K.

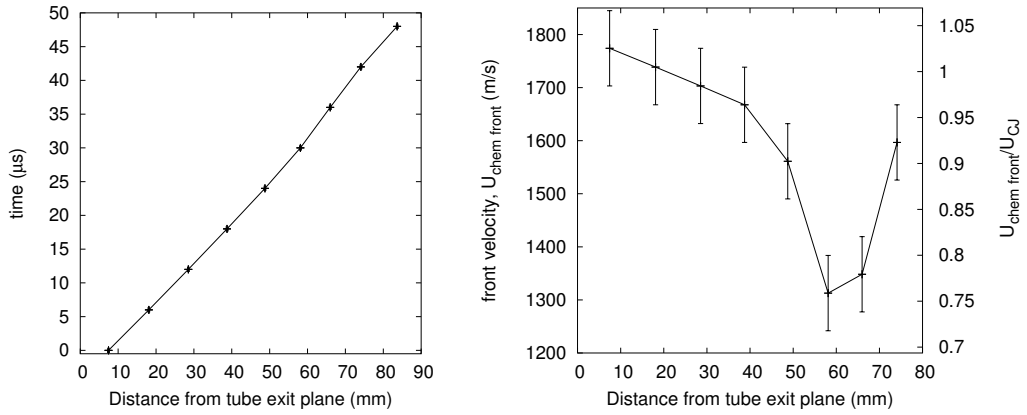

Figure L.39: Velocity profile. Shot 137, 0.22 H_2 + 0.11 O_2 + 0.67 Ar, P_0=100 kPa, T_0=295 K.

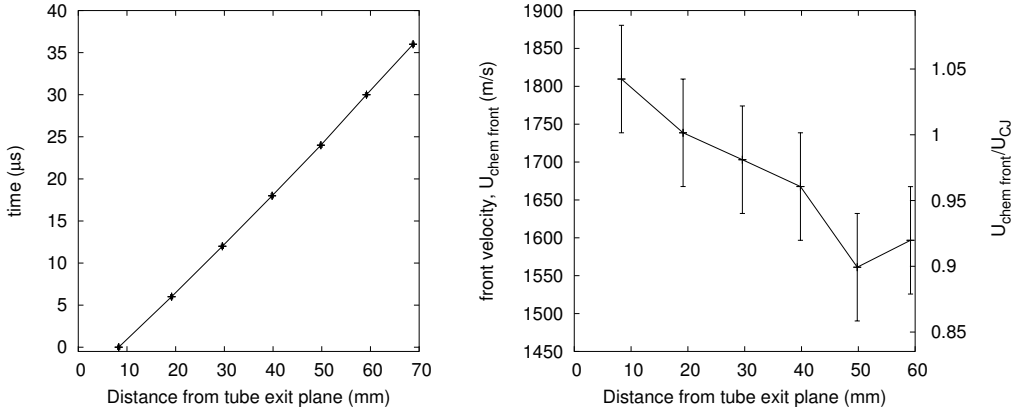

Figure L.40: Velocity profile. Shot 138, 0.223 H_2 + 0.112 O_2 + 0.665 Ar, P_0=100 kPa, T_0=296 K.

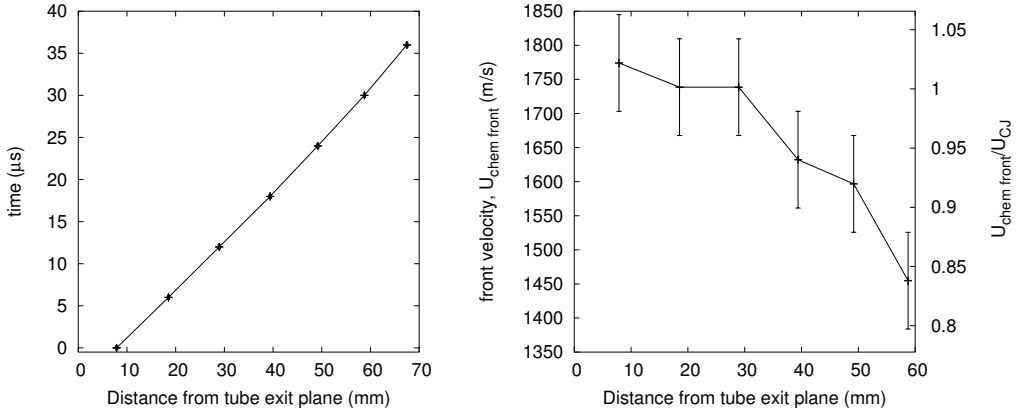

Figure L.41: Velocity profile. Shot 139, 0.223 H_2 + 0.112 O_2 + 0.665 Ar, P_0=100 kPa, T_0=296 K.

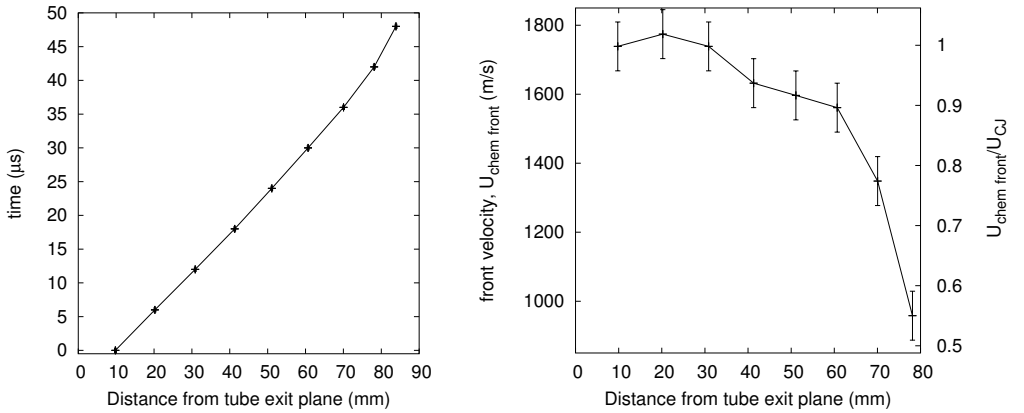

Figure L.42: Velocity profile. Shot 140, 0.227 H_2 + 0.113 O_2 + 0.66 Ar, P_0=100 kPa, T_0=296 K.

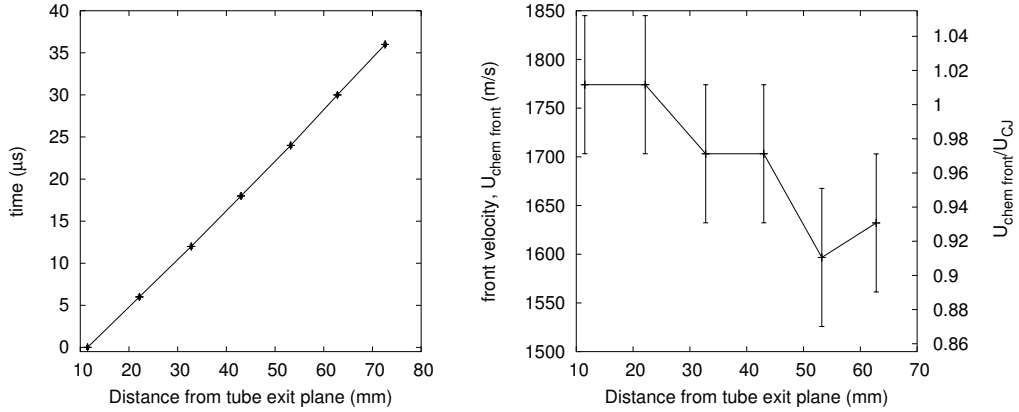

Figure L.43: Velocity profile. Shot 141, 0.233 H_2 + 0.117 O_2 + 0.65 Ar, P_0=100 kPa, T_0=296 K.

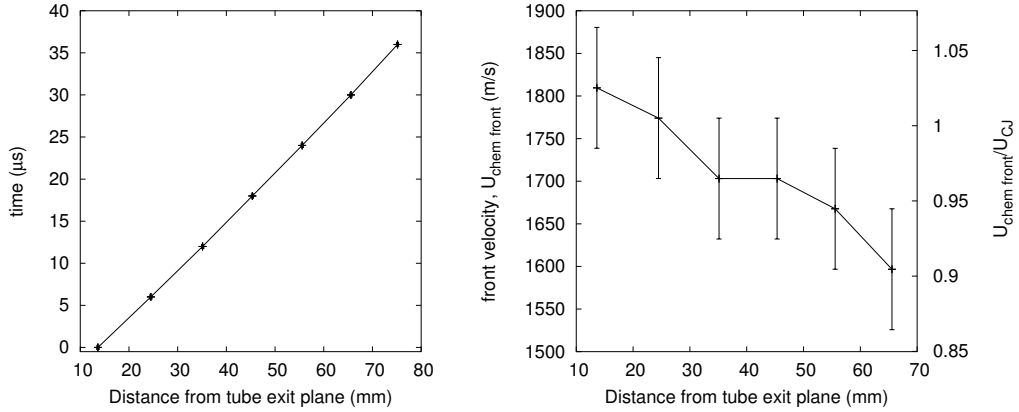

Figure L.44: Velocity profile. Shot 142, 0.24 H_2 + 0.12 O_2 + 0.64 Ar, P_0=100 kPa, T_0=296 K.

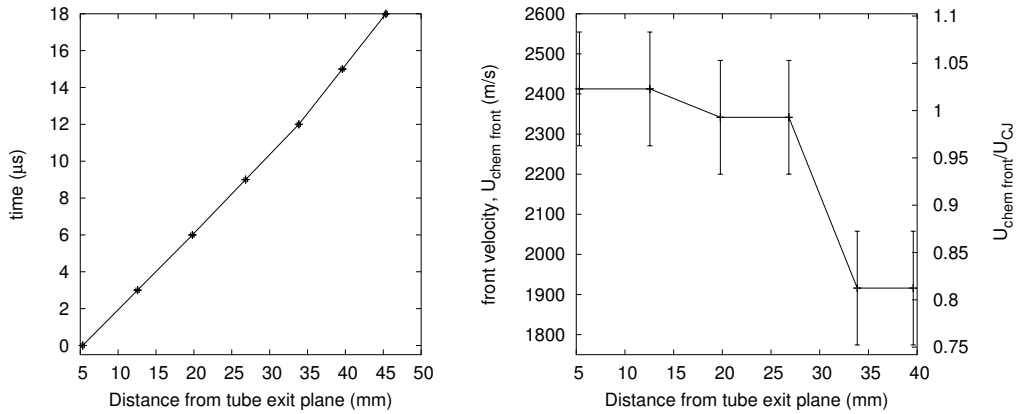

Figure L.45: Velocity profile. Shot 143, 0.5 H_2 + 0.5 N_2O, P_0=45 kPa, T_0=296 K.

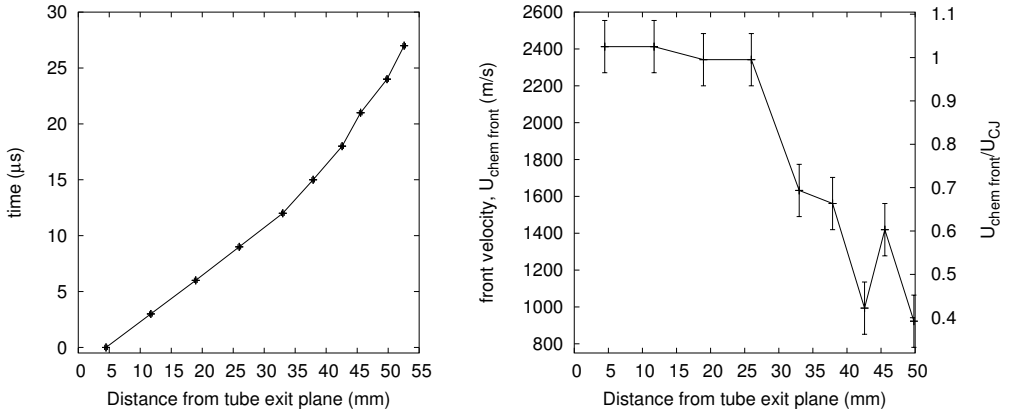

Figure L.46: Velocity profile. Shot 144, 0.5 H_2 + 0.5 N_2O, P_0=40 kPa, T_0=296 K.

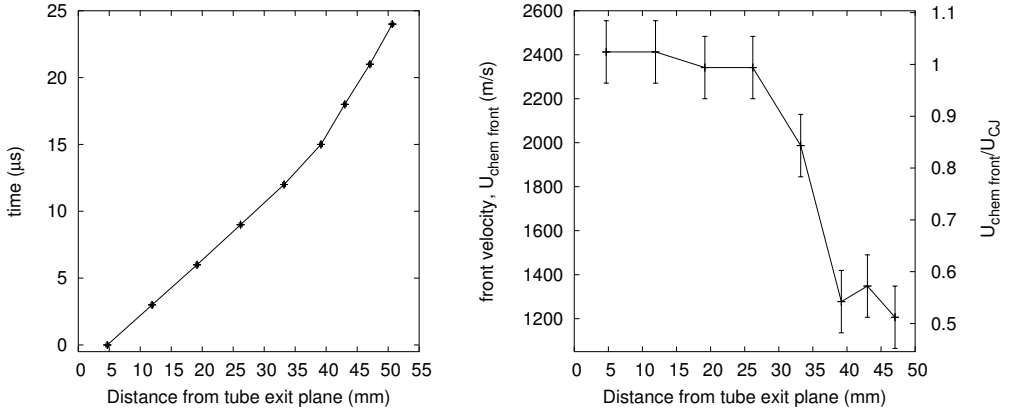

Figure L.47: Velocity profile. Shot 145, 0.5 H_2 + 0.5 N_2O, P_0=42.5 kPa, T_0=296 K.

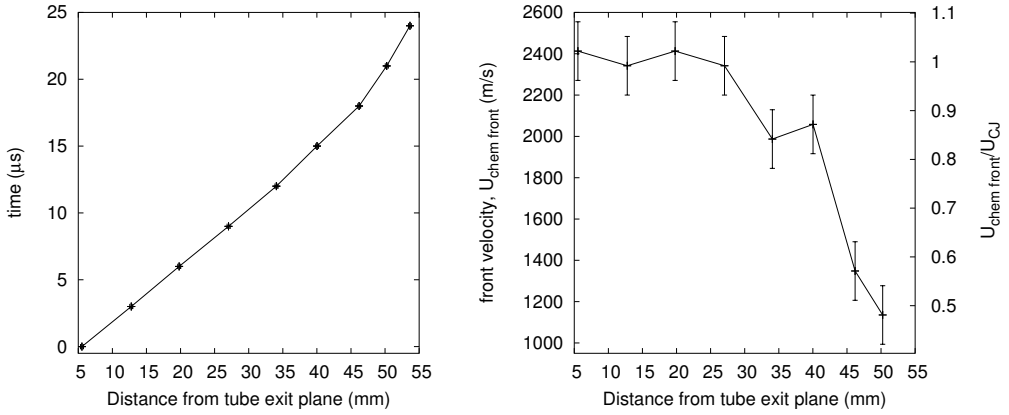

Figure L.48: Velocity profile. Shot 146, 0.5 H_2 + 0.5 N_2O, P_0=47.5 kPa, T_0=297 K.

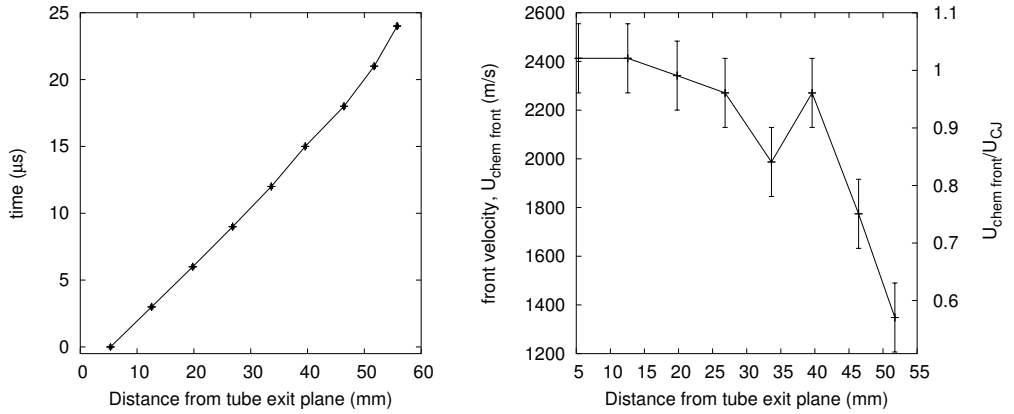

Figure L.49: Velocity profile. Shot 147, 0.5 H_2 + 0.5 N_2O, P_0=50 kPa, T_0=297 K.

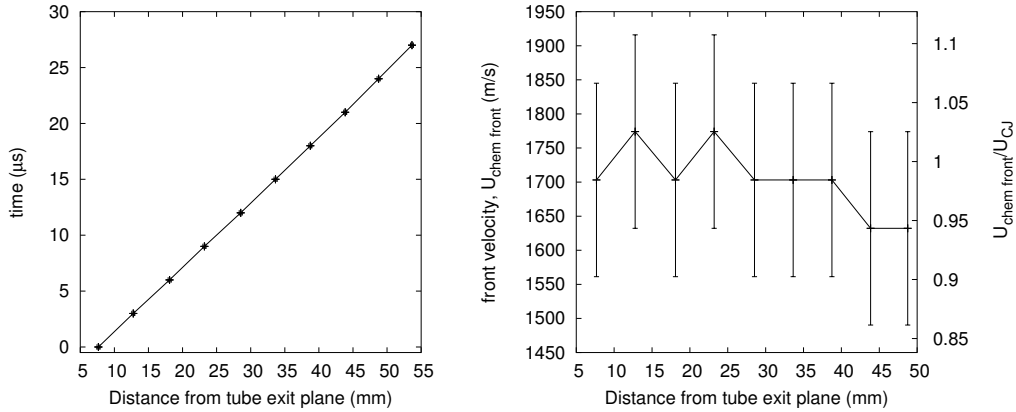

Figure L.50: Velocity profile. Shot 148, 0.22 H_2 + 0.11 O_2 + 0.67 Ar, P_0=100 kPa, T_0=295 K.

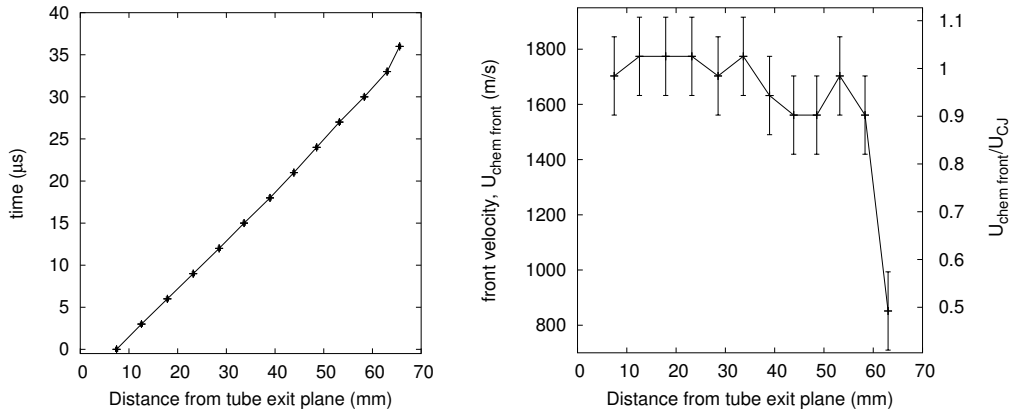

Figure L.51: Velocity profile. Shot 149, 0.22 H_2 + 0.11 O_2 + 0.67 Ar, P_0=100 kPa, T_0=295 K.

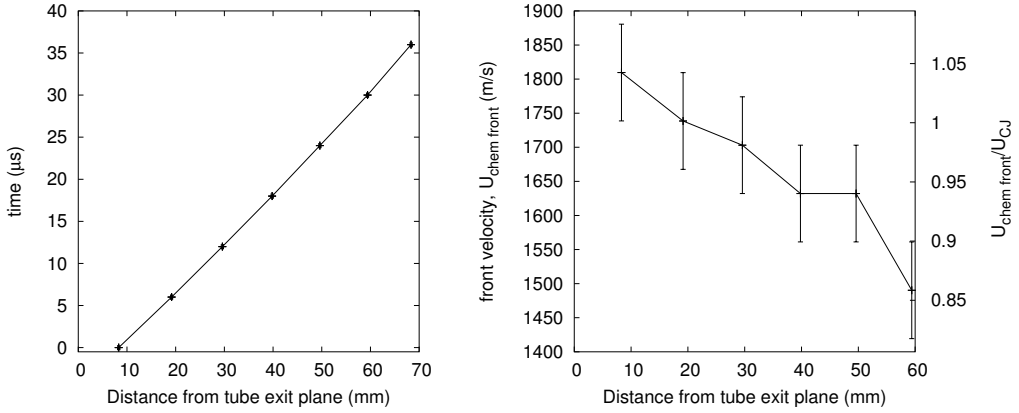

Figure L.52: Velocity profile. Shot 150, 0.223 H_2 + 0.112 O_2 + 0.665 Ar, P_0=100 kPa, T_0=295 K.

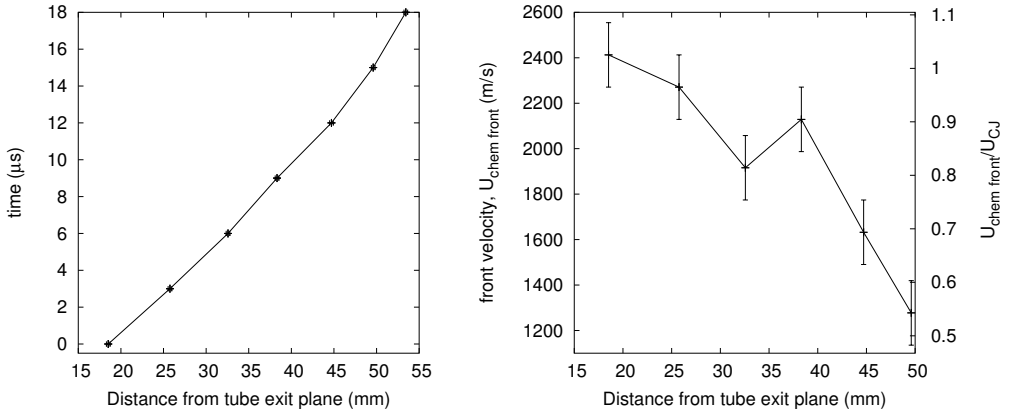

Figure L.53: Velocity profile. Shot 151, 0.5 H_2 + 0.5 N_2O, P_0=40 kPa, T_0=295 K.

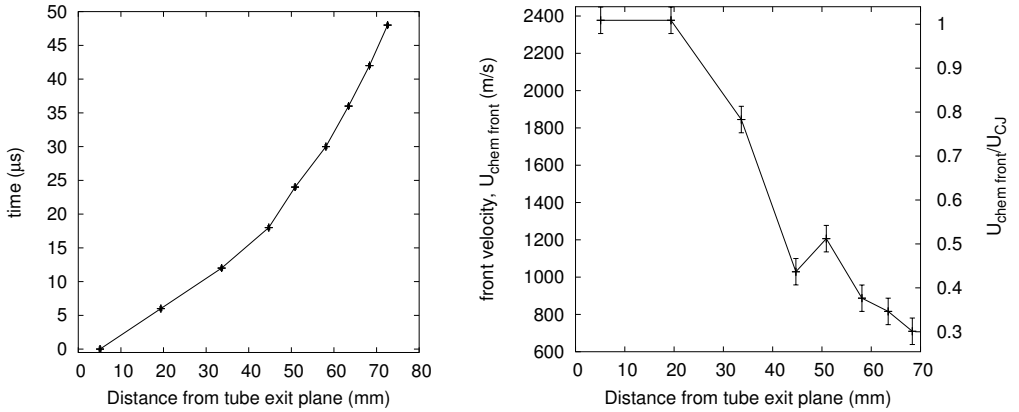

Figure L.54: Velocity profile. Shot 152, 0.5 H_2 + 0.5 N_2O, P_0=42.5 kPa, T_0=295 K.

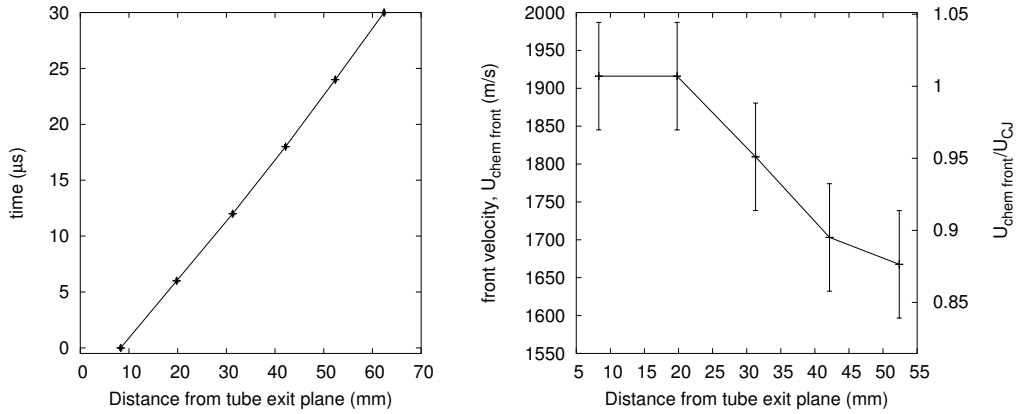

Figure L.55: Velocity profile. Shot 154, 0.333 H_2 + 0.167 O_2 + 0.5 Ar, P_0=55 kPa, T_0=296 K.

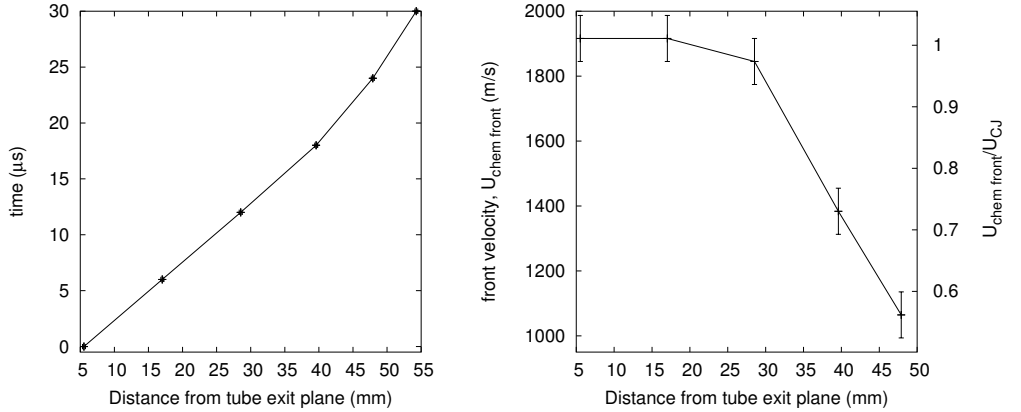

Figure L.56: Velocity profile. Shot 156, 0.333 H_2 + 0.167 O_2 + 0.5 Ar, P_0=45 kPa, T_0=296 K.

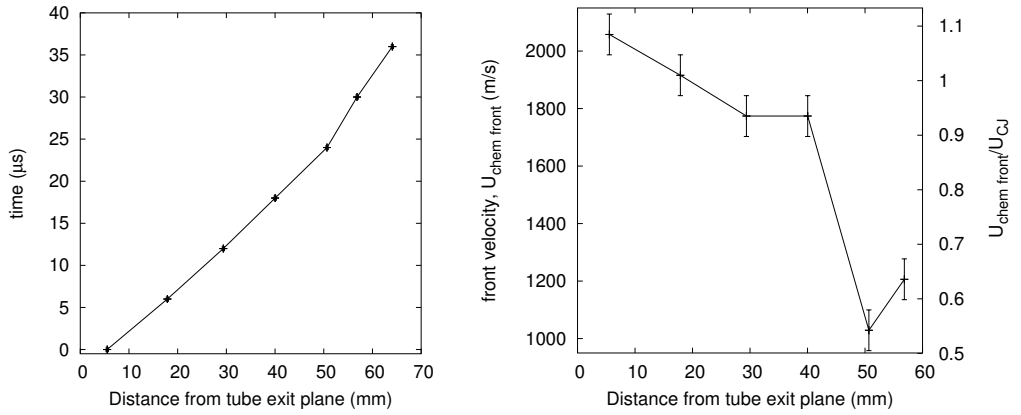

Figure L.57: Velocity profile. Shot 157, 0.333 H_2 + 0.167 O_2 + 0.5 Ar, P_0=47.5 kPa, T_0=296 K.

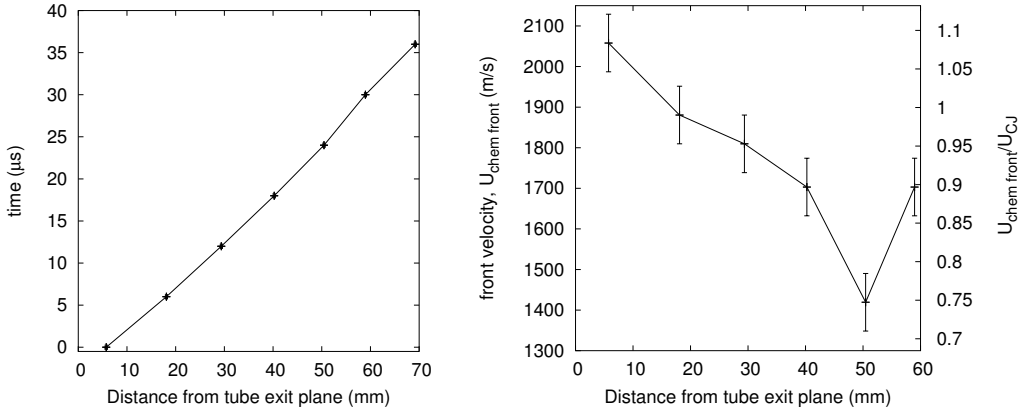

Figure L.58: Velocity profile. Shot 158, 0.333 H_2 + 0.167 O_2 + 0.5 Ar, P_0=50 kPa, T_0=296 K.

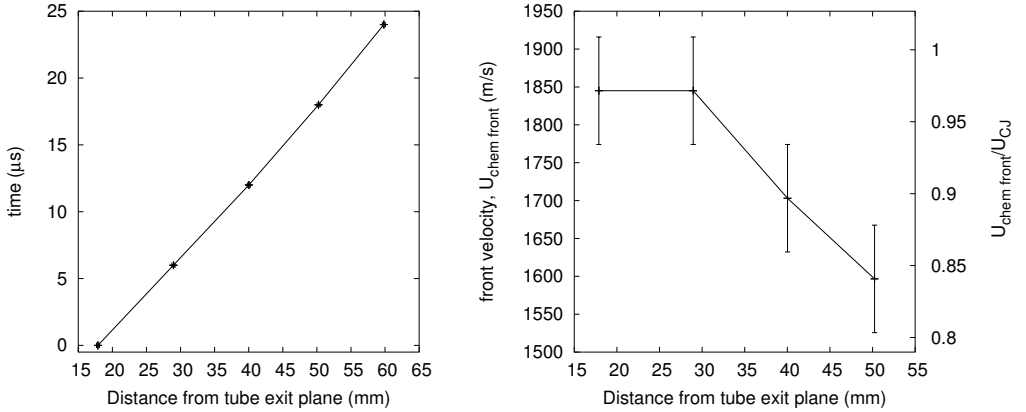

Figure L.59: Velocity profile. Shot 160, 0.333 H_2 + 0.167 O_2 + 0.5 Ar, P_0=50 kPa, T_0=295 K.

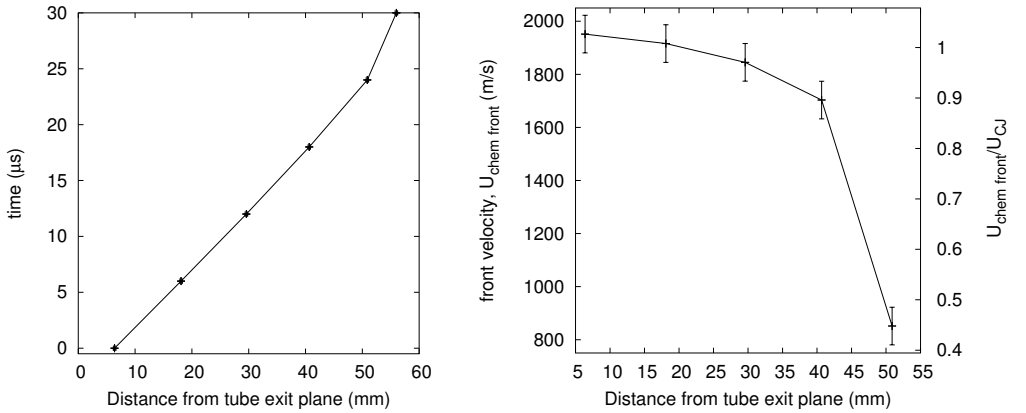

Figure L.60: Velocity profile. Shot 161, 0.333 H_2 + 0.167 O_2 + 0.5 Ar, P_0=52.5 kPa, T_0=295 K.

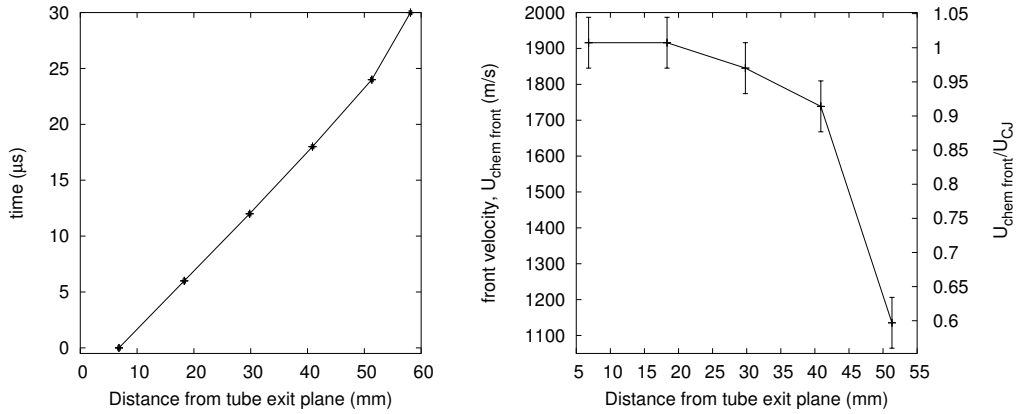

Figure L.61: Velocity profile. Shot 162, 0.333 H_2 + 0.167 O_2 + 0.5 Ar, P_0=53.75 kPa, T_0=296 K.

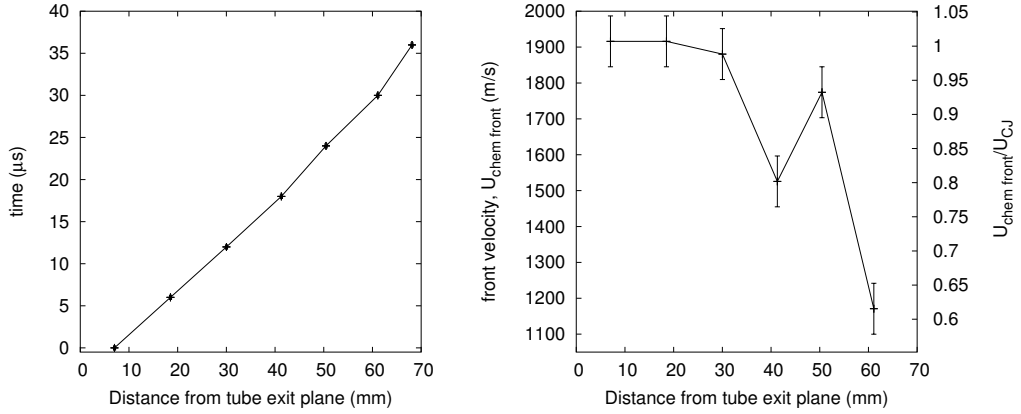

Figure L.62: Velocity profile. Shot 163, 0.333 H_2 + 0.167 O_2 + 0.5 Ar, P_0=55 kPa, T_0=296 K.

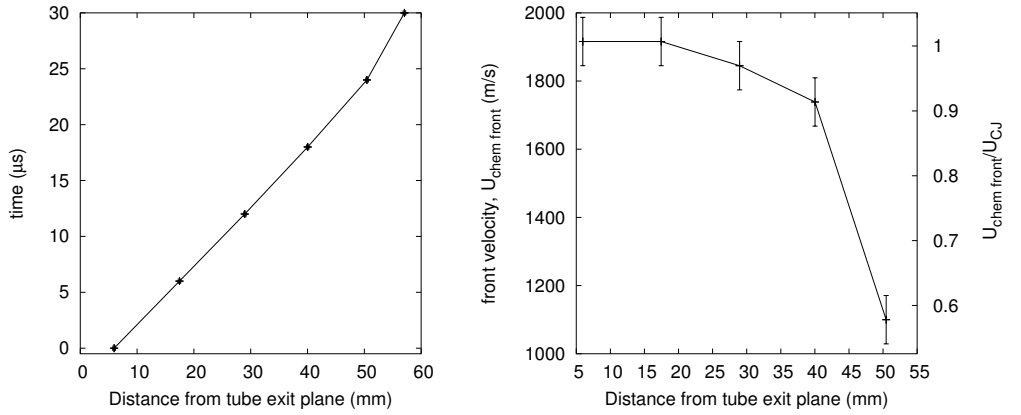

Figure L.63: Velocity profile. Shot 164, 0.333 H_2 + 0.167 O_2 + 0.5 Ar, P_0=55 kPa, T_0=296 K.

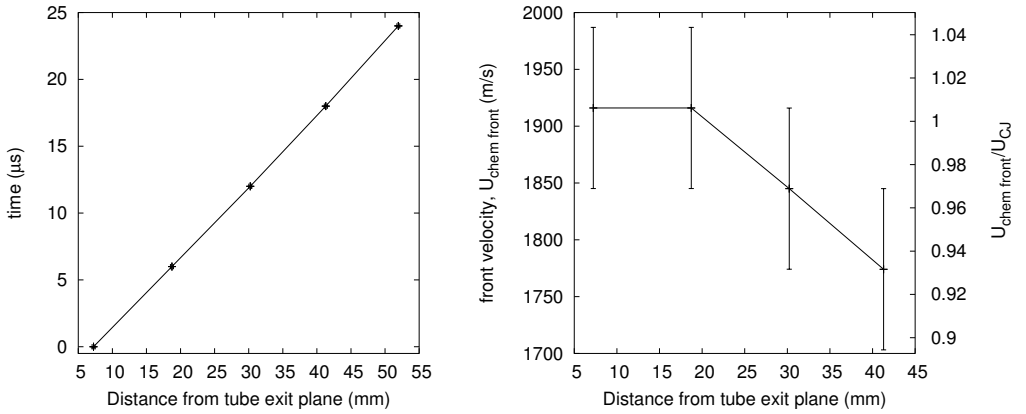

Figure L.64: Velocity profile. Shot 165, 0.333 H_2 + 0.167 O_2 + 0.5 Ar, P_0=57.5 kPa, T_0=296 K.

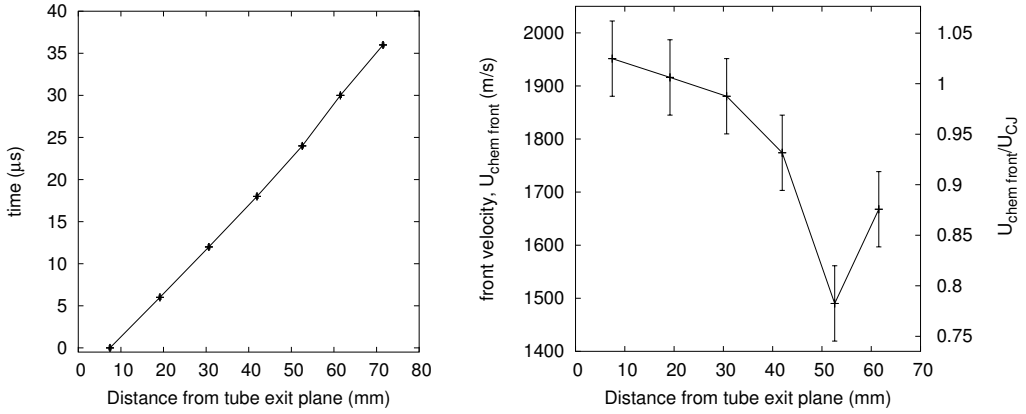

Figure L.65: Velocity profile. Shot 166, 0.333 H_2 + 0.167 O_2 + 0.5 Ar, P_0=57.5 kPa, T_0=296 K.

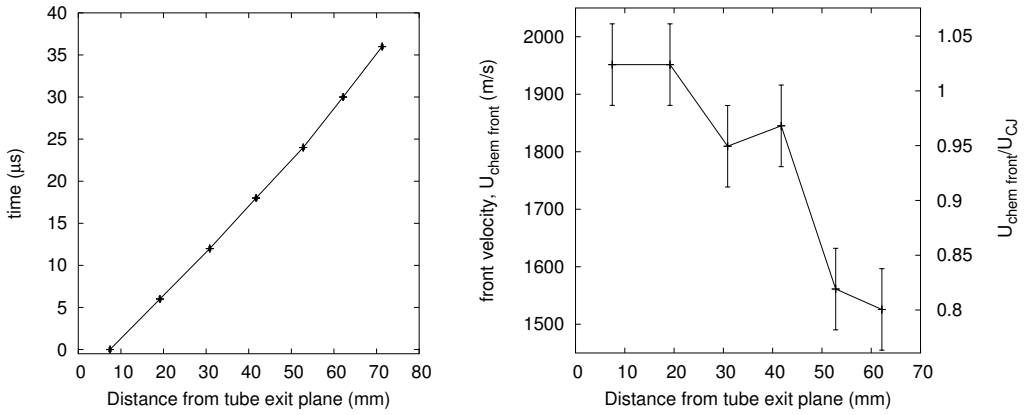

Figure L.66: Velocity profile. Shot 167, 0.333 H_2 + 0.167 O_2 + 0.5 Ar, P_0=60 kPa, T_0=297 K.

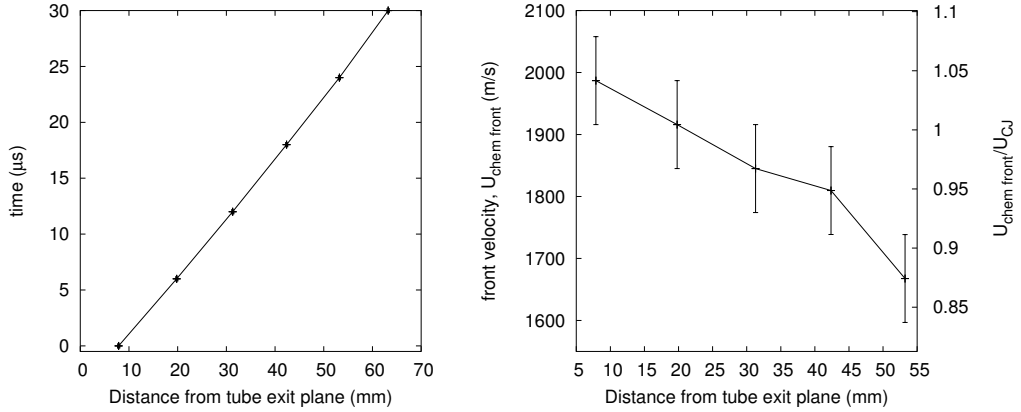

Figure L.67: Velocity profile. Shot 168, 0.333 H_2 + 0.167 O_2 + 0.5 Ar, P_0=62.5 kPa, T_0=296 K.

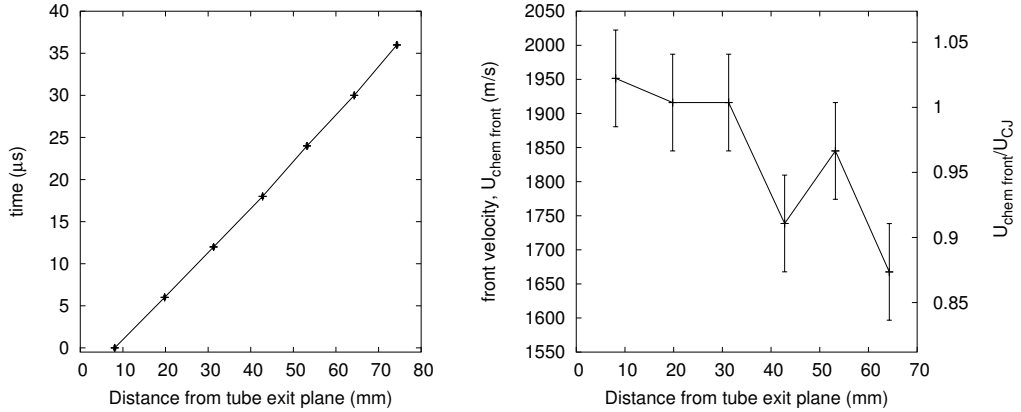

Figure L.68: Velocity profile. Shot 169, 0.333 H_2 + 0.167 O_2 + 0.5 Ar, P_0=65 kPa, T_0=296 K.

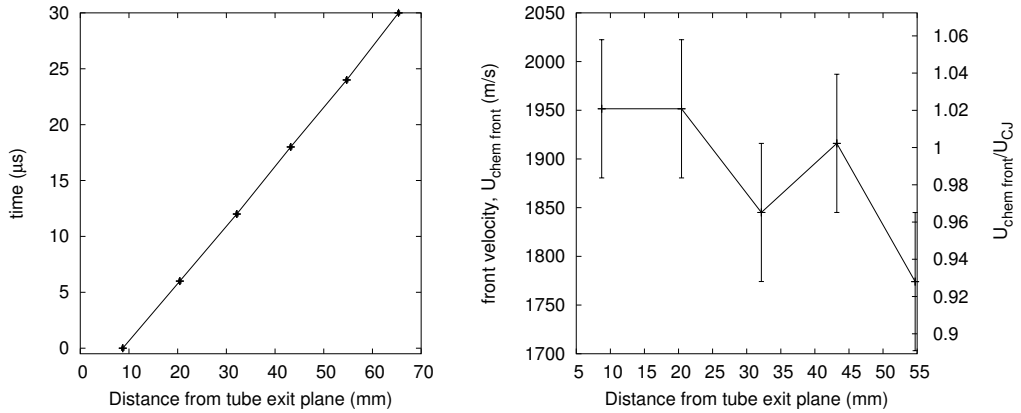

Figure L.69: Velocity profile. Shot 170, 0.333 H_2 + 0.167 O_2 + 0.5 Ar, P_0=70 kPa, T_0=296 K.

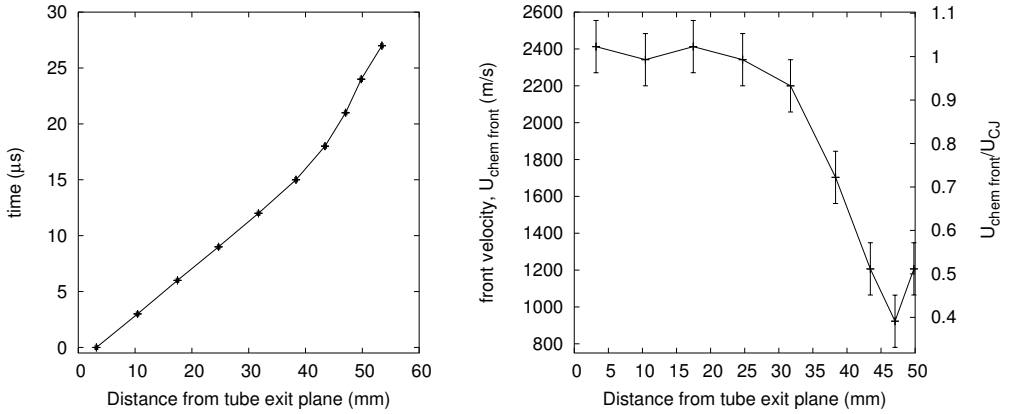

Figure L.70: Velocity profile. Shot 171, 0.5 H_2 + 0.5 N_2O, P_0=45 kPa, T_0=297 K.

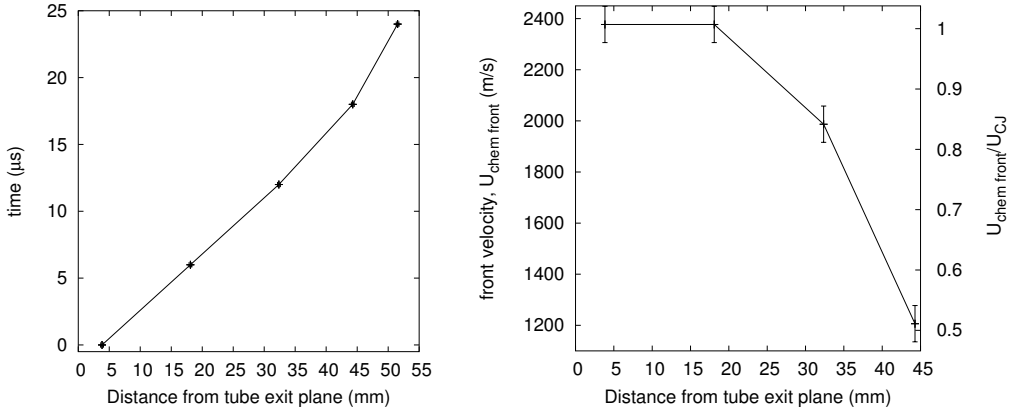

Figure L.71: Velocity profile. Shot 172, 0.5 H_2 + 0.5 N_2O, P_0=47.5 kPa, T_0=297 K.

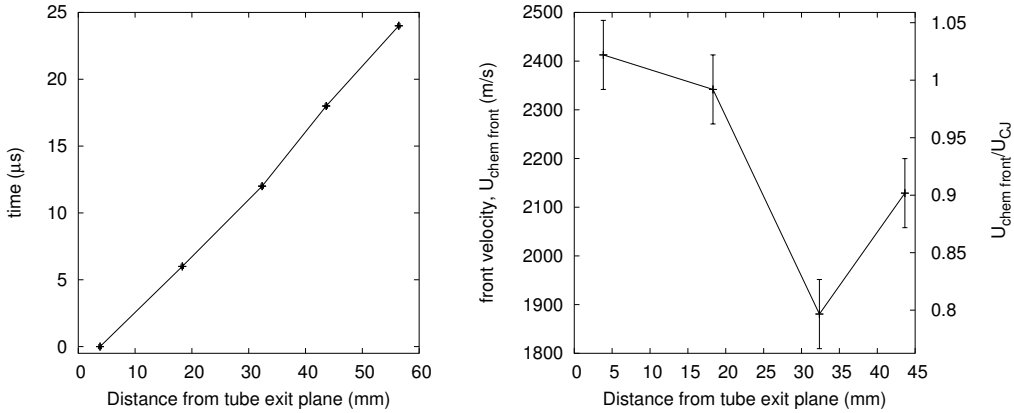

Figure L.72: Velocity profile. Shot 173, 0.5 H_2 + 0.5 N_2O, P_0=47.5 kPa, T_0=297 K.

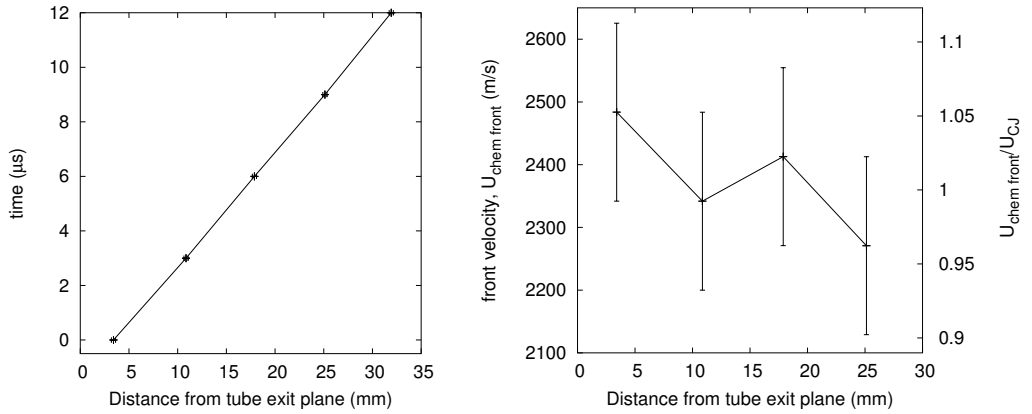

Figure L.73: Velocity profile. Shot 174, 0.5 H_2 + 0.5 N_2O, P_0=46.25 kPa, T_0=297 K.

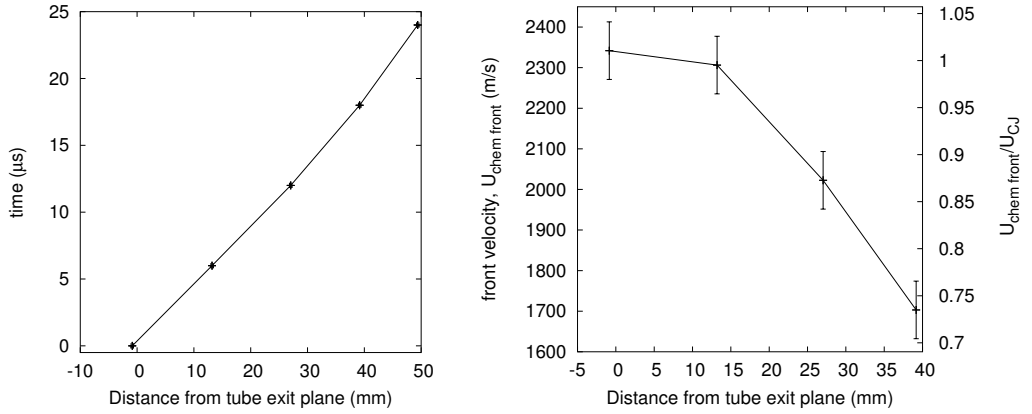

Figure L.74: Velocity profile. Shot 175, 0.222 C_2H_6 + 0.778 O_2, P_0=30 kPa, T_0=297 K.

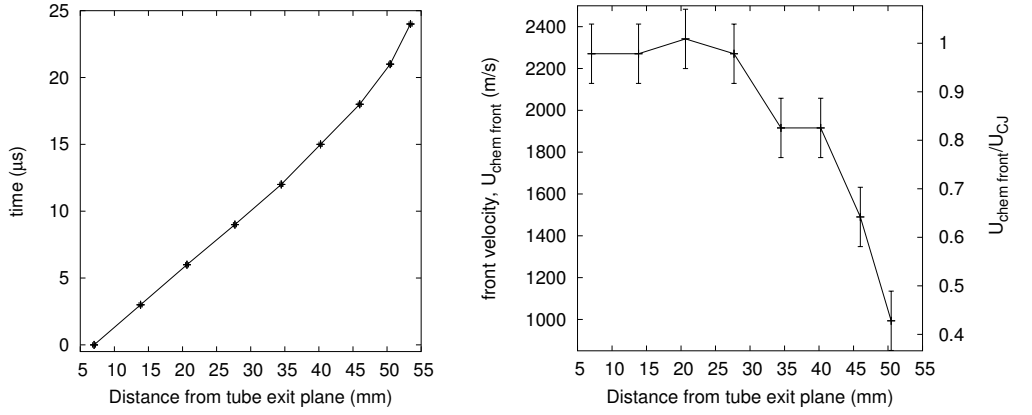

Figure L.75: Velocity profile. Shot 176, 0.222 C_2H_6 + 0.778 O_2, P_0=32.5 kPa, T_0=297 K.

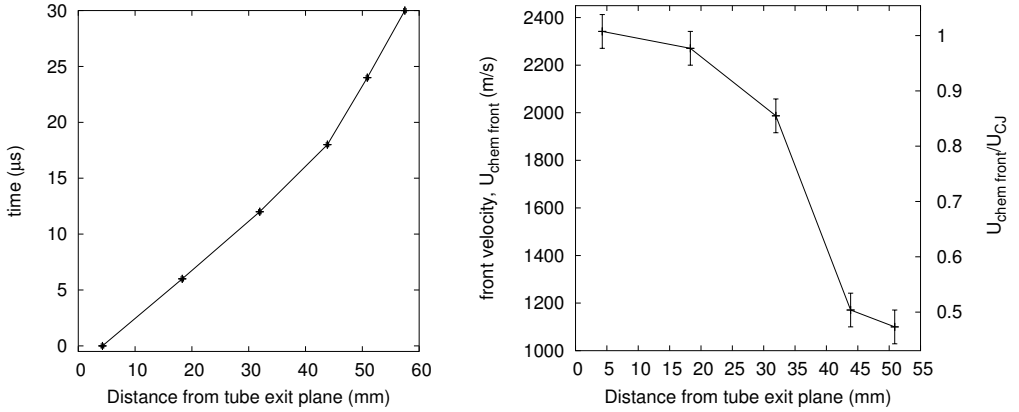

Figure L.76: Velocity profile. Shot 177, 0.222 C_2H_6 + 0.778 O_2, P_0=35 kPa, T_0=297 K.

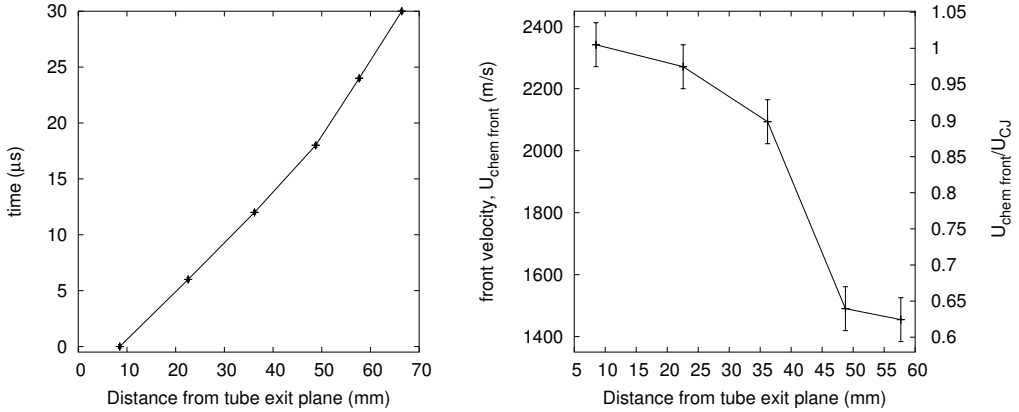

Figure L.77: Velocity profile. Shot 178, 0.222 C_2H_6 + 0.778 O_2, P_0=40 kPa, T_0=297 K.

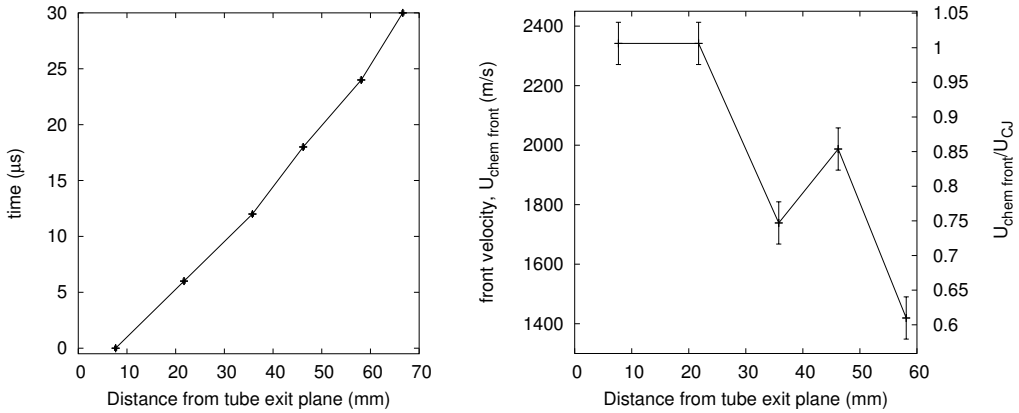

Figure L.78: Velocity profile. Shot 179, 0.222 C_2H_6 + 0.778 O_2, P_0=37.5 kPa, T_0=298 K.

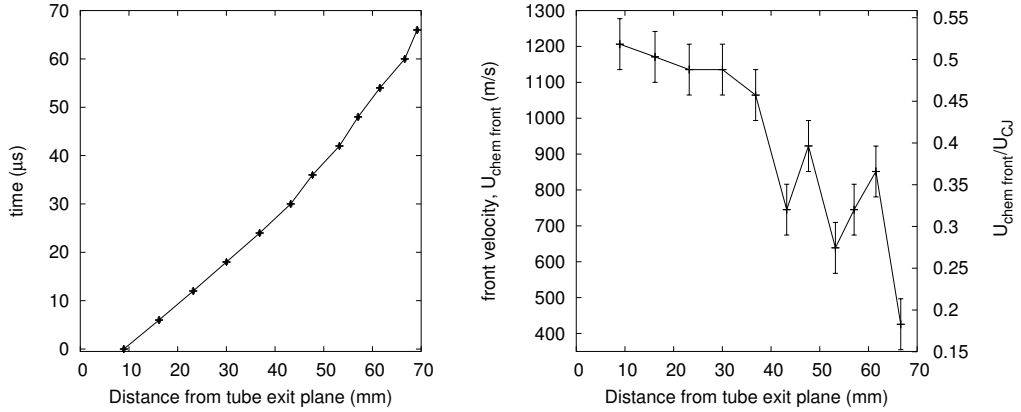

Figure L.79: Velocity profile. Shot 180, 0.222 C_2H_6 + 0.778 O_2, P_0=37.5 kPa, T_0=297 K.

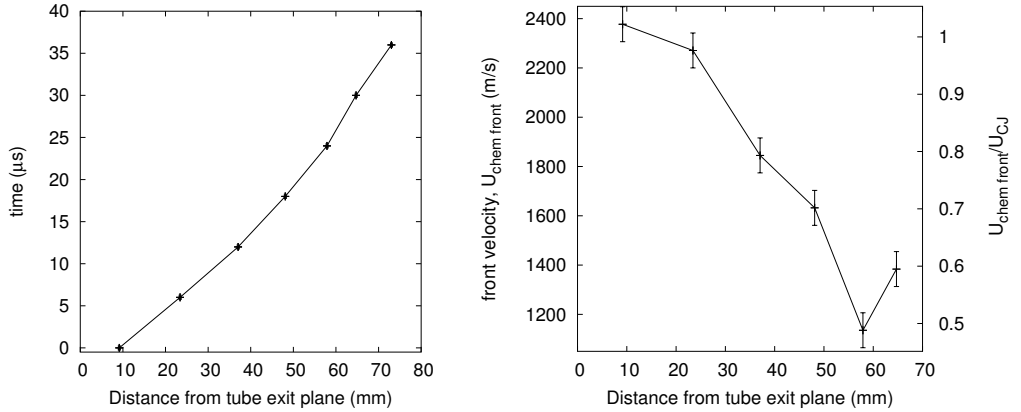

Figure L.80: Velocity profile. Shot 182, 0.222 C_2H_6 + 0.778 O_2, P_0=36.25 kPa, T_0=298 K.

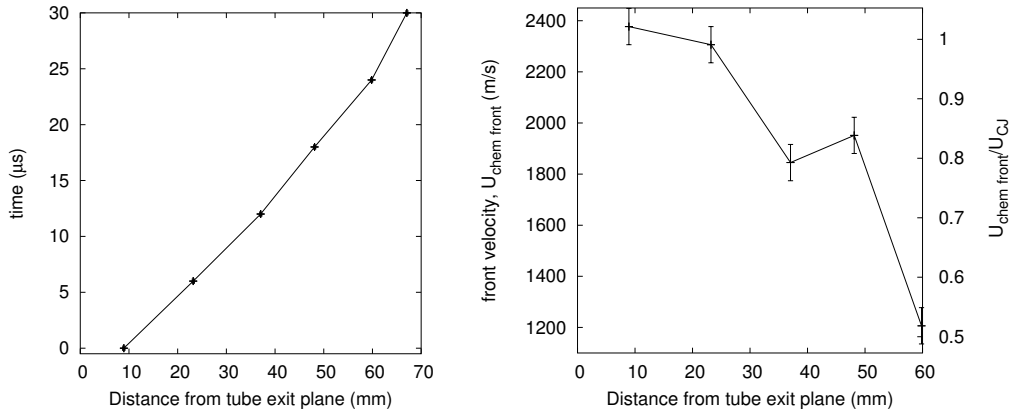

Figure L.81: Velocity profile. Shot 183, 0.222 C_2H_6 + 0.778 O_2, P_0=37.5 kPa, T_0=298 K.

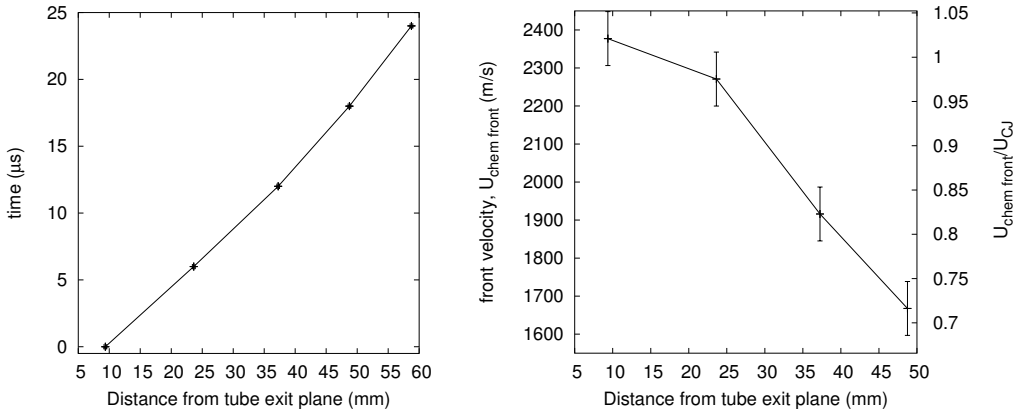

Figure L.82: Velocity profile. Shot 184, 0.222 C_2H_6 + 0.778 O_2, P_0=38.25 kPa, T_0=298 K.

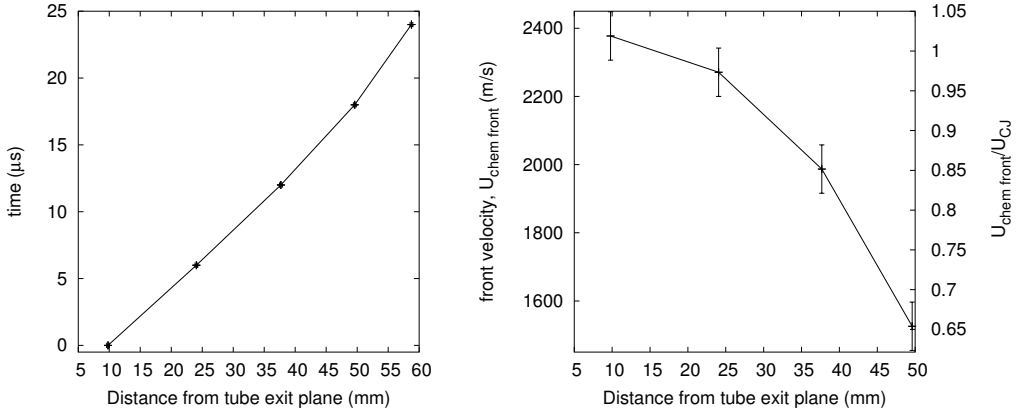

Figure L.83: Velocity profile. Shot 185, 0.222 C_2H_6 + 0.778 O_2, P_0=42.5 kPa, T_0=298 K.

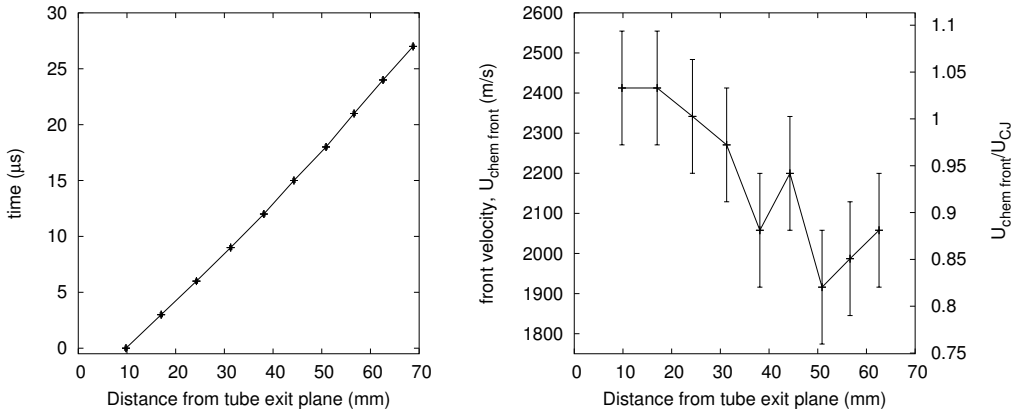

Figure L.84: Velocity profile. Shot 186, 0.222 C_2H_6 + 0.778 O_2, P_0=45 kPa, T_0=299 K.

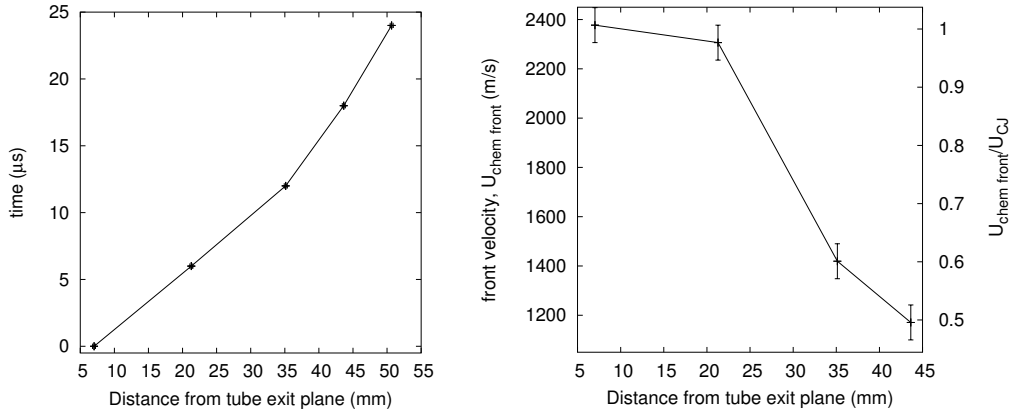

Figure L.85: Velocity profile. Shot 187, 0.333 CH_4 + 0.667 O_2, P_0=50 kPa, T_0=294 K.

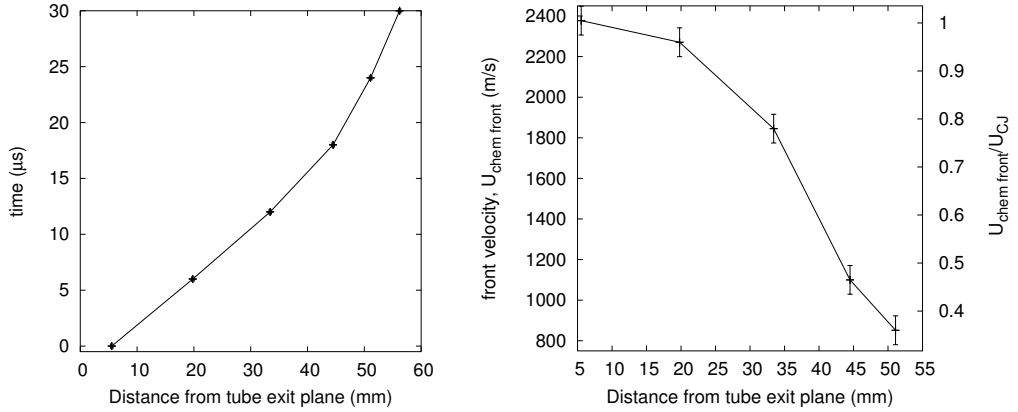

Figure L.86: Velocity profile. Shot 188, 0.333 CH_4 + 0.667 O_2, P_0=55 kPa, T_0=295 K.

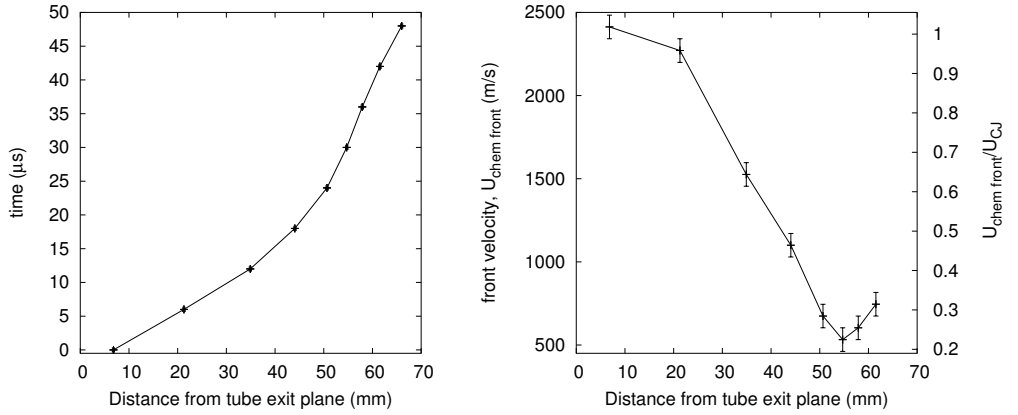

Figure L.87: Velocity profile. Shot 189, 0.333 CH_4 + 0.667 O_2, P_0=60 kPa, T_0=296 K.

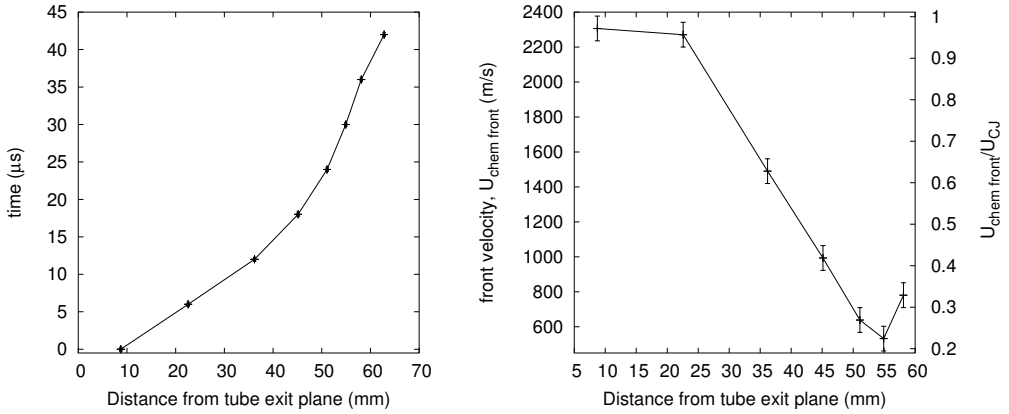

Figure L.88: Velocity profile. Shot 190, 0.333 CH_4 + 0.667 O_2, P_0=65 kPa, T_0=296 K.

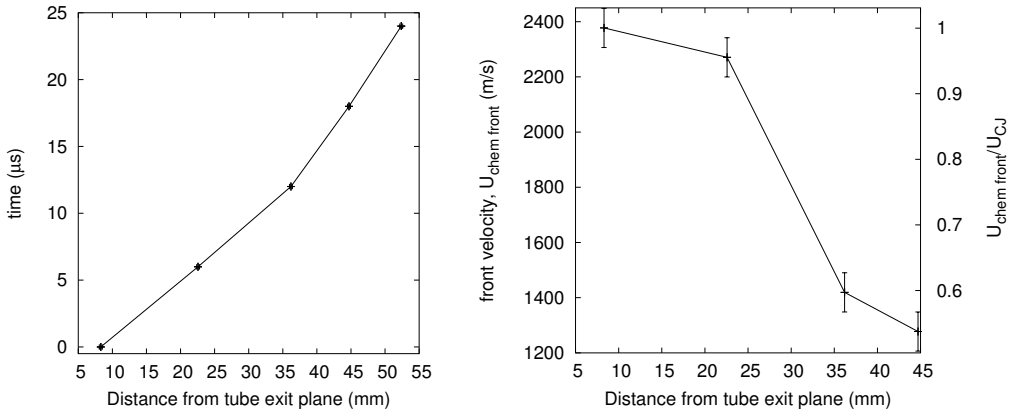

Figure L.89: Velocity profile. Shot 191, 0.333 CH_4 + 0.667 O_2, P_0=70 kPa, T_0=297 K.

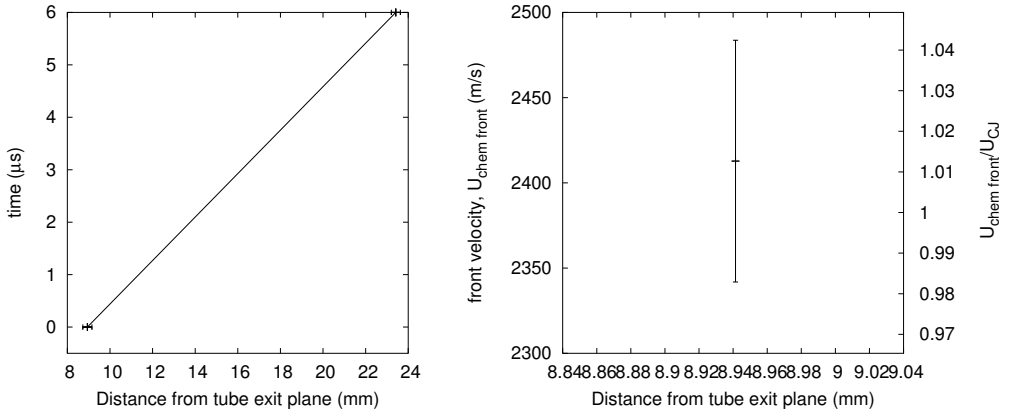

Figure L.90: Velocity profile. Shot 192, 0.333 CH_4 + 0.667 O_2, P_0=80 kPa, T_0=298 K.

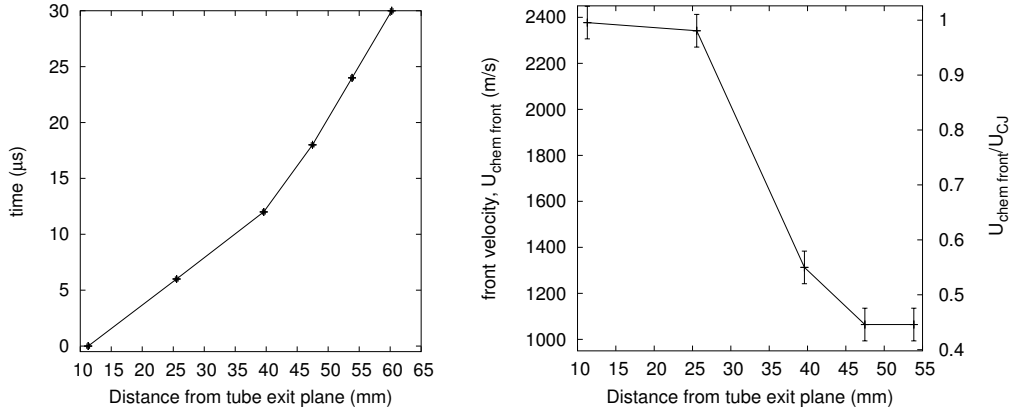

Figure L.91: Velocity profile. Shot 193, 0.333 CH_4 + 0.667 O_2, P_0=90 kPa, T_0=298 K.

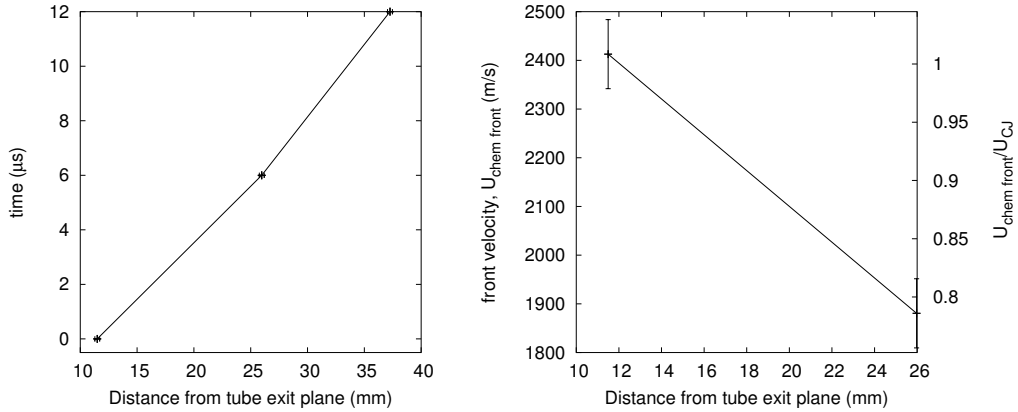

Figure L.92: Velocity profile. Shot 194, 0.333 CH_4 + 0.667 O_2, P_0=100 kPa, T_0=299 K.

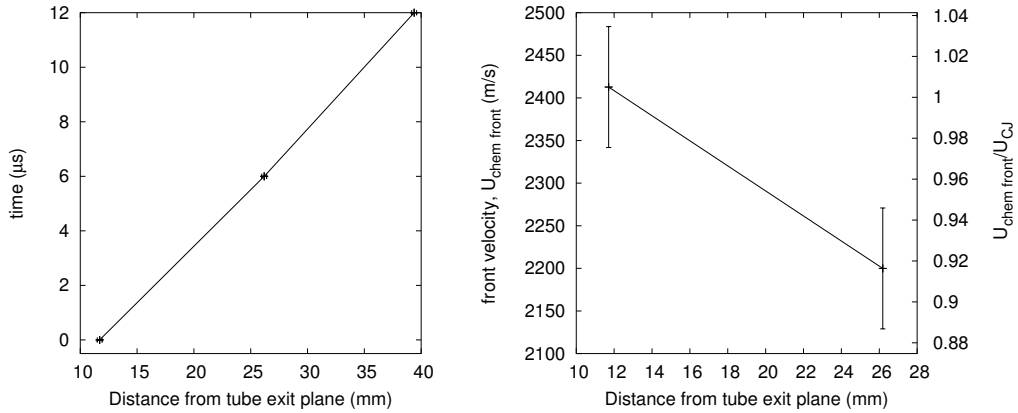

Figure L.93: Velocity profile. Shot 195, 0.333 CH_4 + 0.667 O_2, P_0=120 kPa, T_0=299 K.

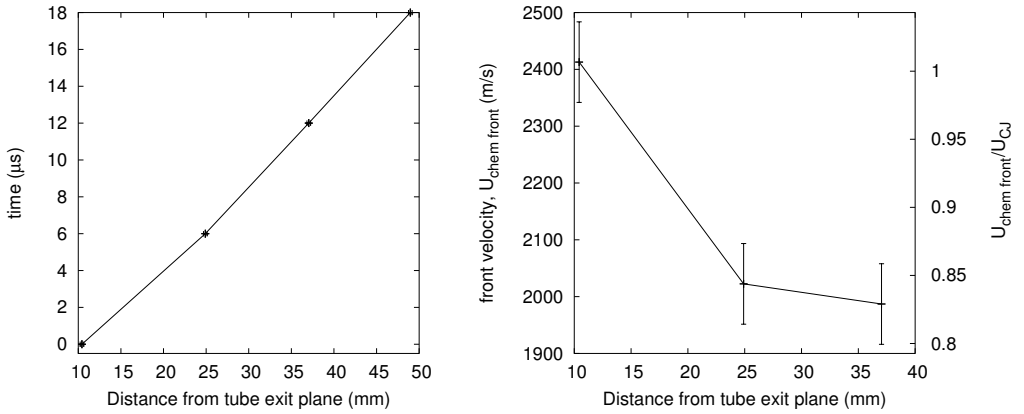

Figure L.94: Velocity profile. Shot 196, 0.333 CH_4 + 0.667 O_2, P_0=110 kPa, T_0=299 K.

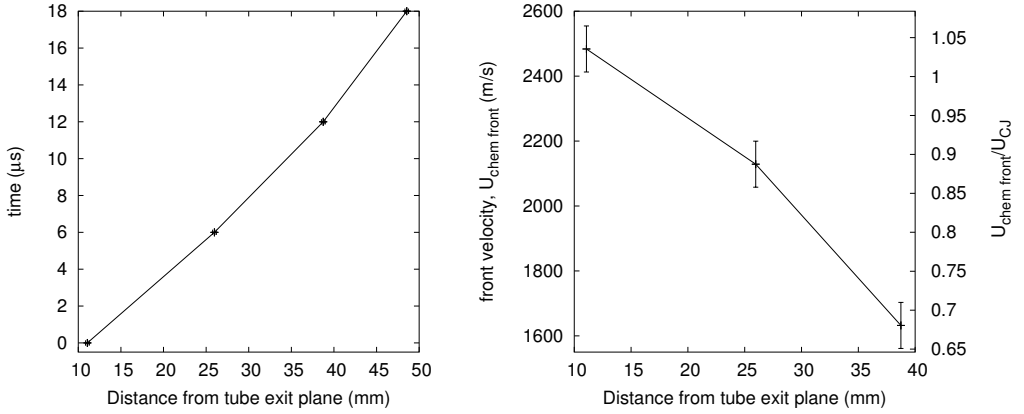

Figure L.95: Velocity profile. Shot 197, 0.333 CH_4 + 0.667 O_2, P_0=115 kPa, T_0=300 K.

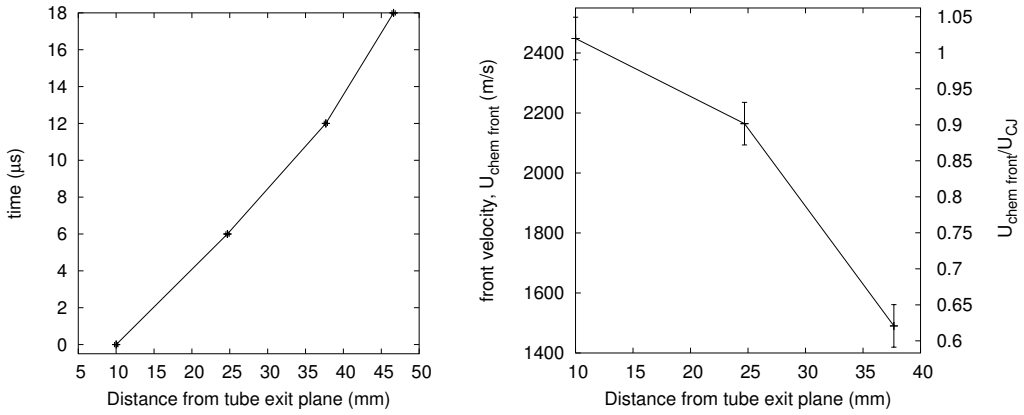

Figure L.96: Velocity profile. Shot 198, 0.333 CH_4 + 0.667 O_2, P_0=120 kPa, T_0=298 K.

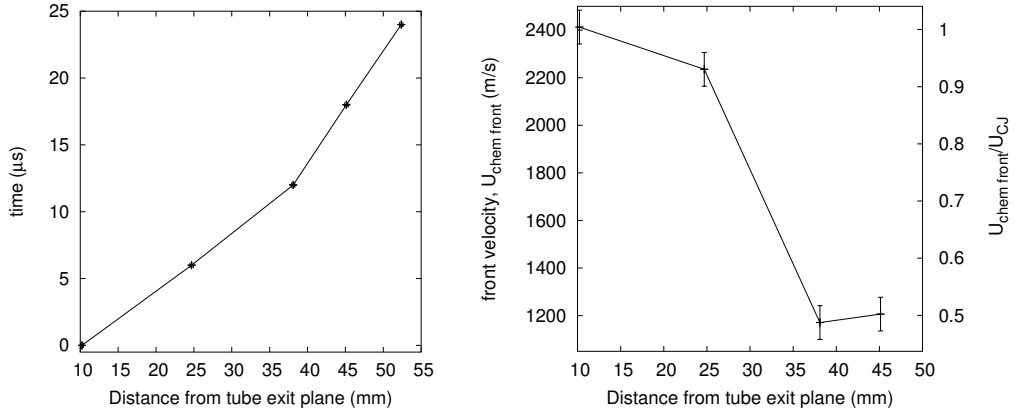

Figure L.97: Velocity profile. Shot 199, 0.333 CH_4 + 0.667 O_2, P_0=125 kPa, T_0=301 K.

Appendix M

Overview of Images from Detonation Diffraction Experiments

In this chapter an overview of the experimentally obtained images is given. The timing parameters and mixture compositions are given in the image caption.

Δ t(P3–PLIF), is the time delay from point in time, the detonation is detected at pressure transducer P3 to the point in time the PLIF image is taken. Δ t(TEP–PLIF) is the time delay from detonation reaching tube exit plane (TEP) to the point in time the PLIF image is taken, assuming CJ velocity between P3 and tube exit plane.

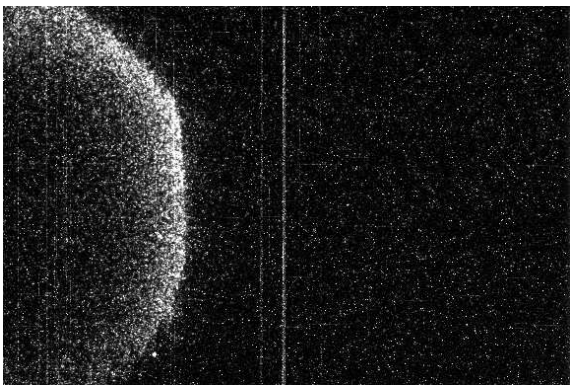

Figure M.1: Shot 16, 0.182 H_2 + 0.091 O_2 + 0.727 Ar, P_0=100 kPa, T_0=297 K. Delays: Δt(P3-PLIF) 193.17 μs; Δt(TEP-PLIF) 13.49 μs. PLIF image height 50 mm.

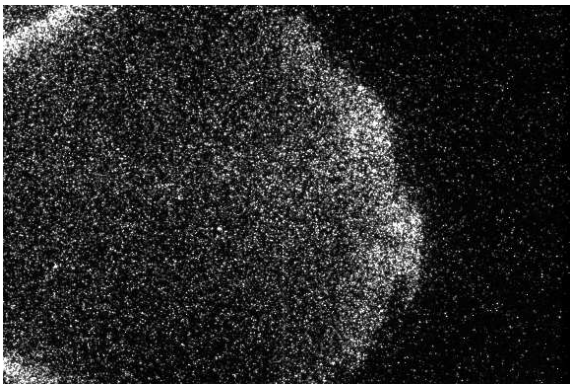

Figure M.2: Shot 17, 0.187 H_2 + 0.093 O_2 + 0.72 Ar, P_0=100 kPa, T_0=297 K. Delays: Δt(P3-PLIF) 193.16 μs; Δt(TEP-PLIF) 14.51 μs. PLIF image height 50 mm.

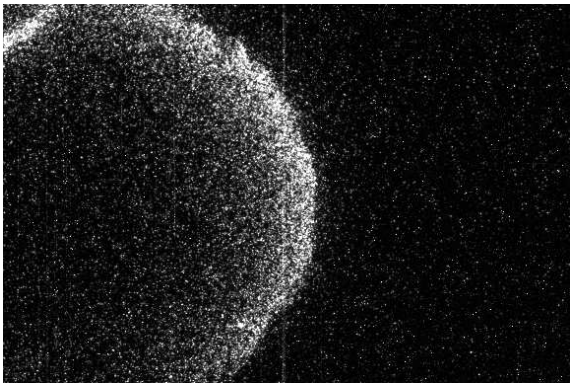

Figure M.3: Shot 18, 0.187 H_2 + 0.093 O_2 + 0.72 Ar, P_0=100 kPa, T_0=296 K. Delays: Δt(P3-PLIF) 200.16 μs; Δt(TEP-PLIF) 21.51 μs. PLIF image height 48 mm.

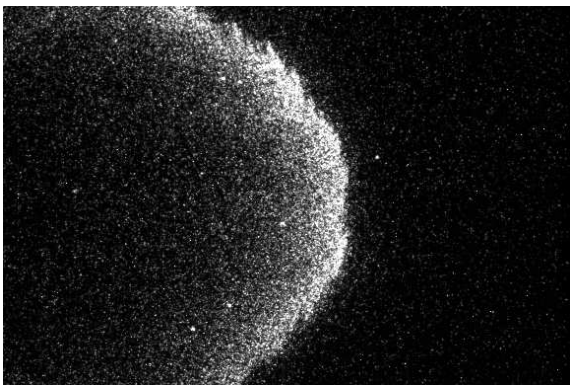

Figure M.4: Shot 19, 0.187 H_2 + 0.093 O_2 + 0.72 Ar, P_0=100 kPa, T_0=297 K. Delays: Δt(P3-PLIF) 200.16 μs; Δt(TEP-PLIF) 21.51 μs. PLIF image height 48 mm.

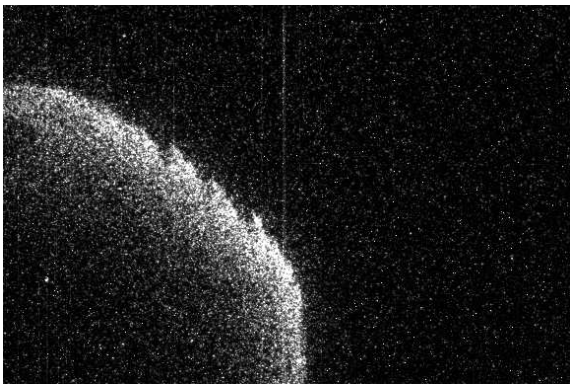

Figure M.5: Shot 20, 0.187 H_2 + 0.093 O_2 + 0.72 Ar, P_0=100 kPa, T_0=296 K. Delays: Δt(P3-PLIF) 200.167 μs; Δt(TEP-PLIF) 21.52 μs. PLIF image height 48 mm.

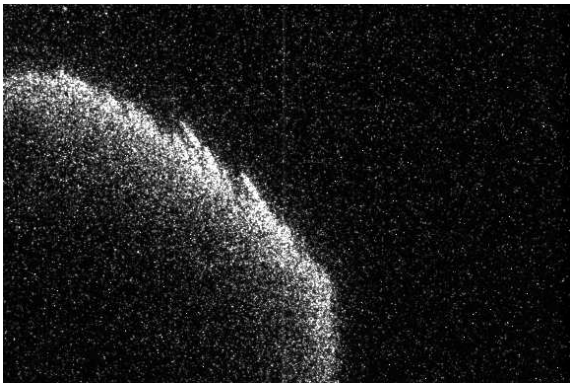

Figure M.6: Shot 21, 0.2 H_2 + 0.1 O_2 + 0.7 Ar, P_0=100 kPa, T_0=297 K. Delays: Δt(P3-PLIF) 200.167 μs; Δt(TEP-PLIF) 24.21 μs. PLIF image height 48 mm.

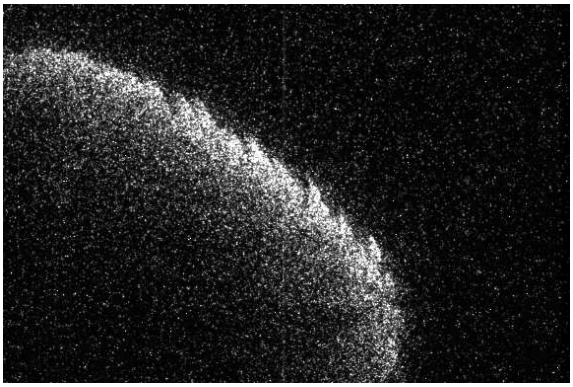

Figure M.7: Shot 22, 0.2 H_2 + 0.1 O_2 + 0.7 Ar, P_0=100 kPa, T_0=298 K. Delays: Δt(P3-PLIF) 206.167 μs; Δt(TEP-PLIF) 30.21 μs. PLIF image height 48 mm.

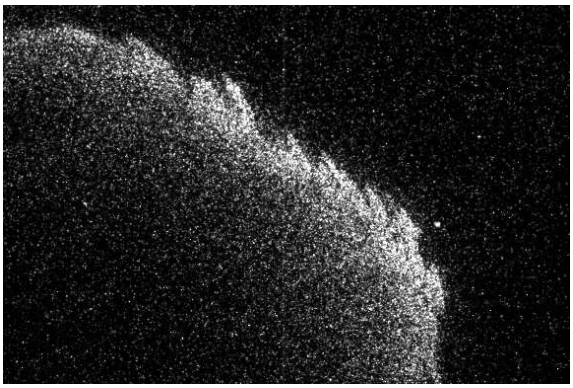

Figure M.8: Shot 23, 0.2 H_2 + 0.1 O_2 + 0.7 Ar, P_0=100 kPa, T_0=298 K. Delays: Δt(P3-PLIF) 212.167 μs; Δt(TEP-PLIF) 36.21 μs. PLIF image height 48 mm.

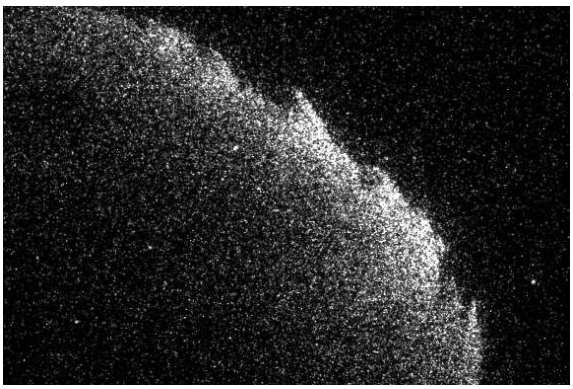

Figure M.9: Shot 24, 0.2 H_2 + 0.1 O_2 + 0.7 Ar, P_0=100 kPa, T_0=298 K. Delays: Δt(P3-PLIF) 218.167 μs; Δt(TEP-PLIF) 42.21 μs. PLIF image height 48 mm.

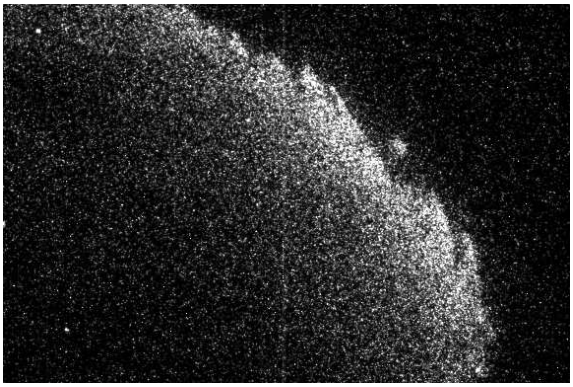

Figure M.10: Shot 25, 0.2 H_2 + 0.1 O_2 + 0.7 Ar, P_0=100 kPa, T_0=298 K. Delays: Δt(P3-PLIF) 224.167 μs; Δt(TEP-PLIF) 48.21 μs. PLIF image height 48 mm.

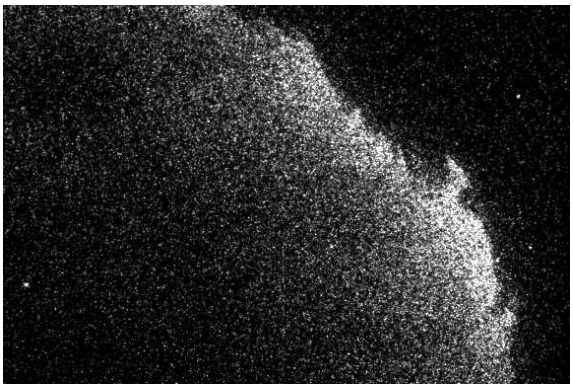

Figure M.11: Shot 26, 0.2 H_2 + 0.1 O_2 + 0.7 Ar, P_0=100 kPa, T_0=298 K. Delays: Δt(P3-PLIF) 230.167 μs; Δt(TEP-PLIF) 54.21 μs. PLIF image height 48 mm.

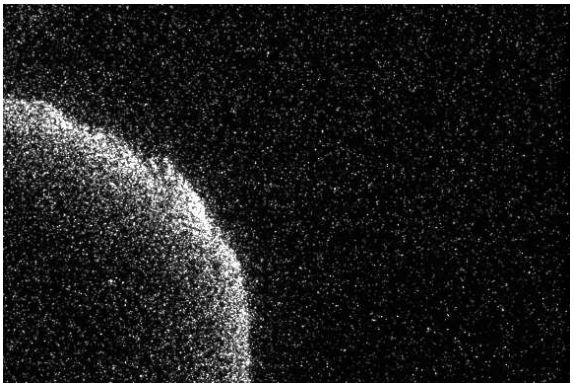

Figure M.12: Shot 27, 0.2 H_2 + 0.1 O_2 + 0.7 Ar, P_0=100 kPa, T_0=298 K. Delays: Δt(P3-PLIF) 190.167 μs; Δt(TEP-PLIF) 14.21 μs. PLIF image height 48 mm.

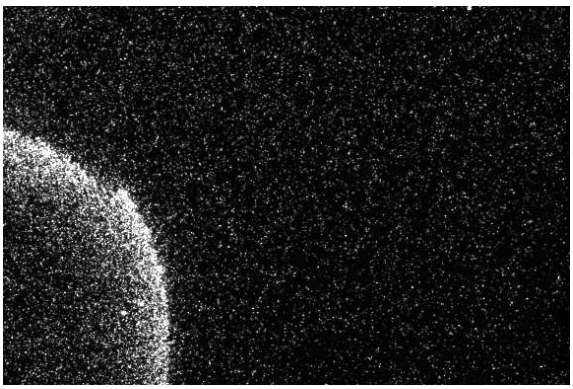

Figure M.13: Shot 28, 0.2 H_2 + 0.1 O_2 + 0.7 Ar, P_0=100 kPa, T_0=298 K. Delays: Δt(P3-PLIF) 187.167 μs; Δt(TEP-PLIF) 11.21 μs. PLIF image height 48 mm.

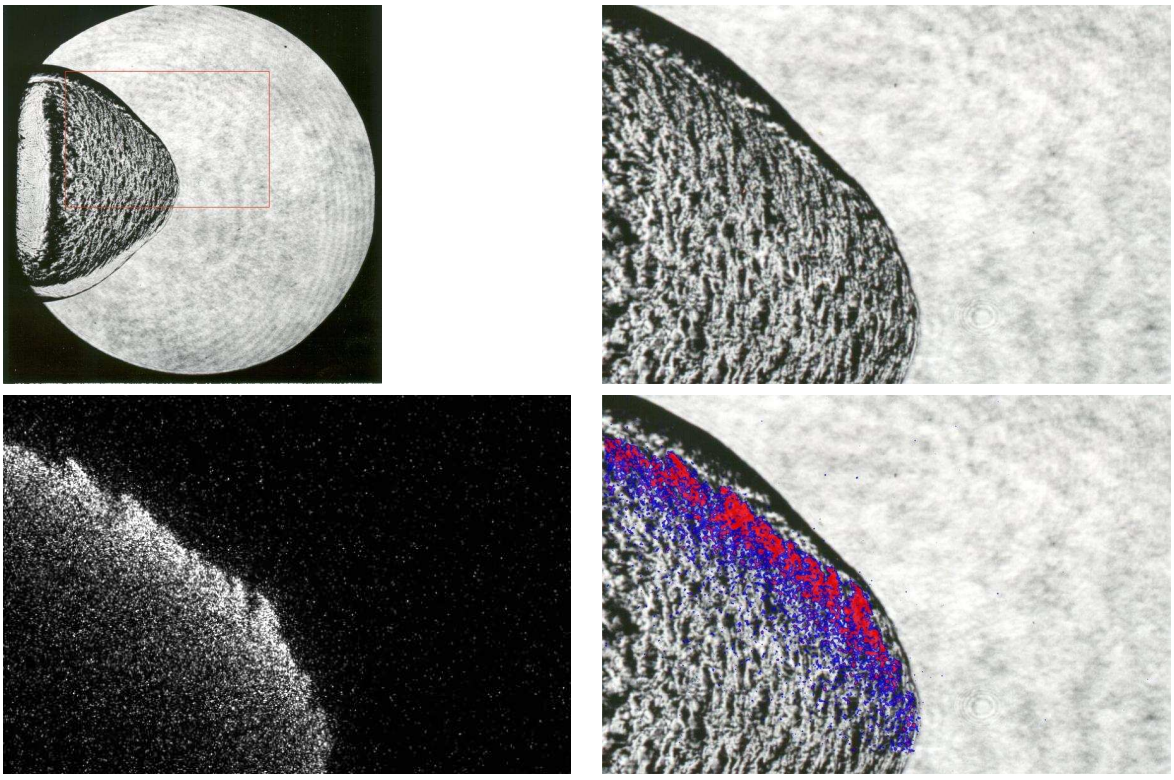

Figure M.14: Shot 30, 0.213 H_2 + 0.107 O_2 + 0.68 Ar, P_0=100 kPa, T_0=296 K. Delays: Δt(P3-PLIF) 208.057 μs; Δt(TEP-PLIF) 34.61 μs. Schlieren image height 150 mm, PLIF image height 50 mm.

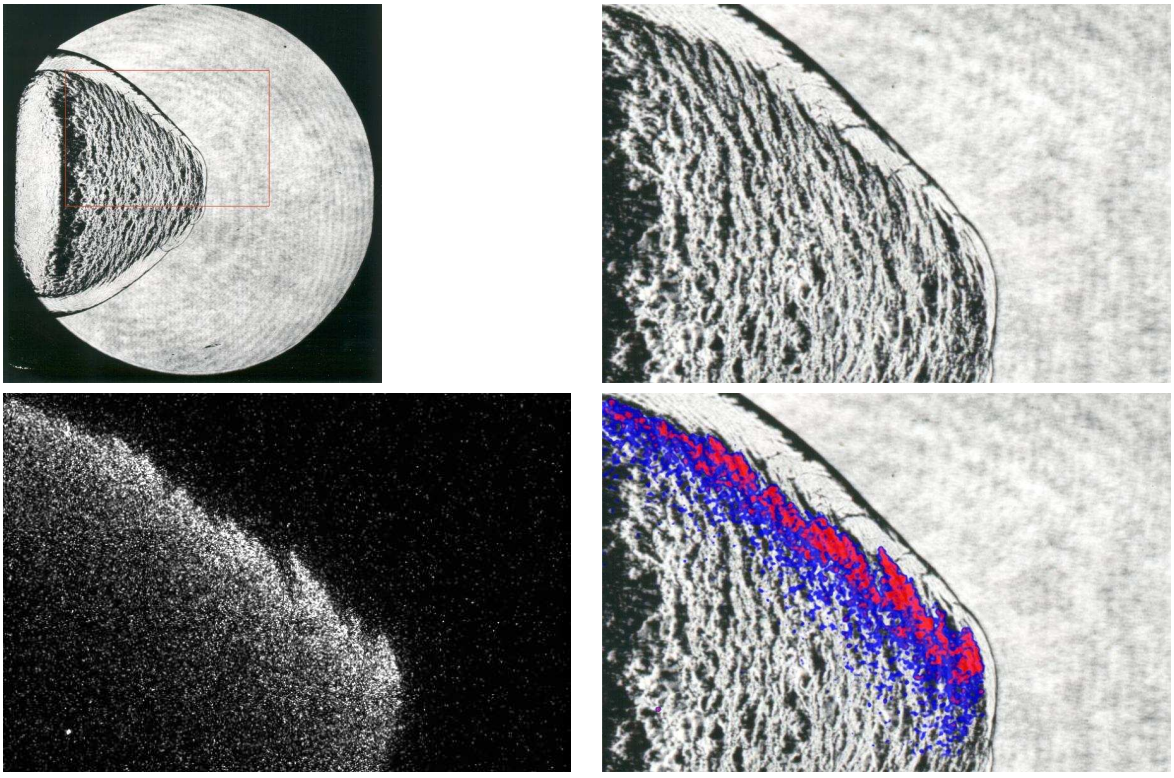

Figure M.15: Shot 31, 0.213 H_2 + 0.107 O_2 + 0.68 Ar, P_0=100 kPa, T_0=296 K. Delays: Δt(P3-PLIF) 217.157 μs; Δt(TEP-PLIF) 43.71 μs. Schlieren image height 150 mm, PLIF image height 50 mm.

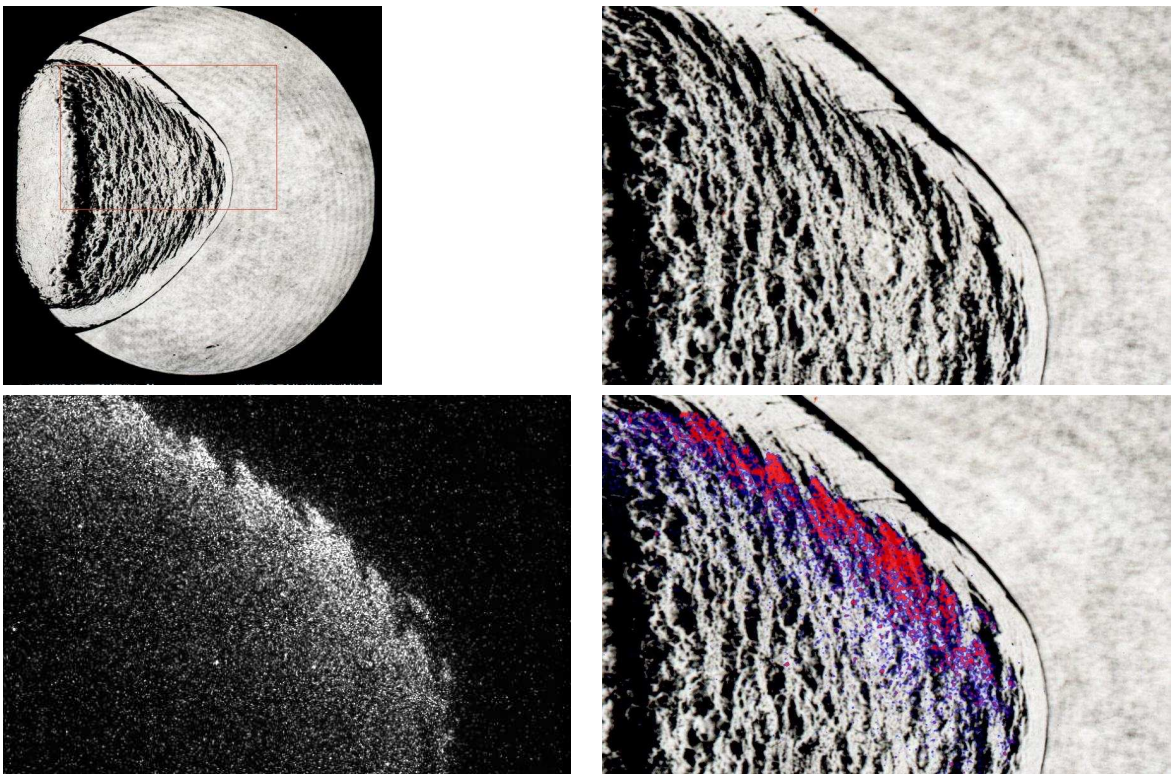

Figure M.16: Shot 32, 0.213 H_2 + 0.107 O_2 + 0.68 Ar, P_0=100 kPa, T_0=296 K. Delays: Δt(P3-PLIF) 227.167 μs; Δt(TEP-PLIF) 53.72 μs. Schlieren image height 150 mm, PLIF image height 50 mm.

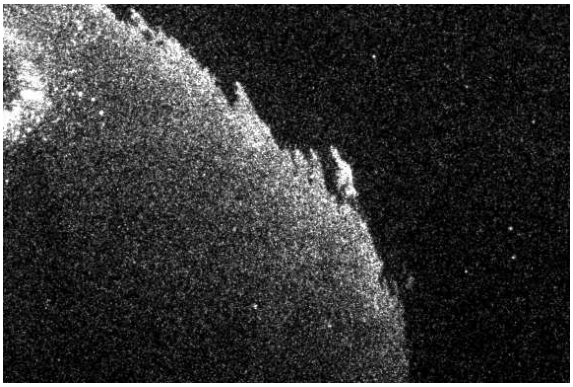

Figure M.17: Shot 33, 0.213 H_2 + 0.107 O_2 + 0.68 Ar, P_0=100 kPa, T_0=296 K. Delays: Δt(P3-PLIF) 227.167 μs; Δt(TEP-PLIF) 53.72 μs. PLIF image height 50 mm.

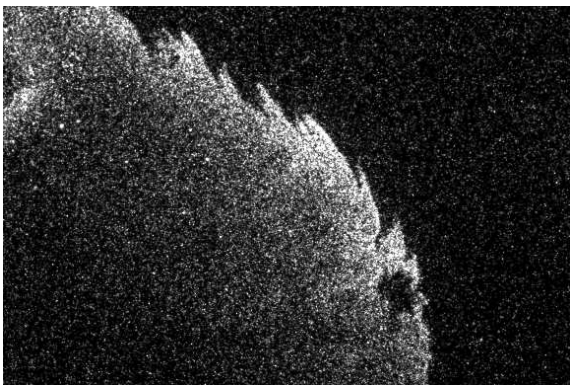

Figure M.18: Shot 34, 0.213 H_2 + 0.107 O_2 + 0.68 Ar, P_0=100 kPa, T_0=297 K. Delays: Δt(P3-PLIF) 227.167 μs; Δt(TEP-PLIF) 53.72 μs. PLIF image height 50 mm.

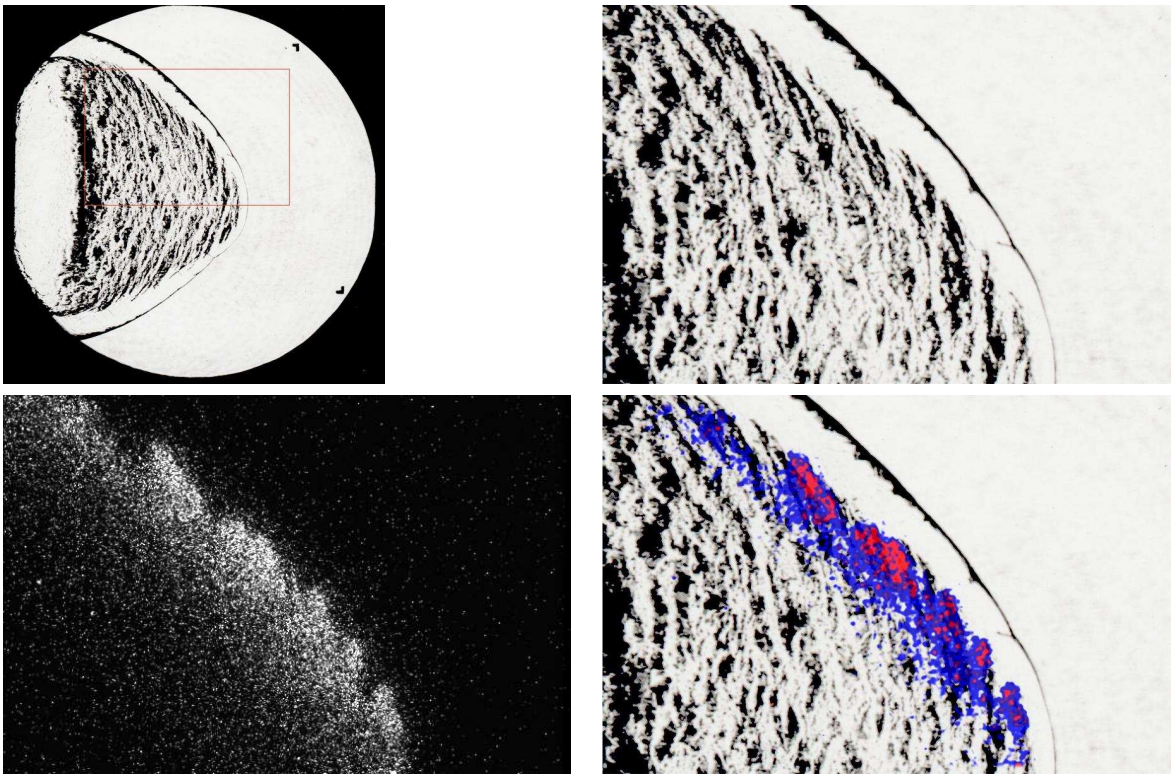

Figure M.19: Shot 35, 0.227 H_2 + 0.113 O_2 + 0.66 Ar, P_0=100 kPa, T_0=294 K. Delays: Δt(P3-PLIF) 227.167 μs; Δt(TEP-PLIF) 56.08 μs. Schlieren image height 150 mm, PLIF image height 50 mm.

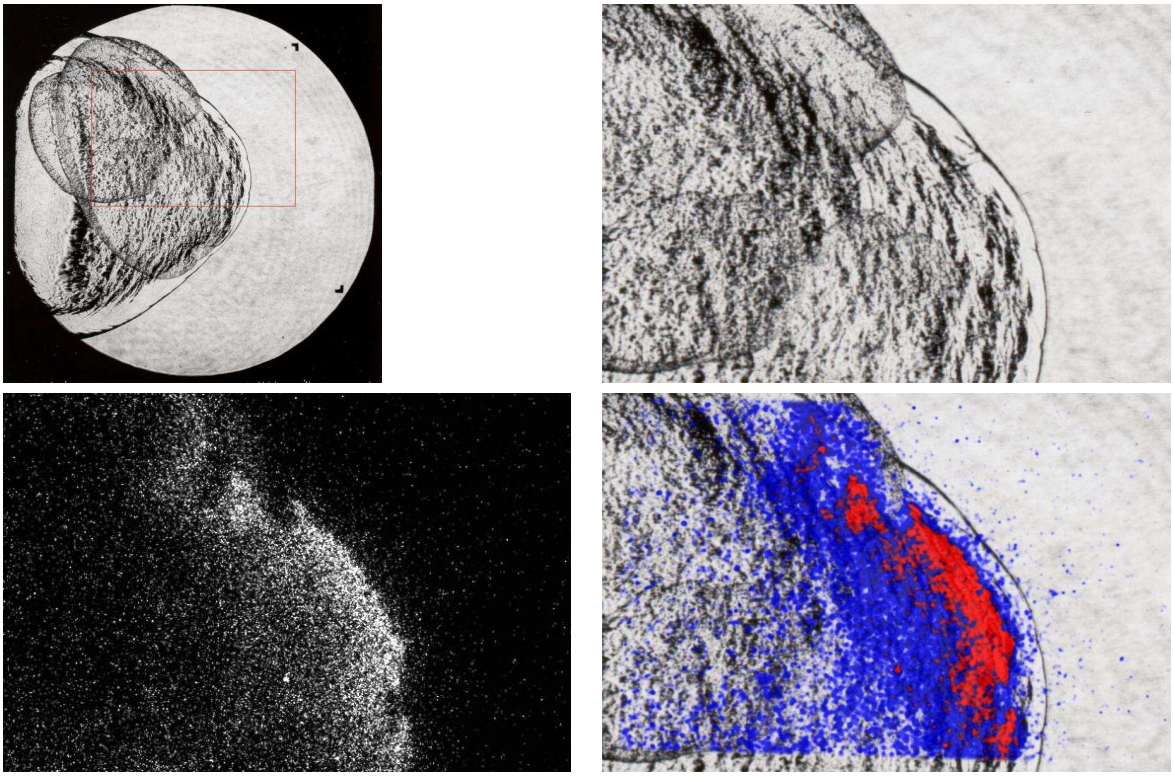

Figure M.20: Shot 36, 0.227 H_2 + 0.113 O_2 + 0.66 Ar, P_0=100 kPa, T_0=294 K. Delays: Δt(P3-PLIF) 227.167 μs; Δt(TEP-PLIF) 56.08 μs. Schlieren image height 150 mm, PLIF image height 50 mm.

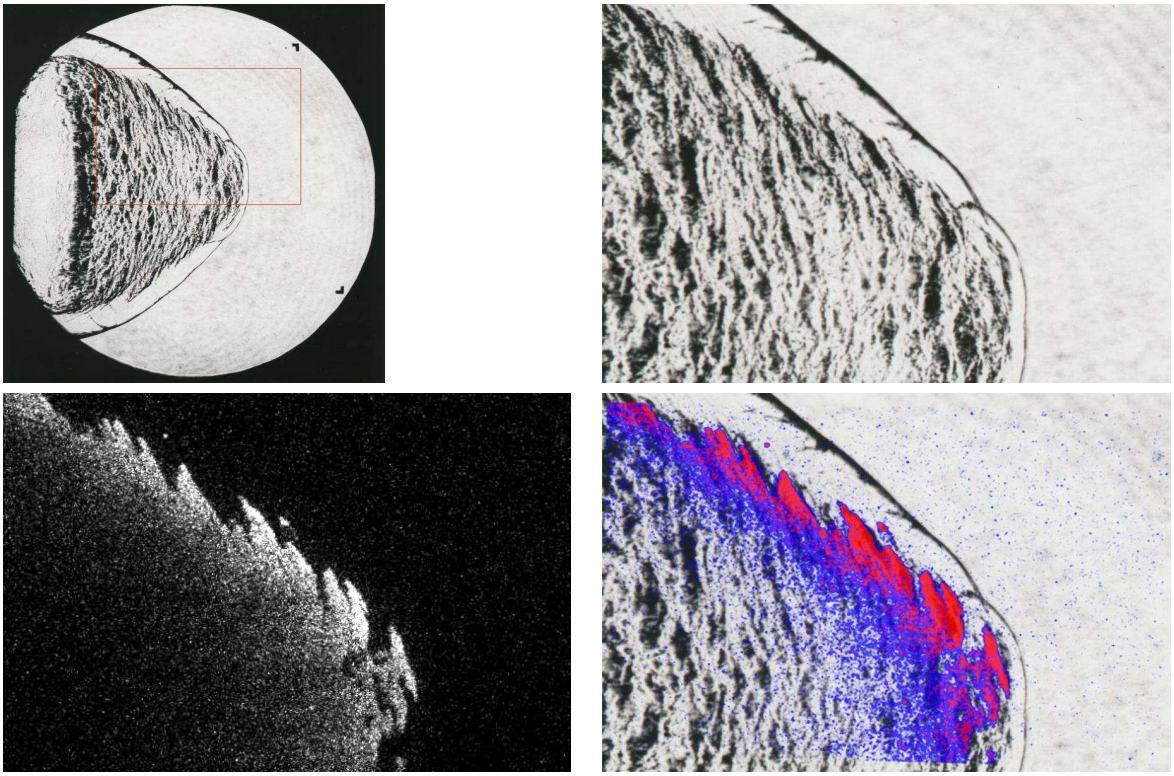

Figure M.21: Shot 37, 0.227 H_2 + 0.113 O_2 + 0.66 Ar, P_0=100 kPa, T_0=295 K. Delays: Δt(P3-PLIF) 227.167 μs; Δt(TEP-PLIF) 56.08 μs. Schlieren image height 150 mm, PLIF image height 50 mm.

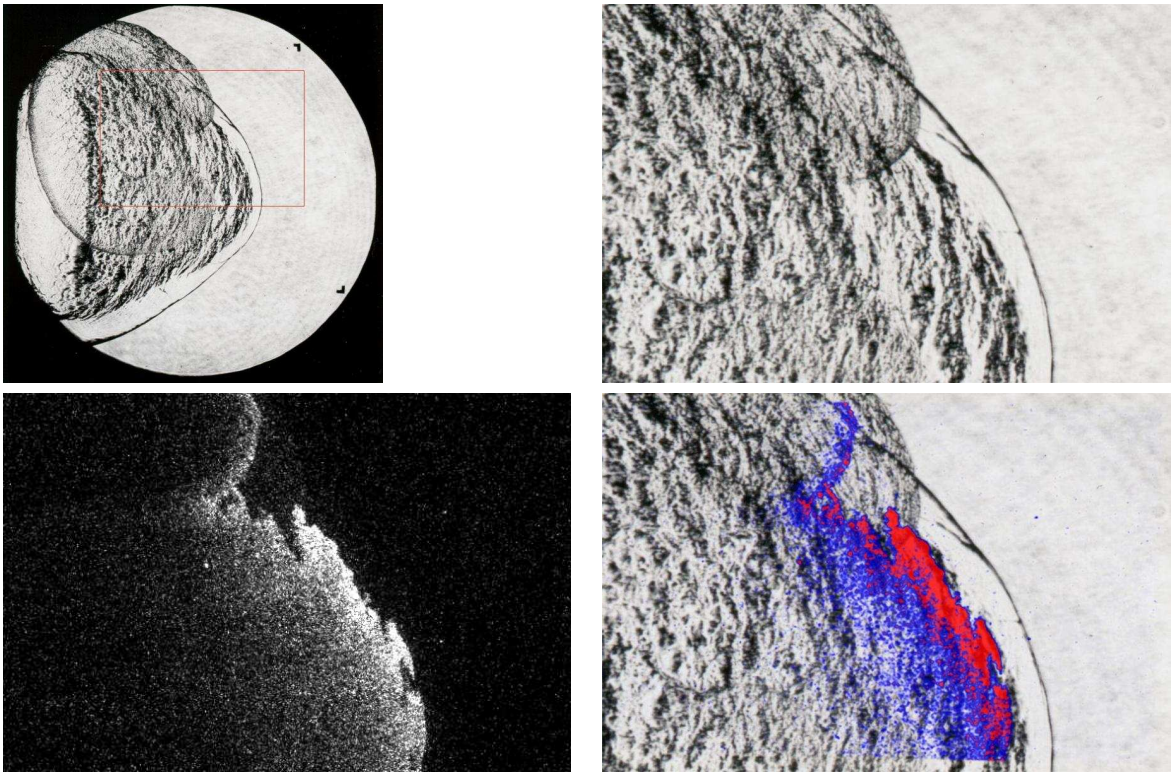

Figure M.22: Shot 38, 0.227 H_2 + 0.113 O_2 + 0.66 Ar, P_0=100 kPa, T_0=295 K. Delays: Δt(P3-PLIF) 232.167 μs; Δt(TEP-PLIF) 61.08 μs. Schlieren image height 150 mm, PLIF image height 50 mm.

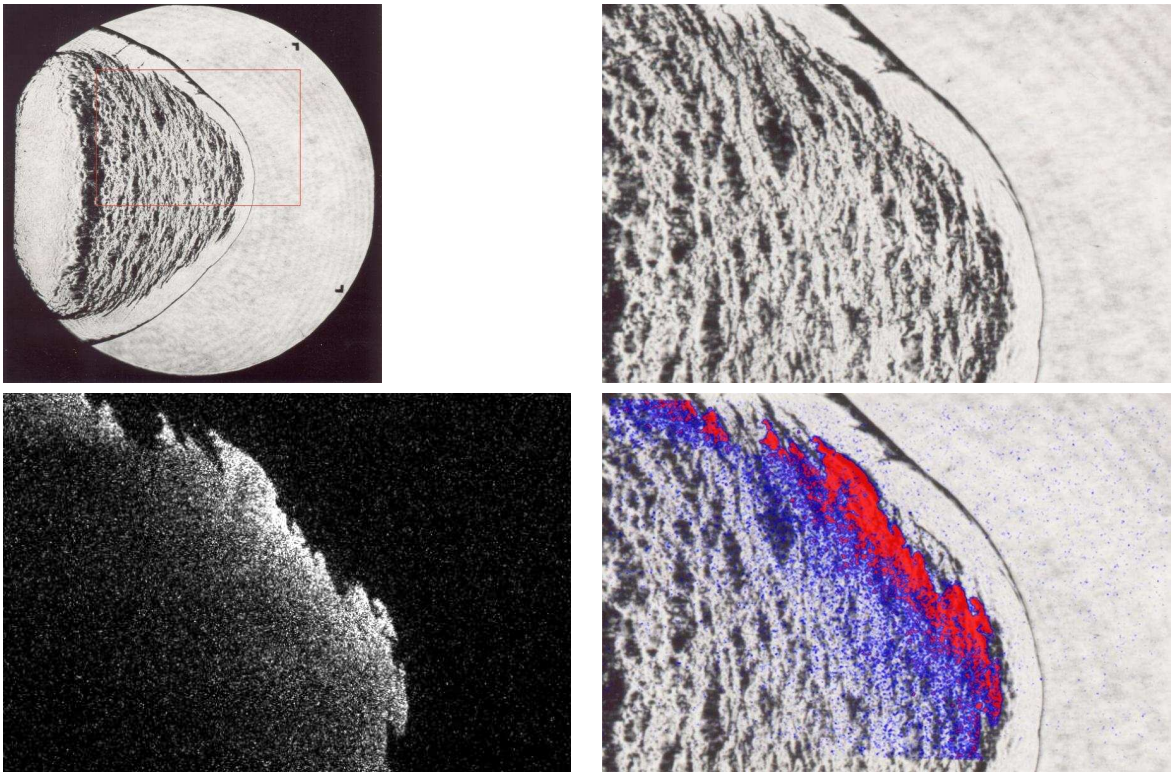

Figure M.23: Shot 39, 0.227 H_2 + 0.113 O_2 + 0.66 Ar, P_0=100 kPa, T_0=295 K. Delays: Δt(P3-PLIF) 232.167 μs; Δt(TEP-PLIF) 61.08 μs. Schlieren image height 150 mm, PLIF image height 50 mm.

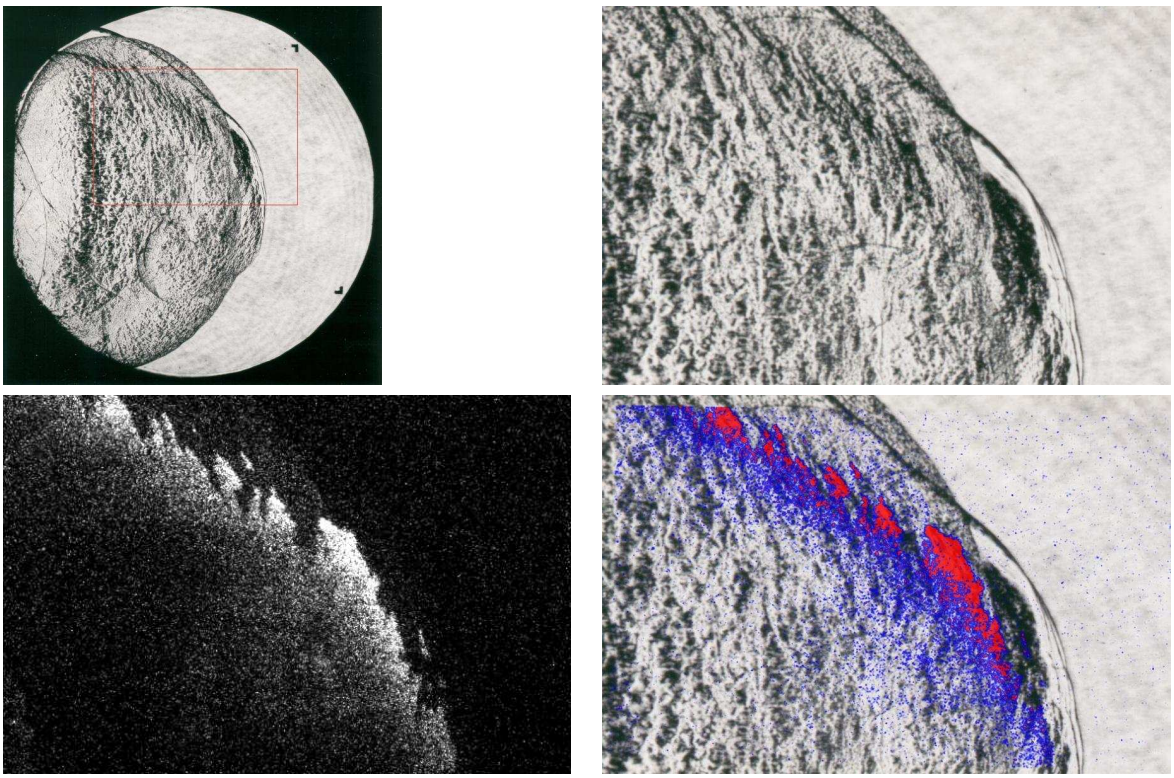

Figure M.24: Shot 40, 0.227 H_2 + 0.113 O_2 + 0.66 Ar, P_0=100 kPa, T_0=295 K. Delays: Δt(P3-PLIF) 232.167 μs; Δt(TEP-PLIF) 61.08 μs. Schlieren image height 150 mm, PLIF image height 50 mm.

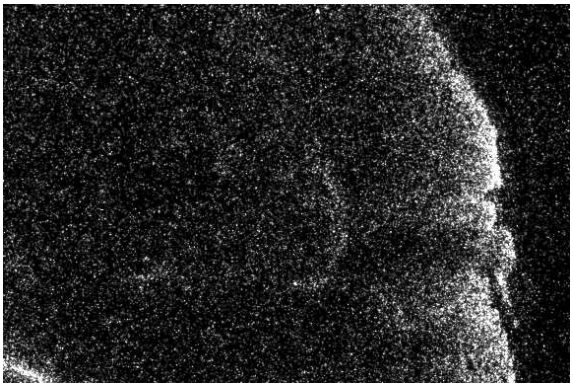

Figure M.25: Shot 41, 0.233 H_2 + 0.117 O_2 + 0.65 Ar, P_0=100 kPa, T_0=296 K. Delays: Δt(P3-PLIF) 232.167 μs; Δt(TEP-PLIF) 62.22 μs. PLIF image height 50 mm.

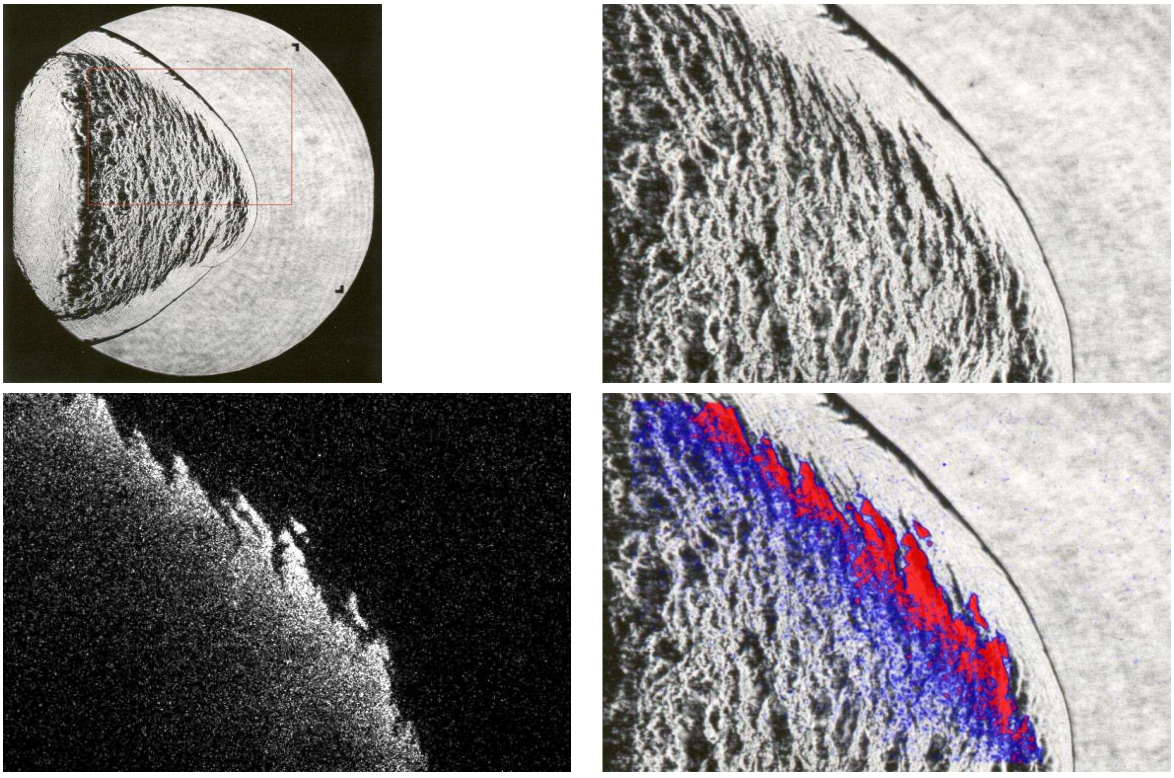

Figure M.26: Shot 42, 0.227 H_2 + 0.113 O_2 + 0.66 Ar, P_0=100 kPa, T_0=296 K. Delays: Δt(P3-PLIF) 232.167 μs; Δt(TEP-PLIF) 61.08 μs. Schlieren image height 150 mm, PLIF image height 50 mm.

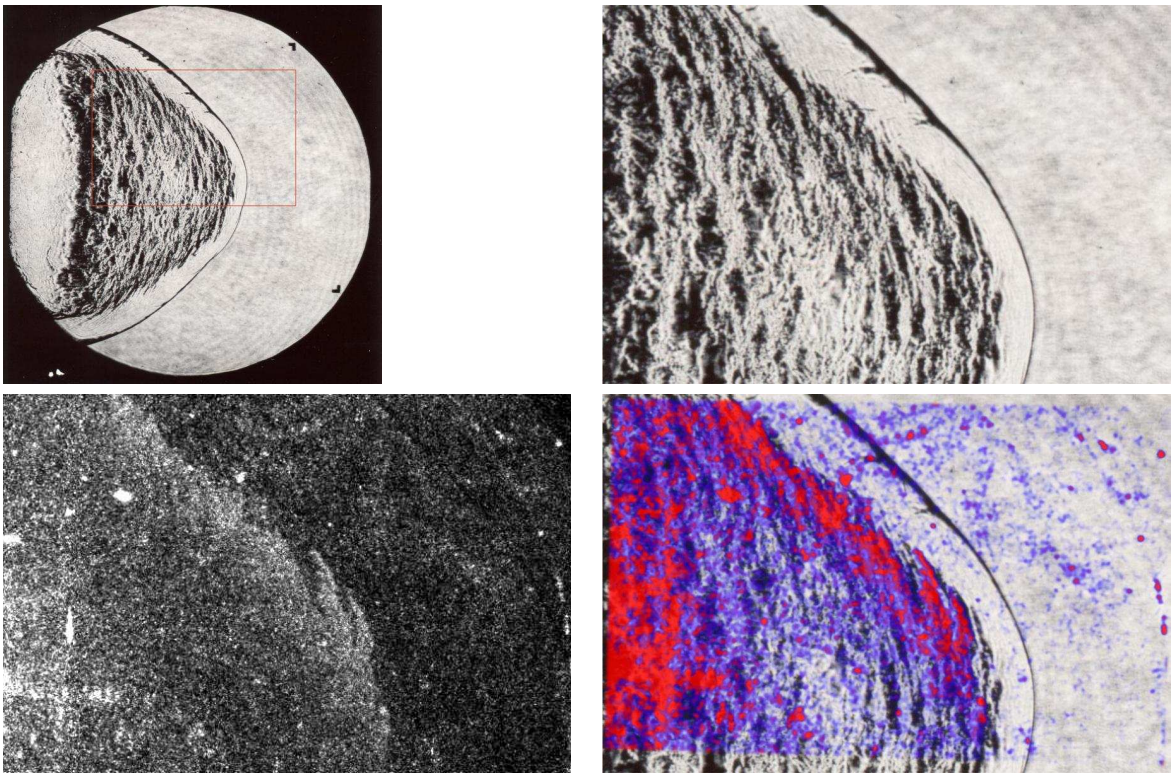

Figure M.27: Shot 43, 0.227 H_2 + 0.113 O_2 + 0.66 Ar, P_0=100 kPa, T_0=296 K. Delays: Δt(P3-PLIF) 232.167 μs; Δt(TEP-PLIF) 61.08 μs. Schlieren image height 150 mm, PLIF image height 50 mm.

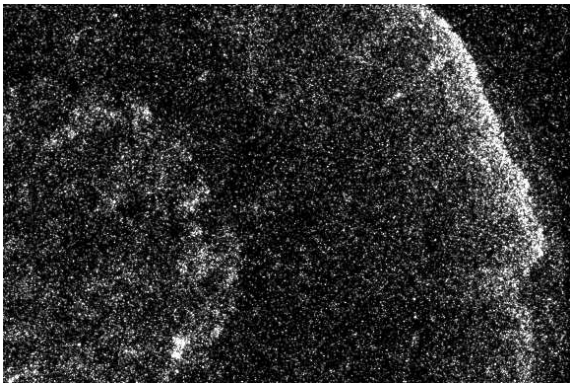

Figure M.28: Shot 44, 0.233 H_2 + 0.117 O_2 + 0.65 Ar, P_0=100 kPa, T_0=296 K. Delays: Δt(P3-PLIF) 232.167 μs; Δt(TEP-PLIF) 62.22 μs. Chemiluminescence image 1 height 50 mm.

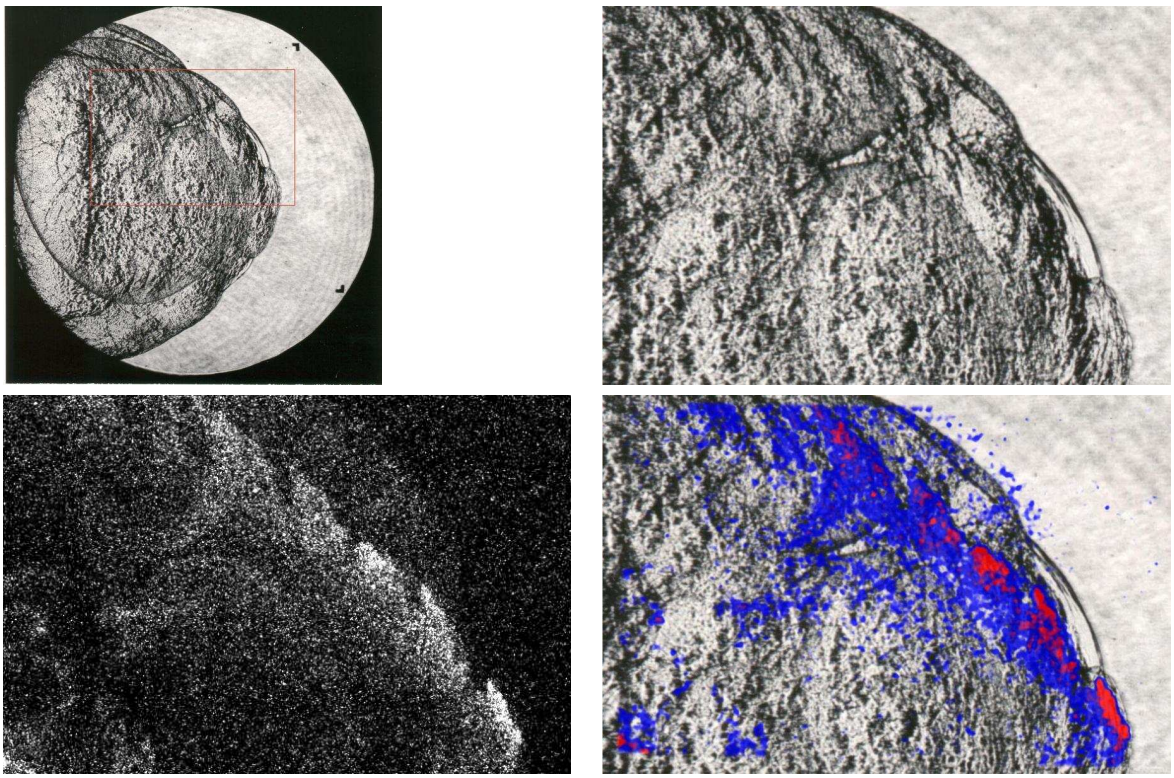

Figure M.29: Shot 45, 0.23 H_2 + 0.115 O_2 + 0.655 Ar, P_0=100 kPa, T_0=296 K. Delays: Δt(P3-PLIF) 232.167 μs; Δt(TEP-PLIF) 61.66 μs. Schlieren image height 150 mm, PLIF image height 50 mm.

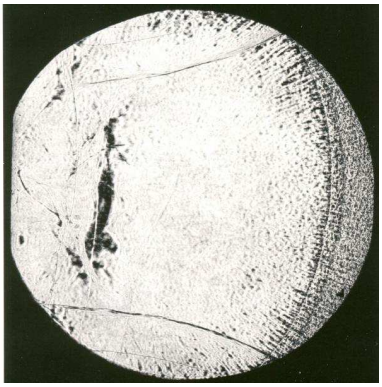

Figure M.30: Shot 49, 0.54 H_2 + 0.27 O_2 + 0.19 N_2, P_0=100 kPa, T_0=295 K. Delays: Δt(P3-schl) 182.22 μs; Δt(TEP-schl) 62.52 μs. Schlieren image height 150 mm.

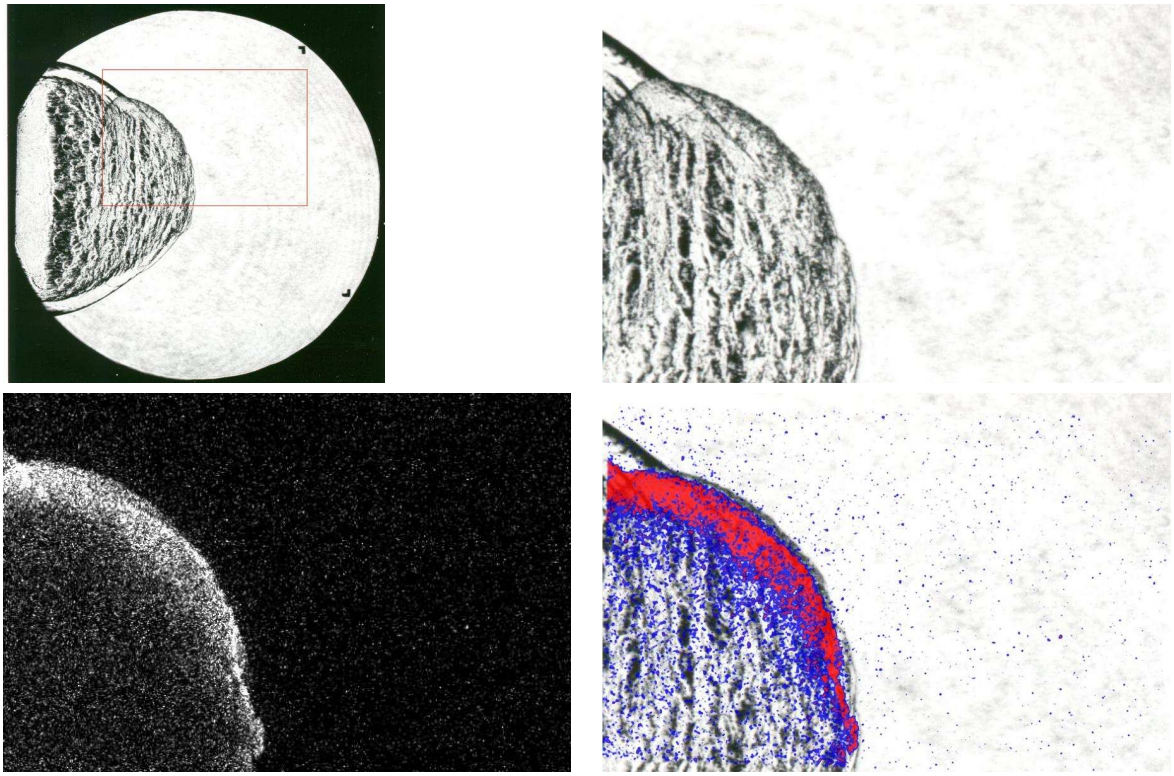

Figure M.31: Shot 50, 0.527 H_2 + 0.263 O_2 + 0.21 N_2, P_0=100 kPa, T_0=295 K. Delays: Δt(P3-PLIF) 150.167 μs; Δt(TEP-PLIF) 28.95 μs. Schlieren image height 150 mm, Chemiluminescence image 1 height 50 mm.

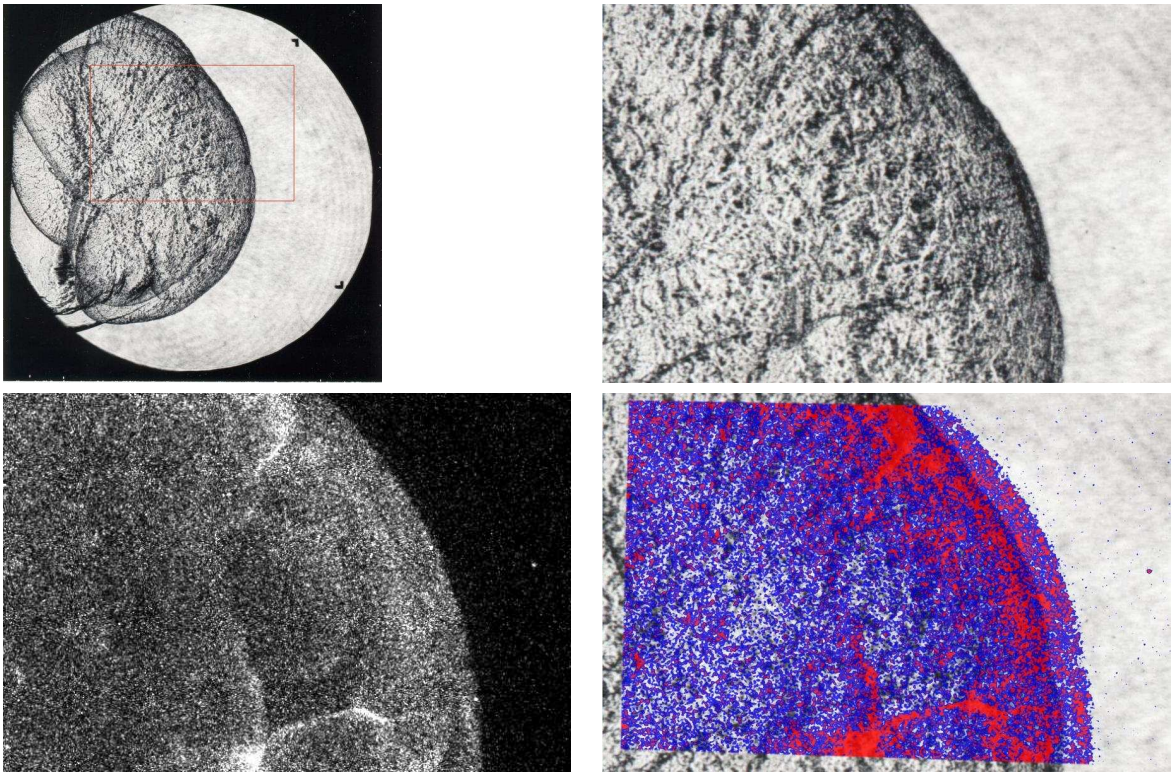

Figure M.32: Shot 51, 0.527 H_2 + 0.263 O_2 + 0.21 N_2, P_0=100 kPa, T_0=295 K. Delays: Δt(P3-PLIF) 160.167 μs; Δt(TEP-PLIF) 38.95 μs. Schlieren image height 150 mm, Chemiluminescence image 1 height 50 mm.

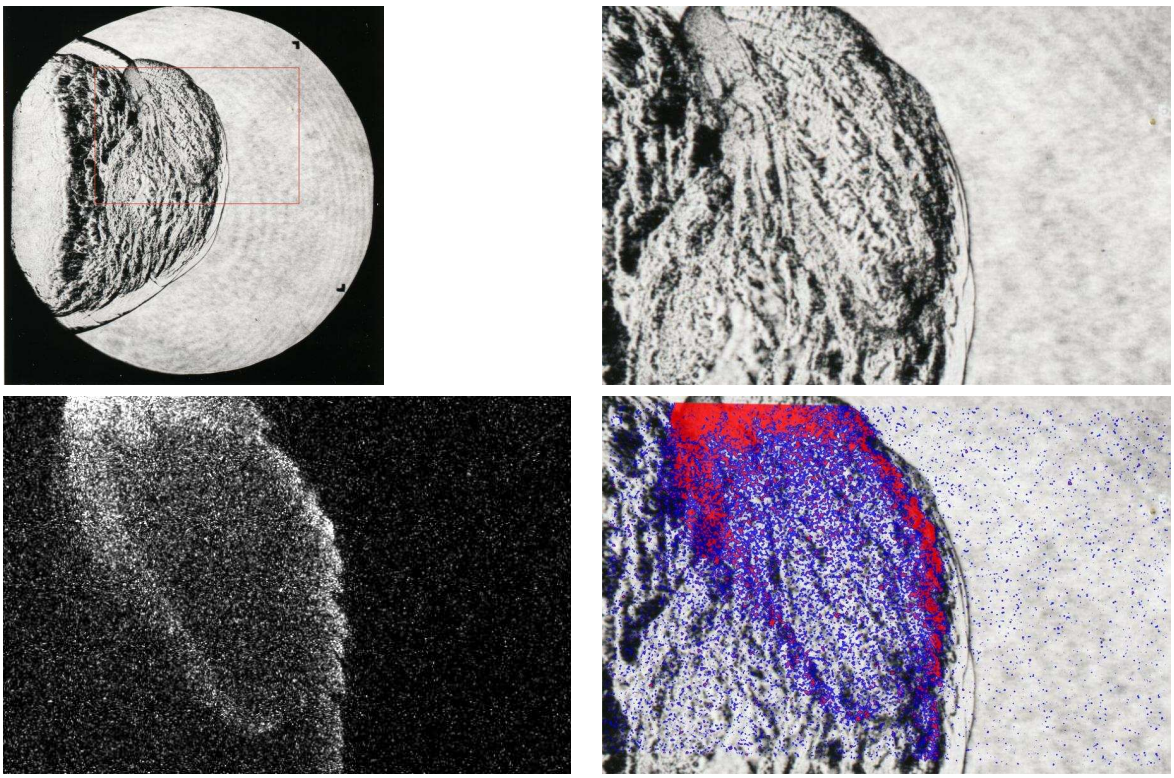

Figure M.33: Shot 52, 0.52 H_2 + 0.26 O_2 + 0.22 N_2, P_0=100 kPa, T_0=296 K. Delays: Δt(P3-PLIF) 160.167 μs; Δt(TEP-PLIF) 38.19 μs. Schlieren image height 150 mm, PLIF image height 50 mm.

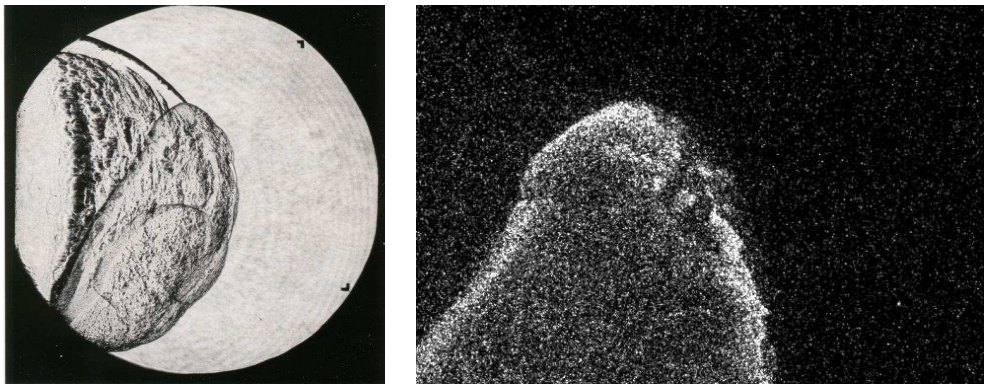

Figure M.34: Shot 53, 0.52 H_2 + 0.26 O_2 + 0.22 N_2, P_0=100 kPa, T_0=295 K. Delays: Δt(P3-schl) 160.22 μs; Δt(TEP-schl) 38.24 μs. Delays: Δt(P3-chem) 7.21 μs; Δt(TEP-chem) -114.77 μs. Schlieren image height 150 mm, PLIF image height 50 mm.

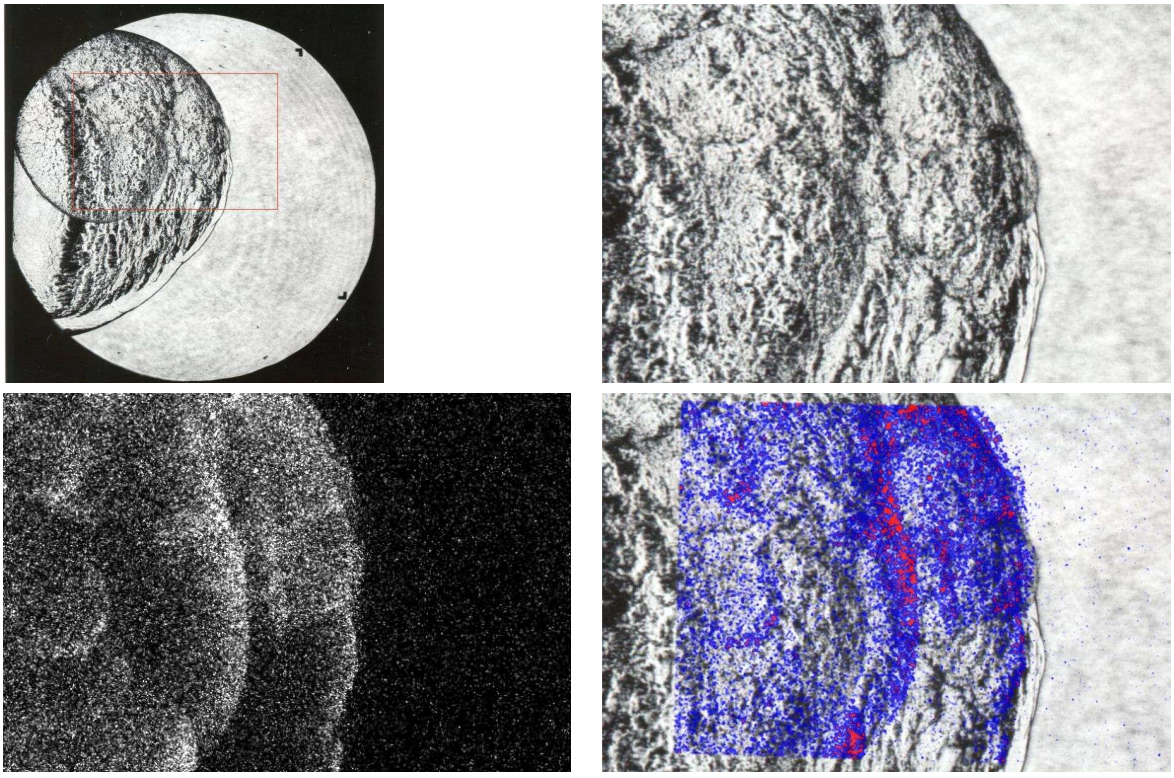

Figure M.35: Shot 54, 0.507 H_2 + 0.253 O_2 + 0.24 N_2, P_0=100 kPa, T_0=297 K. Delays: Δt(P3-PLIF) 160.167 μs; Δt(TEP-PLIF) 36.65 μs. Schlieren image height 150 mm, Chemiluminescence image 1 height 50 mm.

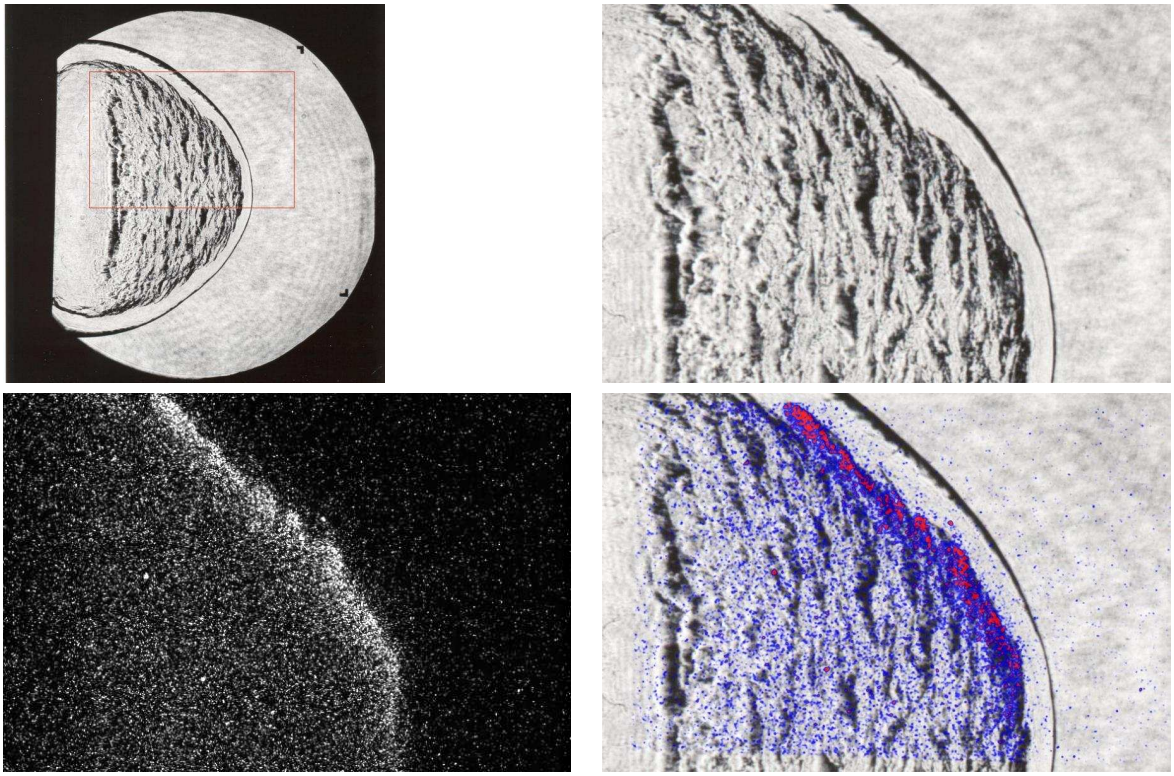

Figure M.36: Shot 55, 0.507 H_2 + 0.253 O_2 + 0.24 N_2, P_0=100 kPa, T_0=294 K. Delays: Δt(P3-PLIF) 160.167 μs; Δt(TEP-PLIF) 36.65 μs. Schlieren image height 150 mm, PLIF image height 50 mm.

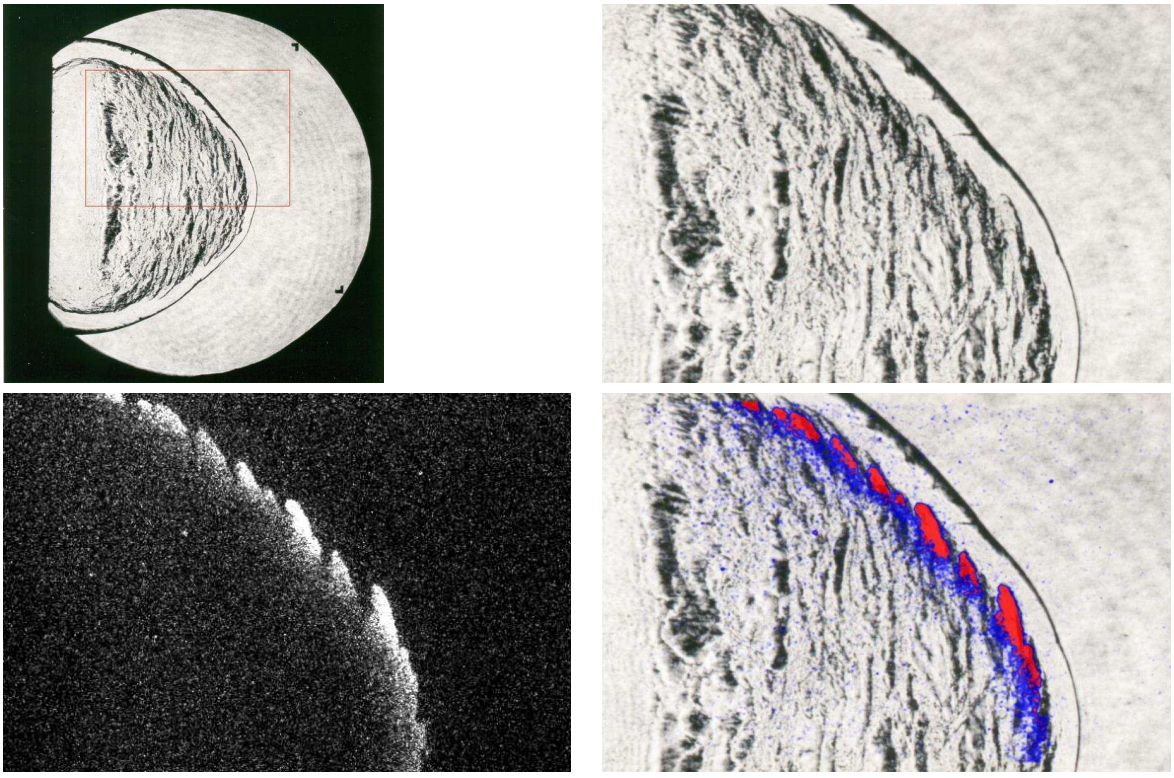

Figure M.37: Shot 56, 0.507 H_2 + 0.253 O_2 + 0.24 N_2, P_0=100 kPa, T_0=295 K. Delays: Δt(P3-PLIF) 160.167 μs; Δt(TEP-PLIF) 36.65 μs. Schlieren image height 150 mm, PLIF image height 50 mm.

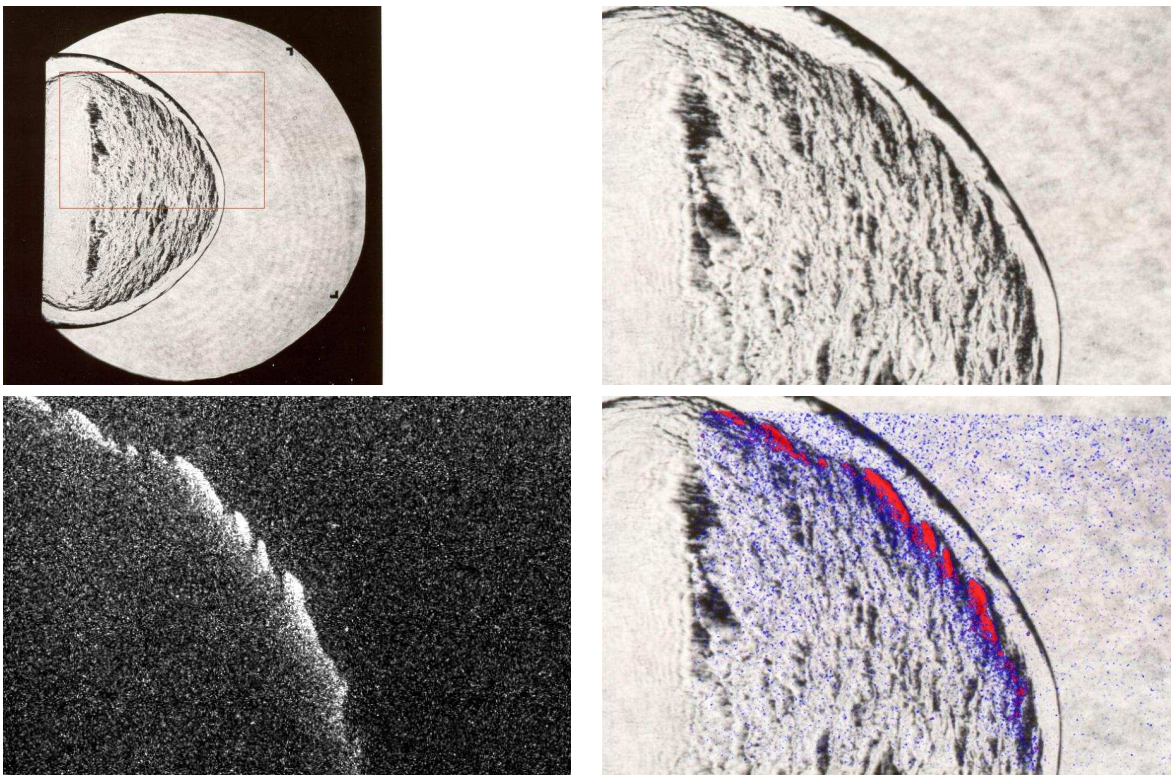

Figure M.38: Shot 57, 0.507 H_2 + 0.253 O_2 + 0.24 N_2, P_0=100 kPa, T_0=296 K. Delays: Δt(P3-PLIF) 155.167 μs; Δt(TEP-PLIF) 31.65 μs. Schlieren image height 150 mm, PLIF image height 50 mm.

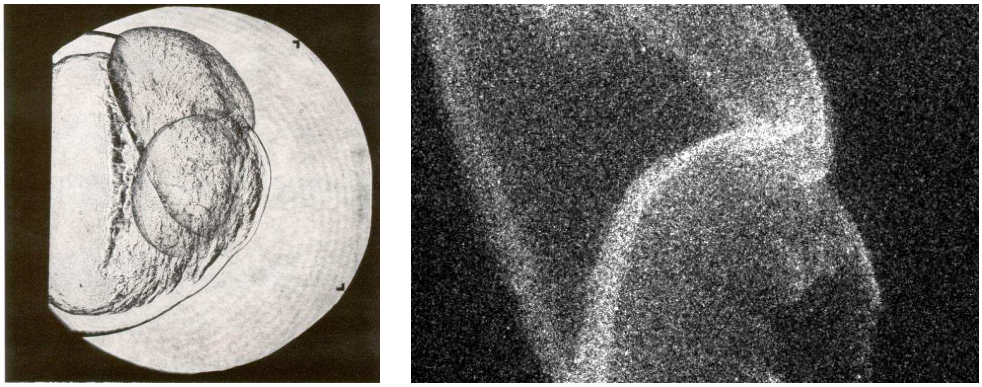

Figure M.39: Shot 58, 0.52 H_2 + 0.26 O_2 + 0.22 N_2, P_0=100 kPa, T_0=296 K. Delays: Δt(P3-schl) 160.19 μs; Δt(TEP-schl) 38.21 μs. Delays: Δt(P3-chem) 7.21 μs; Δt(TEP-chem) -114.77 μs. Schlieren image height 150 mm, Chemiluminescence image 1 height 50 mm.

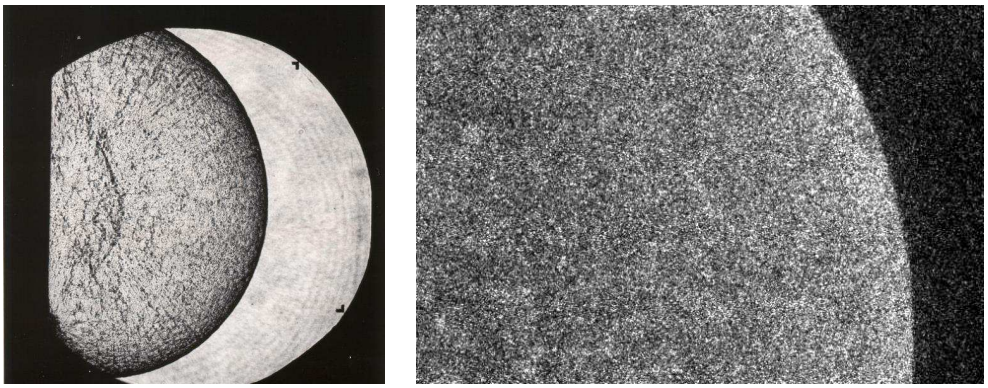

Figure M.40: Shot 59, 0.5 H_2 + 0.5 N_2O, P_0=70 kPa, T_0=296 K. Delays: Δt(P3-schl) 160.19 μs; Δt(TEP-schl) 34.85 μs. Delays: Δt(P3-chem) 7.21 μs; Δt(TEP-chem) -118.13 μs. Schlieren image height 150 mm, Chemiluminescence image 1 height 150 mm.

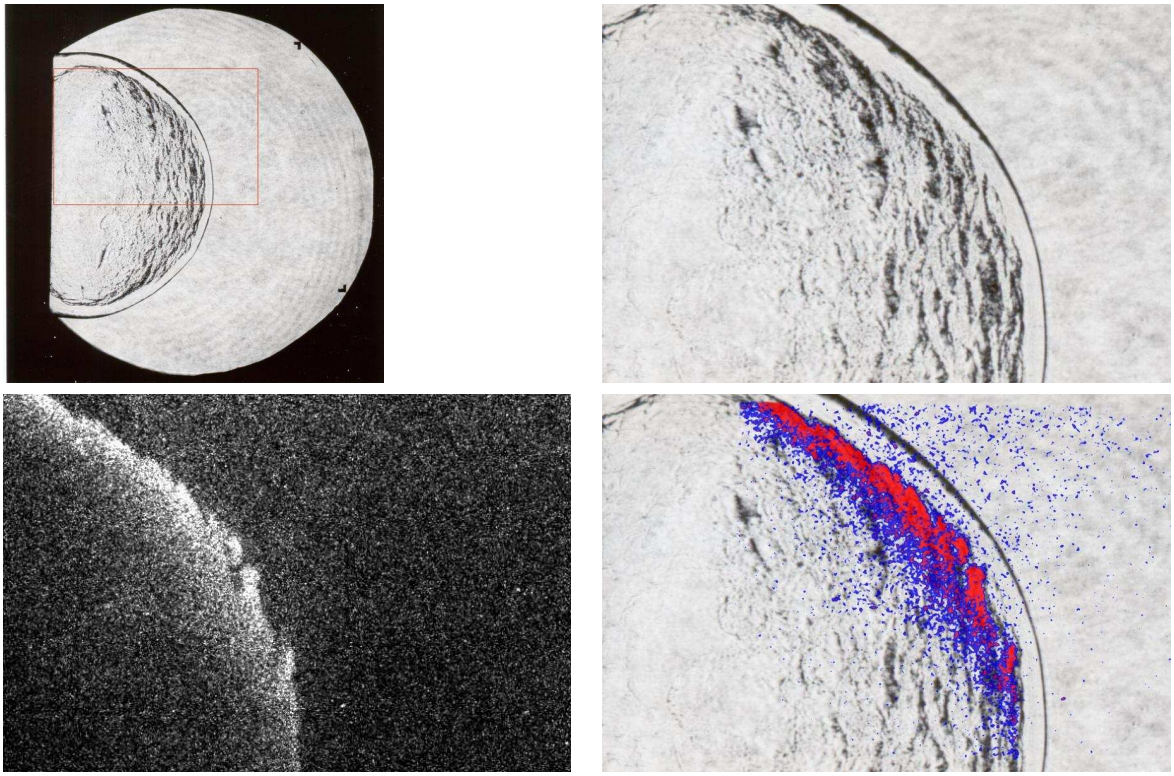

Figure M.41: Shot 60, 0.5 H_2 + 0.5 N_2O, P_0=40 kPa, T_0=296 K. Delays: Δt(P3-PLIF) 160.167 μs; Δt(TEP-PLIF) 33.54 μs. Schlieren image height 150 mm, PLIF image height 50 mm.

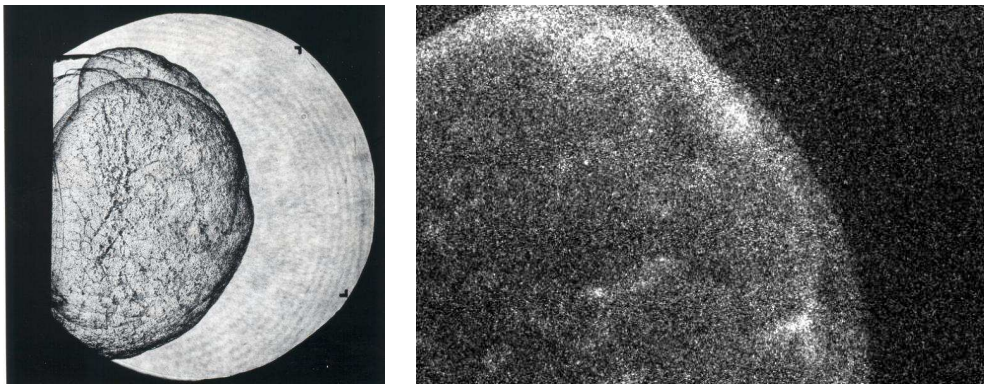

Figure M.42: Shot 61, 0.5 H_2 + 0.5 N_2O, P_0=55 kPa, T_0=296 K. Delays: Δt(P3-schl) 161.22 μs; Δt(TEP-schl) 35.33 μs. Delays: Δt(P3-chem) 7.21 μs; Δt(TEP-chem) -118.68 μs. Schlieren image height 150 mm, Chemiluminescence image 1 height 50 mm.

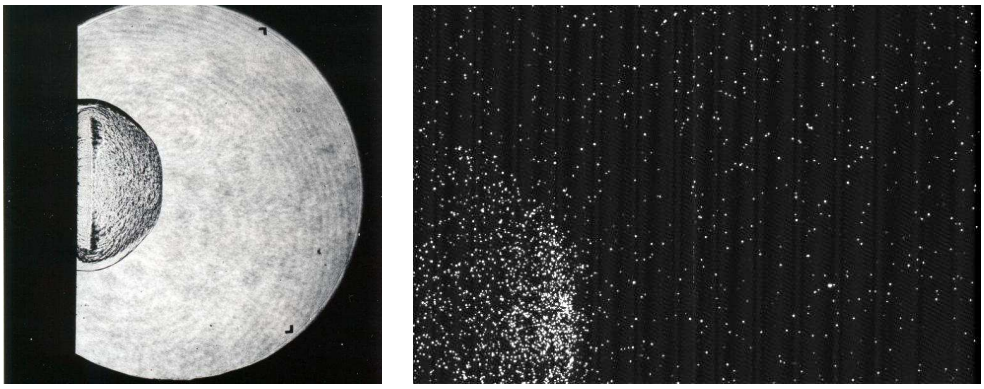

Figure M.43: Shot 64, 0.2 H_2 + 0.1 O_2 + 0.7 Ar, P_0=100 kPa, T_0=294 K. Delays: Δt(P3-schl) 191.26 μs; Δt(TEP-schl) 15.30 μs. Delays: Δt(P3-chem) 7.21 μs; Δt(TEP-chem) -168.75 μs. Schlieren image height 150 mm, Chemiluminescence image 1 height 50 mm.

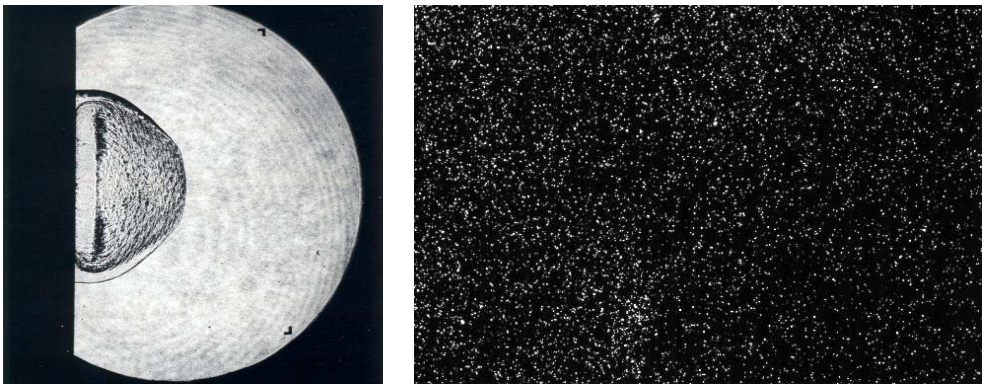

Figure M.44: Shot 65, 0.2 H_2 + 0.1 O_2 + 0.7 Ar, P_0=100 kPa, T_0=295 K. Delays: Δt(P3-schl) 197.28 μs; Δt(TEP-schl) 21.32 μs. Delays: Δt(P3-chem) 7.21 μs; Δt(TEP-chem) -168.75 μs. Schlieren image height 150 mm, Chemiluminescence image 1 height 50 mm.

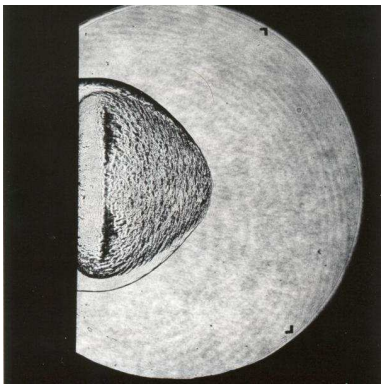

Figure M.45: Shot 66, 0.2 H_2 + 0.1 O_2 + 0.7 Ar, P_0=100 kPa, T_0=294 K. Delays: Δt(P3-schl) 203.23 μs; Δt(TEP-schl) 27.27 μs. Schlieren image height 150 mm.

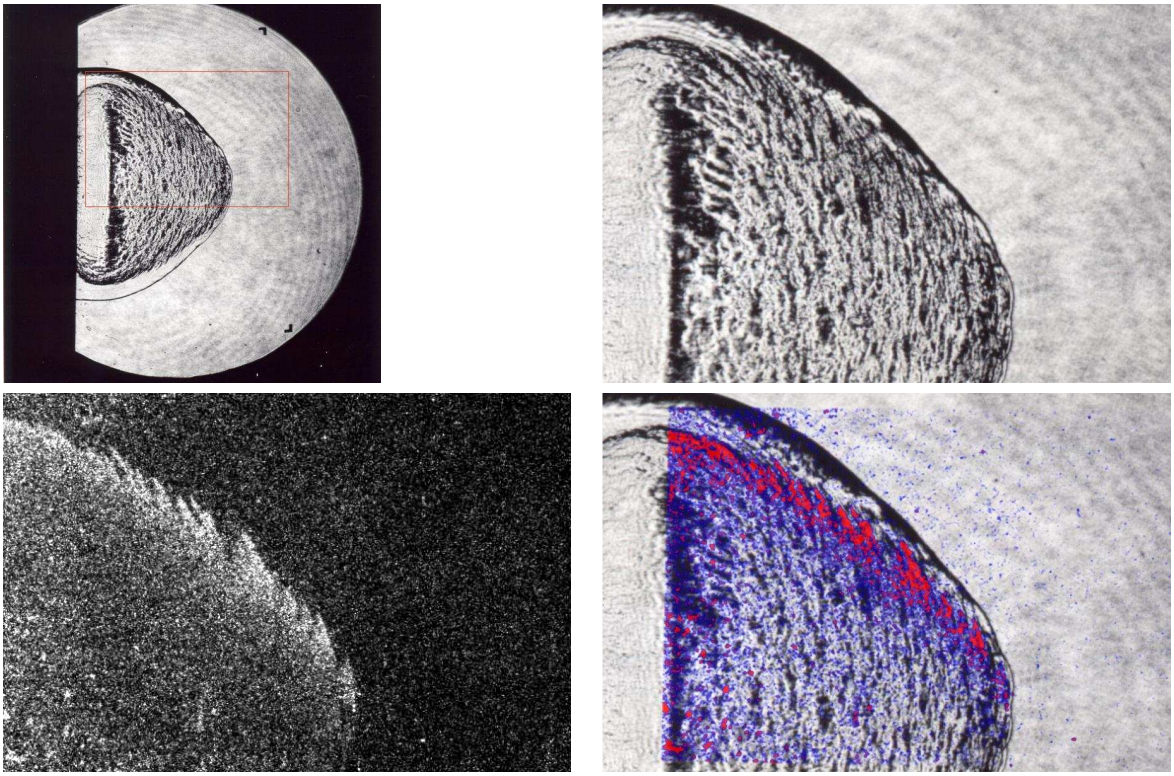

Figure M.46: Shot 67, 0.2 H_2 + 0.1 O_2 + 0.7 Ar, P_0=100 kPa, T_0=295 K. Delays: Δt(P3-PLIF) 208.167 μs; Δt(TEP-PLIF) 32.21 μs. Schlieren image height 150 mm, PLIF image height 50 mm.

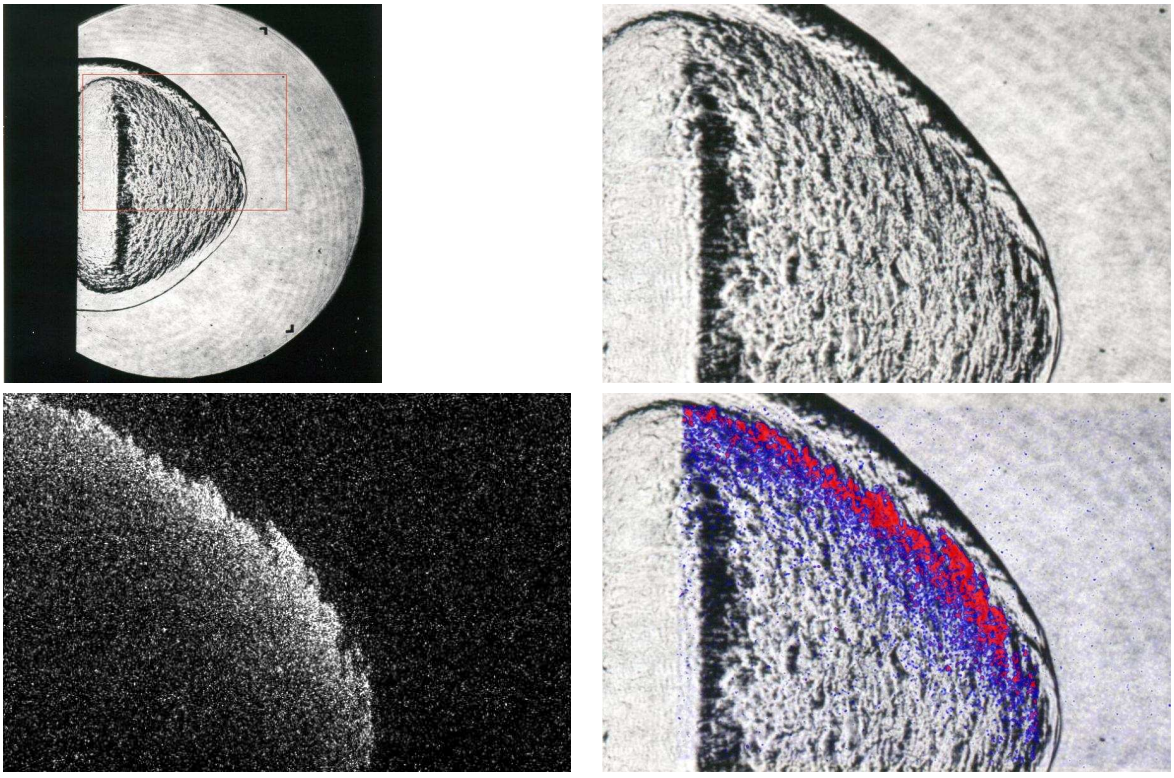

Figure M.47: Shot 68, 0.2 H_2 + 0.1 O_2 + 0.7 Ar, P_0=100 kPa, T_0=295 K. Delays: Δt(P3-PLIF) 214.167 μs; Δt(TEP-PLIF) 38.21 μs. Schlieren image height 150 mm, PLIF image height 50 mm.

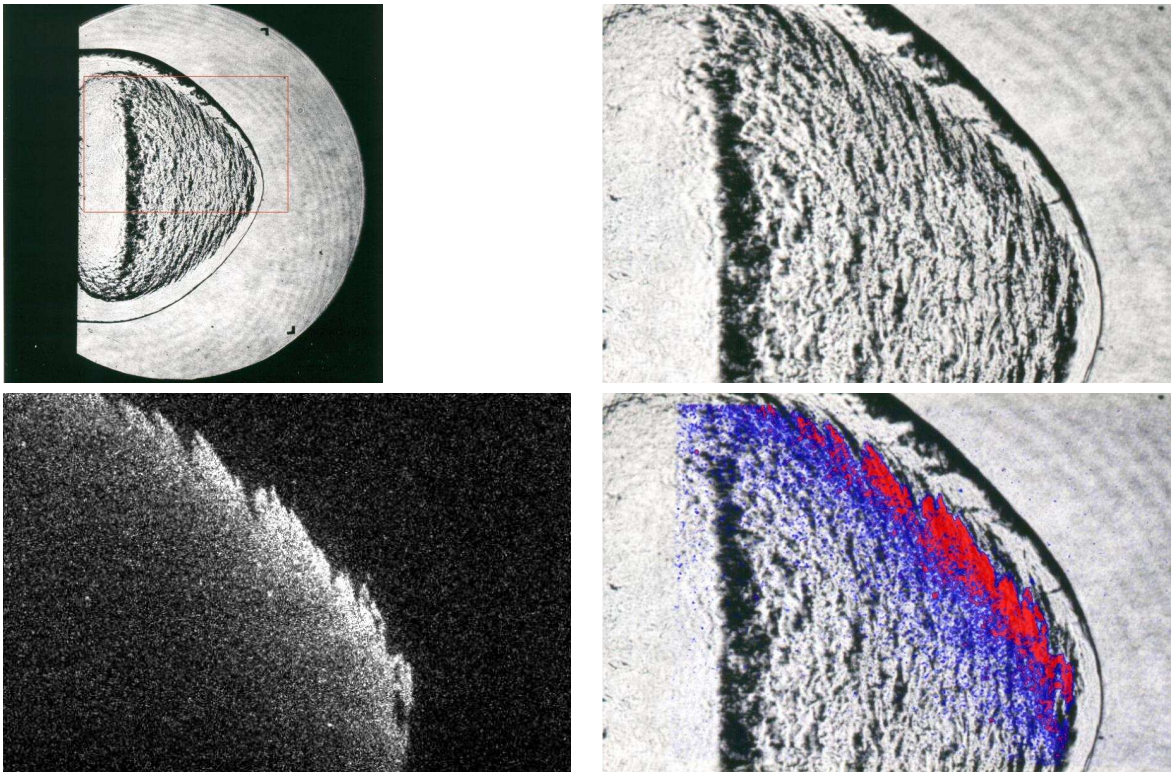

Figure M.48: Shot 69, 0.2 H_2 + 0.1 O_2 + 0.7 Ar, P_0=100 kPa, T_0=295 K. Delays: Δt(P3-PLIF) 220.167 μs; Δt(TEP-PLIF) 44.21 μs. Schlieren image height 150 mm, PLIF image height 50 mm.

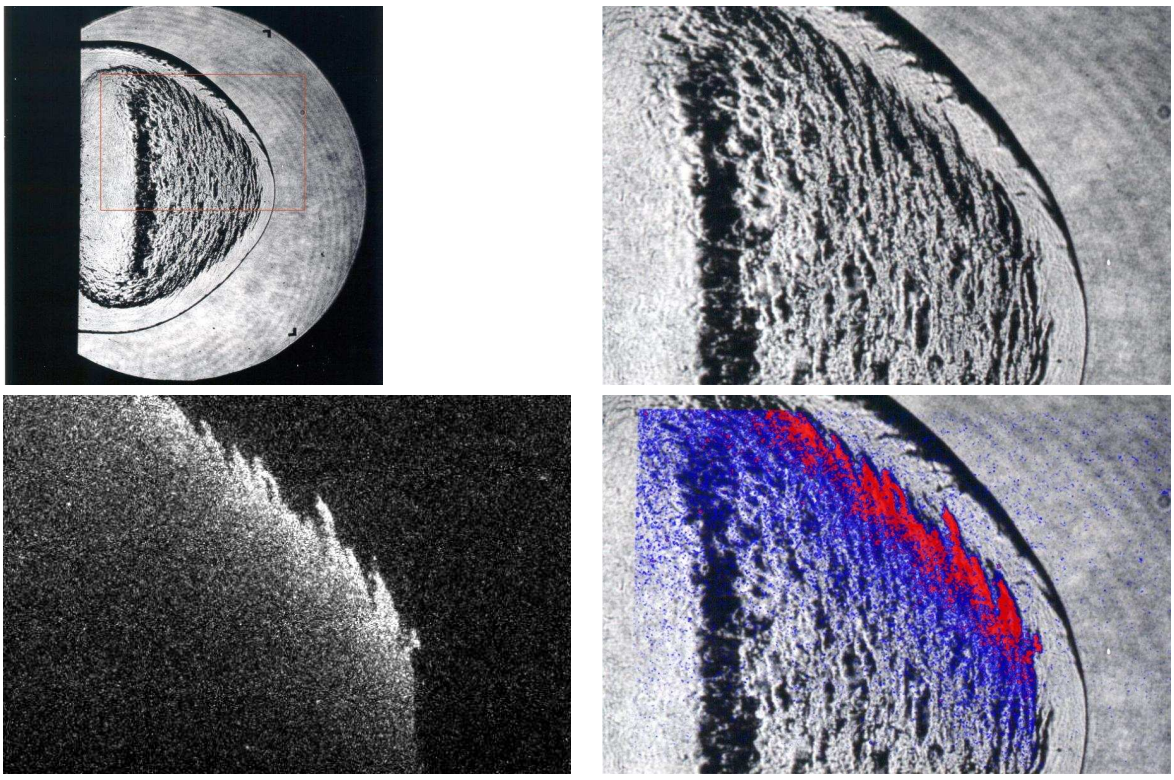

Figure M.49: Shot 70, 0.2 H_2 + 0.1 O_2 + 0.7 Ar, P_0=100 kPa, T_0=296 K. Delays: Δt(P3-PLIF) 226.167 μs; Δt(TEP-PLIF) 50.21 μs. Schlieren image height 150 mm, PLIF image height 50 mm.

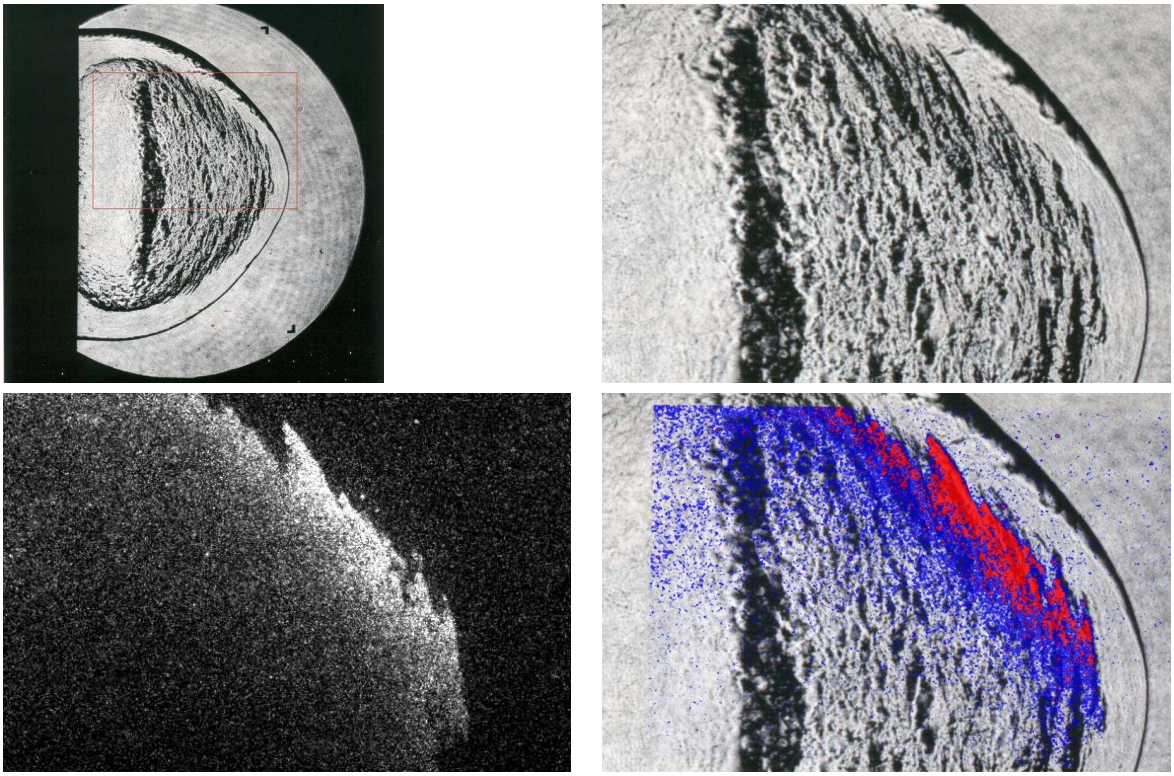

Figure M.50: Shot 71, 0.2 H_2 + 0.1 O_2 + 0.7 Ar, P_0=100 kPa, T_0=296 K. Delays: Δt(P3-PLIF) 232.167 μs; Δt(TEP-PLIF) 56.21 μs. Schlieren image height 150 mm, PLIF image height 50 mm.

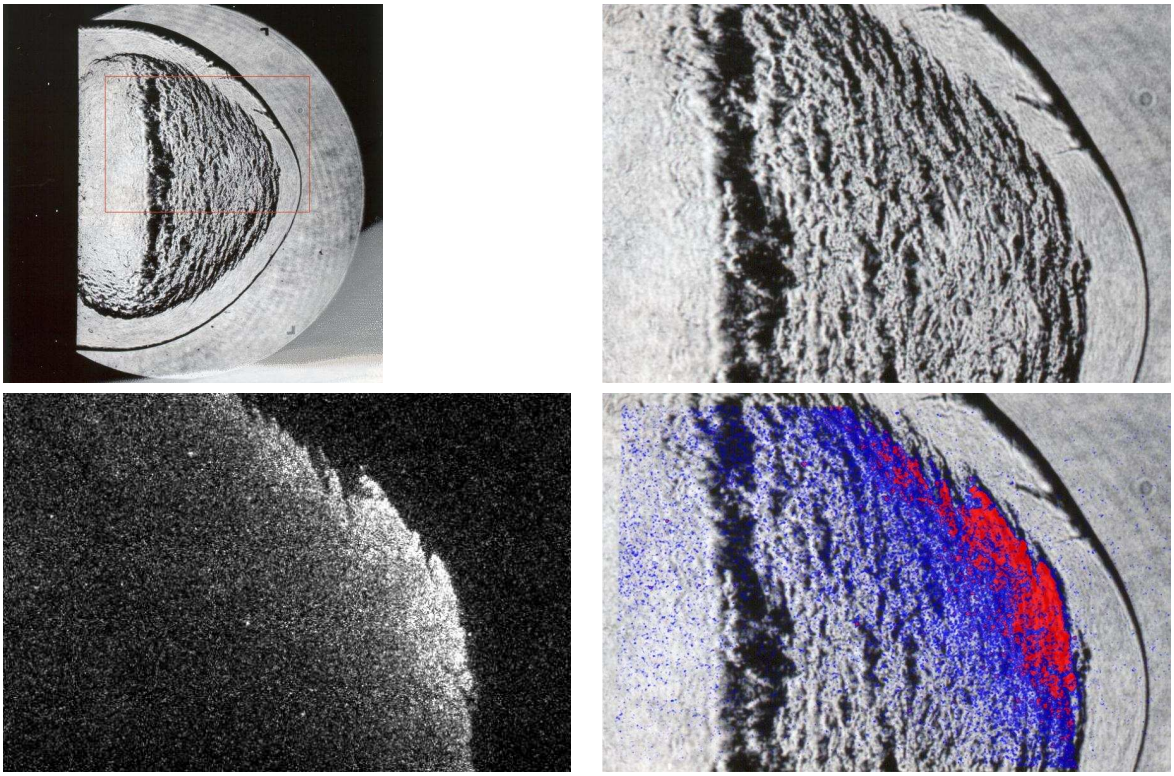

Figure M.51: Shot 72, 0.2 H_2 + 0.1 O_2 + 0.7 Ar, P_0=100 kPa, T_0=296 K. Delays: Δt(P3-PLIF) 238.167 μs; Δt(TEP-PLIF) 62.21 μs. Schlieren image height 150 mm, PLIF image height 50 mm.

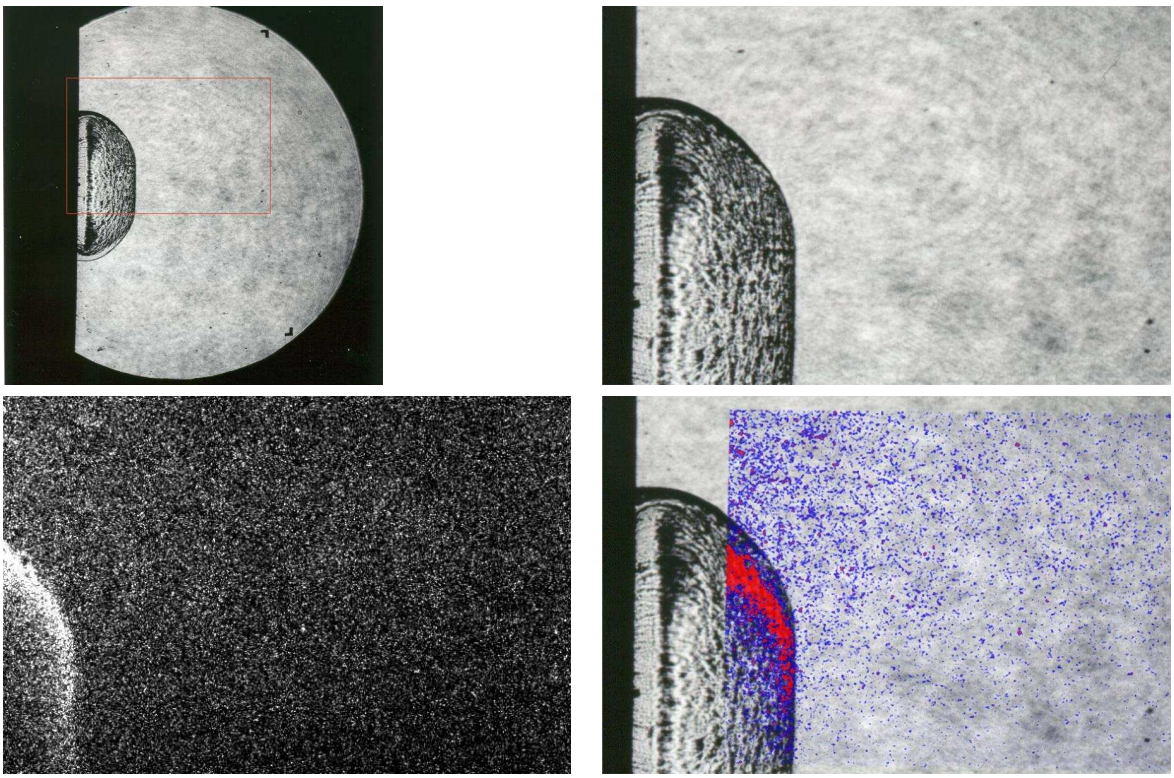

Figure M.52: Shot 73, 0.2 H_2 + 0.1 O_2 + 0.7 Ar, P_0=100 kPa, T_0=296 K. Delays: Δt(P3-PLIF) 184.167 μs; Δt(TEP-PLIF) 8.21 μs. Schlieren image height 150 mm, PLIF image height 50 mm.

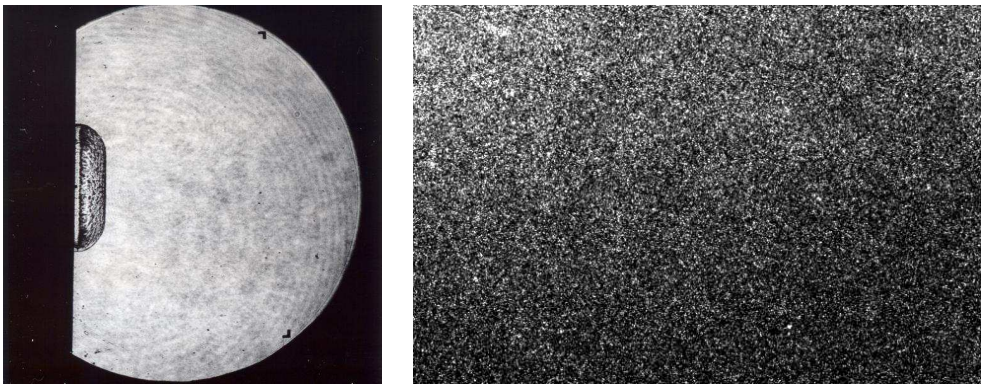

Figure M.53: Shot 74, 0.2 H_2 + 0.1 O_2 + 0.7 Ar, P_0=100 kPa, T_0=296 K. Delays: Δt(P3-schl) 178.28 μs; Δt(TEP-schl) 2.32 μs. Delays: Δt(P3-chem) 7.21 μs; Δt(TEP-chem) -168.75 μs. Schlieren image height 150 mm, PLIF image height 50 mm.

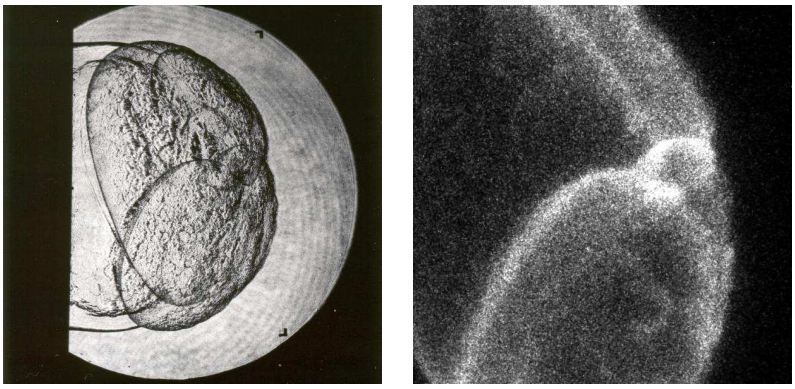

Figure M.54: Shot 75, 0.5 H_2 + 0.5 N_2O, P_0=45 kPa, T_0=294 K. Delays: Δt(P3-schl) 166.23 μs; Δt(TEP-schl) 39.88 μs. Delays: Δt(P3-chem) 7.21 μs; Δt(TEP-chem) -119.14 μs. Schlieren image height 150 mm, Chemiluminescence image 1 height 73 mm.

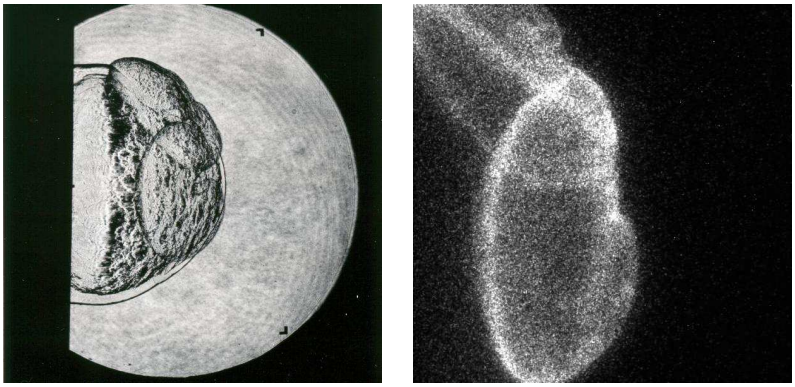

Figure M.55: Shot 76, 0.5 H_2 + 0.5 N_2O, P_0=45 kPa, T_0=295 K. Delays: Δt(P3-schl) 154.23 μs; Δt(TEP-schl) 27.88 μs. Delays: Δt(P3-chem) 7.21 μs; Δt(TEP-chem) -119.14 μs. Schlieren image height 150 mm, Chemiluminescence image 1 height 73 mm.

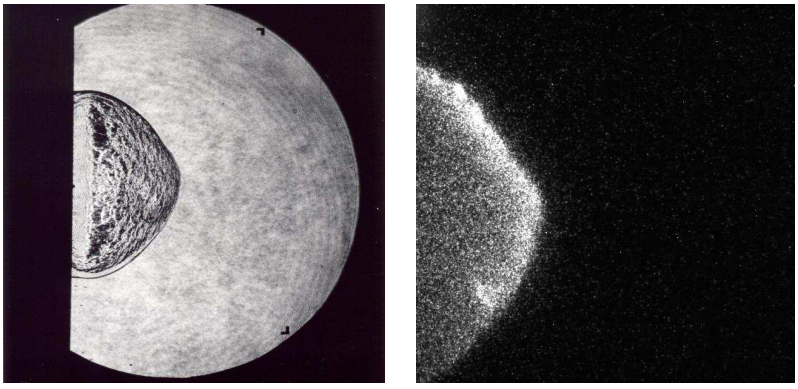

Figure M.56: Shot 77, 0.5 H_2 + 0.5 N_2O, P_0=45 kPa, T_0=295 K. Delays: Δt(P3-schl) 142.23 μs; Δt(TEP-schl) 15.88 μs. Delays: Δt(P3-chem) 7.21 μs; Δt(TEP-chem) -119.14 μs. Schlieren image height 150 mm, Chemiluminescence image 1 height 73 mm.

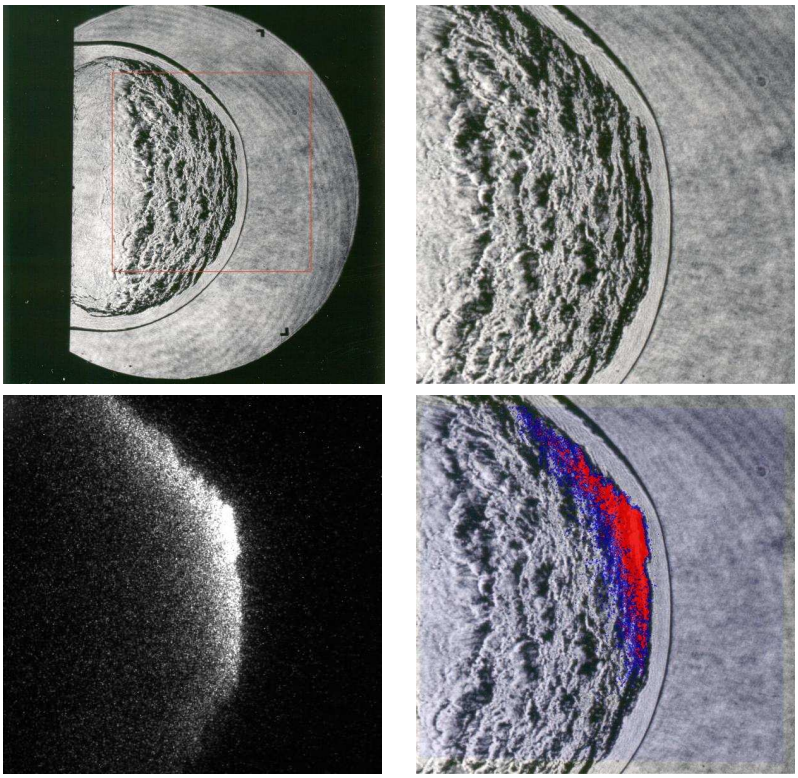

Figure M.57: Shot 78, 0.5 H_2 + 0.5 N_2O, P_0=40 kPa, T_0=295 K. Delays: Δt(P3-PLIF) 166.135 μs; Δt(TEP-PLIF) 39.51 μs. Schlieren image height 150 mm, PLIF image height 73 mm.

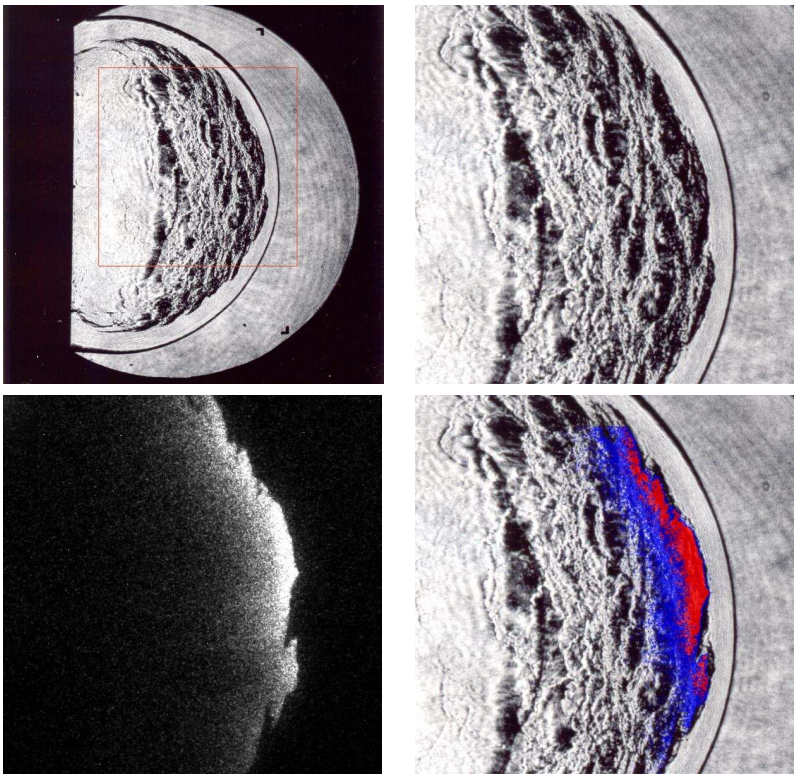

Figure M.58: Shot 79, 0.5 H_2 + 0.5 N_2O, P_0=40 kPa, T_0=295 K. Delays: Δt(P3-PLIF) 178.135 μs; Δt(TEP-PLIF) 51.51 μs. Schlieren image height 150 mm, PLIF image height 73 mm.

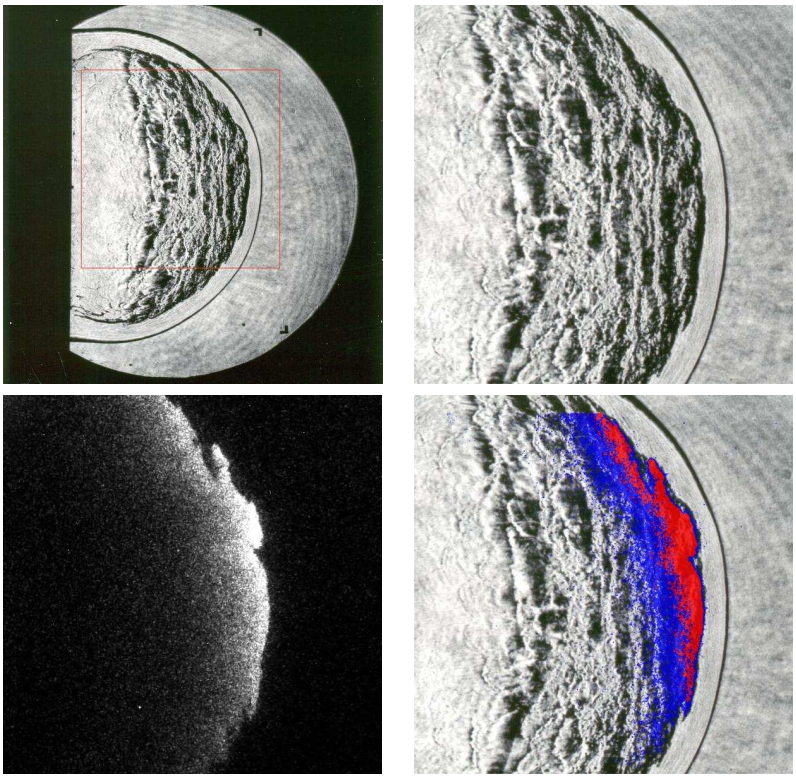

Figure M.59: Shot 80, 0.5 H_2 + 0.5 N_2O, P_0=40 kPa, T_0=296 K. Delays: Δt(P3-PLIF) 172.135 μs; Δt(TEP-PLIF) 45.51 μs. Schlieren image height 150 mm, PLIF image height 73 mm.

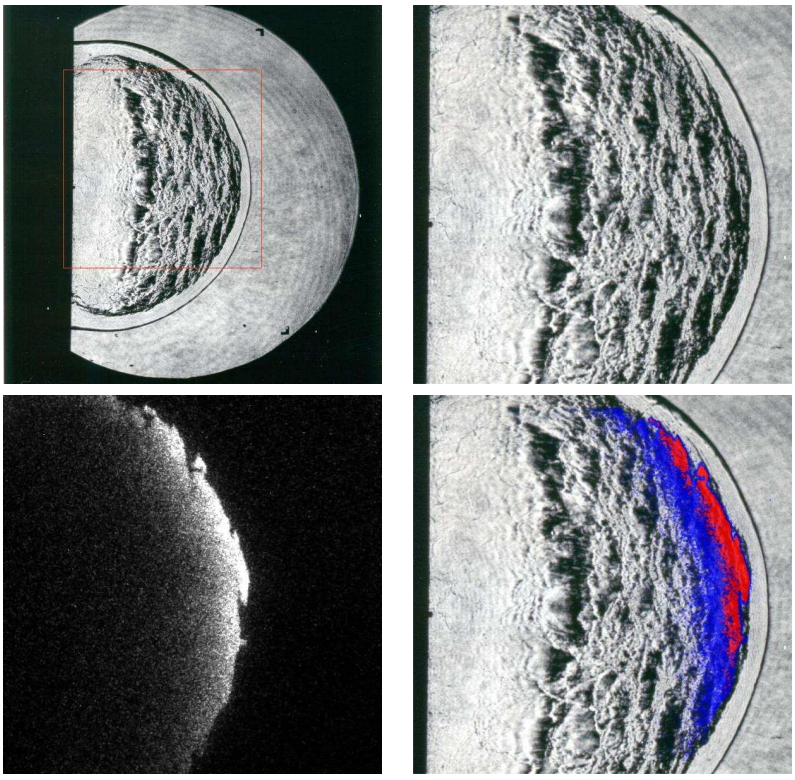

Figure M.60: Shot 81, 0.5 H_2 + 0.5 N_2O, P_0=40 kPa, T_0=296 K. Delays: Δt(P3-PLIF) 166.135 μs; Δt(TEP-PLIF) 39.51 μs. Schlieren image height 150 mm, PLIF image height 73 mm.

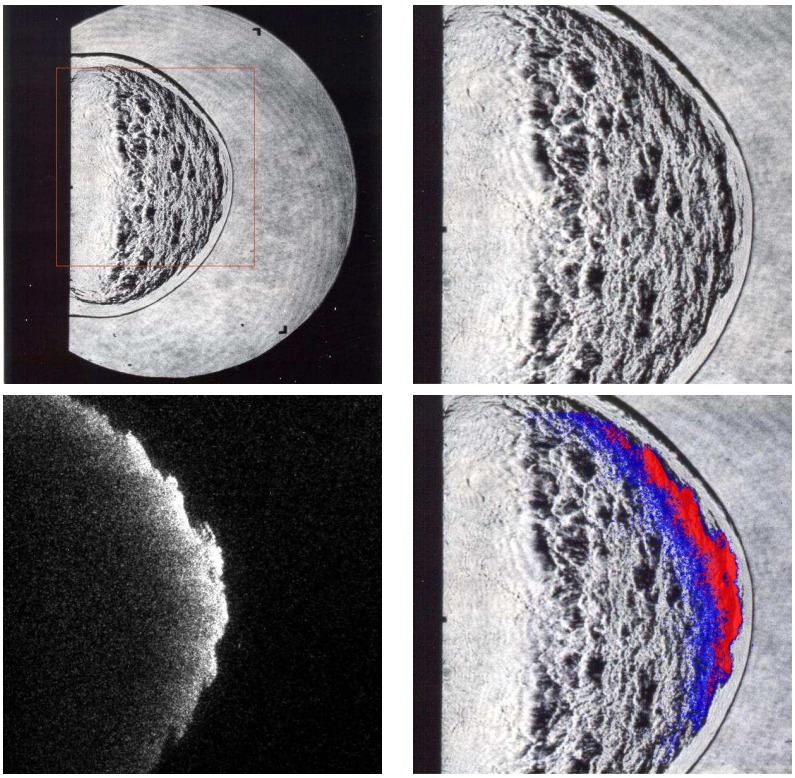

Figure M.61: Shot 82, 0.5 H_2 + 0.5 N_2O, P_0=40 kPa, T_0=296 K. Delays: Δt(P3-PLIF) 160.135 μs; Δt(TEP-PLIF) 33.51 μs. Schlieren image height 150 mm, PLIF image height 73 mm.

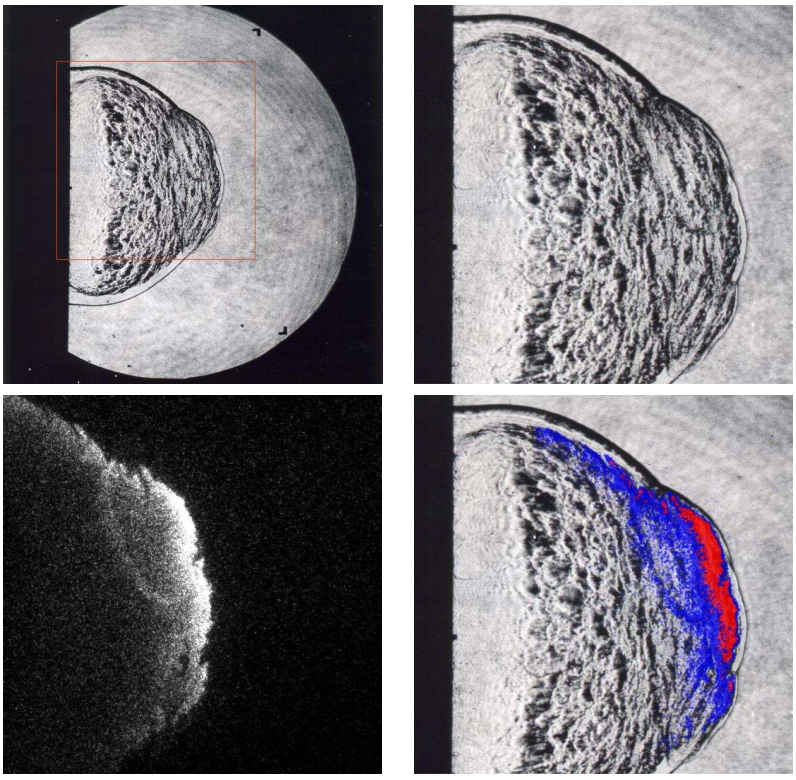

Figure M.62: Shot 83, 0.5 H_2 + 0.5 N_2O, P_0=40 kPa, T_0=296 K. Delays: Δt(P3-PLIF) 154.135 μs; Δt(TEP-PLIF) 27.51 μs. Schlieren image height 150 mm, PLIF image height 73 mm.

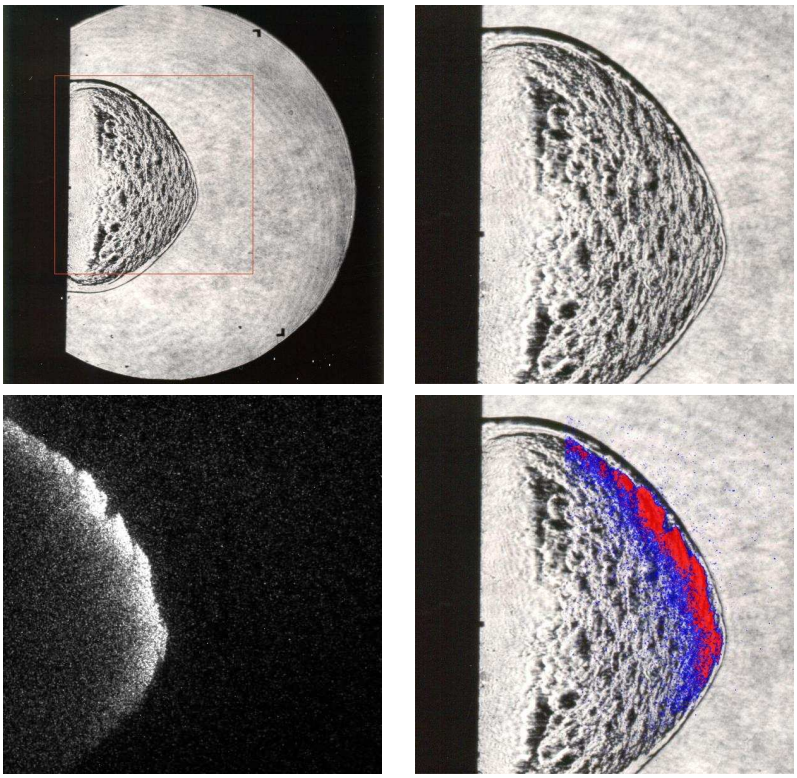

Figure M.63: Shot 84, 0.5 H_2 + 0.5 N_2O, P_0=40 kPa, T_0=296 K. Delays: Δt(P3-PLIF) 148.135 μs; Δt(TEP-PLIF) 21.51 μs. Schlieren image height 150 mm, PLIF image height 73 mm.

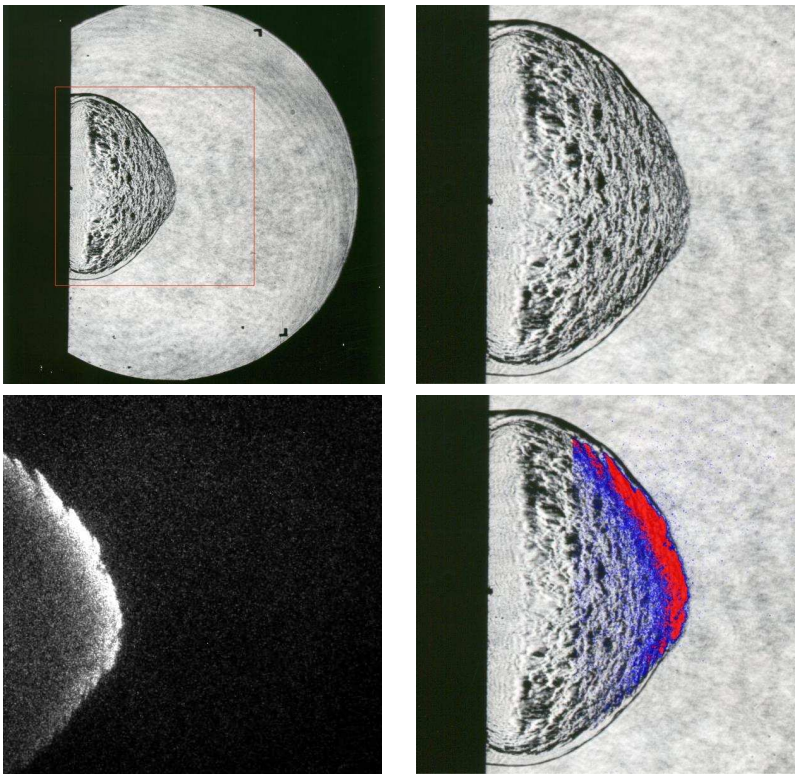

Figure M.64: Shot 85, 0.5 H_2 + 0.5 N_2O, P_0=40 kPa, T_0=296 K. Delays: Δt(P3-PLIF) 142.135 μs; Δt(TEP-PLIF) 15.51 μs. Schlieren image height 150 mm, PLIF image height 73 mm.

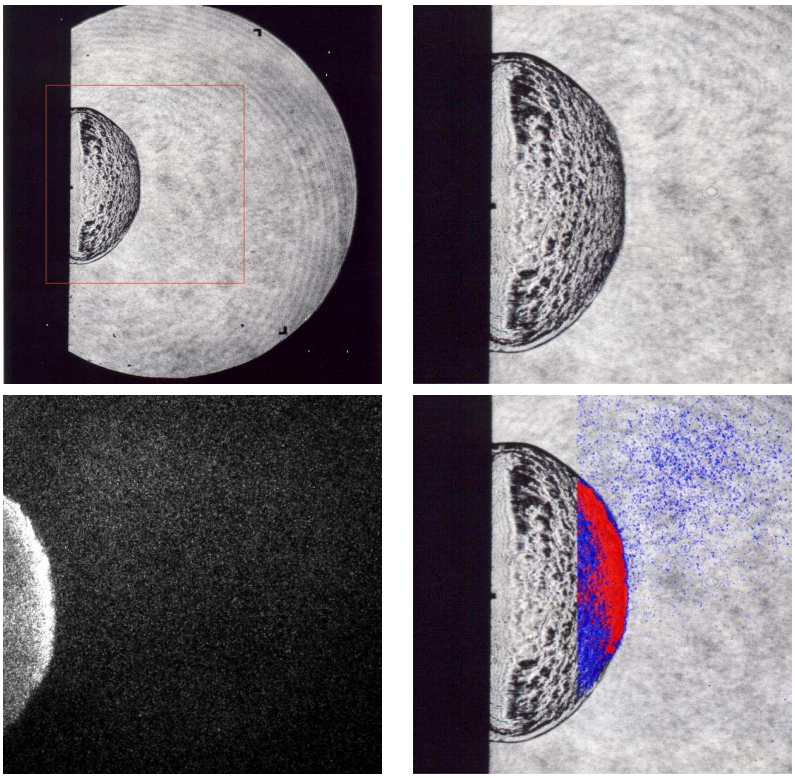

Figure M.65: Shot 86, 0.5 H_2 + 0.5 N_2O, P_0=40 kPa, T_0=296 K. Delays: Δt(P3-PLIF) 136.135 μs; Δt(TEP-PLIF) 9.51 μs. Schlieren image height 150 mm, PLIF image height 73 mm.

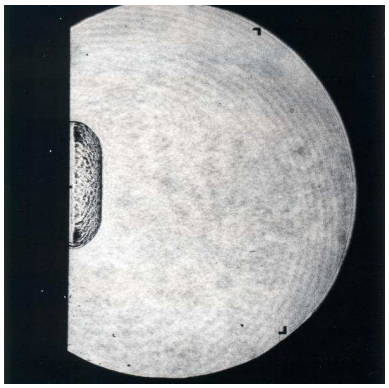

Figure M.66: Shot 87, 0.5 H_2 + 0.5 N_2O, P_0=40 kPa, T_0=296 K. Delays: Δt(P3-schl) 130.15 μs; Δt(TEP-schl) 3.52 μs. Schlieren image height 150 mm.

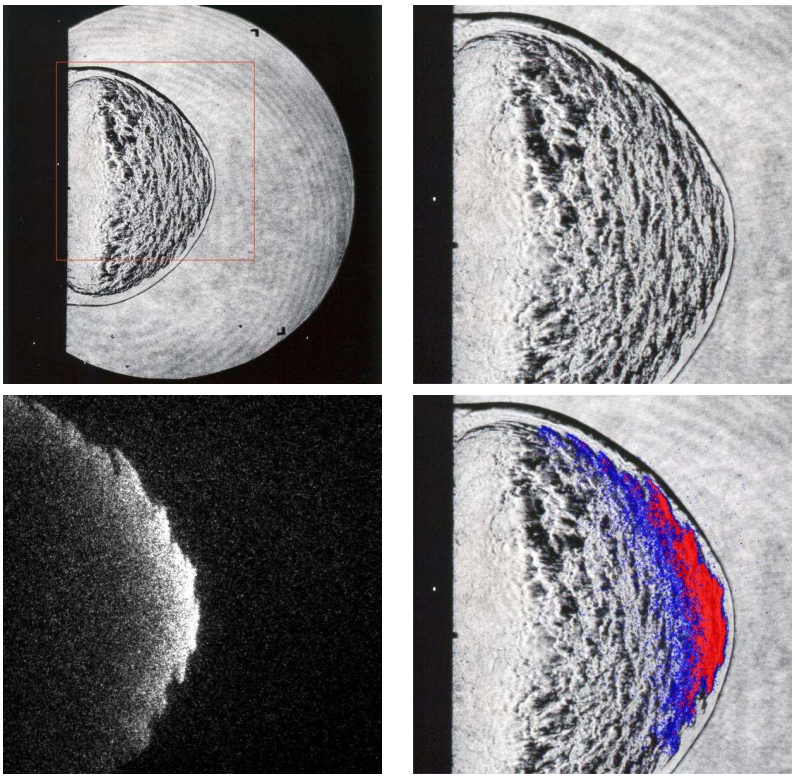

Figure M.67: Shot 88, 0.5 H_2 + 0.5 N_2O, P_0=40 kPa, T_0=296 K. Delays: Δt(P3-PLIF) 154.135 μs; Δt(TEP-PLIF) 27.51 μs. Schlieren image height 150 mm, PLIF image height 73 mm.

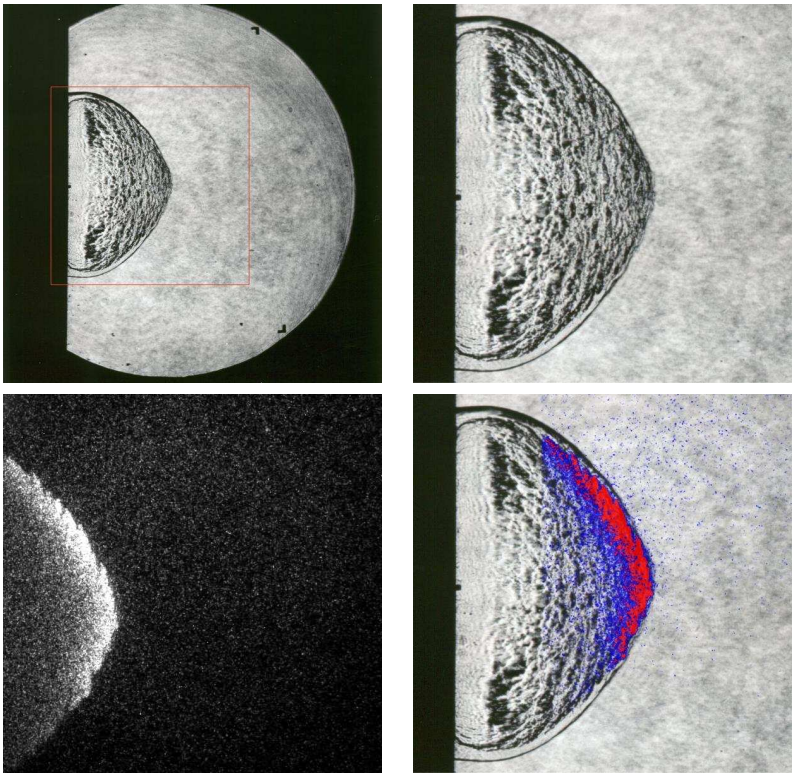

Figure M.68: Shot 89, 0.5 H_2 + 0.5 N_2O, P_0=40 kPa, T_0=296 K. Delays: Δt(P3-PLIF) 142.135 μs; Δt(TEP-PLIF) 15.51 μs. Schlieren image height 150 mm, PLIF image height 73 mm.

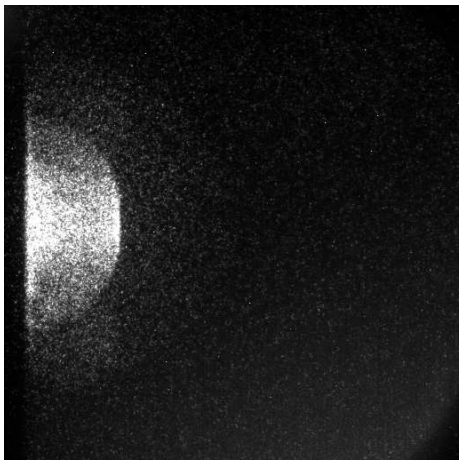

Figure M.69: Shot 90, 0.5 H_2 + 0.5 N_2O, P_0=40 kPa, T_0=294 K. Delays: Δt(P3-chem) 136.245 μs; Δt(TEP-chem) 9.62 μs. Multiple exposure timing: 3×10μs. Chemiluminescence image height 118 mm.

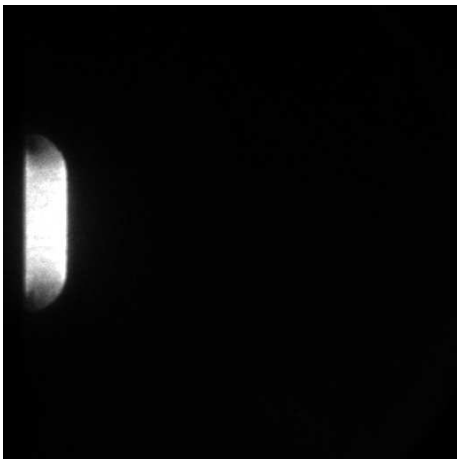

Figure M.70: Shot 92, 0.5 H_2 + 0.5 N_2O, P_0=40 kPa, T_0=294 K. Delays: Δt(P3-chem) 130.245 μs; Δt(TEP-chem) 3.62 μs. Chemiluminescence image height 118 mm.

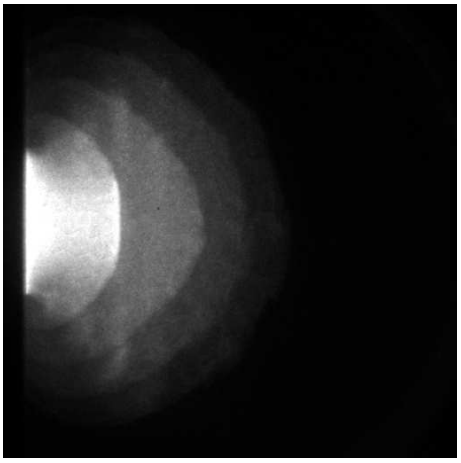

Figure M.71: Shot 93, 0.5 H_2 + 0.5 N_2O, P_0=40 kPa, T_0=294 K. Delays: Δt(P3-chem) 136.245 μs; Δt(TEP-chem) 9.62 μs. Multiple exposure timing: 4×12μs. Chemiluminescence image height 118 mm.

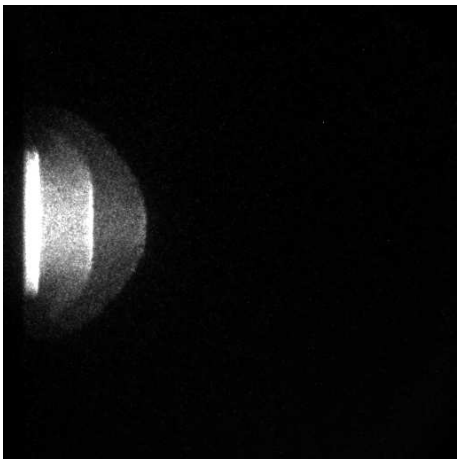

Figure M.72: Shot 96, 0.5 H_2 + 0.5 N_2O, P_0=40 kPa, T_0=295 K. Delays: Δt(P3-chem) 127.245 μs; Δt(TEP-chem) 0.62 μs. Multiple exposure timing: 3×6μs. Chemiluminescence image height 118 mm.

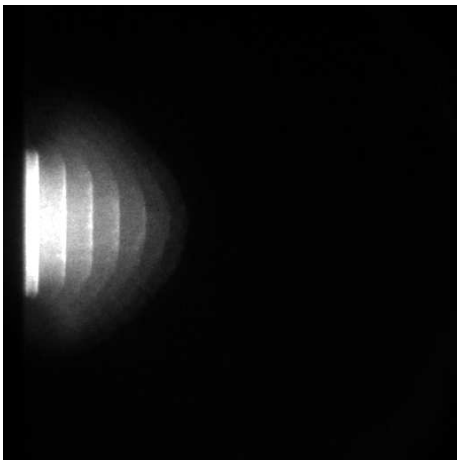

Figure M.73: Shot 97, 0.5 H_2 + 0.5 N_2O, P_0=40 kPa, T_0=295 K. Delays: Δt(P3-chem) 127.245 μs; Δt(TEP-chem) 0.62 μs. Multiple exposure timing: 7×3μs. Chemiluminescence image height 118 mm.

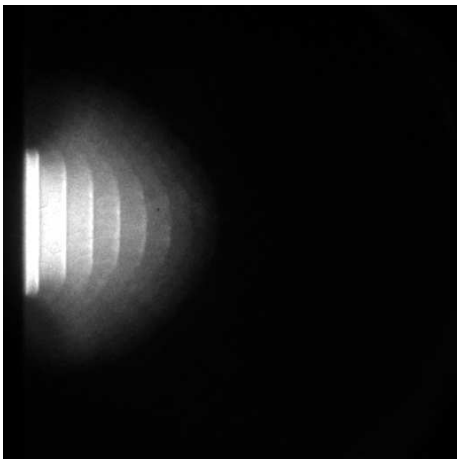

Figure M.74: Shot 98, 0.5 H_2 + 0.5 N_2O, P_0=42.5 kPa, T_0=295 K. Delays: Δt(P3-chem) 127.245 μs; Δt(TEP-chem) 0.76 μs. Multiple exposure timing: 9×3μs. Chemiluminescence image height 118 mm.

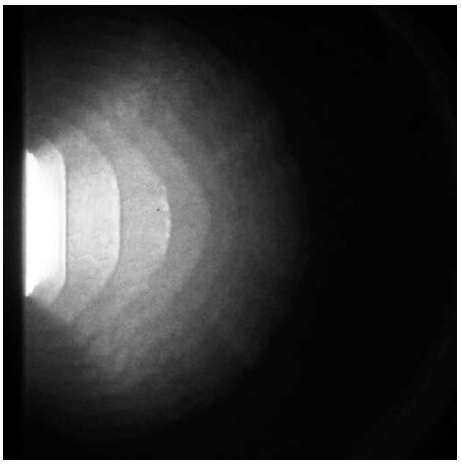

Figure M.75: Shot 99, 0.5 H_2 + 0.5 N_2O, P_0=42.5 kPa, T_0=295 K. Delays: Δt(P3-chem) 130.245 μs; Δt(TEP-chem) 3.76 μs. Multiple exposure timing: 9×6μs. Chemiluminescence image height 118 mm.

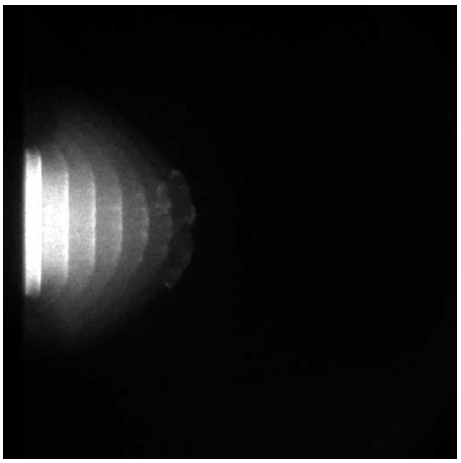

Figure M.76: Shot 100, 0.5 H_2 + 0.5 N_2O, P_0=45 kPa, T_0=295 K. Delays: Δt(P3-chem) 127.245 μs; Δt(TEP-chem) 0.89 μs. Multiple exposure timing: 7×3μs. Chemiluminescence image height 118 mm.

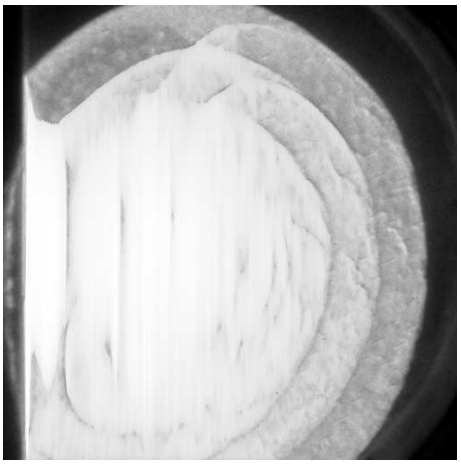

Figure M.77: Shot 101, 0.5 H_2 + 0.5 N_2O, P_0=45 kPa, T_0=295 K. Delays: Δt(P3-chem) 130.245 μs; Δt(TEP-chem) 3.89 μs. Multiple exposure timing: 9×6μs. Chemiluminescence image height 118 mm.

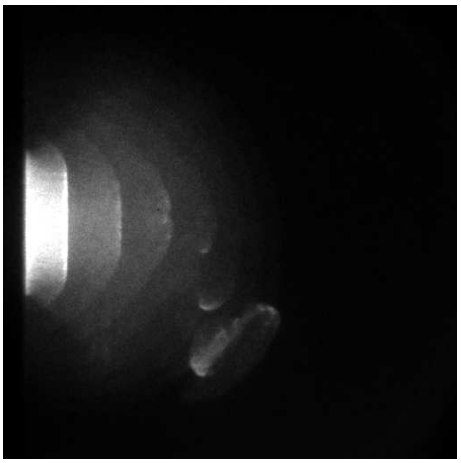

Figure M.78: Shot 102, 0.5 H_2 + 0.5 N_2O, P_0=45 kPa, T_0=296 K. Delays: Δt(P3-chem) 130.245 μs; Δt(TEP-chem) 3.89 μs. Multiple exposure timing: 7×6μs. Chemiluminescence image height 118 mm.

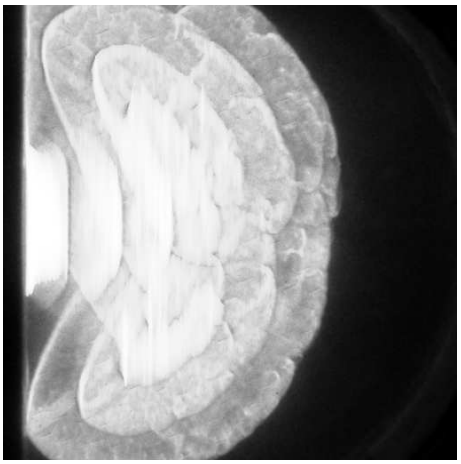

Figure M.79: Shot 103, 0.5 H_2 + 0.5 N_2O, P_0=47.5 kPa, T_0=296 K. Delays: Δt(P3-chem) 130.245 μs; Δt(TEP-chem) 4.02 μs. Multiple exposure timing: 7×6μs. Chemiluminescence image height 118 mm.

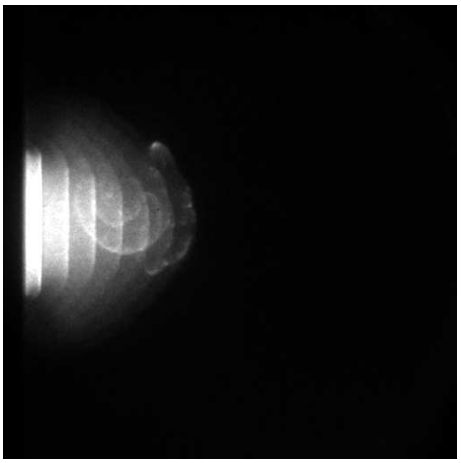

Figure M.80: Shot 104, 0.5 H_2 + 0.5 N_2O, P_0=47.5 kPa, T_0=296 K. Delays: Δt(P3-chem) 127.245 μs; Δt(TEP-chem) 1.02 μs. Multiple exposure timing: 7×3μs. Chemiluminescence image height 118 mm.

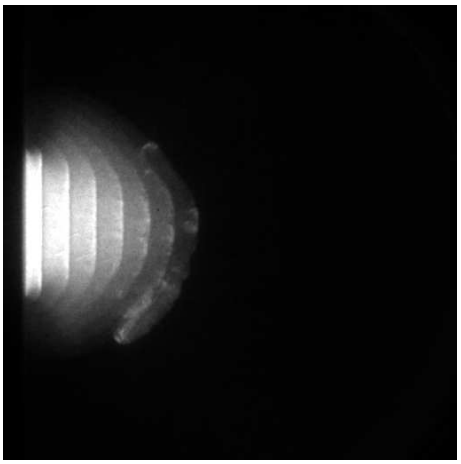

Figure M.81: Shot 105, 0.5 H_2 + 0.5 N_2O, P_0=47.5 kPa, T_0=296 K. Delays: Δt(P3-chem) 127.245 μs; Δt(TEP-chem) 1.02 μs. Multiple exposure timing: 7×3μs. Chemiluminescence image height 118 mm.

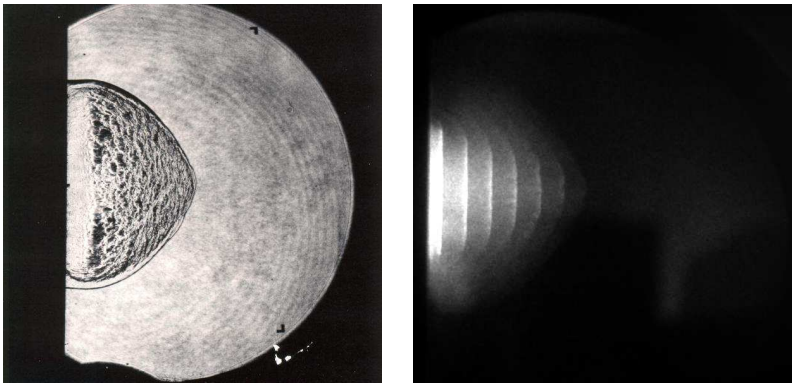

Figure M.82: Shot 106, 0.5 H_2 + 0.5 N_2O, P_0=45 kPa, T_0=294 K. Delays: Δt(P3-schl) 148.18 μs; Δt(TEP-schl) 21.83 μs. Delays: Δt(P3-chem) 127.245 μs; Δt(TEP-chem) 0.89 μs. Multiple exposure timing: 7×3μs. Schlieren image height 150 mm, Chemiluminescence image height 109 mm.

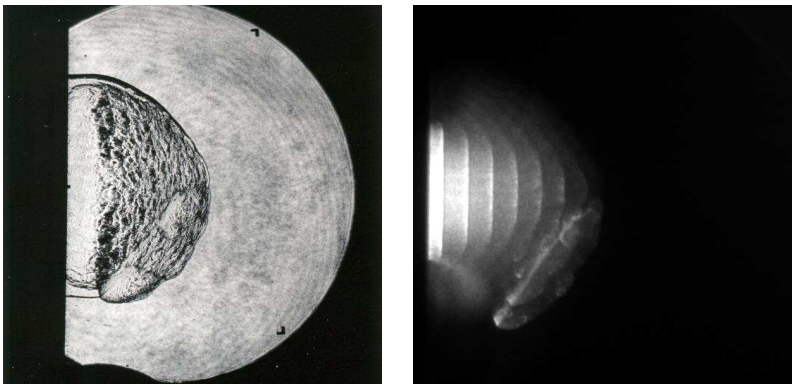

Figure M.83: Shot 107, 0.5 H_2 + 0.5 N_2O, P_0=45 kPa, T_0=294 K. Delays: Δt(P3-schl) 151.18 μs; Δt(TEP-schl) 24.83 μs. Delays: Δt(P3-chem) 127.245 μs; Δt(TEP-chem) 0.89 μs. Multiple exposure timing: 8×3μs. Schlieren image height 150 mm, Chemiluminescence image height 109 mm.

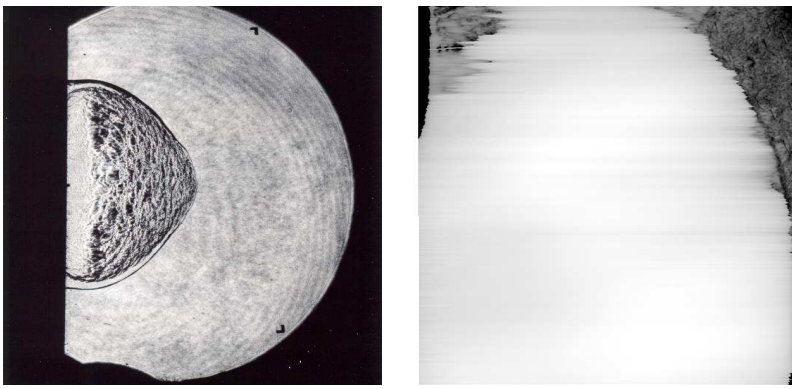

Figure M.84: Shot 108, 0.5 H_2 + 0.5 N_2O, P_0=45 kPa, T_0=295 K. Delays: Δt(P3-schl) 151.18 μs; Δt(TEP-schl) 24.83 μs. Delays: Δt(P3-chem) 127.245 μs; Δt(TEP-chem) 0.89 μs. Multiple exposure timing: 8×3μs. Schlieren image height 150 mm, Chemiluminescence image height 109 mm.

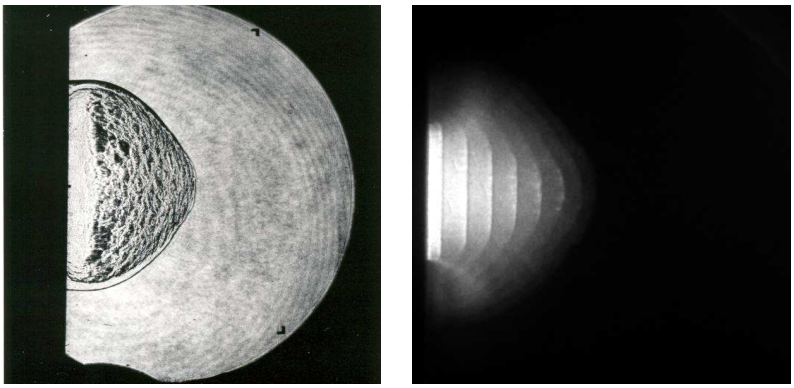

Figure M.85: Shot 109, 0.5 H_2 + 0.5 N_2O, P_0=45 kPa, T_0=295 K. Delays: Δt(P3-schl) 151.18 μs; Δt(TEP-schl) 24.83 μs. Delays: Δt(P3-chem) 127.245 μs; Δt(TEP-chem) 0.89 μs. Multiple exposure timing: 8×3μs. Schlieren image height 150 mm, Chemiluminescence image height 109 mm.

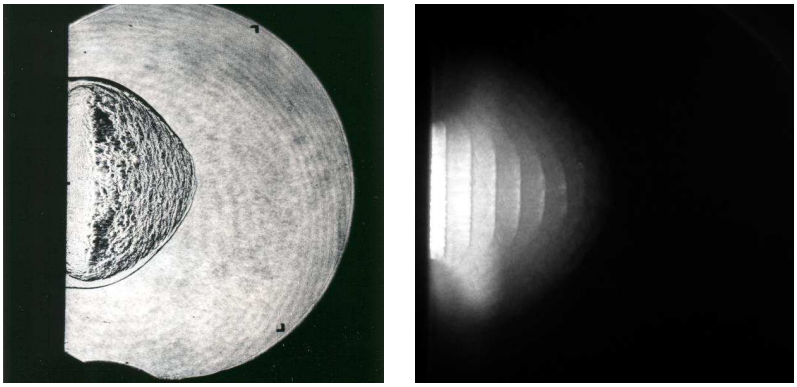

Figure M.86: Shot 110, 0.5 H_2 + 0.5 N_2O, P_0=45 kPa, T_0=295 K. Delays: Δt(P3-schl) 148.18 μs; Δt(TEP-schl) 21.83 μs. Delays: Δt(P3-chem) 127.245 μs; Δt(TEP-chem) 0.89 μs. Multiple exposure timing: 9×3μs. Schlieren image height 150 mm, Chemiluminescence image height 109 mm.

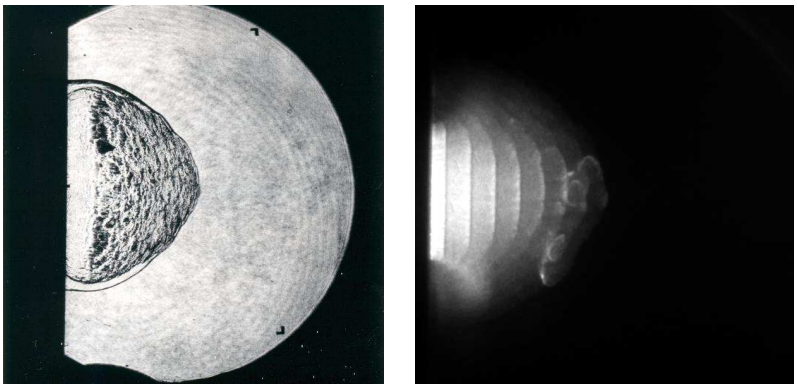

Figure M.87: Shot 111, 0.5 H_2 + 0.5 N_2O, P_0=45 kPa, T_0=295 K. Delays: Δt(P3-schl) 148.18 μs; Δt(TEP-schl) 21.83 μs. Delays: Δt(P3-chem) 127.245 μs; Δt(TEP-chem) 0.89 μs. Multiple exposure timing: 8×3μs. Schlieren image height 150 mm, Chemiluminescence image height 109 mm.

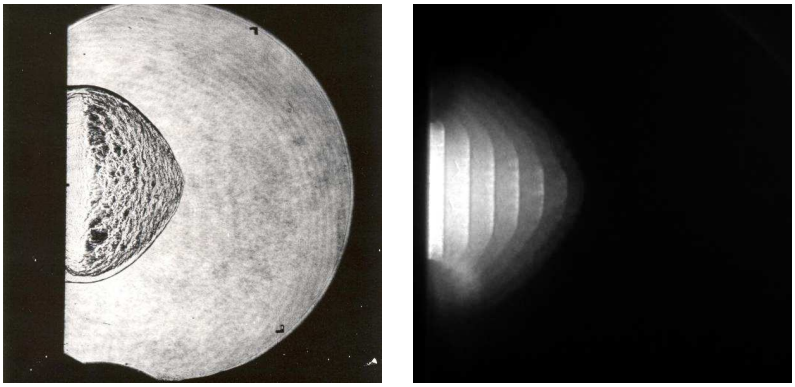

Figure M.88: Shot 112, 0.5 H_2 + 0.5 N_2O, P_0=47.5 kPa, T_0=296 K. Delays: Δt(P3-schl) 145.18 μs; Δt(TEP-schl) 18.95 μs. Delays: Δt(P3-chem) 127.245 μs; Δt(TEP-chem) 1.02 μs. Multiple exposure timing: 7×3μs. Schlieren image height 150 mm, Chemiluminescence image height 109 mm.

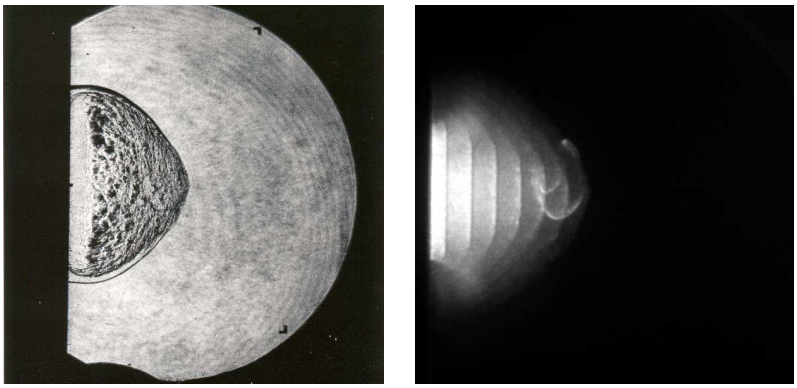

Figure M.89: Shot 113, 0.5 H_2 + 0.5 N_2O, P_0=47.5 kPa, T_0=296 K. Delays: Δt(P3-schl) 145.18 μs; Δt(TEP-schl) 18.95 μs. Delays: Δt(P3-chem) 127.245 μs; Δt(TEP-chem) 1.02 μs. Multiple exposure timing: 7×3μs. Schlieren image height 150 mm, Chemiluminescence image height 109 mm.

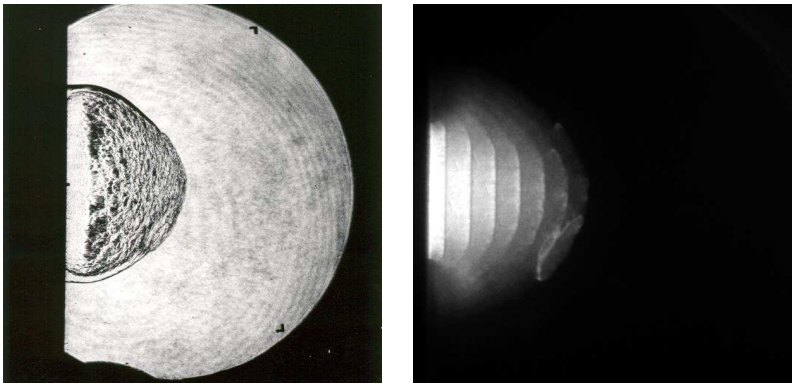

Figure M.90: Shot 114, 0.5 H_2 + 0.5 N_2O, P_0=50 kPa, T_0=296 K. Delays: Δt(P3-schl) 145.18 μs; Δt(TEP-schl) 19.07 μs. Delays: Δt(P3-chem) 127.245 μs; Δt(TEP-chem) 1.14 μs. Multiple exposure timing: 7×3μs. Schlieren image height 150 mm, Chemiluminescence image height 109 mm.

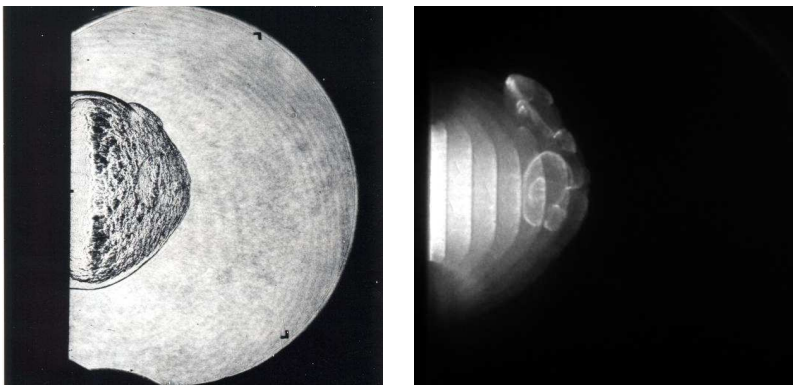

Figure M.91: Shot 115, 0.5 H_2 + 0.5 N_2O, P_0=50 kPa, T_0=296 K. Delays: Δt(P3-schl) 145.18 μs; Δt(TEP-schl) 19.07 μs. Delays: Δt(P3-chem) 127.245 μs; Δt(TEP-chem) 1.14 μs. Multiple exposure timing: 7×3μs. Schlieren image height 150 mm, Chemiluminescence image height 109 mm.

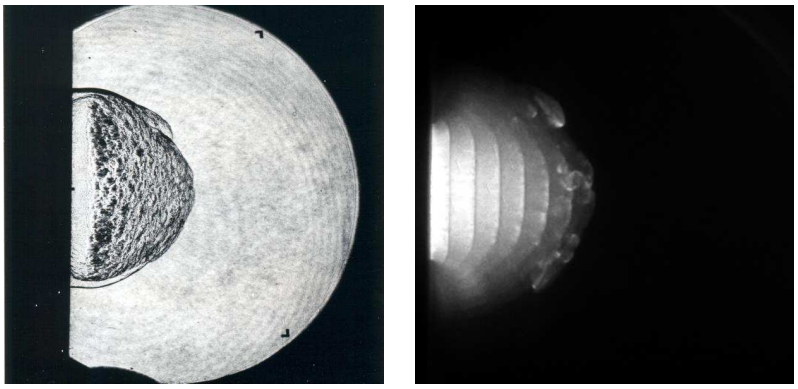

Figure M.92: Shot 116, 0.5 H_2 + 0.5 N_2O, P_0=55 kPa, T_0=296 K. Delays: Δt(P3-schl) 145.18 μs; Δt(TEP-schl) 19.29 μs. Delays: Δt(P3-chem) 127.245 μs; Δt(TEP-chem) 1.36 μs. Multiple exposure timing: 7×3μs. Schlieren image height 150 mm, Chemiluminescence image height 109 mm.

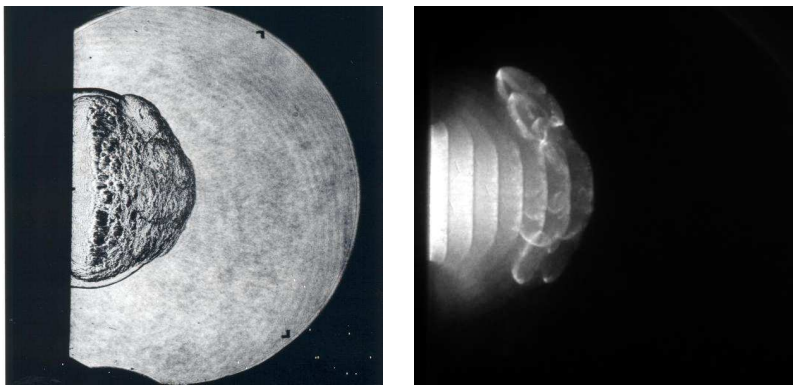

Figure M.93: Shot 117, 0.5 H_2 + 0.5 N_2O, P_0=55 kPa, T_0=296 K. Delays: Δt(P3-schl) 145.18 μs; Δt(TEP-schl) 19.29 μs. Delays: Δt(P3-chem) 127.245 μs; Δt(TEP-chem) 1.36 μs. Multiple exposure timing: 7×3μs. Schlieren image height 150 mm, Chemiluminescence image height 109 mm.

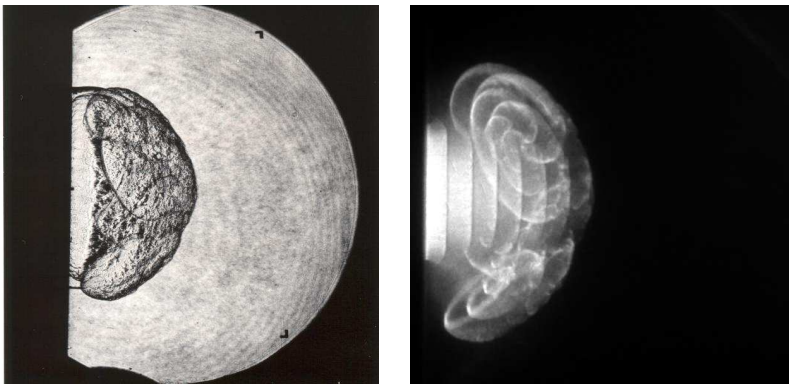

Figure M.94: Shot 118, 0.5 H_2 + 0.5 N_2O, P_0=60 kPa, T_0=296 K. Delays: Δt(P3-schl) 145.18 μs; Δt(TEP-schl) 19.49 μs. Delays: Δt(P3-chem) 127.245 μs; Δt(TEP-chem) 1.56 μs. Multiple exposure timing: 7×3μs. Schlieren image height 150 mm, Chemiluminescence image height 109 mm.

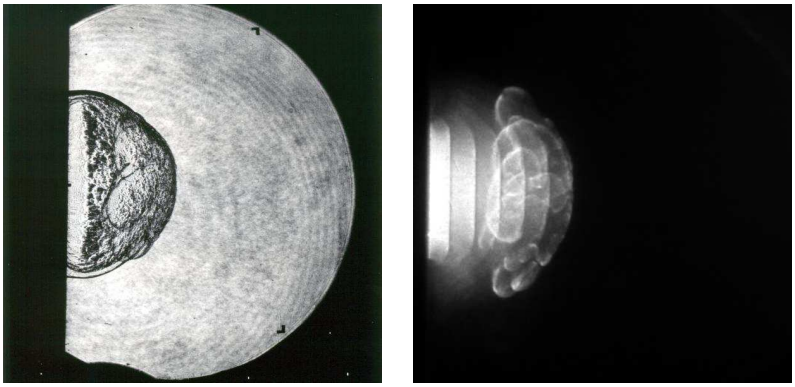

Figure M.95: Shot 119, 0.5 H_2 + 0.5 N_2O, P_0=60 kPa, T_0=296 K. Delays: Δt(P3-schl) 142.18 μs; Δt(TEP-schl) 16.49 μs. Delays: Δt(P3-chem) 127.245 μs; Δt(TEP-chem) 1.56 μs. Multiple exposure timing: 6×3μs. Schlieren image height 150 mm, Chemiluminescence image height 109 mm.

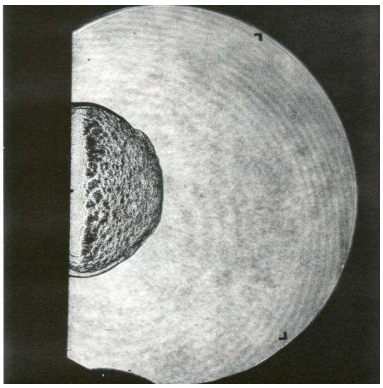

Figure M.96: Shot 120, 0.5 H_2 + 0.5 N_2O, P_0=65 kPa, T_0=297 K. Delays: Δt(P3-schl) 139.28 μs; Δt(TEP-schl) 13.77 μs. Schlieren image height 150 mm.

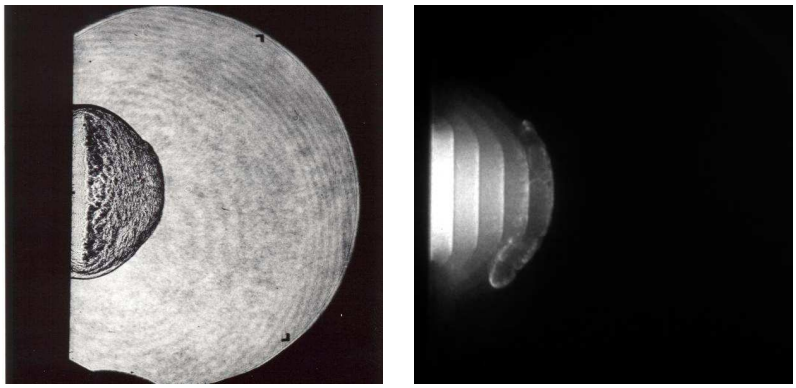

Figure M.97: Shot 121, 0.5 H_2 + 0.5 N_2O, P_0=65 kPa, T_0=297 K. Delays: Δt(P3-schl) 139.18 μs; Δt(TEP-schl) 13.67 μs. Delays: Δt(P3-chem) 127.245 μs; Δt(TEP-chem) 1.74 μs. Multiple exposure timing: 5×3μs. Schlieren image height 150 mm, Chemiluminescence image height 109 mm.

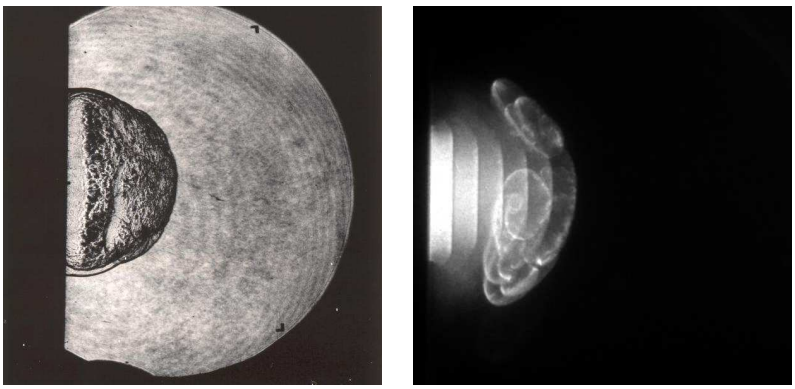

Figure M.98: Shot 122, 0.5 H_2 + 0.5 N_2O, P_0=65 kPa, T_0=297 K. Delays: Δt(P3-schl) 142.18 μs; Δt(TEP-schl) 16.67 μs. Delays: Δt(P3-chem) 127.245 μs; Δt(TEP-chem) 1.74 μs. Multiple exposure timing: 6×3μs. Schlieren image height 150 mm, Chemiluminescence image height 109 mm.

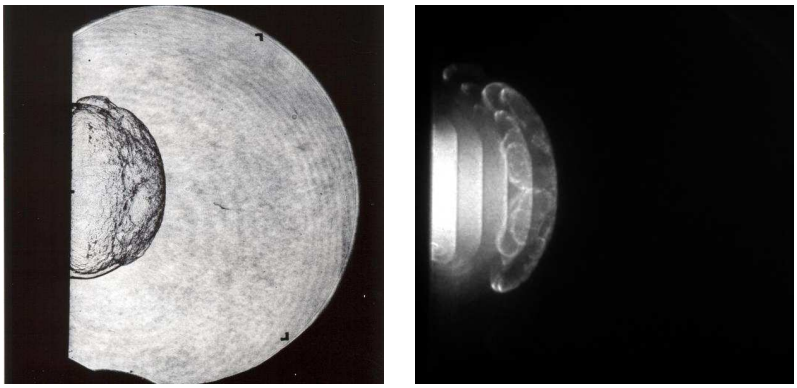

Figure M.99: Shot 123, 0.5 H_2 + 0.5 N_2O, P_0=70 kPa, T_0=297 K. Delays: Δt(P3-schl) 139.18 μs; Δt(TEP-schl) 13.84 μs. Delays: Δt(P3-chem) 127.245 μs; Δt(TEP-chem) 1.91 μs. Multiple exposure timing: 5×3μs. Schlieren image height 150 mm, Chemiluminescence image height 109 mm.

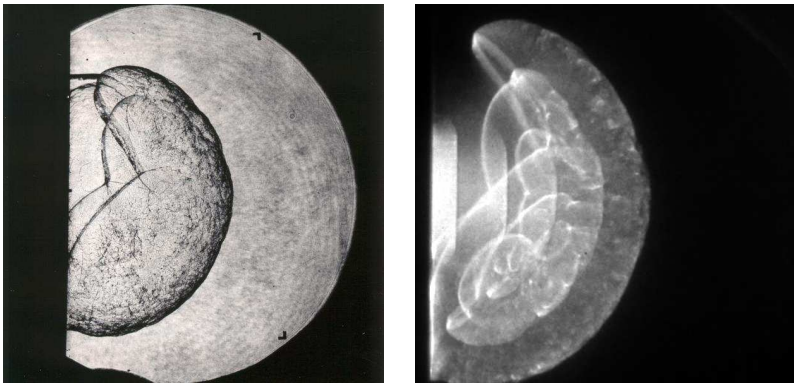

Figure M.100: Shot 124, 0.5 H_2 + 0.5 N_2O, P_0=70 kPa, T_0=297 K. Delays: Δt(P3-schl) 151.18 μs; Δt(TEP-schl) 25.84 μs. Delays: Δt(P3-chem) 127.245 μs; Δt(TEP-chem) 1.91 μs. Multiple exposure timing: 5×6μs. Schlieren image height 150 mm, Chemiluminescence image height 109 mm.

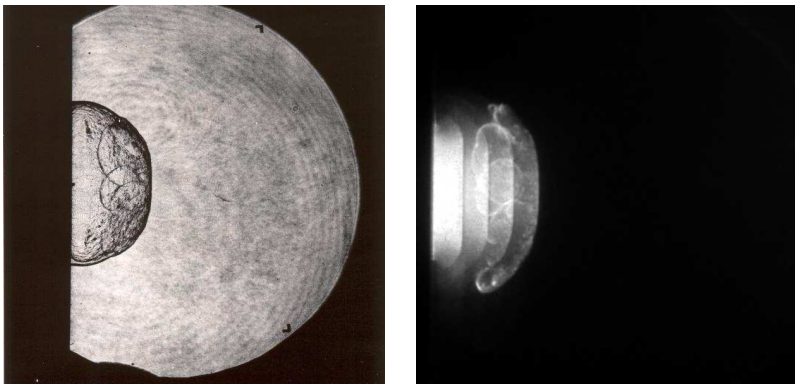

Figure M.101: Shot 125, 0.5 H_2 + 0.5 N_2O, P_0=80 kPa, T_0=297 K. Delays: Δt(P3-schl) 136.18 μs; Δt(TEP-schl) 11.15 μs. Delays: Δt(P3-chem) 127.245 μs; Δt(TEP-chem) 2.21 μs. Multiple exposure timing: 4×3μs. Schlieren image height 150 mm, Chemiluminescence image height 109 mm.

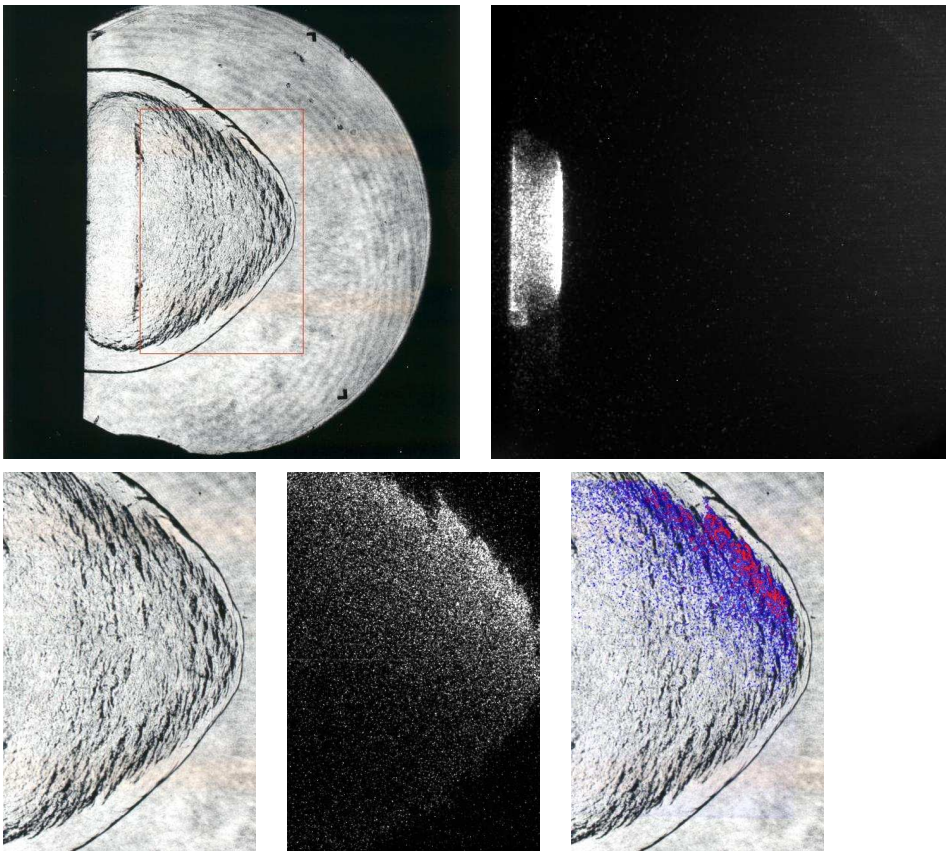

Figure M.102: Shot 126, 0.2 H_2 + 0.1 O_2 + 0.7 Ar, P_0=100 kPa, T_0=294 K. Delays: Δt(P3-PLIF) 214.167 μs; Δt(TEP-PLIF) 38.21 μs. Delays: Δt(P3-chem) 178.285 μs; Δt(TEP-chem) 2.33 μs. Multiple exposure timing: 1×6μs. Schlieren image height 150 mm, PLIF image height 70 mm, Chemiluminescence image height 109 mm.

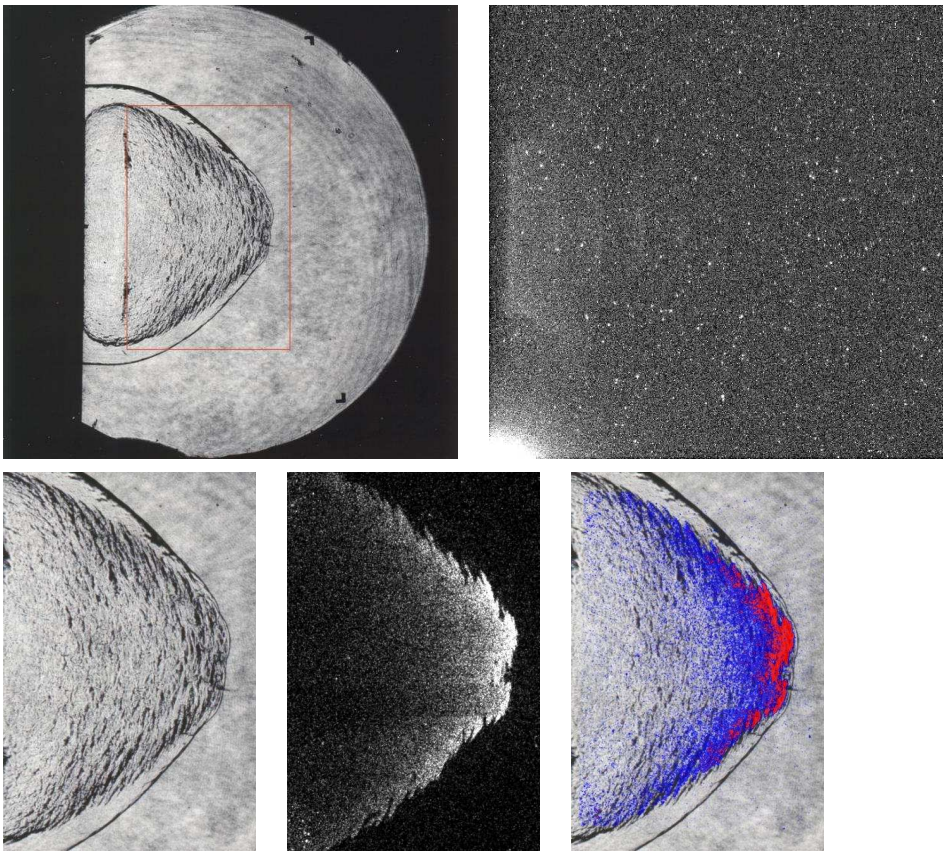

Figure M.103: Shot 127, 0.2 H_2 + 0.1 O_2 + 0.7 Ar, P_0=100 kPa, T_0=294 K. Delays: Δt(P3-PLIF) 208.167 μs; Δt(TEP-PLIF) 32.21 μs. Delays: Δt(P3-chem) 172.285 μs; Δt(TEP-chem) -3.67 μs. Multiple exposure timing: 6×7μs. Schlieren image height 150 mm, PLIF image height 70 mm, Chemiluminescence image height 109 mm.

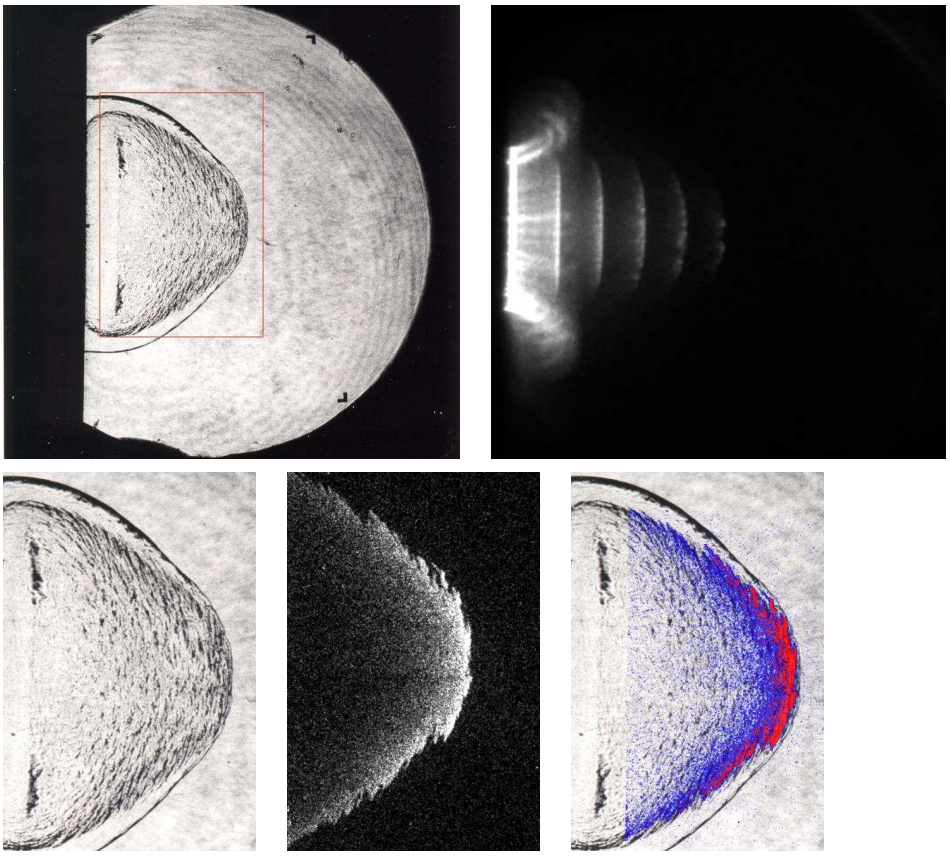

Figure M.104: Shot 128, 0.2 H_2 + 0.1 O_2 + 0.7 Ar, P_0=100 kPa, T_0=295 K. Delays: Δt(P3-PLIF) 202.167 μs; Δt(TEP-PLIF) 26.21 μs. Delays: Δt(P3-chem) 172.285 μs; Δt(TEP-chem) -3.67 μs. Multiple exposure timing: 6×6μs. Schlieren image height 150 mm, PLIF image height 70 mm, Chemiluminescence image height 109 mm.

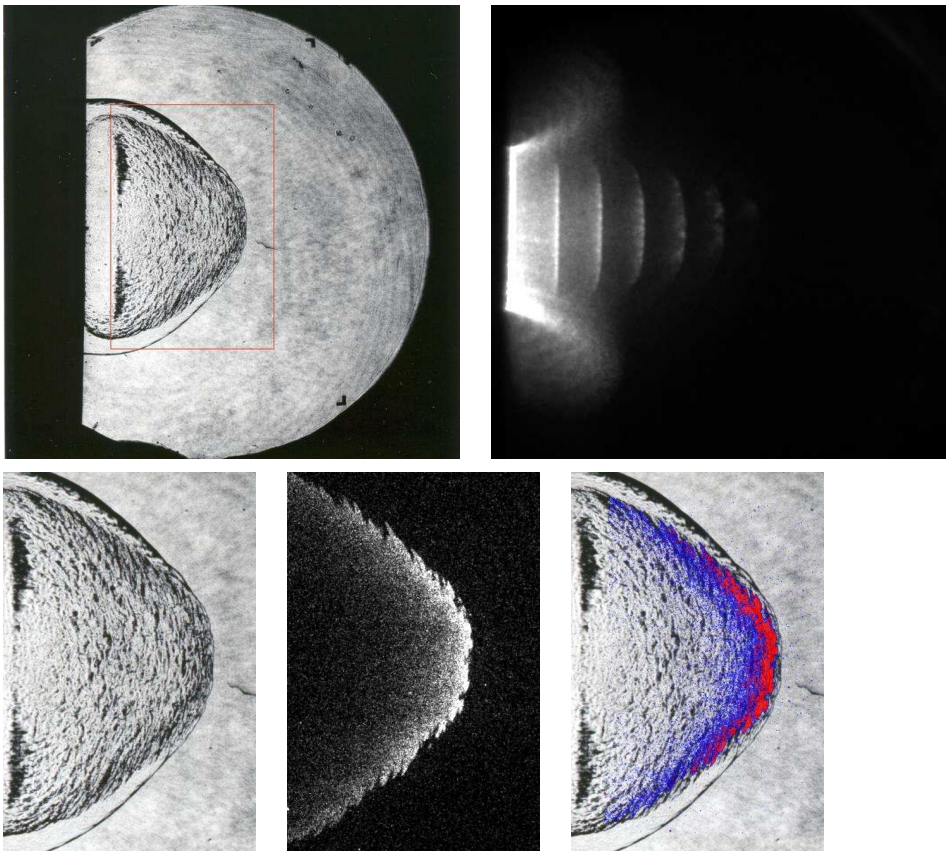

Figure M.105: Shot 129, 0.2 H_2 + 0.1 O_2 + 0.7 Ar, P_0=100 kPa, T_0=295 K. Delays: Δt(P3-PLIF) 202.167 μs; Δt(TEP-PLIF) 26.21 μs. Delays: Δt(P3-chem) 172.285 μs; Δt(TEP-chem) -3.67 μs. Multiple exposure timing: 9×6μs. Schlieren image height 150 mm, PLIF image height 70 mm, Chemiluminescence image height 109 mm.

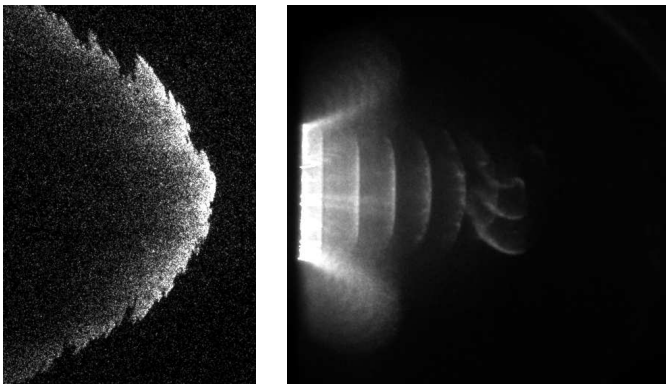

Figure M.106: Shot 130, 0.213 H_2 + 0.107 O_2 + 0.68 Ar, P_0=100 kPa, T_0=295 K. Delays: Δt(P3-chem) 172.285 μs; Δt(TEP-chem) -1.16 μs. Multiple exposure timing: 9×6μs. PLIF image height 70 mm, Chemiluminescence image height 109 mm.

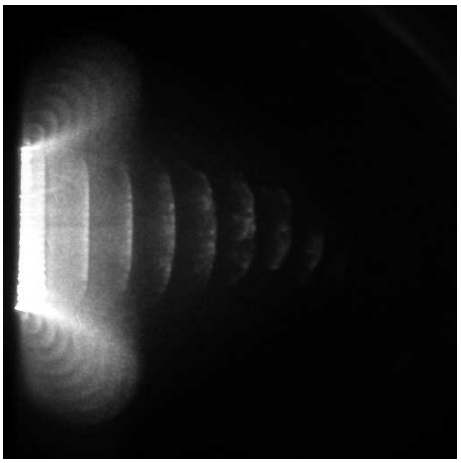

Figure M.107: Shot 131, 0.213 H_2 + 0.107 O_2 + 0.68 Ar, P_0=100 kPa, T_0=296 K. Delays: Δt(P3-chem) 172.285 μs; Δt(TEP-chem) -1.16 μs. Multiple exposure timing: 9×6μs. Chemiluminescence image height 109 mm.

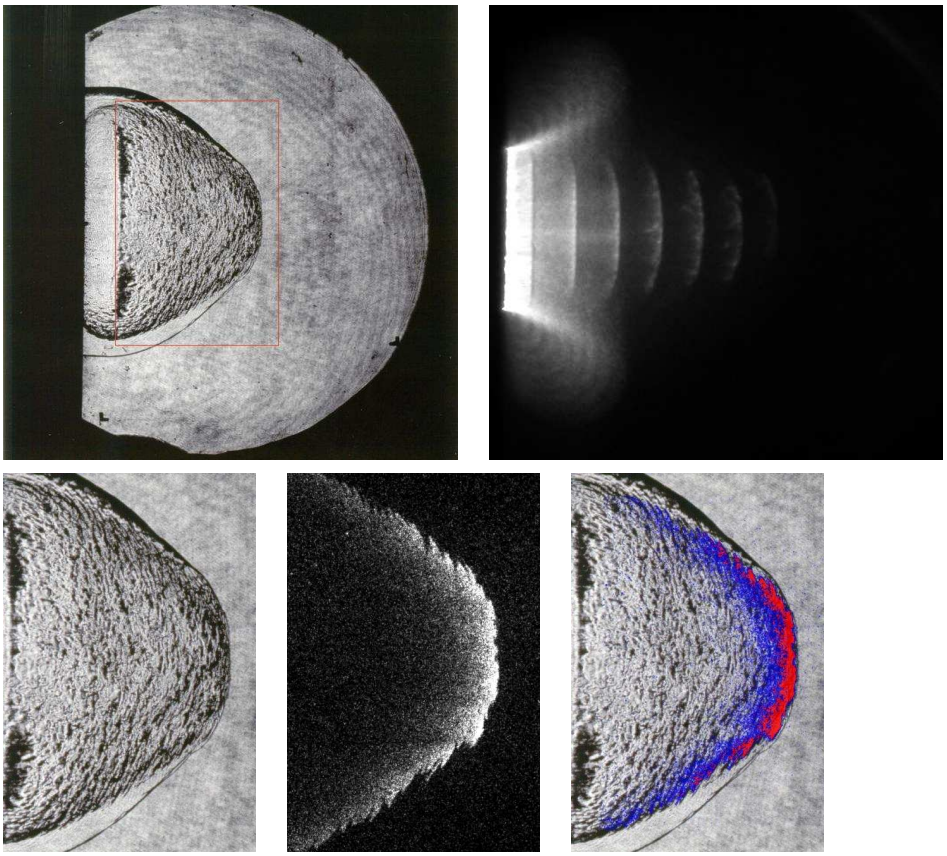

Figure M.108: Shot 132, 0.213 H_2 + 0.107 O_2 + 0.68 Ar, P_0=100 kPa, T_0=296 K. Delays: Δt(P3-PLIF) 202.167 μs; Δt(TEP-PLIF) 28.72 μs. Delays: Δt(P3-chem) 172.285 μs; Δt(TEP-chem) -1.16 μs. Multiple exposure timing: 9×6μs. Schlieren image height 150 mm, PLIF image height 70 mm, Chemiluminescence image height 109 mm.

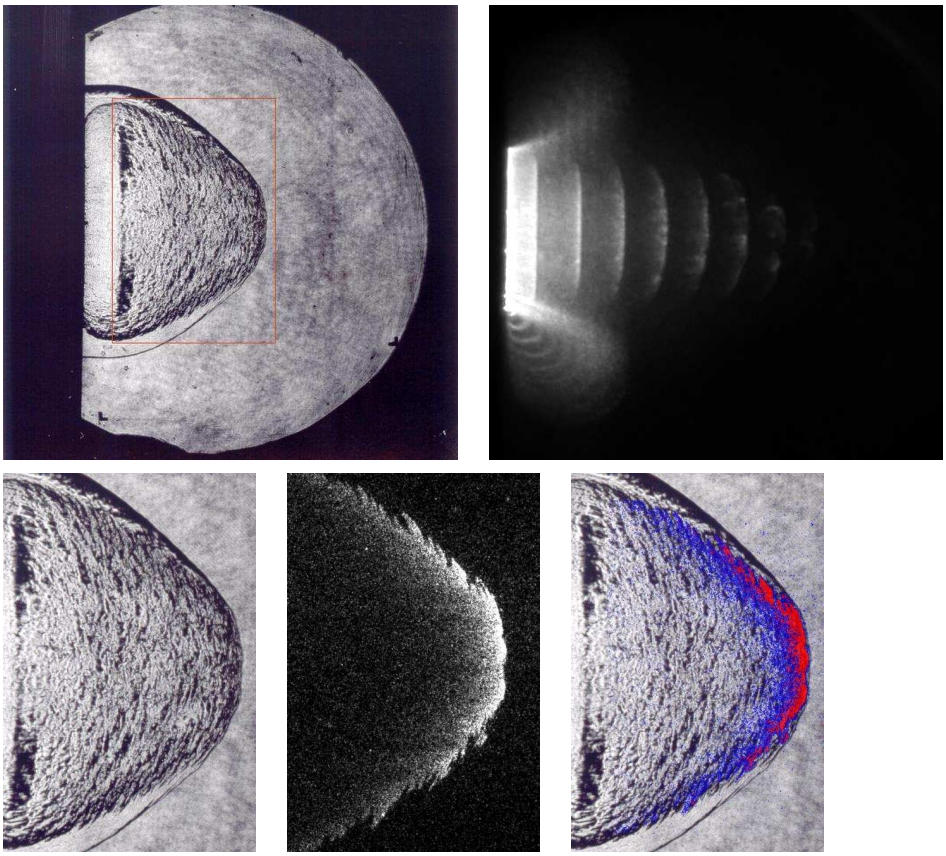

Figure M.109: Shot 133, 0.217 H_2 + 0.108 O_2 + 0.675 Ar, P_0=100 kPa, T_0=296 K. Delays: Δt(P3-PLIF) 202.167 μs; Δt(TEP-PLIF) 29.32 μs. Delays: Δt(P3-chem) 172.285 μs; Δt(TEP-chem) -0.56 μs. Multiple exposure timing: 9×6μs. Schlieren image height 150 mm, PLIF image height 70 mm, Chemiluminescence image height 109 mm.

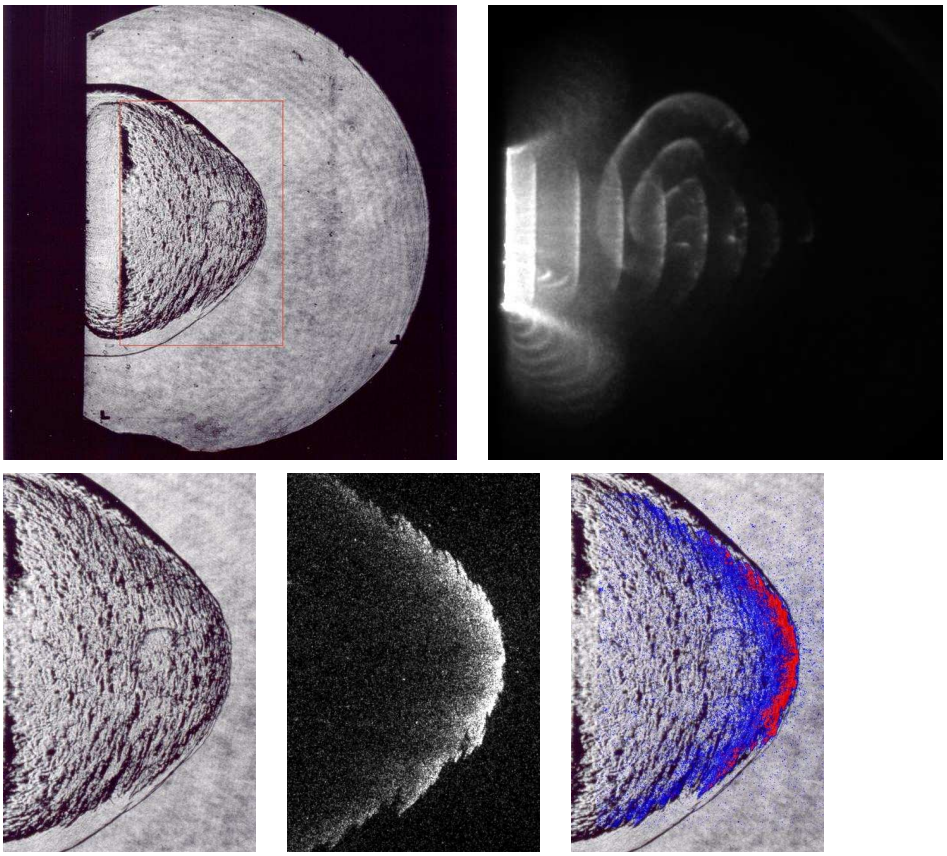

Figure M.110: Shot 134, 0.217 H_2 + 0.108 O_2 + 0.675 Ar, P_0=100 kPa, T_0=296 K. Delays: Δt(P3-PLIF) 202.167 μs; Δt(TEP-PLIF) 29.32 μs. Delays: Δt(P3-chem) 172.285 μs; Δt(TEP-chem) -0.56 μs. Multiple exposure timing: 9×6μs. Schlieren image height 150 mm, PLIF image height 70 mm, Chemiluminescence image height 109 mm.

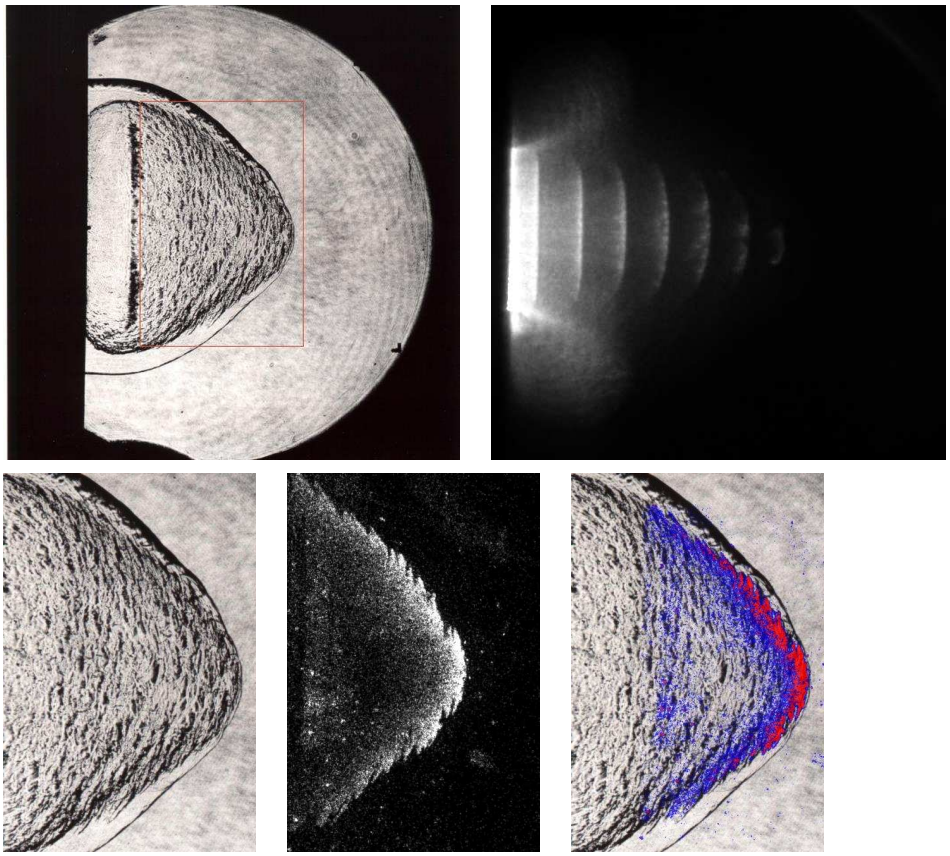

Figure M.111: Shot 135, 0.217 H_2 + 0.108 O_2 + 0.675 Ar, P_0=100 kPa, T_0=294 K. Delays: Δt(P3-PLIF) 208.167 μs; Δt(TEP-PLIF) 35.32 μs. Delays: Δt(P3-chem) 172.285 μs; Δt(TEP-chem) -0.56 μs. Multiple exposure timing: 9×6μs. Schlieren image height 150 mm, PLIF image height 70 mm, Chemiluminescence image height 109 mm.

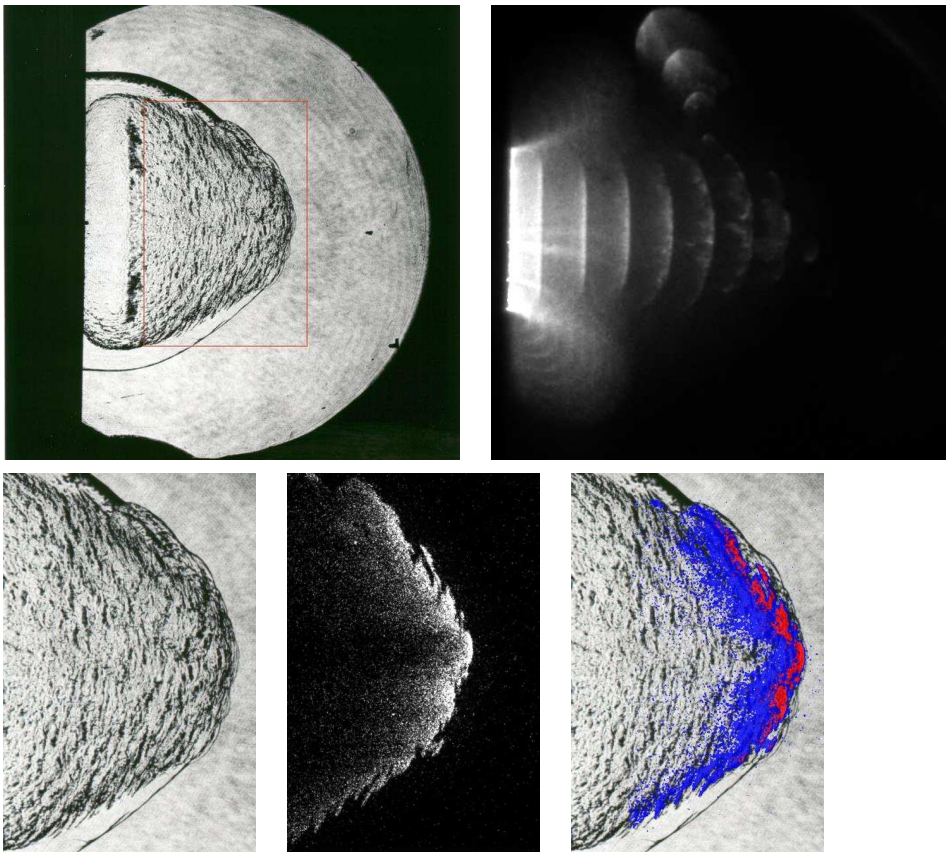

Figure M.112: Shot 136, 0.22 H_2 + 0.11 O_2 + 0.67 Ar, P_0=100 kPa, T_0=295 K. Delays: Δt(P3-PLIF) 208.167 μs; Δt(TEP-PLIF) 35.92 μs. Delays: Δt(P3-chem) 172.285 μs; Δt(TEP-chem) 0.04 μs. Multiple exposure timing: 9×6μs. Schlieren image height 150 mm, PLIF image height 70 mm, Chemiluminescence image height 109 mm.

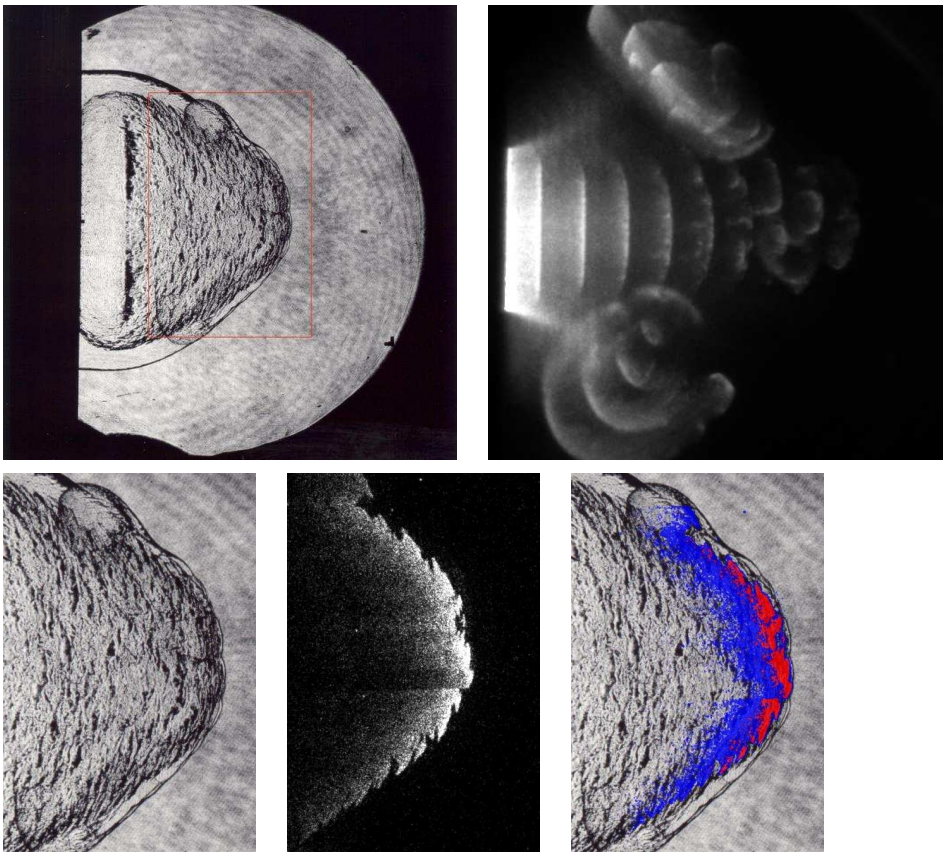

Figure M.113: Shot 137, 0.22 H_2 + 0.11 O_2 + 0.67 Ar, P_0=100 kPa, T_0=295 K. Delays: Δt(P3-PLIF) 208.167 μs; Δt(TEP-PLIF) 35.92 μs. Delays: Δt(P3-chem) 172.285 μs; Δt(TEP-chem) 0.04 μs. Multiple exposure timing: 9×6μs. Schlieren image height 150 mm, PLIF image height 70 mm, Chemiluminescence image height 109 mm.

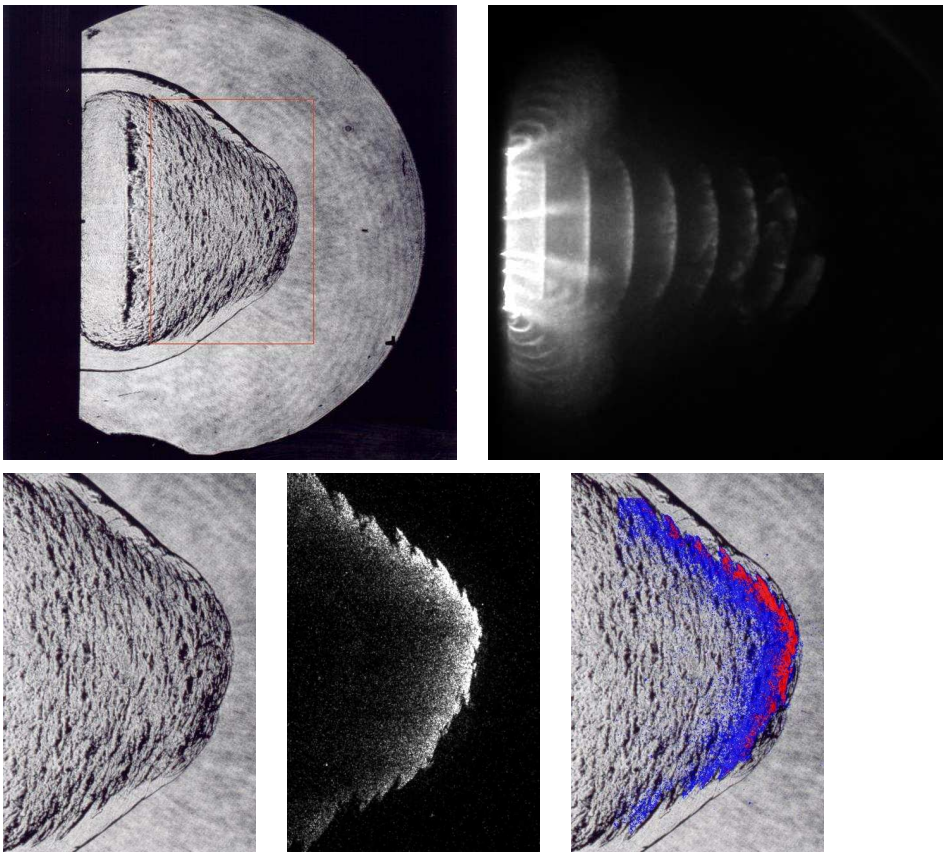

Figure M.114: Shot 138, 0.223 H_2 + 0.112 O_2 + 0.665 Ar, P_0=100 kPa, T_0=296 K. Delays: Δt(P3-PLIF) 208.167 μs; Δt(TEP-PLIF) 36.51 μs. Delays: Δt(P3-chem) 172.285 μs; Δt(TEP-chem) 0.63 μs. Multiple exposure timing: 8×6μs. Schlieren image height 150 mm, PLIF image height 70 mm, Chemiluminescence image height 109 mm.

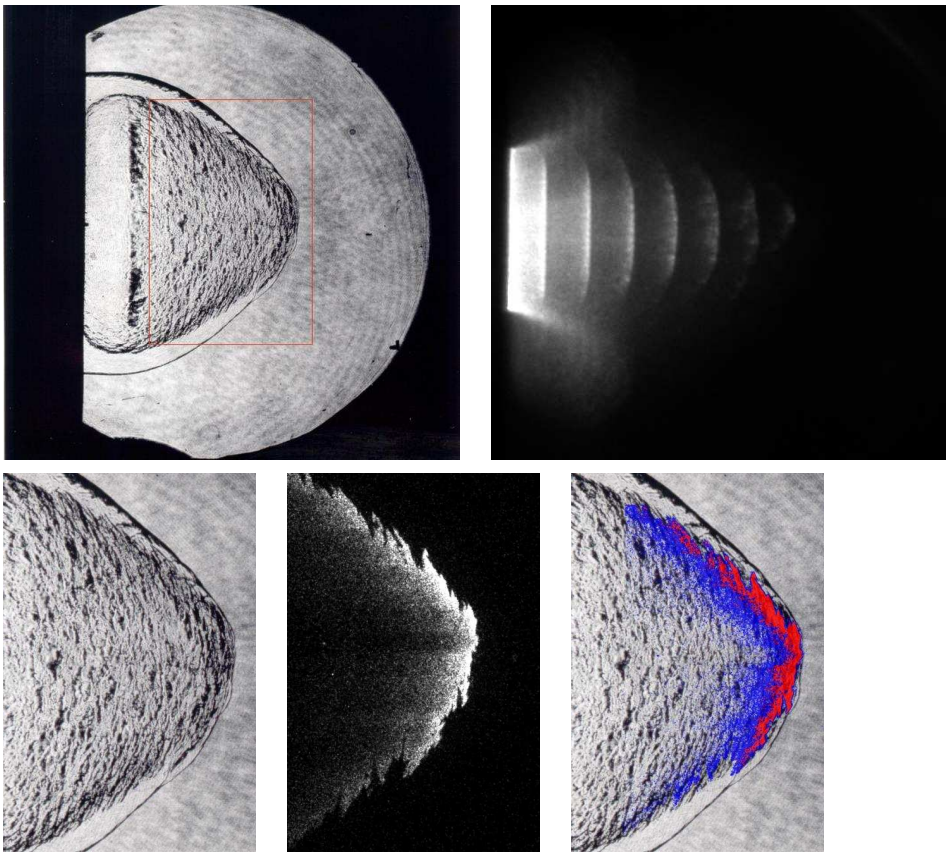

Figure M.115: Shot 139, 0.223 H_2 + 0.112 O_2 + 0.665 Ar, P_0=100 kPa, T_0=296 K. Delays: Δt(P3-PLIF) 208.167 μs; Δt(TEP-PLIF) 36.51 μs. Delays: Δt(P3-chem) 172.285 μs; Δt(TEP-chem) 0.63 μs. Multiple exposure timing: 9×6μs. Schlieren image height 150 mm, PLIF image height 70 mm, Chemiluminescence image height 109 mm.

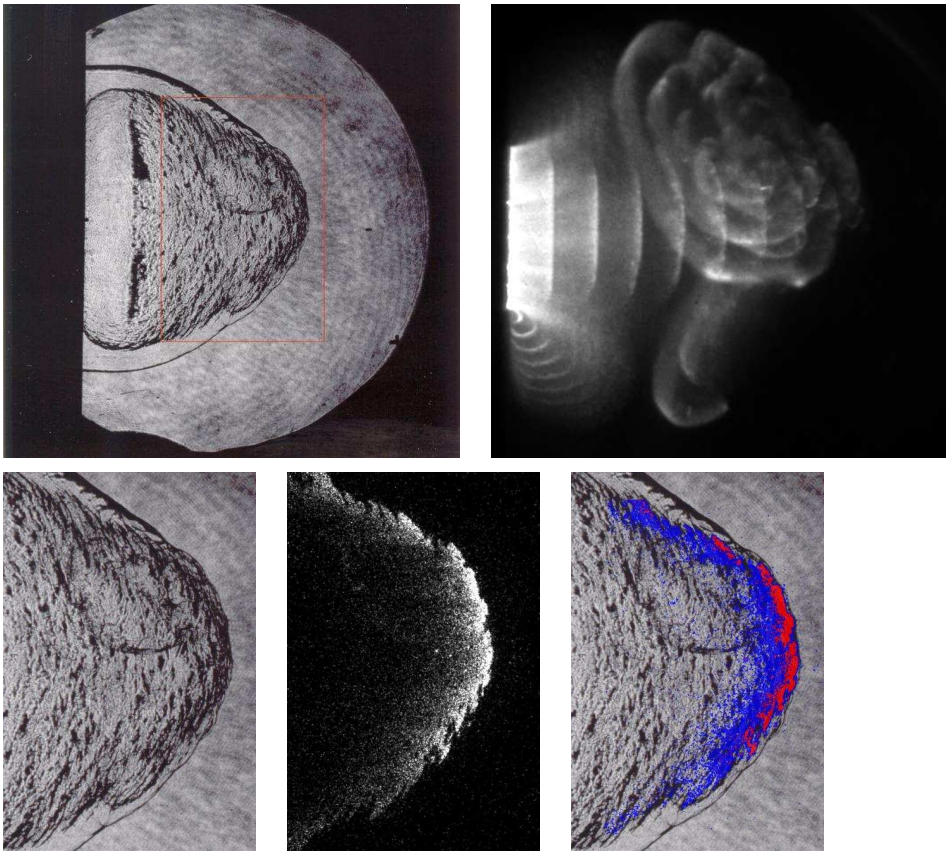

Figure M.116: Shot 140, 0.227 H_2 + 0.113 O_2 + 0.66 Ar, P_0=100 kPa, T_0=296 K. Delays: Δt(P3-PLIF) 208.167 μs; Δt(TEP-PLIF) 37.09 μs. Delays: Δt(P3-chem) 172.285 μs; Δt(TEP-chem) 1.21 μs. Multiple exposure timing: 9×6μs. Schlieren image height 150 mm, PLIF image height 70 mm, Chemiluminescence image height 109 mm.

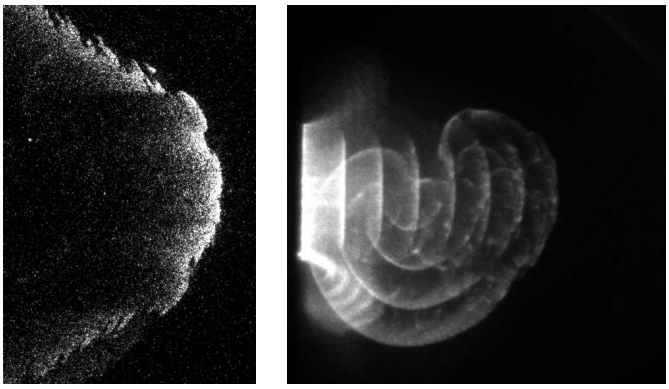

Figure M.117: Shot 141, 0.233 H_2 + 0.117 O_2 + 0.65 Ar, P_0=100 kPa, T_0=296 K. Delays: Δt(P3-chem) 172.285 μs; Δt(TEP-chem) 2.35 μs. Multiple exposure timing: 7×6μs. PLIF image height 70 mm, Chemiluminescence image height 109 mm.

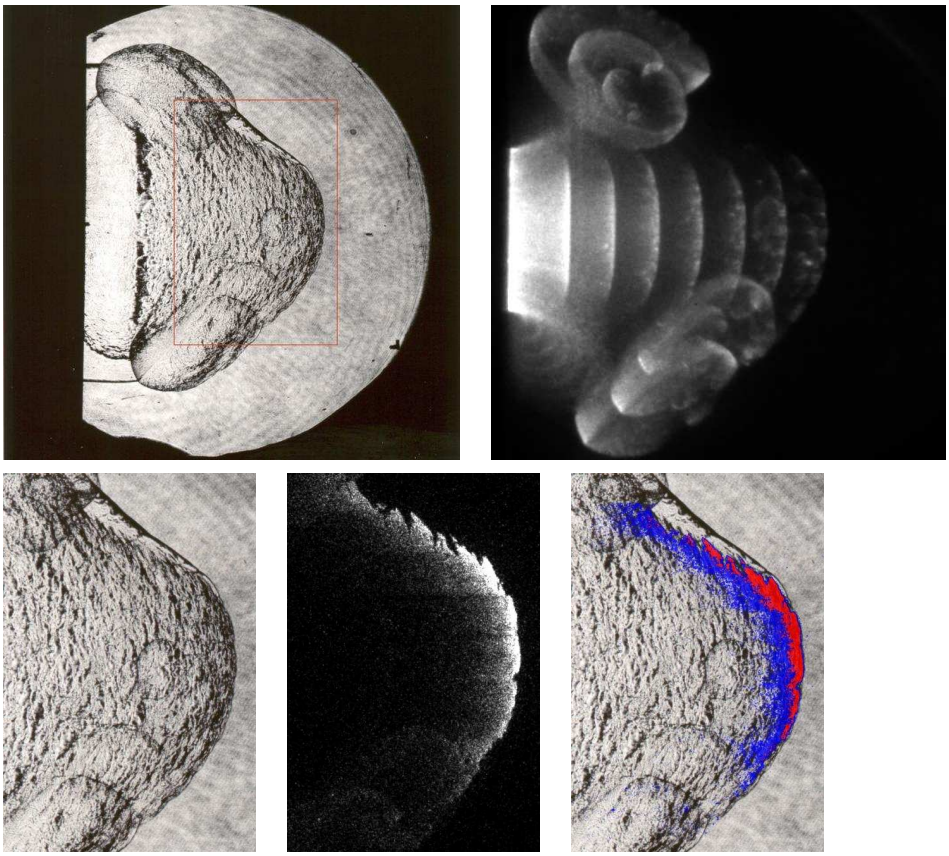

Figure M.118: Shot 142, 0.24 H_2 + 0.12 O_2 + 0.64 Ar, P_0=100 kPa, T_0=296 K. Delays: Δt(P3-PLIF) 208.167 μs; Δt(TEP-PLIF) 39.34 μs. Delays: Δt(P3-chem) 172.285 μs; Δt(TEP-chem) 3.46 μs. Multiple exposure timing: 7×6μs. Schlieren image height 150 mm, PLIF image height 70 mm, Chemiluminescence image height 109 mm.

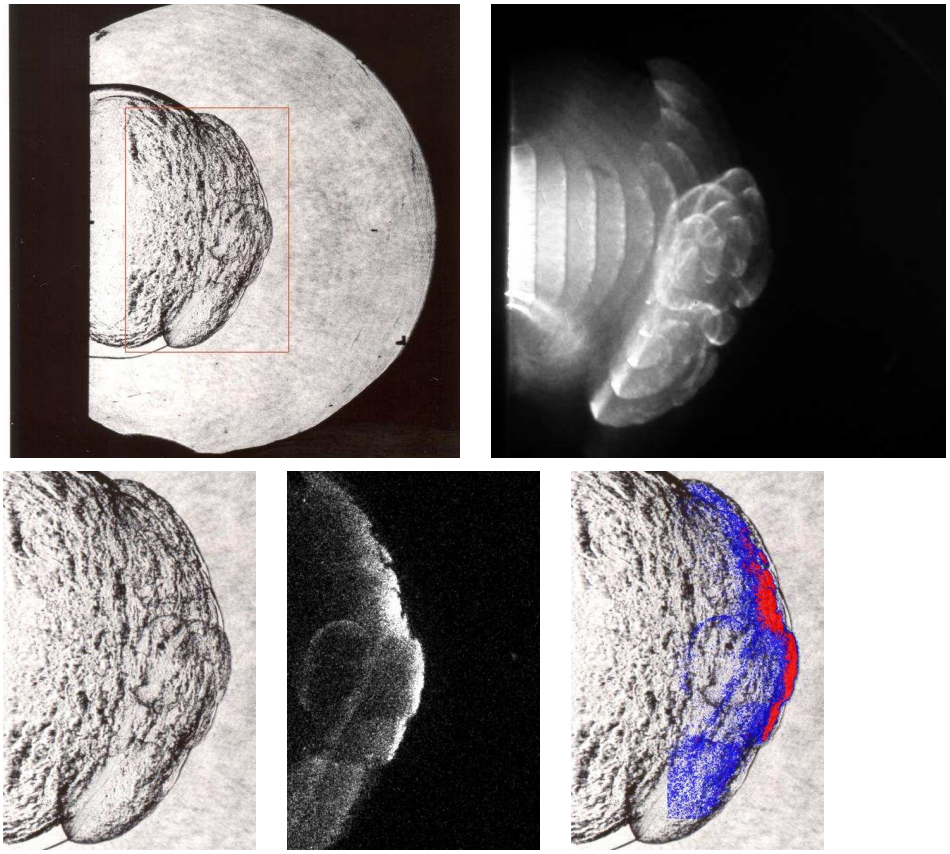

Figure M.119: Shot 143, 0.5 H_2 + 0.5 N_2O, P_0=45 kPa, T_0=296 K. Delays: Δt(P3-PLIF) 151.167 μs; Δt(TEP-PLIF) 24.82 μs. Delays: Δt(P3-chem) 127.285 μs; Δt(TEP-chem) 0.93 μs. Multiple exposure timing: 10×3μs. Schlieren image height 150 mm, PLIF image height 70 mm, Chemiluminescence image height 109 mm.

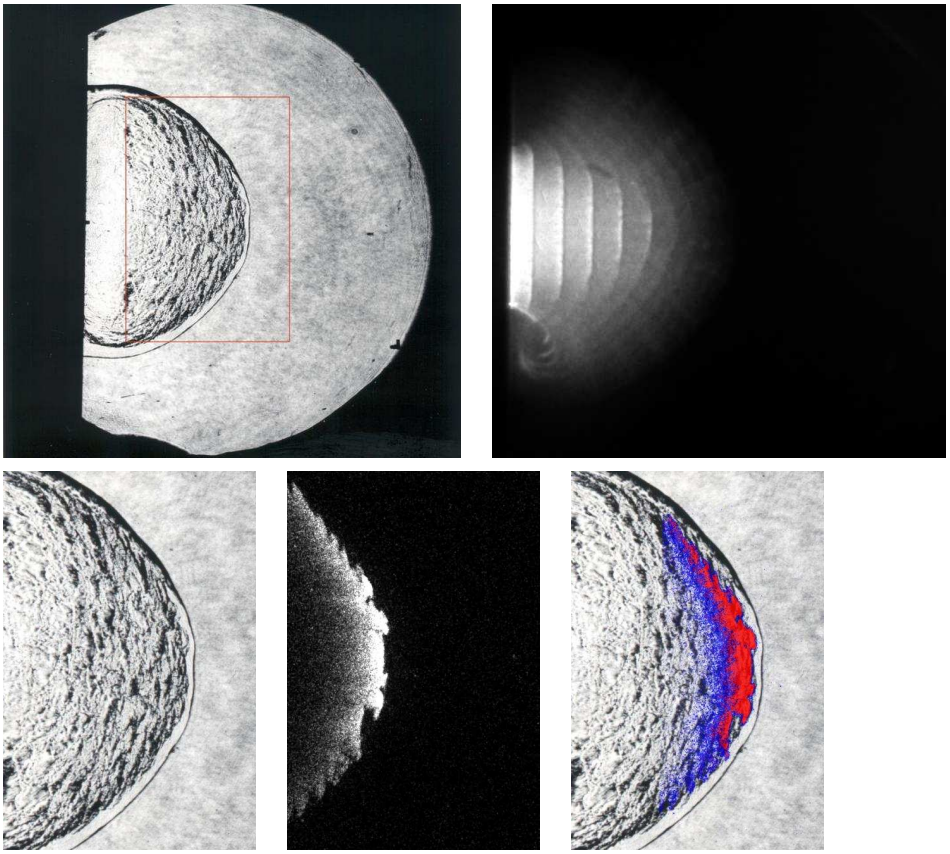

Figure M.120: Shot 144, 0.5 H_2 + 0.5 N_2O, P_0=40 kPa, T_0=296 K. Delays: Δt(P3-PLIF) 151.167 μs; Δt(TEP-PLIF) 24.54 μs. Delays: Δt(P3-chem) 127.285 μs; Δt(TEP-chem) 0.66 μs. Multiple exposure timing: 10×3μs. Schlieren image height 150 mm, PLIF image height 70 mm, Chemiluminescence image height 109 mm.

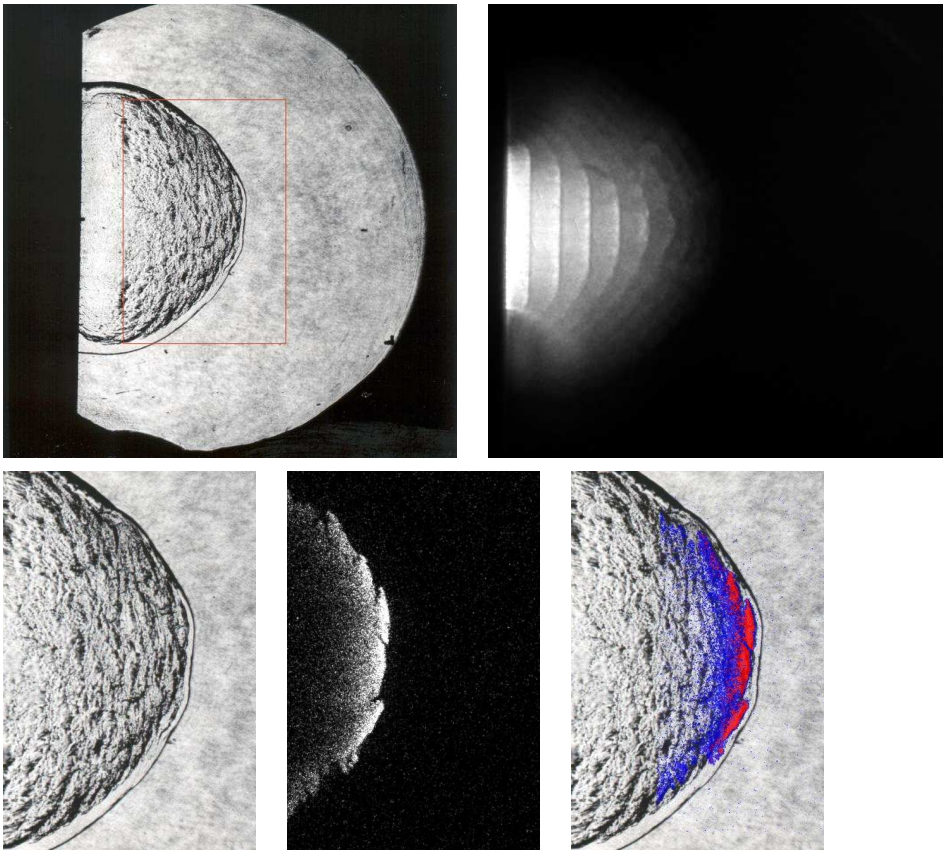

Figure M.121: Shot 145, 0.5 H_2 + 0.5 N_2O, P_0=42.5 kPa, T_0=296 K. Delays: Δt(P3-PLIF) 151.167 μs; Δt(TEP-PLIF) 24.68 μs. Delays: Δt(P3-chem) 127.285 μs; Δt(TEP-chem) 0.80 μs. Multiple exposure timing: 9×3μs. Schlieren image height 150 mm, PLIF image height 70 mm, Chemiluminescence image height 109 mm.

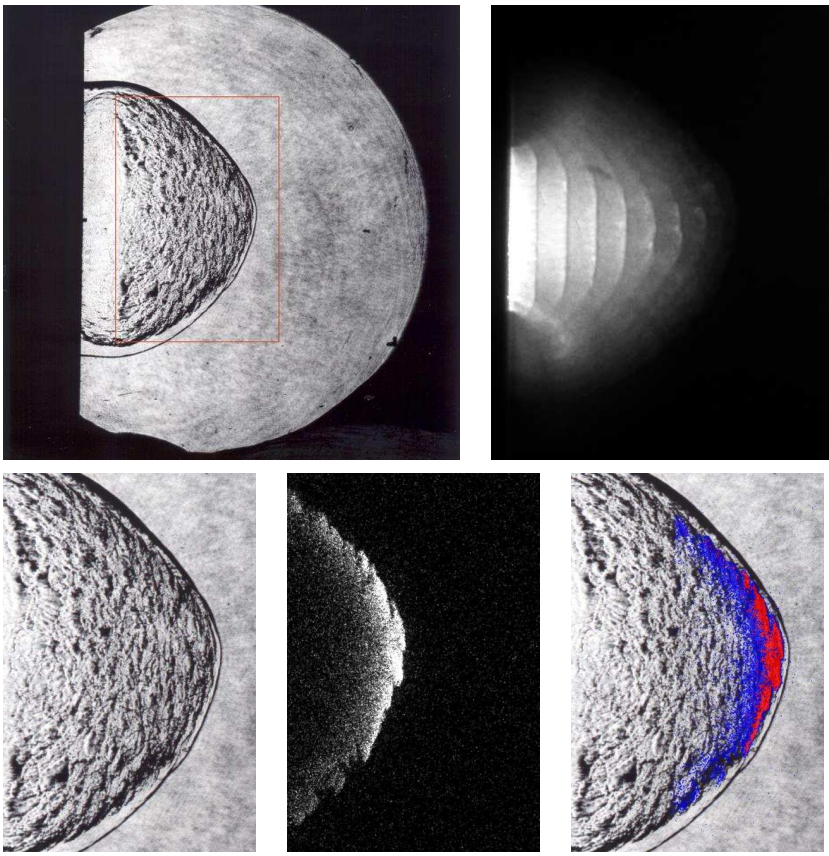

Figure M.122: Shot 146, 0.5 H_2 + 0.5 N_2O, P_0=47.5 kPa, T_0=297 K. Delays: Δt(P3-PLIF) 151.167 μs; Δt(TEP-PLIF) 24.94 μs. Delays: Δt(P3-chem) 127.285 μs; Δt(TEP-chem) 1.06 μs. Multiple exposure timing: 9×3μs. Schlieren image height 150 mm, PLIF image height 70 mm, Chemiluminescence image height 109 mm.

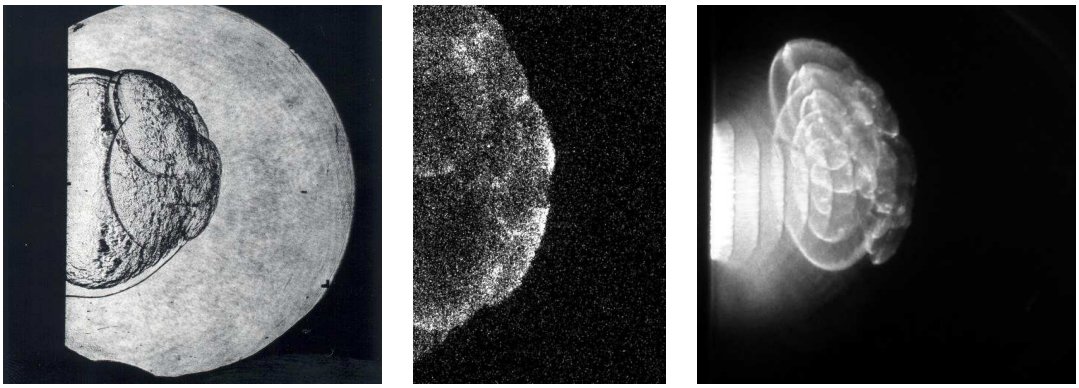

Figure M.123: Shot 147, 0.5 H_2 + 0.5 N_2O, P_0=50 kPa, T_0=297 K. Delays: Δt(P3-PLIF) 151.167 μs; Δt(TEP-PLIF) 25.06 μs. Delays: Δt(P3-chem) 127.285 μs; Δt(TEP-chem) 1.18 μs. Multiple exposure timing: 9×3μs. Schlieren image height 150 mm, PLIF image height 70 mm, Chemiluminescence image height 109 mm.

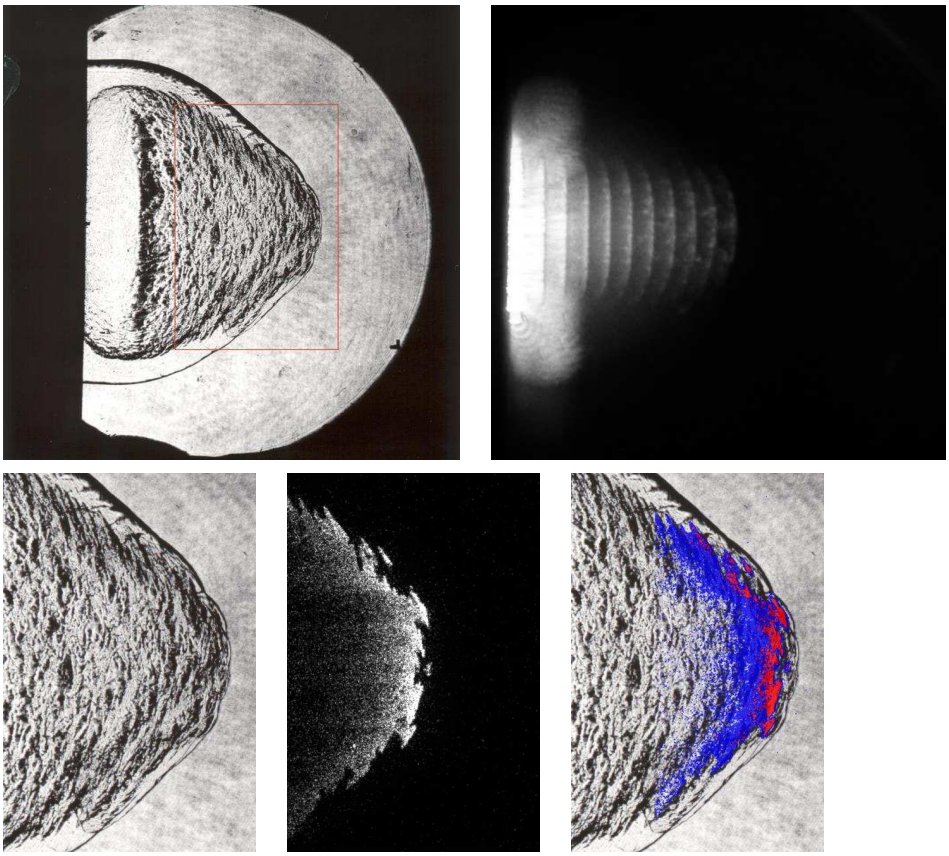

Figure M.124: Shot 148, 0.22 H_2 + 0.11 O_2 + 0.67 Ar, P_0=100 kPa, T_0=295 K. Delays: Δt(P3-PLIF) 214.167 μs; Δt(TEP-PLIF) 41.92 μs. Delays: Δt(P3-chem) 172.285 μs; Δt(TEP-chem) 0.04 μs. Multiple exposure timing: 10×3μs. Schlieren image height 150 mm, PLIF image height 70 mm, Chemiluminescence image height 109 mm.

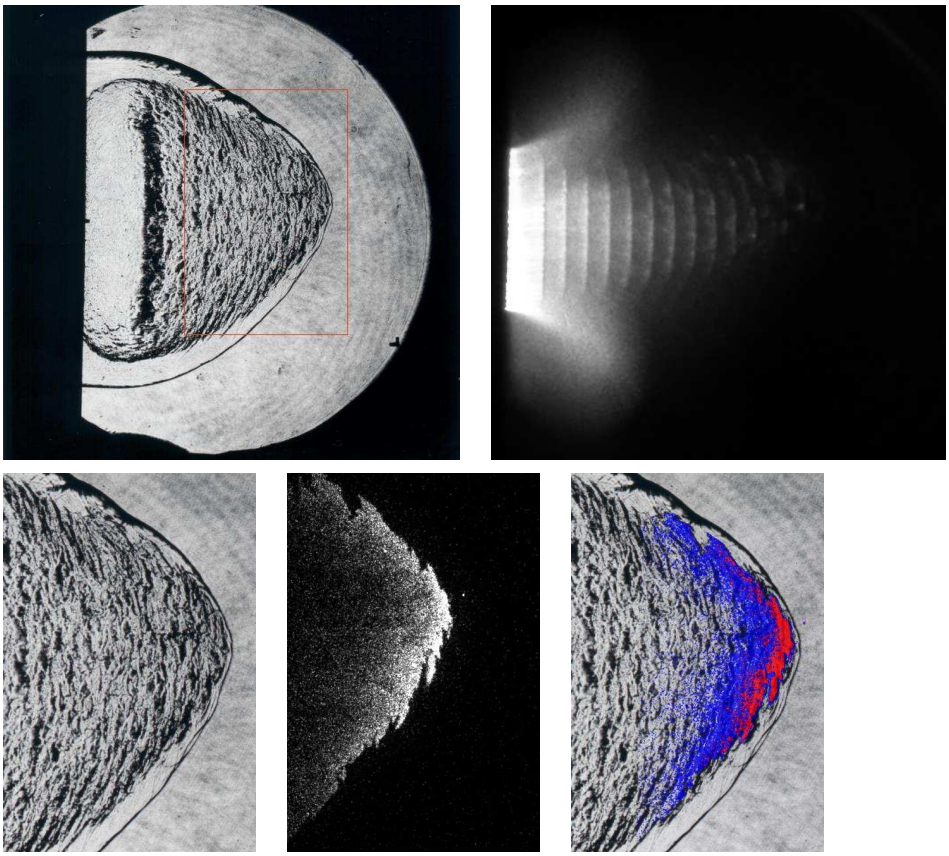

Figure M.125: Shot 149, 0.22 H_2 + 0.11 O_2 + 0.67 Ar, P_0=100 kPa, T_0=295 K. Delays: Δt(P3-PLIF) 217.167 μs; Δt(TEP-PLIF) 44.92 μs. Delays: Δt(P3-chem) 172.285 μs; Δt(TEP-chem) 0.04 μs. Multiple exposure timing: 19×3μs. Schlieren image height 150 mm, PLIF image height 70 mm, Chemiluminescence image height 109 mm.

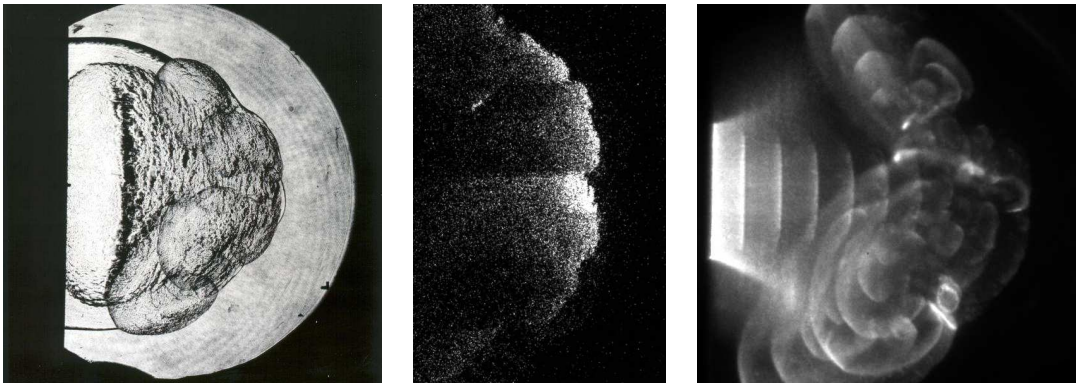

Figure M.126: Shot 150, 0.223 H_2 + 0.112 O_2 + 0.665 Ar, P_0=100 kPa, T_0=295 K. Delays: Δt(P3-PLIF) 220.167 μs; Δt(TEP-PLIF) 48.51 μs. Delays: Δt(P3-chem) 172.285 μs; Δt(TEP-chem) 0.63 μs. Multiple exposure timing: 10×6μs. Schlieren image height 150 mm, PLIF image height 70 mm, Chemiluminescence image height 109 mm.

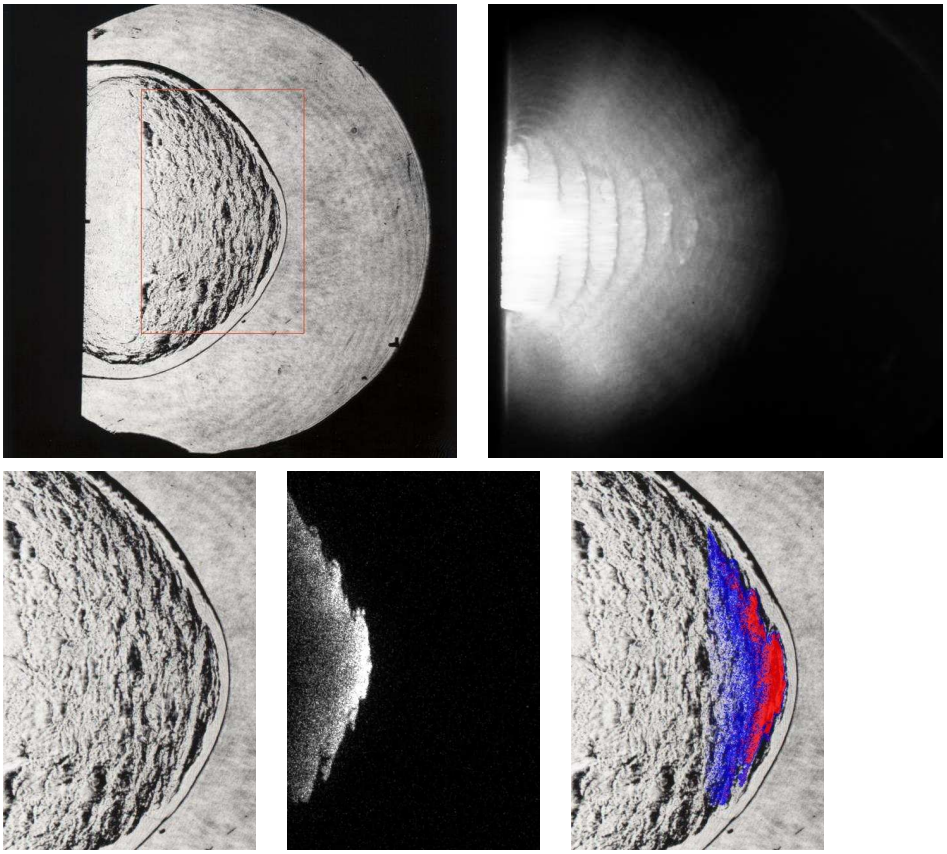

Figure M.127: Shot 151, 0.5 H_2 + 0.5 N_2O, P_0=40 kPa, T_0=295 K. Delays: Δt(P3-PLIF) 160.167 μs; Δt(TEP-PLIF) 33.54 μs. Delays: Δt(P3-chem) 127.285 μs; Δt(TEP-chem) 0.66 μs. Multiple exposure timing: 14×3μs. Schlieren image height 150 mm, PLIF image height 70 mm, Chemiluminescence image height 109 mm.

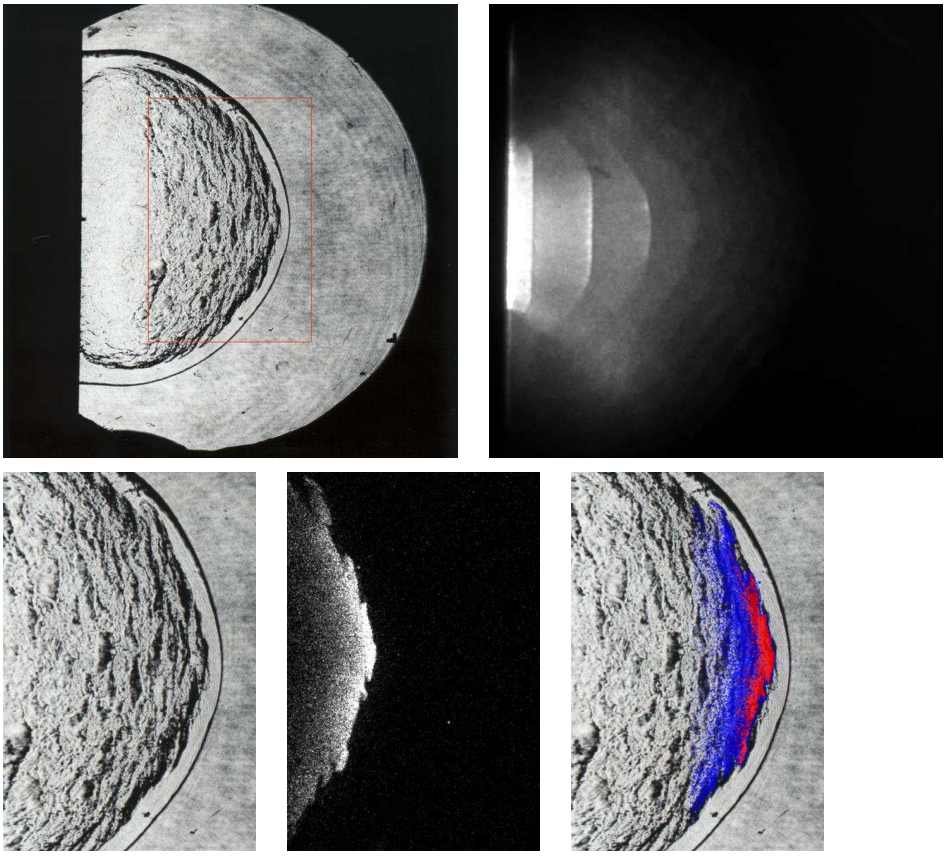

Figure M.128: Shot 152, 0.5 H_2 + 0.5 N_2O, P_0=42.5 kPa, T_0=295 K. Delays: Δt(P3-PLIF) 163.167 μs; Δt(TEP-PLIF) 36.68 μs. Delays: Δt(P3-chem) 127.285 μs; Δt(TEP-chem) 0.80 μs. Multiple exposure timing: 9×6μs. Schlieren image height 150 mm, PLIF image height 70 mm, Chemiluminescence image height 109 mm.

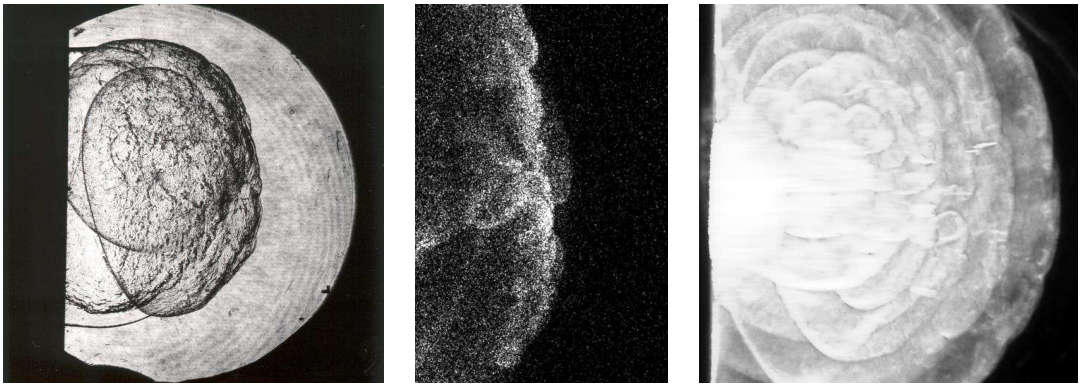

Figure M.129: Shot 153, 0.5 H_2 + 0.5 N_2O, P_0=43.75 kPa, T_0=296 K. Delays: Δt(P3-PLIF) 163.167 μs; Δt(TEP-PLIF) 36.75 μs. Delays: Δt(P3-chem) 127.285 μs; Δt(TEP-chem) 0.87 μs. Multiple exposure timing: 9×6μs. Schlieren image height 150 mm, PLIF image height 70 mm, Chemiluminescence image height 109 mm.

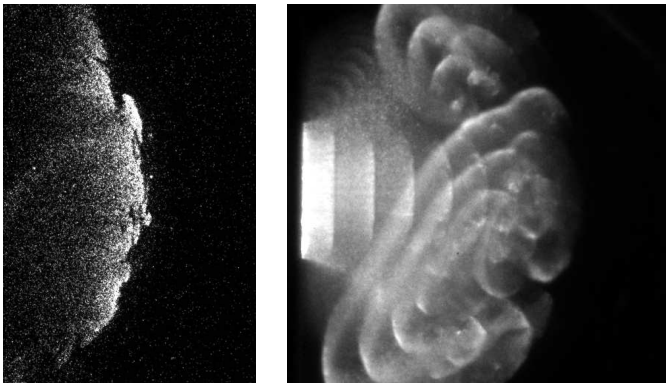

Figure M.130: Shot 154, 0.333 H_2 + 0.167 O_2 + 0.5 Ar, P_0=55 kPa, T_0=296 K. Delays: Δt(P3-chem) 157.285 μs; Δt(TEP-chem) 0.67 μs. Multiple exposure timing: 9×6μs. PLIF image height 70 mm, Chemiluminescence image height 109 mm.

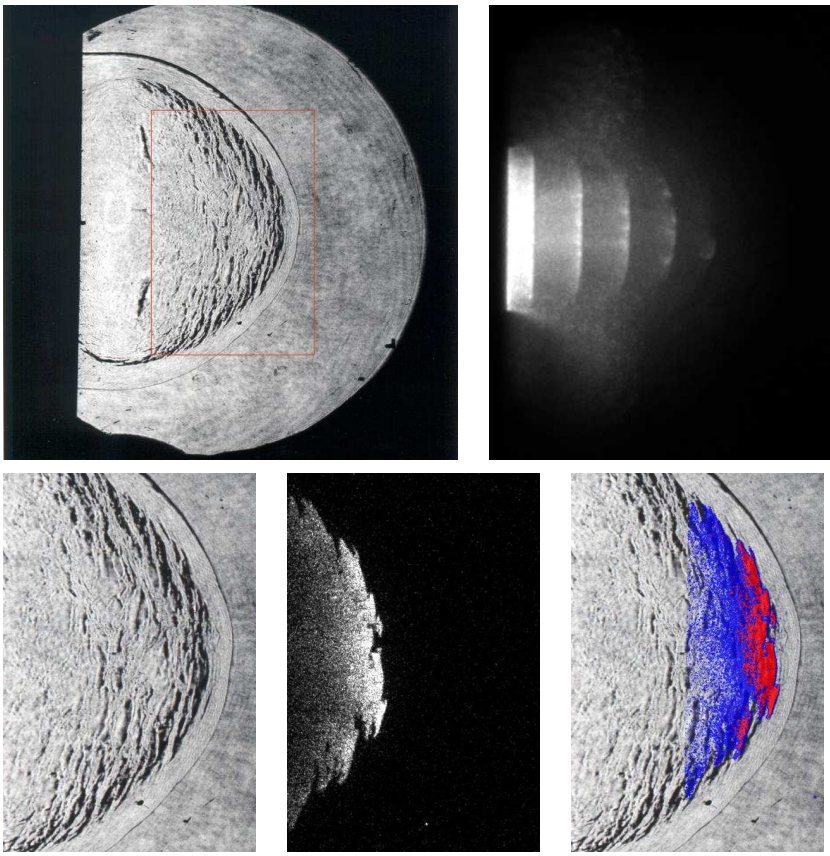

Figure M.131: Shot 156, 0.333 H_2 + 0.167 O_2 + 0.5 Ar, P_0=45 kPa, T_0=296 K. Delays: Δt(P3-PLIF) 199.167 μs; Δt(TEP-PLIF) 41.92 μs. Delays: Δt(P3-chem) 157.285 μs; Δt(TEP-chem) 0.04 μs. Multiple exposure timing: 9×6μs. Schlieren image height 150 mm, PLIF image height 70 mm, Chemiluminescence image height 109 mm.

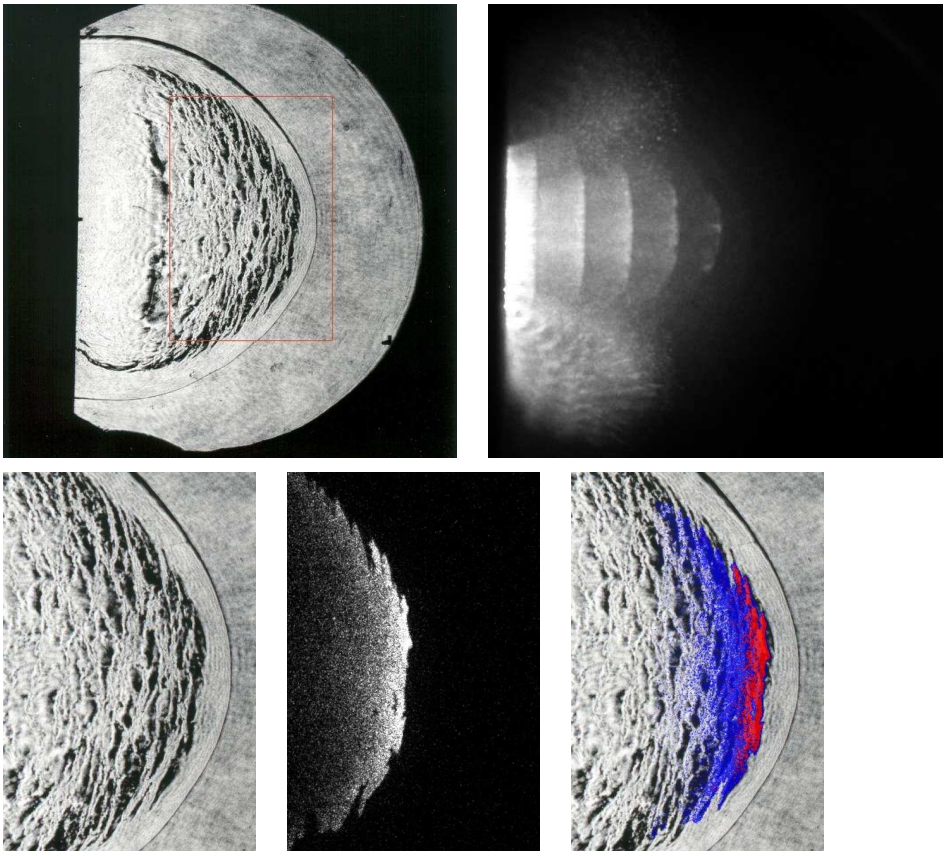

Figure M.132: Shot 157, 0.333 H_2 + 0.167 O_2 + 0.5 Ar, P_0=47.5 kPa, T_0=296 K. Delays: Δt(P3-PLIF) 205.167 μs; Δt(TEP-PLIF) 48.09 μs. Delays: Δt(P3-chem) 157.285 μs; Δt(TEP-chem) 0.21 μs. Multiple exposure timing: 11×6μs. Schlieren image height 150 mm, PLIF image height 70 mm, Chemiluminescence image height 109 mm.

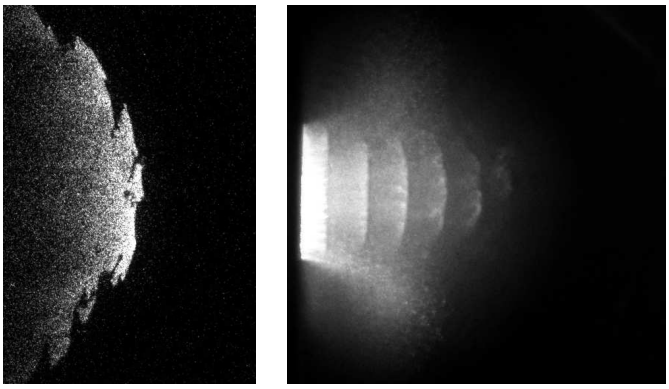

Figure M.133: Shot 158, 0.333 H_2 + 0.167 O_2 + 0.5 Ar, P_0=50 kPa, T_0=296 K. Delays: Δt(P3-chem) 157.285 μs; Δt(TEP-chem) 0.37 μs. Multiple exposure timing: 11×6μs. PLIF image height 70 mm, Chemiluminescence image height 109 mm.

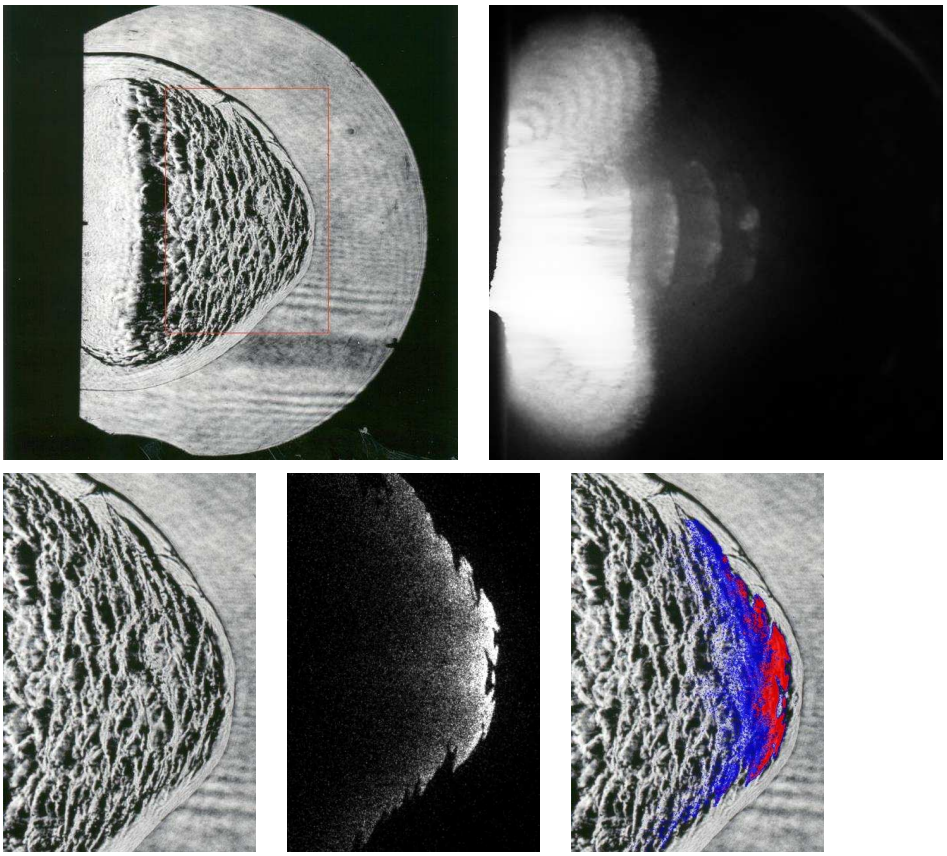

Figure M.134: Shot 160, 0.333 H_2 + 0.167 O_2 + 0.5 Ar, P_0=50 kPa, T_0=295 K. Delays: Δt(P3-PLIF) 199.167 μs; Δt(TEP-PLIF) 42.25 μs. Delays: Δt(P3-chem) 157.285 μs; Δt(TEP-chem) 0.37 μs. Multiple exposure timing: 10×6μs. Schlieren image height 150 mm, PLIF image height 70 mm, Chemiluminescence image height 109 mm.

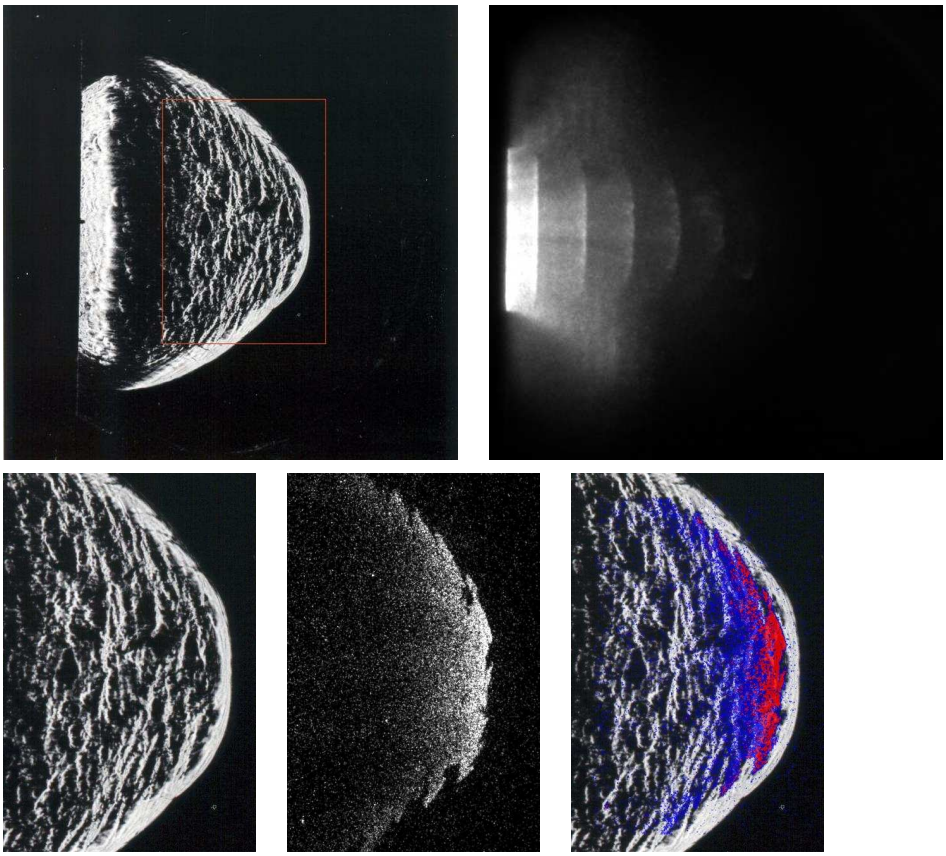

Figure M.135: Shot 161, 0.333 H_2 + 0.167 O_2 + 0.5 Ar, P_0=52.5 kPa, T_0=295 K. Delays: Δt(P3-PLIF) 199.167 μs; Δt(TEP-PLIF) 42.40 μs. Delays: Δt(P3-chem) 157.285 μs; Δt(TEP-chem) 0.52 μs. Multiple exposure timing: 10×6μs. Schlieren image height 150 mm, PLIF image height 70 mm, Chemiluminescence image height 109 mm.

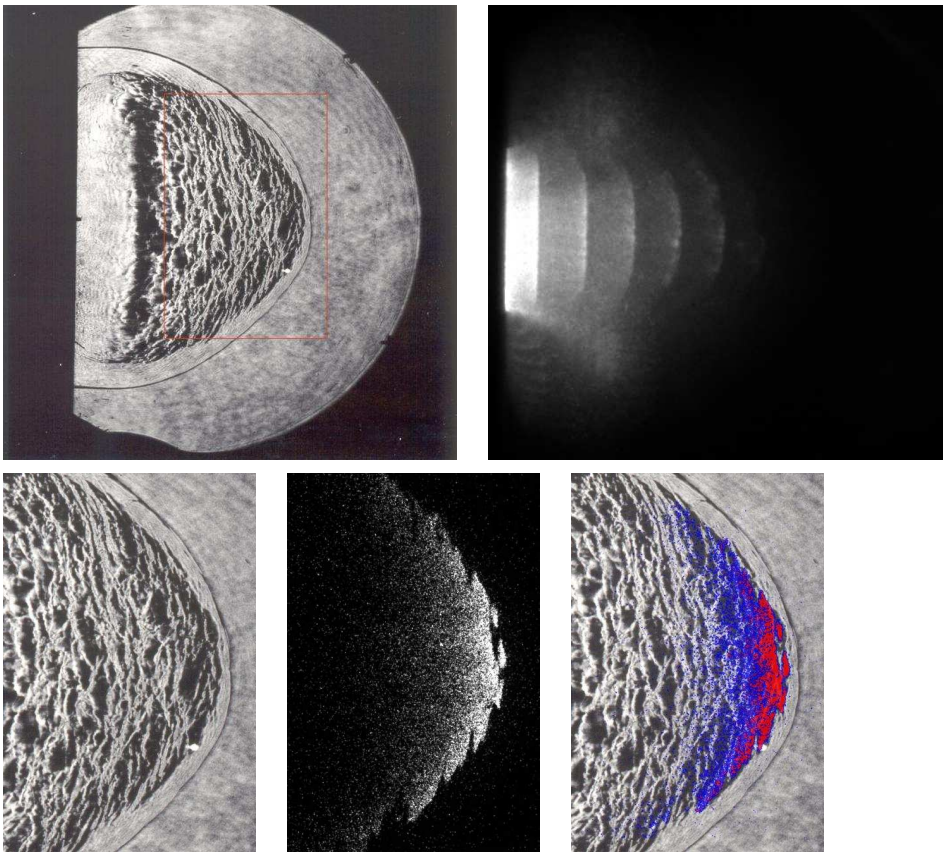

Figure M.136: Shot 162, 0.333 H_2 + 0.167 O_2 + 0.5 Ar, P_0=53.75 kPa, T_0=296 K. Delays: Δt(P3-PLIF) 199.167 μs; Δt(TEP-PLIF) 42.47 μs. Delays: Δt(P3-chem) 157.285 μs; Δt(TEP-chem) 0.59 μs. Multiple exposure timing: 10×6μs. Schlieren image height 150 mm, PLIF image height 70 mm, Chemiluminescence image height 109 mm.

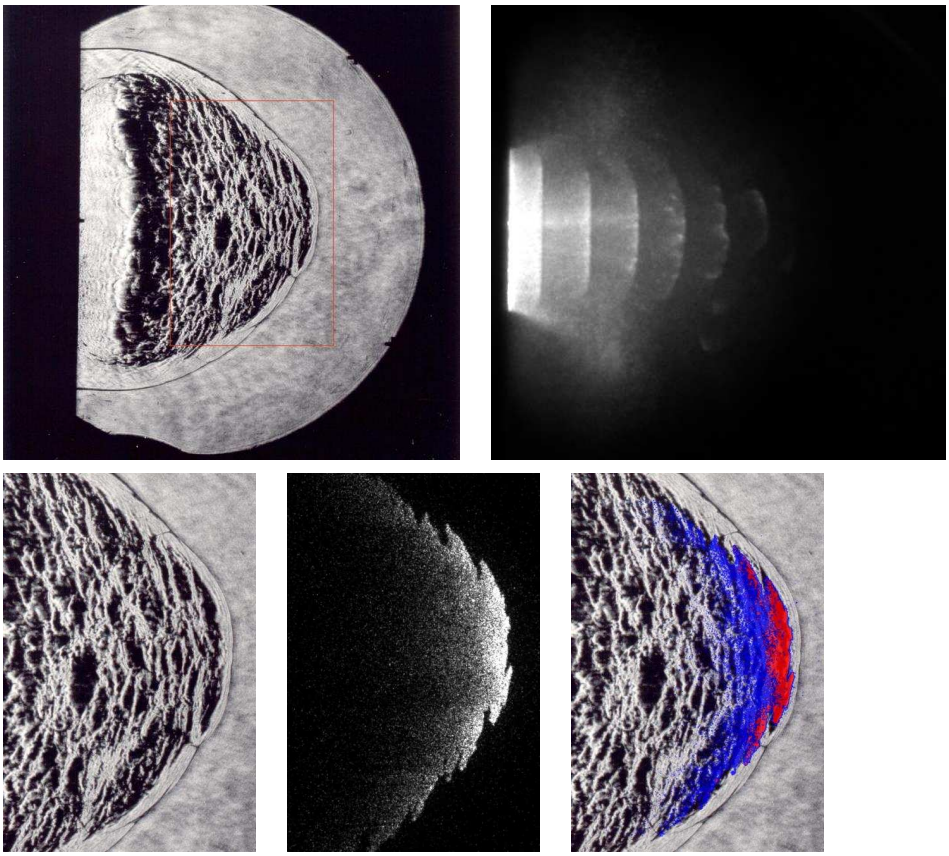

Figure M.137: Shot 163, 0.333 H_2 + 0.167 O_2 + 0.5 Ar, P_0=55 kPa, T_0=296 K. Delays: Δt(P3-PLIF) 199.167 μs; Δt(TEP-PLIF) 42.55 μs. Delays: Δt(P3-chem) 157.285 μs; Δt(TEP-chem) 0.67 μs. Multiple exposure timing: 10×6μs. Schlieren image height 150 mm, PLIF image height 70 mm, Chemiluminescence image height 109 mm.

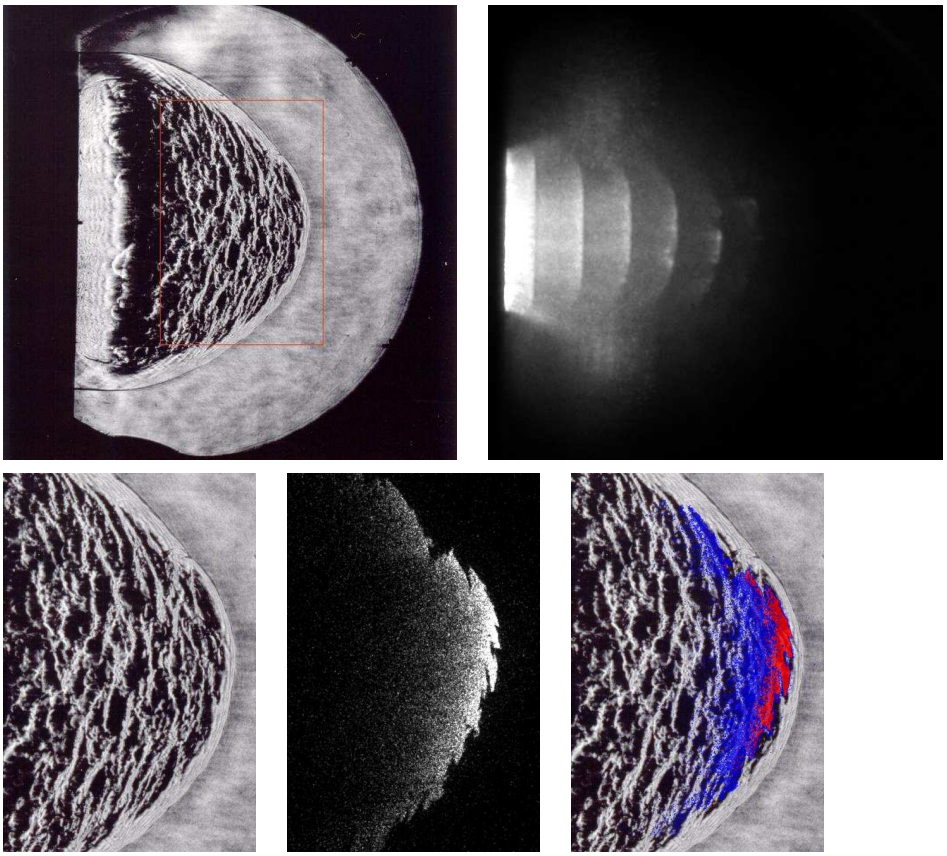

Figure M.138: Shot 164, 0.333 H_2 + 0.167 O_2 + 0.5 Ar, P_0=55 kPa, T_0=296 K. Delays: Δt(P3-PLIF) 199.167 μs; Δt(TEP-PLIF) 42.55 μs. Delays: Δt(P3-chem) 157.285 μs; Δt(TEP-chem) 0.67 μs. Multiple exposure timing: 10×6μs. Schlieren image height 150 mm, PLIF image height 70 mm, Chemiluminescence image height 109 mm.

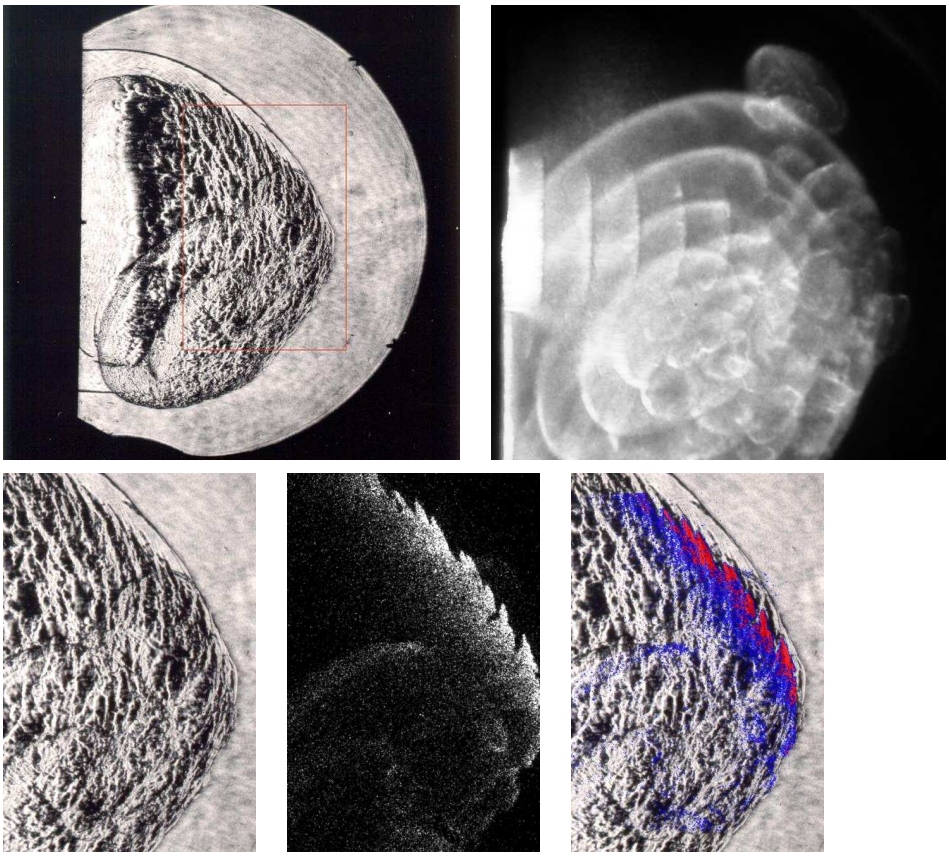

Figure M.139: Shot 165, 0.333 H_2 + 0.167 O_2 + 0.5 Ar, P_0=57.5 kPa, T_0=296 K. Delays: Δt(P3-PLIF) 199.167 μs; Δt(TEP-PLIF) 42.68 μs. Delays: Δt(P3-chem) 157.285 μs; Δt(TEP-chem) 0.80 μs. Multiple exposure timing: 10×6μs. Schlieren image height 150 mm, PLIF image height 70 mm, Chemiluminescence image height 109 mm.

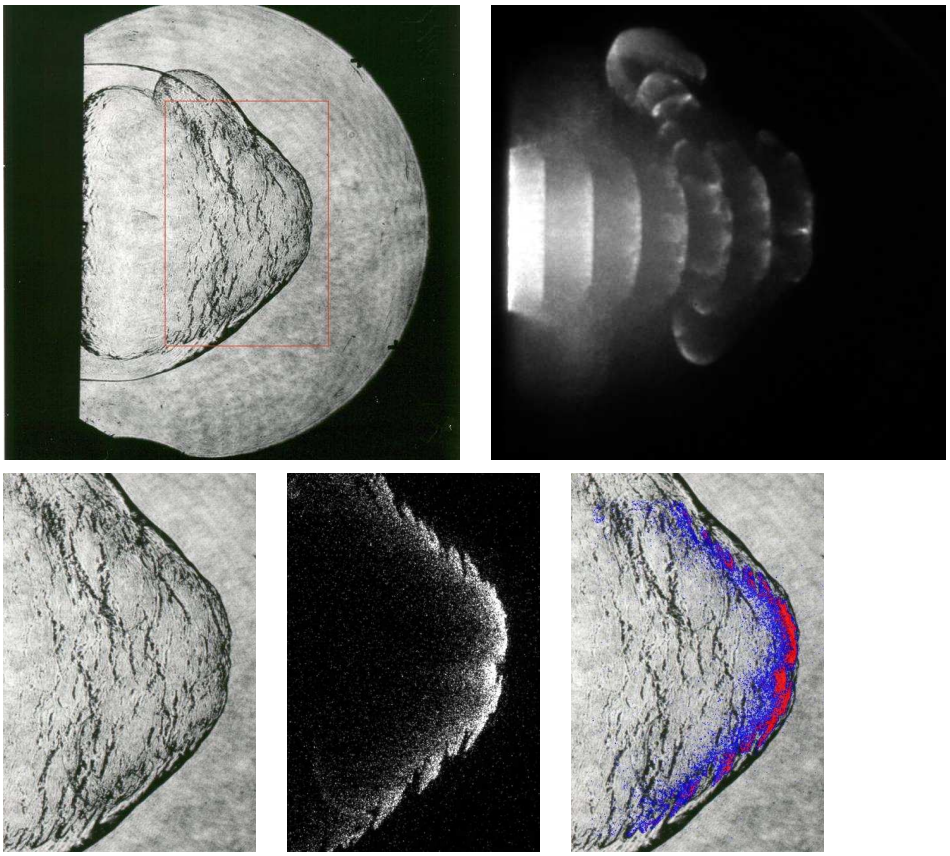

Figure M.140: Shot 166, 0.333 H_2 + 0.167 O_2 + 0.5 Ar, P_0=57.5 kPa, T_0=296 K. Delays: Δt(P3-PLIF) 193.167 μs; Δt(TEP-PLIF) 36.68 μs. Delays: Δt(P3-chem) 157.285 μs; Δt(TEP-chem) 0.80 μs. Multiple exposure timing: 7×6μs. Schlieren image height 150 mm, PLIF image height 70 mm, Chemiluminescence image height 109 mm.

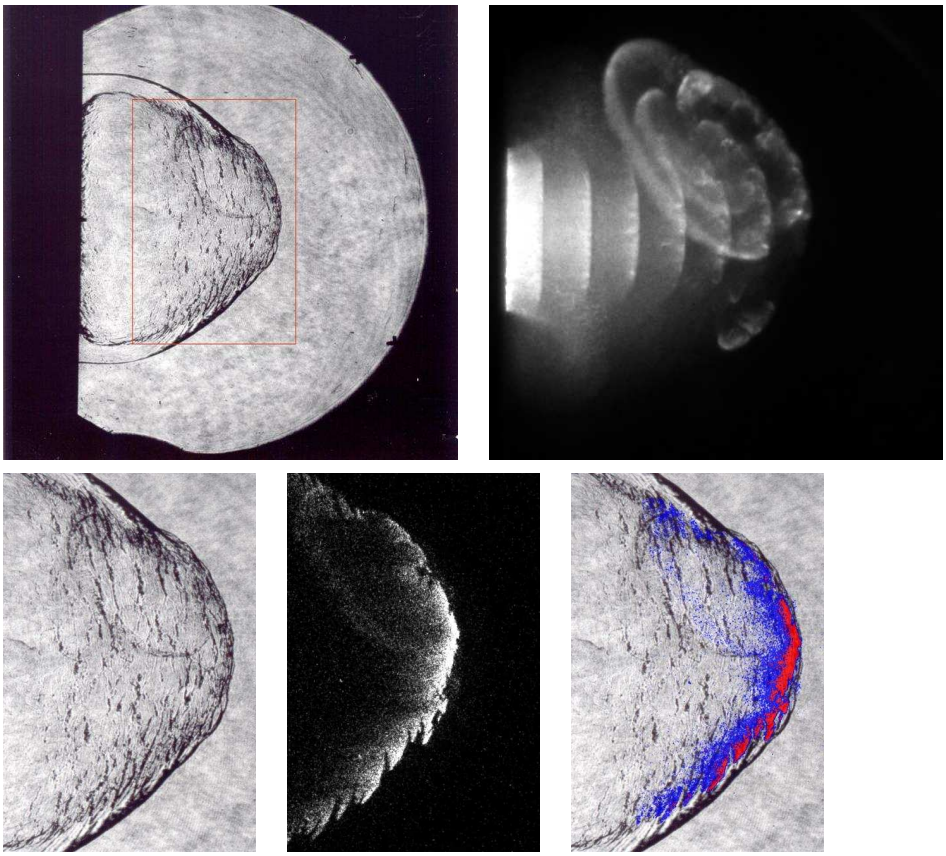

Figure M.141: Shot 167, 0.333 H_2 + 0.167 O_2 + 0.5 Ar, P_0=60 kPa, T_0=297 K. Delays: Δt(P3-PLIF) 187.167 μs; Δt(TEP-PLIF) 30.81 μs. Delays: Δt(P3-chem) 157.285 μs; Δt(TEP-chem) 0.93 μs. Multiple exposure timing: 7×6μs. Schlieren image height 150 mm, PLIF image height 70 mm, Chemiluminescence image height 109 mm.

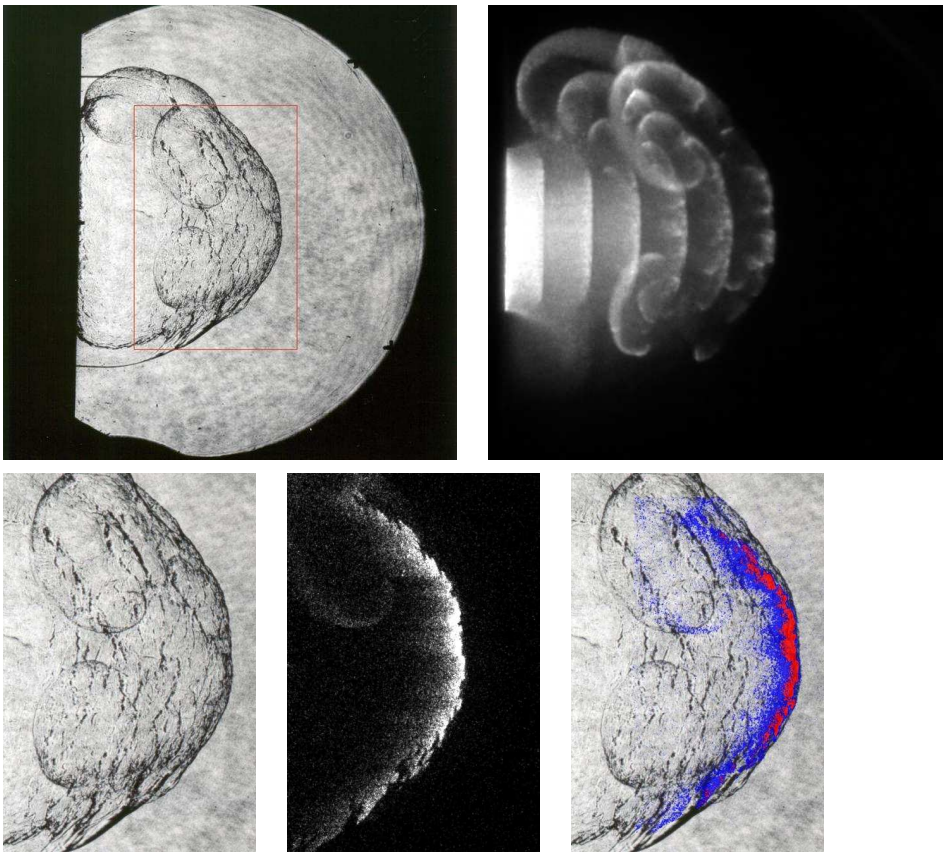

Figure M.142: Shot 168, 0.333 H_2 + 0.167 O_2 + 0.5 Ar, P_0=62.5 kPa, T_0=296 K. Delays: Δt(P3-PLIF) 187.167 μs; Δt(TEP-PLIF) 30.94 μs. Delays: Δt(P3-chem) 157.285 μs; Δt(TEP-chem) 1.06 μs. Multiple exposure timing: 6×6μs. Schlieren image height 150 mm, PLIF image height 70 mm, Chemiluminescence image height 109 mm.

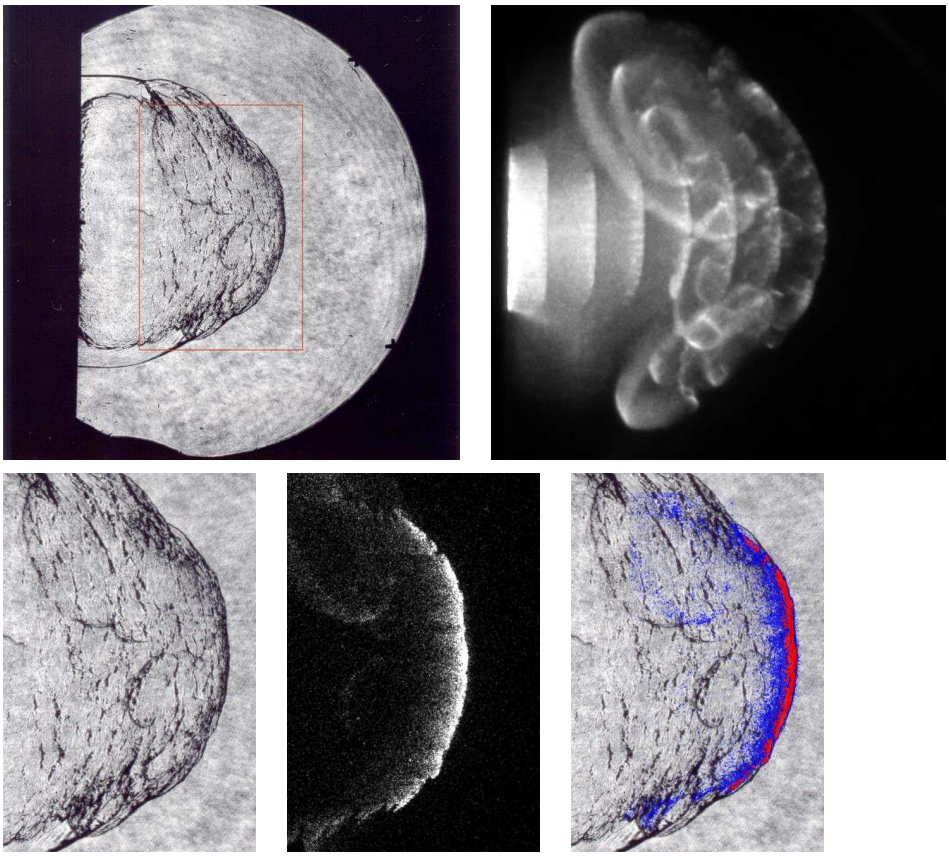

Figure M.143: Shot 169, 0.333 H_2 + 0.167 O_2 + 0.5 Ar, P_0=65 kPa, T_0=296 K. Delays: Δt(P3-PLIF) 187.167 μs; Δt(TEP-PLIF) 31.06 μs. Delays: Δt(P3-chem) 157.285 μs; Δt(TEP-chem) 1.18 μs. Multiple exposure timing: 7×6μs. Schlieren image height 150 mm, PLIF image height 70 mm, Chemiluminescence image height 109 mm.

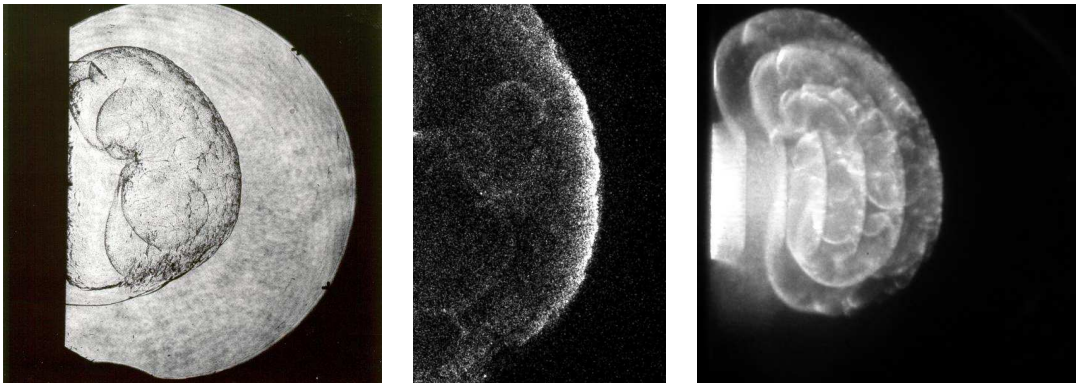

Figure M.144: Shot 170, 0.333 H_2 + 0.167 O_2 + 0.5 Ar, P_0=70 kPa, T_0=296 K. Delays: Δt(P3-PLIF) 187.167 μs; Δt(TEP-PLIF) 31.28 μs. Delays: Δt(P3-chem) 157.285 μs; Δt(TEP-chem) 1.40 μs. Multiple exposure timing: 6×6μs. Schlieren image height 150 mm, PLIF image height 70 mm, Chemiluminescence image height 109 mm.

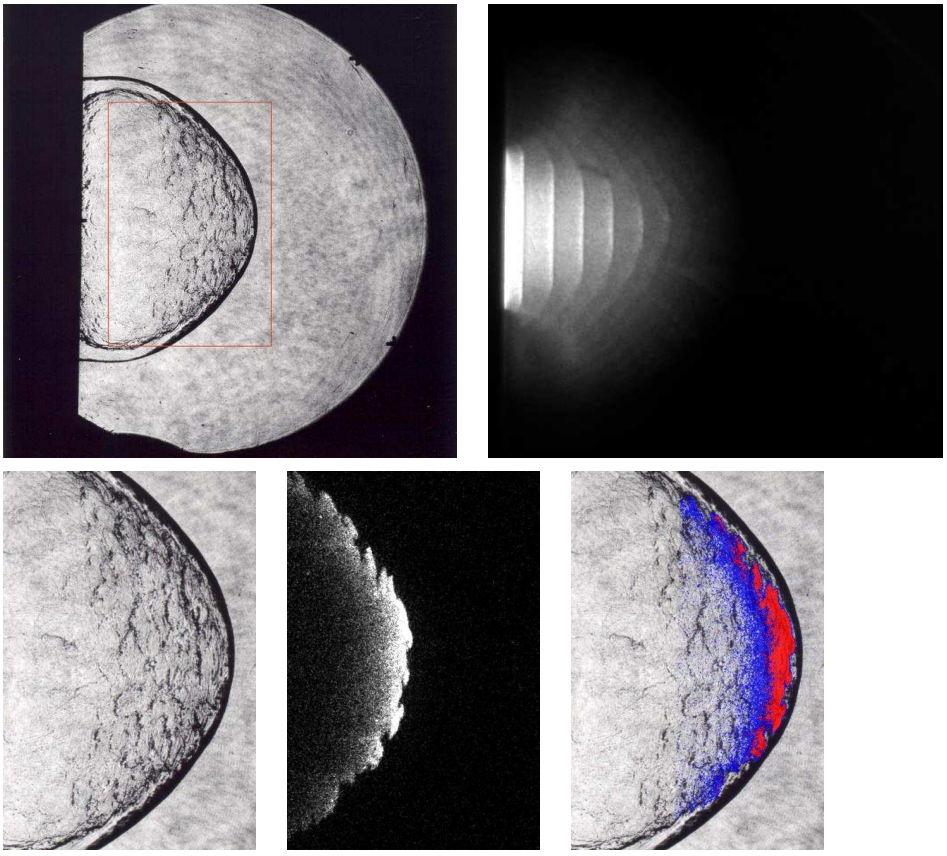

Figure M.145: Shot 171, 0.5 H_2 + 0.5 N_2O, P_0=45 kPa, T_0=297 K. Delays: Δt(P3-PLIF) 154.167 μs; Δt(TEP-PLIF) 27.82 μs. Delays: Δt(P3-chem) 127.285 μs; Δt(TEP-chem) 0.93 μs. Multiple exposure timing: 11×3μs. Schlieren image height 150 mm, PLIF image height 70 mm, Chemiluminescence image height 109 mm.

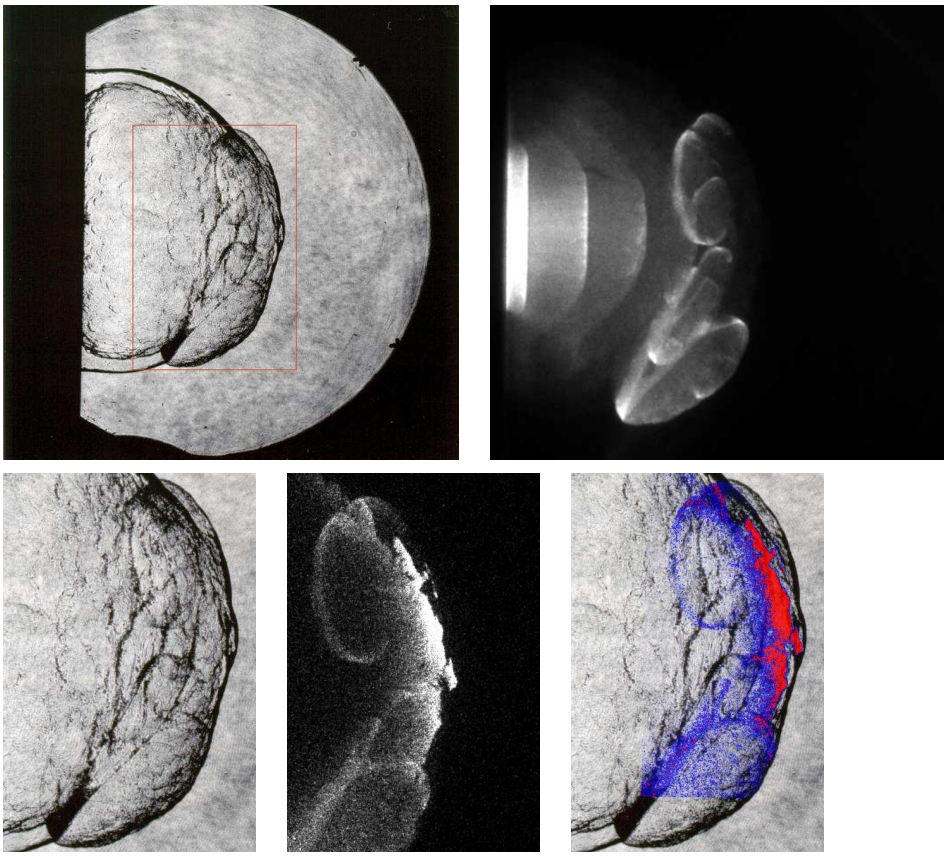

Figure M.146: Shot 172, 0.5 H_2 + 0.5 N_2O, P_0=47.5 kPa, T_0=297 K. Delays: Δt(P3-PLIF) 154.167 μs; Δt(TEP-PLIF) 27.94 μs. Delays: Δt(P3-chem) 127.285 μs; Δt(TEP-chem) 1.06 μs. Multiple exposure timing: 6×6μs. Schlieren image height 150 mm, PLIF image height 70 mm, Chemiluminescence image height 109 mm.

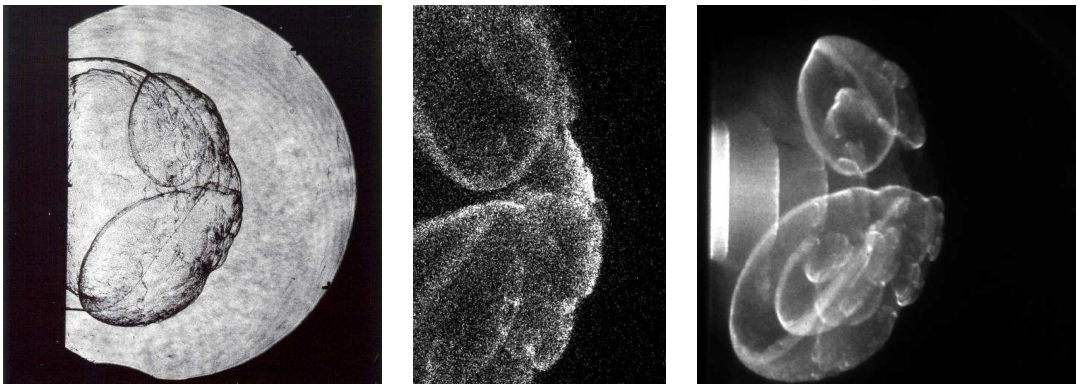

Figure M.147: Shot 173, 0.5 H_2 + 0.5 N_2O, P_0=47.5 kPa, T_0=297 K. Delays: Δt(P3-PLIF) 157.167 μs; Δt(TEP-PLIF) 30.94 μs. Delays: Δt(P3-chem) 127.285 μs; Δt(TEP-chem) 1.06 μs. Multiple exposure timing: 6×6μs. Schlieren image height 150 mm, PLIF image height 70 mm, Chemiluminescence image height 109 mm.

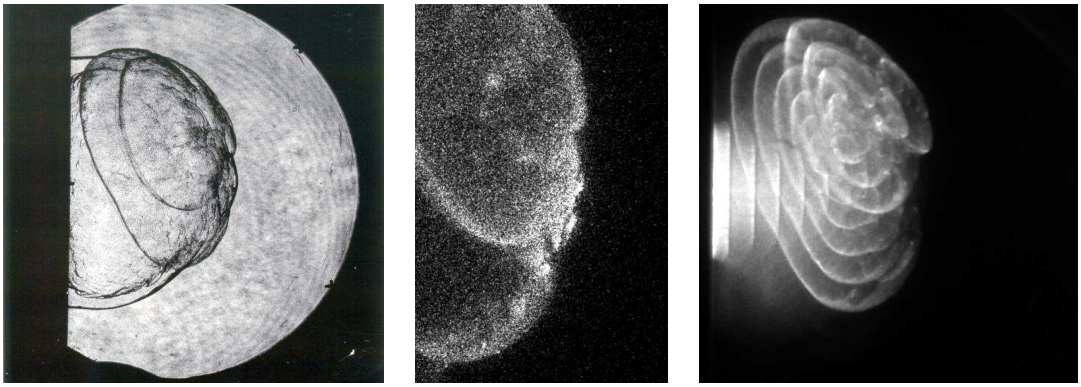

Figure M.148: Shot 174, 0.5 H_2 + 0.5 N_2O, P_0=46.25 kPa, T_0=297 K. Delays: Δt(P3-PLIF) 157.167 μs; Δt(TEP-PLIF) 30.88 μs. Delays: Δt(P3-chem) 127.285 μs; Δt(TEP-chem) 1.00 μs. Multiple exposure timing: 11×3μs. Schlieren image height 150 mm, PLIF image height 70 mm, Chemiluminescence image height 109 mm.

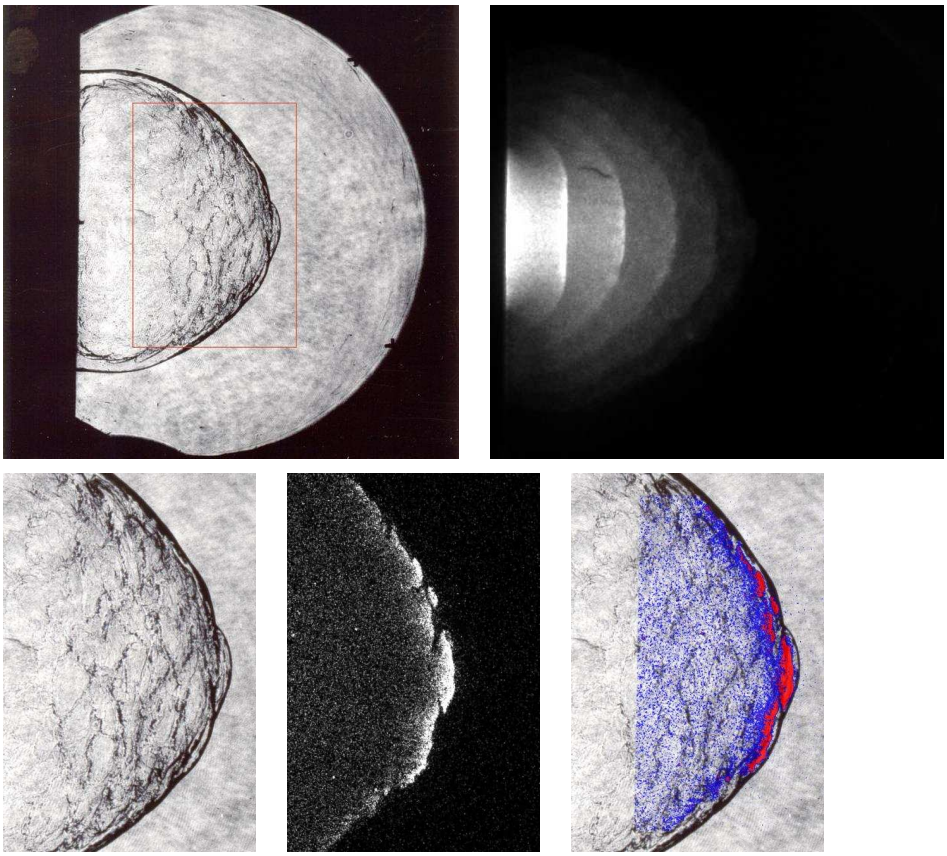

Figure M.149: Shot 175, 0.222 C_2H_6 + 0.778 O_2, P_0=30 kPa, T_0=297 K. Delays: Δt(P3-PLIF) 160.167 μs; Δt(TEP-PLIF) 31.57 μs. Delays: Δt(P3-chem) 127.285 μs; Δt(TEP-chem) -1.31 μs. Multiple exposure timing: 6×6μs. Schlieren image height 150 mm, PLIF image height 70 mm, Chemiluminescence image height 109 mm.

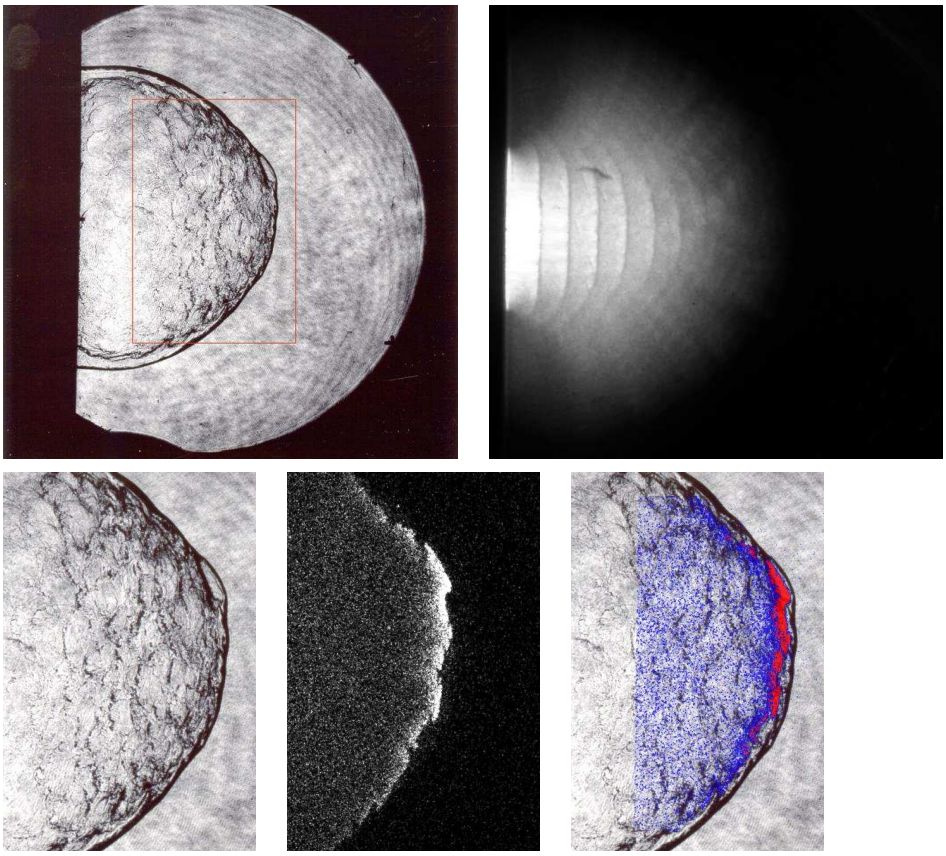

Figure M.150: Shot 176, 0.222 C_2H_6 + 0.778 O_2, P_0=32.5 kPa, T_0=297 K. Delays: Δt(P3-PLIF) 160.167 μs; Δt(TEP-PLIF) 31.77 μs. Delays: Δt(P3-chem) 127.285 μs; Δt(TEP-chem) -1.11 μs. Multiple exposure timing: 14×3μs. Schlieren image height 150 mm, PLIF image height 70 mm, Chemiluminescence image height 109 mm.

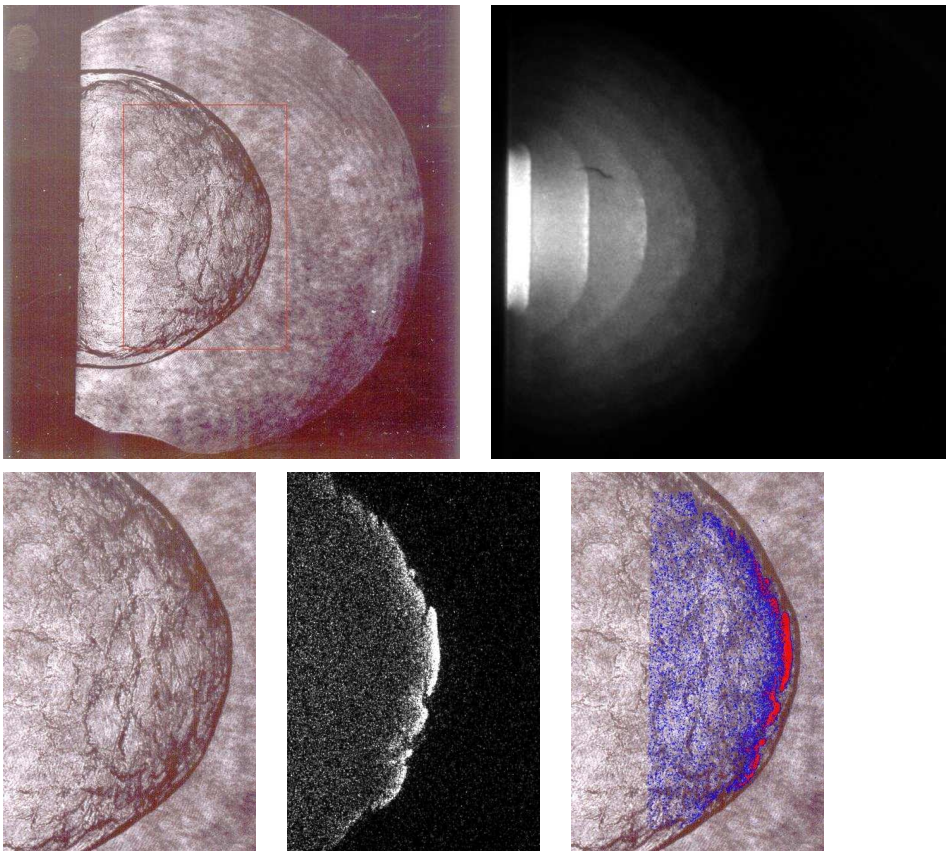

Figure M.151: Shot 177, 0.222 C_2H_6 + 0.778 O_2, P_0=35 kPa, T_0=297 K. Delays: Δt(P3-PLIF) 160.167 μs; Δt(TEP-PLIF) 31.96 μs. Delays: Δt(P3-chem) 130.285 μs; Δt(TEP-chem) 2.07 μs. Multiple exposure timing: 7×6μs. Schlieren image height 150 mm, PLIF image height 70 mm, Chemiluminescence image height 109 mm.

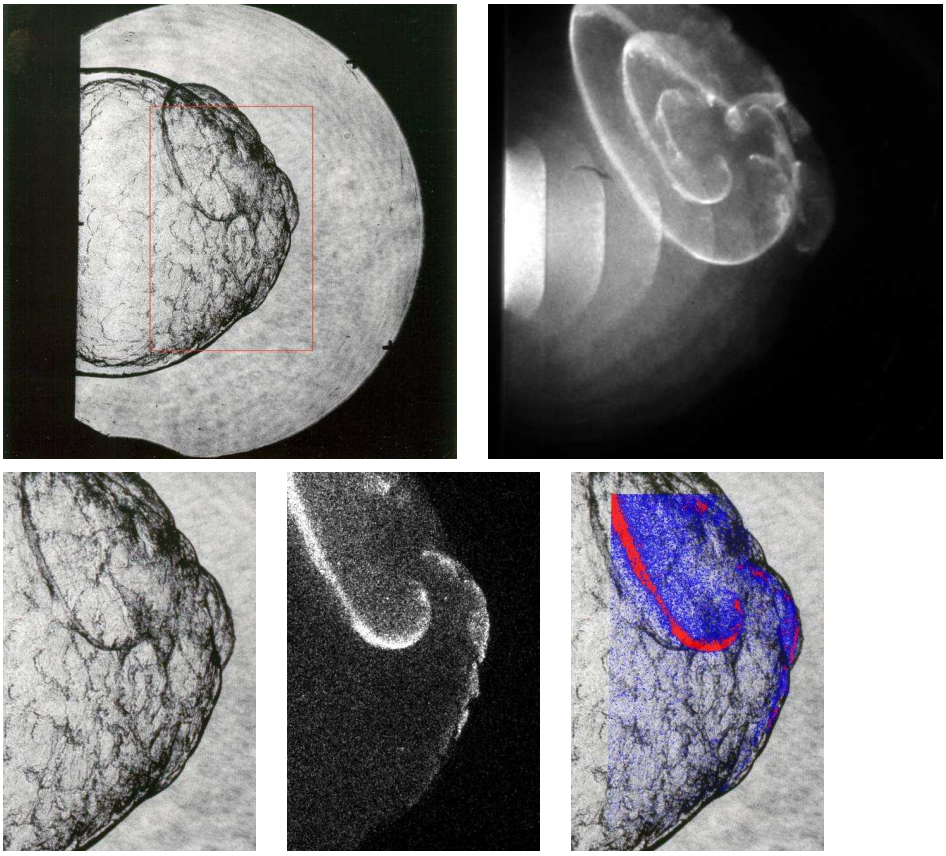

Figure M.152: Shot 178, 0.222 C_2H_6 + 0.778 O_2, P_0=40 kPa, T_0=297 K. Delays: Δt(P3-PLIF) 160.167 μs; Δt(TEP-PLIF) 32.29 μs. Delays: Δt(P3-chem) 130.285 μs; Δt(TEP-chem) 2.40 μs. Multiple exposure timing: 7×6μs. Schlieren image height 150 mm, PLIF image height 70 mm, Chemiluminescence image height 109 mm.

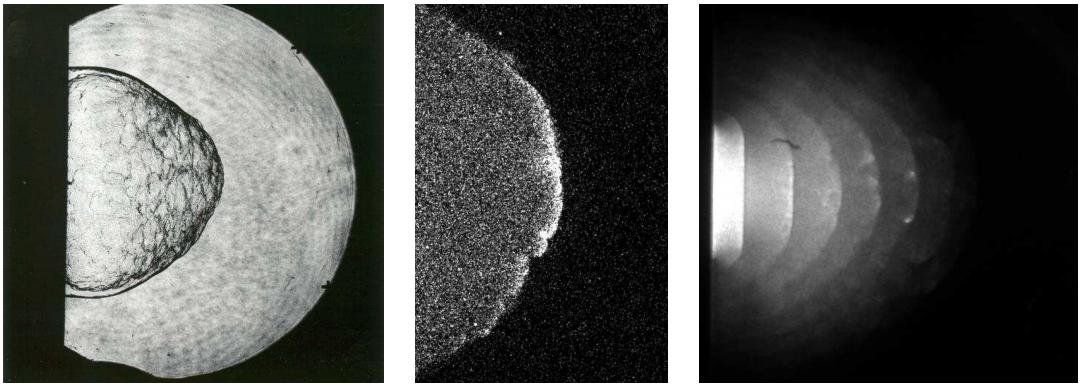

Figure M.153: Shot 179, 0.222 C_2H_6 + 0.778 O_2, P_0=37.5 kPa, T_0=298 K. Delays: Δt(P3-PLIF) 154.167 μs; Δt(TEP-PLIF) 26.13 μs. Delays: Δt(P3-chem) 130.285 μs; Δt(TEP-chem) 2.25 μs. Multiple exposure timing: 7×6μs. Schlieren image height 150 mm, PLIF image height 70 mm, Chemiluminescence image height 109 mm.

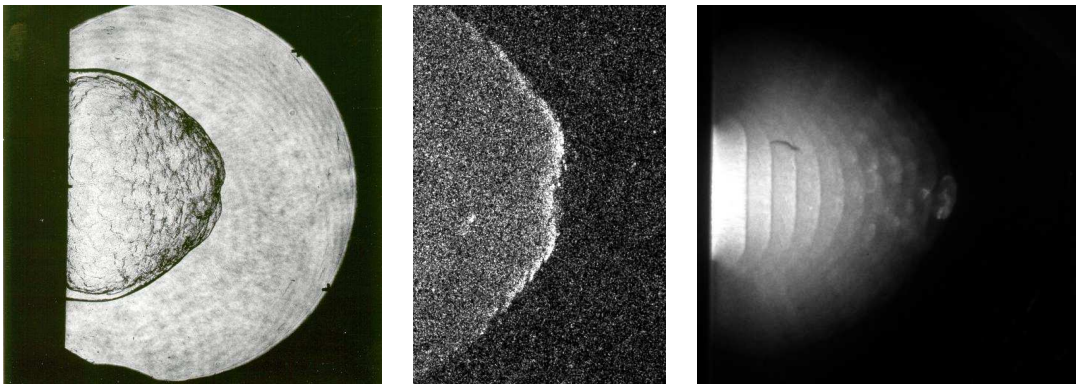

Figure M.154: Shot 180, 0.222 C_2H_6 + 0.778 O_2, P_0=37.5 kPa, T_0=297 K. Delays: Δt(P3-PLIF) 154.167 μs; Δt(TEP-PLIF) 26.13 μs. Delays: Δt(P3-chem) 130.285 μs; Δt(TEP-chem) 2.25 μs. Multiple exposure timing: 11×6μs. Schlieren image height 150 mm, PLIF image height 70 mm, Chemiluminescence image height 109 mm.

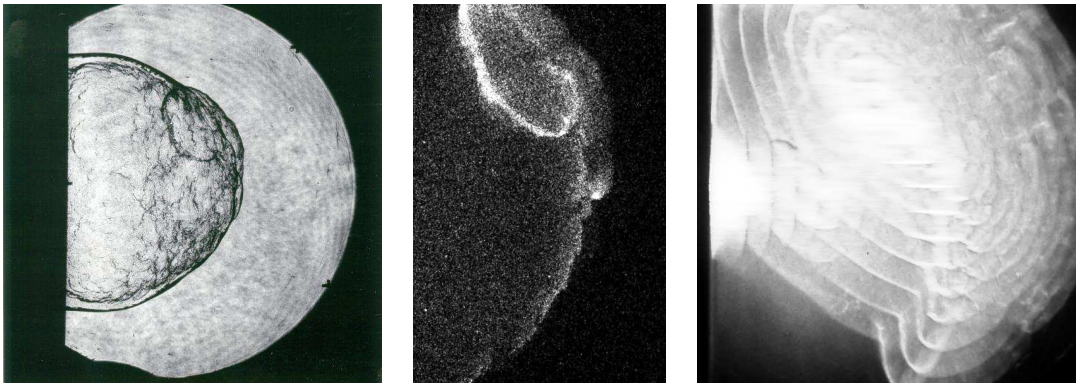

Figure M.155: Shot 181, 0.222 C_2H_6 + 0.778 O_2, P_0=36.25 kPa, T_0=297 K. Delays: Δt(P3-PLIF) 160.167 μs; Δt(TEP-PLIF) 32.04 μs. Delays: Δt(P3-chem) 130.285 μs; Δt(TEP-chem) 2.16 μs. Multiple exposure timing: 11×6μs. Schlieren image height 150 mm, PLIF image height 70 mm, Chemiluminescence image height 109 mm.

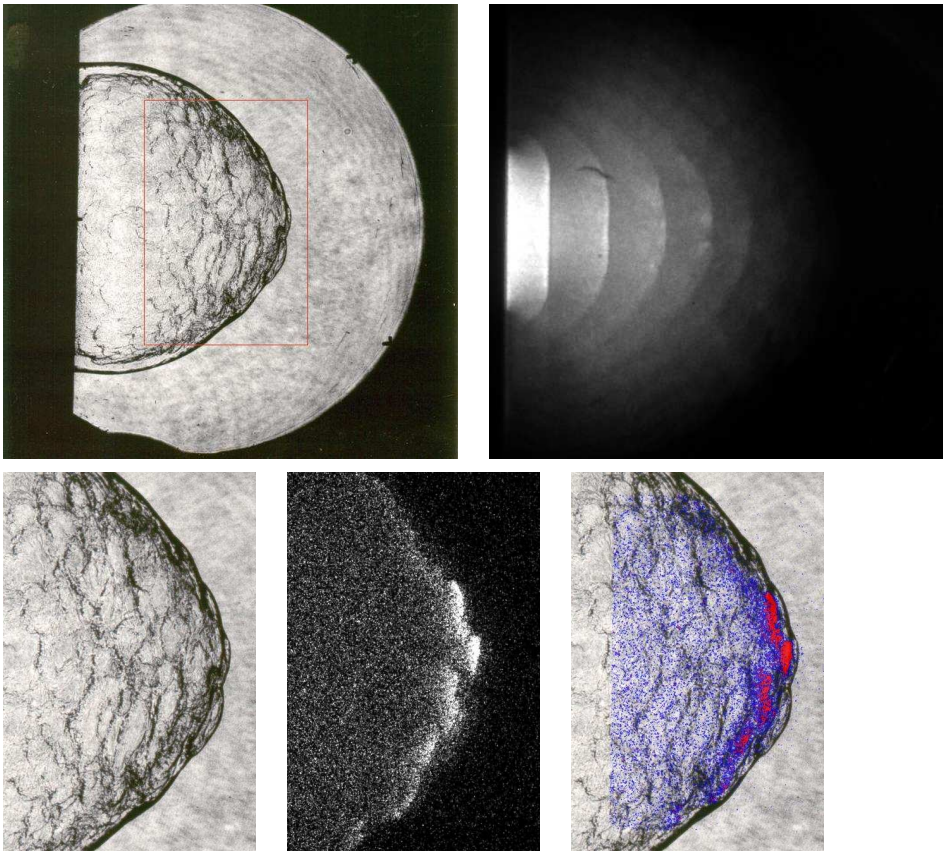

Figure M.156: Shot 182, 0.222 C_2H_6 + 0.778 O_2, P_0=36.25 kPa, T_0=298 K. Delays: Δt(P3-PLIF) 160.175 μs; Δt(TEP-PLIF) 32.05 μs. Delays: Δt(P3-chem) 130.285 μs; Δt(TEP-chem) 2.16 μs. Multiple exposure timing: 9×6μs. Schlieren image height 150 mm, PLIF image height 70 mm, Chemiluminescence image height 109 mm.

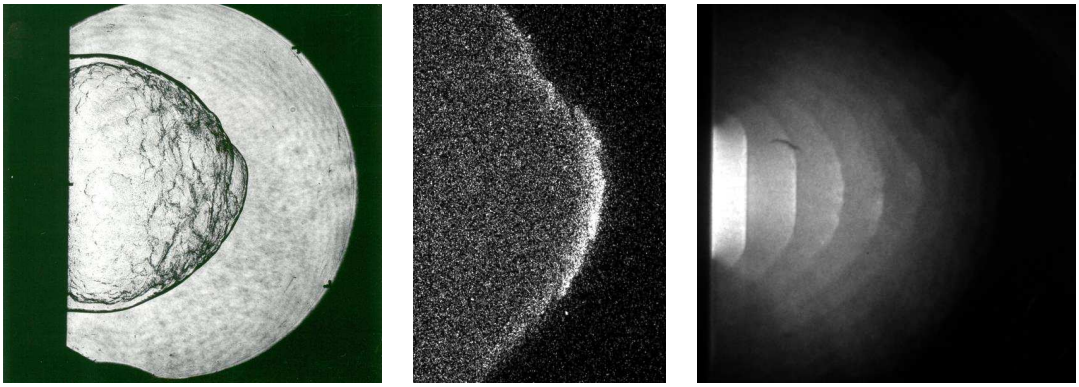

Figure M.157: Shot 183, 0.222 C_2H_6 + 0.778 O_2, P_0=37.5 kPa, T_0=298 K. Delays: Δt(P3-PLIF) 160.175 μs; Δt(TEP-PLIF) 32.14 μs. Delays: Δt(P3-chem) 130.285 μs; Δt(TEP-chem) 2.25 μs. Multiple exposure timing: 9×6μs. Schlieren image height 150 mm, PLIF image height 70 mm, Chemiluminescence image height 109 mm.

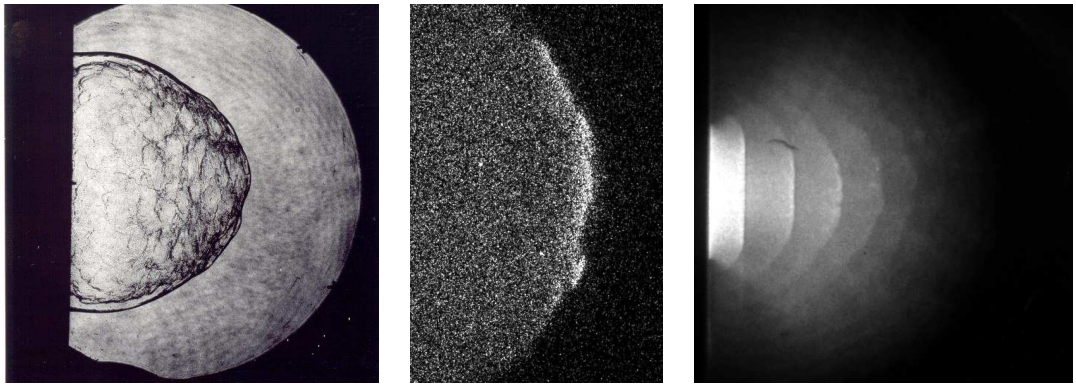

Figure M.158: Shot 184, 0.222 C_2H_6 + 0.778 O_2, P_0=38.25 kPa, T_0=298 K. Delays: Δt(P3-PLIF) 160.175 μs; Δt(TEP-PLIF) 32.18 μs. Delays: Δt(P3-chem) 130.285 μs; Δt(TEP-chem) 2.29 μs. Multiple exposure timing: 9×6μs. Schlieren image height 150 mm, PLIF image height 70 mm, Chemiluminescence image height 109 mm.

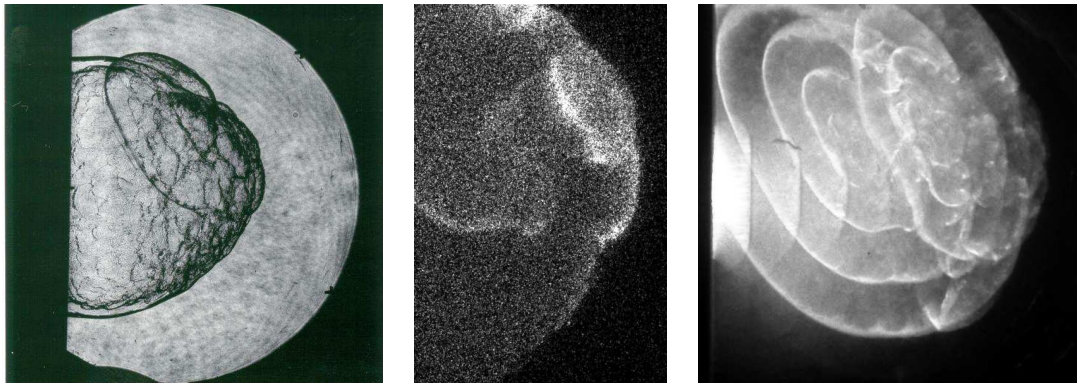

Figure M.159: Shot 185, 0.222 C_2H_6 + 0.778 O_2, P_0=42.5 kPa, T_0=298 K. Delays: Δt(P3-PLIF) 160.175 μs; Δt(TEP-PLIF) 32.45 μs. Delays: Δt(P3-chem) 130.285 μs; Δt(TEP-chem) 2.56 μs. Multiple exposure timing: 9×6μs. Schlieren image height 150 mm, Chemiluminescence image 1 height 70 mm, Chemiluminescence image 2 height 109 mm.

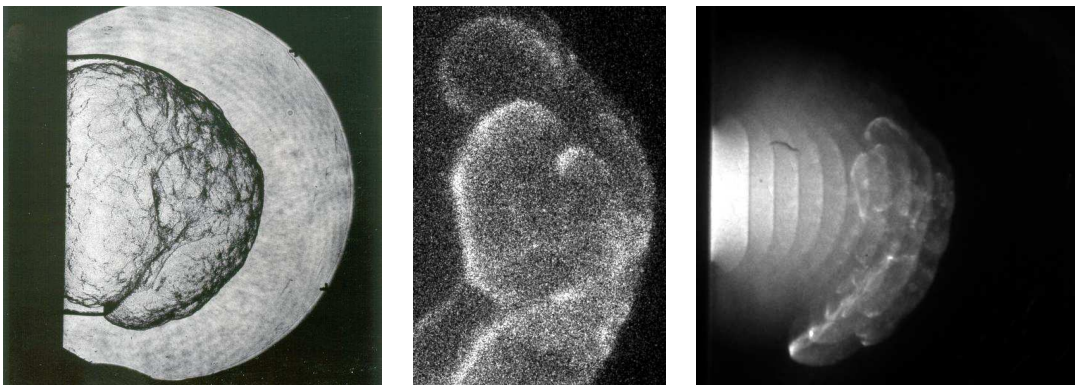

Figure M.160: Shot 186, 0.222 C_2H_6 + 0.778 O_2, P_0=45 kPa, T_0=299 K. Delays: Δt(P3-PLIF) 160.175 μs; Δt(TEP-PLIF) 32.58 μs. Delays: Δt(P3-chem) 130.285 μs; Δt(TEP-chem) 2.69 μs. Multiple exposure timing: 10×3μs. Schlieren image height 150 mm, Chemiluminescence image 1 height 70 mm, Chemiluminescence image 2 height 109 mm.

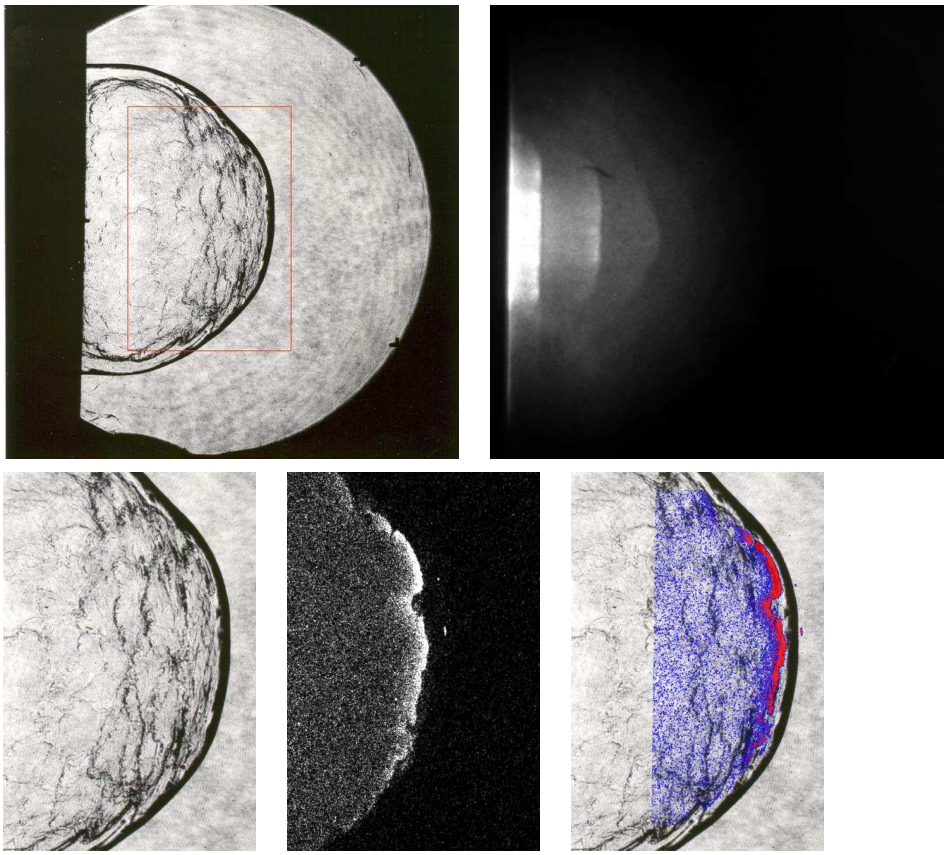

Figure M.161: Shot 187, 0.333 CH_4 + 0.667 O_2, P_0=50 kPa, T_0=294 K. Delays: Δt(P3-PLIF) 157.167 μs; Δt(TEP-PLIF) 30.98 μs. Delays: Δt(P3-chem) 127.285 μs; Δt(TEP-chem) 1.10 μs. Multiple exposure timing: 7×6μs. Schlieren image height 150 mm, PLIF image height 70 mm, Chemiluminescence image height 109 mm.

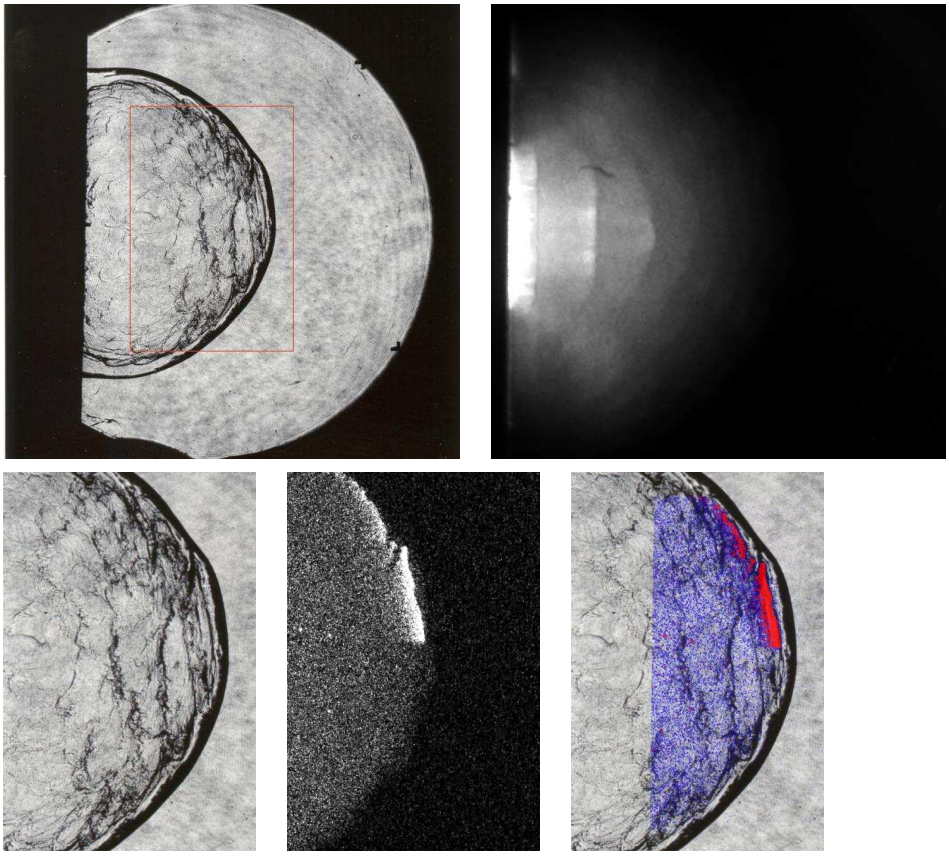

Figure M.162: Shot 188, 0.333 CH_4 + 0.667 O_2, P_0=55 kPa, T_0=295 K. Delays: Δt(P3-PLIF) 157.167 μs; Δt(TEP-PLIF) 31.21 μs. Delays: Δt(P3-chem) 127.285 μs; Δt(TEP-chem) 1.32 μs. Multiple exposure timing: 8×6μs. Schlieren image height 150 mm, PLIF image height 70 mm, Chemiluminescence image height 109 mm.

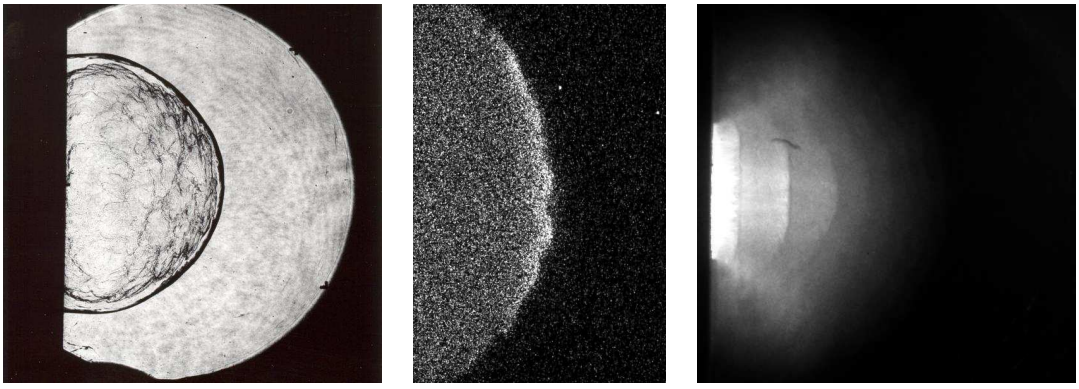

Figure M.163: Shot 189, 0.333 CH_4 + 0.667 O_2, P_0=60 kPa, T_0=296 K. Delays: Δt(P3-PLIF) 157.175 μs; Δt(TEP-PLIF) 31.42 μs. Delays: Δt(P3-chem) 127.285 μs; Δt(TEP-chem) 1.53 μs. Multiple exposure timing: 8×6μs. Schlieren image height 150 mm, PLIF image height 70 mm, Chemiluminescence image height 109 mm.

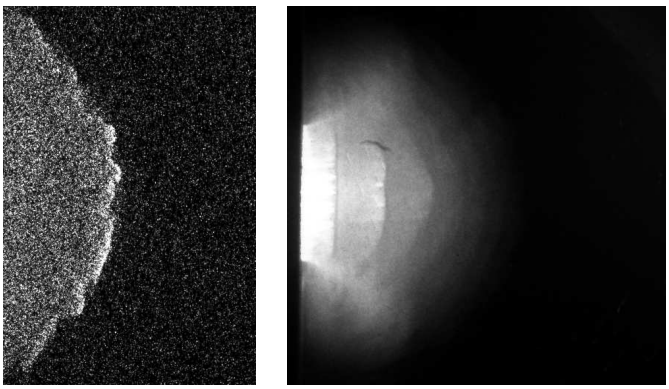

Figure M.164: Shot 190, 0.333 CH_4 + 0.667 O_2, P_0=65 kPa, T_0=296 K. Delays: Δt(P3-chem) 127.285 μs; Δt(TEP-chem) 1.72 μs. Multiple exposure timing: 8×6μs. PLIF image height 70 mm, Chemiluminescence image height 109 mm.

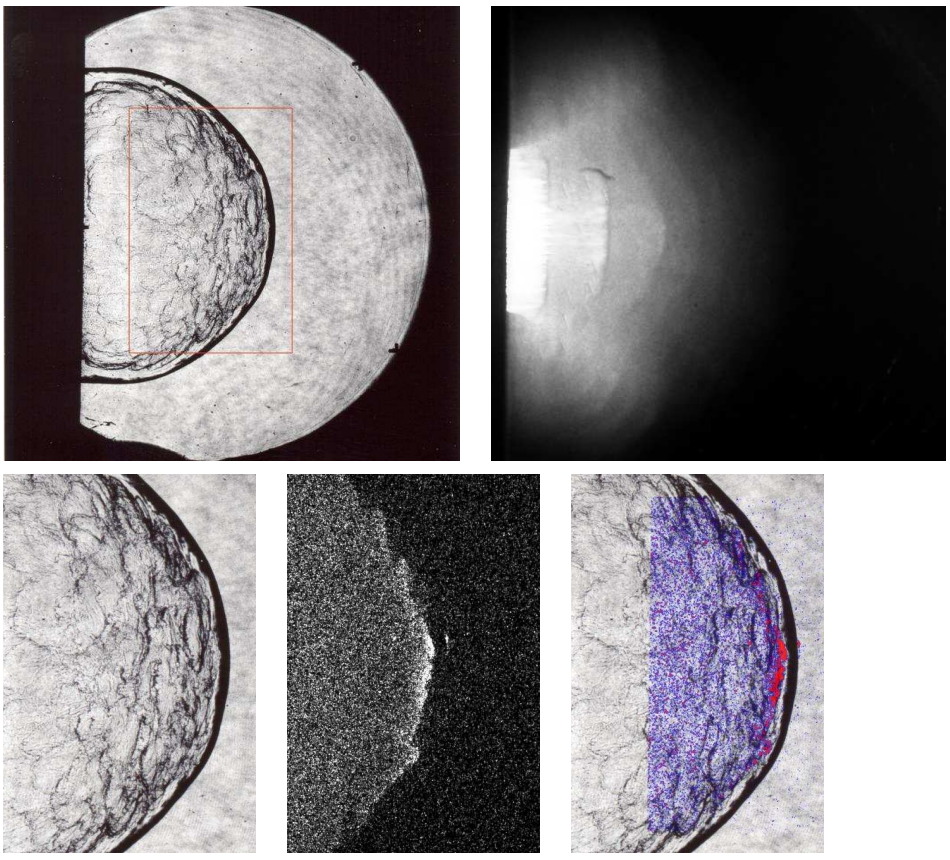

Figure M.165: Shot 191, 0.333 CH_4 + 0.667 O_2, P_0=70 kPa, T_0=297 K. Delays: Δt(P3-PLIF) 157.175 μs; Δt(TEP-PLIF) 31.79 μs. Delays: Δt(P3-chem) 127.285 μs; Δt(TEP-chem) 1.90 μs. Multiple exposure timing: 8×6μs. Schlieren image height 150 mm, PLIF image height 70 mm, Chemiluminescence image height 109 mm.

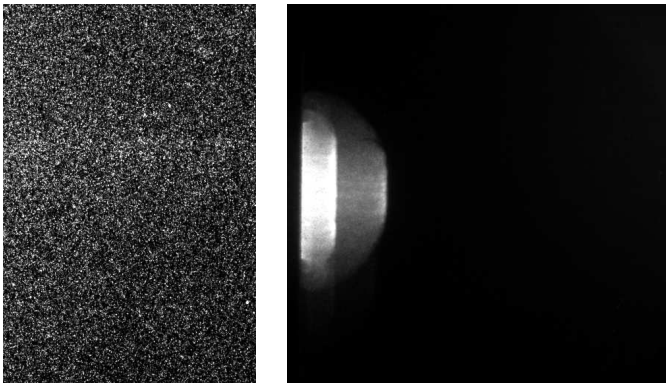

Figure M.166: Shot 192, 0.333 CH_4 + 0.667 O_2, P_0=80 kPa, T_0=298 K. Delays: Δt(P3-chem) 115.285 μs; Δt(TEP-chem) -9.79 μs. Multiple exposure timing: 8×6μs. PLIF image height 0 mm, Chemiluminescence image height 109 mm.

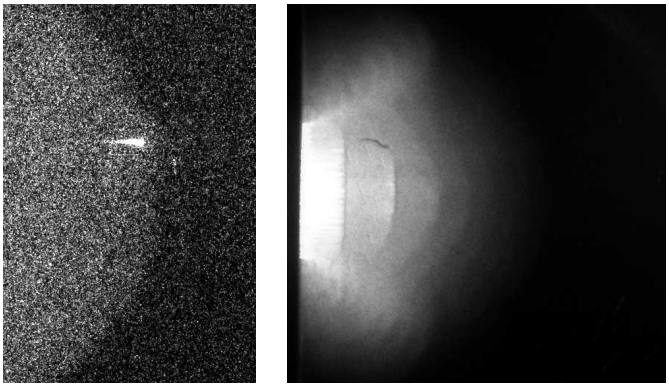

Figure M.167: Shot 193, 0.333 CH_4 + 0.667 O_2, P_0=90 kPa, T_0=298 K. Delays: Δt(P3-chem) 127.285 μs; Δt(TEP-chem) 2.48 μs. Multiple exposure timing: 8×6μs. PLIF image height 70 mm, Chemiluminescence image height 109 mm.

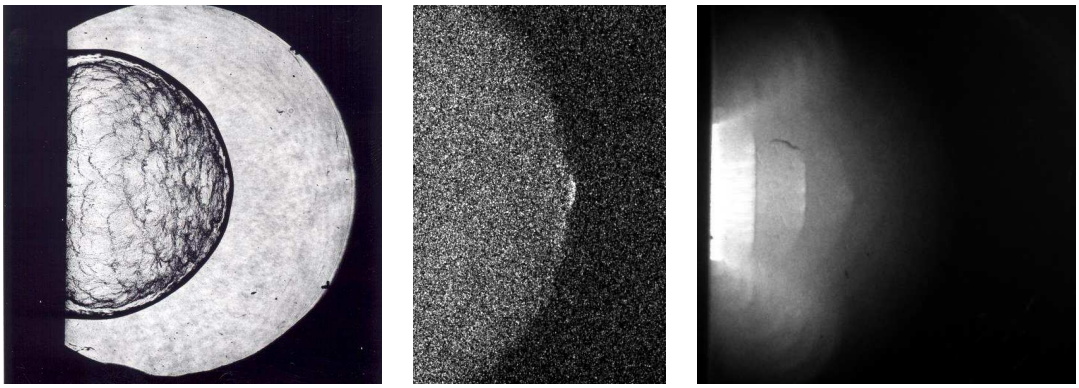

Figure M.168: Shot 194, 0.333 CH_4 + 0.667 O_2, P_0=100 kPa, T_0=299 K. Delays: Δt(P3-PLIF) 157.175 μs; Δt(TEP-PLIF) 32.62 μs. Delays: Δt(P3-chem) 127.285 μs; Δt(TEP-chem) 2.73 μs. Multiple exposure timing: 8×6μs. Schlieren image height 150 mm, PLIF image height 70 mm, Chemiluminescence image height 109 mm.

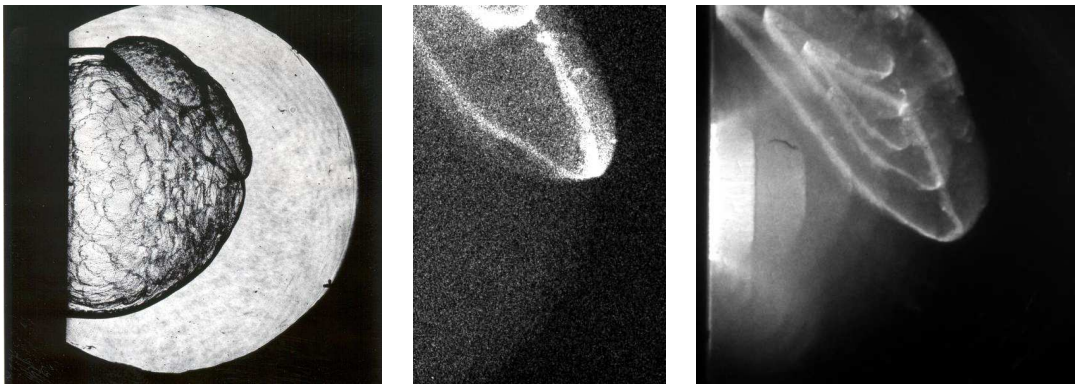

Figure M.169: Shot 195, 0.333 CH_4 + 0.667 O_2, P_0=120 kPa, T_0=299 K. Delays: Δt(P3-PLIF) 157.175 μs; Δt(TEP-PLIF) 33.04 μs. Delays: Δt(P3-chem) 127.285 μs; Δt(TEP-chem) 3.15 μs. Multiple exposure timing: 7×6μs. Schlieren image height 150 mm, Chemiluminescence image 1 height 70 mm, Chemiluminescence image 2 height 109 mm.

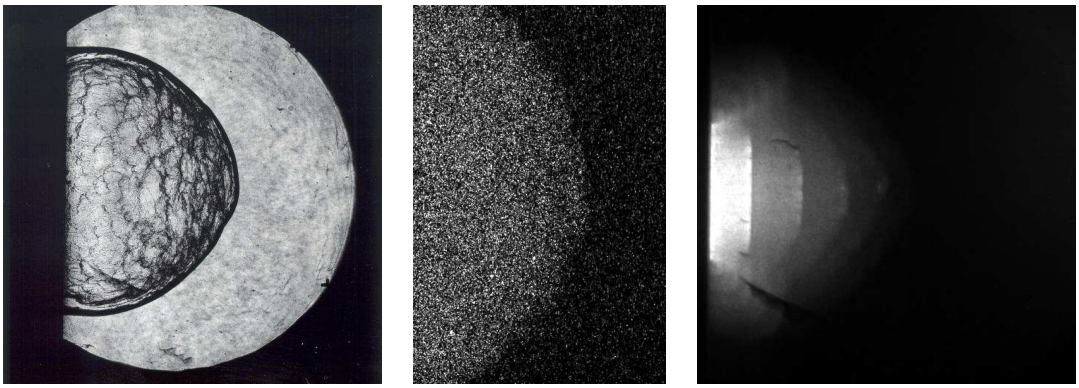

Figure M.170: Shot 196, 0.333 CH_4 + 0.667 O_2, P_0=110 kPa, T_0=299 K. Delays: Δt(P3-PLIF) 157.175 μs; Δt(TEP-PLIF) 32.84 μs. Delays: Δt(P3-chem) 127.285 μs; Δt(TEP-chem) 2.95 μs. Multiple exposure timing: 6×6μs. Schlieren image height 150 mm, Chemiluminescence image 1 height 70 mm, Chemiluminescence image 2 height 109 mm.

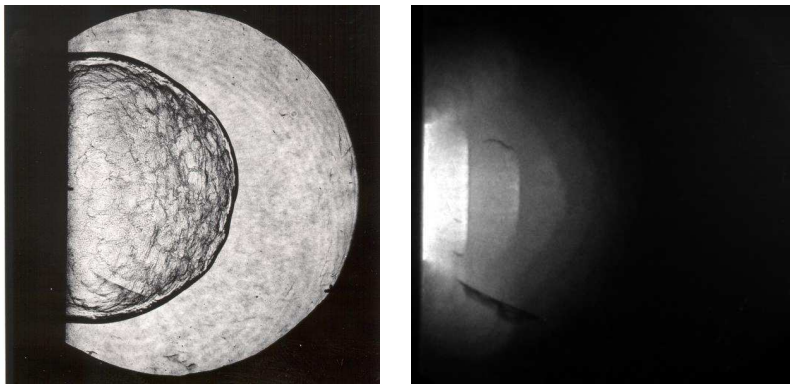

Figure M.171: Shot 197, 0.333 CH_4 + 0.667 O_2, P_0=115 kPa, T_0=300 K. Delays: Δt(P3-schl) 157.17 μs; Δt(TEP-schl) 32.94 μs. Delays: Δt(P3-chem) 127.285 μs; Δt(TEP-chem) 3.06 μs. Multiple exposure timing: 6×6μs. Schlieren image height 150 mm, Chemiluminescence image height 109 mm.

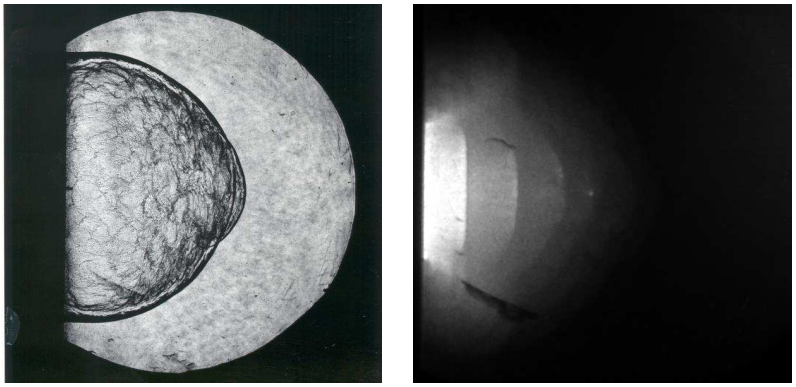

Figure M.172: Shot 198, 0.333 CH_4 + 0.667 O_2, P_0=120 kPa, T_0=298 K. Delays: Δt(P3-schl) 157.2 μs; Δt(TEP-schl) 33.07 μs. Delays: Δt(P3-chem) 127.285 μs; Δt(TEP-chem) 3.15 μs. Multiple exposure timing: 6×6μs. Schlieren image height 150 mm, Chemiluminescence image height 109 mm.

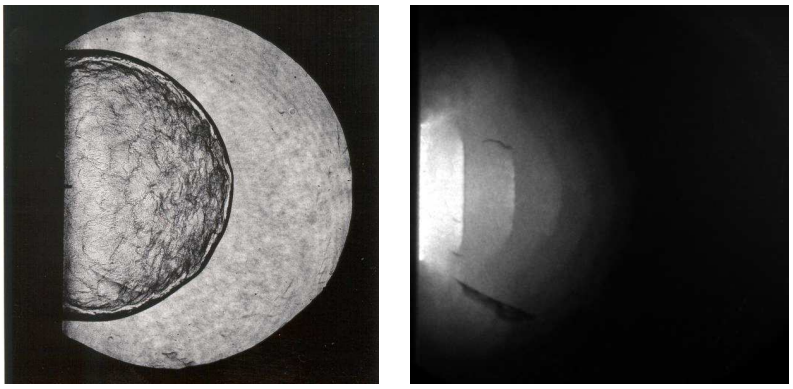

Figure M.173: Shot 199, 0.333 CH_4 + 0.667 O_2, P_0=125 kPa, T_0=301 K. Delays: Δt(P3-schl) 157.23 μs; Δt(TEP-schl) 33.19 μs. Delays: Δt(P3-chem) 127.285 μs; Δt(TEP-chem) 3.25 μs. Multiple exposure timing: 6×6μs. Schlieren image height 150 mm, Chemiluminescence image height 109 mm.

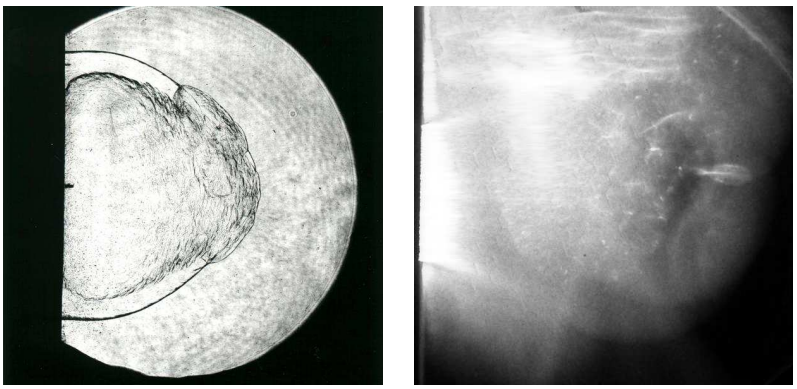

Figure M.174: Shot 200, 0.22 H_2 + 0.11 O_2 + 0.67 Ar, P_0=100 kPa, T_0=293 K. Delays: Δt(P3-schl) 214.2 μs; Δt(TEP-schl) 41.96 μs. Delays: Δt(P3-chem) 172.285 μs; Δt(TEP-chem) 0.04 μs. Multiple exposure timing: 2×43μs. Schlieren image height 150 mm, Chemiluminescence image height 109 mm.

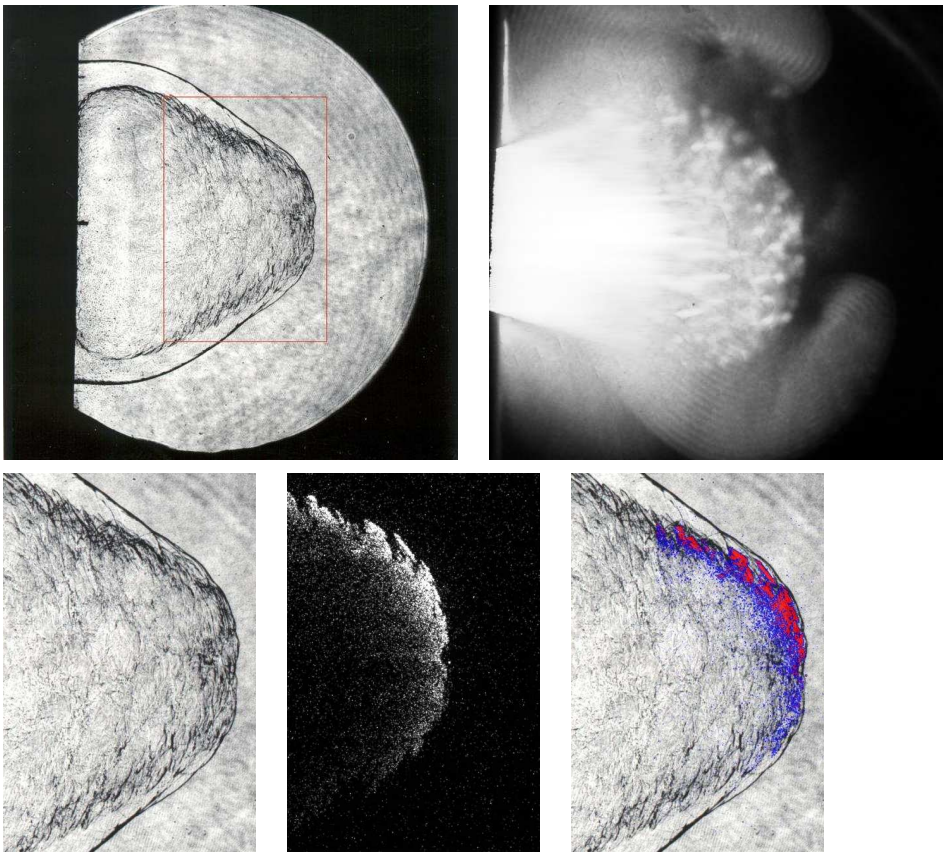

Figure M.175: Shot 201, 0.22 H_2 + 0.11 O_2 + 0.67 Ar, P_0=100 kPa, T_0=294 K. Delays: Δt(P3-PLIF) 214.167 μs; Δt(TEP-PLIF) 41.92 μs. Delays: Δt(P3-chem) 172.285 μs; Δt(TEP-chem) 0.04 μs. Multiple exposure timing: 80×1μs. Schlieren image height 150 mm, PLIF image height 70 mm, Chemiluminescence image height 109 mm.

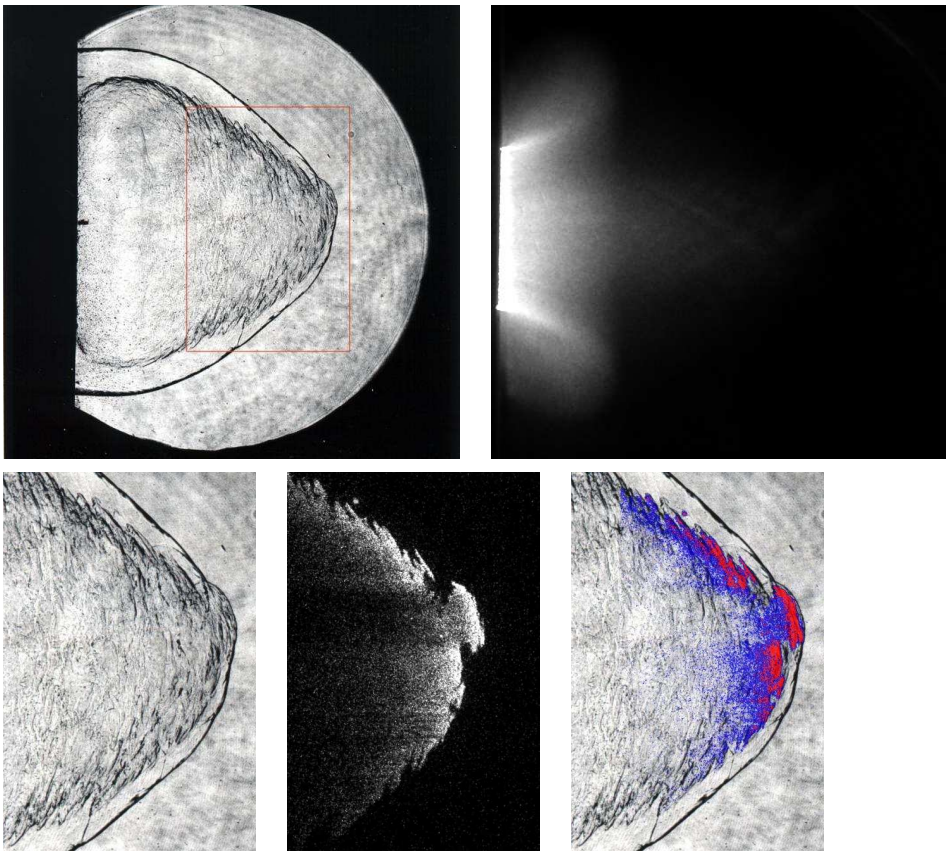

Figure M.176: Shot 202, 0.22 H_2 + 0.11 O_2 + 0.67 Ar, P_0=100 kPa, T_0=294 K. Delays: Δt(P3-PLIF) 220.167 μs; Δt(TEP-PLIF) 47.92 μs. Delays: Δt(P3-chem) 172.285 μs; Δt(TEP-chem) 0.04 μs. Schlieren image height 150 mm, PLIF image height 70 mm, Chemiluminescence image height 109 mm.

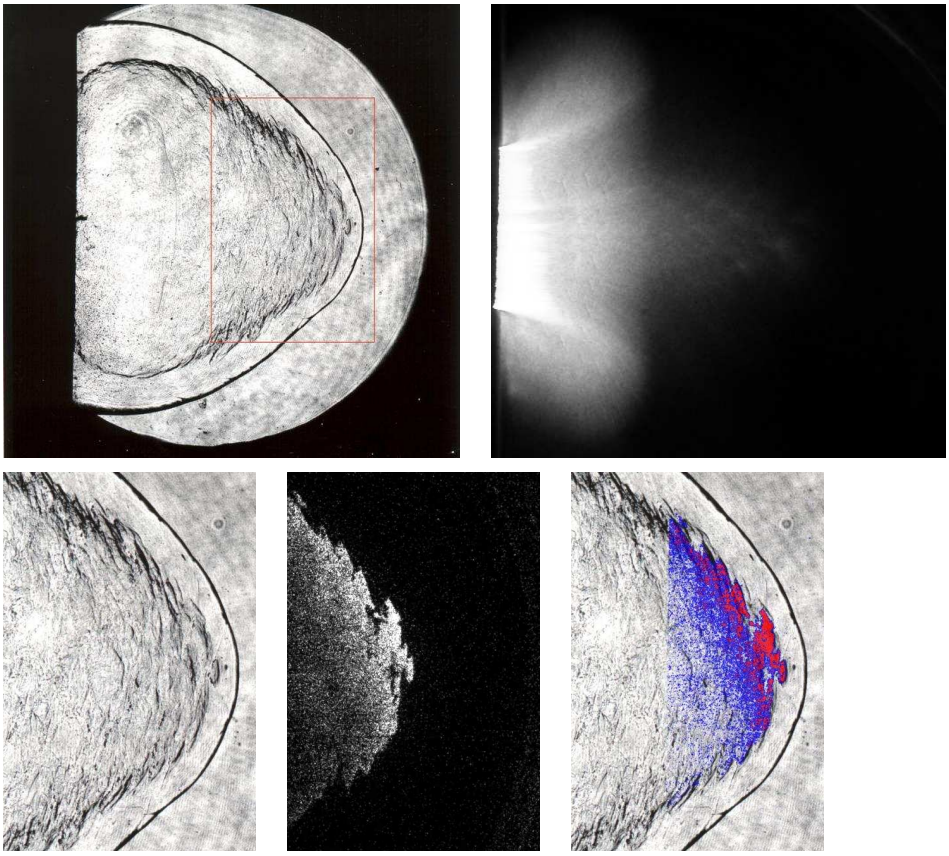

Figure M.177: Shot 203, 0.22 H_2 + 0.11 O_2 + 0.67 Ar, P_0=100 kPa, T_0=294 K. Delays: Δt(P3-PLIF) 232.167 μs; Δt(TEP-PLIF) 59.92 μs. Delays: Δt(P3-chem) 178.285 μs; Δt(TEP-chem) 6.04 μs. Schlieren image height 150 mm, PLIF image height 70 mm, Chemiluminescence image height 109 mm.

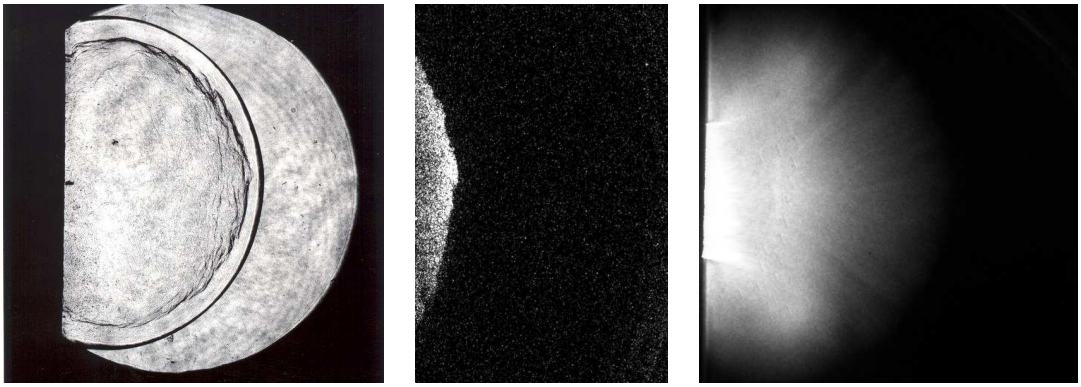

Figure M.178: Shot 204, 0.5 H_2 + 0.5 N_2O, P_0=47.5 kPa, T_0=295 K. Delays: Δt(P3-PLIF) 169.167 μs; Δt(TEP-PLIF) 42.94 μs. Delays: Δt(P3-chem) 127.285 μs; Δt(TEP-chem) 1.06 μs. Schlieren image height 150 mm, PLIF image height 70 mm, Chemiluminescence image height 109 mm.

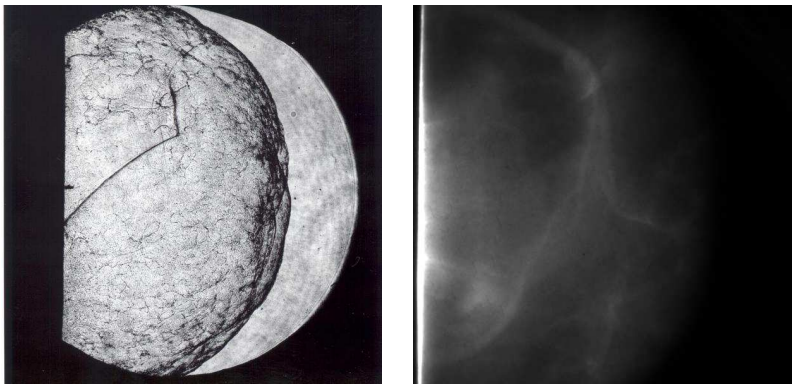

Figure M.179: Shot 205, 0.5 H_2 + 0.5 N_2O, P_0=47.5 kPa, T_0=295 K. Delays: Δt(P3-schl) 169.2 μs; Δt(TEP-schl) 42.97 μs. Delays: Δt(P3-chem) 127.285 μs; Δt(TEP-chem) 1.06 μs. Schlieren image height 150 mm, Chemiluminescence image height 109 mm.

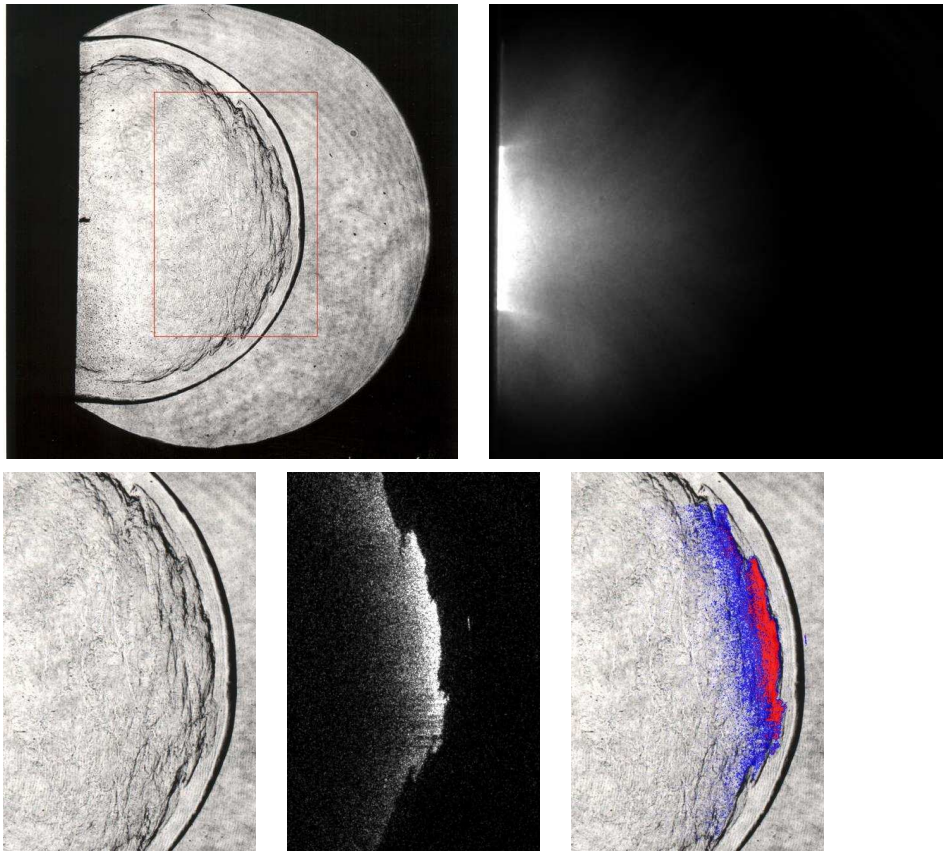

Figure M.180: Shot 206, 0.5 H_2 + 0.5 N_2O, P_0=45 kPa, T_0=295 K. Delays: Δt(P3-PLIF) 169.175 μs; Δt(TEP-PLIF) 42.82 μs. Delays: Δt(P3-chem) 127.285 μs; Δt(TEP-chem) 0.93 μs. Schlieren image height 150 mm, PLIF image height 70 mm, Chemiluminescence image height 109 mm.

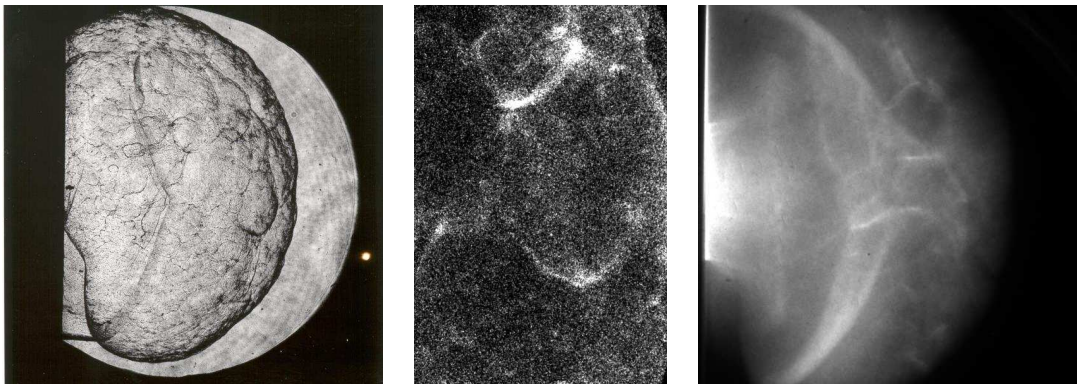

Figure M.181: Shot 207, 0.5 H_2 + 0.5 N_2O, P_0=47.5 kPa, T_0=296 K. Delays: Δt(P3-PLIF) 169.175 μs; Δt(TEP-PLIF) 42.95 μs. Delays: Δt(P3-chem) 127.285 μs; Δt(TEP-chem) 1.06 μs. Schlieren image height 150 mm, Chemiluminescence image 1 height 70 mm, Chemiluminescence image 2 height 109 mm.

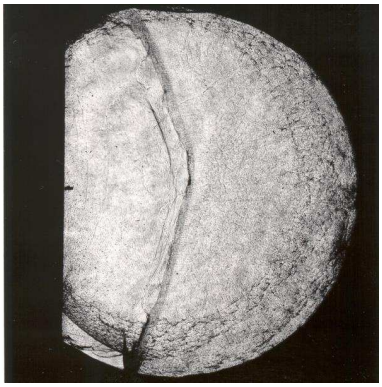

Figure M.182: Shot 208, 0.222 C_2H_6 + 0.778 O_2, P_0=40 kPa, T_0=295 K. Delays: Δt(P3-schl) 190.2 μs; Δt(TEP-schl) 62.32 μs. Schlieren image height 150 mm.

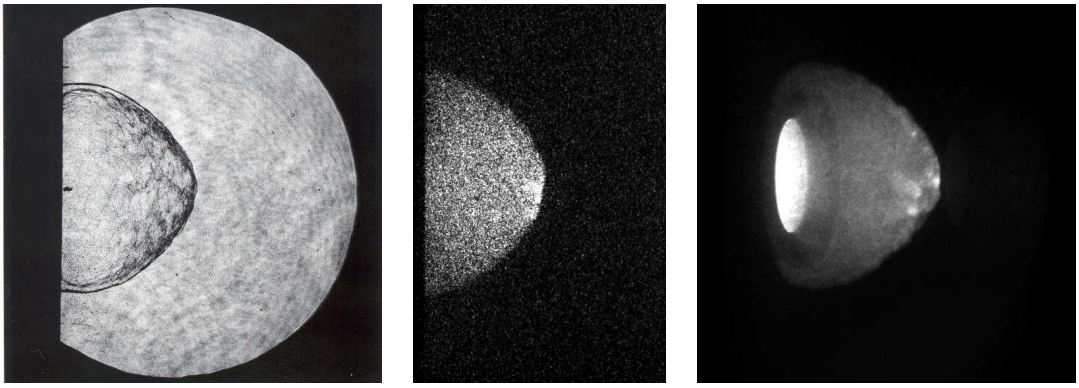

Figure M.183: Shot 209, 0.222 C_2H_6 + 0.778 O_2, P_0=40 kPa, T_0=296 K. Delays: Δt(P3-PLIF) 148.3 μs; Δt(TEP-PLIF) 20.42 μs. Delays: Δt(P3-chem) 148.3 μs; Δt(TEP-chem) 20.42 μs. Schlieren image height 150 mm, Chemiluminescence image 1 height 140 mm, Chemiluminescence image 2 height 140 mm.

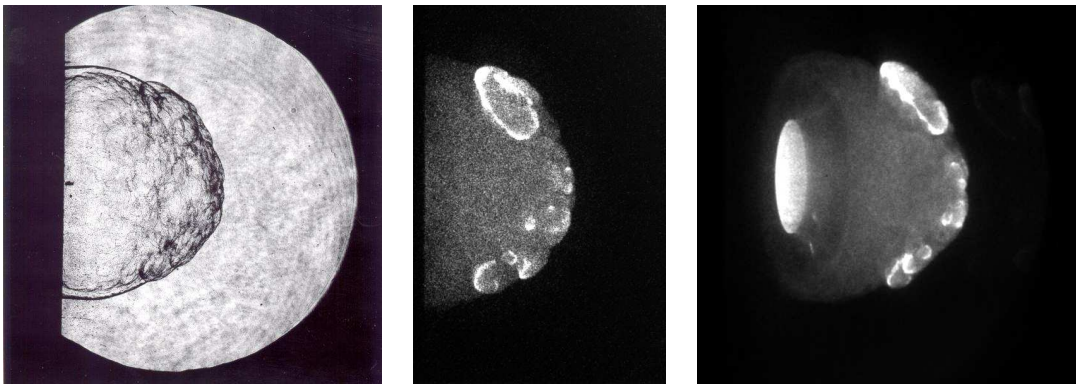

Figure M.184: Shot 210, 0.222 C_2H_6 + 0.778 O_2, P_0=42.5 kPa, T_0=296 K. Delays: Δt(P3-PLIF) 154.6 μs; Δt(TEP-PLIF) 26.87 μs. Delays: Δt(P3-chem) 153.6 μs; Δt(TEP-chem) 25.87 μs. Schlieren image height 150 mm, Chemiluminescence image 1 height 140 mm, Chemiluminescence image 2 height 140 mm.

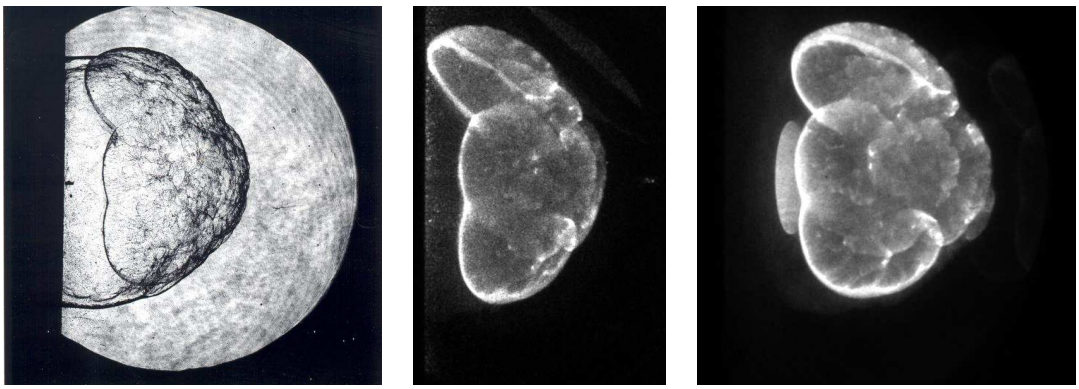

Figure M.185: Shot 211, 0.222 C_2H_6 + 0.778 O_2, P_0=42.5 kPa, T_0=297 K. Delays: Δt(P3-PLIF) 157.6 μs; Δt(TEP-PLIF) 29.87 μs. Delays: Δt(P3-chem) 156.6 μs; Δt(TEP-chem) 28.87 μs. Schlieren image height 150 mm, Chemiluminescence image 1 height 140 mm, Chemiluminescence image 2 height 140 mm.

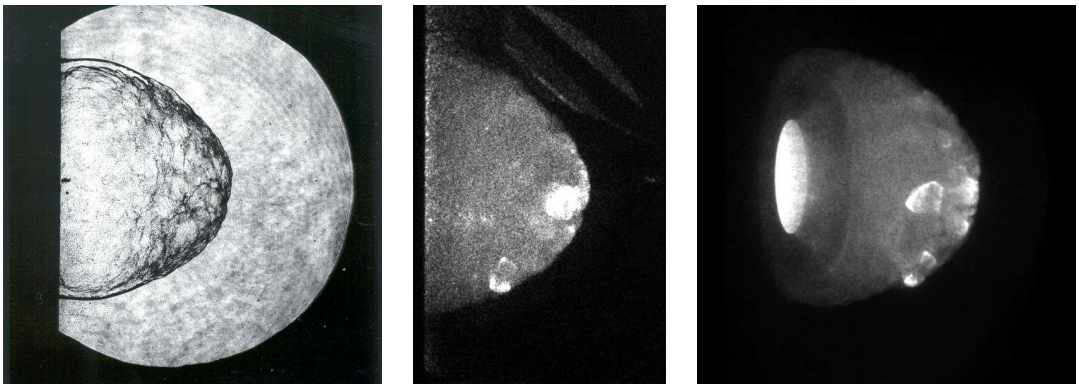

Figure M.186: Shot 212, 0.222 C_2H_6 + 0.778 O_2, P_0=42.5 kPa, T_0=297 K. Delays: Δt(P3-PLIF) 155.6 μs; Δt(TEP-PLIF) 27.87 μs. Delays: Δt(P3-chem) 154.6 μs; Δt(TEP-chem) 26.87 μs. Schlieren image height 150 mm, Chemiluminescence image 1 height 140 mm, Chemiluminescence image 2 height 140 mm.

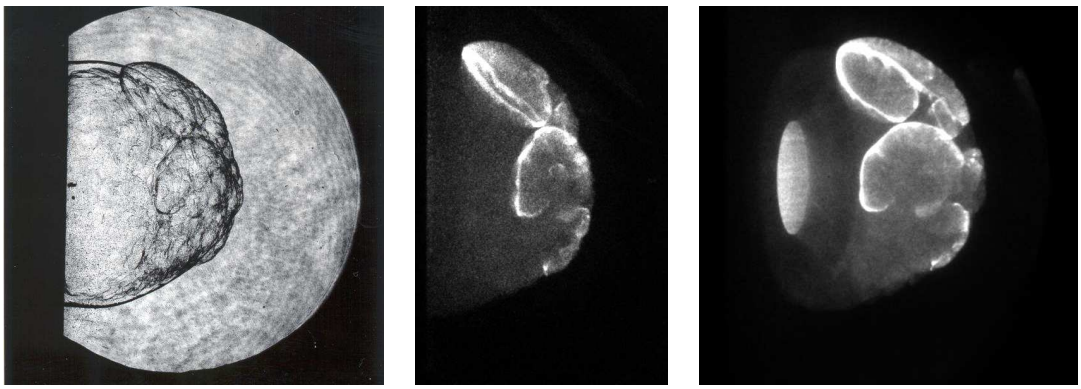

Figure M.187: Shot 213, 0.222 C_2H_6 + 0.778 O_2, P_0=42.5 kPa, T_0=298 K. Delays: Δt(P3-PLIF) 156.6 μs; Δt(TEP-PLIF) 28.87 μs. Delays: Δt(P3-chem) 155.6 μs; Δt(TEP-chem) 27.87 μs. Schlieren image height 150 mm, Chemiluminescence image 1 height 140 mm, Chemiluminescence image 2 height 140 mm.

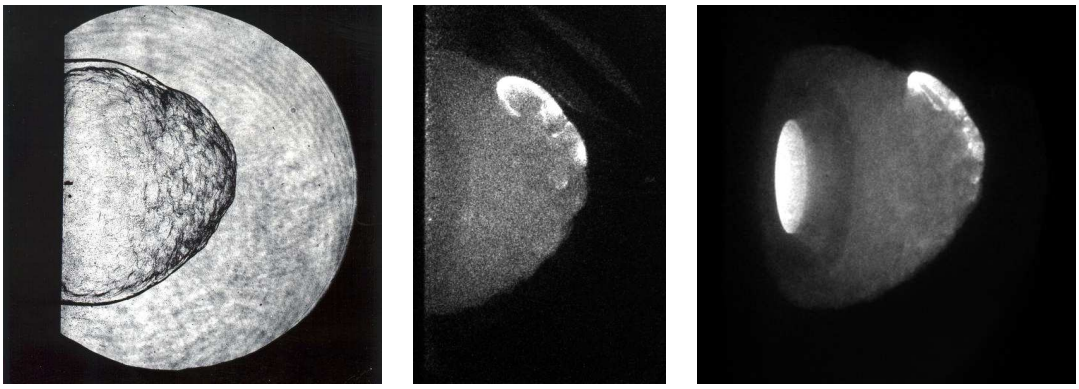

Figure M.188: Shot 214, 0.222 C_2H_6 + 0.778 O_2, P_0=42.5 kPa, T_0=298 K. Delays: Δt(P3-PLIF) 156.6 μs; Δt(TEP-PLIF) 28.87 μs. Delays: Δt(P3-chem) 155.6 μs; Δt(TEP-chem) 27.87 μs. Schlieren image height 150 mm, Chemiluminescence image 1 height 140 mm, Chemiluminescence image 2 height 140 mm.

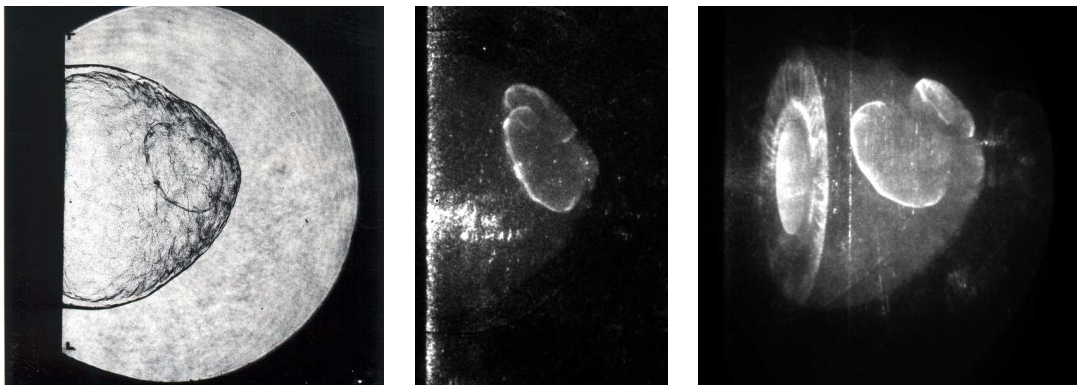

Figure M.189: Shot 215, 0.222 C_2H_6 + 0.778 O_2, P_0=42.5 kPa, T_0=294 K. Delays: Δt(P3-PLIF) 156.36 μs; Δt(TEP-PLIF) 28.63 μs. Delays: Δt(P3-chem) 156.36 μs; Δt(TEP-chem) 28.63 μs. Schlieren image height 150 mm, Chemiluminescence image 1 height 140 mm, Chemiluminescence image 2 height 140 mm.

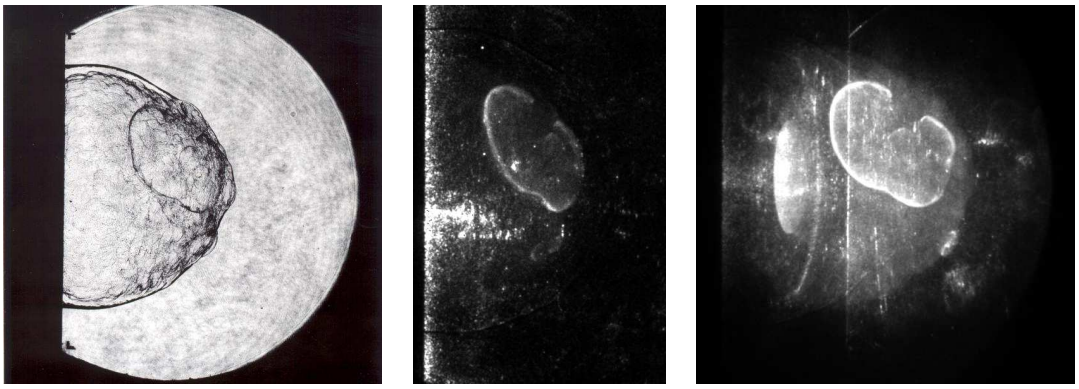

Figure M.190: Shot 216, 0.222 C_2H_6 + 0.778 O_2, P_0=42.5 kPa, T_0=295 K. Delays: Δt(P3-PLIF) 156.36 μs; Δt(TEP-PLIF) 28.63 μs. Delays: Δt(P3-chem) 156.36 μs; Δt(TEP-chem) 28.63 μs. Schlieren image height 150 mm, Chemiluminescence image 1 height 140 mm, Chemiluminescence image 2 height 140 mm.

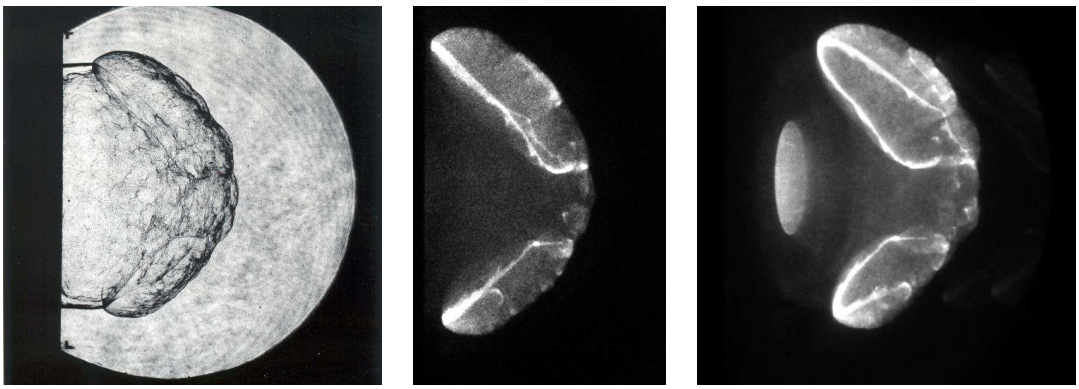

Figure M.191: Shot 217, 0.222 C_2H_6 + 0.778 O_2, P_0=42.5 kPa, T_0=295 K. Delays: Δt(P3-PLIF) 156.36 μs; Δt(TEP-PLIF) 28.63 μs. Delays: Δt(P3-chem) 156.36 μs; Δt(TEP-chem) 28.63 μs. Schlieren image height 150 mm, Chemiluminescence image 1 height 140 mm, Chemiluminescence image 2 height 140 mm.

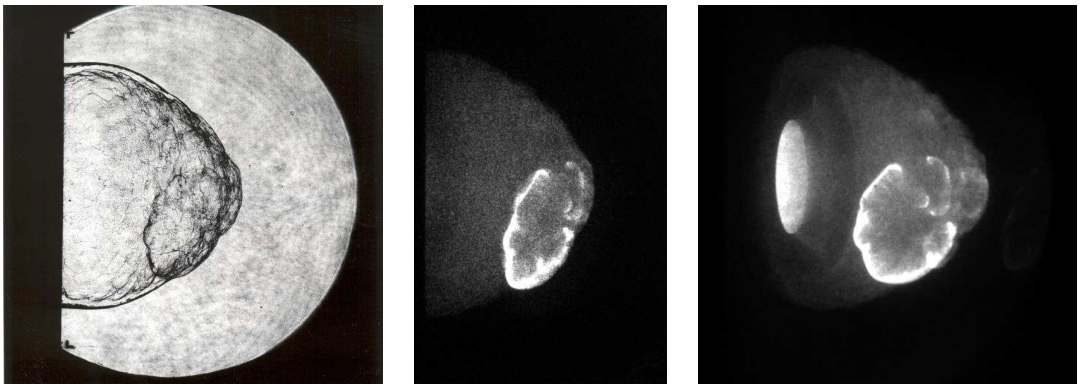

Figure M.192: Shot 218, 0.222 C_2H_6 + 0.778 O_2, P_0=42.5 kPa, T_0=296 K. Delays: Δt(P3-PLIF) 156.36 μs; Δt(TEP-PLIF) 28.63 μs. Delays: Δt(P3-chem) 156.36 μs; Δt(TEP-chem) 28.63 μs. Schlieren image height 150 mm, Chemiluminescence image 1 height 140 mm, Chemiluminescence image 2 height 140 mm.

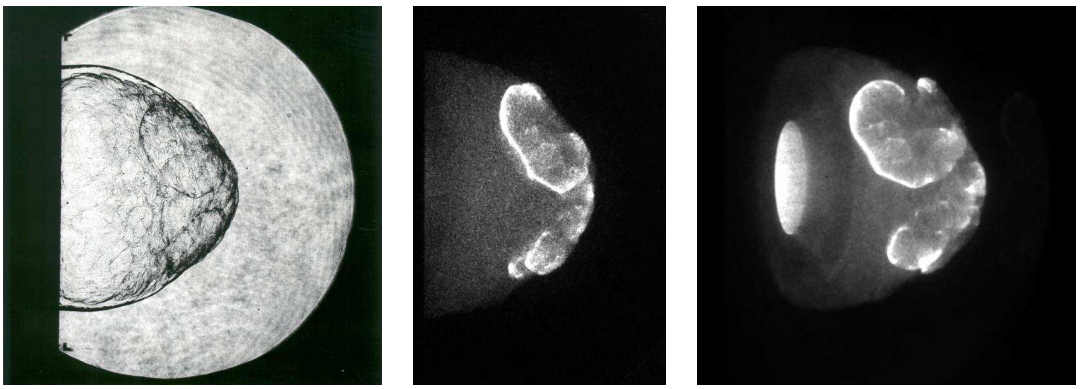

Figure M.193: Shot 219, 0.222 C_2H_6 + 0.778 O_2, P_0=42.5 kPa, T_0=296 K. Delays: Δt(P3-PLIF) 156.36 μs; Δt(TEP-PLIF) 28.63 μs. Delays: Δt(P3-chem) 156.36 μs; Δt(TEP-chem) 28.63 μs. Schlieren image height 150 mm, Chemiluminescence image 1 height 140 mm, Chemiluminescence image 2 height 140 mm.

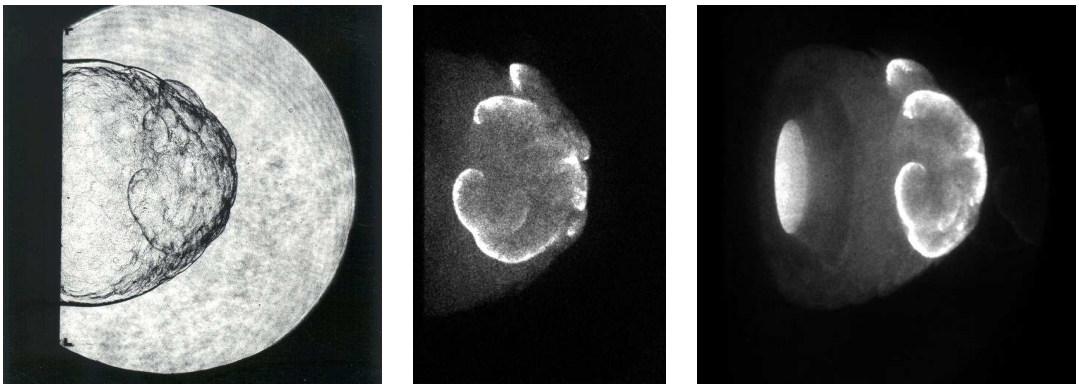

Figure M.194: Shot 220, 0.222 C_2H_6 + 0.778 O_2, P_0=42.5 kPa, T_0=297 K. Delays: Δt(P3-PLIF) 156.36 μs; Δt(TEP-PLIF) 28.63 μs. Delays: Δt(P3-chem) 156.36 μs; Δt(TEP-chem) 28.63 μs. Schlieren image height 150 mm, Chemiluminescence image 1 height 140 mm, Chemiluminescence image 2 height 140 mm.

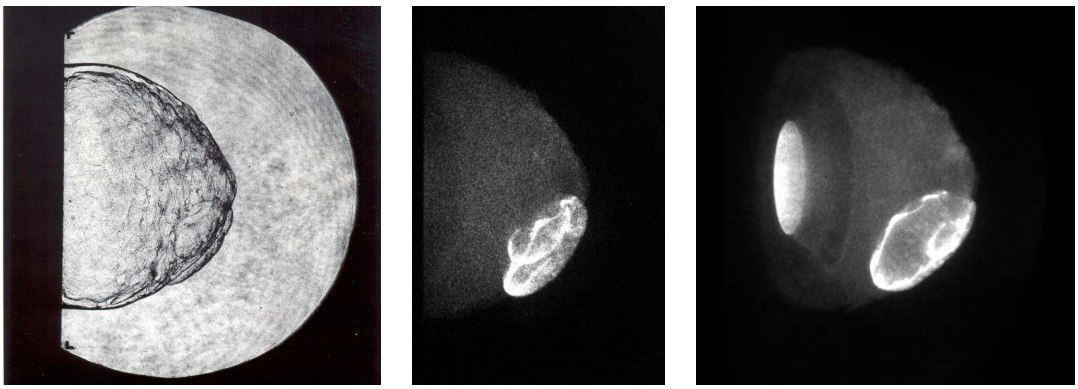

Figure M.195: Shot 221, 0.222 C_2H_6 + 0.778 O_2, P_0=42.5 kPa, T_0=297 K. Delays: Δt(P3-PLIF) 156.36 μs; Δt(TEP-PLIF) 28.63 μs. Delays: Δt(P3-chem) 156.36 μs; Δt(TEP-chem) 28.63 μs. Schlieren image height 150 mm, Chemiluminescence image 1 height 140 mm, Chemiluminescence image 2 height 140 mm.

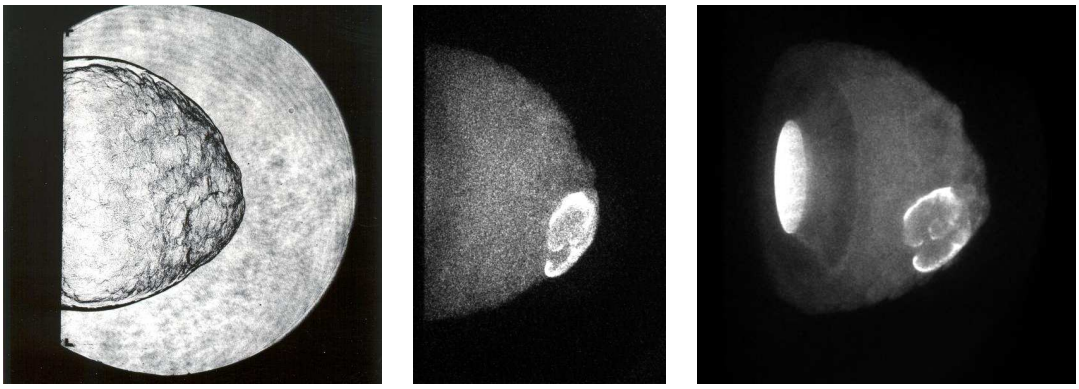

Figure M.196: Shot 222, 0.222 C_2H_6 + 0.778 O_2, P_0=42.5 kPa, T_0=297 K. Delays: Δt(P3-PLIF) 158.36 μs; Δt(TEP-PLIF) 30.63 μs. Delays: Δt(P3-chem) 156.36 μs; Δt(TEP-chem) 28.63 μs. Schlieren image height 150 mm, Chemiluminescence image 1 height 140 mm, Chemiluminescence image 2 height 140 mm.

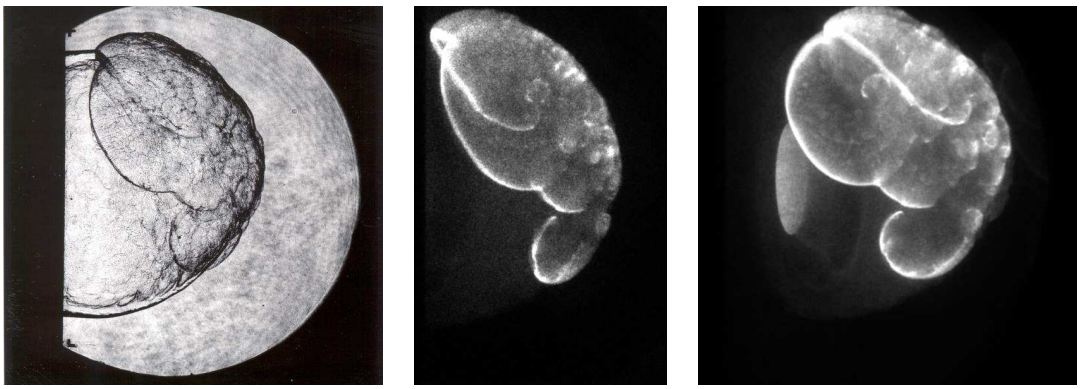

Figure M.197: Shot 223, 0.222 C_2H_6 + 0.778 O_2, P_0=42.5 kPa, T_0=298 K. Delays: Δt(P3-PLIF) 161.36 μs; Δt(TEP-PLIF) 33.63 μs. Delays: Δt(P3-chem) 156.36 μs; Δt(TEP-chem) 28.63 μs. Schlieren image height 150 mm, Chemiluminescence image 1 height 140 mm, Chemiluminescence image 2 height 140 mm.

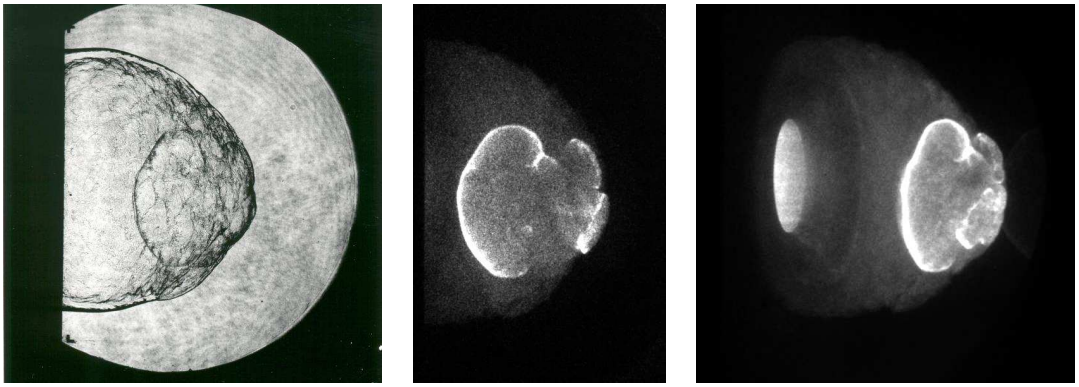

Figure M.198: Shot 224, 0.222 C_2H_6 + 0.778 O_2, P_0=42.5 kPa, T_0=298 K. Delays: Δt(P3-PLIF) 160.36 μs; Δt(TEP-PLIF) 32.63 μs. Delays: Δt(P3-chem) 156.36 μs; Δt(TEP-chem) 28.63 μs. Schlieren image height 150 mm, Chemiluminescence image 1 height 140 mm, Chemiluminescence image 2 height 140 mm.

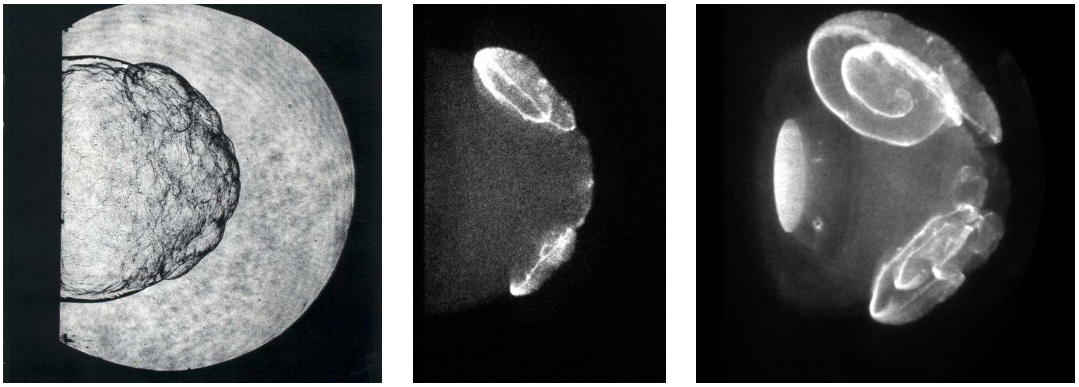

Figure M.199: Shot 226, 0.222 C_2H_6 + 0.778 O_2, P_0=42.5 kPa, T_0=297 K. Delays: Δt(P3-PLIF) 156.36 μs; Δt(TEP-PLIF) 28.63 μs. Delays: Δt(P3-chem) 156.36 μs; Δt(TEP-chem) 28.63 μs. Multiple exposure timing: 2×5μs. Schlieren image height 150 mm, Chemiluminescence image 1 height 140 mm, Chemiluminescence image 2 height 140 mm.

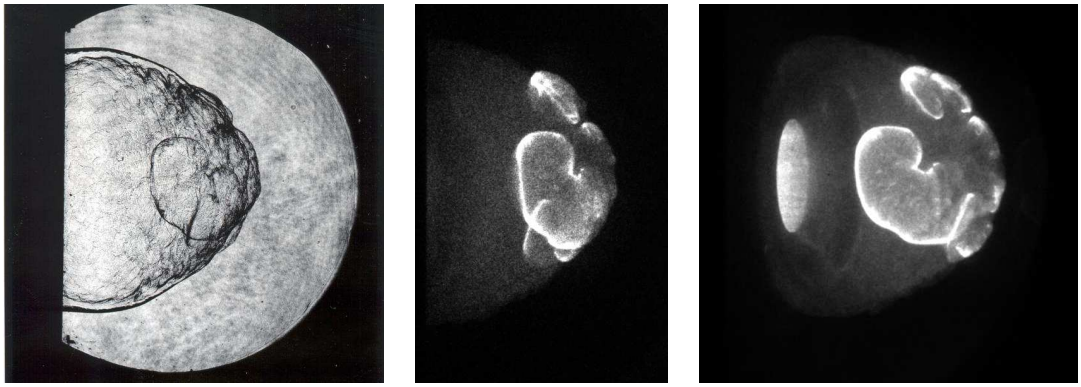

Figure M.200: Shot 227, 0.222 C_2H_6 + 0.778 O_2, P_0=42.5 kPa, T_0=298 K. Delays: Δt(P3-PLIF) 160.36 μs; Δt(TEP-PLIF) 32.63 μs. Delays: Δt(P3-chem) 156.36 μs; Δt(TEP-chem) 28.63 μs. Schlieren image height 150 mm, Chemiluminescence image 1 height 140 mm, Chemiluminescence image 2 height 140 mm.

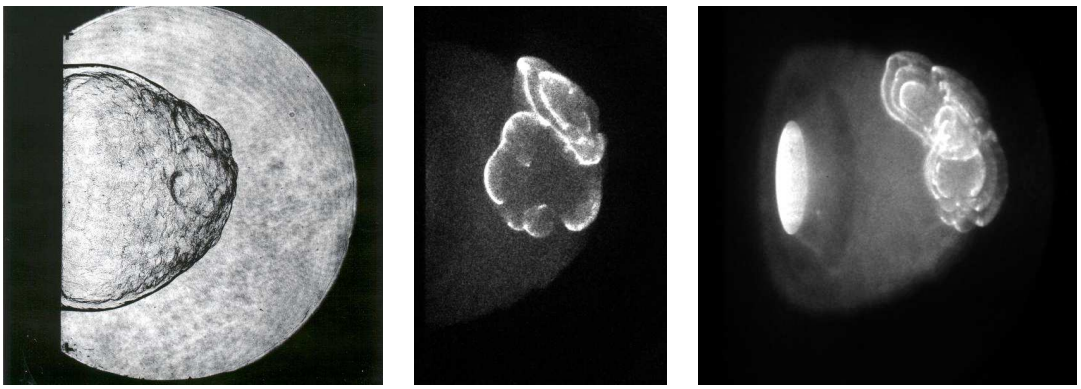

Figure M.201: Shot 228, 0.222 C_2H_6 + 0.778 O_2, P_0=42.5 kPa, T_0=298 K. Delays: Δt(P3-PLIF) 160.36 μs; Δt(TEP-PLIF) 32.63 μs. Delays: Δt(P3-chem) 156.36 μs; Δt(TEP-chem) 28.63 μs. Multiple exposure timing: 3×2μs. Schlieren image height 150 mm, Chemiluminescence image 1 height 140 mm, Chemiluminescence image 2 height 140 mm.

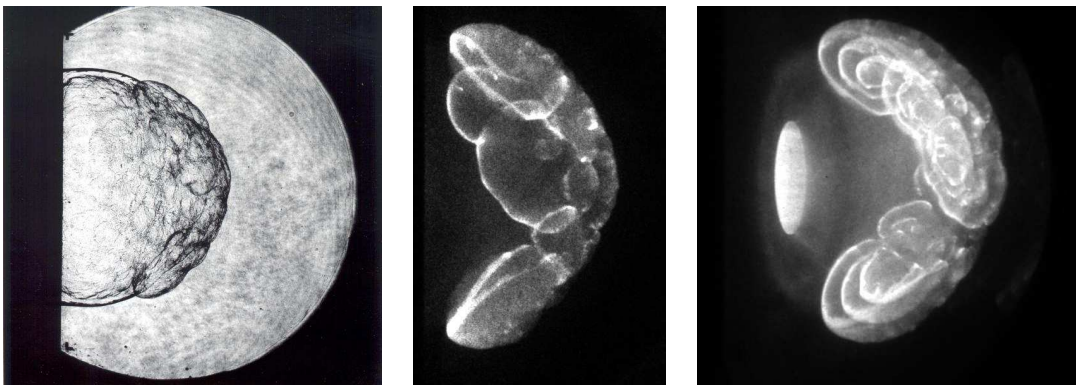

Figure M.202: Shot 229, 0.222 C_2H_6 + 0.778 O_2, P_0=42.5 kPa, T_0=298 K. Delays: Δt(P3-PLIF) 160.36 μs; Δt(TEP-PLIF) 32.63 μs. Delays: Δt(P3-chem) 154.36 μs; Δt(TEP-chem) 26.63 μs. Multiple exposure timing: 3×3μs. Schlieren image height 150 mm, Chemiluminescence image 1 height 140 mm, Chemiluminescence image 2 height 140 mm.